Smart Innovation, Systems and Technologies 372

P. H. V. Sesha Talpa Sai
Srikar Potnuru
Mehmet Avcar
Vishesh Ranjan Kar *Editors*



Intelligent Manufacturing and Energy Sustainability

Proceedings of ICIMES 2023

KES International

Springer

Smart Innovation, Systems and Technologies

Volume 372

The Smart Innovation, Systems and Technologies book series encompasses the topics of knowledge, intelligence, innovation and sustainability. The aim of the series is to make available a platform for the publication of books on all aspects of single and multi-disciplinary research on these themes in order to make the latest results available in a readily-accessible form. Volumes on interdisciplinary research combining two or more of these areas is particularly sought.

The series covers systems and paradigms that employ knowledge and intelligence in a broad sense. Its scope is systems having embedded knowledge and intelligence, which may be applied to the solution of world problems in industry, the environment and the community. It also focusses on the knowledge-transfer methodologies and innovation strategies employed to make this happen effectively. The combination of intelligent systems tools and a broad range of applications introduces a need for a synergy of disciplines from science, technology, business and the humanities. The series will include conference proceedings, edited collections, monographs, handbooks, reference books, and other relevant types of book in areas of science and technology where smart systems and technologies can offer innovative solutions.

High quality content is an essential feature for all book proposals accepted for the series. It is expected that editors of all accepted volumes will ensure that contributions are subjected to an appropriate level of reviewing process and adhere to KES quality principles.

Indexed by SCOPUS, EI Compendex, INSPEC, WTI Frankfurt eG, zbMATH, Japanese Science and Technology Agency (JST), SCImago, DBLP.

All books published in the series are submitted for consideration in Web of Science.

P. H. V. Sesha Talpa Sai · Srikar Potnuru ·
Mehmet Avcar · Vishesh Ranjan Kar
Editors

Intelligent Manufacturing and Energy Sustainability

Proceedings of ICIMES 2023

Springer

Editors
P. H. V. Sesha Talpa Sai
Department of Mechanical Engineering
Malla Reddy College of Engineering
and Technology
Hyderabad, Telangana, India

Srikar Potnuru
Department of Mechanical Engineering
Malla Reddy College of Engineering
and Technology
Hyderabad, Telangana, India

Mehmet Avcar
Faculty of Engineering
Department of Civil Engineering
Suleyman Demirel University
Isparta, Türkiye

Vishesh Ranjan Kar
Department of Mechanical Engineering
National Institute of Technology
Jamshedpur, Jharkhand, India

ISSN 2190-3018 ISSN 2190-3026 (electronic)
Smart Innovation, Systems and Technologies
ISBN 978-981-99-6773-5 ISBN 978-981-99-6774-2 (eBook)
https://doi.org/10.1007/978-981-99-6774-2

This Springer imprint is published by the registered company Springer Nature Singapore Pte Ltd.
The registered company address is: 152 Beach Road, #21-01/04 Gateway East, Singapore 189721, Singapore

Paper in this product is recyclable.

ICIMES 2023 Committees

Conference Committee

Chief Patron

Sri. CH. Malla Reddy—Founder Chairman, MRGI, Hon'ble Minister, Government of Telangana

Patrons

Sri. CH. Mahendar Reddy, Secretary, MRGI
Sri. CH. Bhadra Reddy, President, MRGI

Conference Chair

Dr. V. S. K. Reddy—Director

Honorary Chair

Dr. Lakshmi C. Jain—University of Technology Sydney, Sydney, Australia

Publication Chair

Dr. Suresh Chandra Satapathy—Professor, KIIT, Bhubaneswar, India

Organizing Chair

Dr. Srikar Potnuru—Professor and HOD—MECH

Convener

Dr. S. Srinivasa Rao, Principal

Co-conveners

Dr. P. H. V. Sesha Talpa Sai, Dean R&D, MRCET
Dr. T. Venugopal, Dean-Students Welfare

Organizing Secretaries

Dr. M. Sharanya, Professor and HOD, EEE, MRCET
Dr. Misba Mehdi, Associate Professor and HOD, AERO, MRCET

Coordinators

Dr. R. Hussain Vali—Assistant Professor
Dr. Ajith Raj Rajendran—Associate Professor
Dr. G. Madhu Mohan—Assistant Professor
Mr. V. Gopala Krishna—Assistant Professor

Editorial Board

Prof. (Dr.) PHV Sesha Talpa Sai, Dean, R&D, Department of Mechanical Engineering, MRCET, India
Prof. (Dr.) Srikar Potnuru, Head and Professor, Department of Mechanical Engineering, Malla Reddy College of Engineering and Technology, India
Prof. (Dr.) Mehmet Avcar, Department of Civil Engineering, Faculty of Engineering, Suleyman Demirel University, 32260 Isparta, Turkey
Prof. (Dr.) Vishesh Ranjan Kar, Department of Mechanical Engineering, National Institute of Technology, Jamshedpur, India

International Advisory Committee

Dr. Lakshmi C. Jain—University of Technology Sydney, Sydney, Australia
Prof. (Dr.) Shahrol Mohamaddan—Shibaura Institute of Technology, Japan
Prof. (Dr.) Sinin Hamdan—Universiti Malaysia Sarawak (UNIMAS), Malaysia
Prof. (Dr.) Amiya Bhaumik—Lincoln University College, Malaysia
Prof. (Dr.) Bhaskar Kura—University of New Orleans, LA, USA
Prof. (Dr.) K. C. Devarayapalli—Kyungpook University, South Korea
Prof. (Dr.) Angel Sanz Anderes—UPM, Madrid, Spain
Prof. (Dr.) S. V. Prabhakar—Yeunagnam University, South Korea
Prof. (Dr.) Yequing Bao—University of Alabama, USA
Prof. (Dr.) Sabastian Franchini—UPM, Madrid, Spain

Industry Advisory Committee

Mr. Sunil Maheshwari, Senior Regional Manager, Adroitec Engineering Solutions Pvt. Ltd. India
Mr. Bhushan Prasad M., Vice President, Renewable Energy Systems Ltd. India
Mr. Uma Shankar, Head Automation, Farm Division, Mahindra & Mahindra, Zaheerabad, India
Mr. Ramana Rao P. V., ADM, SMC Corporation India Pvt. Ltd.
Mr. Sandeep Arora, Associate Director, Verizon, India

National Advisory Committee

Prof. (Dr.) G. Balu—DOAD, DRDL, Telangana, India

Prof. (Dr.) Soumya Gangopadhy—Indian Institute of Technology, Bhilai, Chhattisgarh
Prof (Dr.) P. K. Jain—Centre for Carbon Materials, ARCI, Hyderabad, Telangana, India
Prof (Dr.) K. Vijay Kumar Reddy—Jawaharlal Nehru Technological University Hyderabad, Telangana, India
Prof. (Dr.) Jose Immanuel—Indian Institute of Technology, Bhilai, India
Prof. (Dr.) Vishesh Ranjan Kar—National Institute of Technology, Jamshedpur, Jharkhand, India
Prof. (Dr.) K. S. Reddy—Indian Institute of Technology, Madras, Tamil Nadu, India
Prof. (Dr.) Susanta Kumar Sahoo—National Institute of Technology Rourkela, Odisha, India
Prof. (Dr.) G. Raghavendra—National Institute of Technology Warangal, Telangana, India
Prof. (Dr.) Chinmay—National Institute of Technology Silchar, Assam, India
Prof. (Dr.) Swami Naidu—National Institute of Technology Raipur, Chhattisgarh, India
Prof. (Dr.) P. Narsimha Reddy—Sreenidhi Institute of Science and Technology, Hyderabad, Telangana, India
Prof. (Dr.) U. S. Paul Russel—Air India, India
Prof. (Dr.) Ajit Behera—Metallurgical and Materials Engineering National Institute of Technology, Rourkela

Institute Committee

Prof. (Dr.) V. Madhusudhana Reddy, Professor
Prof. (Dr.) K. Chandra Sekhar, Professor
Prof. (Dr.) T. Lokeswara Rao, Professor
Prof. (Dr.) B. Sandhya Rani, Professor
Prof. (Dr.) D. Damodara Reddy, Professor
Prof. (Mr.) Y. Dilip Kumar, Professor

Preface

The International Conference on Intelligent Manufacturing and Energy Sustainability (ICIMES 2023) was successfully organized by Malla Reddy College of Engineering and Technology, an UGC Autonomous Institution, during 23 and 24 June 2023 at Hyderabad. The objective of this conference was to provide opportunities for the researchers, academicians and industry persons to interact and exchange the ideas, experience and gain expertise in the cutting-edge technologies pertaining to Industry 5.0. Research papers were received and subjected to a rigorous peer-reviewed process with the help of editorial board, program committee and external reviewers. The editorial committee has finally accepted 21.5% manuscripts for publication in a single volume with Springer SIST series.

Our sincere thanks to Chief Guest and Keynote Sessions by Dr. Naeem M. S. Hanoon—Faculty of Electrical Engineering, University Technology Mara, Sarawak, Malaysia, Professor Dr. Hushairi Zen—Dean, Faculty of Science and Technology, ICATS UC-Malaysia, and Prof. Siba K. Udgata—Professor School of Computer and Information Sciences, University of Hyderabad. Our special thanks to all the session chairs for their immense support. The sessions chairs are:

1. Dr. Jose Immanuel R., Professor, Department of Mechanical Engineering, Indian Institute of Technology Bhilai, India.
2. Dr. Ajit Behera, Professor, Department of Metallurgical and Materials Engineering, National Institute of Technology Rourkela, India.
3. Dr. Obbu Chandra Sekhar, Department of Electrical Engineering, National Institute of Technology Delhi, India.
4. Dr. Vishesh Ranjan Kar, Professor, Department of Mechanical Engineering, National Institute of Technology Jamshedpur, India.
5. Dr. Dinesh Kumar R., Professor, Department of Mechanical Engineering, National Institute of Technology Srinagar, India.
6. Dr. T. Karthikeya Sharma, Professor, Department of Mechanical Engineering, National Institute of Technology Andhra Pradesh, India.
7. Dr. Thrinadh J., Professor, Mechanical Department (SOE), Malla Reddy University, India.

We are indebted to the editorial board, program committee and external reviewers who have produced critical reviews in a short time. We would like to express our special gratitude to publication chair Dr. Suresh Chandra Satapathy, Professor and Dean, KIIT, Bhubaneswar, for his valuable support and encouragement till the successful conclusion of the conference.

We express our heartfelt thanks to our Chief Patron Sri. CH. Malla Reddy, Founder Chairman, MRGI, Patrons Sri. CH. Mahendar Reddy, Secretary, MRGI, Sri. CH. Bhadra Reddy, President, MRGI, Conference Chair Dr. V. S. K. Reddy, Convener Dr. S. Srinivasa Rao, Organizing Chair Dr. Srikar Potnuru, Organizing Secretary Dr. M. Sharanya and Dr. Misba Mehidi, and Coordinators Dr. R. Husain Vali, Dr. Ajith Raj R., Dr. G. Madhu Mohan and Mr. V. Gopala Krishna for their valuable contribution to successful conduct the conference. Last, but certainly not least, our special thanks to all the authors without whom the conference would not have taken place. Their technical contributions have made our proceedings rich and praiseworthy.

Hyderabad, India Dr. P. H. V. Sesha Talpa Sai
Hyderabad, India Dr. Srikar Potnuru
Isparta, Turkey Dr. Mehmet Avcar
Jamshedpur, India Dr. Vishesh Ranjan Kar

Contents

About the Editors

Dr. P. H. V. Sesha Talpa Sai, Ph.D. Professor, Department of Mechanical Engineering, Malla Reddy College of Engineering and Technology, India

Brief Profile:

Dr. P. H. V. Sesha Talpa Sai, Professor and Director (R&D), and Coordinator, Centre for Innovation, Incubation and Entrepreneurship (CIIE), is a dynamic and multi-talented personality with research orientation. He obtained his B.Tech. degree from SV University, M.E. degree from Osmania University and Doctoral degree from JNTU, Hyderabad. He is having 16 years of industry experience in reputed organizations (automobile and manufacturing). He is having association with industries such as HAL, BDL and BHEL during his industrial career. He is also having 15 years of teaching and research experience. He is visiting faculty to Lincoln University College (LUC), Malaysia. He is guiding four Ph.D. scholars from different universities. He has 52 international and national publications/conference proceedings. He also organized and participated in number of national and international seminars/conferences and workshops. He is a life member of Solar Energy Society of India (SESI), Institute of Engineers (India), Institute of Valuers, SAE and ISTE.

Dr. Srikar Potnuru, Ph.D. Head and Associate Professor, Department of Mechanical Engineering, Malla Reddy College of Engineering and Technology, India

Brief Profile:

Dr. Srikar is currently heading the Department of Mechanical Engineering at MRCET. He started working with MRCET in 2017. His mechanical engineering education includes a B.Tech. from JNTUK and M.Tech. and Ph.D. from NIT Rourkela. His whole experience spans ten years. More than 20 of his research publications have been published and are indexed in SCI and Scopus. He is also a member for ASME, ISTE, IEI and Indian Science Congress. He has organized seminars, FDPs, workshops and other events as well as attended numerous national and international conferences. He has two patents, which are to his credit. Springer's International Conference ICIMES was successfully organized by him four times. To present his technical work at an ASME meeting that was supported by UGC, he flew to the University of Southern California in the States. For other academic and research endeavours, he has also been to nations like Singapore and the UAE.

Dr. Mehmet Avcar, Ph.D. Associate Professor, Department of Civil Engineering, Suleyman Demirel University, Turkey

Brief Profile:

Dr. Avcar has been working as an associate professor in the Department of Civil Engineering at Suleyman Demirel University, Turkey, since 2018. He has over 18 years of teaching and research experience. Dr. Avcar received his doctoral degree from Suleyman Demirel University in 2011 in the Department of Civil Engineering at the Branch of Mechanics. His research interests are mechanics of solids, advanced composite structures and structural mechanics. To this point, he has authored (and co-authored) over 70 research articles in peer-reviewed journals, books and conferences on the analysis of mechanical behaviours of different composite structures. He has been involved in the "Stanford University World Ranking Best 2% list of Scientists" three times (for the single year 2019, 2020 and 2021). He is acting as an editor of the *Journal of Engineering Sciences and Design* (e-ISSN: 1308-6693). He has worked on several national projects as a researcher. He is also serving as a reviewer for many reputed international journals. In addition to teaching and research activities, he is also involved in administration facilities, such as Head of the Branch of Mechanics, Faculty Associate Professor Representative, etc.

Dr. Vishesh Ranjan Kar, Ph.D. Assistant Professor, Department of Mechanical Engineering, National Institute of Technology, Jamshedpur, India

Brief Profile:

Dr. Kar is presently working as Assistant Professor in the Department of Mechanical Engineering, NIT-Jamshedpur, India, since 2018. He has over 14 years of teaching, research and industrial experience. He received his doctoral degree from NIT Rourkela in 2015 on Computational Solid Mechanics. So far, he authored (and co-authored) over 90 research articles in peer-reviewed journals, books and conferences. He is also Editorial Board Member of *Journal of the Mechanical Behaviour of Materials*. He has handled and also handling various research projects as Principal Investigator funded by government and private agencies. Under his guidance, 07 Ph.D. students are pursuing Ph.D. in the area of advanced composite structures. He is the recipient of Early Career Research Award 2017 from DST, Government of India. He has been recognized as one of the Top 2% Scientists in the world by Elsevier and currently holding the position of Associate Dean (Academic: Recognition and Accreditation).

Chapter 1
A Multi-objective Optimization Model for Economic-Environmental Operation of Microgrid

Mohan Kumar Gowrisetty, Manjunath Yalagala, Vineeth Reddy LakkiReddy, Ravivarma Kamireddy, and Lokeshgupta Bhamidi

Abstract This paper investigates a multi-objective optimization model for the microgrid operation problem under grid-connected mode and isolated mode. The proposed operation problem is modelled as mixed integer linear programming and multiple objective functions such as minimization of daily operation cost and minimization of daily emission output are considered from the financial and ecological perspectives. The proposed bi-objective problem is transformed into a single-objective problem using a fuzzy satisfaction-maximizing approach in this model. The problem is then solved using the mixed-integer linear programming method. The proposed microgrid consists of diesel generators, wind turbines, battery storage system and solar PV panels to meet the local load demand. In addition, after satisfying the overall local load demand, the microgrid participates in the energy trading process with the main grid. In this model, the proposed cost objective function also includes the expenses of energy traded from the main grid, which will enhance the local renewable energy utilization as well as maximize the microgrid's extra renewable energy selling revenue. The effectiveness of the proposed bi-objective model is analyzed with two different case studies and various scenarios are considered for the microgrid optimal operation under grid connected as well as islanded modes. From

M. K. Gowrisetty (✉) · M. Yalagala · V. R. LakkiReddy · R. Kamireddy · L. Bhamidi
Department of Electrical and Electronics Engineering, SRM University, Amaravati, Andhra Pradesh 522502, India
e-mail: mohankumar_gowrisetty@srmap.edu.in

M. Yalagala
e-mail: manjunath_yalagala@srmap.edu.in

V. R. LakkiReddy
e-mail: vineeth_lakkireddy@srmap.edu.in

R. Kamireddy
e-mail: k30ravivarma@gmail.com

L. Bhamidi
e-mail: lokesh206@gmail.com

P. H. V. S. Talpa Sai et al. (eds.), *Intelligent Manufacturing and Energy Sustainability*, Smart Innovation, Systems and Technologies 372,
https://doi.org/10.1007/978-981-99-6774-2_1

the overall simulation result analysis, it shows that the bi-objective proposed model is able to create a better optimal economic and environmental microgrid operation.

1.1 Introduction

Due to ecological -economic concerns and rising fuel costs, the governments of various countries are providing incentives for the production of clean and sustainable energy through renewable energy resources (RERs). RERs play a vital role in the reduction of air pollution and greenhouse gas emissions [1]. The generation of electricity through renewable resources has operational limitations such as the intermittent nature of generation, that can undermine the reliability of system. A hybrid power system, which combines solar photo voltaic (PV) units, wind turbines (WTs), diesel generators, microturbines and battery storage system, is helpful to manage the irregular generation of electricity and encourages the integration of clean energy sources. A microgrid (MG) is a local energy system that operates autonomously from the main power grid and utilizes renewable energy sources to provide reliable and sustainable electricity to local communities. Microgrids have a number of advantages, including to improve the reliable and secure power supply for consumers, better energy management for local loads, and also reduce the carbon emissions, transportation losses, and overall operating costs [2, 3].

The MG can be operated in two different ways: islanded mode and grid-connected mode. By combining the benefits of both islanded mode and grid-connected modes, the microgrid can provide a reliable power supply during outages and also utilize the main grid power as a backup source [4–6]. The optimal scheduling of MGs primarily focuses on the objectives of minimization of daily operating cost, minimizing of emission pollution, improvement of system reliability, and so on. In recent years, the research study on MG models has been extensively focused on because of various new technology developments in RERs and energy management schemes. The primary focus of many literature works on the MG operation problem is modelled as the single-objective optimization problem with the objective function of either minimization of overall operation cost or minimization of emission output, these works come under the first category. The optimal scheduling of MG operation problem was developed in [7] with a group of RERs in conjunction with electric vehicles and batteries. To solve the proposed model, a hybrid algorithm called the hybrid DE-HS (Differential Evolution and Harmony Search was employed in this work. The authors in [8] have presented a reduced gradient algorithm to reduce the operation and maintenance cost of the MG system. The authors in [9] proposed a day-ahead operational planning model for an urban microgrid, which takes into account predefined values for distributed generation (DG). This model aims to minimize daily fuel consumption costs and reduction of CO2 emissions. In [10], the authors takes into account of combined heat and power (CHP) system for load distribution model to minimize consumed fuel while meeting the local load demand. Most of the abovementioned works considered only a single-objective optimization model for MG operation, however, multiple objectives need to be considered in a practical environment to satisfy various MG entities. In addition to the operation cost objective, other different objectives such as emission, line power loss, reliability, and quality can also be considered for better optimal MG operation. Therefore, a comprehensive multi-objective optimization model is needed to operate the MG system effectively.

The second category involves an optimal operation of MG problem with multiple objectives. In [11], the authors investigated the operational benefits of multi-objective optimal energy management scheme in MG environment. In [12], the authors proposed a model of deterministic multi-objective MG operational optimization problem, a heuristic optimizer is used to solve the proposed problem. The main objective of this model is to minimize both operation cost and emission of MG simultaneously. In [13], a stochastic model was presented for achieving the optimal energy management of MG to minimize both operation cost and emission. In this model, the scenario-based stochastic programming is considered to address the uncertainties corresponding to wind turbine speed, electrical demand, and solar radiation. A game theory-based optimization model was proposed in [14] to solve the multi-objective MG operation problem.

In this paper, a bi-objective optimal MG operation problem is developed to reduce the overall operating cost and environmental pollutant emission. To solve the proposed bi-objective optimization problem, the combination of a maximum fuzzy satisfaction method and MILP approach is used. The proposed multi-objective model is transformed into single objective problem by employing a maximum fuzzy satisfaction method and the final single objective MG model is solved by using the MILP method.

1.2 Proposed Model of Microgrid

Figure 1.1 depicts the structure of proposed MG model, which comprises the various distributed energy resources (DERs) such as PV units, diesel engines (DEs), WTs, micro-turbines (MTs), and battery energy storage system (BES) along with the controllable and non-controllable loads. The DERs are the local generation sources in the MG and the BES is used for energy storage purpose when there is an excess RER energy. The MG system has the capability to operate either in grid connect mode or isolation mode with the help of common coupler. For efficient and effective operation, all the components within the MG system are interconnected using a two-way communication link. The energy exchange between the components is facilitated by a bidirectional power link. The different components in the MG network are coordinated with a central controller (CC) through a communication network for optimal operation. If the local power generation is unable to satisfy local load demand of the MG, the power can be imported from the main grid and utilized to balance the load power demand.

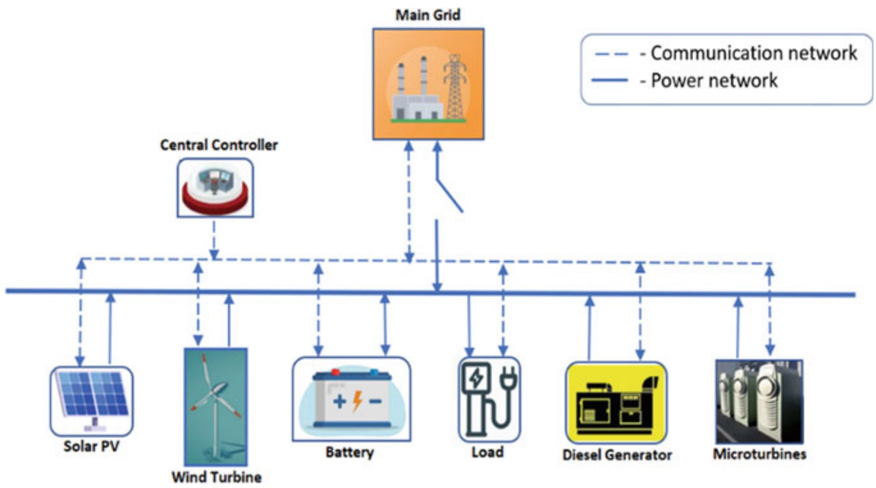

Fig. 1.1 Structure of microgrid model

1.3 Microgrid Components

1.3.1 Modelling of WT and PV Units

The mathematical modelling of wind turbine output power [15] is given by

$$P_{wt}^{t} = \begin{cases} 0; & V_w^t \le V_{ci},\, V_w^t \ge V_{co} \\ \left(\frac{V_w^t - V_{ci}}{V_r - V_{co}}\right) P_{rw}; & V_{ci} \le V_w^t \le V_r \\ P_{rw}; & V_r \le V_w^t \le V_{co} \end{cases} \tag{1.1}$$

here, P_{rw} is the WT rated output power, cut-out speed of WT (V_{co}) considered as 25 m/s, cut-in speed of WT (V_{ci}) considered as 3 m/s, rated speed of WT (V_r) which is 12 m/s respectively. Solar energy is the most prevalent and accessible type of renewable energy. The mathematical modelling of output power of solar PV unit [16] is given by

$$P_{PV}^{t} = \begin{cases} P_{rs}\frac{(I^t)^2}{I_c I_{std}}; & 0 \le I^t \le I_c \\ P_{rs}\frac{I^t}{I_{std}}; & I_c \le I^t \le I_{std} \\ P_{rs}; & I^t \ge I_{std} \end{cases} \tag{1.2}$$

here, P_{rs} is the PV rated output power, certain irradiation point of solar panel (I_c) which is normally set to 0.15 kW/m^2, standard irradiance of solar panel (I_{std}) which is 1 kW/m^2 and I^t is solar irradiance at time t.

1.3.2 Modelling of Micro Turbine (MT)

A microturbine is a compact gas turbine operates at high speed that can be used to generate electricity in the local areas such as residential or commercial buildings, and remote or off-grid locations. The output power generation cost of MT (C^t_{MT}) is calculated by [17]

$$C^t_{MT} = \frac{c_{ng}}{L_h} * \left(\frac{P^t_{MT}}{\eta_{MT}}\right) \tag{1.3}$$

where natural gas price (c_{ng}) in USD/m^3, low hot value of natural gas (L_h) in kWh/m^3, P^t_{MT} is power generated by MT and η_{MT} is the efficiency of MT.

1.3.3 Modelling of Diesel Generator

DEs are typically employed as a backup power source. The mathematical model for consumed fuel of DE (F^t_{DE}) and power generated cost (C^t_{DE}) are given by

$$F^t_{DE} = F_0 * P_{DE-R} + F_1 * P^t_{DE} \tag{1.4}$$

$$C^t_{DE} = c_{dsl} * F^t_{DE} \tag{1.5}$$

here, F_0 and F_1 are curve fitting coefficients of consumed fuel, P_{DE-R} is the DE rated output power.

1.4 Problem Formulation

The main goals of the proposed model is to minimize the total daily operation cost and the minimization of daily pollutant emission. The objective functions and corresponding constraints are mathematically formulated as follows:

1.4.1 Islanded Mode

In this scenario, the main aim is to reduce the overall daily operation cost and environmental pollutant emission of MG connected in islanded mode. The objective functions are mathematically given by:

$$\min\ F_1 = \sum_{t=1}^{T} \left[C_{DE}^{t} + C_{MT}^{t} + C_{Cur} \left| P_{net}^{t} \right| \right] \tag{1.6}$$

$$\min\ F_2 = \sum_{t=1}^{T} \left(E_{DE}^{CO_2} + E_{DE}^{SO_2} + E_{DE}^{\mathrm{NO}_2} \right) * P_{DE}^{t} + \left(E_{MT}^{\mathrm{CO}_2} + E_{MT}^{\mathrm{SO}_2} + E_{MT}^{NO_x} \right) * P_{MT}^{t} \tag{1.7}$$

where C_{Cur} is the curtailed power cost and the net available power at time instant t.

The power balance equation is given as

$$P_{DE}^{t} + P_{MT}^{t} + P_{PV}^{t} + P_{WT}^{t} - P_{BC}^{t} + P_{BD}^{t} - P_{\mathrm{Load}}^{t} = 0 \tag{1.8}$$

1.4.2 Grid Connected Mode

In this scenario, the main goal is to minimize the MG operation cost which is associated with energy production, operation and maintenance, purchased power from the main grid, and minimization of pollutant emission simultaneously. The objective functions are as follows:

$$\min\ F_1 = \sum_{t=1}^{T} \left[C_{DE}^{t} + C_{MT}^{t} + C_{\mathrm{buy}}^{t}\, P_{FG}^{t} - C_{\mathrm{sell}}^{t}\, P_{TG}^{t} \right] \tag{1.9}$$

$$\min\ F_2 = \sum_{t=1}^{T} \left(E_{DE}^{CO_2} + E_{DE}^{SO_2} + E_{DE}^{\mathrm{NO}_2} \right) * P_{DE}^{t} + \left(E_{MT}^{\mathrm{CO}_2} + E_{MT}^{\mathrm{SO}_2} + E_{MT}^{NO_x} \right) * P_{MT}^{t} \left(E_{\mathrm{grid}}^{\mathrm{CO}_2} + E_{\mathrm{grit}}^{\mathrm{SO}_2} + E_{\mathrm{grid}}^{\mathrm{NO}_x} \right) * P_{FG}^{t} \tag{1.10}$$

where imported electricity price from the main grid at instant time t is C_{buy}^{t} , imported power from main grid is P_{FG}^{t}, C_{sell}^{t} is the electricity exported energy price to main grid, exported power to main grid is P_{TG}^{t}. The power balance equation for grid connected mode is

$$P_{DE}^{t} + P_{MT}^{t} + P_{PV}^{t} + P_{WT}^{t} - P_{BC}^{t} + P_{BD}^{t} + P_{FG}^{t} - P_{TG}^{t} - P_{\mathrm{Load}}^{t} = 0 \tag{1.11}$$

1.4.3 Constraints

$$P_{DE}^{\min} \le P_{DE}^{t} \le P_{DE}^{\max} \tag{1.12}$$

$$P_{MT}^{\max} \leq P_{MT}^{t} \leq P_{MT}^{\max} \tag{1.13}$$

$$0 \leq P_{FG}^{t} \leq P_{FG}^{max} b_{fg}^{t} \tag{1.14}$$

$$0 \leq P_{TG}^{t} \leq P_{TG}^{\max} b_{tg}^{t} \tag{1.15}$$

$$b_{\mathrm{fg}}^{t} + b_{\mathrm{tg}}^{t} \leq 1, b_{\mathrm{fg}}^{t}, b_{\mathrm{tg}}^{t} \in \{0, 1\} \tag{1.16}$$

$$0 \leq P_{bd}^{t} \leq P_{bd}^{\max} * d^{t} \tag{1.17}$$

$$0 \leq P_{bc}^{t} \leq P_{bc}^{\max} * b^{t} \tag{1.18}$$

$$b^{t} + d^{t} \leq 1 \tag{1.19}$$

$$S^{\min} \leq S^{t} \leq S^{\max} \tag{1.20}$$

$$S^{t} = S^{t-1} + \frac{\left(\eta_{c} P_{BC}^{t} \delta t - P_{BD}^{t} \delta t / \eta_{d}\right)}{\Omega_{BESS}} \tag{1.21}$$

The maximum and minimum power limits of DE and MT are represented in Eqs. (1.12) and (1.13), respectively. The power exchanging limits between main grid and MG are represented in Eqs. (1.14) and (1.15). The simultaneous buying and selling operations are not possible at any time instant t, which is shown in Eq. (1.16). The Eqs. (1.17) and (1.18) represents the limits for the charging ($P_{bc}^{\max}$) and discharging ($P_{bd}^{\max}$) operations of BES. The operations of the BES cannot be happened simultaneously, which is represented by Eq. (1.19). The state of charge (SOC) limits for the BES are shown in Eq. (1.20), and the SOC level is calculated by using Eq. (1.21).

1.4.4 Maximum Fuzzy Satisfaction Method

In this stage, the proposed bi-objective optimization problem is transformed into a single-objective problem using the maximum fuzzy satisfaction method [18]. The two objective functions are defined with fuzzy membership functions based on this method. According to the maximum fuzzy satisfaction method, the minimization objective function can be converted into upward half trapezoidal membership function and similarly maximization objective function is converted into downward half trapezoidal membership function. Finally, the MILP method is used to solve the final single objective model. If the function F is the minimization function, then the fuzzy membership function is given as follows:

$$\mu(F) = \begin{cases} 1 & if \quad F \le F^{\min} \\ \frac{F^{\max} - F}{F^{\max} - F^{\min}} & if \quad F^{\min} < \mathrm{F} < F^{\max} \\ 0 & if \quad F \ge F^{\max} \end{cases} \tag{1.22}$$

If the function F is the maximization function, then the fuzzy membership function is represented as:

$$\mu(F) = \begin{cases} 0 & if \quad F \le F^{\min} \\ \frac{F - F^{\min}}{F^{\max} - F^{\min}} & if \quad F^{\min} < F < F^{\max} \\ 1 & if \quad F \ge F^{\max} \end{cases} \tag{1.23}$$

In the proposed model, both objective functions daily operation cost (F_1) and daily emission (F_2) are minimization functions, so both objectives are converted into the fuzzy membership functions with the help of Eq. (1.22).

The final single objective function (γ) and corresponding constraints are given by

$$\max \gamma = \min\{\mu(F_1), \mu(F_2)\} \tag{1.24}$$

$$\text{s.t} \begin{cases} \gamma \le \mu(F_1) \\ \gamma \le \mu(F_2) \\ 0 \le \gamma \le 1 \\ \text{constraints (11) to (21)} \end{cases} \tag{1.25}$$

1.5 Results and Discussions

In this section, three different case studies were used to analyze the effectiveness of the proposed multi-objective optimization problem for a grid-tied MG and each case study is analyzed with the operation of islanded and grid connected modes. The Case1 and Case 2 represent the single objective optimization problem where the operation cost and pollutant emission are minimized individually. In case 3, a multi-objective optimization problem is formulated, and the maximum fuzzy satisfaction method and MILP method are used to optimize both the objectives simultaneously. In all case studies, the MG optimal operation problem is solved by using MILP solver in laptop intel core i5 using MATLAB R2021a toolbox.

Case 1: Daily operation cost minimization:

In this case, the proposed model is formulated as a single objective optimization problem with the minimization of daily operation cost function. This model is tested in two MG operating modes such as islanded and grid-connected operations. The simulation output results for this case study are shown in Tables 1.1 and 1.2. From the results, it is noted that the optimal daily operation cost is 6.2065 k$/day in islanded mode and 4.7833 k$/day in grid connected mode. The daily curtailment load is 2.345 MWh in islanded mode and there is 12.469 MWh imported power and 0.928 MWh exported power from/to the main grid in grid connected mode.

Case 2: Environmental pollutant emission minimization:

In this case, the proposed model is formulated as a single objective optimization problem with the minimization of daily pollutant emission. The simulation output results for this case study are shown Table 1.1 and 1.2. From the results, it is noted that the optimal environmental pollutant emission is 2.146 tons/day in islanded mode and 12.448 tons/day in grid connected mode. The daily curtailment load is 12.85 MWh in islanded mode and there is 2.459 MWh imported power and 0.7584 MWh exported power from/to the main grid in grid connected mode.

Case 3: Minimization of both daily operation cost and environmental pollutant emission:

In this case study, the suggested model aims to minimize both economic and environmental objectives simultaneously. Case 1 and Case 2 examined the optimization problem with the focus of a single objective function. As a result, the simultaneous optimal values are not achieved in both cases. Hence, both the objectives are simultaneously optimized in case 3 using proposed multi-objective optimization model. The simulation output results for this case study are shown Tables 1.1 and 1.2. From results, it is clearly noted that the optimal daily operating cost is 7.6369 k$/day along with optimal pollutant emission is 4.918 tons/day in islanded mode. The optimal daily operation cost and environmental pollution emission is 5.036 k$/day and 12.68 tons/day in grid connected mode.

Table 1.1 Minimization of optimal operation problem under islanded mode

Cases	Isolated mode			
	Daily operation cost (k$/day)	Daily emission (tons/day)	Daily curtailment load (MWh)	Daily unutilized RERs (MWh)
Case 1	**6.2065**	10.232	2.345	0.638
Case 2	10.38	**2.146**	12.85	1.409
Case 3	**7.6369**	**4.918**	8.554	0.638

Table 1.2 Minimization of optimal operation problem under grid connected mode

Cases	Grid connected mode			
	Daily operation cost (k$/day)	Daily emission (tons/day)	Import power (MWh)	Export power (MWh)
Case 1	**4.783**	14.02	12.469	0.928
Case 2	6.438	**12.448**	2.459	0.7584
Case 3	**5.036**	**12.68**	3.92	0.85

From the overall analysis of results in islanded mode, it is observed that the load curtailment is very high in case 2, low in case 1 and moderate in case 3. Similarly unutilized RER energy is high in case 2 when compared with remaining cases. In grid connected mode, the power imported from main grid is high value in case 1, low value in case 2 and moderate in case 3. Similarly, the power exported to main grid is high in case 1, low and medium in case 2 and case 3 respectively.

From the overall discussion, it is concluded that the proposed multi objective MG operation model able to provide the better optimal solutions when compared to single objective MG operation models. It is also found the proposed multi-objective model maximizes the effective renewable energy utilization, lower the daily load curtailment, and also reduces the daily imported energy from the main grid.

The optimal scheduling of different RERs and energy storage devices in proposed bi-objective model case are shown in Figs. 1.2 and 1.3 respectively.

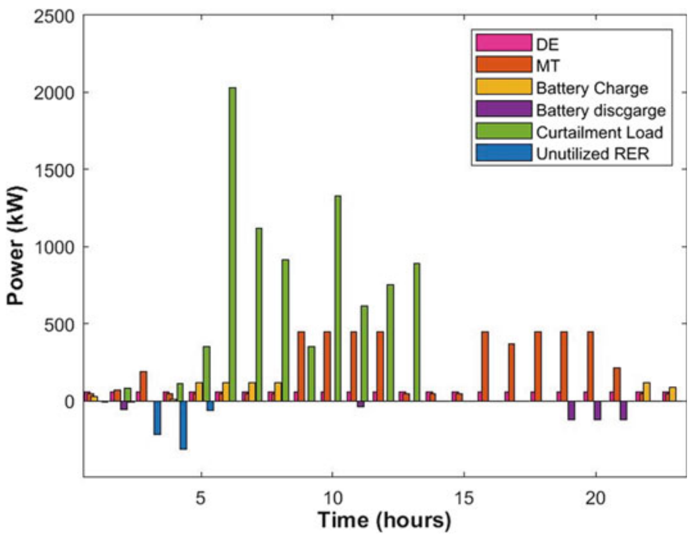

Fig. 1.2 Daily optimal operation outputs of different RERs and ESS in case 3 for islanded mode of operation

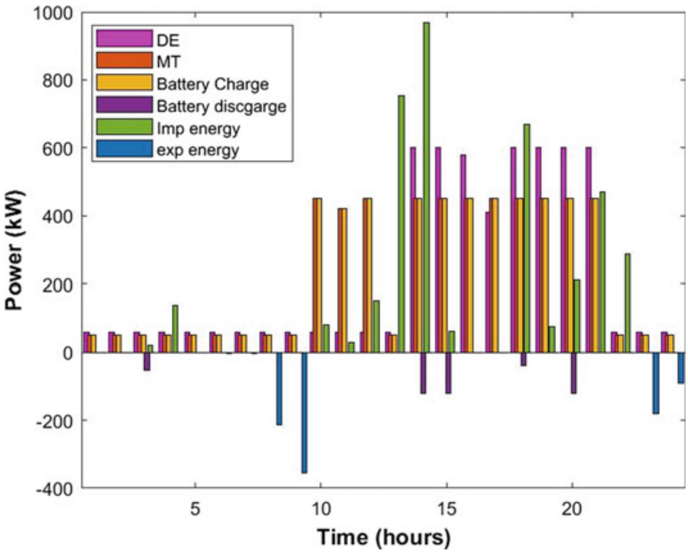

Fig. 1.3 Daily optimal operation outputs of different RERs and ESS in case 3 for grid connected mode of operation

1.6 Conclusion

A bi-objective optimization model for an optimal energy scheduling strategy of MG with economic and environmental objectives is proposed in this paper for both isolated and grid-connected modes. The minimization of daily operation cost and minimization of daily emission are the primary objectives for the proposed multi-objective problem. By using a maximum fuzzy satisfaction and MILP method, the proposed multi-objective model is solved. Three distinct case studies are used to analyze the effectiveness of the proposed model and each case study is evaluated with two different operating modes i.e., isolated mode and grid-connected mode. The comprehensive analysis of results indicates that the proposed bi-objective MG operation model is capable to provide the better optimal solution.

References

1. Abolhosseini, S., Heshmati, A., Altmann, J.: A review of renewable energy supply and energy efficiency technologies. Tech. Rep., Apr 2014 [online]. Available: http://ftp.iza.org/dp8145.pdf
2. Nwulu, N.I., Xia, X.: Optimal dispatch for a microgrid incorporating renewables and demand response. Renewable Energy **101**, 16–28 (2017)
3. Zhou, K., Yang, S., Chen, Z., Ding, S.: Optimal load distribution model of microgrid in the smart grid environment. Renewable Sustain. Energy Rev. **35**, 304–310 (2014)

4. Morstyn, T., Hredzak, B., Demetriades, G.D., Agelidis, V.G.: Unified distributed control for DC microgrid operating modes. IEEE Trans. Power Syst. **31**(1), 802–812 (2016). https://doi.org/10.1109/TPWRS.2015.2406871
5. Ortega, R., Carranza, O., Sosa, J.C., García, V.H., Rodríguez,J.J.: Modeling and design of photovoltaic inverters for island mode operation within a microgrid. In: 2015 IEEE Thirty Fifth Central American and Panama Convention (CONCAPAN XXXV), Tegucigalpa, Honduras, 2015, pp. 1–6. https://doi.org/10.1109/CONCAPAN.2015.7428487
6. Jiang, Q., Xue, M., Geng, G.: Energy management of microgrid in grid-connected and stand-alone modes. IEEE Trans. Power Syst. **28**(3), 3380–3389 (2013). https://doi.org/10.1109/TPWRS.2013.2244104
7. Surender Reddy, S., Park, J.Y., Jung, C.M.: Optimal operation of microgrid using hybrid differential evolution and harmony search algorithm. Front. Energy **10**(3), 355–362 (2016). https://doi.org/10.1007/s11708-016-0414-x
8. Ramabhotla, S., Bayne, S., Giesselmann, M.: Operation and maintenance cost optimization in the grid connected mode of microgrid. In: 2016 IEEE Green Technologies Conference (GreenTech), Kansas City, MO, USA, 2016, pp. 56–61. https://doi.org/10.1109/GreenTech.2016.18
9. Kanchev, H., Colas, F., Lazarov, V., Francois, B.: Emission reduction and economical optimization of an urban microgrid operation including dispatched PV-based active generators. IEEE Trans. Sustain. Energy **5**(4), 1397–1405 (2014)
10. Hernandez-Aramburo, C.A., Green, T.C., Mugniot, N.: Fuel consumption minimization of a microgrid. IEEE Trans. Ind. Appl. **41**, 673–681 (2005)
11. Aghajani, G., Shayanfar, H., Shayeghi, H.: Presenting a multi-objective generation scheduling model for pricing demand response rate in micro-grid energy management. Energy Convers. Manage. **106**, 308–321 (2015)
12. Motevasel, M., Seifi, A.R.: Expert energy management of a micro-grid considering wind energy uncertainty. Energy Convers. Manage. **83**, 58–72 (2014)
13. Niknam, T., Azizipanah-Abarghooee, R., Narimani, M.R.: An efficient scenario-based stochastic programming framework for multi-objective optimal micro-grid operation. Appl. Energy **99**, 455–470 (2012)
14. Li, P., Ma, J., Zhao, B.: Game theory method for multi-objective optimal operation of microgrid. In: 2015 IEEE Power & Energy Society General Meeting, Denver, CO, 2015, pp. 1–5. https://doi.org/10.1109/PESGM.2015.7286075
15. Giorsetto P., Utsurogi, K.F.: Development of a new procedure forreliability modeling of wind turbine generators. IEEE Trans. Power Apparatus Syst. **1**, 134–143 (1983)
16. Aien, M., Fotuhi-Firuzabad, M., Rashidinejad, M.: Probabilistic optimal power flow in correlated hybrid wind–photovoltaic power systems. IEEE Trans. Smart Grid **5**(1), 130–138 (2014)
17. Nikmehr, N., Najafi-Ravadanegh, S.: Optimal operation of distributed generations in micro-grids under uncertainties in load and renewable power generation using heuristic algorithm. IET Renew. Power Gener. **9**(8), 982–990 (2015)
18. Chen, J., et al.: Optimal sizing for grid-tied microgrids with consideration of joint optimization of planning and operation. IEEE Trans. Sustain. Energy **9**(1), 237–248 (2018)

Chapter 2
A Review of Biodegradable Oil Derived from Biomass for Internal Combustion Engine Lubrication

Wasihun Diriba Keno, Kannaki Shanmugam Pondicherry, Dieter Fauconnier, Venkata Ramayya Ancha, and Patrick De Baets

Abstract Due to the current devastating environmental concerns caused by petroleum-derived lubricants in internal combustion (IC) engines (because of their toxicity, non-biodegradability and not environmental adaptability), and the increase in oil prices, as well as the degradation of the global crude oil reserves, researchers all over the world are working to develop innovative ideas for sustainable development in biomass-derived biodegradable lubricant oil which the perform equivalent or more than the commercial petroleum-based oils in engine lubrication. This review paper's major purpose is to provide those researchers and particularly engineers interested in IC engine biolubricant oil derived from renewable biomass with appropriate information and perspective.

2.1 Introduction

An engine is a mechanical device in any automobile that can transform the chemical energy of the fuel into mechanical power by moving the piston's position from the top dead center to the bottom dead center. Due to this up-and-down piston movement, friction occurs at the interface, generating frictional heat [1]. Among all parts of the engine which are in relative motion when the automobile moves, the most important part which consists of the piston, piston ring, cylinder liner, and connecting components affects the performance of the engine. Because friction and wear reduce the performance of the engine, a lubrication mechanism is used to mitigate the effects of friction and wear on the contact surface. Lubrication is the process of applying

W. D. Keno (✉) · K. S. Pondicherry · D. Fauconnier · P. De Baets
Department of Electromechanical, Systems and Metal Engineering, Soete Laboratory, Ghent University, 9052 Zwijnaarde, Belgium
e-mail: wasihun.diribo@ju.edu.et

W. D. Keno · V. R. Ancha
Faculty of Mechanical Engineering, Jimma University, 378 Jimma, Ethiopia

P. H. V. S. Talpa Sai et al. (eds.), *Intelligent Manufacturing and Energy Sustainability*, Smart Innovation, Systems and Technologies 372,
https://doi.org/10.1007/978-981-99-6774-2_2

lubricant oil to the surface interface in contact that moves inside the engine relative to one another to reduce friction, wear, heat loss, oxidation, and corrosion, provide an insulator environment, and protect engine parts against moisture, dirt, and dust. In IC engines, engine lubrication largely influences friction, which reduces fuel economy. Engine fuel economy is connected to engine power losses, and minimizing power losses can result in improved fuel economy. Engine lubricants greatly minimize friction and wear between two surfaces in contact by forming a thin film between two engine mating surfaces, keeping them from contacting each other and being worn out or broken. When the right engine lubricant is selected, the engine works smoothly because the lubricant helps to keep the engine clean and protected while also preventing corrosion and cooling the engine.

Biolubricant generated from biomass have been used for engine lubrication for hundreds of years in the past. However, due to the discovery of crude oil and the availability of lower cost lubricating oils, this proposal was abandoned [2]. Currently, crude oils derived from fossil fuels are utilized as raw materials in the production of commercial lubricant oils. However, the gradual exhaustion of petroleum sources, accompanied by a growing understanding of environmental problems, has caused widespread alarm throughout the globe. Mineral oils extracted by refining crude oil are the most used engine oil lubricants, however, they are neither sustainable nor environmentally friendly. Therefore, there is a need to invest efforts to find environmentally friendly, biodegradable and sustainable alternatives. Additionally, mineral oils are expensive, and this becomes of relevance in economically weaker countries (Fig. 2.1).

Biomass derived bio-lubricants attract attention nowadays as the best lubricants due to their high biodegradability and low human/environmental toxicity. Moreover, they have molecular structures with the capacity to degrade biologically over time through the processes of bacterial decomposition or thematic biodegradation. Biolubricant are extremely lubricious, have a high flash point, and have a high viscosity index. Because of their biodegradability, they are less harmful than mineral-based lubricants and are frequently renewable. Several studies indicated that a large biomass vegetable oils such coconut, olive, sunflower seed, corn, soybean, rice bran and rubber seed oils might be employed as lubricants in engine lubrication purposes. The use of biomass derived oil as a biolubricant oil has been well-established, however, to match the performance to a conventional mineral oil further research is necessary particularly concerning the additives, such as, antioxidants, friction modifiers, anti-wear agents etc. [4–6].

2.1.1 Sources of Bio-Based Engine Lubricants

Bio-lubricants are derived from large plant biomass such as rapeseed, sunflower, castor, palm, soybean and coconut, jojoba, Karanja, and etc. [7]. Even though it depends on geographical locations, more than 350 oil-bearing crops/vegetables are known to be the source of bio-lubricants around the world.

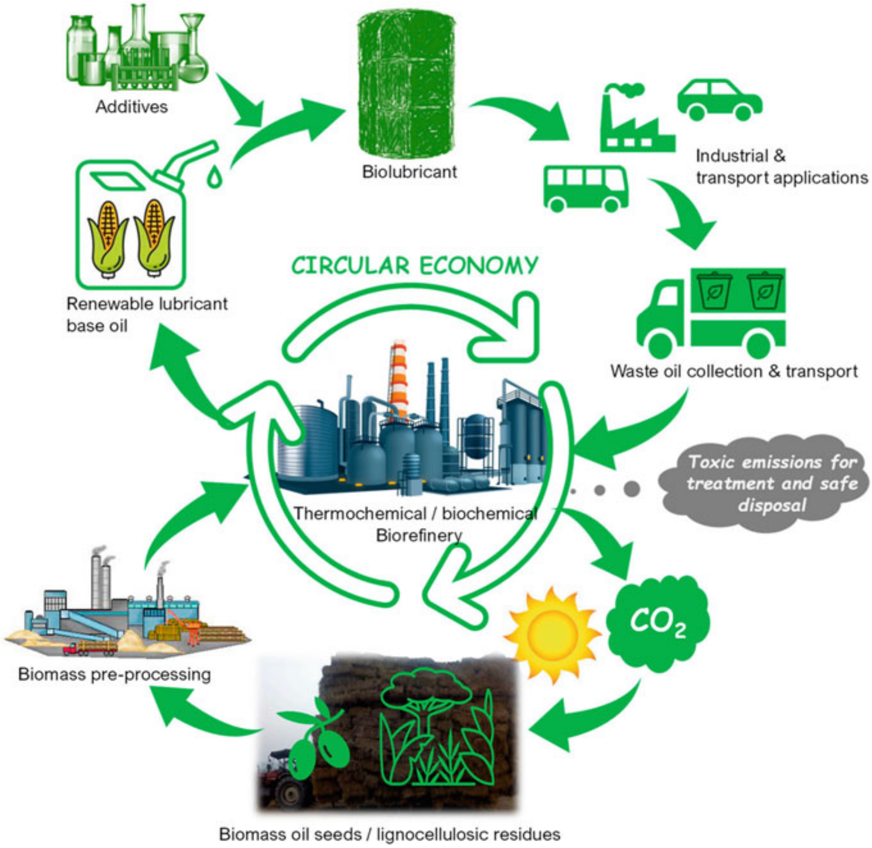

Fig. 2.1 Life cycle of biolubricant oil derived from biomass [3]

2.1.2 Advantages and Limitations of Biomass Derived Engine Biolubricant

Biomass derived engine biolubricant oils have certain advantages and disadvantages depending upon the biomass feedstock used to produce lubricants when considered for engine and various industrial lubrication processes. The benefit of using biomass derived biolubricant oil over petroleum-derived mineral oil lies in the fact it has higher lubricity [8]. As an advantages, biomass derived biolubricant have countable advantages when considered for IC engine lubrication compared with mineral oils in their excellent lubricity, high VI, high flash points, high percentage of biodegradability (90–98%), less toxicity, and renewability. Most significantly, vegetable oils are biodegradable, non-toxic, and renewable, reducing reliance on imported petroleum oils.

Low harmful effects, attractive lubricating properties, higher VI, high ignition temperature, raised machinery lifespan, high load-carrying capacity, suitable anti-wear characteristic, great coefficient of friction, natural multi-grade properties, low evaporation rates, reduced emissions into the environment, and rapid biodegradability are among the benefits of using bio-based lubricants according to [7]. Biomass derived biolubricant oils also have certain limitations (disadvantages) such as low oxidative stability and may lack sufficient oxidative stability in their natural form for lubricant use and poor cold flow performance. The use of antioxidants and other types of additives can be used to overcome this limitation.

2.1.3 Current Status of Biomass Derived Biolubricant as Alternative for IC Engines

Different scholars [1, 7, 9–11] reported the potential of bio-based lubricants in automotive applications and addressed their origin, characteristics, benefits, drawbacks, possibilities, and limitations as a potential replacement candidate for conventional lubricants in automotive applications such as IC engines. Kalam et al. [4] recently released a study on the impact of thermal stability and lubrication performance of biodegradable olive oil as an engine lubricant on the performance of heavy-duty diesel engines. The result revealed that olive oil has good oxidation stability due to the high percentages of oleic acid in the fatty acid makeup (Fig. 2.2).

Zulkifli et al. [12] evaluated the wear-reduction properties of a palm oil as an engine lubricant in a for different lubrication regimes. The result of the evaluation found that the palm oil lubricant improves the coefficient of friction and the wear in terms of the wear scar diameter (WSD). Moreover, Cheenkachorn et al. [13]

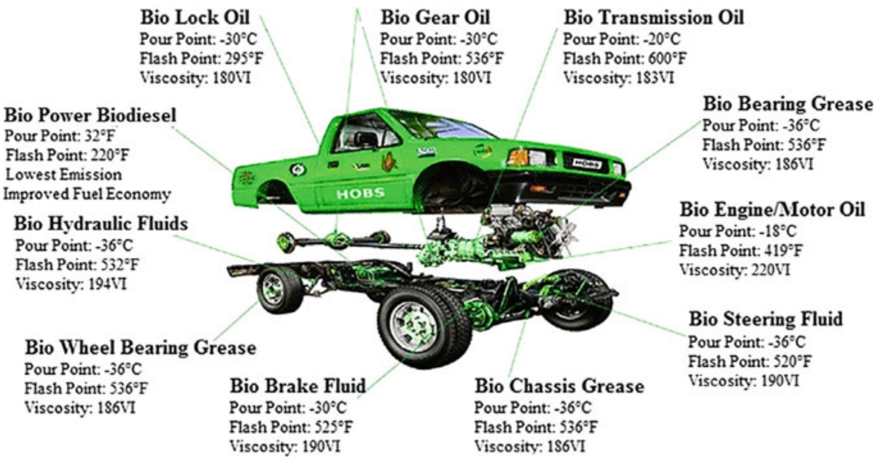

Fig. 2.2 Lubrication requirements for a pick-up truck [7]

found that palm-based engine oil blends were comparable to conventional engine oils when fueling single-cylinder, four-stroke diesel engines. The palm oil biolubricant outperforms commercial SAE 40 oil in terms of tribological qualities.

Arumugam et al. [14] investigated the influence of biolubricant on the tribological characteristics of a pin-on-disc cylinder liner piston ring pair tribometer. The result showed that the biolubricant reduced the coefficient of friction and wear and exhibited better lubricity. Ting et al. [15] analyzed the viscosity and working efficiency of soybean oil lubricant as engine lubricant. The analysis revealed that the viscosity of the soybean oil is much higher than that of the engine oils. Nagendramma et al. [16] explored the development of eco-friendly biodegradable lubricants and discovered that artificial and vegetable oil-based esters provide the best alternatives for formulating non-toxic lubricants for automotive gearbox fluids and automotive gear oils, either alone or in a blend. In similar manner, Bekal et al. [17] conducted a research using Pongamia oil instead of conventional mineral oil in an engine and the Pongamia oil shows the minimum brake-specific energy consumption and the highest brake thermal efficiency at medium- and high-load conditions because of its low viscosity.

Bhat [9, 18] studied the application of Karanja oil as a biolubricant in compression ignition engines. The results showed that the Karanja oil has a good potential to replace mineral oil base stocks in 4-stroke diesel engine oil formulations. Aravind et al. [5] investigated the lubricant properties of biodegradable rubber tree seed (*Hevea brasiliensis* Muell. Arg) oil using a four-ball tester and estimated the coefficient of friction and the wear preventive characteristics of the oil. It was discovered that rubber seed oil possesses features that make it well-suited for development into a bio-lubricant, and that its capabilities may be enhanced further with the addition of appropriate additives.

Reddy et al. [19] experimentally investigated the usage of Palm oil as a lubricant to substitute mineral oil in compression ignition (CI) engines and found that the palm oil-based lubricant revealed appreciable expedience on engine and emission performance. Furthermore, to investigate vegetable oils' degradation rate during engine operation and the effect towards tribological characteristics, Mannekote and Kailas [20] tested fresh and aged coconut and palm oils after 100 h of 4-stroke engine endurance testing. The results suggested that during the initial stages, the anti-wear characteristics of fresh bio-based oils were comparable to the conventional engine oil (Table 2.1).

2.1.4 Thermal Stability and Low Temperature Performance of Biomass Derived Engine Biolubricant

Thermal instability, low hydrolytic stability, and low temperature performance are major limits in the application of biomass derived lubricating oils in IC engine lubrication as compared to mineral or synthetic oil-based lubricants. As a result of long-term

Table 2.1 Plant biomass plant derived oils used as a biolubricant in IC Engine

Biomass derived oil	Major properties of oil	References
Coconut oil	High anti-wear, better lubricity, low coefficient of friction	[7, 20, 21]
Sunflower oil	High VI, flash point, lubricity, and low evaporative loss, co-efficient of friction, and non-toxic	[7, 21, 22]
Soybean oil		[7, 15, 21]
Olive oil		[4, 7, 21]
Castor oil	Low volatility, high viscosity index (VI), high antioxidants, low deposit formation	[7, 11, 21, 23]
Jatropha oil	Low wear, high VI, loss, low cumulative weight loss, low coefficient of friction	[7, 11, 24]
Rapeseed oil	Higher density, viscosity, flashpoint, fire-point, and calorific value was determined	[2, 14, 21, 25, 26]
Jojoba oil		[21, 27]
Palm oil		[12, 19–21]
Pongamia oil		[17, 26]
Karanja oil		[11, 18, 28, 29]
Rubber tree seed oil	Highest viscosity index and a low pour point, thermally stable up to 250 °C	[5, 30, 31]

exposure to low temperatures, cloudiness and solidification appear at low temperatures, resulting in poor flow characteristics. The pour point, as defined by the ASTM D97 standard, is the lowest temperature at which a lubricant may flow or be handled without freezing in a machine element [32, 33].

Some drawbacks of biomass-derived lubricating oils include low oxidative stability, and many bio-based oils lack adequate oxidative stability in their native state for lubricant application in engine. The lubrication performance of any oil depends on oxidation stability, which may change the characteristics of the oil. To address this constraint, antioxidants can be utilized; nevertheless, with this chemical, a modification will result in the shifting of its fatty acids owing to the partial hydrogenation process, increasing the cost of the final product. The presence of bis-allylic carbons in the double bonds in biomass derived oils is one of the main reason for poor oxidation stability; but, this problem can be improved by the addition of additives and chemical modification.

An antioxidant is any compound capable of preventing the oxidation of a biological substrate or molecule initiated by any reactive compound, either free radicals or other species that are capable of initiating or inducing the oxidation of any substrate [34, 35]. From a broad perspective, molecules capable of reducing oxidation phenomena can be broadly classified as primary antioxidants, or chain-breaking radical scavengers; secondary antioxidants, also known as oxygen scavengers and peroxide decomposers; and those that act through a combination of the functionalities of both.

2.1.5 Literature Gap and Scope for Future Researchers Work.

Mineral oils extracted by refining crude oil are the most used engine oil lubricants, however, they are neither sustainable nor environmentally friendly. Therefore, there is a need to invest efforts to find environmentally friendly, biodegradable, and sustainable alternatives. Additionally, mineral oils are expensive, and this becomes of relevance in economically weaker countries. The use of biomass derived biolubricant oil has been well-established, however, to match the performance to a conventional mineral oil further research is necessary particularly modifying the engine components, surface modifications and using green and smart lubrication system with compatible additives such as, antioxidants, friction modifiers, anti-wear agents [36].

Therefore, the researchers and engineers around the globe should aim to enhance the state of the art in the direction of finding a sustainable, environmentally friendly, relatively more biodegradable, and economically affordable alternative biolubricant and their additives to conventional engine oil lubricants.

2.2 Conclusion

Reciprocating internal combustion engines are still considered as the primary means of propulsion for vehicles operating in land or sea. However, the efficiency of such engines is low due to heat loss and friction. Therefore, the role of lubricants becomes utmost essential as they not only aid in reducing friction and wear but also enable efficient heat transfer, removal of contaminants and hinder corrosion.

Because of their natural and ecologically benign properties, plant biomass derived lubricant can be used as an alternative for mineral oil-based lubricants in IC engines. It has been demonstrated in the literature that the functionality and endurance of biomass-derived bio-lubricants are quite poor in an engine without any additive. As a result, adding additives to biolubricant oil is critical for the smooth operation of a contemporary IC engine. Antioxidants, anti-seizure, antifriction, anti-wear, extreme pressure, corrosion inhibitor, and anti-foam additives are commonly added to biomass-derived biolubricant to increase their desirable qualities, minimize their unpleasant features, and improve their lubrication performance in the IC engine. Some additives perform their function within the body of the base oil such as antioxidants, while others do their work on the surface of the metal such as anti-wear additives and rust inhibitors.

Because of their better intrinsic properties, biomass derived biolubricant oils provide substantial benefits as alternative lubricants for internal combustion engines, industrial and maintenance applications. Biomass derived biolubricant is one of the most important fields because it provides a simple, non-toxic, and renewable product that has the potential to save the environment while also meeting the demands of modern industry to reduce friction and wear for better movement of components that are in mutual contact with each other in IC engine parts.

Acknowledgements I would like to thank Prof. Dr. ir. Patrick De Baets, Prof. Dr. ir. Venkata Ramayya Ancha, Prof. Dr. ir. Dieter Fauconnier, and Dr. ir. Kannaki Shanmugam Pondicherry for their valuable advice and support during the preparation of the paper. This research work was supported and funded by NASCRE Jimma University and Ghent University.

References

1. Pathak, M.K., Joshi, A., Mer, K.K.S., Katiyar, J.K., Patel, V.K.: Potential of Bio-lubricants in Automotive Tribology (2019). https://doi.org/10.1007/978-981-15-0434-1_11
2. Zainal, N.A., Zulkifli, N.W.M., Gulzar, M., Masjuki, H.H.: A review on the chemistry, production, and technological potential of bio-based lubricants. Renew. Sustain. Energy Rev. **82**, 80–102 (2018). https://doi.org/10.1016/j.rser.2017.09.004
3. Sarma, R.N., Vinu, R.: Current status and future prospects of biolubricants: properties and applications. Lubricants **10**, 1–21 (2022). https://doi.org/10.3390/lubricants10040070
4. Kalam, M.A., Masjuki, H.H., Cho, H.M., Mosarof, M.H., Mahmud, M.I., Chowdhury, M.A., Zulkifli, N.W.M.: Influences of thermal stability, and lubrication performance of biodegradable oil as an engine oil for improving the efficiency of heavy duty diesel engine. Fuel **196**, 36–46 (2017). https://doi.org/10.1016/j.fuel.2017.01.071
5. Aravind, A., Joy, M.L., Nair, K.P.: Lubricant properties of biodegradable rubber tree seed (*Hevea brasiliensis* Muell. Arg) oil. Ind. Crops Prod. **74**, 14–19 (2015). https://doi.org/10.1016/j.indcrop.2015.04.014
6. Rani, S., Joy, M.L., Nair, K.P.: Evaluation of physiochemical and tribological properties of rice bran oil—biodegradable and potential base stoke for industrial lubricants. Ind. Crops Prod. **65**, 328–333 (2015). https://doi.org/10.1016/j.indcrop.2014.12.020
7. Mobarak, H.M., Niza Mohamad, E., Masjuki, H.H., Kalam, M.A., Al Mahmud, K.A.H., Habibullah, M., Ashraful, A.M.: The prospects of biolubricants as alternatives in automotive applications. Renew. Sustain. Energy Rev. **33**, 34–43 (2014). https://doi.org/10.1016/j.rser.2014.01.062.
8. Negi, P., Singh, Y., Tiwari, K.: A review on the production and characterization methods of bio-based lubricants. Mater. Today Proc. **46**, 10503–10506 (2021). https://doi.org/10.1016/j.matpr.2020.12.1211
9. Syahir, A.Z., Zulkifli, N.W.M., Masjuki, H.H., Kalam, M.A., Alabdulkarem, A., Gulzar, M., Khuong, L.S., Harith, M.H.: A review on bio-based lubricants and their applications. J. Clean. Prod. **168**, 997–1016 (2017). https://doi.org/10.1016/j.jclepro.2017.09.106
10. Panchal, T.M., Patel, A., Chauhan, D.D., Thomas, M., Patel, J.V.: A methodological review on bio-lubricants from vegetable oil based resources. Renew. Sustain. Energy Rev. **70**, 65–70 (2017). https://doi.org/10.1016/j.rser.2016.11.105
11. Suhane, A.: Potential of non edible vegetable oils as an alternative lubricants in automotive applications. Int. J. Eng. Res. Appl. **2**, 1330–1335 (2012)
12. Zulkifli, N.W.M., Kalam, M.A., Masjuki, H.H., Shahabuddin, M., Yunus, R.: Wear prevention characteristics of a palm oil-based TMP (trimethylolpropane) ester as an engine lubricant. Energy **54**, 167–173 (2013). https://doi.org/10.1016/j.energy.2013.01.038
13. Cheenkachorn, K., Fungtammasan, B.: Development of engine oil using palm oil as a base stock for four-stroke engines. Energy **35**, 2552–2556 (2010). https://doi.org/10.1016/j.energy.2010.03.002
14. Arumugam, S., Sriram, G.: Effect of bio-lubricant and biodiesel-contaminated lubricant on tribological behavior of cylinder liner-piston ring combination. Tribol. Trans. **55**, 438–445 (2012). https://doi.org/10.1080/10402004.2012.667517

15. Ting, C.C., Chen, C.C.: Viscosity and working efficiency analysis of soybean oil based bio-lubricants. Meas. J. Int. Meas. Confed. **44**, 1337–1341 (2011). https://doi.org/10.1016/j.measurement.2011.04.005
16. Nagendramma, P., Kaul, S.: Development of ecofriendly/biodegradable lubricants: an overview. Renew. Sustain. Energy Rev. **16**, 764–774 (2012). https://doi.org/10.1016/j.rser.2011.09.002
17. Bekal, S., Bhat, N.R.: Bio-lubricant as an alternative to mineral oil for a CI engine—an experimental investigation with pongamia oil as a lubricant. Energy Sour. Part A Recover. Util. Environ. Eff. **34**, 1016–1026 (2012). https://doi.org/10.1080/15567031003735303
18. Bhat, R., N. Associate: A study on the use of Karanja oil as lubricant in compression ignition engines. Natl. Conf. Adv. Mech. Eng. Sci. **2016** (2016). http://www.ijettjournal.org
19. Reddy, K.S.V.K., Kabra, N., Kunchum, U., Vijayakumar, T.: Experimental investigation on usage of palm oil as a lubricant to substitute mineral oil in CI engines. Chinese J. Eng. **2014**, 1–5 (2014). https://doi.org/10.1155/2014/643521
20. Mannekote, J.K., Kailas, S.V.: Experimental investigation of coconut and palm oils as lubricants in four-stroke engine. Tribol. Online **6**, 76–82 (2011). https://doi.org/10.2474/trol.6.76
21. Cecilia, J.A., Plata, D.B., Saboya, R.M.A., de Luna, F.M.T., Cavalcante, C.L., Rodríguez-Castellón, E.: An overview of the biolubricant production process: challenges and future perspectives. Processes **8**, 1–24 (2020). https://doi.org/10.3390/pr8030257
22. Jabal, M.H., Abdulmunem, A.R., Abd, H.S.: Experimental investigation of tribological characteristics and emissions with nonedible sunflower oil as a biolubricant. J. Air Waste Manag. Assoc. **69**, 109–118 (2019). https://doi.org/10.1080/10962247.2018.1523070
23. Singh, A.K.: Castor oil-based lubricant reduces smoke emission in two-stroke engines. Ind. Crops Prod. **33**, 287–295 (2011). https://doi.org/10.1016/j.indcrop.2010.12.014
24. Shahabuddin, M., Masjuki, H.H., Kalam, M.A.: Experimental investigation into tribological characteristics of biolubricant formulated from Jatropha oil. Procedia Eng. **56**, 597–606 (2013). https://doi.org/10.1016/j.proeng.2013.03.165
25. Arumugam, S., Sriram, G., Ellappan, R.: Bio-lubricant-biodiesel combination of rapeseed oil: an experimental investigation on engine oil tribology, performance, and emissions of variable compression engine. Energy **72**, 618–627 (2014). https://doi.org/10.1016/j.energy.2014.05.087
26. Mercier, G.: WEMCOL capacitor fluid development. Electr. Insul. Conf. **10**, 2348–2355 (1997)
27. Gupta, M., Pandey, N.K., Mishra, G.C., Singhal, S.: Development and performance aspects of jojoba based lubricant formulations for two stroke gasoline engines. SAE Tech. Pap. (1993). https://doi.org/10.4271/932795
28. Sudan Reddy Dandu, M., Nanthagopal, K.: Tribological aspects of biofuels—a review. Fuel **258**, 116066 (2019). https://doi.org/10.1016/j.fuel.2019.116066
29. Sharma, U.C., Sachan, S.: Friction and wear behavior of Karanja oil derived biolubricant base oil. SN Appl. Sci. **1**, 1–11 (2019). https://doi.org/10.1007/s42452-019-0706-y
30. Nwokolo, E.: Rubber (*Hevea brasiliensis* L.) seed, oil and meal. In: Food Feed from Legumes and Oilseeds, 333–344 (1996). https://doi.org/10.1007/978-1-4613-0433-3_35
31. Yang, M., Zhu, W., Cao, H.: Biorefinery methods for extraction of oil and protein from rubber seed. Bioresour. Bioprocess. **8** (2021). https://doi.org/10.1186/s40643-021-00386-2
32. Hernández-Sierra, M.T., Aguilera-Camacho, L.D., Báez-García, J.E., García-Miranda, J.S., Moreno, K.J.: Thermal stability and lubrication properties of biodegradable castor oil on AISI 4140 steel. Metals **8**, 1–15 (2018). https://doi.org/10.3390/met8060428
33. Quinchia, L.A., Delgado, M.A., Franco, J.M., Spikes, H.A., Gallegos, C.: Low-temperature flow behaviour of vegetable oil-based lubricants. Ind. Crops Prod. **37**, 383–388 (2012). https://doi.org/10.1016/j.indcrop.2011.12.021
34. Luna, F.M.T., Salmin, D.C., Santiago, V.S., Maia, F.J.N., Silva, F.O.N., Mazzetto, S.E., Cavalcante, C.L.: Oxidative stability of acylated and hydrogenated ricinoleates using synthetic and natural antioxidants. J. Chem. **2019** (2019). https://doi.org/10.1155/2019/3973657
35. González, M., Gallego, R., Romero, M.A., González-Delgado, J.A., Arteaga, J.F., Valencia, C., Franco, J.M.: Impact of natural sources-derived antioxidants on the oxidative stability and rheological properties of castor oil based-lubricating greases. Ind. Crops Prod. **87**, 297–303 (2016). https://doi.org/10.1016/j.indcrop.2016.04.068

36. Rajammagari, H.V., Mohmad, M.W.: The effect of mixed nanoadditive-blended diesel–water emulsion on the performance, combustion, and emission characteristics of a DI diesel engine. Heat Transf. **49**, 3531–3548 (2020). https://doi.org/10.1002/htj.21786

Chapter 3
Advancing Scientific Research in Computer Science by ChatGPT and LLaMA—A Review

Esraa Hassan, Roheet Bhatnagar, and Mahmoud Y. Shams

Abstract ChatGPT and LLaMA AI Modelling are advancing computer science scientific research in several ways. We discuss the capabilities of ChatGPT and LLaMA to advance computer science research in this review. Whereas LLaMA is an automated dialogue system that can respond to questions about scientific subjects, ChatGPT is an NLP model that can create dialogues. The authors contend that by offering scientists more effective methods for data collection and analysis, these two technologies have the potential to fundamentally alter the way they conduct research. According to the authors, ChatGPT and LLaMA could be used to speed up data collection and analysis and give researchers more accurate findings. Additionally, they propose that similar technologies may be employed to develop virtual assistants for scientists, enabling them to easily access pertinent data and take better decisions. Additionally, they think that these technologies could be utilized to enhance inter-scientist communication, facilitating more productive collaboration. There are many benefits of employing LLaMA and ChatGPT in scientific research. These innovations may shorten the time required for data gathering and analysis while also giving researchers more precise findings. These might also help scientists communicate more effectively with one another, which would improve collaboration. Using these tools for scientific study does have certain restrictions. In the real world, it is unknown, for instance, how trustworthy the outcomes produced by ChatGPT and LLaMA would be. Furthermore, it's not obvious how long it would take to train these models

E. Hassan · M. Y. Shams
Faculty of Artificial Intelligence, Kafrelsheikh University, Kafrelsheikh 33516, Egypt
e-mail: esraa.hassan@ai.kfs.edu.eg

M. Y. Shams
e-mail: mahmoud.yasin@ai.kfs.edu.eg

R. Bhatnagar (✉)
Department of Computer Science and Engineering, Manipal University Jaipur, Jaipur, Rajasthan, India
e-mail: roheet.bhatnagar@jaipur.manipal.edu

P. H. V. S. Talpa Sai et al. (eds.), *Intelligent Manufacturing and Energy Sustainability*, Smart Innovation, Systems and Technologies 372,
https://doi.org/10.1007/978-981-99-6774-2_3

before they could be put to good use in a research environment. Prior to putting AI-based systems into practice in the real world, it is important to consider the ethical issues surrounding their use for scientific study.

3.1 Introduction

Generative AI modelling can assist computer scientists in developing new algorithms and applications faster than ever before. As shown in Figure, ChatGPT is a natural language processing (NLP) system that employs deep learning to create conversations based on a given context. It aims to revolutionise the way computer scientists conduct research by creating conversations between humans and machines, enabling more natural interactions as shown in Fig. 3.1. ChatGPT and LLaMA can help computer scientists better understand how humans interact with machines. By generating conversations between humans and machines, researchers can gain insights into how people communicate with computers, which can then be used to improve the user experience of existing technologies [1]. Despite these challenges, generative AI offers numerous advantages for advancing computer science scientific research. LLaMA can be used to produce text that closely resembles the input or entirely differs from it. It functions by dissecting a sentence into its component words or phrases. Thereafter, words are converted into numerical vectors and supplied to the LSTM network. It can be used for many different things, such as providing natural language answers to user inquiries, summarizing lengthy texts, producing original content, performing sentiment analysis, and other things that call for natural language comprehension. It requires large amounts of training data to produce accurate results. Additionally, it may not be able to accurately capture nuances in language or understand complex concepts. It can generate high-quality text quickly and with minimal effort and be used for a variety of tasks, such as summarization and sentiment analysis. Training steps of ChatGPT, combining supervised learning with reinforcement learning. (1) Pre-training the model using supervised learning on a large corpus of text data to generate text that is like the training data. (2) Fine-tune the model using reinforcement learning: Once the model has been pre-trained, it can be fine-tuned using reinforcement learning techniques for providing rewards for generating text. (3) Evaluate and refine the model: After fine-tuning, it is important to evaluate the performance of the model and refine it as needed by adjusting hyperparameters.

3.2 Related Works

Recent developments in computer science research like ChatGPT and LLaMA have been created to make it easier to conduct scientific research. An open-source natural language processing (NLP) toolbox called ChatGPT enables researchers to have conversational interactions with their data. LLaMA is a machine learning-based

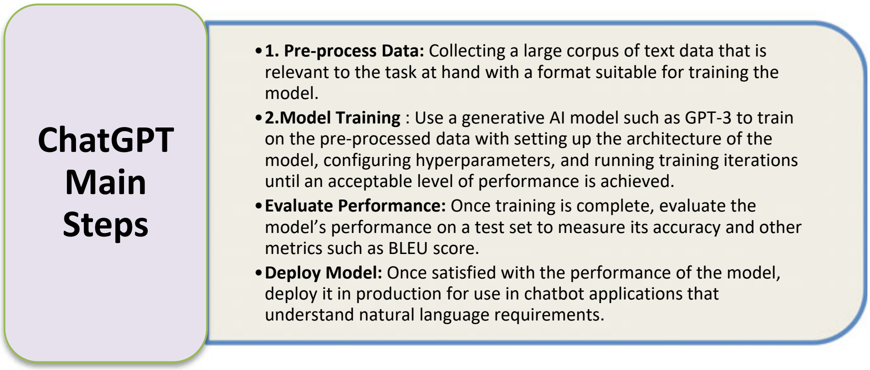

Fig. 3.1 ChatGPT and LLaMA AI modelling main steps

system that autonomously creates research articles from unstructured data using deep learning techniques. These two technologies have been created to make conducting scientific research more straightforward and effective. Mitrovic et al. [2] examine the ability of a machine learning model to detect and explain decisions made by a chatbot (CHATGPT) when generating short text. The authors used a dataset of human-generated and CHATGPT-generated text to train the model, which was then tested on unseen data. The results showed that the model was able to accurately detect whether a given text was generated by CHATGPT or a human, and it was also able to explain its decision-making process. Guo et al. [3] examine the performance of ChatGPT, a chatbot based on the GPT-3 language model, in comparison to human experts. A comparison corpus was created to evaluate ChatGPT's performance, and a detection method was developed to identify when ChatGPT is providing an answer. Results show that ChatGPT can provide answers that are comparable to those of human experts in terms of accuracy and fluency. Megahed et al. [4] explore how generative AI models such as ChatGPT can be used in SPC practice, education, and research. Through an exploratory study, the authors analyze the potential applications of ChatGPT in various contexts and discuss the implications of its use. The authors conclude that ChatGPT has potential to be used in SPC practice, education, and research, but caution that it should be used with care to ensure ethical considerations are considered. Omar et al. [5] examines the current state of chatbot technology for knowledge graphs and proposes future directions for improvement. It compares ChatGPT, a recently developed model, to traditional question-answering approaches. The authors found that ChatGPT outperforms traditional methods in terms of accuracy and response time. Susnjak et al. [6] presents a prescriptive learning analytics framework that combines predictive modelling and explainable AI with prescriptive analytics and chat GPT. The framework is composed of four components: predictive modelling, explainable AI, prescriptive analytics, and chat GPT. The paper concludes that ChatGPT has potential to be a disruptive technology, but further research is needed to understand user sentiment and trust in the system. Jeblick et al. [7] explore the use of ChatGPT, a simplified natural language processing (NLP) system, to generate simplified radiology reports. The authors conducted an exploratory case study with a group of radiologists and medical students to evaluate the effectiveness of ChatGPT in producing accurate and understandable reports. The results showed that ChatGPT was able to generate reports that were both accurate and easy to understand, with most participants rating them as “very good” or “excellent”. The authors conclude that ChatGPT is a promising tool for simplifying radiology reports, making them easier for patients to understand. Tang et al. [8] present a pilot evaluation of two artificial intelligence (AI) models, ChatGPT and DALL-E 2, on decision making and spatial reasoning tasks. The results show that both models can successfully complete the tasks with high accuracy. However, ChatGPT outperformed DALL-E 2 in terms of accuracy and speed. The authors conclude that AI models such as ChatGPT and DALL-E 2 can be used to improve decision making and spatial reasoning capabilities in various applications. Subaveerapandiyan et al. [9] examines the opinions of netizens, academicians, and information professionals about artificial intelligence (AI) with special reference to ChatGPT. However, there were concerns about the potential for misuse of AI and its impact on privacy. Zhou et al. [10] provide a comprehensive survey of pretrained foundation models, from BERT to ChatGPT. The authors also discuss the challenges and opportunities for future research in this field. They provide a summary of the current state-of-the-art pretrained foundation models and their potential applications. Teo et al. [6] explore the use of two natural language processing (NLP) models, BERT and ChatGPT, for sentiment analysis of scientific literature on Lyme disease. The authors found that both models achieved good performance in terms of accuracy and F1 score. They also found that BERT outperformed ChatGPT in terms of precision, recall, and F1 score. The authors concluded that both models can be used for sentiment analysis of scientific literature on Lyme disease. Bang et al. [11] present a comprehensive evaluation of ChatGPT, a multitask, multilingual, multimodal chatbot. The evaluation focuses on three main aspects: reasoning, hallucination, and interactivity. The authors conducted experiments to measure the performance of ChatGPT in English and Chinese on various tasks such as question answering, dialogue generation, and natural language understanding. The results showed that ChatGPT achieved state-of-the-art performance in all tasks. Additionally, the authors discussed the implications of their findings for future research in chatbot development. Tu et al. [12] examine the causal-discovery performance of ChatGPT, a natural language processing model, in the context of neuropathic pain diagnosis. The authors tested ChatGPT on a dataset of patient records from a Swedish hospital and found that it was able to accurately identify causal relationships between symptoms and diagnoses. The results suggest that ChatGPT could be used to improve the accuracy and speed of medical diagnosis in the future. Yang et al. [13] explore the limits of ChatGPT, a transformer-based language model, for query or aspect-based text summarization. The authors conducted experiments on two datasets, the CNN/Daily Mail dataset and the Chinese Gigaword dataset. The results showed that ChatGPT achieved competitive performance compared to other state-of-the-art models. However, it was found that ChatGPT was not able to capture long-term dependencies in the text and had difficulty in generating summaries with multiple aspects. The authors also discussed potential solutions to these issues. Hartmanna et al. [14] examine the political ideology of conversational AI, specifically ChatGPT. Through a series of experiments, the authors found evidence that ChatGPT has a pro-environmental, left-libertarian orientation. The authors suggest that this ideological bias may be due to the data used to train the model or the algorithms used in its development. They conclude by calling for further research into the implications of this bias and how it can be addressed. Qin et al. [15] examines the potential of ChatGPT, a natural language processing task solver, as a general-purpose tool. The authors evaluate the performance of ChatGPT on a variety of tasks, including question answering, dialogue generation, and natural language inference. The results show that ChatGPT can perform well on these tasks and can be used as a general-purpose tool for natural language processing. Pardos et al. [16] examine the learning gain differences between ChatGPT, a natural language processing-based automated tutoring system, and human tutors in providing algebra hints. The study was conducted by Zachary A. Pardos from the Berkeley School of Education at the University of California, Berkeley, USA, and Shreya Bhandari. Results showed that ChatGPT outperformed human tutors in terms of providing algebra hints that were more accurate and helpful to students. Prieto et al. [17] investigate the use of ChatGPT, a natural language processing tool, for the scheduling of construction projects. The authors tested the tool on a real-world project and found that it was able to generate a feasible schedule with minimal user input. They also found that ChatGPT was able to generate more accurate schedules than traditional methods, and that it could be used to reduce the time needed for scheduling tasks. The authors conclude that ChatGPT could be a useful tool for construction project scheduling. White et al. [18] present a Prompt Pattern Catalog (PPC) to enhance prompt engineering with ChatGPT. The PPC is a collection of patterns that can be used to generate effective prompts for conversations with ChatGPT. The authors discuss the importance of prompt engineering and how the PPC can help in this process. They also provide an example of how the PPC can be used to generate effective prompts for a given conversation topic. Huang et al. [19] explore the ethical implications of using ChatGPT, a natural language processing (NLP) model, for conversational AI applications. Through a diagnostic analysis, the authors examine the ethical issues that arise from using ChatGPT in terms of privacy, fairness, and transparency. They also discuss potential solutions to these issues, such as introducing ethical guidelines for developers and users of ChatGPT and developing tools to monitor its use. They suggest further research into the ethical implications of using AI models like ChatGPT in conversational AI applications. Khalil et al. [20] examine the potential of using ChatGPT, a natural language generation system, to detect plagiarism. The authors analyze the performance of ChatGPT on two datasets and compare it to existing plagiarism detection systems. Wei et al. [21] present a novel approach to zero-shot information extraction via chatting with ChatGPT. The authors propose a method that combines the natural language understanding capabilities of ChatGPT with a multi-task learning framework to enable zero-shot information extraction from conversations. Experiments on two real-world datasets show that the proposed method outperforms existing methods in both accuracy and speed. The results demonstrate the effectiveness of the proposed approach for zero-shot information extraction. Huang et al. [22] examine the potential and limitations of ChatGPT, a natural language processing model, in detecting implicit hate speech. The authors conclude that while ChatGPT can be a useful tool for detecting explicit hate speech, it is not suitable for detecting implicit hate speech and should be used in conjunction with human annotators to ensure accuracy. Guo et al. [23] present a novel approach to semantic communications with ordered importance using ChatGPT. The authors propose a method that uses an encoder-decoder framework to generate responses with ordered importance. The proposed model is evaluated on two datasets and achieves state-of-the-art performance in terms of both automatic and human evaluation metrics. The results demonstrate the effectiveness of the proposed approach in generating meaningful and informative responses with ordered importance. Krügel et al. [24] examine the moral authority of ChatGPT, a natural language processing model. It explores the implications of using such models in ethical decision-making and discusses the potential for ChatGPT to be used as a moral authority. The authors analyze the ethical implications of using ChatGPT in various scenarios and discuss how it could be used to provide advice on ethical issues. They conclude that ChatGPT has potential to be used as a moral authority, but that further research is needed to understand its limitations and capabilities. Frieder et al. [25] examine the mathematical capabilities of ChatGPT, a natural language processing model. The authors conducted experiments to evaluate the model's ability to answer questions related to basic arithmetic, algebra, and calculus. They found that ChatGPT was able to accurately answer simple arithmetic questions but struggled with more complex algebraic and calculus problems. The authors also found that ChatGPT was able to understand and respond to questions in a conversational manner. Overall, the results suggest that ChatGPT has some potential for use in educational settings. Chen et al. [26] present a novel end-to-end approach for generating humorous titles from scientific abstracts. The authors use a transformer-based model to generate titles that are both grammatically correct and humorous. Sierra et al. [27] examine the linguistic ambiguity of ChatGPT, a natural language processing model developed by dezzai and the University Complutense of Madrid (UCM). The authors analyze the model's ability to recognize and resolve ambiguities in language, such as homonyms and polysemy. They also discuss how ChatGPT can be used to improve natural language understanding in chatbots and other applications. They provide recommendations for further research into linguistic ambiguity analysis in ChatGPT. Belouadi et al. [28] present a novel approach to end-to-end style-conditioned poetry generation with token-free language models Experiments show that GPT5 outperforms existing models in terms of both quality and diversity of generated poems. Furthermore, the model can generate poems in different styles, demonstrating its ability to capture stylistic features of the data. Hendy et al. [29] present a comprehensive evaluation of GPT models for machine translation. The authors compare the performance of GPT models to other existing machine translation models, such as Transformer and LSTM. They evaluate the models on two language pairs: English German and English French. The results show that GPT models outperform the other models in terms of BLEU scores, while also providing faster inference times. The authors also discuss potential applications of GPT models in machine translation and conclude that they are a promising approach for this task. Borji et al. [30] This paper by Ali Borji of Quintic AI presents a categorical archive of ChatGPT failures. It gives a summary of the different kinds of mistakes that might happen when utilising ChatGPT, a natural language processing model, and offers advice on how to fix them. The significance of knowing how to use ChatGPT and the environment in which it is used are also covered in the study. With the help of ChatGPT and LLaMA, researchers may interact with their data in a conversational style and automatically produce research papers from unprocessed data, making the process of doing scientific research simpler and more effective.

3.3 AI Modelling Datasets

3.3.1 ChatGPT Software Testing Dataset

The ChatGPT Software Testing dataset is a collection of conversations between humans and chatbots. Its purpose is to aid in the performance testing and enhancement of chatbot apps. Furthermore, it might be difficult to gauge the success of a discussion because it depends on how well the user comprehends the chatbot's response. Jalil et al. [31] examine the potential of using ChatGPT, a natural language processing technology, to improve software testing education. It discusses the promises and perils of using ChatGPT in this context, including its potential to enhance student engagement and reduce instructor workloads, as well as the risks of relying too heavily on automated systems. The authors also provide recommendations on how to use ChatGPT in software testing education. Conversations between people and chatbots are included in the Human ChatGPT Comparison Corpus dataset. It was developed to assess how well various chatbot models performed in NLP tasks. The dataset is made up of exchanges between chatbots and people that were gathered from a variety of places, including Reddit, Twitter, and other online discussion boards. This dataset's objective is to serve as a baseline for comparing the effectiveness of various chatbot models in NLP tasks. Researchers can learn which model works best in specific settings by comparing the performance of several models on this dataset. Additionally, new chatbot models that are better suited for activities or applications can be created using this dataset.

3.3.2 Human ChatGPT Comparison Corpus Dataset

Conversations between humans and chatbots are included in the Human ChatGPT Comparison Corpus dataset, which was compiled from a number of sources. Each talk is assigned a score that reflects how well it went. This rating is based on details

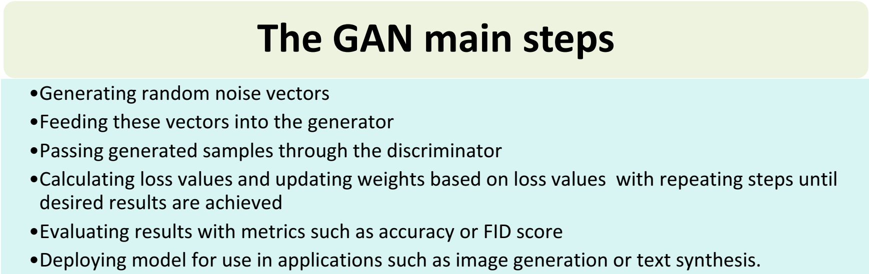

Fig. 3.2 The main steps of GAN architecture

including how long the conversation lasted, how many turns each person took, and if it finished satisfactorily. The lack of real-world data in this dataset, where all talks are generated by current chatbot models or human simulations, is a drawback. Additionally, it doesn't offer any information about how effectively a model functions when engaging with real people in realistic situations because it only includes chats between humans and chatbots.

3.4 AI Approaches

3.4.1 Generative Adversarial Networks (GANs)

Unsupervised learning is accomplished using generative adversarial networks (GANs), an artificial intelligence (AI) model. They are made up of a generator and a discriminator, two neural networks that compete with one another to produce data that seems plausible enough to trick the discriminator into believing it is real. The discriminator then analyses the properties of the created data as illustrated in Fig. 3.2 to differentiate between actual and generated data. If the discriminator is tricked, it gives the generator feedback so that it can do better in subsequent iterations.

3.4.2 Variational Autoencoders (VAEs)

VAEs, which are a type of generative model used in AI modeling, consist of two neural networks: an encoder and a decoder. Their purpose is to learn the underlying structure of data. The encoder compresses input data into a latent space representation, while the decoder reconstructs the data from this latent space representation, as illustrated in Fig. 3.3).

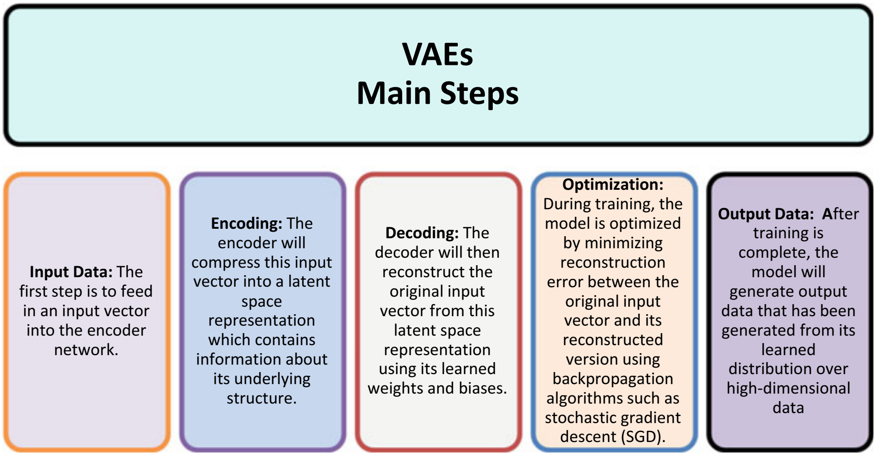

Fig. 3.3 VAEs model main steps

3.4.3 *Autoregressive Models (ARMs)*

Autoregressive models (ARMs) are a type of AI model that utilize past data to predict future values. They are commonly utilized in natural language processing (NLP) applications such as text summarization, machine translation, and chatbots, as illustrated in Fig. 3.4. They create predictions about future values by using a sequence of past values to forecast the following value in the sequence.

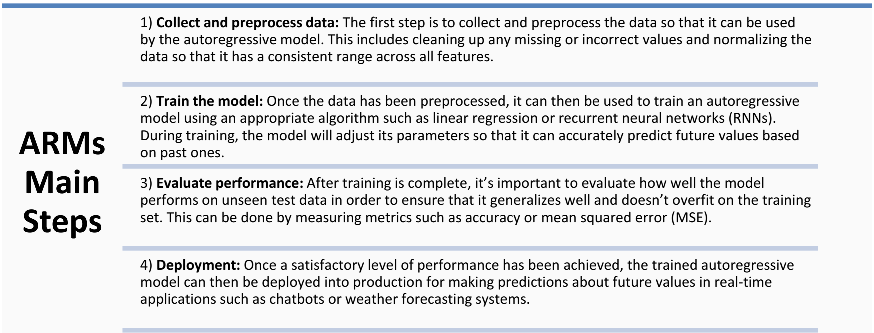

Fig. 3.4 ARMs model main steps

3.4.4 Flow-Based Generative Models (FBGMs)

FBGMs are advantageous for producing realistic data for applications such as image generation, text generation, and audio synthesis, as well as for unsupervised learning tasks like anomaly detection. Additionally, they can be utilized for generative modeling tasks like VAEs. However, FBGMs require a significant amount of training data to generate convincing outputs. The key steps involved in using flow-based generative models are: (1) Preprocessing data; (2) Defining the model; (3) Training the model; (4) Making inferences; (5) Evaluating the model; (6) Deploying the model.

3.4.5 Recurrent Neural Networks (RNNs)

Recurrent Neural Networks (RNNs) are a type of artificial neural network utilized in AI modeling. They are specifically designed for processing sequences of data, such as text, audio, or video. RNNs have numerous applications, including natural language processing (NLP), speech recognition, image captioning, and machine translation. Examples of RNNs include ChatGPT and LLaMA. RNNs employ a type of memory called long short-term memory (LSTM) to retain information from previous inputs, enabling the network to learn patterns in the data over time.

3.4.6 Generative Stochastic Networks (GSNs)

Generative Stochastic Networks (GSNs) are a type of AI model that utilizes deep learning and probabilistic graphical models to generate new data from existing data. GSNs are commonly used in NLP applications like chatbots, machine translation, and text-to-speech systems. These networks are trained on large datasets of text or other data and can subsequently produce new data that resembles the original dataset. Furthermore, GSNs may not be able to generate entirely novel data; instead, they may only be capable of producing variations on existing data.

3.4.7 Generative Moment Matching Networks (GMMNs)

GMMN is a generative model used in AI modeling that combines deep learning and reinforcement learning techniques to generate natural language responses. It is commonly employed in tasks such as chatbot conversations, dialogue generation, and question answering. GMMN functions by initially encoding the input text into a vector representation utilizing an encoder network. This vector representation is

Table 3.1 The hyperparameters for LLMA and ChatGPT

Type	Dimension	*n* heads	*n* layers	Learning rate	Batch size	*n* tokens
LLaMA	4096	32	32	3.0^{e-4}	4 M	1.0 T
ChatGPT	768	12	12	0.00002	32	50,000

then utilized by a decoder network to generate a response based on the context of the conversation.

3.4.8 Deep Convolutional Generative Adversarial Networks (DCGANs)

Deep Convolutional Generative Adversarial Networks (DCGAN) are a subclass of generative adversarial networks (GAN) that create new data from existing data using convolutional neural networks. It is a kind of method for unsupervised learning that can be used to produce accurate pictures, movies, and other kinds of data. AI modelling applications like ChatGPT and LLaMA leverage DCGANs. A generator and a discriminator are the two neural networks that make up a DCGAN. The two networks operate in an adversarial manner, with the generator attempting to deceive the discriminator into believing that its generated data is genuine, while the discriminator seeks to differentiate between real and fake data (Table 3.1).

3.5 Chat GPT-3 and LLaMA-I Examples

3.5.1 Chat GPT-3

Question: How do I send an HTTP request in Javascript?

Answer:

```
// Create an XMLHttpRequest object
var xhr = new XMLHttpRequest();

// Open a connection to the server
xhr.open('GET', 'http://www.example.com/data.json', true);

// Set up a handler for when the request finishes
xhr.onload = function () {

 // Check if the request was successful
 if (xhr.status === 200) {

  // If successful, process the response data (e.g., parse JSON)
  var data = JSON.parse(xhr.responseText);

  // Do something with the data here...

 } else {

  // If unsuccessful, log the error code and message
  console.log('Error: ' + xhr.status + ' - ' + xhr.statusText);

 }
};
```

Question: Write a regex to remove all the HTML tags in a python string.

Answer:

```
import re

regex = re.compile(r'<[^>]*>')
string = '<html><body><p>Hello World!</p></body></html>
result = regex.sub('', string)
print(result) # Hello World!
```

3.5.2 LLaMA-I

In this section, we represent some examples of generations obtained with LLaMA-I that are related with computer science tasks [1].

Question: How do I send an HTTP request in JavaScript?
Answer:

Here's an example of how to make a GET request using the JS HTTP API:

```
var request = new XMLHttpRequest();
request.open('GET', '/url/to/resource', true);

request.onload = function() {
    if (request.status >= 200 && request.status < 400) {
        // Success!
    } else {
        // Error!
    }
};

request.send();
```

Question: Write a regex to remove all the HTML tags in a python string.
Answer:

```
import re
def removeHtmlTags(text):
    return re.sub('<[^>]*>', '', text)
```

3.6 Discussion and Conclusion

ChatGPT is a large language model that can understand natural language input and produce suitable answers based on its comprehension of the conversation. It was trained using large datasets of conversations and can be used for tasks like text summarization, language translation, and story creation. Researchers can use ChatGPT to analyze large datasets of conversations, gain insights into how people interact with each other and with computers, and develop new applications or technologies. However, ChatGPT requires big datasets of discussions and a lot of processing power to produce reliable results. Despite these challenges, ChatGPT outperforms conventional techniques for evaluating natural language interactions. In a study involving three construction companies, ChatGPT was found to be an effective solution for project scheduling that improved efficiency and cost savings while providing an intuitive user interface. ChatGPT and related generative AI can also be used to aid computer scientists in understanding how artificial intelligence functions, which could enhance current AI systems or create new ones.

Availability of Data and Materials There is no applied data.

Competing Interests There is no conflict of interest.

Funding There is no conflict of funding.

Authors' Contributions The researchers participated in all parts of the research equally.

Acknowledgements I would like to thank the ChatGPT for providing some important information., Thanks to the editors and reviewers.

References

1. Touvron, H., et al.: LLaMA: Open and Efficient Foundation Language Models [online]. Available https://github.com/facebookresearch/xformers
2. Bošnjak, M., et al.: SemPPL: predicting pseudo-labels for better contrastive representations, Jan 2023 [online]. Available http://arxiv.org/abs/2301.05158
3. Guo, B., et al.: How Close is ChatGPT to Human Experts? Comparison Corpus, Evaluation, and Detection [online]. Available https://chat.openai.com/chat
4. Megahed, F.M., Chen, Y.-J., Ferris, J.A., Knoth, S., Jones-Farmer, L.A.: How Generative AI models such as ChatGPT can be (Mis)Used in SPC Practice, Education, and Research? An Exploratory Study, Feb 2023 [online]. Available http://arxiv.org/abs/2302.10916
5. Omar, R., Mangukiya, O., Kalnis, P., Mansour, E.: ChatGPT Versus Traditional Question Answering for Knowledge Graphs: Current Status and Future Directions Towards Knowledge Graph Chatbots, Feb 2023 [online]. Available http://arxiv.org/abs/2302.06466
6. Susnjak, T.: Applying BERT and ChatGPT for Sentiment Analysis of Lyme Disease in Scientific Literature, Feb 2023 [online]. Available http://arxiv.org/abs/2302.06474
7. Jeblick, K., et al.: ChatGPT Makes Medicine Easy to Swallow: An Exploratory Case Study on Simplified Radiology Reports, Dec 2022 [online]. Available http://arxiv.org/abs/2212.14882
8. Tang, Z., Kejriwal, M.: A Pilot Evaluation of ChatGPT and DALL-E 2 on Decision Making and Spatial Reasoning.
9. Subaveerapandiyan, A., Vinoth, A., Tiwary, N.: Netizens, Academicians, and Information Professionals' Opinions About AI With Special Reference To ChatGPT [online]. Available https://digitalcommons.unl.edu/libphilprac
10. Zhou, C., et al.: A Comprehensive Survey on Pretrained Foundation Models: A History from BERT to ChatGPT, Feb 2023 [online]. Available http://arxiv.org/abs/2302.09419
11. Bang, Y., et al.: A Multitask, Multilingual, Multimodal Evaluation of ChatGPT on Reasoning, Hallucination, and Interactivity, Feb 2023 [online]. Available http://arxiv.org/abs/2302.04023
12. Tu, R., Ma, C., Zhang, C.: Causal-Discovery Performance of ChatGPT in the context of Neuropathic Pain Diagnosis, Jan 2023 [online]. Available http://arxiv.org/abs/2301.13819
13. Yang, X., Li, Y., Zhang, X., Chen, H., Cheng, W.: Exploring the Limits of ChatGPT for Query or Aspect-based Text Summarization, Feb 2023 [online]. Available http://arxiv.org/abs/2302.08081
14. Hartmann, J., Schwenzow, J., Witte, M.: The political ideology of conversational AI: converging evidence on ChatGPT's pro-environmental, left-libertarian orientation
15. Qin, C., Zhang, A., Zhang, Z., Chen, J., Yasunaga, M., Yang, D.: Is ChatGPT a General-Purpose Natural Language Processing Task Solver? Feb 2023 [online]. Available http://arxiv.org/abs/2302.06476

16. Pardos, Z.A., Bhandari, S.: Learning Gain Differences Between ChatGPT and Human Tutor Generated Algebra Hints, Feb 2023 [online]. Available http://arxiv.org/abs/2302.06871
17. Prieto, S.A., Mengiste, E.T., García De Soto, B.: Investigating the use of ChatGPT for the scheduling of construction projects
18. White, J., et al.: A Prompt Pattern Catalog to Enhance Prompt Engineering with ChatGPT, Feb 2023 [online]. Available http://arxiv.org/abs/2302.11382
19. Zhuo, T.Y., Huang, Y., Chen, C., Xing, Z.: Exploring AI Ethics of ChatGPT: A Diagnostic Analysis, Jan 2023 [online]. Available http://arxiv.org/abs/2301.12867
20. Khalil, M., Er, E.: Will ChatGPT get you caught? Rethinking of Plagiarism Detection [online]. Available https://www.ithenticate.com/
21. Wei, X., et al.: Zero-Shot Information Extraction via Chatting with ChatGPT, Feb 2023 [online]. Available http://arxiv.org/abs/2302.10205
22. Huang, F., Kwak, H., An, J.: Is ChatGPT better than Human Annotators? Potential and Limitations of ChatGPT in Explaining Implicit Hate Speech, Feb 2023 [online]. Available http://arxiv.org/abs/2302.07736
23. Guo, S., Wang, Y., Li, S., Saeed, N.: Semantic Communications with Ordered Importance using ChatGPT, Feb 2023 [online]. Available http://arxiv.org/abs/2302.07142
24. Krügel, S., Ostermaier, A., Uhl, M.: The moral authority of ChatGPT.
25. Frieder, S., et al.: Mathematical Capabilities of ChatGPT, Jan 2023 [online]. Available http://arxiv.org/abs/2301.13867
26. Chen, Y., Eger, S.: Transformers Go for the LOLs: Generating (Humourous) Titles from Scientific Abstracts End-to-End, Dec 2022 [online]. Available http://arxiv.org/abs/2212.10522
27. Ortega-Martín, M., García-Sierra, Ó., Ardoiz, A., Álvarez, J., Armenteros, J.C., Alonso, A.: Linguistic ambiguity analysis in ChatGPT, Feb 2023 [online]. Available http://arxiv.org/abs/2302.06426
28. Belouadi, J., Eger, S.: ByGPT5: End-to-End Style-conditioned Poetry Generation with Token-free Language Models, Dec 2022 [online]. Available http://arxiv.org/abs/2212.10474
29. Hendy, A., et al.: How Good Are GPT Models at Machine Translation? A Comprehensive Evaluation, Feb 2023 [online]. Available http://arxiv.org/abs/2302.09210
30. Borji, A.: A Categorical Archive of ChatGPT Failures, Feb 2023 [online]. Available http://arxiv.org/abs/2302.03494
31. Jalil, S., Rafi, S., LaToza, T.D., Moran, K., Lam, W.: ChatGPT and Software Testing Education: Promises & Perils, Feb 2023 [online]. Available http://arxiv.org/abs/2302.03287

Chapter 4
An Effective Traffic Guidance and Support for Emergency Vehicles Using RFID Technology

P. H. V. Sesha Talpa Sai, Nandakishore Anand, Akuthota Viswajeeth, M. S. Nirmal Raj, R. Ajith Raj, and Potnuru Srikar

Abstract In India Emergency Vehicles like Ambulances, Police Vehicles, Firemen, Disaster Management vehicles and so on are dealing with issue every day because of the gridlock at the traffic lights in the vast majority of the urban communities which prompts issues like passing because of rescue vehicle delay, slow methodology at crime location or at mishap site and so on. To handle this issue the development is to utilize RFID (Radio Frequency ID) tag and peruse for detecting the coming emergency vehicle from a sufficient distance and giving an earlier traffic freedom by managing the traffic signals. In complex circumstance like numerous EVs at same intersection from same or different bearing, higher gridlock rate and so forth. The artificial intelligence calculation is utilized by taking the contributions from RFID reader. The excellent consideration is given to the gadget which can be created by the reconciliation of RFID arrangement and Lo-Ra innovation with the fundamental regulator board bringing about productive execution in rush hour gridlock the executives for EVs without uncovering higher costs.

P. H. V. Sesha Talpa Sai (✉) · P. Srikar
Department of Mechanical Engineering, Malla Reddy College of Engineering and Technology, Hyderabad, India

N. Anand · A. Viswajeeth · M. S. Nirmal Raj
School of Electronics and Communication Engineering, Lincoln University College, Kuala Lumpur, Malaysia

R. Ajith Raj
Department of Aerospace Engineering, Karunya Institute of Technology and Sciences, Coimbatore, India

P. H. V. S. Talpa Sai et al. (eds.), *Intelligent Manufacturing and Energy Sustainability*, Smart Innovation, Systems and Technologies 372,
https://doi.org/10.1007/978-981-99-6774-2_4

4.1 Introduction

Emergency vehicles (EV) like ambulances, fire engines, police vans for the most part need to cross a traffic signal n number of times prior to arriving at the expected objective however frequently we find, the EV's neglect to arrive at the objective in time in light of weighty traffic blockage at traffic signals with no real way to get the traffic inside brief period free from time. This has prompted a ton of bombed salvage tasks and cost many lives.

We ordinarily view as the majority of the emergency vehicles relying upon the ordinary sources like alarms, emergency blazing lights to arrive at the objective yet will not have the option to clear the traffic preceding their methodology towards the traffic intersection. There are likewise different variables that become an integral factor while moving toward a traffic signal like individuals under disarray, individuals with disabled hearing, different wellsprings of gigantic commotions and some more. These elements could have an outrageous cost for the emergency circumstance.

Alongside everyday expanding populace and in this way expanding traffic blockage even with the most complex traffic frameworks, there are still high possibilities of EV cannot arrive at the objective in time. These circumstances actually request an answer for the emergency vehicles. There have been numerous arrangements that have recently proposed in regards to the traffic leeway for emergency vehicles, however the emergency benefits actually face challenges in arriving at their objections which just demonstrates that the arrangements probably won't have been adequately proficient.

4.2 Background of the Research

Even though various researchers have worked on this topic still there is a demand to make the model more reliable and accurate. This strategy looks at the versatile adjusting calculation to make a bunch of plan boundaries of two well- characterized modules. PC reproduction result are given, showing that the network execution regarding the everyday mean speed, which is achieved by the proposed versatile enhancement system, is essentially better compared to the first TUC Framework for the situation in which the-previously mentioned plan boundaries are fine together with flawlessness by the framework activity [1]. By using a minimal amount of cooperative memory, the framework generates the three road case designs of void road case, usual road case, and crowded road case. Using a stream of images that are independent from the road video cameras, the programme may decide on a variety of environmental road cases [2]. To deal with blockage in metropolitan traffic stream through cutting edge computerized reasoning methods is a significant examination region. Different smart and approach have been created utilizing lush figuring strategies to handle with this issue. This paper is an endeavor towards returning to such move toward in creating current traffic control systems [3].

This study center around the use of RFID as a method of traffic stream identification, which communicates assortment data associated with traffic stream directly to a control framework utilizing a RS 232 connection point, simultaneously, the sensor breaks down and Judges the data utilizing an expansion calculation intended for controlling traffic progression. Furthermore, it can likewise successfully control traffic stream while lessening traffic defer time and keep up with the normal traffic progression [4]. The main goal of this framework is to reduce road congestion by allowing emergency vehicles to arrive at a certain location without having to stop anywhere until the assignment is reached. This framework combines Lab View programming and RFID technology. The connected emergency car RFID tag is scanned by the RFID reader, which then sends the information to the modified tiny regulator LPC 1768H with the help of the added C instructions. The indicator won't turn red until the other reader in a different course recognizes a tag that looks identical [5].

Other researchers used ultrasonic sensors to measure the thickness of the traffic, but this method has more drawbacks because it is particularly sensitive to temperature variations and has difficulties reading reflection from delicate, bent, slight, and small objects [6, 7]. In addition, it will detect anything that comes within its range, including people, animals, and other objects. In our study, RFID is used to measure the volume of traffic; it simply looks for vehicles having RFID tags in order to accurately calculate the volume of traffic [8].

In this study, they suggest the LabVIEW simulation for time-based traffic light control. The truth is that the clock doesn't care whether there is high or low traffic flow; it will still run at the appointed time. They only use reproduction as a solution to this. In our paper, we utilize RFID to measure the traffic thickness. Depending on the traffic thickness, the sign timing will be altered. In addition, we employ reproduction in LabVIEW and equipment execution using my RIO to handle this. The picture handling approach comprises edge detection, changing RGB to grayscale, and other functions. Therefore, it is complicated when used to continuous, but in our work, we use RFID to measure the thickness, which is a simple and accurate method in comparison to picture handling [9, 10].

The current development conquers the current issues and gives a greatly improved method for clearing traffic regardless of how serious the clog might be, the creation defeats even the most uncommon instances of traffic blockage which stretch out as much as a few kilometers out and out. Since we are utilizing radio waves we have long scope of transmission that could be conceivable with a right blend of receiving wires and RFID frameworks. The RFID framework utilized in the creation is a mix of RFID tag that is introduced in the emergency vehicle as well as the reader at the traffic signal. The significant part of the creation which distinguishes itself from the remainder of comparable licenses involving RFID for traffic leeway is that our creation is coordinated with an improvement board which runs under the choice tree calculation thusly can manage complex circumstances where multiple emergency vehicles are moving toward a convergence and in the extended traffic predicaments. The improvement board is the focal piece of our gadget associated with RFID Reader and other upheld modules and points of interaction. In most pessimistic scenarios of broadened tough situations, the two-way correspondence is laid out between back to back signals in the characterized range. By this implies the general control of the traffic blockage is in the possession of the emergency vehicle when it comes in nearness to a traffic signal helping to flawlessly traffic freedom. As such the vehicle can arrive at the objective on time.

The innovation likewise considers a wide range of weather patterns dissimilar to certain proposition that utilize IR beams which are impacted by weather patterns. Radio waves are not impacted by any weather conditions changes and are generally dependable and compelling in emergency circumstances which make it ideal.

4.3 Proposed System

Emergency vehicles like ambulances, fire engines, police vans for the most part need to cross a traffic light n number of times prior to arriving at the expected objective yet frequently we find, the EV's neglect to arrive at the objective in time due to weighty gridlock at traffic lights with no real way to get the traffic inside brief period free from time. This has prompted a great deal of bombed salvage tasks and cost many lives.

We usually see as the greater part of the emergency vehicles relying upon the ordinary sources like alarms, emergency blazing lights to arrive at the objective yet will not have the option to clear the traffic preceding their methodology towards the traffic intersection. There are additionally different variables that become possibly the most important factor while moving toward a traffic light like individuals under disarray, individuals with disabled hearing, different wellsprings of tremendous clamors and some more. These variables could have an outrageous cost for the emergency circumstance.

Alongside everyday expanding populace and in this way expanding gridlock even with the most modern traffic executives frameworks, there are still high possibilities of EV cannot arrive at the objective in time. These circumstances actually request an answer for the emergency vehicles. There have been numerous arrangements that have recently proposed with respect to the traffic freedom for emergency vehicles, however the emergency benefits actually face hardships in arriving at their objections which just demonstrates that the arrangements probably won't have been sufficiently effective.

The current development conquers the current issues and gives a vastly improved method for clearing traffic regardless of how serious the blockage might be, the innovation defeats even the most extraordinary instances of gridlock which reach out as much as a few kilometers out and out. Since we are utilizing radio waves we have long scope of transmission that could be conceivable with a right mix of receiving wires and RFID frameworks. The RFID framework utilized in the creation is a blend of RFID label that is introduced in the emergency vehicle as well as the reader at the traffic light. The significant part of the creation which differentiates itself from the remainder of comparable licenses involving RFID for traffic freedom is that our development is coordinated with an improvement board which runs under the choice tree calculation in this way can manage complex circumstances where multiple emergency vehicles are moving toward a crossing point and in the extensive rush hour gridlock tough situations. The improvement board is the focal piece of our gadget associated with RFID Reader and other upheld modules and connection points. In most pessimistic scenarios of broadened predicaments, the two-way correspondence is laid out between successive signs in the characterized range. By this implies the general control of the gridlock is in the possession of the emergency vehicle when it comes in closeness to a traffic light supporting to consistently traffic leeway. As such the vehicle can arrive at the objective on time.

The innovation additionally considers a wide range of weather patterns dissimilar to certain recommendations that utilize IR beams which are impacted by weather patterns. Radio waves are not impacted by any weather conditions changes and are consistently solid and powerful in emergency circumstances which make it ideal.

The capacity to handle traffic circumstances is partitioned into two sorts:

- In the event of single Emergency Vehicle.
- In the event of numerous Emergency Vehicles.

Single Emergency Vehicle:

In this present circumstance, the artificial intelligence calculation doesn't assume a significant part, rather the straightforward RFID correspondence would do the trick for the freedom, as recently determined, the connection between Regulator board and the TAG will aid deferral of the traffic signal by changing from red to a green sign in this manner clearing the traffic.

Multiple Emergency Vehicles:

In this present circumstance the man-made intelligence calculation becomes possibly the most important factor, the regulator board is coordinated "Choice TREE Calculation" which examinations in light of previous boundaries.

The boundaries that will be given to the calculation depend on:

- TIME CONTROL In view of TRAFFIC Clog
- PRIORITY In view of Moving toward DISTANCE.

The framework comprises of essential parts, for example,

- RFID reader
- RFID tag
- Improvement board for supporting artificial intelligence calculation
- Fundamental E-parts
- Lo-Ra tech module.

For better getting it, assuming we consider a numerous traffic signal intersection like a go across Street, and we expect that there are different emergency vehicles drawing closer, for this situation the man-made intelligence calculation becomes possibly the most important factor and focuses on the emergency vehicle which has first moved toward inside the scope of RFID READER while holding off all the excess traffic lights on red, the regulator board likewise ensures that the emergency vehicle has left the reach intersection, if not, it gives a drawn out green sign in the path of approach to ensure the EV has left the intersection.

Subsequent to ensuring that the main EV has left the intersection, it continues on toward the following EV in path from which it has gotten the sign (by means of the RFID TAG on the EV), in this way the regulator load up handles various EV'S simultaneously. The target market for the implementation has been shown in Fig. 4.1 and the working of this technology has been shown in Fig. 4.2. Figures 4.3 and 4.4 shows the design of RFID and it outer cover.

The execution of this work is focused on for traffic the executives, so crisis vehicle on street gets freedom to arrive at their objective quicker than expected with next to no human intercession. The RFID TAG is put on the crisis vehicle and the READER is incorporated into a regulator board which runs on a simulated intelligence calculation which is set close to the traffic light. The regulator board which is outfitted with the artificial intelligence calculation is answerable for clearing the crisis vehicles

Fig. 4.1 Target market

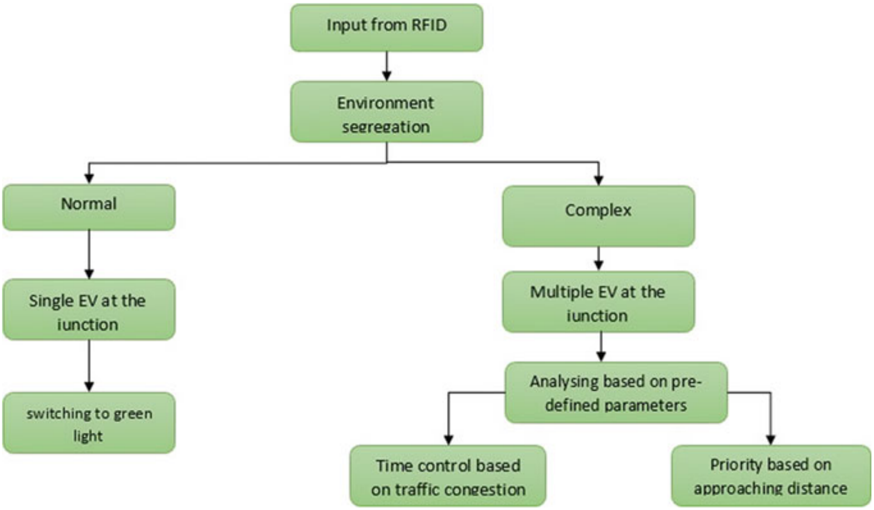

Fig. 4.2 Software overview

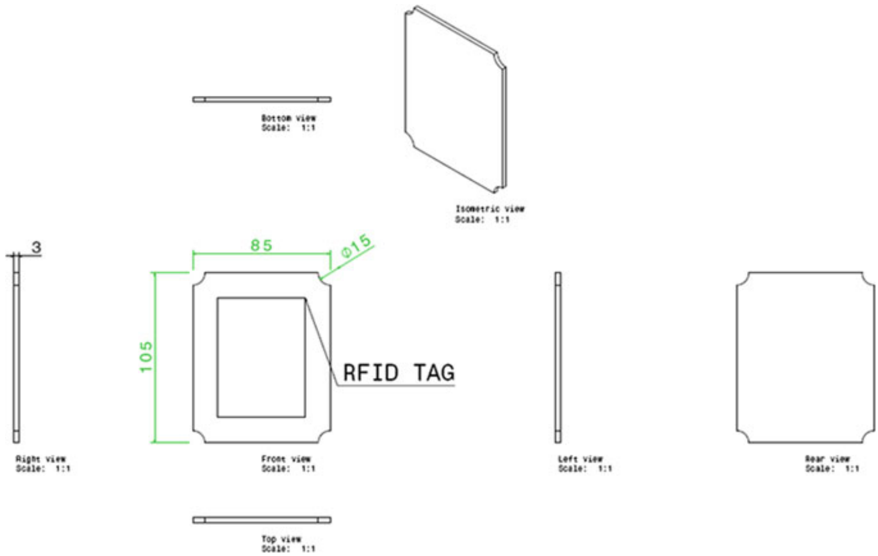

Fig. 4.3 Design of RFID

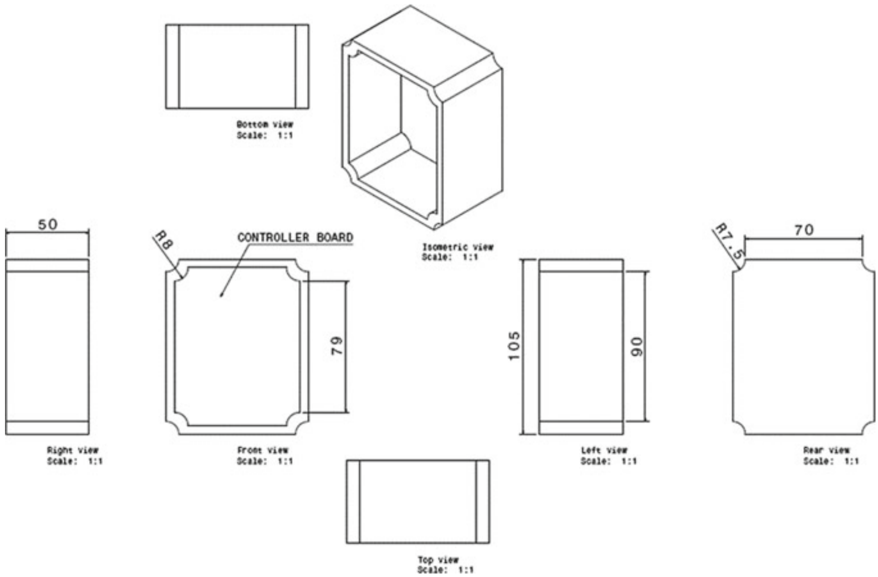

Fig. 4.4 Design of outer frame

when the RFID Label comes extremely close to the READER. In view of the RFID READER'S feedback the traffic light's guideline will be controlled and helping the earlier traffic leeway on the particular way by changing to green light of the sign. The RFID labels are indicated with special recognizable proof code which makes it more straightforward for the READER to separate between the common and crisis vehicle. The RFID READER in the regulator board can take in various data sources like distance, speed, position which will help in breaking down complex conditions.

Moderate to thickly populated nations deal with issues of gridlock in everyday life. This gridlock is a serious issue for emergency vehicles (EV's) like ambulances, fire engines that need to arrive at the emergency site on time. Despite boisterous alarms while working, the gridlock before a traffic light actually stays to be a significant issue.

4.4 Conclusion

The essential thought this paper is to help emergency vehicles by clearing the traffic a long time before hand during an emergency circumstance. The execution of this idea is focused on for traffic the executives, so emergency vehicle on street gets leeway to arrive at their objective significantly quicker with practically no human intercession. The RFID TAG is put on the emergency vehicle and the READER is incorporated into a regulator board which runs on a simulated intelligence calculation which is set close to the traffic signal. The regulator board which is outfitted with the computer-based intelligence calculation is liable for clearing the emergency vehicles when the RFID TAG comes quite close to the READER. In view of the RFID reader's feedback the traffic sign's guideline will be controlled and supporting the earlier traffic leeway on the separate way by changing to green light of the sign. The RFID tags are determined with novel recognizable proof code which makes it more straightforward for the reader to separate between the conventional and emergency vehicle. The RFID READER in the regulator board can take in numerous data sources like distance, speed, position which will help in dissecting complex conditions.

References

1. Kouveals, A., Aboudolas, K., Kosmatopoulos, E.B., Papageorgious, M., IEEE: Adaptive performance optimization for large-scale traffic control systems. IEEE Trans. Intell. Transp. Syst. **12**(4) (2011)
2. Chinyere, O.U., Francisca, O., Amano, O.E., Computer Science Department, Nnamdi Azikiwe University, Awka, Nigeria Computer Science Department, University of Benin, Benin City, Nigeria: Design and simulation of an intelligent traffic control system. Int. J. Adv. Eng. Technol. (2011)

3. Tahilyani, S., Darbari, M., Shukla, P.K., Department of electronics and communication engineering, Babu Banarais Das University, Licknow: Soft computing approaches in traffic control system. In: Conference on Intelligent Systems and Control
4. Chao, K.-H., Chen, P.-Y., Department of Electrical Engineering, National Chin-Yi University of Technology: An intelligent traffic flow control system based on radio frequency identification and wireless sensor networks. Int. J. Distrib. Sensor Netw.
5. Chandrakanth Sagar, S., Narayana, M.: Ambulance controlled traffic system using RFID technology using lab view simulation. Int. J. RFID Technol. (2014)
6. Madhura, R., Arpitha, A.N., Hemanth Kumar, S.R., Indushree, B.C., Kumar, R.: Density based traffic control system with priority for emergency vehicles. IJSTE Int. J. Sci. Technol. Eng. **3**(12) (2017)
7. Mshelia, D.E., Alkali, A.H., Dada, E.G., Ismail, K.: Design and development of a traffic density detection and signal adjustment system. Asian J. Appl. Sci. Technol (AJAST) **3**(1), 86–98 (2019)
8. Dhiman, A., Kumar, A., Kumar, A., Sokhal, Y., Channi, H.K.: Modelling of traffic light control using LabVIEW. Int. J. Sci. Res. Comput. Sci. Eng. Inf. Technol. IJSRCSEIT **2**(6) (2017). ISSN: 2456-3307
9. Abbas, N., Tayyab, M., Tahir Qadri, M.: Real-time area based traffic density estimation by image processing for traffic signal control system. Int. J. Comput. Appl. **83**(9) (2013)
10. Tahmid, T., Hossain, E.: Density based smart traffic control system using canny edge detection algorithm for congregating traffic information. In: 2017 3rd International Conference on Electrical Information and Communication Technology (EICT), 7–9 Dec 2017

Chapter 5
Analytical Study of the Propagation of GPS Constellation

Sachin Srivastava, Amit Kumar Thakur, Abu Sufiyan, K. Haripriya, and R. Ajith Raj

Abstract Today's scenario is more demanding on the accuracy of position or location so that without wasting time people will reach their place. The current work on the propagation of the Global Positioning System constellation and their prognosis of the service availability necessitates repeating the procedure carried out by each receiver to determine the location of the received source. The information from the ALMANAC is used to calculate the constellation's satellites' positions in an Earth-cantered, Earth-fixed system. The appropriate relations are derived from literature with the help of MATLAB software. Neglect higher-order adjustments offered by ephemerides for initial approximation. This paper also discusses the Geometric Dilution of the Precision curve for various periods of the day to evaluate the accuracy of our Global Positioning System.

5.1 Introduction

For the best positioning system, the Global Positioning System (GPS) is fully operational in the 1960s. Users with the necessary receiving equipment can access accurate, globally accessible, three-dimensional location and velocity information from the GPS. A version of Coordinated Universal Time (UTC) is also broadcast by GPS. The constellation of satellites typically consists of 24 satellites [there are currently 30 satellites] distributed across 6 orbital planes, each with four satellites. Due to the user

S. Srivastava · A. K. Thakur (✉)
Department of Aerospace, Lovely Professional University, Phagwara, Punjab 144001, India
e-mail: amit.25010@lpu.co.in

A. Sufiyan · K. Haripriya
Department of Aeronautical Engineering, Malla Reddy College of Engineering and Technology, Hyderabad, India

R. Ajith Raj
Department of Aerospace Engineering, Karunya Institute of Technology and Sciences, Coimbatore, India

P. H. V. S. Talpa Sai et al. (eds.), *Intelligent Manufacturing and Energy Sustainability*, Smart Innovation, Systems and Technologies 372,
https://doi.org/10.1007/978-981-99-6774-2_5

receivers' passive operation, GPS can serve multiple users (i.e., receive only). The system makes use of the one-way time of arrival (TOA) ranging concept [1, 9, 10].

Dr. Ivan Getting developed a 3-D position-finding method that accommodated the delay in radio signal reception in 1951. Based on that, Russia launched Sputnik in 1957, which successfully reached orbit from Earth it was the first satellite but unfortunately the mission was unsuccessful. This Sputnik allows scientists and researchers to use radio signals and track the satellite's location from the Earth's surface and develop more and more satellite-related technology. The John Hopkins University's APL developed the concept for the Transit satellite system, which could offer navigation for the military as well as commercial also for submarines. In the 1960's they launched the first Transit satellite.

It was suggested in 1966 to use an architecture that would use measurements from four satellites to do away with the need for receivers to include highly accurate clocks. The Department of Defence's attempt to combine the Transit and Timation satellite system's success led to the creation of the NavStar-GPS in 1973. Initiated in 1978, the primary launches culminated in 1993 with the whole constellation of 24 GPS satellites. Science has advanced to the point where each satellite must have its clock, the ability to communicate with ground stations, solid-state microprocessors, computers, and bandwidth utilization strategies to track GPS positions with extreme precision. To increase the accuracy of the NavStar satellites and their use by commercial civilian airlines, 700 tests were carried out on them. GPS underwent several advances in the 1980s and 1990s that allowed it to be used for a variety of purposes. Initially, navigation techniques are used in the car to find the correct location of the destination and provide proper services, later they included these services in shipping, sailing and so many more where society required them. The NAVSTAR GPS is the navigation device of the modern era. It is still in research stage for its validation. According to consumer, estimation and prediction should be precise and it is crucial point [2, 8].

Analysing the viability of using GPS L2C signals with the space service volume (SSV) receiver on satellites in geostationary orbit (GEO) that are part of the satellite-based augmentation system (SBAS) and include signal transmitters in the L1 and L5 bands [3]. The same bands of the SSV GPS-receiving antennas may be affected by augmentation signals from SBAS GEO satellites that are sent in the L1 and L5 frequencies. As a result, the GPS L2C signal is chosen instead of the L1 and L5 band signals for the GPS SSV receiver on SBAS GEO satellites. The different restrictions on space exploration in GEO should be taken into account, unlike ground systems. Before contemplating the use of new Global Navigation Satellite System (GNSS) signals in GEO, a signal feasibility analysis is therefore required.

To increase the positioning precision and accuracy of the receiver in satellite positioning systems, optimization of the navigation satellite constellation and reduction of the observation residuals are typically utilised. To mimic the experiment, observational data from the CAPS and GPS systems are employed. The root mean square of positioning error, improvement percentage, and standard deviation are determined when the number of downlink frequencies varies. The root mean square of positioning error in three dimensions is $1/\sqrt{k}$ of that in a single frequency when the number of descending frequencies is k. Theoretical derivation and empirical results demonstrate that the use of multi-frequency navigation signals can significantly increase the accuracy of satellite location [4].

Particularly true for satellite constellations that provide imaging, communications, and other services that are staged in low Earth orbit. With easier access to space, more and more space-faring organisations are developing constellations of hundreds or thousands of satellites, whereas such large satellite constellations were previously only fielded by a few numbers of governments. A new issue has arisen as a result of this: how to manage satellite inventory effectively. Author suggests using Markov decision process (MDP) models to determine the best fielding strategy for satellites within a constellation based on the current situation in order to solve this problem. The MDP model takes into account a number of stochastic forces, including hardware failure, launch-related issues, and the potential of satellite collisions by leveraging earlier work on managing this risk. The Global Positioning System (GPS), which has about 30 satellites in medium-Earth orbit but necessitates at least 24 for system-level operations, is the system to which we apply our concept. The mathematically ideal steady-state inventory level for the GPS constellation, according to our research, which was conducted completely independently from the GPS sustainment reasoning, is 31 satellites, which supports both the GPS sustainment policy and our suggested model [5].

GPS is a strong tool that gives users access to data they may use to create accurate reports and surveys, measure time precisely, track their location, and do other tasks including mapping, emergency response, transportation, and aerial surveys. The number of available satellites, physical impediments, atmospheric impacts, ephemerides, and most recent technology incorporating artificial intelligence all affect GPS accuracy.

As GPS is following the dual-use method and offers facilities for military and civilian service in the form of Precise Positioning Service (PPS) and Standard Positioning Services (SPS). The PPS gives precise positioning for military service and SPS gives the space-based positioning [1, 9, 10].

5.1.1 Constellation Design

30 satellites make up the constellation arrangement, and they are arranged in such a way that 4 or 5 satellites are fixed in one orbital plane. Normally, the satellite period for one orbit is 11 h, 58 min, or sometimes called half of a sidereal day [6]. Around the equator at a 60-degree angle, the orbits are nearly circular and similarly spaced apart separation having a nominal inclination of 55° about the equatorial plane. The orbital radius is roughly 26,600 km. This constellation of satellites offers users throughout the world the capacity to navigate and determine the time continuously. This illustration opens each orbit, treating it like a ring, and presents it as a plane. The equator on Earth looks similar to a ring that has been unpacked and flat. Each equator on Earth tilted 55° from the equatorial plane of the Earth.

The position of the orbital plane from Earth is obtained by the use of ascending node's longitude, although, the placement of the satellite in the orbital plane is calculated with the mean anomaly. Every orbital plane crosses the equatorial plane at the longitude of the ascending node. The Greenwich meridian is the reference point at which the ascending node's longitude is zero. Nearby the equator, which shows as a reference point, the Mean Anomaly, which describes the angular positions of each satellite within the orbit, is zero.

ALMANAC is the basic information about the overall constellation. It allows for identifying which satellites are visible from a defined user location.

5.1.2 Ephemerides

The ephemerides that each satellite transmits are unique. The validity of each set is limited to 4 h, and new ephemerides can be communicated every 2 h. For accurate satellite orbit calculation, take the higher-order corrections to the standard Keplerian parameter, and the clock settings.

The receiver's Latitude, Longitude, and Altitude can be easily calculated using the Earth-Centered Earth-Fixed (ECEF) Coordinate System. The 0° longitudes towards the x-axis direction, 90° longitudes towards the y-axis direction, and to complete the right-hand coordinate system, the perpendicular of the equatorial plane is showing the geographical north. Here, for describing the inertial axis these three X, Y and Z are enough and it will show all rotational axis also.

Here, Kepler's law will explain the earth's center is in focus and the rest are vacant. The satellite's speed varies with its distance from the earth's center. The closest point in the orbit of the earth, called Perigee, has the highest speed, whereas point Apogee has the lowest speed.

We took into account WGS 84, which offers a model of an ellipsoid that resembles the Earth. As we want to know all the activity of satellites before sending the correct location of users. To determine the location of the satellite we need to apply Newton's Laws for the force acting on it [1, 7] (Fig. 5.1).

$\frac{d^2r}{dt^2} = -\frac{\mu}{r^3}r$ is the statement of a two-body motion of Keplerian's, in which the point-mass Earth is the only force acting on the satellite. The gravitational pull of the Sun and Moon, sometimes known as a third body, is another force at work on satellites. The location and velocity vector of a satellite in a two-body orbit can be determined from the beginning conditions at any moment, even though GPS depends on the accuracy supplied by the two-body motion. The sizing, form, and orientation of an orbit in space, as well as the location of the satellite within an orbit, are determined by six orbital elements.

a Semi-major axis length.

e Eccentricity.

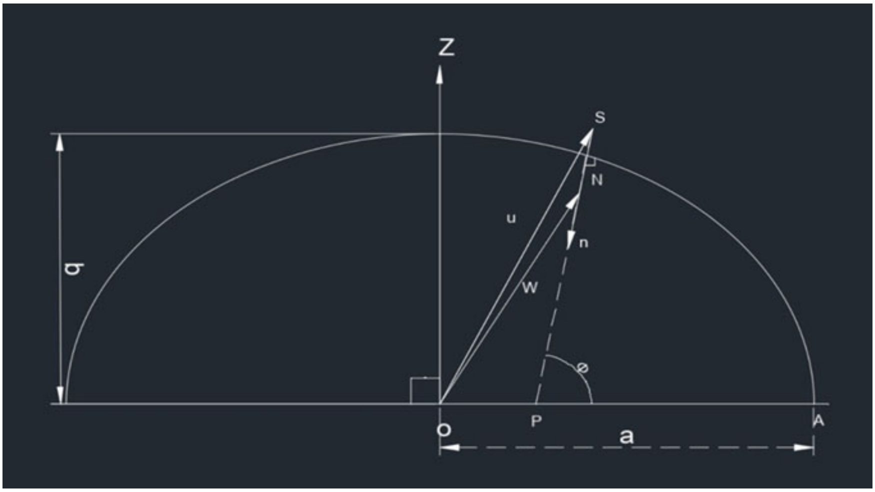

Fig. 5.1 Ellipsoidal model of earth, by Courtesy: Kaplan and Hegarty [1, 8, 9]

i Angle of Inclination.
Ω Right accession of the Ascending Node (RAAN).
ω Argument of Perigee (AOP).

The first five elements provide the Size, Shape, and Orientation of the Orbit in space.

t_p Time value used to locate the satellite in its orbit.

The time at which the satellite passes a specific place is known as the moment it passes another point can be determined because it moves in a relatively predictable manner and follows a schedule.

Except for t_p converting to mean anomaly, satellites transmit GPS almanac and ephemeride data that include osculating Keplerian orbital elements. The message from the GPS ephemerides should be accurate information about the satellite's position and velocity [1, 9, 10].

The procedure (definition through formulas) used by a GPS receiver to obtain the satellite's position vector (x_s, y_s, and z_s) in the ECEF coordinate system is displayed in Table 5.1.

5.2 Results and Discussion

This is how the satellite propagation of GPS constellation and the forecast of the service availability. By using MATLAB coding, obtain the 30-satellite orbit, ground track, and geometry of dilution of precision smoothly and verified by kinds of literature.

Table1 GPS ephemeris and computation of satellite's ECEF position vector, by courtesy Kaplan and Hegarty [1, 9, 10]

1	t_{0e}	Ephemeris reference time
2	$\sqrt{a}$	Semi-major axis in square root
3	e	Eccentricity
4	i_0	The angle of Inclination (at the time t_{0e})
5	Ω_0	Longitudinally ascending node (at weekly epoch)
6	ω	The argument of perigee (at the time t_{0e})
7	M_0	Mean anomaly (at time t_{0e})
8	$\frac{d_i}{d_t}$	Rate of change of angle of Inclination
9	$\dot{\Omega}$	Rate of change of longitude of the ascending node
10	Δn	Mean motion correction
11	$\mathrm{a} = (\sqrt{a})^2$	Semi-major axis
12	$\mathrm{n} = \sqrt{\frac{\mu}{a^3}} + \Delta n$	Corrected mean motion, μ= 398,600.5 × 10^8 m^3/s^2
13	$t_k = t - t_{0e}$	Time from ephemeris epoch
14	$M_k = M_0 + n(t_k)$	Mean anomaly
15	$\sin v_k = \frac{\sqrt{1-e^2 \sin v_k}}{1-e\cos E_k}$	Eccentric anomaly
16	$\cos v_k = \frac{\cos E_k - e}{1-e\cos E_k}$	Eccentric anomaly

5.2.1 30-Satellite Orbit

The satellite's followed path is called the orbit and it coordinates the ability and aim of the sensor which the satellite carried. A satellite constellation is a collection of man-made satellites that function as a unit to support a system. To ensure that at all times at least one satellite is visible anywhere on Earth, a constellation can offer permanent or nearly worldwide coverage. They are positioned in groups of orbital planes and linked to earthly stations all around the world. Additionally, they are employed in inter-satellite communication. 24 satellites are required for the GPS satellite, and they are evenly divided across six orbital planes [11, 12] (Fig. 5.2).

5.2.2 Ground Track

Sometimes called a ground trace, it shows the locus on the Earth's surface just beneath of trajectory of the satellite. Some scientists also called this track suborbital track and it is the vertical projection of the satellite path onto the Earth's surface.

Here, the satellite gives several different ground tracks based on orbital parameters and these parameters defined the sizing, shaping, and location of the orbit which is followed by the satellite.

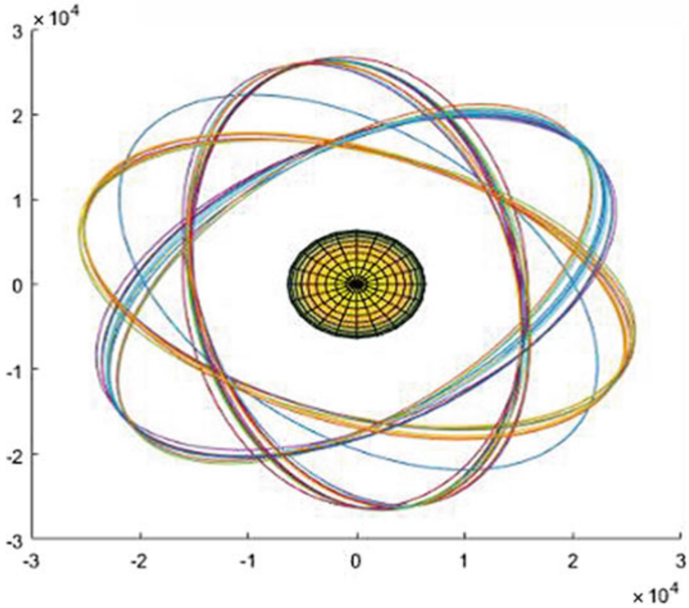

Fig. 5.2 Satellite view

A path along the ground that follows the motion of a hypothetical line connecting the satellite and, hence, the center of the world is what is known as a satellite ground track. Additionally, ground stations could be positioned in the earth's atmosphere or on its surface. Earth stations can transmit with spacecraft by transmitting and receiving radio waves in the Super High Frequency (SHF) or Extremely High Frequency (EHF) bands. The ground track of a satellite can has a range of several shapes depending on the values of the orbital components, which are elements that govern the sizing, type, and positioning of the satellite's orbit. The ground route of satellites frequently has a broad sinusoidal shape (Fig. 5.3).

5.2.3 Geometric Dilution of Precision (GDOP)

Geomatics and satellite navigation engineers use the terms "Dilution of Precision" (DOP) and "Geometric Dilution of Precision" (GDOP) to describe the mathematical influence that navigation satellite geometry has on the accuracy of positional measurements. In general, a GPS receiver can be more exact the more signals it can "see" (spread apart versus near together). The position of the particular satellite is specified in the ephemeris data. But this could be a source of inaccuracy if you don't know where they are precisely at that precise moment. The GPS receiver has an excellent GDOP if the satellites are dispersed over the sky. The GDOP, however, is

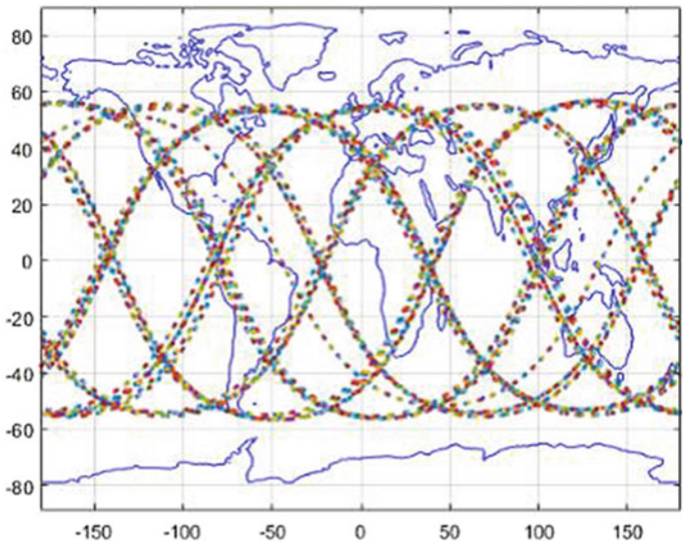

Fig. 5.3 Ground track

inadequate if the satellites are physical approximations. This potentially reduces the accuracy of your GPS positioning by meters.

The position error in the geometry of the satellites is said as Geometric Dilution of Precision (GDOP). And mathematically, it is the ratio of position error to range error. GDOP value is better when the number of satellites is more (Fig. 5.4).

5.3 Conclusion and Future Scope

Nowadays, people are much depending on Global Positioning Systems for their daily life. That's why locating the accurate location, using a Global Positioning System has still had a scientific interest as the precise location is not yet fully achieved. The current approach used in the work gives a useful insight into intensifying the precise location with the number of satellites. As the number of satellites can be accessed for a single location, the geometrical accuracy of the location will be increased due to the reduction of tolerance proximity. Hence the current approach is viable to detect the location with GPS using at least three numbers of satellites, and using four satellites will give a more accurate and precise location which is desired.

For the future, changes in shape, sizing, and location of orbits with the changes in orbital parameters give more accuracy.

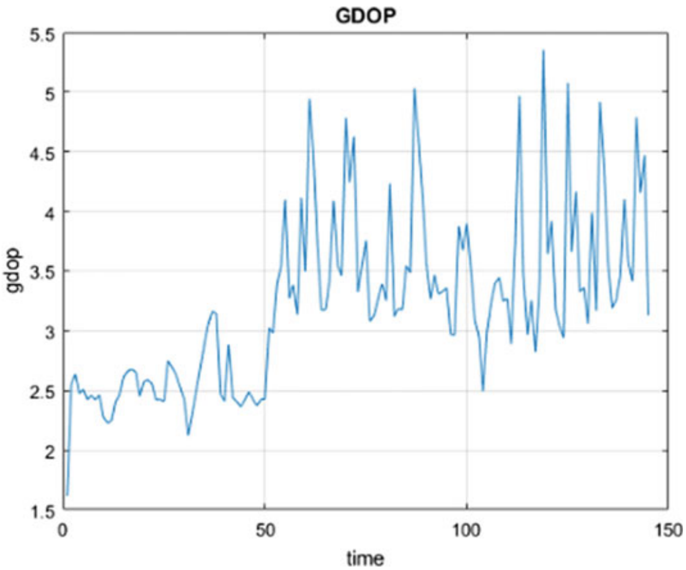

Fig. 5.4 Geometry dilution of precision (GDOP)

References

1. Kaplan, E.D., Hegarty, C., eds.: Understanding GPS/GNSS: Principles and Applications. Artech House (2017)
2. Navstar, G.: Joint Program Office (JPO). GPS NAVETAR User's Overview. YEE-82-009D. GPS JPO (1991). https://doi.org/10.1002/j.2161-4296.1976.tb01853.x
3. Lee, H.B., Kwon, K.H., Won, J.H.: Feasibility analysis of GPS L2C signals for SSV receivers on SBAS GEO satellites. Remote Sensing **14**(21), 5329 (2022)
4. Kong, T., Ma, L., Ai, G.: Research on improving satellite positioning precision based on multi-frequency navigation signals. Sensors **22**(11), 4210 (2022)
5. Kim, R.: Stochastic inventory control modeling for satellite constellations. J. Spacecr. Rocket.Spacecr. Rocket. **57**(3), 612–620 (2020)
6. Bahder, T.B.: GPS for Land Combat Applications: Summary Report of Army Workshop Held at University of North Carolina, 2 and 3 Aug 1995. Army Research Lab Adelphi, MD (1995)
7. Cappellari, J.O., Vélez, C.E., Fuchs, A.J. eds.: Mathematical Theory of the Goddard Trajectory Determination System, vol. 71106. Goddard Space Flight Center (1976)
8. Navstar, G.P.S.: Joint Program Office. NAVSTAR GPS Space Segment/Navigation User Interfaces. Technical Report IS-GPS-200. ARINC Engineering Services, LLC (2004)
9. Battin, R.H.: An Introduction to the Mathematics and Methods of Astrodynamics. AIAA, New York (1987)
10. Van Dierendonck, A.J., Russell, S.S., Kopitzke, E.R., Birnbaum, M.: The GPS navigation message. Navigation **25**(2), 147–165 (1978). https://doi.org/10.1002/j.2161-4296.1978.tb01326.x
11. Ulybyshev, Y.: Satellite constellation design for continuous coverage: short historical survey, current status and new solutions. In: 5th International Workshop on Constellations and Formation Flying (2008)
12. Bancroft, S.: An algebraic solution of the GPS equations. IEEE Trans. Aerosp. Electron. Syst.Aerosp. Electron. Syst. **1**, 56–59 (1985). https://doi.org/10.1109/TAES.1985.310538

Chapter 6
Angular RxJS for E-commerce Development

Swarom Padalkar, Maheshwar D. Jaybhaye, and Sangita M. Jaybhaye

Abstract This paper explores the use of RxJS in combination with Angular for dynamic filtering and sorting in e-commerce websites. It highlights the importance of filtering and sorting in e-commerce and the challenges faced in implementing effective filtering and sorting systems. The paper then explains how RxJS operators such as map, filter, and scan can be used to create responsive and scalable filtering and sorting systems. Additionally, it discusses the advantages of using Angular for e-commerce websites and how it facilitates the implementation of dynamic filtering and sorting systems. Code examples and case studies are provided to demonstrate the effectiveness of using RxJS and Angular for dynamic filtering and sorting in e-commerce.

6.1 Introduction

Angular and RxJS play a significant role in the development of e-commerce applications, offering powerful tools and capabilities for building robust and responsive web applications. Angular, a widely adopted framework for web development, provides a comprehensive set of features and tools for creating scalable and maintainable applications. RxJS, on the other hand, is a reactive programming library that enhances Angular applications by enabling efficient handling of asynchronous events and managing complex data flows.

Hevery and Erickson [1] aforementioned, Angular provides a structured and modular approach to application development, making it suitable for building large-scale e-commerce platforms. It offers a rich set of features, such as component-based architecture, dependency injection, and a powerful templating system, which facilitate the development of dynamic and interactive user interfaces.

S. Padalkar (✉) · M. D. Jaybhaye
COEP Technological University, Pune, India
e-mail: padalkarsj19.prod@coeptech.ac.in

S. M. Jaybhaye
Vishwakarma Institute of Technology, Pune, India

P. H. V. S. Talpa Sai et al. (eds.), *Intelligent Manufacturing and Energy Sustainability*, Smart Innovation, Systems and Technologies 372,
https://doi.org/10.1007/978-981-99-6774-2_6

Kaluža [2], compared Angular with other popular frameworks, including React, to evaluate their suitability for web application development. The study highlights Angular's robustness, maintainability, and extensive ecosystem, making it an excellent choice for complex e-commerce projects.

Bulgakova [3] explored the effectiveness of reactive programming, of which RxJS is a key component, in web development. The study showcases the benefits of reactive programming in handling asynchronous operations, managing state, and composing complex data streams, all of which are crucial aspects of e-commerce application development.

By leveraging the capabilities of Angular and RxJS, e-commerce developers can build feature-rich and responsive applications that provide seamless user experiences, efficient data handling, and real-time updates. These technologies enable the creation of dynamic product catalogs, interactive shopping carts, real-time notifications, and smooth checkout processes.

The study focuses on the use of RxJS for filtering and sorting in e-commerce development, providing practical insights and recommendations for optimizing website performance and enhancing the user experience.

The study also explores the broader applications of reactive programming in web development and the potential for future research in this area.

The study aims to contribute to the field of e-commerce development and provide practical guidance for businesses looking to improve their website functionality and user experience.

6.1.1 Angular for E-commerce Development

Angular is a front-end framework that enables developers to create dynamic, responsive, and intuitive user interfaces. With its built-in components and modules, Angular offers a flexible and scalable framework that is ideal for e-commerce development.

Some of the key features of Angular for e-commerce development include:

1. Dynamic User Interfaces: Angular allows developers to create dynamic and responsive user interfaces that adapt to user input and changes in data.
2. Powerful Shopping Cart Features: Angular provides powerful shopping cart features that enable developers to manage and update shopping carts in real-time.
3. Robust Security Features: Angular provides a range of security features that help protect sensitive user data, including built-in support for HTTPS, CSRF protection, and content security policies [4, 5].

6.1.2 RxJS for E-commerce Development

RxJS is a reactive programming library that enables developers to create complex data streams and manipulate data in real-time. With RxJS, developers can create observable data streams that can be easily managed and transformed. This is particularly useful in e-commerce development, where real-time data updates and dynamic user interfaces are critical. Some of the key features of RxJS for e-commerce development include:

1. Asynchronous Data Management: RxJS enables developers to manage asynchronous data streams and manipulate data in real-time.
2. Reactive Forms: RxJS provides support for reactive forms, which can respond to user input in real-time and provide an interactive user experience.
3. Real-Time Data Updates: RxJS enables real-time data updates, which can be particularly useful in e-commerce development for managing product catalogues, shopping carts, and other critical aspects of the user experience [6].

6.1.3 Significance of Study

E-commerce websites are a critical component of modern business, and optimizing their performance and user experience is crucial for success.

Filtering and sorting functionality is a key feature of e-commerce websites, but traditional approaches can be inefficient and lead to poor user experience.

RxJS offers a reactive programming approach that can handle complex data streams in real-time, making it an ideal solution for dynamic filtering and sorting in e-commerce websites.

By studying the use of RxJS for filtering and sorting in e-commerce development, we can identify best practices and strategies for optimizing performance and enhancing the user experience.

This study can contribute to the broader field of reactive programming and its application in web development, as well as provide practical insights and recommendations for e-commerce businesses looking to improve their website performance and user experience. Some of companies which uses angular for its e-commerce websites are-

1. Google Shopping: Google Shopping is an e-commerce platform developed by Google. The website is developed using Angular and offers online shopping services for various products.
2. Nike: Nike is a well-known sports brand that sells its products online. The website is developed using Angular and provides customers with a range of products to choose from.
3. iStock: iStock is a popular website that provides users with a wide range of stock photos, vectors, illustrations, and videos. The website is developed using Angular and is known for its easy-to-use interface and fast search results.

6.2 Angular and Its Features for E-commerce Development

Angular is a widely used front-end framework for building web applications, including e-commerce websites. It offers a range of features that make it an ideal choice for e-commerce development. In this section, we will explore some of the key features of Angular and their benefits for e-commerce development.

Angular is a TypeScript-based open-source front-end web application platform that was developed by Google. It is a complete rewrite of AngularJS, which is also a front-end framework. Angular uses a component-based architecture, which makes it easier to develop, test, and maintain complex web applications. It is designed to work well with other libraries and tools, such as RxJS, which makes it ideal for e-commerce development [1, 2, 4].

6.2.1 Angular Modules and Components

Angular modules are used to organize related functionality into cohesive blocks of code. They can be used to separate functionality, such as authentication or product management, into discrete modules. Angular components are the building blocks of an Angular application. They are responsible for rendering the user interface and responding to user events. Components can be nested within other components to create complex user interfaces.

6.2.2 Angular Routing and Navigation

Angular offers a powerful routing and navigation system that allows developers to create single-page applications (SPAs) that can handle multiple views and states. This is particularly useful for e-commerce websites, where users may need to navigate through multiple pages to find what they are looking for. Angular routing makes it easy to manage the state of an application and to handle user navigation.

6.2.3 Angular Forms and Templates

Angular offers a range of features for building forms and templates, which are essential for e-commerce websites. Angular forms are built using reactive programming techniques, which makes it easy to manage complex form data and validation. Angular templates are used to define the layout and structure of an application's user interface. They can be used to create dynamic, responsive interfaces that are tailored to the needs of e-commerce websites.

6.2.4 Angular Animations

Angular animations allow developers to create engaging and dynamic user interfaces that can help to increase user engagement and retention. Angular animations can be used to add visual cues and feedback to user interactions, such as hover effects or transitions between pages. This can make an e-commerce website feel more responsive and intuitive, which can help to improve the overall user experience.

In summary, Angular offers a range of features that make it an ideal choice for e-commerce development. Its component-based architecture, powerful routing system, and features for building forms and templates make it easy to create responsive and user-friendly e-commerce websites. Additionally, its support for animations can help to create engaging and dynamic user interfaces that can help to improve user engagement and retention.

6.3 RxJS and Its Features for E-commerce Development

RxJS is a popular reactive programming library that is widely used in web development, particularly with front-end frameworks like Angular. In e-commerce development, RxJS offers several features that can improve the performance, reliability, and user experience of web applications. This section will provide an overview of RxJS and its key features for e-commerce development [7].

RxJS, short for Reactive Extensions for JavaScript, is a library that allows developers to create asynchronous and event-driven applications using observable sequences. RxJS is built on the concept of observables, which represent streams of data that can change over time. Observables can be used to manage complex data flows and handle events such as user input, network requests, and real-time updates [4].

6.3.1 Reactive Programming and Observables

Reactive programming is a programming paradigm that focuses on declarative programming and the propagation of changes. Reactive programming involves using observables to represent data streams and reacting to changes in those streams. Observables can be thought of as a sequence of values that are emitted over time, and subscribers can react to those values as they arrive [3, 4, 6].

6.3.2 RxJS Operators and Functions

RxJS provides a variety of operators and functions that can be used to manipulate and transform observable sequences. Operators like **map()**, **filter()**, and **reduce()** can be used to transform and filter data streams, while functions like **debounceTime()** and **throttleTime()** can be used to control the frequency of emissions. Additionally, RxJS provides utility functions for creating observables from existing data sources, such as **fromEvent()** and **fromPromise()** [3, 8].

6.3.3 Real-Time Data Streams and Updates

One of the key benefits of RxJS in e-commerce development is its ability to handle real-time data streams and updates. With observables, developers can create data streams that update in real-time based on user actions, server responses, or other events. This can enable features like real-time search results, live product updates, and dynamic shopping carts [9].

6.3.4 Use Cases for RxJS in E-commerce Development

RxJS can be used in a variety of ways in e-commerce development. Some common use cases include:

1. Filtering and sorting products based on user preferences.
2. Handling real-time updates for product availability and pricing.
3. Creating dynamic shopping carts that update in real-time.
4. Implementing autocomplete search suggestions for products.
5. Managing complex user input forms with validation and error handling.

6.4 Filtering and Sorting in E-commerce with RxJS

Filtering and sorting allow customers to quickly find the products they need and reduce the amount of time spent searching for them. It is crucial for e-commerce websites to provide an excellent user experience to increase customer satisfaction and conversion rates. According to a study by Baymard Institute [9], 30% of online shoppers abandon their cart due to a complicated checkout process, including difficulties in product searching and filtering. Effective filtering and sorting can help overcome these issues and increase sales [4].

6.4.1 Challenges in Implementing Filtering and Sorting

Implementing filtering and sorting can be challenging due to the large amount of data involved and the need to update the user interface dynamically. Traditional approaches to filtering and sorting often result in slow page loading times and poor user experience. Additionally, designing a filter and sorting system that is both flexible and easy to use can be difficult [4, 5, 10].

6.4.2 Using RxJS for Dynamic Filtering and Sorting

RxJS is a reactive programming library that can be used in conjunction with Angular to manage complex data streams and create dynamic user interfaces. RxJS operators such as map, filter, and scan can be used to filter and sort data in real-time, allowing for a more responsive user experience. RxJS also provides a flexible and scalable approach to filtering and sorting, making it easier to implement and update [4, 5, 10].

6.4.3 Code Example

Here is an example of multiple filters using RxJS in Angular for an e-commerce website:

```
import { Component } from '@angular/core';
import { Observable } from 'rxjs';
import { filter, map, tap } from 'rxjs/operators';
import { ProductService } from './product.service';
@Component({
  selector: 'app-product-list',
  templateUrl: './product-list.component.html',
  styleUrls: ['./product-list.component.css']
})
export class ProductListComponent {
  products$: Observable<any[]>; searchText: string;
  minPrice: number; maxPrice: number;
  selectedCategory: string; selectedBrand: string;
constructor(private productService: ProductService) {
// Initialize products$ with all products from
//ProductService and log them to console using tap
//operator
this.products$ =
this.productService.getProducts().pipe(
    tap(products => console.log('Initial products:', products))
  );
 }
// Filter the products based on user's inputs
filterProducts() {
```

```
  this.products$ =
this.productService.getProducts().pipe(
// Apply map operator to filter the products based on
// name, price, category, and brand and return the
// filtered products
map(products => products.filter(product => {const
nameMatch =
product.name.toLowerCase().includes(this.searchText.toL
owerCase());
const priceMatch = (this.minPrice == null ||
product.price >= this.minPrice) && (this.maxPrice ==
null || product.price <= this.maxPrice);
      const categoryMatch = (this.selectedCategory
== null || product.category === this.selectedCategory);
    const brandMatch = (this.selectedBrand == null
|| product.brand === this.selectedBrand);
    return nameMatch && priceMatch && categoryMatch
&& brandMatch;
  })),
// Apply filter operator to remove the empty products
//array
filter(products => products.length > 0),
// Log the filtered products to console using tap
//operator
  tap(products => console.log('Filtered products:', products))
)}
  resetFilter() {
    this.searchText = '';
    this.minPrice = null;
    this.maxPrice = null;
   this.selectedCategory = null;
    this.selectedBrand = null;
        this.products$ = this.productService.getProducts().pipe(
      tap(products => console.log('Reset products:',
products)))}}
```

Code Output:

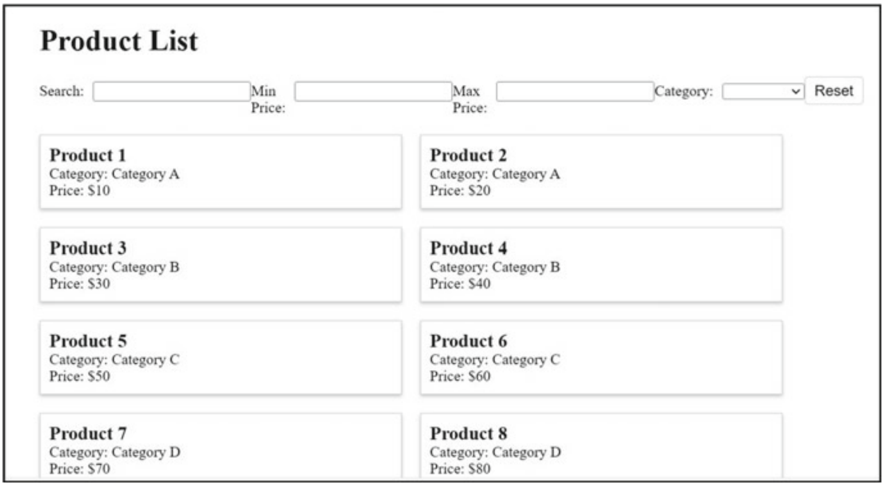

This is an Angular component that displays a list of products and allows the user to filter the list based on various criteria such as product name, price range, category, and brand. The component uses **Observable** to asynchronously load and update the list of products based on the user's filter inputs.

- searchText: a string used to filter products based on their names. It is initialized to an empty string and can be set by the user.
- minPrice: a number used to filter products based on their price. It represents the minimum price and can be set by the user.
- maxPrice: a number used to filter products based on their price. It represents the maximum price and can be set by the user.
- selectedCategory: a string used to filter products based on their category. It represents the selected category and can be set by the user.

selectedBrand: a string used to filter products based on their brand. It represents the selected brand and can be set by the user.

The **ProductListComponent** class is defined as an Angular component and is annotated with the @Component decorator. The component has a template file (product-list.component.html) and a stylesheet file (product-list.component.css) associated with it.

The component has several properties:

- products$—an observable that holds an array of products.
- searchText, minPrice, maxPrice, selectedCategory, selectedBrand—variables that hold the user's input for filtering the products.

The constructor function initializes the products$ observable by calling the getProducts function from the ProductService and passing it through several operators to log the initial products to the console.

The 'filterProducts' function is called when the user applies a filter. It first calls 'getProducts' from the 'ProductService', and then applies several operators to the resulting observable. The 'map' operator is used to filter the products based on the user's input for name, price, category, and brand. 'The filter' operator is used to remove any empty product arrays. The resulting filtered products are logged to the console using the tap operator.

The resetFilter method is called when the user resets the filter. It sets all filter inputs to null and re-initializes the products$ observable with all products from the ProductService. The tap operator is then applied to log the reset products to the console.

Overall, this code defines a component that allows the user to filter products based on their name, price, category, and brand. It uses RxJS operators to create an observable that emits the filtered products and logs them to the console.

6.5 Conclusions

It can be concluded that the use of RxJS in conjunction with Angular for dynamic filtering and sorting in e-commerce websites is highly effective. The study highlighted the importance of filtering and sorting in e-commerce, as well as the challenges faced in implementing effective filtering and sorting systems. Using RxJS operators such as map, filter, and scan, it demonstrated how responsive and scalable filtering and sorting systems can be created. The advantages of using Angular for e-commerce websites were also discussed, particularly its ability to facilitate the implementation of dynamic filtering and sorting systems.

The significance of this study lies in its contribution to the field of e-commerce development and its potential to provide practical insights and recommendations for businesses looking to optimize their website performance and enhance the user experience. However, it is important to note that the study's scope and limitations should be taken into consideration when applying its findings to other types of e-commerce websites or development frameworks.

References

1. Hevery, M., Erickson, K.: Angular: A Framework for Building Web Applications
2. Kaluža, M., Troskot, K., Vukelić, B.: Comparison of front-end frameworks for web applications development. Zbornik Veleučilišta u Rijeci **6**(1), 261–282 (2018)
3. Bulgakova, O., Zosimov, V.: Reactive Programming Paradigm for Development User Interfaces. Control Syst. Comput. 62–69 (2019). https://doi.org/10.15407/csc.2019.05.062
4. Choudhary, V., Chauhan, K.: E-commerce: sorting and filtering techniques for product search. Int. J. Eng. Sci. Comput. **7**(10), 15110–15115 (2017)
5. Seif, M., Zaki, M.: E-commerce product search and filtering using angular and RxJS. Int. J. Comput. Sci. Inf. Secur. **15**(6), 53–60 (2017)
6. Daniels, P., Atencio, L.: RxJS in Action. Simon and Schuster (2017)
7. Kurata, D.: Angular + RxJS in-depth tutorial. https://app.pluralsight.com/library/courses/angular-rxjs-web-applications/table-of-contents
8. Farhi, O.: Reactive Programming with Angular and Ngrx (2017)
9. Baymard Institute: Cart Abandonment Rate Statistics (2021). https://baymard.com/lists/cart-abandonment-rate
10. Schwarz, L.: Real-time Filtering and Sorting with RxJS (2018). https://blog.angularindepth.com/real-time-filtering-and-sorting-with-rxjs-888458cc210

Chapter 7
Application of Artificial Intelligence Method for Predicting of Compressive Strength and Materials Required for Self-Compacting Concrete

M. Sivashankar, Sk. Abdul Rahman, C. Arvind Kumar, and G. Manohar

Abstract The compressive strength of concrete is a major parameter to assess the overall quality of concrete as other mechanical prosperities are directly related to the compressive strength. It can be determined using the non-destructive testing (NDT) method which is carried out without destroying the concrete specimen. Whereas the NDT methods like the rebound (Schmitz) hammer and Ultrasonic Pulse velocity (UPV) are most popular because they are much quicker; their values are more of an approximation than exact compressive strength values. The newly developed soft computing techniques like ANN, Fuzzy logic, Genetic programming etc. may be used to prepare a better numerical model correlating NDT results. Therefore, the present work uses the ANN tool to predict the required compressive strength and materials. The performance of the proposed model was evaluated using a dataset of 80 SCC specimens which are collected from journals. The proposed approach provides a reliable and accurate means for predicting the compressive strength and materials required for SCC. It is a time-consuming process and difficult to determine the compression strength of concrete in the laboratory. In this project, we predict the material quantities required for the different mixes and we cast cubes of 150 mm with those quantities and did NDT and compression tests after 28 days of curing, and with those quantities using ANN, we predict the compression strength of the SCC. After that, we just compare the results which we are getting from NDT, compression test and ANN predicted values.

M. Sivashankar · Sk. Abdul Rahman · C. Arvind Kumar (✉) · G. Manohar
Department of Civil Engineering, Matrusri Engineering College, Saidabad, Hyderabad 500059, India
e-mail: arvind.cholker@gmail.com

P. H. V. S. Talpa Sai et al. (eds.), *Intelligent Manufacturing and Energy Sustainability*, Smart Innovation, Systems and Technologies 372,
https://doi.org/10.1007/978-981-99-6774-2_7

7.1 Introduction

The prediction of compression strength and material quantities for SCC is a challenging task due to the complex interactions between various constituent materials, and mix proportions. Achieving the desired strength in SCC requires precise control over the proportions of cement, aggregates, water, and admixtures, as well as careful consideration of mix design parameters such as water-to-cement ratio, aggregate grading, and viscosity modifying agents [1–3]. Therefore, accurate prediction of the compression strength of SCC is crucial for ensuring its structural performance and durability [4, 5]. The objective of this project report is to develop a reliable prediction model for estimating the compression strength or material quantities of self-compacting concrete. The report will review the existing literature on SCC, including its properties, mixed design considerations, and factors affecting its strength development [6–8]. Various statistical and machine-learning techniques will be employed to analyze the experimental data on SCC mixtures with different compositions. The findings of this study will contribute to the understanding of SCC behaviour and provide practical guidelines for optimizing its mix design and predicting its compression strength or material quantities in real-world construction applications.

7.2 Objectives

- Predicting the material quantities for Mix-1(M30), Mix-2(M35) and Mix-3(M40) using Artificial Neural Networks (ANN) and Manufacture Self Compacting Concrete (SCC) of the above mixes which are obtained from ANN and check its Fresh properties.
- Predicting the compressive strength of Self Compacting Concrete (SCC) using Artificial Neural Networks (ANN) and finding the compression strength of Cubes using Non-Destructive Test (NDT) and experimentally.
- Comparing the compression test results which are obtained from ANN, NDT, and experiment values.

7.3 Materials Used

- Cement: OPC 53 grade cement which was having a specific gravity of about 3.15.
- Fly ash: Class—f fly ash was used in this study. The specific gravity of Fly ash is 2.2.
- Coarse Aggregate: The size of the aggregate is 10 mm and the specific gravity is 2.74.
- Fine Aggregate: River sand was used and its specific gravity is 2.64.
- Super Plasticizer: ConplastSP430 was used as water reducing agent and the specific gravity is 1.1.

- Water.

7.4 Artificial Neural Networks (ANN)

Artificial neural networks (ANNs) are a type of machine learning model inspired by the structure and function of the human brain [9]. At a high level, ANNs consist of interconnected nodes or neurons, organized into layers as shown in Fig. 7.1 [10]. Each neuron receives input from one or more neurons in the previous layer, processes it, and produces an output that is passed on to the next layer [11–13]. This process is repeated through the layers until the final output is generated. ANNs can have multiple layers, and the number of neurons in each layer can vary. One of the most commonly used types of ANN is the neural net fitting, here information flows only in one direction, from input to output [14]. Training ANN's process is usually done using optimization techniques such as gradient descent, and the quality of the training data and the architecture of the network can greatly affect the performance of the model.

7.4.1 Data Employed

The performance of the proposed model was evaluated using a dataset of 80 SCC specimens. The data used in this technique was taken from Siddique et al. [7].

- Training dataset: This is required to construct the model. In this project, 64 (80% of total data) out of the 80 values are considered as the training dataset.
- Validation dataset: This is required to assess the performance of a model during the training process. The remaining 8 (10% of total data) values are considered validation datasets in this project.
- A testing dataset: This is required to estimate the model performance. In this project, the remaining 8 (10% of total data) values are considered as testing datasets.

Fig. 7.1 Artificial neural networking

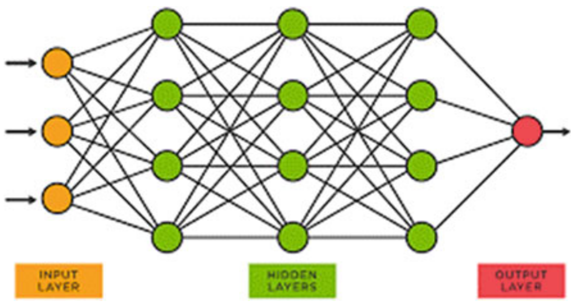

7.5 ANN Modeling

ANN stands for Artificial Neural Network, a machine-learning model inspired by the structure and function of biological neurons in the human brain [15]. ANN models consist of multiple interconnected layers of nodes, or artificial neurons, that perform mathematical computations on input data and generate output predictions. ANNs are commonly used for tasks such as image recognition, natural language processing, and prediction. They can learn complex patterns and relationships in data, and can often outperform traditional machine-learning models in terms of accuracy and efficiency. This topic deals with the information about prediction of material quantities and compression strength of self-compacting concrete.

7.5.1 Prediction of Material Quantities for Different Mixes Using ANN

The input and output parameters should be assigned to the appropriate layers in the ANN model, and the number of nodes in the input and output layers should match the number of input and output parameters, respectively.

- Input Parameters: Compression strength.
- Output Parameters: Cement, Fly ash, w/c ratio, Super plasticizer, FA and CA.

Figure 7.2 represents the network diagram while prediction of material quantities. The ANN should be trained to converge to the optimal solution quickly without overfitting. There are some figures related to training the ANN. We trained the neural network for predicting the material quantities for M30, M35 and M40 SCC mixes.

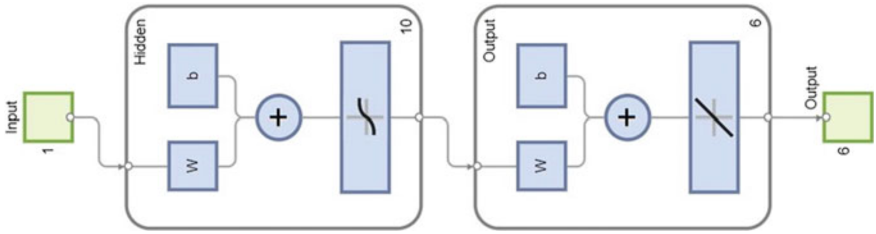

Fig. 7.2 ANN network diagram while prediction of material quantities

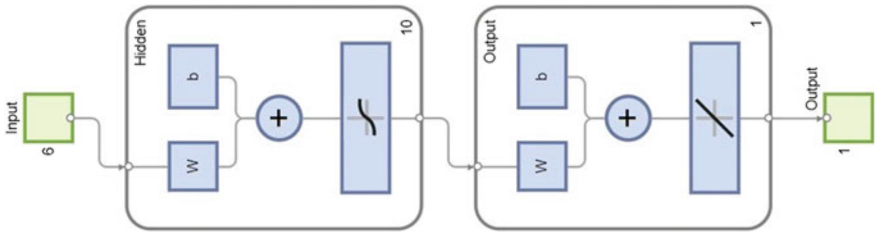

Fig. 7.3 Neural network diagram for prediction of compression strength

7.5.2 Prediction of Compression Strength Using ANN

We trained the neural network for predicting the compression strength of mix–1, mix-2 and mix-3. The input and output parameters used in the training of the network are:

- Input Parameters: Cement, Fly ash, Water-Cement ratio, Super Plasticizer, Fine aggregate, Coarse Aggregate.
- Input Parameters: Compression strength (Fig. 7.3).

7.6 Experimental Procedure

This topic is related to what we did in the laboratory, like the description of the laboratory test procedure in step by step.

7.6.1 Production of SCC and Its Fresh Property Tests

Casting cubes using concrete is a common process in construction and civil engineering, where concrete cubes are cast and tested to assess the strength and durability of the concrete. The process involves the following steps:

Material preparation: Here we used ANN-predicted material quantities

- Mould preparation and Manufacture of SCC
- Fresh property tests on SCC: Slump flow test and V-funnel test
- Pouring
- Demolding and curing: The curing period is 28 days.

7.6.2 Non-destructive Test

Non-destructive testing (NDT) methods can be used to estimate the compressive strength of concrete without damaging the structure. The most commonly used NDT methods for this purpose are:

- Ultrasonic Pulse Velocity (UPV) Test: In this method, a pulse of high-frequency sound waves is sent through the concrete using a transducer. The time taken for the sound waves to travel through the concrete and back to the receiver is measured. The UPV is then calculated using the formula UPV = distance/time. The UPV values can be correlated with the compressive strength of the concrete using empirical relationships.
- Rebound Hammer Test: In this method, a spring-loaded hammer is used to strike the concrete surface, and the rebound distance of the hammer is measured using a graduated scale. The rebound distance is correlated with the compressive strength of the concrete using empirical relationships.
- It's important to note that NDT methods provide an estimate of the compressive strength of concrete, and the results should be used in conjunction with other information, such as the mix design, curing conditions, and construction practices, to assess the overall.

7.7 Results and Discussions

The results and discussion section of this study on SCC compressive strength or material quantities prediction would typically include the following.

7.7.1 Predicted Output Values of ANN

The predicted material quantities and compression strength values are listed in Tables 7.1 and 7.2 (Figs. 7.4 and 7.5).

7.7.2 Fresh Property Test Results of SCC

The fresh property test slump flow and V-funnel tests on fresh concrete results are which we got were within the range and the test values are satisfactory. The test values are given in Table 7.3.

Table 7.1 Predicted material quantities using ANN

S. No.	Materials	Mix-1 (M30)	Mix-2 (M35)	Mix-2 (M40)
1	Cement (kg/m^3)	277.58	267.885	251.34
2	Fly ash (kg/m^3)	132.63	135.155	153.40
3	Water–cement ratio	0.44	0.40	0.36
4	Superplasticizer dosage (%)	0.52	0.46	0.44
5	Fine aggregate (kg/m^3)	830.165	895.29	910.45
6	Coarse aggregate (kg/m^3)	842.26	854.87	868.32

Table 7.2 ANN predicted compression strength

Mixes	Mix-1 (M30)	Mix-2 (M35)	Mix-3 (M40)
Compression strength (N/mm^2)	36.72	38.44	43.62

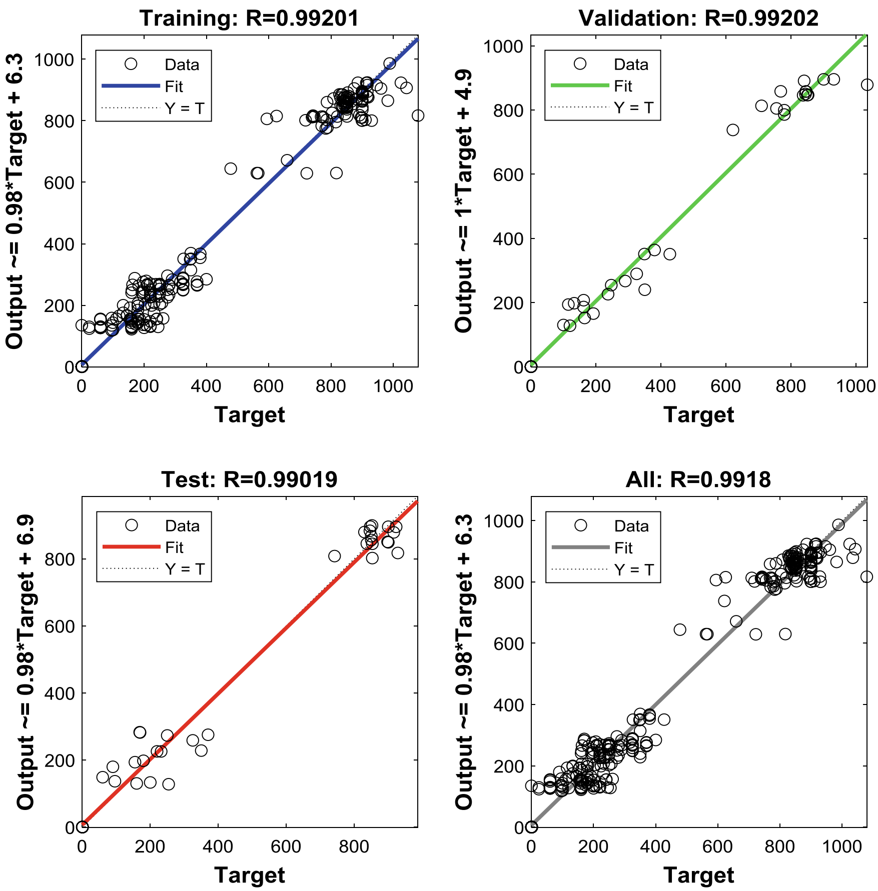

Fig. 7.4 Performance of ANN while predicting the material quantities

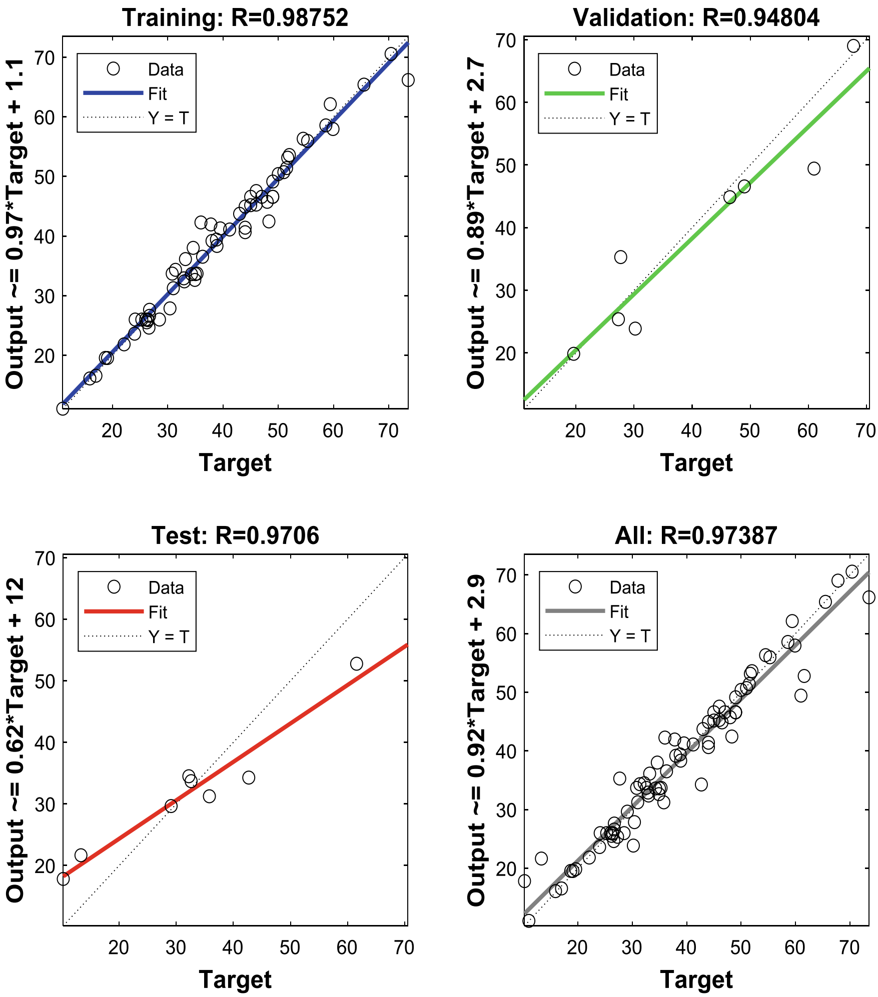

Fig. 7.5 Performance of ANN while predicting the compression strength

Table 7.3 Fresh property test values

Methods	Typical range of values	Test values		
		Mix-1 (M30)	Mix-2 (M35)	Mix-3 (M40)
Slump flow (mm)	500–800 mm	590	557	563
V-funnel (s)	$\leq$ 8 s	4	6	6

Table 7.4 Non-destructive test values

S. No.	Mix	Specimen no.	Rebound hammer (N/mm^2)		Ultrasonic pulse velocity speed (N/mm^2)	
			Individual	Average	Individual	Average
1	Mix-1 (M30)	1	38.4	39.4	39.2	38.4
		2	38		40.5	
		3	41.4		35.5	
2	Mix-2 (M35)	1	46.5	42.8	44.8	40.8
		2	38.7		39.1	
		3	43.2		38.5	
3	Mix-3 (M40)	1	45.5	44.3	48.3	47.6
		2	44.1		48.8	
		3	43.3		45.7	

7.7.3 NDT Test Results

NDT techniques are not used directly for cube compression strength testing, they can be valuable tools for assessing the properties and integrity of the cube before and after the test, as well as for monitoring the test process and ensuring its accuracy. The test results are mentioned in Table 7.4.

7.7.4 Compression Strength Test Results

The compression strength test on cubes is a commonly used method for assessing the strength of concrete. In this test, standard-sized cubes (150 mm × 150 mm × 150 mm) are cast from a representative sample of the concrete and cured under controlled conditions. After a 28 days curing period, the cubes are subjected to a compressive load until they fail. The maximum load sustained by the cube before failure is recorded as the compressive strength of the concrete. Table 7.5 provides the compression strength test results.

7.7.5 Comparison of Compression Strength Results

When comparing the compression strength results of ANN, NDT, and experimental values listed in Table 7.6, it is important to consider the sources of variability and error in each method. Experimental values obtained from the compression strength test on cubes are generally considered the most accurate and reliable, as they directly

Table 7.5 Experimental compression strength test results

S. No.	Mix	Specimen no	Compression strength (N/mm^2)	Avg. compression strength (N/mm^2)
1	Mix-1 (M30)	1	40.22	39.6
		2	36.22	
		3	42.22	
2	Mix-2 (M35)	1	43.11	40.1
		2	41.33	
		3	38.00	
3	Mix-3 (M40)	1	45.56	47.5
		2	42.22	
		3	54.89	

measure the strength of the concrete under controlled conditions. However, there can be variability in the test results due to factors such as the size and shape of the cubes, the loading rate, and the specimen preparation.

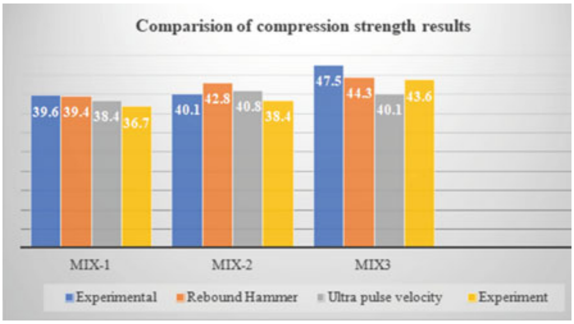

- The performance of the ANN model in predicting the compressive strength of SCC, including the accuracy of the predictions compared to NDT and Experimental test results.

Table 7.6 Compression strength results

S. No.	Mix	Compression strength values in N/mm^2			
		Experimental	Rebound hammer	Ultrasonic pulse velocity	ANN
1	Mix-1 (M30)	39.6	39.4	38.4	36.7
2	Mix-2 (M35)	40.1	42.8	40.8	38.4
3	Mix-3 (M40)	47.5	44.3	40.1	43.6

- The number of training, validation, and testing data sets used, as well as the criteria used for selecting these data sets.
- The architecture of the ANN model, including the number of neurons, hidden layers, activation functions, and learning algorithms used.
- The statistical indicators used to evaluate the accuracy of the ANN model, such as the mean squared error (MSE), mean absolute error (MAE), and correlation coefficient (R).
- The significance of the results and their implications for the concrete industry, including potential cost and time savings from using ANN for compressive strength prediction.
- The effectiveness of the selected ANN architecture and training parameters in predicting the compressive strength of SCC, and any limitations or challenges in the ANN approach.
- The potential for further research in using ANN or other prediction methods for SCC compressive strength, including ways to improve the accuracy and efficiency of the predictions.

7.8 Conclusion

- Based on the available data and analysis, the prediction of compression strength and material quantities for self-compacting concrete appears to be a feasible and effective approach.
- Through the use of various models and methods, such as regression analysis and artificial neural networks, it is possible to accurately estimate the compressive strength or material quantities of SCC based on a range of input factors such as mix design, aggregate properties, curing conditions, and more.
- However, it is important to note that there may be limitations to the accuracy of these predictions, as there are numerous factors that can influence the strength of SCC that may not be fully captured by the available data.
- It is also important to consider the specific conditions and requirements of each project when making predictions, as there may be unique factors that can impact the performance of the concrete.
- Overall, while there are some potential limitations and challenges to predicting the compression strength of SCC, it remains a promising area of research and has the potential to improve the efficiency and effectiveness of concrete design and construction in the future.
- The obtained results after comparison showed that the proposed model of ANN for predicting compressive strength has good capability of accuracy 95%.

References

1. Kathiravan, T., Vidivelli, B.: Mechanical properties of self-compacting & curing concrete. Civ. Eng. **94**, 39954–39959 (2016)
2. Patel, A., Bhuva, P.: Compressive Strength and Modulus of Elasticity of Self Compacting Concrete, PG Students, Dept. of Structure Engg. B.V.M Engg., College V.V.Nagar. Gujarat Technological University, Gujarat, India on 13–14 May (2011)
3. Cussigh, F., Sonebi, M.: Testing SCC—segregation test methods. University of Niš, Faculty of Civil Engineering and Architecture, Serbia (Jan 2005)
4. Garlic, Z., Despotovic, I., Curcic, G.T.: Properties of Self-Compacting Concrete With Different Types of Additives. The University of Niš, Faculty of Civil Engineering and Architecture, Serbia (Jan 2008)
5. Sugathan, A.: Self-Compacting High-Performance Concrete with Steel Fibres. Assistant Professor, Department of Civil Engineering, New Horizon College of Engineering, Visvesvara Technological University Bangalore, Karnataka. ISSN (Online): 2347-3878, Impact Factor (2015): 3.791
6. Kumar, A., et al.: Behaviour of fibre reinforce concrete beam in pure torsion. Int. J. Res. Eng. Technol. **4**(5), 551–556 (2015)
7. Siddique, R., Aggarwal, P., Aggarwal, Y.: Prediction of compressive strength of self-compacting concrete containing bottom ash using artificial neural network. Adv. Eng. Softw.Softw. **42**(10), 780–786 (2011)
8. Yaman, M.A., Elaty, M.A., Taman, M.: Predicting the ingredients of self-compacting concrete using artificial neural network. Alexandria Eng. J. **56**, 523–532 (2017)
9. Cholker, A.K., Tantray, M.A.: Strain-sensing characteristics of self-consolidating concrete with micro-carbon fibre. Austr. J. Civ. Eng. **18**(1), 46–55 (2020)
10. de-Prado-Gil, J., Palencia, C., Silva-Monteiro, N., Martinez-Garcia, R.: To predict the compressive strength of self-compacting concrete with recycled aggregates utilizing ensemble machine learning models. Case Stud. Constr. Mater. **16** (2022)
11. Rajakarunakaran, S.A., Lourdu, A.R., Muthusamy, S.: Prediction of strength and analysis in self-compacting concrete using machine learning based regression techniques. Adv. Eng. Softw. **173** (2022)
12. Cholker, A., Tantray, M.: Strain and damage sensing property of self-compacting concrete reinforced with carbon fibers. Int. J. Eng. **32**(11), 1577–1583 (2019)
13. Cui, T., Kulasegaram, S., Li, H.: Predicting fresh and hardened properties of self-compacting concrete containing fly ash by artificial neural network model. MATEC Web Conf. **361** (2022)
14. Dutta, S., Ramachandra Murthy, A., Samui, P.: Prediction of compressive strength pf self-compacting concrete using intelligent computational modeling. CMC **53**(2), 167–185 (2017)
15. Akram Hossain, M., Sadiqul Islam, G.M., Mallick, A.: Compressive strength prediction for industrial waste-based SCC using artificial neural network. J. Civ. Eng. Forum (Jan 2023)

Chapter 8
CFD of HVAC System to Simulate the Vertical Farm Facility Using OpenFOAM

Rathan Babu Athota, Sai Puravardhan Korani, Surya Hevanth Nimmala, Prem Kumar Bet, and Sathvik Merugu

Abstract The Indoor plant industrial facilities are one of the elective approaches to satisfy the needs of food creation for the expanded metropolitan tenants. It empowers cultivators to develop food crops reliably and locally with a superior grade. In confined solitary container, a controlled agriculture environment, ventilation and solitary rack system is utilized to control the changing climate and to maintain the atmosphere consistency. Lettuce is a highly produced crop in vertical farm lines and an ill-advised plan could cause the tip burn of lettuces which ordinarily happens at internal and recently occurring leaves with the less transpiration rate because of the presence of a boundary layer. A three-dimensional computational (CFD) model is created by reproducing the developing climate in a solitary rack framework. And further developed airflow framework was planned and proposed to help give a dynamic and uniform limit layer that could help stall tip consumption events in lettuce production. An inlet at the roof is installed for the supply of air which was intended to give vertical wind currents down through the canopy of the crop by decreasing the temperature and relative humidity. Different cases were studied using CFD and controlled treatment was employed.

R. B. Athota (✉) · S. P. Korani · S. H. Nimmala · P. K. Bet · S. Merugu
Department of Aeronautical Engineering, Institute of Aeronautical Engineering, Dundigal, Hyderabad, Telangana 500043, India
e-mail: a.rathanbabu@iare.ac.in

S. P. Korani
e-mail: 20951A2164@iare.ac.in

S. H. Nimmala
e-mail: 20951A2192@iare.ac.in

P. K. Bet
e-mail: 20951a2152@iare.ac.in

S. Merugu
e-mail: 20951a2173@iare.ac.in

P. H. V. S. Talpa Sai et al. (eds.), *Intelligent Manufacturing and Energy Sustainability*, Smart Innovation, Systems and Technologies 372,
https://doi.org/10.1007/978-981-99-6774-2_8

8.1 Introduction

Vertical farming is a technique of growing crops inside a concealed building with artificial resources or growing them with naturally available resources in vertically placed layers. As it has constant supply of artificial light source by using L.E.Ds, Air conditioning, and controlled environment for agriculture. Vertical farms can be set up anywhere, regardless of the weather [1]. If we talk about controlled environment, vertical farms require ideal climate conditions inside the growth chamber. The HVAC system controls airflow, relative humidity, and temperature [2]. So, to ensure the capacity of HVAC for handling the load is unsure and requires a lot of energy. If we likely to reduce the tip-burn of lettuce, the stagnant boundary layer should be removed for that the air supply position plays key role. To investigate this HVAC setup CFD tool can be an effective tool for evaluate and analyze the heating load and air circulation in the farm facility. Therefore, here we have created one-dimensional model using CATIA and Open Foam was developed to study the air-flow and heating load inside the container for new farm design. The results of CFD simulations can be utilized to study and interpret airflow. By this CFD results can be used for future scope to optimize the design of the workplace and positions of inlets and further provide guidance to develop full scale model. Particularly Open Foam is chosen for it's reliable, flexible and open access to source code to perform analysis of the air-flow and heating load of HVAC systems used in vertical farm [3].

8.1.1 K-Epsilon Turbulence Model

For simulations, the turbulent k-model is commonly utilized. The kinetic energy is used as the model's base variable (k). To capture all the turbulence length and time scales, two transport equations are solved. Whereas the typical k-epsilon model solves for two variables: turbulent kinetic energy (k) and the rate of kinetic energy dissipation, epsilon ().

Turbulence energy transport equation:

Equation 8.1:

$$\frac{\partial k}{\partial t} + uj * \frac{\partial kj}{\partial xj} = -ui_i' uj_j' * \frac{\partial ui}{\partial xj} - \varepsilon + \frac{\partial}{\partial xj}\left(\nu + \frac{\nu T}{\sigma k}\right)\frac{\partial k}{\partial xj} \tag{8.1}$$

Turbulence dissipation transport equation:

Equation 8.2:

$$\frac{\partial \varepsilon}{\partial t} + uj\frac{\partial \varepsilon}{\partial xj} = -C\varepsilon 1 * \frac{\varepsilon}{k}u_i{}' u_j{}' \frac{\partial ui}{\partial xj} - C\varepsilon * 2\frac{\varepsilon^2}{k} + \frac{\partial}{\partial xj}\left(\nu + \frac{\nu T}{\sigma k}\right)\frac{\partial \varepsilon}{\partial xj} \tag{8.2}$$

Many upgradations are done in k-ε model as it has some drawbacks like no slip walls, Insensitive to pressure gradients, inefficient for strong curvatures, and which makes difficult to solve epsilon. Solver which we are used is buoyant BoussinesqSimpleFoam with compressible flow solvers. As the design simulations are done in OpenFoam.

8.2 Literature Review

In computational fluid dynamics as a tool for simulating and validating the performance of HVAC in the vertical is the best option [1]. They have also conducted series of experiments by employing different types of air circulation systems and observed which case has the best results. They used the Boussinesq approximation for airflow to obtain faster convergence in these tests, and the k-model as a turbulence model for simulation of indoor wall-bounded air flows for ventilation systems [4].

The authors also have developed a one-dimensional model based on transient analysis using MATLAB and Simulink to study the interaction between the HVAC operation and indoor climate conditions in the growing chamber. The study has explained by the comparison of the results between the existing farm and model that with the extra cooling capacity we can eliminate the vapor pressure deficit, with one HVAC malfunction the two operational units cannot handle if the temperature upsurges 500 °C and the sudden drop in temperature the humidity does not vary [2]. At last, they recommended instead of the 1D model the 3D (using laminar NAVIER STOKES equations) model can give optimal results with given parameters and also recommended HVACs with higher cooling loads to create better-growing conditions [5].

CFD models were used to validate and analyze the performance of the system and to analyze the airflow and temperature distribution uniformity in a shipping container by changing the inlets and outlet in 6 different positions, and finally, Mohd Noh et al., recommended the best positions for inlets and outlet.

BIM is software that is used to design building facilities and manages operations more efficiently. By using BIM software to develop a 3D digital prototype of a vertical farm and simulate its performance by using CEA (Control Environment Agriculture) and using Design science they have improved the prototype for nD integration [6].

The study of HVAC system performances and the effect of plants on its performance by Lalonde et al. (2019) was to decrease the energy demand. They examined the energy performance of two HVAC systems by evaluating sensible and latent heat parameters using TRNSYS for BIAS simulation (TRNSYS is a simulation package for buildings and renewable engineering). They majorly focused on condensation on the walls and to supply uniform CO_2. They also conducted experiment on different cultivated densities [7]. The system was studied by structural analysis of a Reentry module for a return mission to 2010TK7 [8]. For the adaption of modern technology the system can also useful for various automobile industries for thermal and different parametric study is done [9].

8.3 Methodology

We use container with solitary rack confinement is considered as a vertical farming for this experiment. Because the for the mini structure the energy demand is less compared to the actual vertical farm as compared to standard shipping container is best. Where the controlled environmental agriculture needs HVAC to maintain the temperature, humidity inside the container.

8.3.1 Design

Factors which are driven are position of inlet and outlet, Transpiration rate, Energy consumption, Temperature and Humidity…etc. where it is said to be the position to fix the inlet is at the roof forcing the wind vertically downwards penetrating through the canopy surface of the plant. The lettuce crop is the most grown plant by using CEA technique. Where the vertical wind velocity of 2.3 m/s is used for air-flow inside the container.

And the experiment was conducted with two temperature and humidity intakes. At first, the velocity was increased to reduce the temperature with initial conditions of 23 °C and relative humidity of 30% of atmospheric humidity. The extra cooling capacity is used to control the temperature and humidity. For better optimal results the 3-dimensional model was used and HVACs with higher cooling loads to create better-growing conditions (Table 8.1).

There are total of 8 racks, placed 4 racks at each side of the short wall horizontally for the bottom rack is placed at a distance of 1.6 ft, where we assume each rack contains 360 pant units. At the roof intel is placed with air cooling condition. The downward direction air is 2.3 m/s (Fig. 8.1).

Where we have used LEDs for heat flux, which are set as artificial lightning source for plant growth. It has a wavelength of 400–700 nm emitted and the LED have 68 W/m^2. Which access for better plant growth and high yield.

Table 8.1 Design parameters

Standard shipping container dimensions (for vertical farm)	40 ft × 8 ft × 8 ft
Surface length (ft)	18.5
Thickness (ft)	0.25
Width (ft)	5

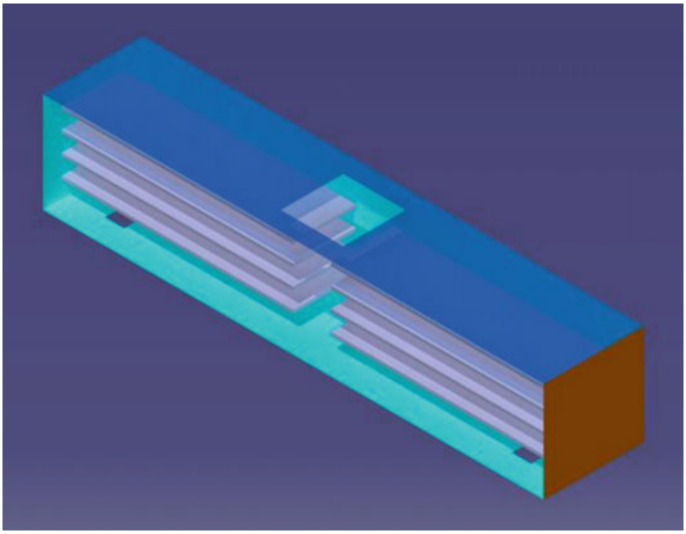

Fig. 8.1 3D representation of solitary confinement

8.3.2 Meshing

We have used PolyMesh for the model in OpenFOAM as in meshing process. From the CFD toolbox operations are allowed for user-system. Time at the initial is given as Patch points are created for the Mesh stats where points taken are 48,510, faces are 128,000 and internal faces is about 112,000, Hence the cells are 40,000 and face per cell is up to 6 and we have boundary patches of 3. It has a hexahedra-cells of overall cells (Fig. 8.2).

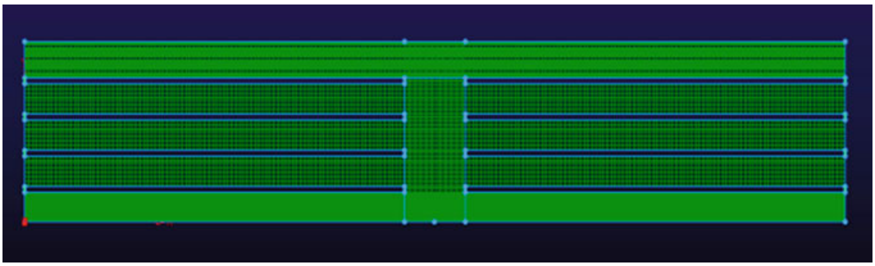

Fig. 8.2 Mesh

8.3.3 *Boundary Conditions*

For the Foam file the we use the polyboundaryMesh, for the floor, ceiling are taken as wall at n faces at different values. As the boundary condition for different parameters are taken into consideration, as for the velocity (U) we have a vector field and inter field is taken as uniform as for the inlet and outlet is considered as zero gradient.

The adjustable airflow rate, adjustable temperature with user-defined flow profile can make energy consumption less. With small infrastructure like standard 40 ft container the use of medium cooling load HVACs can reduce the energy consumption.

Where the experiment was conducted with two temperature and humidity intakes. At first, the velocity was increased to reduce the temperature with initial conditions of 23 °C and relative humidity of 30% of atmospheric humidity. The extra cooling capacity is used to control the temperature and humidity. For better optimal results the 3-dimensional model was used and HVACs with higher cooling loads to create better-growing conditions. The design simulations are done in OpenFoam using the buoyantBoussinesqSimpleFoam solver with compressible flow solvers.

The transpiration rate of plant is loss of water from their surfaces through stomata. When they are closed the transpiration rate decreases. They are closed due to the presence of boundary layer at the tip of the leaf due to that there will a calcium deficiency and it causes the tip burn. So, by position inlet correctly and the enough vertically downwind will remove the tip. So, the inlet positioned at the roof facing downward will force the removal of boundary layer as air penetrates through the 11 canopy surface and the transpiration rate of the plant increases which increases the water uptake.

8.4 Results and Discussions

8.4.1 *Velocity*

See Figs. 8.3 and 8.4.

8.4.2 *Temperature*

See Figs. 8.5 and 8.6.

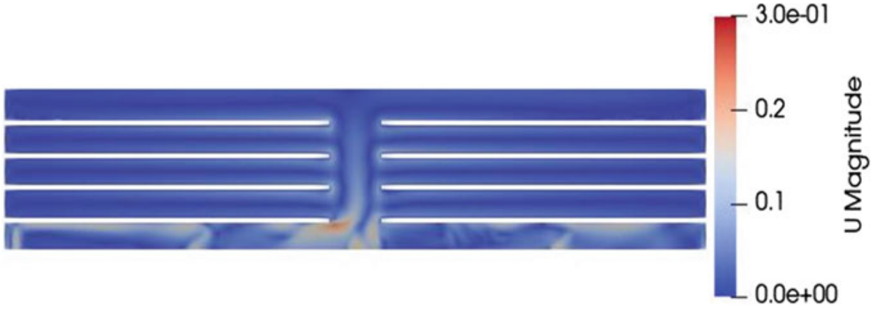

Fig. 8.3 Initial velocity at temperature above 310 k

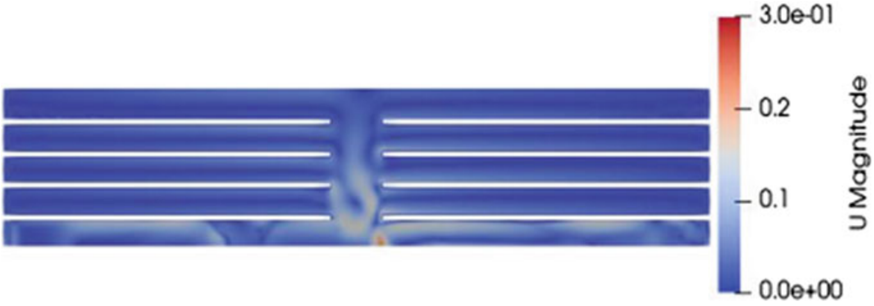

Fig. 8.4 Velocity at temperature below 300 k ideal condition for plant growth

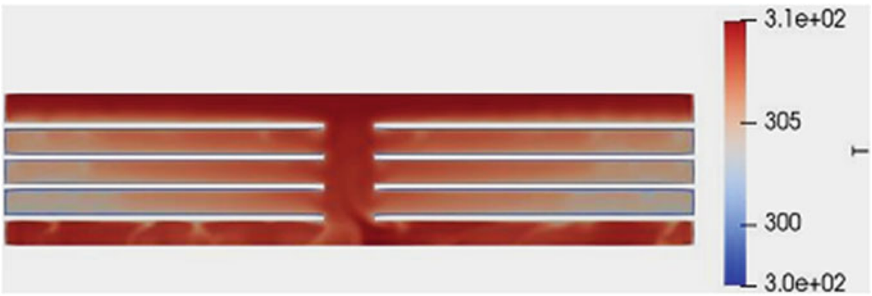

Fig. 8.5 Temperature of the container initially above 310 k

8.4.3 Energy

As we look in to the velocity (Figs. 8.3 and 8.4) the airflow temperature developed from initial high room temperatures around 310 k where it is gradually decreased less than 300 k which shows high velocity formation around the corners of racks.

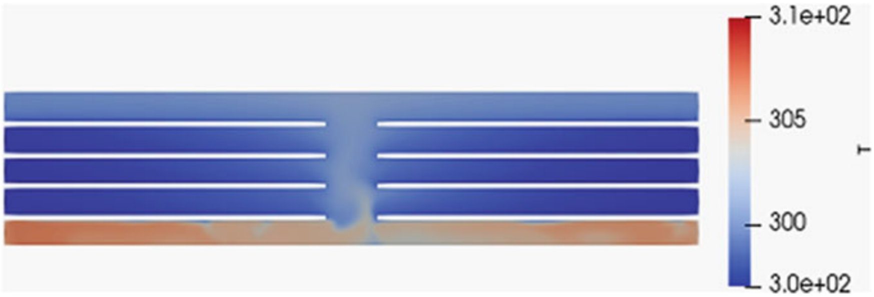

Fig. 8.6 Temperature of container ideal condition to grow the crop below 300 k

So, by using K-Epsilon model we simulated the turbulence model to counter high velocities.

As a result, we got ideal conditions to grow plant with less heating load capacity.

If we see (Figs. 8.5 and 8.6) the temperatures at initial is above 310 k is considered and difference can be observed when the temperature is at decreasing gradually where for less than 300 k we have perfect condition for crop growth. If we see the energy results (Figs. 8.7 and 8.8) the energy is moving corner of racks from initial and they end up at the stamp.

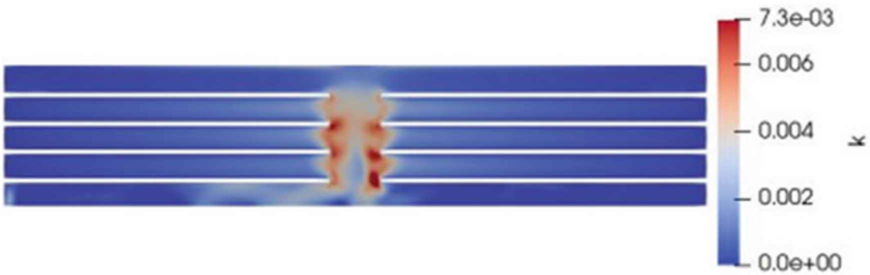

Fig. 8.7 Energy at coroners of racks

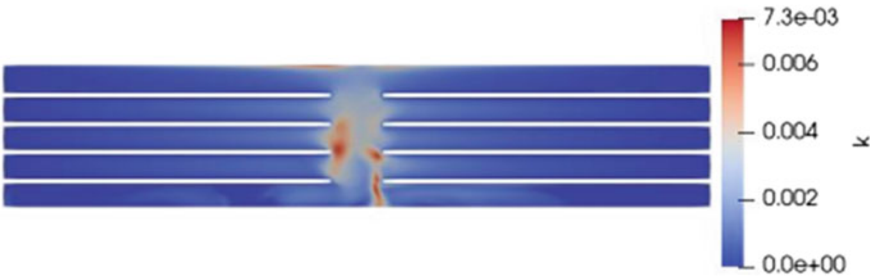

Fig. 8.8 Energy at end time stamp

Fig. 8.9 Rate of dissipation initially

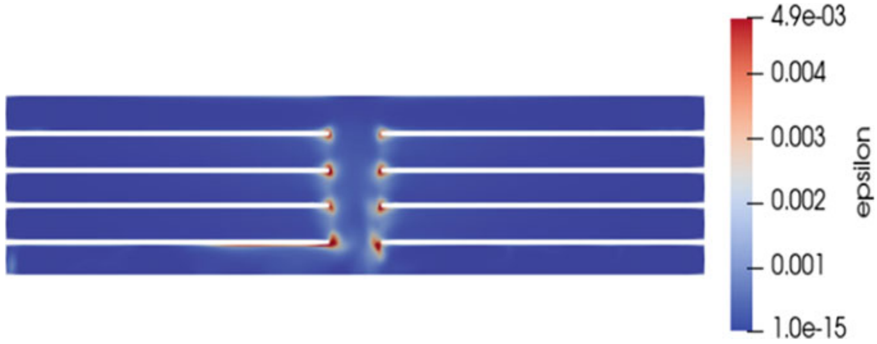

Fig. 8.10 Rate of dissipation

8.4.4 Dissipation Rate

If we observe the model the dissipation at initial state the flow diffusion effect varying as in Fig. 8.10 the rate of airflow is much higher at the edge of the system and later at the end of the flow distribution the flow is negligible as we can see in Figs. 8.9 and 8.11.

8.5 Conclusion and Future Work

The HAVAC system at different parametric study is observed at variations in paraview software.

By this vertical farming equipment is simulated using OpenFoam software. The buoyantBoussineqsimple Foam solver is used for CFD simulation. K-epsilon turbulent model is used for indoor agriculture farming using simulation. To rectify the problem in vertical farming industries which basically take more energy. So, by

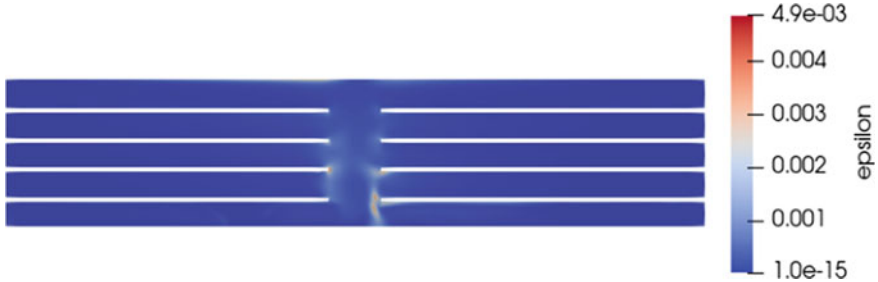

Fig. 8.11 Rate of dissipation at end

using shipping containers, we can produce maximum yield and with less usage of energy. As it requires to understand the different computational time step results and other turbulence models which will be studied further. For different velocities gradients the evaluation can be done for vertical farming as future work. We also try to build optimizations and advance designs for vertical farm. The HVAC capacity can be decreased by using solitary Rack system from the results I can conclude that the by having less free place can decrease the energy consumption. The problem with conventional vertical farming industries is they have more free space to run the machines which conserves more energy. By using shipping containers, we can produce maximum yield and use less energy. We can distribute the airflow sufficiently to remove the boundary layer and can increase the transpiration rate by using less heating load on HVAC.

In future work we try to develop system with finite elemental analysis where the heat flow in the HAVAC system and different parametric study can be studied. By applying different thickness for the model all constraints are measured.

References

1. Zhang, Y., Kacira, M., An, L.: A CFD study on improving airflow uniformity indoor plant factors system. Biosyst. Eng. **147**, 193–205 (2016)
2. Zhang, S., Schulman, B.: A numerical model for simulating the in door climate inside the growing chambers of vertical farms with case studies. Int. J. Environ. Sci. Dev. **8**, 728–735 (2017)
3. Martkos, S., Vani De Voort, S., Li, Z., Voog, M., Krijn, M.: Lettuce growth and quality optimization in a plant factory. In: VIII International Symposium on Light in Hort Culture, 1134, pp. 231–238, May 2016
4. Brooksa, J., Kumara, S., Goyalb, S., Subramanyc, R., Barooaha, P.: Energy-efficient control of under-actuated HVAC zones in commercial buildings
5. Randolph, O., Asia Banpour, B.: Energy consumption optimization in off-grid vertical farming. In: IIE Annual Conference. Proceedings, pp. 861–866. Institute of Industrial and Systems Engineers (IISE) (2020)
6. Khan, R.R.A., Ahmed, V.: Building Information Modelling and Vertical Farming: Data Integration to Manage Facilities and Processes. Facilities (2017)
7. Eleftheriadis, G., Hamdy, M.: The impact of insulation and HVAC degradation on overall building energy performance: a case study. Buildings **8**(2), 23 (2018)

8. Babu, A.R., George, N.A., Harsha Vardhan Reddy, V., Govardhan, D.: Dynamics and structural Analysis of a Reentry Module for a Sample return mission to 2010TK7
9. Shiva Prasad, U., Babu, A.R., Sairaju, B., Amirishetty, S., Deepak, D.: Automotive chassis design material selection for road and race vehicles. J. Mech. Eng. Search Dev. **43**(3), 274–282 (2020)

Chapter 9
Computational Analysis and Comparative Study on Ballistic Impact Properties of Composite Materials

A. R. S. Nikhil Aanandhan, M. Ashwin, G. Gokul Sree, A. Ashwin, J. Jensin Joshua, and S. Seralathan

Abstract Composite materials assist all types of aircraft, rockets, and missiles to fly higher and faster. However, impacts at high speeds affect aircraft and causes partial or complete penetration. To comprehend the consequences of hybrid composites made of Kevlar and Kenaf fibers when exposed to a high-velocity bullet, this study examines the ballistic impact characteristics. Three plates are designed with three different stacking sequences and impacted with a projectile at different velocities to spot the combination which could withstand the high-velocity impacts. Impact properties like total deformation, direction deformation, equivalent stress, and maximum shear stress are observed and analyzed using ANSYS software. Plate 1 with kenaf as its third layer shows better resistance to high velocity impacts than the other two stacking sequences. Therefore, Plate 1 can be effectively used in high velocity impact applications.

9.1 Introduction

High-performance aircraft and ground vehicles need composite materials to handle shock loads as well as static and cyclic stresses. Some instances of impact loads include hail damage, runway pebbles, and engine hoods striking fan blades, damage from foreign objects, wrecks, and projectiles striking aircraft. Low-velocity impacts, high-velocity impacts, and hyper-velocity impacts are the three groups into which impact loads is categorized. The basis for this categorization is that when the projectile's velocity varies, the processes for energy transfer, energy dissipation, and

A. R. S. Nikhil Aanandhan · M. Ashwin · G. Gokul Sree · A. Ashwin · J. Jensin Joshua · S. Seralathan (✉)
Department of Aeronatuical Engineering, Hindustan Institute of Technology and Science, Chennai, Tamil Nadu 603103, India
e-mail: siva.seralathan@gmail.com

P. H. V. S. Talpa Sai et al. (eds.), *Intelligent Manufacturing and Energy Sustainability*, Smart Innovation, Systems and Technologies 372,
https://doi.org/10.1007/978-981-99-6774-2_9

damage propagation all undergo significant modifications. The usage of composite materials in high-performance applications including armor, ground vehicles, and aircraft has expanded due to the necessity for robust, lightweight materials with high strength and rigidity for structural purposes. Utilizing fiber-reinforced composites (woven, knitted, or braided) is one method that could be used to increase the ballistic limit. The literature on ballistic impact on composite constructions has been carried out by various researchers. Soydan et al. [1] examined the technical viability of the construction in which ANSYS simulation software was used to simulate the composite structure made of fiber cement, aramid fabric, and steel layer laminated. A fiber cement layer of 8 mm, a Kevlar 29 layer of 2.4 mm, and a layer of 1006 steel of 3 mm stopped a 9 mm FMJ bullet with just minor distortion. Yahaya et al. [2] investigated how moisture affected the dynamic characteristics of polymer-based composites. They found that the degradation of fiber/matrix interface and the plasticization of the matrix determined the basis on which moisture affected the composites high strain rate characteristics. Shunmugam and Velmurugan [3] carried out studies in which two non-deformable projectiles were used to directly hit the laminate, including penetration and delamination. The ballistic characteristics of laminated Kevlar 29 and 129 composite panels were studied numerically and experimentally [4]. These panels were struck at a speed between 130 and 250 m/s, which was less than the panel's penetration limit. Maximum dynamic displacement, which is one of the important performance metrics for the usage of personal protective equipment, was studied numerically to ascertain its properties. The mechanical property data for the numerical simulation may then be determined by the experimental characterization of the material, which demonstrated high consistency [5].

Therefore, the purpose of this study is to propose a numerical analysis model for analyzing the ballistic impact based only on the dynamic and mechanical characteristics of the target material destruction, geometric parameters of the target, and parameters of the projectile such as velocity, shape, and size. The fibers, kenaf is chosen for its impact resistance and load-bearing capabilities. The investigation is being carried out using a commercial code, ANSYS Mechanical Workbench.

9.2 Methodology

The data used in this study are collected after studying several articles on ballistic impact testing using gas gun equipment as well as simulation to decide the best properties with different stacking sequence that suited for load-bearing capabilities damage resistance, cut or puncture strength. Materials used in this study were Kevlar and Kenaf and Global-drop off material viz., Epoxy Resin. The setup is modeled using ANSYS ACP pre which is a module within the ANSYS Workbench dedicated mainly for modeling of layered composite structures. Modeling of the plates began by updating engineering data with the material properties. The engineering data as per Table 9.1 is updated with the qualities of Kevlar and Kenaf fibers, epoxy resin, and steel 6001. The geometry of both the hybrid plates and the projectile is modelled using ANSYS Design Modeller. The hybrid plate is created initially, followed by the projectile. The ANSYS Mechanical is used to mesh the designed model. The setup is completed using ACP pre by modeling the fiber layers into the designed model as solid materials with specified thickness for each layer. The setup is then imported into ANSYS Explicit dynamics, a flagship suite where the impact simulation and analysis of the simulation is performed. A plate with five layers of diverse materials, including Kenaf and Kevlar woven textiles is created. Each material's attributes require to be modelled independently into Engineering data. It is decided to simulate three plate samples of different thicknesses to quickly effect the behavior of the entire system.

ANSYS Design Modeller is used to represent the stack shape as solid materials with varying thicknesses for each layer. The geometry and projectile are then transferred into ANSYS mechanical at a 20 mm offset for fine meshing. The 3D mesh of ANSYS Explicit dynamics mesh modeler with linear element order with explicit physics preference and hex dominant element type is used while meshing the composite plate. Three different composite plates are modeled in a similar way with different stacking sequences. However, the thickness (1.1 mm), orientation and symmetry remain the same for all the three plates. Epoxy resin is used as the global drop off material for all the three plates whose material properties are predefined in ANSYS engineering data.

Plate 1 with stacking sequence Kevlar/Kevlar/Kenaf/Kevlar/Kevlar is shown in Fig. 9.1a. The thickness of four Kevlar layers is 0.8 mm and the thickness of a single Kenaf layer is 0.3 mm. Figure 9.1a represents the thickness of each layer and has an overall thickness of 0.11 mm. Plate 2 has a thickness dimension of four layers of Kevlar of 0.8 mm and a single kenaf layer of 0.3 mm with stacking sequence of Kevlar/Kenaf/Kevlar/Kevlar/Kevlar. Figure 9.1b represents the thickness of each layer and represents an overall thickness of 0.11 mm. Plate 3 has a stacking sequence of Kevlar/Kevlar/Kevlar/Kenaf/Kevlar. Plate 3 has thickness dimensions of four layers of Kevlar fabric of 0.8 mm, and a single layer of kenaf fiber of 0.3 mm thickness. Figure 9.1c represents the thickness of each layer and represents an overall thickness

Table 9.1 Mechanical properties

	Kenaf fiber	Kelvar fiber	Resin Epoxy
Young's modulus x direction (Pa)	$4.21e^{+09}$	$1.85e^{+010}$	$3.78e^{+09}$
Young's modulus y direction (Pa)	$2.103e^{+09}$	$1.85e^{+010}$	
Young's modulus z direction (Pa)	$4.21e^{+09}$	$6e^{+009}$	
Poisson's ratio XY	0.362	0.25	0.35
Poisson's ratio YZ	0.181	0.33	
Poisson's ratio ZX	0.362	0.33	
Shear modulus XY (Pa)	$1.54e^{+09}$	$7.7e^{+008}$	$1.4e^{+09}$
Shear modulus YZ (Pa)	$8.90e^{+09}$	$5.43e^{+009}$	
Shear modulus ZX (Pa)	$1.54e^{+09}$	$5.43e^{+009}$	
Density (Kg/m^3)	1400	1440	1160

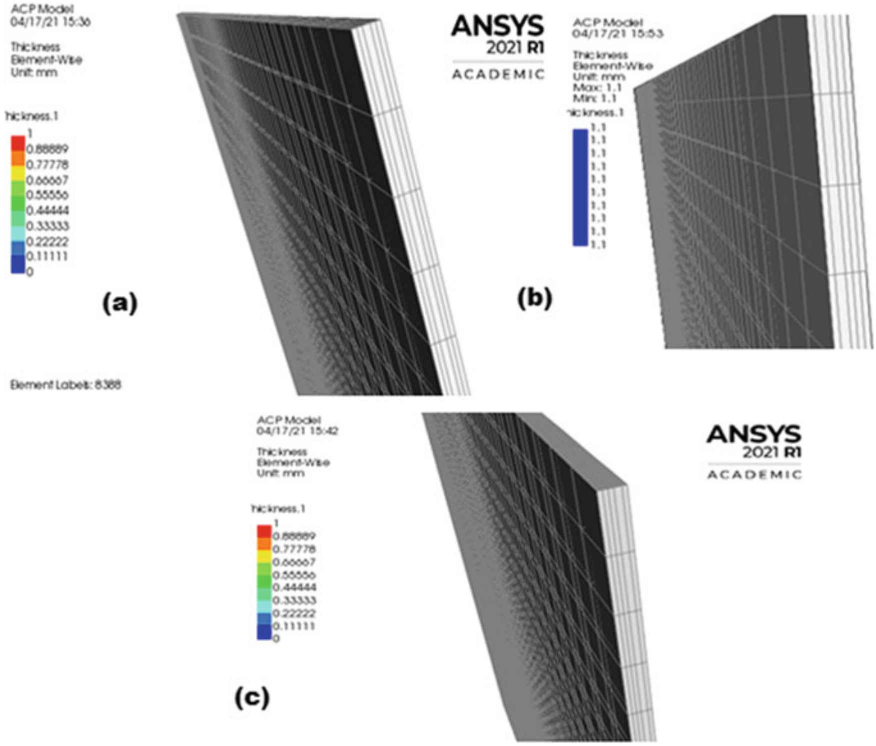

Fig. 9.1 Solid model of **a** Plate 1, **b** Plate 2 and **c** Plate 3

of 0.11 mm. Kevlar layers are modelled using a macro homogeneous model, which assumes that the whole layer is homogenous in shape and has orthotropic mechanical characteristics.

The projectile geometry is modeled using ANSYS Design modeler along with the composite plates. A projectile is supposed to be 20 mm away from the composite plate/origin. The projectile's substance is Steel 1006 (LA-4167-MS. May 1, 1969. EOS 7th International Symposium on Ballistics, Johnson and Cook) and it is chosen from the ANSYS Explicit Dynamics material database. ANSYS Explicit dynamics mesh modeller with linear element order and explicit physics preference is used to construct the 3D mesh of the bullet.

The plate dimensions are 100 mm $\times$ 100 mm $\times$ 3.5 mm. ANSYS Explicit elements and Ansys Explicit dynamics are used to handle the problem. The programme has automatically configured body interactions for the Kenaf and Kevlar layers. Body contact between the projectile and the composite is deemed frictionless. To foresee the ballistic conduct of the framework, the solver yields set to figure aggregate and 'z' directional distortion of the stack layers. Furthermore, equivalent stress (Von-Mises) is set to show the residual stress of the entire framework. Erosion is included in the solver, a numerical mechanism automatically removes elements (deletion) that allows simulation of penetration, material fracture and cutting. The velocity of the projectile is assigned as an initial component in the global coordinate system and is varied in the 'z' direction and x and y components of the system are assigned with fixed support boundary conditions. A time of $3e^{-004}$ s is set as the end time with a maximum number of cycles of $1e^{+07}$. All the three plates are configured with the same type of analysis settings and the temperature is also made constant for all three plates when the simulation is done. All simulations presented here use a 9 mm 1006 steel bullet with a Johnson–Cook strength model that includes strain and strain rate hardening constants, as well as the Gruneisen Coefficient. The projectile and composite target are modelled using a Lagrannian reference frame, which means that the mesh is attached to the material and thus deforms together, but the stiffness behaviour of the projectile is assumed to be rigid as the study is limited to the impact on composite plate. These, along with a material model and a set of initial and boundary conditions define the entire problem solution. The plates are impacted with different velocities and the velocity at which the materials failed (i.e., when complete penetration is observed) is noted and the plate's total deformation, directional deformation, Von-Misses stress, and maximum shear stress are studied and compared for that velocity.

9.3 Results and Discussion

Figure 9.2 represents the deformation observed in Plate 1 after the impact simulation. The projectile penetrated the plate completely at a velocity of 1142 m/s. It is observed that the maximum deformation is 41.414 mm. Figure 9.3 provides a visual representation of the deformation seen in Plate 1 after the impact simulation. The largest deformation measured is 41.414 mm, and the maximum deformation takes place at $1.2e^{-4}$ s. With respect to Plate 2, maximum deformation is observed as 41.503 mm at a velocity of 1131.5 m/s. It is observed that Plate 2 is completely penetrated at a velocity of 1131.5 m/s. Figure 9.4 provides a visual representation of the deformation seen in Plate 2 after the impact simulation. The largest deformation measured is 41.503 mm, and the maximum deformation takes place at $1.3e^{-4}$ s. With respect to Plate 3, the maximum deformation observed is 45.289 mm at a velocity of 1139.5 m/s. Plate 3 got completely penetrated at a velocity of 1139.5 m/s. Figure 9.5 provides a visual representation of the deformation seen in Plate 3 after the impact simulation. The largest deformation measured is 45.289 mm, and the maximum deformation takes place at $1.3e^{-4}$ s.

Table 9.2 lists the total deformation that results from a bullet striking Plate 1 at 1142 m/s, Plate 2 at 1131.5 m/s and Plate 3 at 1139.5 m/s is 41.414 mm, 41.503 mm, and 45.289 mm, respectively. Plate 1 has less total deformation than compared to hybrid composite plates with different stacking sequences with the same mechanical properties and considering the layers of Kevlar and Kenaf as homogeneous in nature. Plate 3 takes more deformation compared with the other two plates and this may

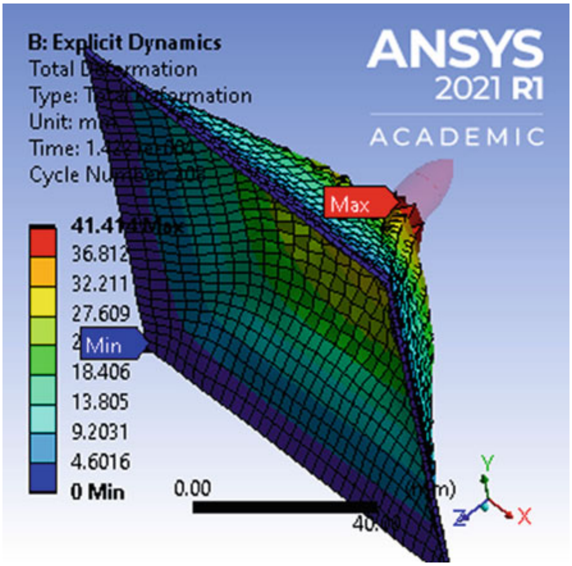

Fig. 9.2 Total deformation of Plate 1

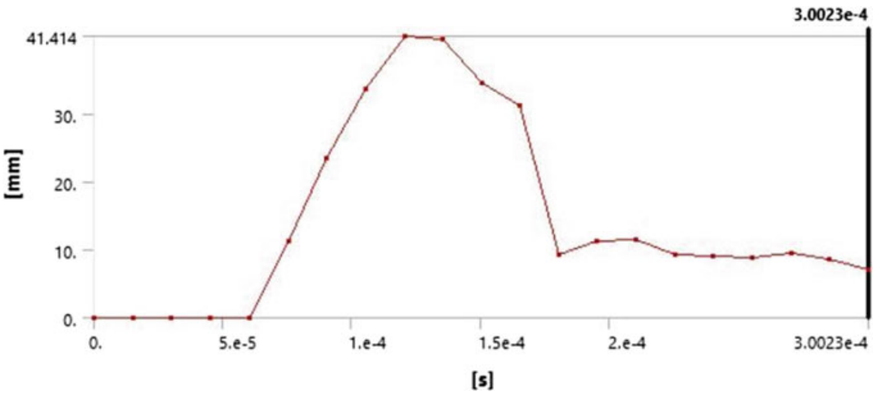

Fig. 9.3 Deformation versus time graph of Plate 1

be due to its stacking sequence and the type of material chosen. Plate 1 takes lesser deformation than others and it can be used as impact material in ballistic applications.

Figure 9.6 represents the maximum shear stress of Plate 1 after the impact simulation. The maximum shear stress observed is found to be 7543.2 MPa. Figure 9.7 provides a visual representation of the maximum shear stress seen in Plate 1 after the impact simulation. The maximum shear stress observed is found to be 7543.2 MPa, and the maximum time taken for it to occur is nearly $1.6e^{-4}$ s. With reference to Plate 2, maximum shear stress observed is 6528.3 MPa when the velocity of the projectile is

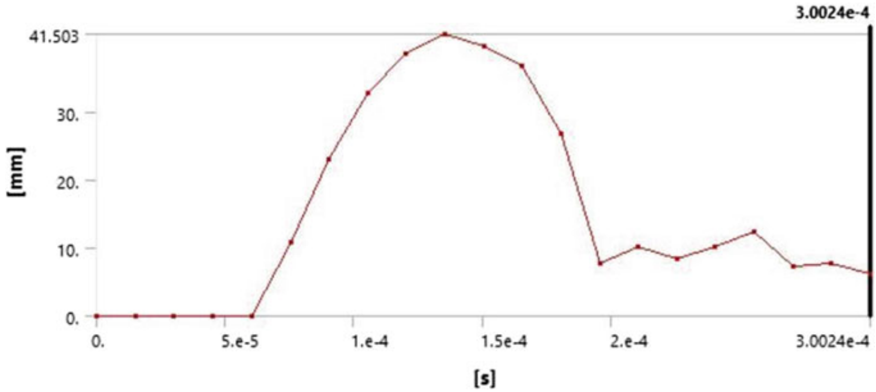

Fig. 9.4 Deformation versus time graph of Plate 2

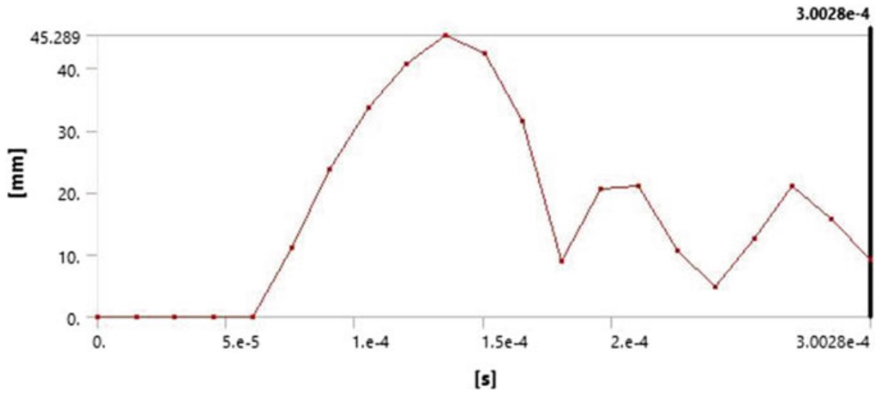

Fig. 9.5 Deformation versus time graph of Plate 3

Table 9.2 Investigated parameters of all three plates

	Velocity (m/s)	Total deformation (mm)	Maximum shear stress (MPa)	Equivalent stress (MPa)	Directional deformation (mm)
Plate 1	1142	41.414	7543.2	13,242	3.8425
Plate 2	1131.5	41.503	6528.3	12,232	4.4191
Plate 3	1139.5	45.289	6010.8	11,358	4.7192

1131.5 m/s. Figure 9.8 provides a visual representation of the maximum shear stress seen in Plate 2 after the impact simulation. The maximum shear stress observed is 6528.3 MPa, and the maximum time taken for it to occur is nearly 1.8e^{-4} s. In Plate 3, maximum shear stress of 6010.8 MPa has been observed. Figure 9.9 provides a visual representation of the maximum shear stress seen in Plate 3 after the impact simulation. The maximum shear stress is found to be 6010.8 MPa, and the maximum time taken for it to occur is nearly 1.5e^{-4} s.

Table 9.2 lists the maximum shear stress that results from a bullet striking Plate 1 at 1142 m/s, Plate 2 at 1131.5 m/s and Plate 3 at 1139.5 m/s is 7543.2 MPa, 6528.3 MPa, and 6010.8 MPa respectively. The maximum shear stress of Plate 1 is found to be the highest at an impact velocity of 1142 m/s with boundary conditions as fixed on four sides. The Kevlar and Kenaf layers are homogenous in nature. Plate 3 takes less stress compared with the other two plates and this may be due to its stacking sequence and the type of material chosen. Figure 9.10 represents the equivalent stress

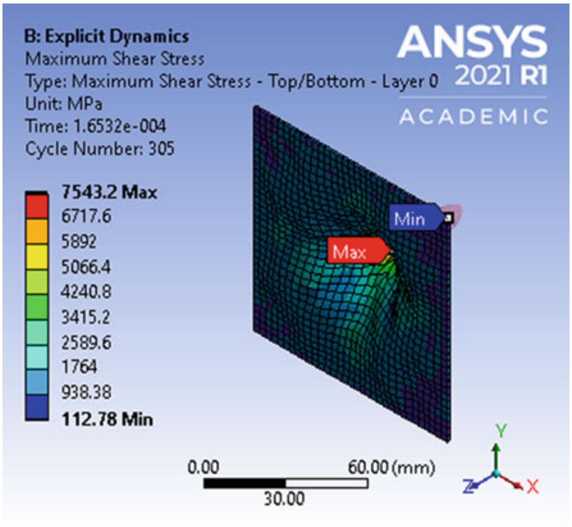

Fig. 9.6 Maximum shear stress of Plate 1

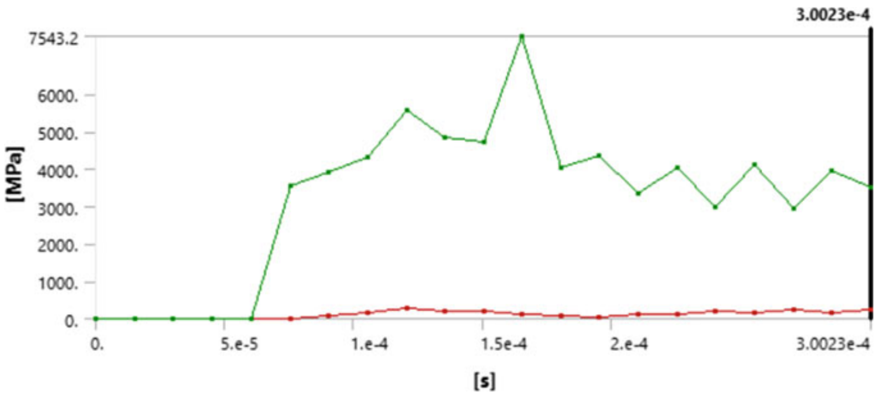

Fig. 9.7 Maximum shear stress versus time graph of Plate 1

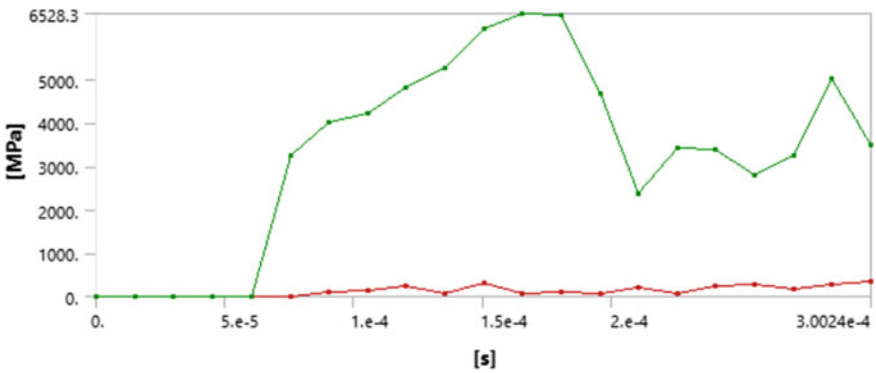

Fig. 9.8 Maximum shear stress versus time graph of Plate 2

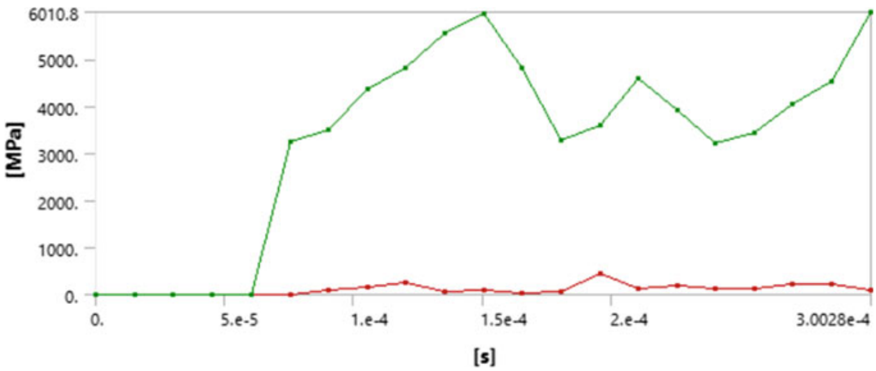

Fig. 9.9 Maximum shear stress versus time graph of Plate 3

observed in Plate 1 after the projectile impact. Maximum equivalent stress observed after complete penetration is found to be 13,424 MPa.

Figure 9.11a provides a visual representation of the equivalent stress seen in Plate 1. Maximum Equivalent stress observed after complete penetration is 13,424 MPa, and the maximum time taken for it to occur is nearly $1.6e^{-4}$ s. In Plate 2, maximum equivalent stress observed is 11,358 MPa when the impact velocity is 1131.5 m/s. Figure 9.11b provides a visual representation of the equivalent stress seen in Plate 2 after the impact simulation and the maximum equivalent stress observed after complete penetration is found to be 11,358 MPa, and the maximum time taken for it to occur is nearly $1.4e^{-4}$ s. Plate 3 has a maximum equivalent stress as 12,232 MPa when the projectile is impacted at a velocity of 1139.5 m/s. Figure 9.12 provides a visual representation of the equivalent stress seen in Plate 3 after the impact simulation. Maximum Equivalent stress observed after complete penetration is found to be 12,232 MPa, and the maximum time taken for it to occur is nearly $1.6e^{-4}$ s. Table 9.2 lists the maximum equivalent stress and maximum directional deformation. During

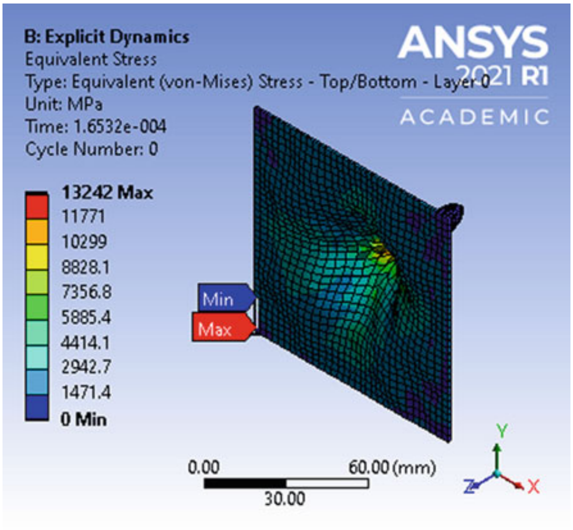

Fig. 9.10 Equivalent stress of the Plate 1

the impact of the composite panel, Panel 1 has a maximum equivalent stress value of 13,242 MPa at a velocity of 1142 m/s. This further confirms that Plate 1 has better impact resistance than the other two plates. The maximum deformation of Plate 3 is greater when compared to the other two plates. This confirms that the stacking sequence does have influence over the deformation and plate 1 with kenaf as third layer in the stacking sequence showed lesser deformation than the other two Plates.

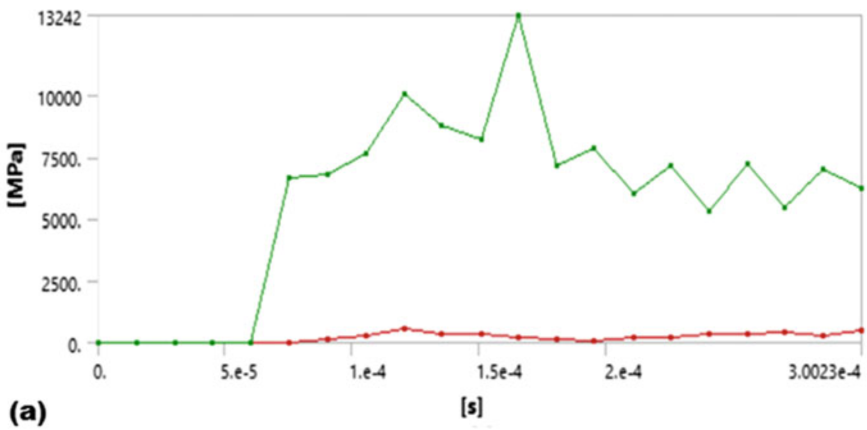

Fig. 9.11 Equivalent stress versus time graph of **a** Plate 1 and **b** Plate 2

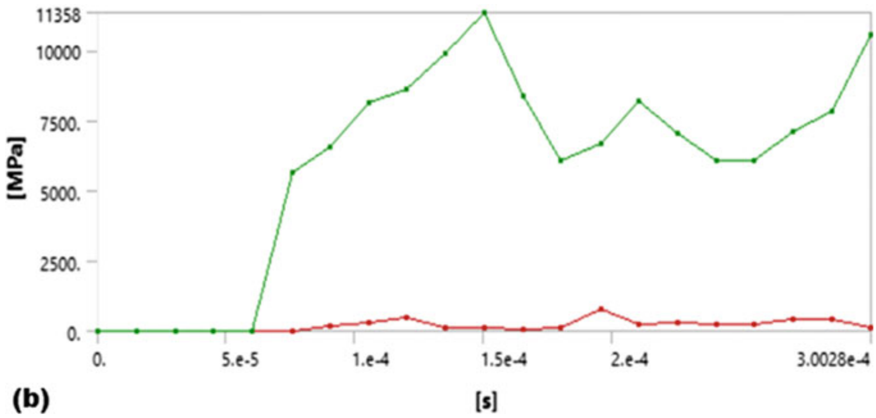

Fig. 9.11 (continued)

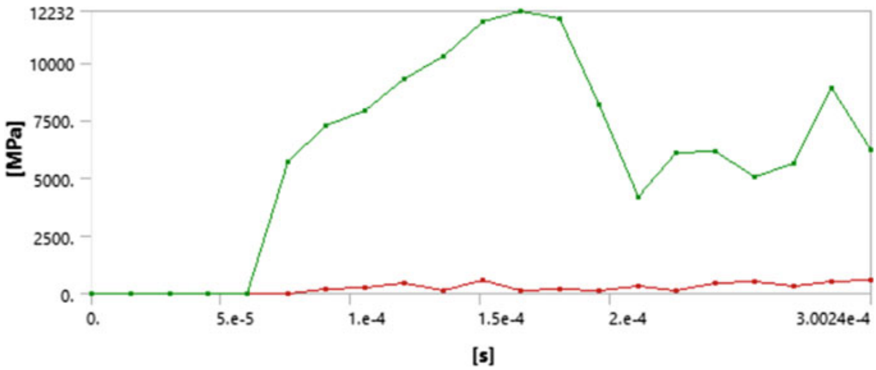

Fig. 9.12 Equivalent stress versus time graph of Plate 3

9.4 Conclusion

Ballistic impact test is performed successfully on all three hybrid composite plates with varied velocity impacts. A nonlinear equation of state is used in combination with an orthotropic stiffness matrix to accurately simulate the behavior of a composite material under impact circumstances. Plate 1 has shown very less flexural deformation and a high equivalent stress. So, Plate 1 has the potential for use in places where high structural strength apart from a lower flexural value is required. Plate 2 is penetrated completely at a velocity of 1131 m/s which is the earliest compared to the other two plates. Therefore, the stacking sequence of composite Plate 2 is weakest compared to the other two plates. All three plates withstood projectile impacts up to a velocity of 1100 m/s. Even though Plate 2 failed at the earliest, Plate 3 showed the highest deformation among the other 2 plates. Plate 1 with kenaf as its 3rd layer shows better resistance to high velocity impacts than the other two stacking sequences. Total deformation, Von-Mises stress also shows the effectiveness of Plate 1. Hence, Plate 1 can be effectively used in high velocity impact applications.

References

1. Soydan, A.M., Tunaboylu, B., Elsabagh, A.G., Sar, A.K., Akdeniz, R.: Simulation and experimental tests of ballistic impact on composite laminate armor. Adv. Mater. Sci. Eng. **2018** (2018). Article ID 4696143
2. Yahaya, R., Sapuan, S.M., Jawaid, M., Leman, Z., Zainudin, E.S.: Investigating ballistic impact properties of Woven Kenaf-Aramid hybrid composites. Fibers Polym. **17**, 275–281 (2016)
3. Balaji Shunmugam, A., Velmurugan, R.: Comparative study of ballistic performance parameter of Kevlar/Epoxy composite laminate. In: Tadepalli, T., Narayanamurthy, V. (eds) Recent Advances in Applied Mechanics. Lecture Notes in Mechanical Engineering. Springer, Singapore (2022)
4. Sikarwar, R.S., Velumurugan, R., Gupta, N.K.: Ballistic performance of Kvlar/Epoxy composite laminates. Proc. Indian Natl. Sci. Acad. **79**(4), 789–799 (2013)
5. Kumar, S., Gupta, D.S., Singh, I., Sharma, A.: Behavior of Kevlar/Epoxy composite plates under ballistic impact. J. Reinforced Plastics Compos. **29**(13), 2048–2064 (2010)

Chapter 10
Computational Modelling on Lithium-Ion Battery Pack Forced Convection Cooling

Prakash Ghose, Swarup Kumar Nayak, Basanta Kumar Rana, and Jitendra Kumar Patel

Abstract Lithium-ion batteries are widely used in cell phones, laptops and battery vehicles. However, during discharge, a huge amount of heat is generated in the cell core. Thermal management of the battery pack is much important, particularly for electric vehicles to reduce fire hazards. In this work, CFD simulations are performed to evaluate the cooling effect of a 4 × 4 Lithium-ion battery pack with different discharge rates and different airflow velocities. From the results it is observed that cells present downstream have a higher temperature as compared to the cells placed upstream irrespective of discharge rate and airflow rate. The two mid-cells in the last row have the highest temperature in any operating condition. When the discharge rate increases, the amount of heat generation in the cells increases. Hence, the temperature of the corresponding cell in each row is relatively higher as compared to the low discharge rate condition. Similarly, with an increase in airflow velocity, the cooling rate of the battery pack is enhanced.

10.1 Introduction

Hydrocarbon fuel-driven automobiles are one of the major sources of air pollution. CO_2, CO, NOx emissions from automobiles affect human health and are also responsible for global warming. Today electric vehicles are the most prominent alternative to fuel-driven vehicles. Though electric vehicle technology is not a new concept but due to the poor energy storage capacity of lead-acid and Nickel–cadmium batteries, electric vehicles were not popular. Lithium-Ion battery technology now changed the scenario of electric vehicles due to its high energy storage ability. However, during charging and particularly during discharging, a huge amount of heat is generated from the Li-Ion battery. Therefore, the thermal management of the battery is an

P. Ghose (✉) · S. K. Nayak · B. K. Rana · J. K. Patel
School of Mechanical Engineering, KIIT Deemed to be University, Bhubaneswar 751024, India
e-mail: pghosefme@kiit.ac.in

P. H. V. S. Talpa Sai et al. (eds.), *Intelligent Manufacturing and Energy Sustainability*, Smart Innovation, Systems and Technologies 372,
https://doi.org/10.1007/978-981-99-6774-2_10

important factor hence cooling system should be designed properly. Otherwise, fire hazards may cause a severe accidents.

Wang et al. [1] investigated battery cooling through forced convection with various cell arrangement structures. It has been reported that a fan placed on the top of the module is the best cooling method. A cubic arrangement of cells is a better option for cooling and also it is cost-effective. On the other hand, hexagonal cell arrangement is best as space utilization is a concern. In another work, Wang et al. [2] conducted CFD simulations to investigate the temperature distribution and heat transfer of Lithium-Ion batteries through air cooling. It is suggested that if the ambient temperature is below 20 °C, forced convection for cooling is not required. Also, it is mentioned that the upper ambient temperature limit is 35 °C with forced convection cooling. Saw et al. [3] developed new correlations for the Nussetl number and Reynolds number from their experimental and CFD study, where the air is used as a cooling fluid. Xu et al. [4, 5] used U-shaped duct and baffle plates respectively to enhance the battery cooling using air as working fluid. Many researchers also used heat pipes to improve the heat transfer rate on battery cooling [6–8]. Battery cooling using phase change material is also a method [9, 10] that is investigated by many researchers. Hybrid cooling processes such as; (i) PCM is used as a primary coolant and water is used as a secondary coolant (ii) PCM used in heat pipe etc. are also investigated for cooling enhancement [11, 12]. To increase the cooling effect, Ethyl glycol–water, Al_2O_3-water, ZnO-water and CuO_2-water nanofluids are also used for battery cooling and performance has been investigated [13, 14].

In the current simulation, a 4 × 4 lithium-Ion battery pack is used for simulation to investigate the cooling effect of the battery pack with different battery discharge rates and airflow velocities are acceptable.

10.2 Methodology

A 4 × 4 lithium-Ion battery pack is used for simulation as shown in Fig. 10.1. The gap between two consecutive cells in the lateral direction is 3 mm and the gap between two consecutive cells in the longitudinal direction is 6 mm. The height of the cell is 90 mm and the diameter of the lithium-ion core is 18 mm and it is covered with a 1.5 mm thick steel casing. The battery pack cover dimension is 91 mm × 82 mm × 100 mm.

The computational geometry has three domains such as; (i) Fluid domain (ii) Lithium-ion core and an (iii) Steel cover. The geometry is prepared with the help of Ansys Design modeler and meshed using Ansys Meshing tool. The entire domain has meshed with 1.5 million hexahedra cells. The interfaces between the overlapping domains are converted to the coupled boundary so that only heat exchanges between the domains will be possible. One face of the fluid domain along the longitudinal direction is given as the inlet boundary and the opposite plane is kept as the outlet boundary. The remaining faces of the fluid domain are the adiabatic boundaries.

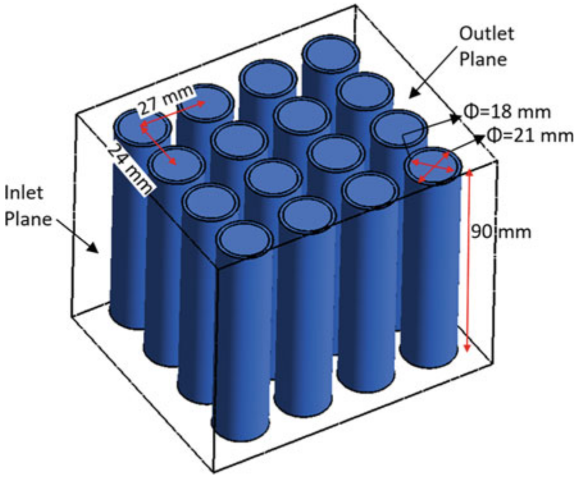

Fig. 10.1 Lithium-ion battery pack geometrical configuration

Table 10.1 Properties of lithium-ion cell [15]

Property	Values
Rated voltage	3.2 V
Rated current	1.35 Ah
Density	2018 kg/m^3
Specific heat	1282 J/kg K
Volume	0.0000227 m^3
Thermal conductivity	Radial: 0.9 W/mK Axial: 2.7 W/mK

In this simulation, a 18,650 battery is used. The physical properties of the battery core are given in Table 10.1.

Orthogonal conductivity is used for the Lithium-ion core. The standard constant thermophysical properties of steel are used for the battery cover. Also, the standard constant thermophysical properties of air are used for the fluid domain. Buoyancy-driven heat transfer is not considered in this work. Only force convection cooling is considered. Continuous cooling is required for the battery as heat generates during battery discharge. The heat generation theory proposed by Bernadi [16] is used as given in Eq. (10.1).

$$Q_g = \frac{1}{V_{battery}}\left[i^2 R_i + iT\frac{\mathrm{d}U_0}{\mathrm{d}T}\right] \tag{10.1}$$

The first parameter in the bracket of Eq. (10.1) is the polarization heating effect and the second term is the Joule heating effect. $V_{battery}$ is the battery volume, i is the current flow during discharge, R_i is the internal resistance, T is the battery temperature and the term $\frac{\mathrm{d}U_0}{\mathrm{d}T}$ is the parameter which is related to an electrochemical

Table 10.2 Operating conditions

Cases	Discharge rate	Current (A)	Heat rate (W/m^3)	Airflow velocity (m/s)
1	1C (discharge in 1 h)	1.35	5318	0.01
2	2C (discharge in 30 min)	2.07	19,452	0.01
3	2C (discharge in 30 min)	2.07	19,452	0.1

reaction. In this work, the internal resistance is set as 0.04 Ω and the term $T\frac{dU_0}{dT}$ is taken as 0.01116 × rated voltage [15].

Simulations are conducted for two discharging conditions where the air flow rate is kept as 0.01 m/s. Simulations are also performed with different air flow rates where the discharge rate is kept constant. The cases simulated are given in Table 10.2.

Steady-state mass, momentum and energy conservation equations in Reynolds averaged form are solved along with k and ε equations of the standard k-ε model. The heat rate values given in Table 10.2 are set as a constant source of the lithium-ion core. SIMPLE velocity–pressure coupling approach and second-order upwind spatial discretization scheme are used. Convergence criteria 10^{-4} is set for all governing equations except the energy equation. For the energy equation, it is set as 10^{-6}.

10.3 Results and Discussion

10.3.1 Effect of Battery Discharge Rate

Figure 2a shows the temperature distribution across the mid-horizontal plane for case-1 and case-2. Figure 2c shows the 3-D view of the cell cover temperature distribution and the air velocity pattern on the mid-plane for case-1 and case-2.

From both figures, it is observed that in case-1 (1C discharge rate), the temperature across the cells is less than in case-2 (2C discharge rate). In both cases, the air mass flow rate is the same but the heat generation in case-2 is around 4 times greater than in case-1 in the cell core. Therefore, in every row of the cell in the battery pack of case-2 (shown in Table 10.2), the temperature is higher as compared to case-1. It is obvious that the surface temperature of cell covers is higher in case-2 as the amount of heat generation is higher in this case. As a result, relatively a higher amount of heat is transferred from cell covers to the air. Hence, the air temperature is also high for case-2.

In both cases (case-1 and 2), it can be visualized that the air temperature increases along the downstream direction. Moreover, the temperature of the cells in the first row is the lowest and it increases consecutively for the cells placed downstream. The air received heat from the first row of cells and its temperature rises. The hot air cannot receive more amount of heat from the next row of cells because the temperature difference between cell cover and air decreases. Hence, the cell temperature placed downstream is higher.

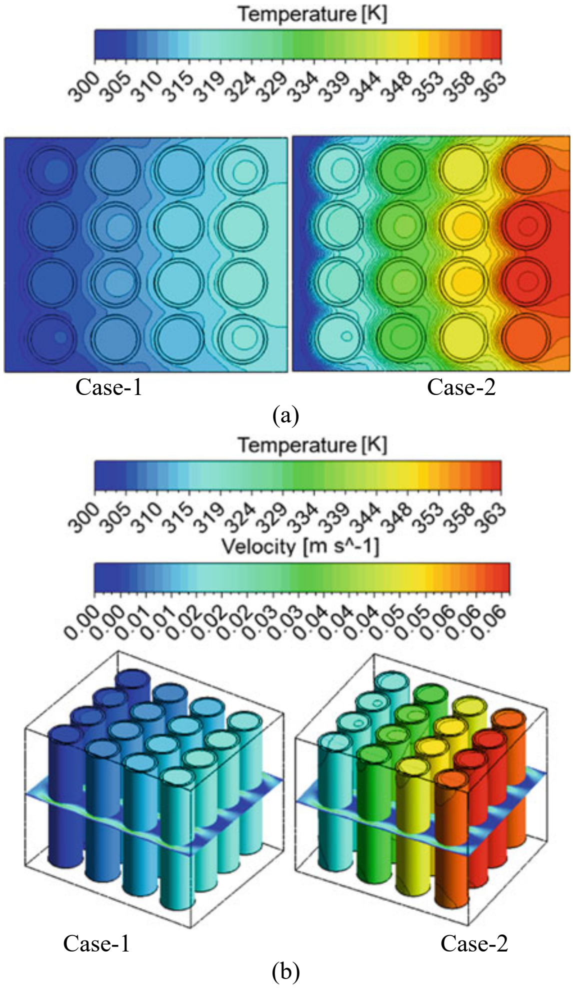

Fig. 10.2 **a** Temperature distribution across the mid-plane of the domain. **b** Cell outer surface temperature and velocity contour at the mid-plane, for case-1 and 2

The cell cover surface temperature for case-1 and case-2 is also shown in Fig. 2b. It can be visualized that the temperature of two mid cells in every row has a higher temperature than the side cells. The airflow between the side cells and battery casing receives heat from one side. On another side, it is the battery casing wall. Hence no heat is received from another side. But airflow across the middle cells received heat from both sides. As a result, the air temperature between cells increases. Hence, due to the decrease in temperature difference between mid-cells and air less heat transfer occurs from mid-cells. Therefore, the temperature of two mid cells in every row becomes higher than the side cells.

10.3.2 Effect of Air Flow Rate

Figure 10.3a, b, shows the temperature distribution across the mid-plane and surface temperature of cells respectively. In both cases (case-2 and case-3), the discharge rate is maintained at 2C with different air flow rates. From the figures, it has been observed that as the airflow velocity increases, the cell temperature decreases throughout. A huge temperature drop across the cells is observed when the air velocity increases from 0.1 to 0.1 m/s. From Fig. 10.3b, it is observed that the maximum air velocity in the cell gap is around 0.02 m/s for case-2, whereas it is around 0.18 m/s for case-3. When the air velocity increases, the local Reynolds number increases. Hence Nusselt number increases. As a result, the heat transfer coefficient increases with an increase in air velocity. Therefore, the battery cooling is enhanced with an increase in air velocity.

From Fig. 10.4, it is observed that in case-2, the temperature of the cell is highest (363 °C) and it is the lowest for case-3. The highest temperature is obtained at the two mid cells of the last row. In case-2, the 2C discharge rate generates the highest amount of heat while the airflow velocity is maintained at 0.01 m/s. In case-3 it is increased to 10 times. Hence, the cell maximum temperature is the lowest among all the cases.

Table 10.3 depicts the amount of heat generated, the amount of heat that enters through inlet air, the total heat energy that moves out from the system, the pressure drop across the battery and the average temperature of outlet air for various cases.

It is observed that in case-1 and case-2, different amount of heat is generated because they have different discharge rate but the airflow velocity is the same. The average temperature of outflow gas is less for case-1 because it has a smaller energy source. However, the pressure drop is the same for case-1 and case-2 because the airflow velocities are the same for both cases. It is observed that in case-2 and case-3 same amount of heat is generated in the cells due to the high discharge rate. In case-3, the heat rejected out is maximum in case-3 due to high airflow velocity and the average temperature of outlet air is 304.87 K. The pressure drop in case-3 is the highest because high flow velocity causes higher frictional losses.

10.4 Conclusion

CFD simulations are conducted to determine the cooling of 4×4 Lithium-ion battery pack with different discharge rate and with different air flow velocity. The heat generation from cell are determined using the correlation developed by Bernadi. From the result it is observed that with an airflow velocity of 0.01 m/s, when the battery discharge rate is 1C, 2.153 W of heat energy is rejected out from the cells and the average air temperature at the outlet is around 315 K. When the discharge rate increases up to 2C, heat rejection increases to 238% and the temperature of outlet air increases to 13.15%. Similarly, with increase in air flow velocity considering

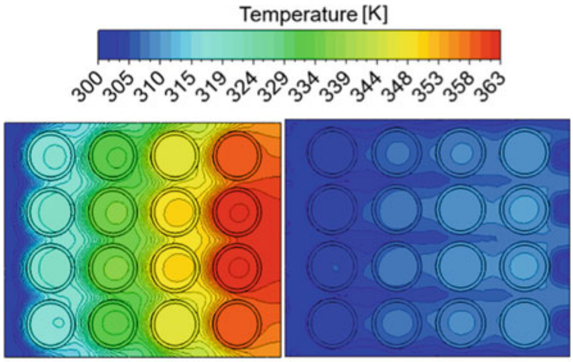

Case-2 Case-3

(a)

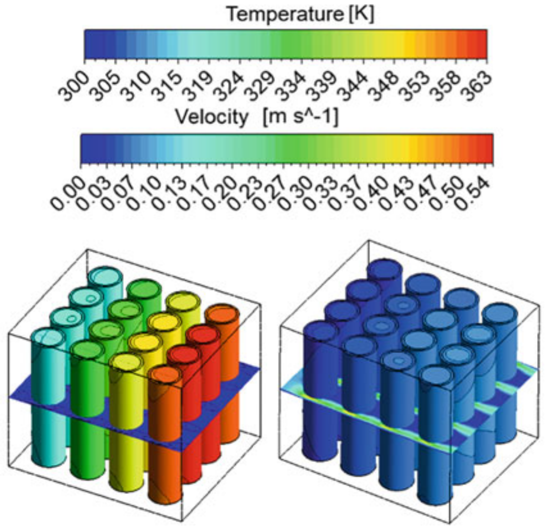

Case-2 Case-3

(b)

Fig. 10.3 **a** Temperature distribution across the mid-plane of the domain. **b** Cell outer surface temperature and velocity contour at the mid-plane, for case-2 and 3

2C discharge rate, the amount of heat rejection increase to 28% and the outlet air temperature decreases to 15%. The pressure drop also increases across the battery pack with increase in airflow velocity.

It is also observed that the last row cells have the highest temperature and the first row cells have the lowest temperature regardless of discharge rate and airflow velocity. The two middle cells of the last row have the highest temperature among all irrespective of discharge and flow conditions. For case-1, case-2 and case-3 the middle cells of the last row have 317 K, 362 K and 310 K respectively.

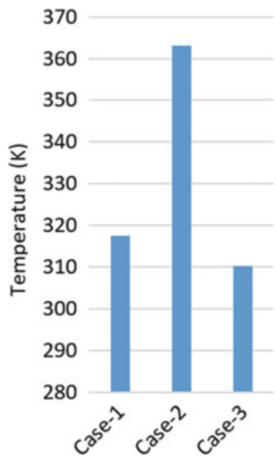

Fig. 10.4 Maximum temperature inside the cell

Table 10.3 Various variables at inlet and outlet for different cases

Case	Flow area (m^2)	Mass flow rate (kg/s)	Inlet (W)	Energy source (W)	Outlet (W)	Avg. Pressure drop (Pa)	Avg. Temp Outlet (K)
1	0.01	0.0001225	0.2213	1.9323	2.1536	0.0271	315.61
2		0.0001225	0.2213	7.0682	7.2895	0.0271	357.12
3		0.001225	2.2808	7.0682	9.3485	0.4265	304.87

References

1. Wang, T., et al.: Thermal investigation of lithium-ion battery module with different cell arrangement structures and forced air-cooling strategies. J. Appl. Energ. **134**, 229–238 (2014)
2. Wang, T., Tseng, K., Zhao, J.: Development of efficient air-cooling strategies for lithium-ion battery module based on empirical heat source model. J. Appl. Therm. Eng. **90**, 521–529 (2015)
3. Saw, L.H., et al.: Computational fluid dynamic and thermal analysis of Lithium-ion battery pack with air cooling. J. Appl. Energ. **177**, 783–792 (2016)
4. Xu, X., He, R.: Research on the heat dissipation performance of battery pack based on forced air cooling. J. Power Sour. **240**, 33–41 (2013)
5. Jiaqiang, E., et al.: Effects of the different air cooling strategies on cooling performance of a lithium-ion battery module with baffle. J. Appl. Therm. Eng. **144**, 231–241 (2018)
6. Tran, T.-H., Harmand, S., Sahut, B.: Experimental investigation on heat pipe cooling for hybrid electric vehicle and electric vehicle lithium-ion battery. J. Power Sour. **265**, 262–272 (2014)
7. Wang, Q., et al.: Experimental investigation on EV battery cooling and heating by heat pipes. J. Appl. Therm. Eng. **88**, 54–60 (2015)
8. Liang, J., Gan, Y., Li, Y.: Investigation on the thermal performance of a battery thermal management system using heat pipe under different ambient temperatures. J. Energ. Convers. Manage. **155**, 1–9 (2018)
9. Chen, F., et al.: Air and PCM cooling for battery thermal management considering battery cycle life. J. Appl. Therm. Eng. **173**, 115154 (2020)
10. Verma, A., Shashidhara, S., Rakshit, D.: A comparative study on battery thermal management using phase change material (PCM). J. Therm. Sci. Eng. Prog. **11**, 74–83 (2019)

11. Bai, F., et al.: Thermal management performances of PCM/water cooling-plate using for lithium-ion battery module based on non-uniform internal heat source. J. Appl. Therm. Eng. **126**, 17–27 (2017)
12. Putra, N., et al.: Performance of beeswax phase change material (PCM) and heat pipe as passive battery cooling system for electric vehicles. J. Case Stud. Therm. Eng. **21**, 100655 (2020)
13. Jilte, R., Kumar, R., Ahmadi, M.H.: Cooling performance of nanofluid submerged vs. nanofluid circulated battery thermal management systems. J. Clean. Prod. **240**, 118131 (2019)
14. Wiriyasart, S., et al.: Thermal management system with nanofluids for electric vehicle battery cooling modules. J. Case Stud. Therm. Eng. **18**, 100583 (2020)
15. Huang, Y., et al.: Study on the thermal interaction and heat dissipation of cylindrical lithium-ion battery cells. J. Energ. Procedia **142**, 4029–4036 (2017)
16. Bernardi, D., Pawlikowski, E., Newman, J.: A general energy balance for battery systems. J. Electrochem. Soc. **132**(1), 5 (1985)

Chapter 11
Computational Studies on Single-Wall Rotating Vaneless Diffuser of a Centrifugal Compressor Stage

Anusha Yagnamurthy, Jyothsna Dokala, George Ratna Vamsi Preggam, S. Seralathan, S. Sathish, and A. Muthuram

Abstract This paper focuses on the computational study on the effect of single wall rotation of vaneless diffuser, namely hub side wall and shroud side wall of the vaneless diffuser. ANSYS CFX software is used to analyze the flow parameters and performance of the single wall rotating vaneless diffuser. The rotating diffusers are examined at five dimensionless mass flow rates using SVD as the base model. Using the same impeller, SVD, HRVD, SRVD, and RVD configurations are simulated and compared. Static pressure and total pressure in stationary frame are measured to understand the diffusion process in the single wall rotating vaneless diffuser. Based on the investigations, HRVD outperforms all other configurations with overall improved performance in terms of pressure rise and flow dynamics.

11.1 Introduction

Centrifugal compressors have three main components: impeller, diffuser, and casing. A centrifugal compressor is a device which uses an impeller to accelerate the fluid radially and compress the fluid. At the downstream, the diffuser further converts the velocity of fluid into pressure energy. Centrifugal compressor efficiency is impacted by diffuser losses and non-uniformity in flow at impeller's outlet. This results in a large loss in total pressure and a decrease in centrifugal compressor performance. Rotating a portion of the stationary vaneless diffuser walls at the impeller speed significantly reduces the shear forces between the diffuser walls and the flow. As a result, the operating range and performance are improved [1]. Dean and Senoo did research on vaneless diffuser-equipped centrifugal compressors. The results illustrated on the flow at diffuser entry region is irregular, unstable, and three-dimensional.

A. Yagnamurthy · J. Dokala · G. R. V. Preggam · S. Seralathan (✉) · S. Sathish · A. Muthuram
Department of Aerospace Engineering, Hindustan Institute of Technology and Science, 603103, Chennai, Tamil Nadu, India
e-mail: siva.seralathan@gmail.com

P. H. V. S. Talpa Sai et al. (eds.), *Intelligent Manufacturing and Energy Sustainability*, Smart Innovation, Systems and Technologies 372,
https://doi.org/10.1007/978-981-99-6774-2_11

This causes secondary flow zones to emerge in the diffuser flow domain and subpar compressor performances [2].

To minimize the energy losses in centrifugal compressors due to diffusion, many radial diffuser designs are proposed. A rotating vanless diffuser (RVD) with shroud extension is a straightforward and practical design solution that can significantly improve centrifugal compressor efficiency and lower energy losses. It has been found from a research study that RVD had the capacity to smooth out the incoming distorted particles and enhance the performance of the centrifugal compressor. However, it has been proved that impellers with extended shrouds will only benefit high-speed stage to a small extent and have a minimal impact on the efficiency of low-specific-speed stages [3]. Recently initial numerical studies on a forced RVD with a centrifugal impeller compressor stage having exit blade angle $\beta = 90^\circ$ were completed by Seralathan and Roy Chowdhury [4] and Govardhan and Seralathan [3]. Sivamani and Ghosh [5] also studied a backswept impeller with impeller's disc that extended 40% past the tip diameter of the impeller blade. The investigations showed a greater static pressure rise was enhanced by reduced stagnation pressure losses [6].

The walls of the vaneless area of an RVD rotate independently of the impeller. Hence, the diffuser speed will be much less than the impeller speed [7]. Blade trimming or blade cutback is another way of accomplishing additional static pressure recovery, but it has failed and proved to be not suitable to achieve the desired static pressure.

Studies had shown that a free-rotating vaneless diffuser with a rotational speed more than 0.50 times the speed of the impeller was more effective in terms of diffusion. Thus, it had been demonstrated that free-rotating vaneless diffusers can produce high static pressure with minimal energy consumption in low-speed centrifugal compressors [8]. The working range of a centrifugal compressor with a vaned diffuser is less than that of a vaneless diffuser. Vaneless diffusers are employed in a variety of applications due to their wide working range, ease of manufacture, and simple design.

However, all earlier studies attempted to understand the diameter ratio of the RVD portion that outperforms all other diameter ratios. Computational research by a few authors focused on the performance of the forced RVD compressor stage with low specific speed and pressure ratio demonstrated the existence of an optimum dimensional details of the centrifugal compressor.

Hence, the focus of this study is to make one wall of the RVD rotate while the other wall remains stationary viz., the hub side wall of the diffuser rotates while the shroud side wall is stationary and vice versa. All the comparison in terms of performance and flow parameters of a compressor are made with base stationary vaneless diffuser and rotating vaneless diffusers. The commercial CFD code, ANSYS CFX [3] is used for this study and the simulations are carried out for different mass flow rates ($\phi =$ 0.025, 0.045, 0.054, 0.1, 0.25).

11.2 Computational Methodology

Table 11.1 shows the parameters of the compressor and diffuser. Geometrical models are generated using ANSYS Design Modeller with the dimensions listed here. The diffuser is made to rotate at equivalent speed of the impeller (RVD) and make one wall of the RVD rotate while the other wall remains stationary viz., the hub side wall of the diffuser rotates while the shroud side wall is stationary (HRVD) and vice versa (SRVD). All the comparisons are made with conventional stationary vaneless diffuser (SVD). Figure 11.1 shows the impeller chosen for the present study with its dimensional details listed in Table 11.1.

The meshing of impeller geometry is done in ANSYS Turbo grid [4] with elements count of 339,420 and total number of nodes are 368,714. Target mesh size method is used to generate fine meshing. Figure 11.2 shows the meshed computations domain based on single passage approach chosen here to minimize the computational resources [5]. To reduce the expenses of processing and time, the current work

Table 11.1 Dimensional information

Inducer hub diameter	D_1	98.40 mm	Thickness of the blade	T	6 mm
Inducer tip diameter	D_2	215.20 mm	Width of the blade at inlet	b_1	58.5 mm
Impeller exit diameter	D_3	570 mm	Width of the blade at exit	b_2	27.6 mm
Diffuser exit diameter	D_4	798 mm	Blade angle at the inlet	β_1	44.6°
Rotational speed of the impeller	N	1500 rpm	Blade angle at the exit	β_2	90°
Diffuser diameter ratio	D_4/D_3	1.4	Number of blades	Z	18

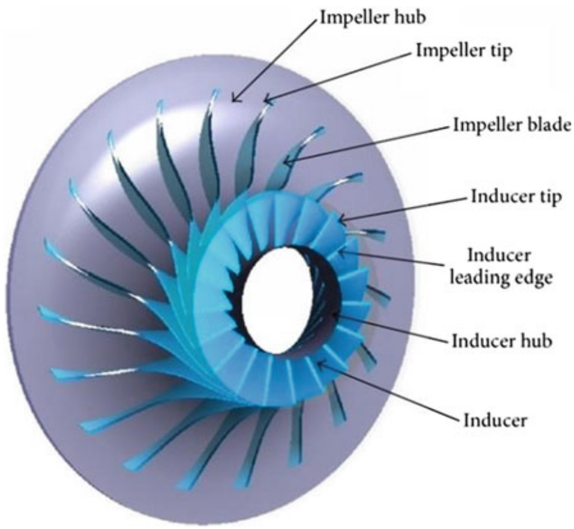

Fig. 11.1 Centrifugal impeller

Fig. 11.2 Meshed domain

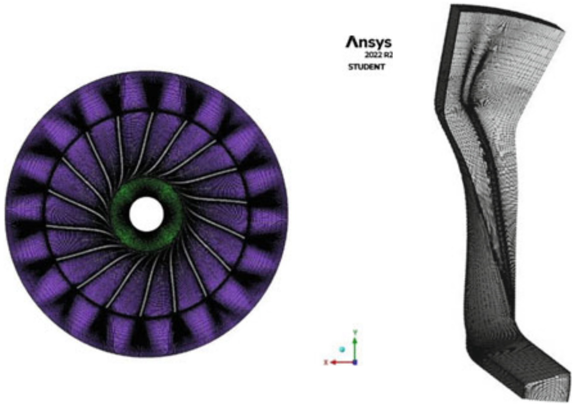

examines using single passage approach for simulation as shown in Fig. 11.2, by assuming that fluid flow in each fluid flow passage is periodic. Boundary conditions are steady state circumstances with total pressure in stationary frame at inlet, and the outlet it is given mass flow rate. The non-rotating and rotating domains are linked through frozen rotor interface [6]. In the conventional diffuser, the diffuser walls are stationary, and it is specified as counter rotating wall as the whole domain is defined as rotating domain initially. Every wall has a no-slip border condition [7]. Air (at 25 °C) is defined as the fluid, total energy is invoked for heat transfer model, and the boundary conditions at the walls are indicated as smooth and adiabatic. The turbulence model kω-SST is used to compute the 3D RANS equations [3, 8]. Due to time and computational resource constraints, the convergence threshold is set at 10^{-4}. All simulations are adiabatic and steady-state conditions. Governing equations such as continuity and momentum are used with advection scheme high resolution as solver performs the simulations [9]. The boundary conditions imposed are specified in Fig. 11.3.

11.3 Results and Discussion

The computational analysis is done for five different dimensionless mass flow rates namely, $\phi = 0.025, 0.045, 0.054, 0.1, 0.25$. It is found that rise in mass flow rate results in stagnation pressure losses. The plots for total pressure in stationary frame of reference, and static pressure is plotted for SVD, HRVD, SRVD, and RVD (refer Figs. 11.4, 11.5, 11.6, 11.7, 11.8, 11.9, 11.10, 11.11, 11.12 and 11.13). The outcomes for various mass flow rates are discussed here.

As can be seen in Fig. 11.4, SVD, HRVD, SRVD, and RVD are displaying a similar pattern. The pressure is declining faster after mass flow 0.10 kg/s, and a steep curve is seen after 0.10 kg/s mass flow. All the rotating vaneless diffuser concepts such as RVD, HRVD and SRVD are outperforming SVD. The difference in pressure

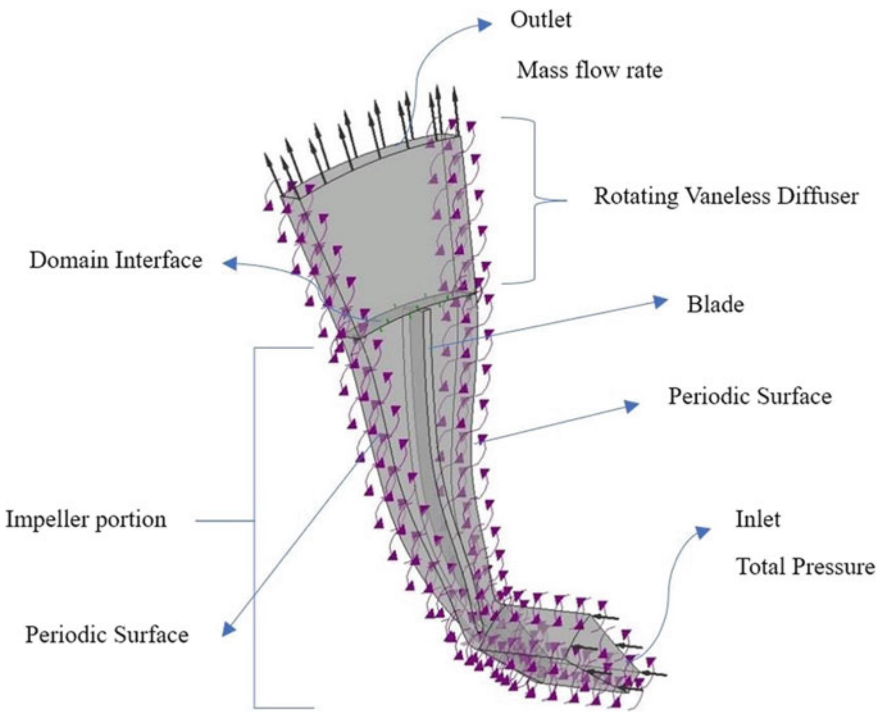

Fig. 11.3 Boundary conditions

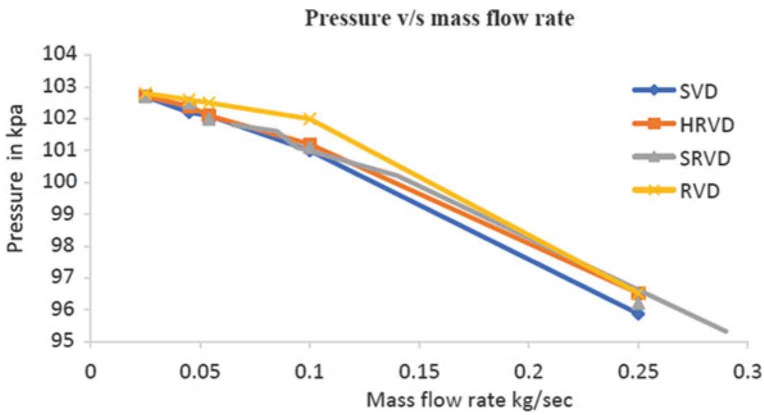

Fig. 11.4 Mass flow rates (kg/s) versus pressures (kPa)

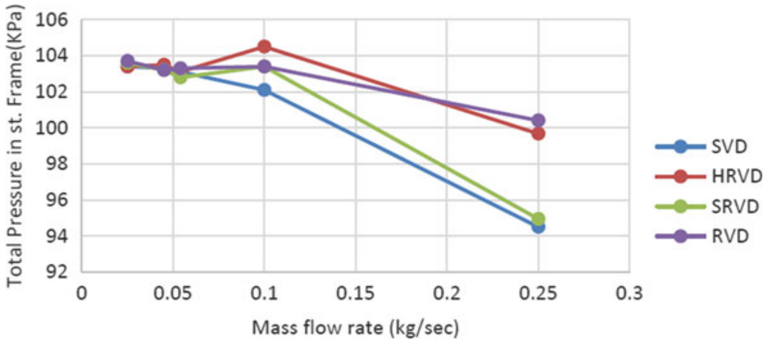

Fig. 11.5 Mass flow rates (kg/s) versus total pressures in stationary frame (kPa)

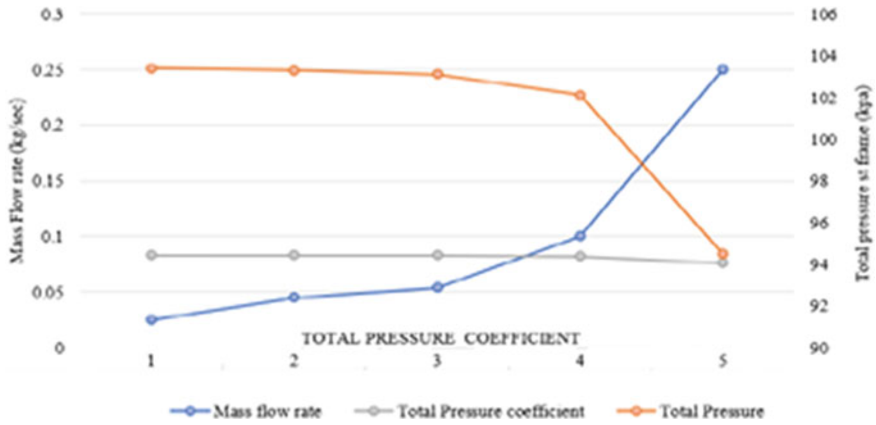

Fig. 11.6 Total pressure coefficients for varied mass flow rates of SVD

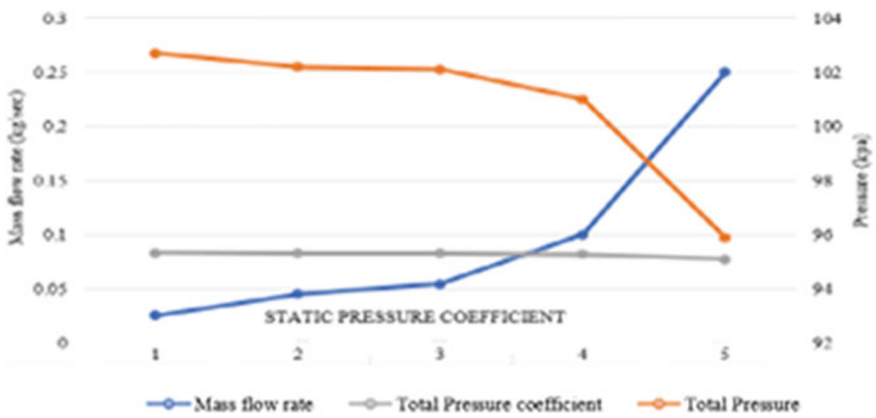

Fig. 11.7 Static pressure coefficients for varied mass flow rates of SVD

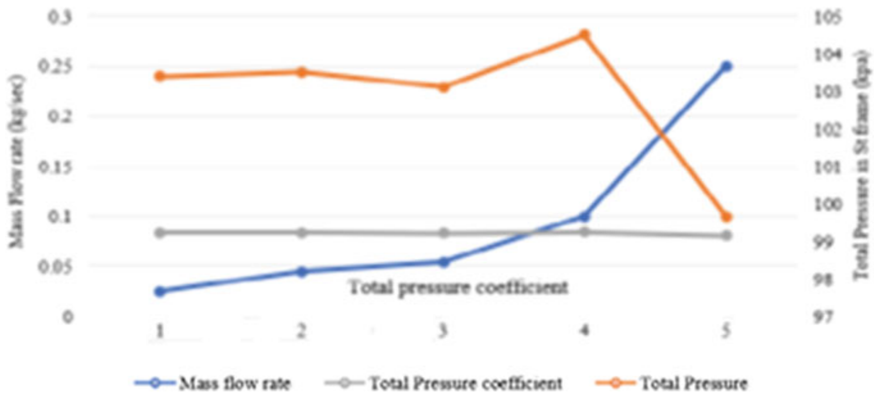

Fig. 11.8 Total pressure coefficients for varied mass flow rates of HRVD

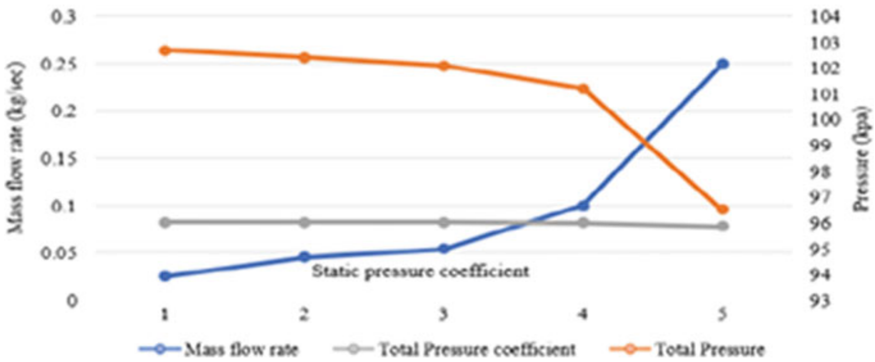

Fig. 11.9 Static pressure coefficients for varied mass flow rates of HRVD

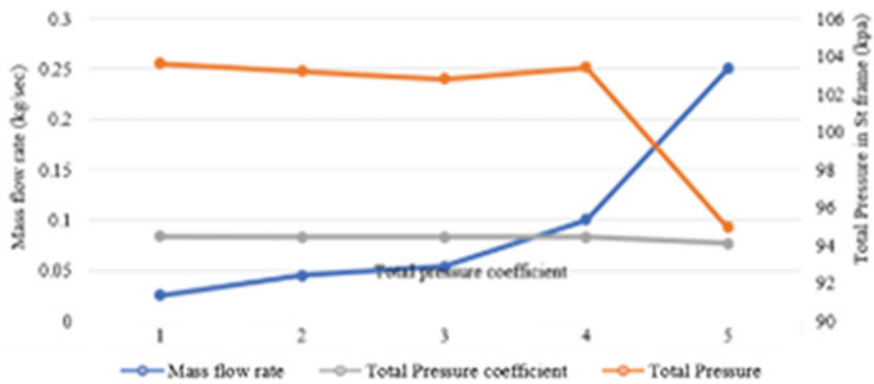

Fig. 11.10 Total pressure coefficients for varied mass flow rates of SRVD

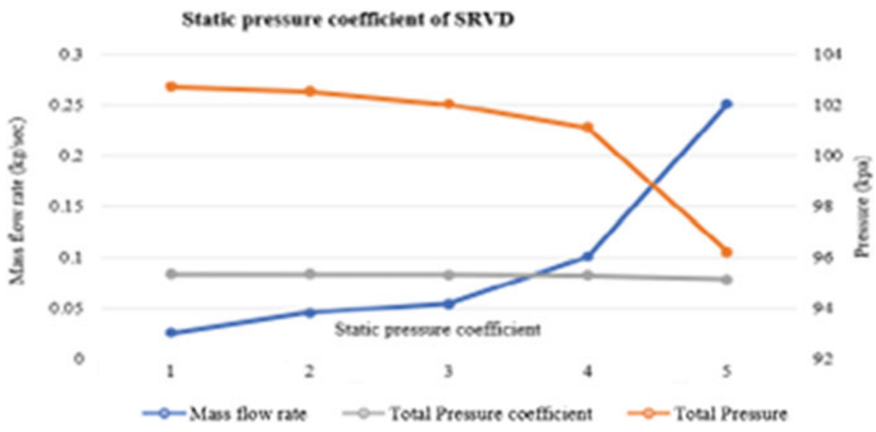

Fig. 11.11 Static pressure coefficients for varied mass flow rates of SRVD

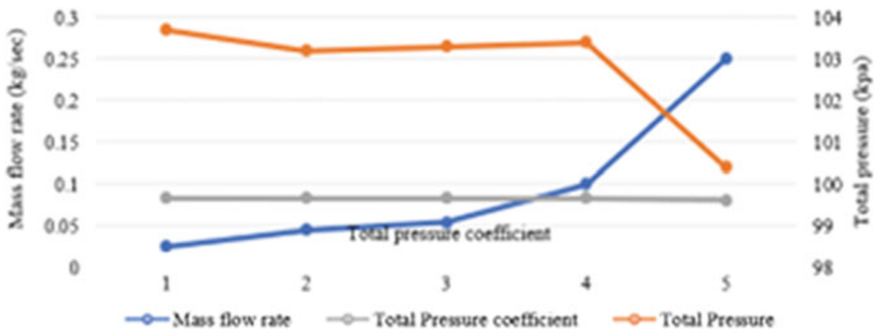

Fig. 11.12 Total pressure coefficients for varied mass flow rates of RVD

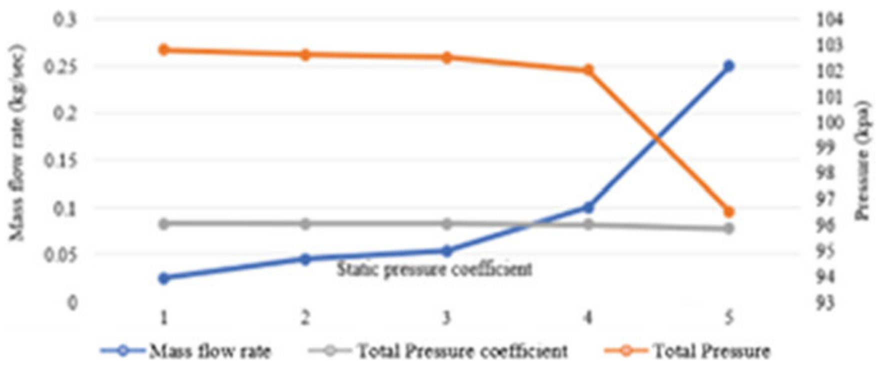

Fig. 11.13 Static pressure coefficient for various mass flow rates of RVD

is very small at mass flow of 0.25 kg/s. It is also observed that SVD, SRVD, and HRVD have nearly the same pressure at 0.10 kg/s mass flow.

Figure 11.5 depicts the total pressure variations for all cases, and it is same at the beginning. For RVD, HRVD, and SRVD, the total pressure increases to 0.10 kg/s whereas on the contrary, the total pressure of the SVD is decreasing. In all cases, behavior after 0.10 kg/s in SVD has the steepest slope, followed by the SRVD, and HRVD. The change in the total pressure of RVD is very small and thus it can be seen clearly that it has a very small slope.

In Fig. 11.6, it can be observed that the total pressure varies with negligible change with respect to the mass flow rate for SVD. When the mass flow rate increases, there is a small change in the total pressure up to 0.10 kg/s mass flow rate, but after 0.10 kg/s, there is a steep decrease in pressure.

Figure 11.7 shows the variations in static pressure in stationary frame for SVD. The total pressure increases gradually up to 0.054 kg/s mass flow rate and after that there is steep increase. Figure 11.8 shows the total pressure variations for HRVD. A rise in the mass flow rate results in total pressure constantly changing with small difference. The total pressure decreases up to mass flow rate 0.054 kg/s and after that it increased and then steep decreased from 0.10 to 0.25 kg/s mass flow rates.

Figure 11.9 lists the variations of static pressure rise for HRVD. The static pressure is constantly decreasing with small changes with the mass flow rate and the pressure is decreasing with some small change up to mass flow rate 0.10 kg/s after that it is steeply decreased.

Figure 11.10 depicts the variations in total pressure in the stationary frame for SRVD. The total pressure is decreasing constantly with small changes and the total pressure is decreasing up to 0.054 kg/s mass flow rate after that it is increases at 0.10 kg/s mass flow rate and then decreased steeply at 0.25 kg/s mass flow rate.

Figure 11.11 shows the variations of static pressure for SRVD. Static pressure decreases with small changes with the mass flow rate and the pressure decreases gradually up to 0.10 kg/s mass flow rate and then it is steeply decreased. Figure 11.12 shows the variations in total pressure in stationary frame for RVD. The total pressure is same as the previous cases, and it decreases with small changes with respect to mass flow rate. The total pressure decreases from 0.025 to 0.045 kg/s mass flow rates and after that it increased constantly with small changes and then it decreased steeply from mass flow rate 0.10 to 0.25 kg/s. Figure 11.13 depicts the variations of static pressure for RVD. The pressure coefficient decreases constantly with some small changes with respect to mass flow rate and the pressure is decreasing gradually with mass flow rate from 0.10 to 0.25 kg/s mass flow rates.

For the sake of brevity, the static pressure and total pressure in stationary frame contours of HRVD at mass flow rates 0.025, 0.045 and 0.10 kg/s are shown here (refer Figs. 11.14, 11.15 and 11.16). The energy transfer from the impeller and diffuser and simultaneous diffusion happening within the passage are clearly captured in the contours. Static pressure gradually increases throughout the passage and the maximum pressures are observed at the domain outlet.

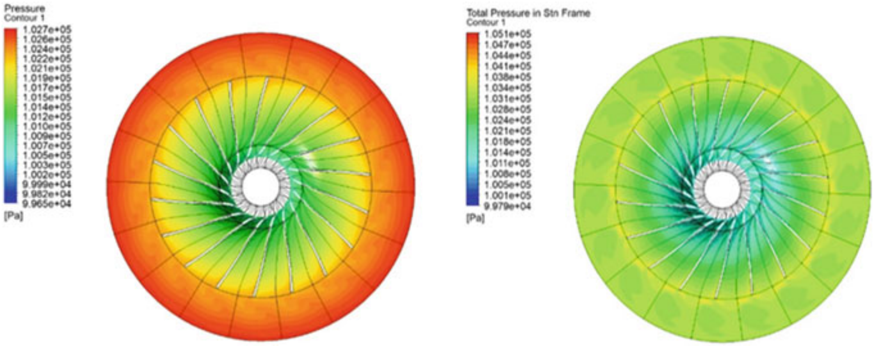

Fig. 11.14 Contours of HRVD for mass flow rate 0.025 kg/s

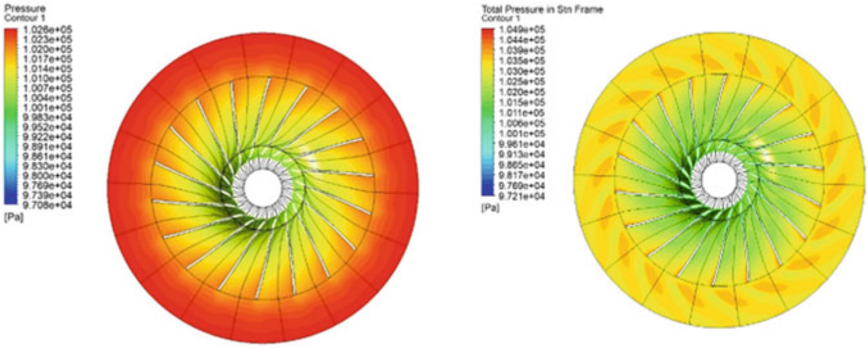

Fig. 11.15 Contours of HRVD for mass flow rate 0.045 kg/s

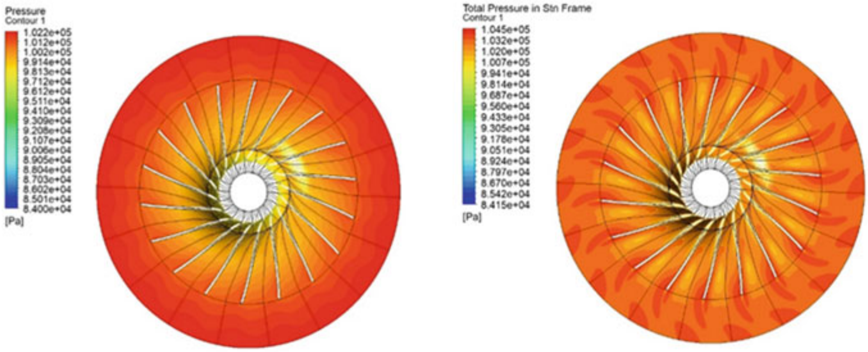

Fig. 11.16 Contours of HRVD with mass flow rate 0.1 kg/s

11.4 Conclusion

On analyzing the SVD, HRVD, SRVD, and RVD configurations, it is observed that increase in mass flow rate resulted in a decrease in total pressure and pressure. RVD is outperforming than SVD, HRVD, and SRVD. It is observed that SVD, SRVD, and HRVD have nearly the same pressure at a 0.10 kg/s mass flow rate. In all cases, the flow behavior after 0.1 kg/s, the SVD has the steepest slope, followed by SRVD, and HRVD. The change in the total pressure of RVD is very small. Static pressure coefficient for various mass flow rates of HRVD is declining with the increment in terms of mass flow rates. The static pressure coefficients for various mass flow rates of HRVD is reducing at a very small rate but reduces with a steep slope when the mass flow is increased from 0.1 to 0.25 kg/s. On comparing all the cases, HRVD gives an optimum performance with respect to rise in static pressure when compared to the base SVD model.

References

1. Konakala, S.R., Govardhan, M.: CFD studies on the performance of a centrifugal compressor with single wall rotating vaneless diffusers at the wall extension ratios of 1.1 and 1.15. In: ASME 2017 Gas Turbine India Conference, GTINDIA2017, Bangalore (2017)
2. Niveditha, P., Prasad, B.V.S.S.S.: Computational study of influence by rotating vaneless diffuser on the performance of centrifugal compressor. AIP Conf. Proc. **2316**(1), 030025 (2021)
3. Govardhan, M., Seralathan, S.: Effect of forced rotating vaneless diffusers on centrifugal compressor stage performance. J. Eng. Sci. Technol. **6**(5), 562–578 (2011)
4. Seralathan, S., Roy Chowdhury, D.G.: Performance enhancement of a low-pressure ratio centrifugal compressor stage with a rotating vaneless diffuser by impeller disk extended shrouds. J. Appl. Fluid Mech. **9**(8), 2933–2947 (2016)
5. Sivamani, S., Ghosh, R.C.D.: Performance enhancement of the centrifugal compressor stage with a rotating vaneless diffuser—a numerical study. In: ASME 2014 Gas Turbine India Conference, GTINDIA 2014, New Delhi (2014)
6. Sivamani, S., Ghosh, R.D.: Numerical investigation to assess the performance of free rotating vaneless diffuser for a centrifugal compressor stage. In: ASME 2017 Gas Turbine India Conference, GTINDIA 2017, Bangalore (2017)
7. Seralathan, S., Roy, C.D.G.: Free rotating vaneless diffuser of diffuser diameter ratio 1.30 with different speed ratios and its effect on centrifugal compressor performance improvement. Energ. Procedia **54**, 506–517 (2014)
8. Seralathan, S., Roychowdhury, D.G.: Numerical studies on the effect of diffuser rotational speeds on low pressure ratio centrifugal compressor performance. J. Appl. Fluid Mech. **10**(3), 785–799 (2017)
9. Seralathan, S., Chowdhury, D.G.R., Jaswal, A.K.: Enhancement of flow diffusion in a centrifugal compressor stage with backward curved impeller by shroud extension—a numerical study. Adv. Mater. Res. **984–985**, 1102–1107 (2014)

Chapter 12
Conceptual Design and Structural Analysis of a Multipurpose Agricultural Robot

Mervin Joe Thomas, Rekala Sai Bharani Kumar Goud, Nagamalla Jayaprakash, and Santhakumar Mohan

Abstract Modern farmers face several challenges in meeting the food needs of the increasing population growth. In order to meet the growing demand without compromising on the quality and quantity within available constraint spaces of farming, they must transform from conventional methods to precision agriculture, reducing direct human intervention. The advancements in agricultural operations from traditional to technological methods improve efficiency and offer a safer work environment. This paper focuses on the preliminary conceptual design and working of a low-cost all-terrain agricultural robot suitable for small/medium-scale farmers. The robot is designed to perform two individual operations—transplanting and weed removal. A brief description of the various components used to perform the two operations is highlighted in this paper.

12.1 Introduction

Recent times have shown a drastic transition from manual operations to technological intervention to overcome the challenges faced by modern farmers. The significant difficulties include high operational and production costs, environmental impacts, reduced farming grounds, lack of available labour and livestock, and plant diseases. Besides manual operations with sensitive plants, health concerns during the direct harvest of edible fruits/vegetables and fatigue due to monotonous, repetitive tasks

M. J. Thomas (✉) · R. S. B. K. Goud · N. Jayaprakash · S. Mohan
Department of Mechanical Engineering, Indian Institute of Technology, Palakkad 678623, India
e-mail: mervinjoethomas@iptif.tech

S. Mohan
e-mail: santhakumar@iitpkd.ac.in

M. J. Thomas
Post Doctoral Fellow, IIT Palakkad Technology IHub Foundation, Palakkad, India

P. H. V. S. Talpa Sai et al. (eds.), *Intelligent Manufacturing and Energy Sustainability*, Smart Innovation, Systems and Technologies 372,
https://doi.org/10.1007/978-981-99-6774-2_12

worsens the situation. This reason has directed researchers towards precision agriculture, which involves grouping robotics, Artificial Intelligence (AI) and the Internet of Things (IoT) in farming [1]. Nowadays, agricultural robots perform operations such as cultivation [2], pest [3] and weed control [4], inspection [5], and harvesting [6]. However, in the current scenario, agricultural robots exhibit drawbacks like high initial costs, low operational efficiency, bulky and complex mechanisms fitted with large sprayers for weed control [7]. In order to ensure a high yield and good quality harvest, weed control is critical. However, the challenge here is that the weeds exist in random patterns. Therefore, it is necessary to remove or retard the growth of the weeds without affecting the nearby plants. This very reason motivates researchers to devise novel designs to ensure precision.

Transplanting is a process of planting seedlings from containers grown in nurseries at equal spacing and desired depths. Manually performing this operation is a labour-intensive and time-consuming process. On the other hand, weeds' growth affects plants' growth, thereby compromising yield. The traditional and effective way to remove weeds is by eradicating and gathering them by hand. This manual process is, however, very monotonous, time-consuming and involves high labour costs. Similarly, spraying fertilizers or herbicides in bulk to control weed growth is hazardous to the plants and leads to much wastage. Besides, herbicides at undesired locations may gradually create problems like skin rashes and reduce soil quality, making it impotent [8]. Therefore, this paper presents a robot mechanism to perform transplanting operations and weed removal similar to hand-weeding. The robot is designed to be robust and adaptable to varying climatic conditions, removing weeds of different shapes and patterns. With this technology, the weeding process can be carried out without disturbing the desired crop.

This paper is organized as follows: Sect. 12.2 describes the robot architecture and conceptual design of the proposed robot mechanism. The robot's working in transplanting and weeding modes are detailed in Sect. 12.3. Section 12.4 explains the structural analysis results of the robot structure. Finally, a brief summary of this work and the scope for future work are given in Sect. 12.5.

12.2 Robot Architecture and Conceptual Design

This section describes the conceptual design of the proposed robot mechanism. The robot consists of a cart used in common for transplanting and weeding operations. Figure 12.1a, b show the robot's CAD model in both configurations. Since transplanting and weed operations happen at two instants of farming, the top portion of the robot can be changed as per the needs. The cart is made using an Aluminium T-slot frame. The cross-section of the frame is a double profile with six T-slots. The frames are connected using gussets. Gussets are used to hold the aluminium frame in a fixed position. This component permits easy assembly and disassembly. The robot base consists of four wheels powered by two motors on either side of the cart on the T-slot frame. The motors are connected to the wheels using a belt drive. The

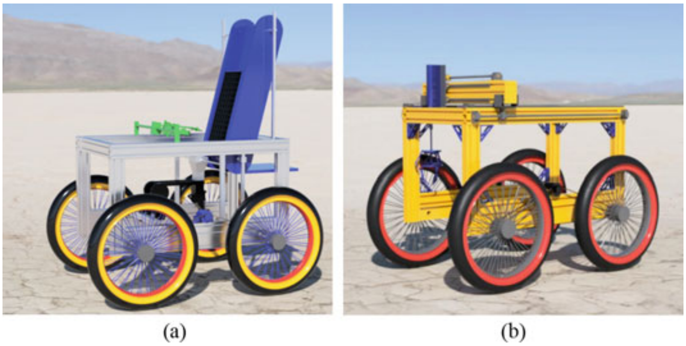

Fig. 12.1 CAD model of the proposed robot in **a** transplanting mode; and **b** weeding mode

following two subsections describe the transplanting and weeding mechanisms used in the proposed robot.

12.2.1 Transplanting Mechanism

The transplanting mechanism consists of three major components. The first component is the seedling tray with a holder. The seedling tray contains the seedlings that are to be planted. The seedling tray has fifteen rows and seven columns in the proposed design, with a total capacity to hold 105 seedlings.

Figure 12.2a shows the seedling tray with holder. The seedling tray holder contains a belt on which the seedling tray is placed. The seedling tray holder moves horizontally when the gripper takes a seedling from the seedling tray. When an entire row of seedlings is completed, the belt on which the seedling tray is placed rotates such that the seedling tray moves down by one row. The seedling tray holder moves horizontally using the lead screw mechanism powered by a stepper motor. The second major component is the gripper. The gripper is placed such that when it is in the extended position, it reaches the seedling in the seedling tray, and when it goes into the retracted position, it plucks the seedling from the seedling tray and drops it into the funnel-shaped component. Figure 12.2b shows the proposed gripper. The gripper moves from the retracted to the extended position using the x-bar mechanism powered by a motor. The rings placed on the needles act as sliders, as shown in Fig. 12.2c. When the rings move forward, the needles will move away from each other. When the rings move backwards, the needles move towards each other and vice-versa. A stepper motor powers the slider-crank mechanism. The third major component is the planting mechanism shown in Fig. 12.2d, which plants the seedlings into the soil that the gripper drops.

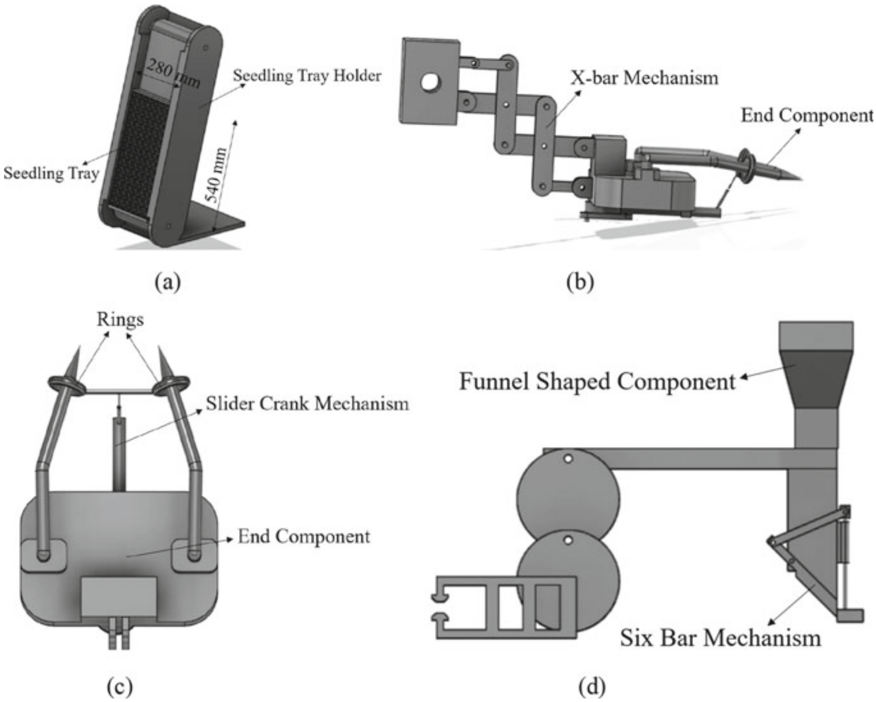

Fig. 12.2 Transplanting mechanism components **a** seedling tray with holder; **b** gripper; **c** end component; and **d** planter

12.2.2 Weeding Mechanism

The weeding mechanism consists of an additional Aluminium rail placed laterally over the cart to which the gripper and slider are attached. This rail can be translated longitudinally using the ball screw mechanism placed along the longitudinal rail of the cart on either side. Three ball screws are used in the design for the translational motion of the components. The ball screw transforms the rotational motion into linear motion. Figure 12.3a shows the CAD model of the ball screw assembly. The rail is mounted on ball-bearing carriages, allowing smooth rail translation motion. The ball-bearing carriages are guided by guide rails placed on T-slots in the cart. A slider is attached to the lateral rail, which helps the gripper move vertically, reaching weed roots. The slider is translated laterally along the rail with the help of a ball-screw mechanism. As shown in Fig. 12.1b, telescopic slides are mounted onto the lateral frame using ball-bearing carriages and guideways. Figure 12.3b shows a close-up view of the telescopic slides. The gripper shown in Fig. 12.3c is mounted on the telescopic slides to adjust the heights as per requirements. The end effector is a three-fingered parallel gripper.

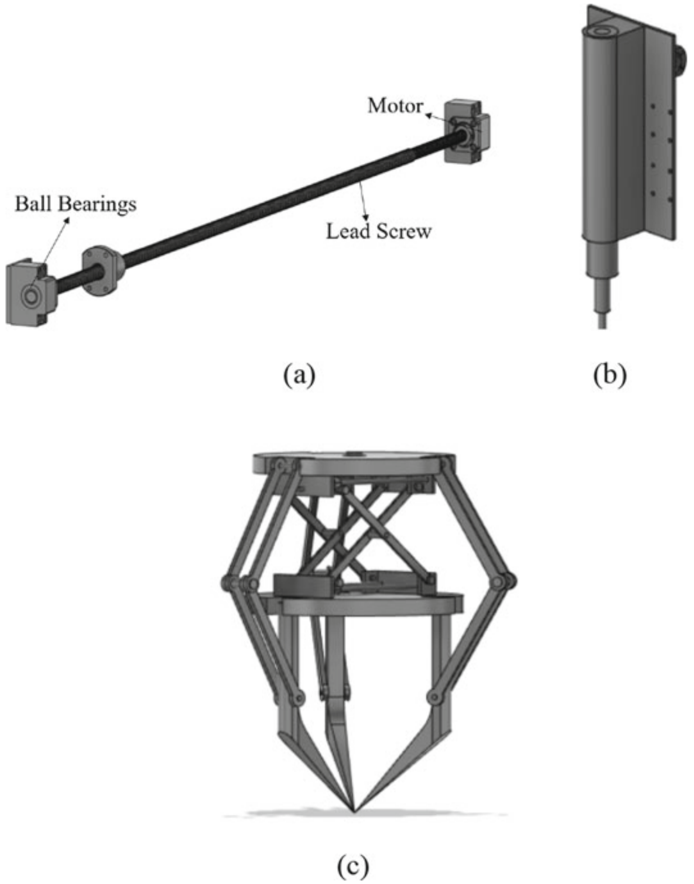

Fig. 12.3 Weeding mechanism components **a** ball screw assembly; **b** telescopic slides; and **c** end effector gripper

12.3 Working

This section describes the robot's working during the transplanting and weeding modes. The mobile cart is operated similarly to the tiller truck mechanism. This mechanism permits them to take sharper turns by manoeuvring the rear wheels. As explained earlier, transplanting is planting seedlings into the soil. The mobile robot base will have the components explained in Sect. 2.2(a) during the transplanting mode. Figure 12.4a shows a line diagram of the transplanting mechanism with the direction of motion of each component. The seedlings produced in seedling trays from the nursury are placed on the seedling tray holder. The seedling tray holder moves horizontally using the leadscrew mechanism, and the seedling tray is pushed downwards via belt drive. The gripper from the reverted position moves to the extended position using the X-bar mechanism. As the gripper moves towards the extended

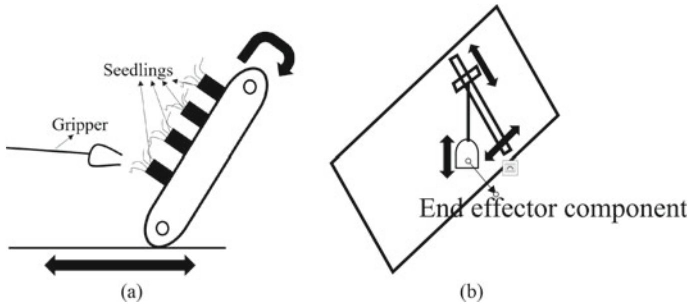

Fig. 12.4 Schematic line diagram **a** transplanting mechanism, and **b** weeding mechanism

position, the needles of the gripper are made closer and the gripper gets hold of the seedling in the tray. On retracting the gripper, the seedling is pulled out from the tray. Then the needles of the gripper are moved away, resulting in the seedling falling into the funnel-shaped component and then dropping into the planter. The planter can move vertically up and down. The planter takes the seedling dropped by the gripper and moves it into the soil. When the planter moves into the soil, the slider at the bottom of the planter moves upward due to the force applied by the ground, resulting in the bottom of the planter to open. This further drops the seedling into the hole made by the planter mechanism. This completes one cycle of the seedling process. The cart then moves to the next seedling position. When all the seedlings in a row are planted, the belt on which the seedling tray is placed rotates, causing the seedling tray to move a row down.

Ball-screw mechanisms are used for lateral and longitudinal end-effector movement during the weeding process. The sliders attached to the lateral aluminium frame will help the gripper adjust its height vertically to remove weeds from roots by penetrating the soil. The sliders would also protect the gripper from any obstacle on the ground. The three-fingered, self-centred, parallel gripper is operated parallel using a scissor lifting mechanism. A lead screw mechanism is used to slide the scissor lift mechanism. Figure 12.4b shows the line diagram of the gantry mechanism used for the weeding process.

12.4 Static Structural Analysis

This section explains the static structural analysis results of the mobile cart on which all the other components are placed. The structural analysis is performed using the ANSYS Workbench software package. The simulation study is done for two cases—Case 1: A static load of 200 N is applied to the top of the cart on each frame (Fig. 12.5a), and Case 2: A static load of 1000 N is applied at the centre of the cart (Fig. 12.5b. The material assigned for the analysis is Aluminium 6061 T6 hot formed. The parameters assigned for the simulation study are listed in Table 12.1. The element type chosen for the study is tetrahedral. The total number of elements and nodes in the study were 213,863 and 1,382,681, respectively. Figures 12.6 and 12.7 show the simulation results for the two cases described earlier. Table 12.2 lists the results obtained from the simulation study for the two cases. It is clear from the simulation results that the stresses and the deformation induced within the frame are within the safe limits and, therefore, can further proceed for the prototype fabrication for proof of concept. The maximum deformation induced in the frame is 0.08 mm, and the maximum Von-Mises stress induced is 14.442 MPa.

12.5 Conclusion and Scope for Future Work

This paper explains the conceptual design and preliminary results of an agricultural robot for transplanting and weed removal operations. A detailed description of the individual components of the robot when in use for the two modes is described. The static structural analysis is carried out for the robot base for two loading conditions. The results indicate that the design is safe and can be further used for hardware fabrication. Additionally, the robot will be equipped with a basic level of autonomy to make the process more user-friendly for the farmer. Also, incorporating solar technology for power and Bluetooth connectivity for remote control can enable untethered operations on the ground.

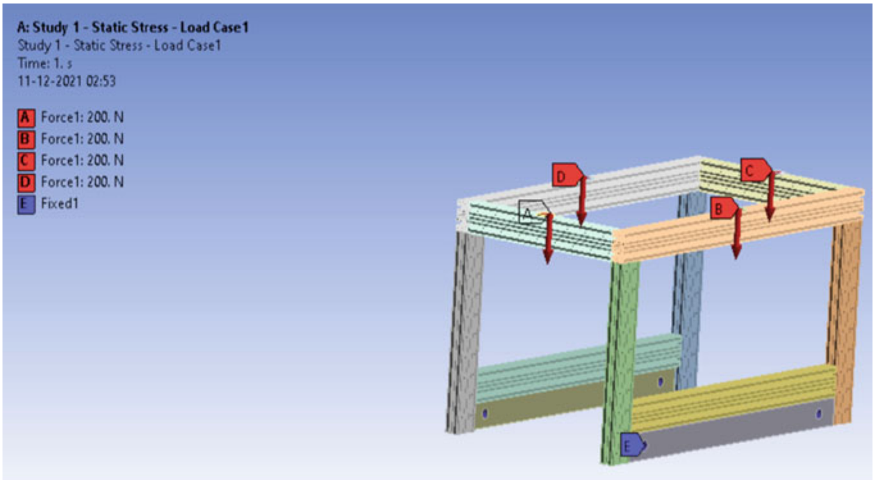

(a)

Fig. 12.5 Structural analysis loading conditions **a** Case 1; and **b** Case 2

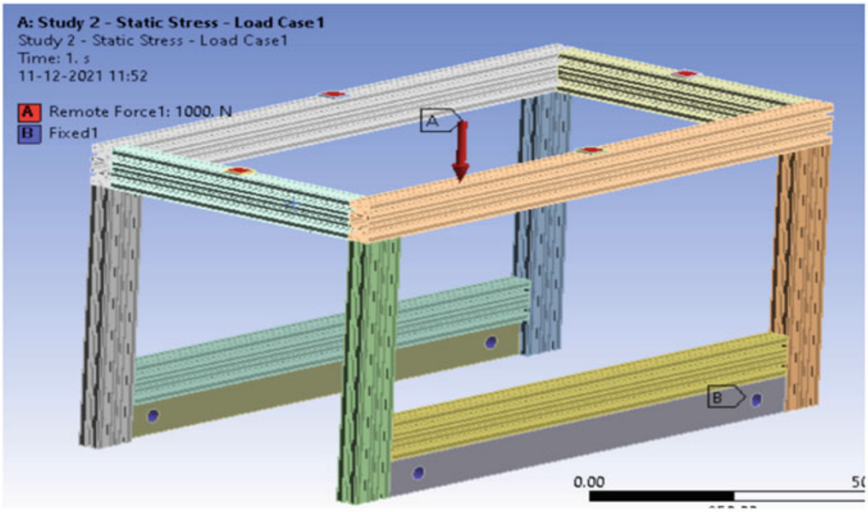

(b)

Fig. 12.5 (continued)

Table 12.1 List of parameters assigned for the simulation study

S. No	Parameter	Magnitude
1	Density (kg/mm^3)	2.7e−6
2	Thermal conductivity (W/mm C)	0.167
3	Specific heat (mJ/kg C)	8.96e5
4	Youngs modulus (MPa)	72,700
5	Poisson's ratio	0.33
6	Bulk modulus (MPa)	71,275
7	Shear modulus (MPa)	27,331
8	Ultimate tensile strength (MPa)	340
9	Yield strength (MPa)	313

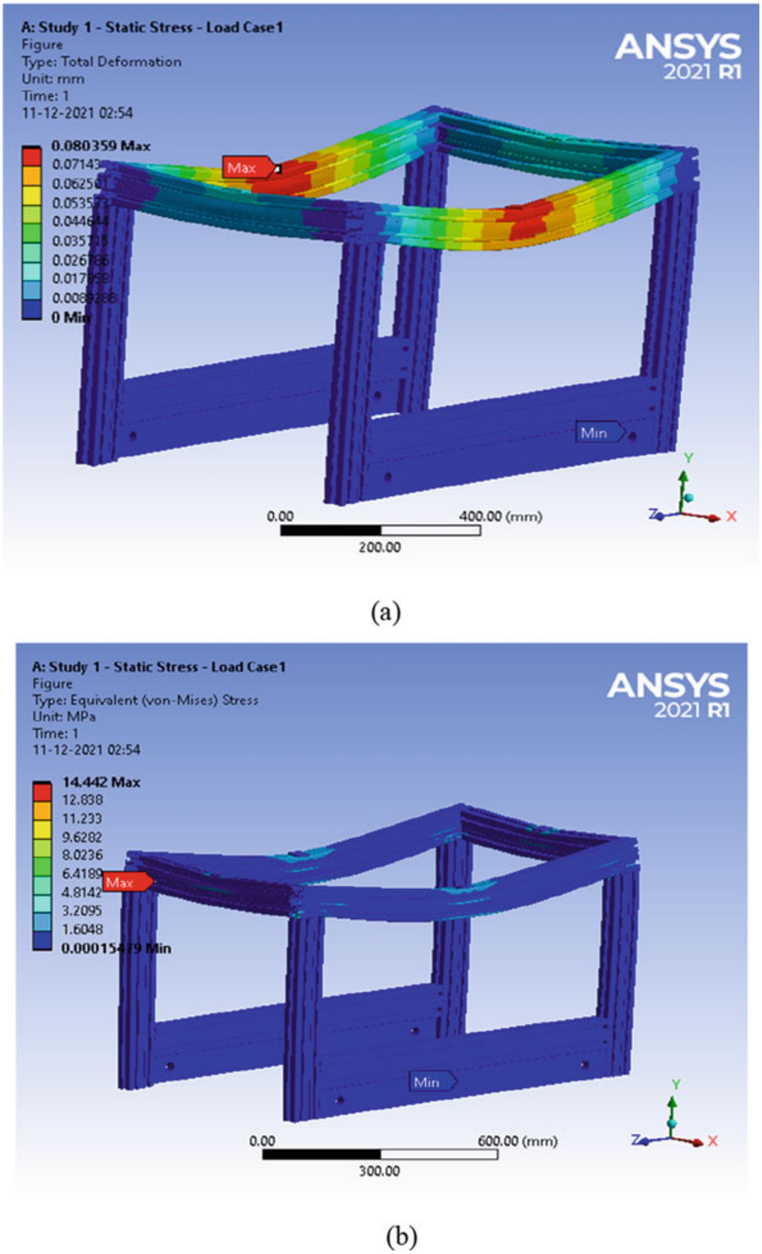

Fig. 12.6 ANSYS simulation results for Case 1 **a** total deformation; and **b** Von-Mises stress

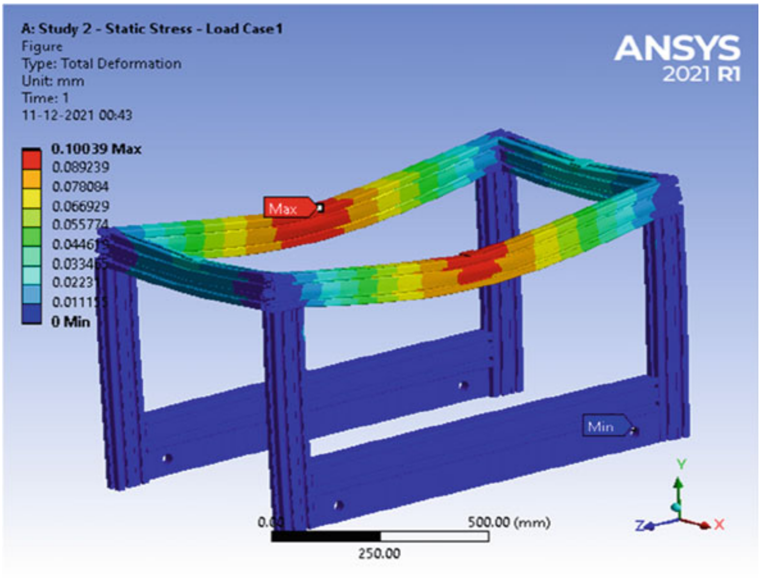

(a)

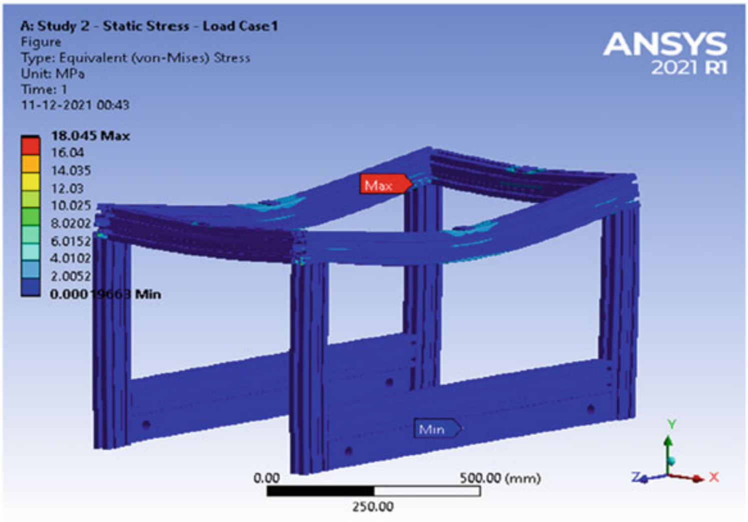

(b)

Fig. 12.7 ANSYS simulation results for Case 1 **a** total deformation; and **b** Von-Mises stress

Table 12.2 Simulation results

Case 1	Total deformation (mm)	0.08
	Von-Mises stress (MPa)	14.442
Case 2	Total deformation (mm)	0.10039
	Von-Mises stress (MPa)	18.045

Acknowledgements This research is partially supported by the Ministry of Electronics and Information Technology (4(16)/2019-ITEA), Government of India. Also, IIT Palakkad Technology IHub Foundation (IPTIF), India, financially supports the first author's postdoctoral fellowship.

References

1. Torky, M., Hassanein, A.E.: Integrating blockchain and the internet of things in precision agriculture: analysis, opportunities, and challenges. Comput. Electron. Agric. **178**, 1–23 (2020). https://doi.org/10.1016/j.compag.2020.105476
2. Polic, M., Ivanovic, A., Maric, B., Arbanas, B., Tabak, J., Orsag, M.: Structured ecological cultivation with autonomous robots in indoor agriculture. In: Proceedings of the 16th International Conference on Telecommunications, ConTEL, pp. 189–195. University of Zagreb, Faculty of Electrical Engineering and Computing (2021). https://doi.org/10.23919/ConTEL52528.2021.9495963
3. Vibhute, A.S., Deshmukh, K.R.T., Hindule, R.S., Sonawane, S.M.: Pest Management System Using Agriculture Robot. In: Techno-Societal 2020, pp. 802–810. Springer (2021). https://doi.org/10.1007/978-3-030-69925-3
4. Wu, X., Aravecchia, S., Lottes, P., Stachniss, C., Pradalier, C.: Robotic weed control using automated weed and crop classification. J. Field Robot. **37**, 322–340 (2020). https://doi.org/10.1002/rob.21938
5. Barbosa, W.S., Oliveira, A.I.S., Barbosa, G.B.P., Leite, A.C., Figueiredo, K.T., Vellasco, M.M.B.R., Caarls, W.: Design and development of an autonomous mobile robot for inspection of soy and cotton crops. In: Proceedings of International Conference on Developments in eSystems Engineering, DeSE, pp. 557–562 (2019). https://doi.org/10.1109/DeSE.2019.00107
6. Mao, W., Liu, Z., Liu, H., Yang, F., Wang, M.: Research progress on synergistic technologies of agricultural multi-robots. Appl. Sci. **11**, 1–34 (2021). https://doi.org/10.3390/app11041448
7. Steward, B., Gai, J., Tang, L.: The use of agricultural robots in weed management and control. In: Robotics and Automation for Improving Agriculture, pp. 161–186 (2019). https://doi.org/10.19103/as.2019.0056.13
8. Wołejko, E., Wydro, U., Odziejewicz, J.I., Koronkiewicz, A., Jabłońska-Trypuć, A.: Biomonitoring of soil contaminated with herbicides. Water **14**, 1–19 (2022). https://doi.org/10.3390/w1410153

Chapter 13
Condition Based Assessment and Diagnostics of Transformer in Smart Grid Network Using Adaptive Neuro Fuzzy Inference System Framework

Rahul Soni and Bhinal Mehta

Abstract In smart grid infrastructure, power transformers are one of the most integral assets that must be constantly monitored during their operational life. Several diagnostic methods, such as interfacial tension (IFT), moisture presence, degree of polymerization (DP), harmonics, temperature rise furans compound have detrimental effect on transformer insulation. This research article introduces a novel adaptive neural fuzzy inference system (ANFIS) model to analyse the insulation degradation for oil and paper based on the datasets of moisture contents, IFT, harmonics and temperature rise within the insulation. The proposed study findings are verified using real data gathered from various transformers used in utilities, industry and literatures including the impacts of electric vehicles (EV) and Distributed energy resources (DER). Time varying harmonics and temperature effect is important aspect of this research. The novel proposed ANFIS model is more than 90% efficient and errors of less than 1% for training and testing data sets utilized for study.

13.1 Introduction

The daily rise in load demand and the substantial number of ageing power transformers have contributed to a high failure rate over the past two decades. According to an IEEE statistical survey, 10% of an oil-immersed power transformer fleet should experience a catastrophic breakdown during a 16-year period. This encouraged global utilities to switch from time-based maintenance plans to more dependable condition-based maintenance strategies. According to a CIGRE survey, 11% of transformer failures are caused by problems with the insulation system. Therefore, a thorough

---

R. Soni (✉) · B. Mehta
Department of Electrical Engineering, School of Energy Technology, Pandit Deendayal Energy University, Gandhinagar, Gujarat 382426, India
e-mail: rahulsoni2302@gmail.com

P. H. V. S. Talpa Sai et al. (eds.), *Intelligent Manufacturing and Energy Sustainability*, Smart Innovation, Systems and Technologies 372,
https://doi.org/10.1007/978-981-99-6774-2_13

understanding of the mechanism underlying insulation system ageing and the quantification of the extent of its integrity are necessary in order to develop a dependable condition-based maintenance approach [1, 2].

In addition to electrical and mechanical stresses within the transformer, ageing of the transformer insulation system is attributed to a number of factors, including oxygen, which determines reaction regime (oxidation or pyrolysis), temperature, which affects the rate of the reaction, moisture content, which determines the mobility of peroxides, and temperature. For instance, the mechanical strains and over-temperature that transformers experience during frequent energization processes may cause the transformers to age prematurely. Although the ageing of an insulation system is an inevitable process, exposing a transformer to too much of the factors that accelerate ageing causes it to age more quickly. Due to a lack of financial resources, utilities must implement trustworthy and affordable models for estimating transformer life and making asset management decisions [3, 4].

Even though this model is comprehensive for asset management decisions, it can still be criticized for its regular applicability because it includes several factors that are not monitored during routine transformer testing. Additionally, the transformer needs to be turned off in order to analyse some of the metrics used in this model, such the sweep frequency response analysis. In, a score system or method for evaluating transformer condition were described. Based on historical data, failure statistics, and previous loading, a predetermined weighing factor is pre-assigned to each parameter in this method. This method's analysis displays inconsistency because it depends on personnel knowledge [5–7].

The literature contains a number of papers looking at different estimation models for transformer remnant life, but the majority of these models are static expert system rules, without considering how these rules might be modified adaptively over time based on the history and experience of actual measurements. This research aims to introduce an adaptive neuro fuzzy logic inference system (ANFIS)-based remnant life prediction model for power transformers. The continual evaluation of the measured parameters and model output can increase the accuracy of this ANFIS-based model. The variables in this model are regularly monitored diagnostic indications, such as IFT, 2-FAL content in oil, and moisture content in cellulose insulation, which have a positive correlation with transformer ageing [8, 9].

In this research, the use of frequently measured characteristics during routine transformer inspection is a major component of the proposed ageing model. Other factors that exhibit a relationship with the transformer's remaining life but are not measured during normal inspection were thus excluded from the suggested model. Degree of Polymerization (DP) is a good predictor for the condition of solid insulation, for instance. One of the ageing by-products that results from the deterioration of paper insulation is 2-FAL, which can be used as a gauge for the paper's overall health. The winding insulation's breakdown rate is also accelerated by a number of by-products, including moisture [10, 11]. The novel proposed ANFIS model is more than 90% efficient and errors of less than 1% for training and testing data sets utilized for study.

13.2 Adaptive Neuro Fuzzy Inference System

The ANFIS system is an adaptable neuro-fuzzy inference machine, as its name implies. It functions as a universal approximate, much like "pure" artificial neural networks (i.e., non-fuzzy) or traditional fuzzy systems. Its goal is to approximate or "learn" simple or complex mappings (i.e., nonlinear functions) from an input space (often multivariate) to a univariate or multivariate output space.

The traditional ANFIS has five layers. Starting from input layer to output layer. A brief explanation of each layer's functionality in the lines that follow [12].

Layer No.1 (Inputs Layer)

Fuzzification of the input occurs in this layer. This indicates that each fuzzy subset that makes up an input's universe of discourse is given a membership value. This function has the following mathematical expression:

$$Output_{ij}^{(1)} = \mu_j\left(Input_i^{(1)}\right) \tag{13.1}$$

where, $Output_{ij}^{(1)}$ is the output of the layer 1 node, which corresponds to the i-th input variable's j-th linguistic phrase. For each ANFIS system in this library, the generalized Gaussian function has been chosen as the default membership function.

Layer No.2 (Fuzzy with AND Operation)

This layer's nodes all carry out fuzzy-AND operations. The T-norm operator of the algebraic product was chosen for all of the library's ANFIS networks. This has the effect of making every node's output equal to the sum of all of its inputs (i.e., every input term node connected to that rule node):

$$Output_k^{(2)} = W_k = \prod_{i=1}^{N_{Inputs}} Ouptput_{(ij)}^1 \tag{13.2}$$

Each node in this layer produces an output that corresponds to the firing strength (or activation value) of the associated fuzzy rule. K = 1…, number of rules.

Layer No.3 (Normalization Step)

The firing strength of each rule divided by the entire sum of the activation values of all the fuzzy rules determines the output of the k-th node. As a result, the activation value for each fuzzy rule is normalized. The simplest way to write this operation is:

$$Output_k^{(3)} = \overline{W_k} = \frac{Output_k^{(2)}}{\sum_{m=1}^{N_{Rules}} output_m^2} \tag{13.3}$$

Layer No.4 (Adjustable Layer)

The linear function is implemented by each node k in this layer and is accustomed by a set of adjustable parameters a_k.

$$Output_k^{(4)} = \overline{W_k} f_k = \overline{W_k}(a_{1k} Input_1^{(1)} + \cdots + a_{N_{Inputs}k} Inputs_{N_{Inputs}}^{(1)} + a_{0_k}) \tag{13.4}$$

The weight is determined by using (13.3) to compute the normalized activation value of the k-th rule. These parameters, which are changed by the RLS (Recursive Least Square) algorithm, are known as the linear parameters of the ANFIS system.

Layer No.5 (Output Layer)

For ANFIS (MISO), this layer consists of just one node, which adds its inputs algebraically to produce the output of the network:

$$Output_k^{(5)} = \sum_{k=1}^{N_{rules}} Output_k^{(4)} = \sum_{k=1}^{N_{rules}} \overline{W_k} f_k = \frac{\sum_{k=1}^{N_{rules}} W_k f_k}{\sum_{k=1}^{N_{rules}} W_k} \tag{13.5}$$

13.2.1 Transformer Insulation Deformation in Smart Grid Network

The main contributing factor to the ageing of a transformer is determined to be the cumulative influence of temperature, moisture, acids, and oxygen. One of these by-products, acids, is produced by the oxidation of oil and the breakdown of cellulose Despite the fact that different forms of acids are produced when oil oxidizes, only a few particular acid types that function as catalysts and have a poor solubility in oil are aggressive and quicken the ageing process of paper insulation.

The integration of the Distributed Energy Resources (DER) has an effect on the transmission and sub transmission in terms of power quality issues, in addition to the low voltage distribution system, according to research on the influence on high-voltage networks. The proposed study is shown in Fig. 13.1.

The performance of the transformer is somewhat improved by the PV integration. However, the harmonics effects brought on by solar PV panels have a detrimental effect on transformer performance. One of the detrimental effects of PV penetration is power reversal. Additionally, the solar integration increased the OLTC's working frequency by 45%, which may increase the likelihood that transformers will fail [13].

Transformer power flow is typically fixed in one direction in a traditional power grid. However, the grid's power flow becomes erratic and uncertain with the addition of renewable energy sources, such as wind farms, which could result in the transformer's reverse power flow. For instance, high reverse power flow may increase

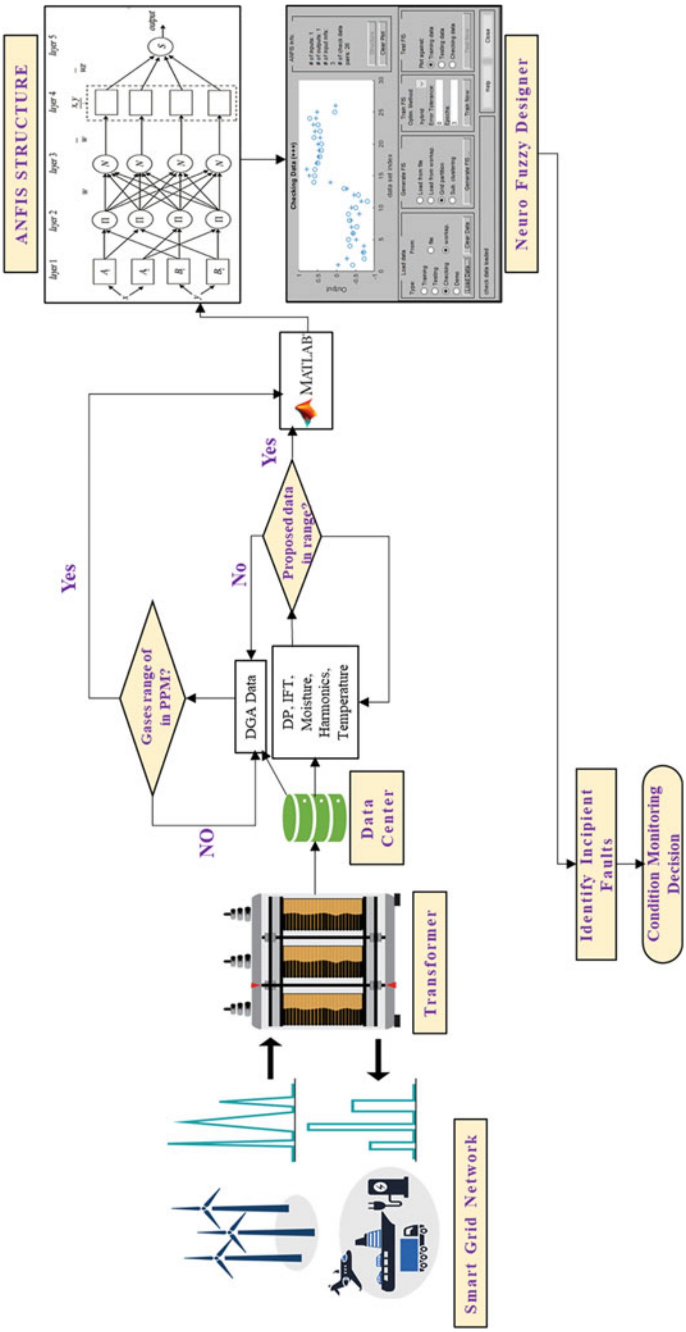

Fig. 13.1 Condition assessment of transformer in smart grid network using ANFIS

transformer power loss and jeopardize the transformer's thermal stability. The simultaneous charging of several EVs may cause the grid to be insufficient in terms of capacity and security. If EVs are correctly connected into the grid, such incidents might be prevented. If EVs are managed effectively, there is a great possibility to integrate them into the grid. The grid may encounter voltage sag, feeder congestion, line overloads, etc. without the aforementioned integration [14, 15].

13.3 Results and Discussion

13.3.1 Transformer Paper Deformation Under Moisture and IFT Examination

This research work proposes novel ANFIS based system for transformer condition assessment in smart grid infrastructure. Firstly, the moisture content and IFT is being diagnosed from the simulation analysis and literature. The insulation status is being diagnosed in terms of healthy insulation, medium risk, high risk and immediate failure respectively. The rules execution from Sugeno FIS, surface plot and contour plot are shown in Figs. 13.2 and 13.3 for immediate failure of paper insulation.

Furthermore, ANFIS based analysis is also done for detailed analysis of training and testing data with structure representation with training error of 0.97742 (precisely) as shown in Figs. 13.4 and 13.5. respectively.

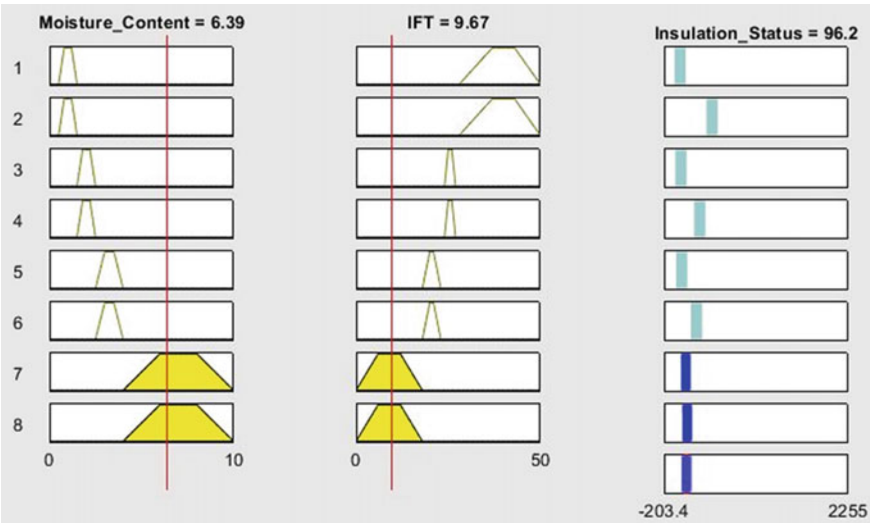

Fig. 13.2 Rules execution for paper insulation analysis using Takagi–Sugeno FIS

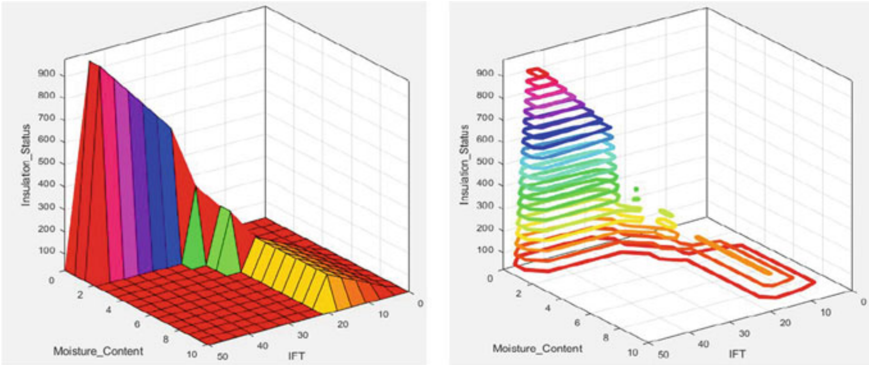

Fig. 13.3 Surface and contour plots of paper insulation using Takagi–Sugeno FIS

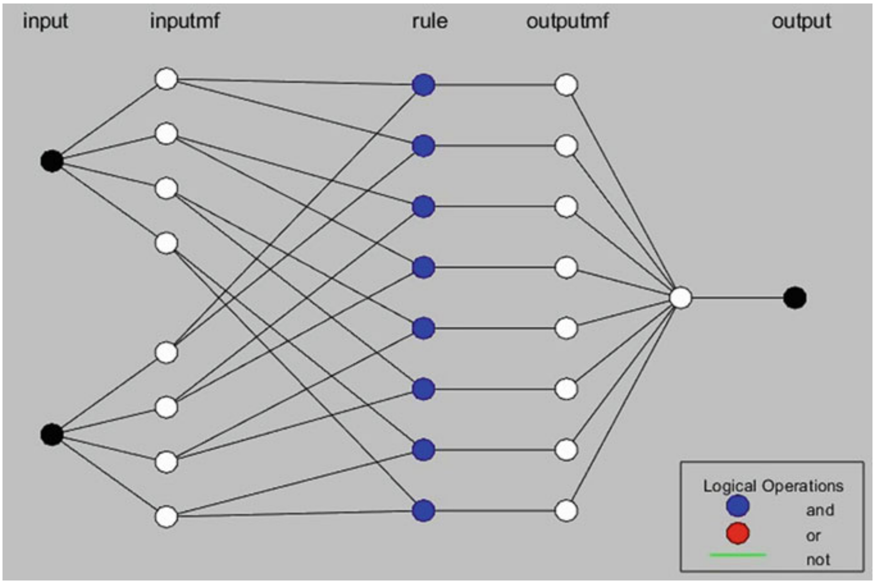

Fig. 13.4 Transformer paper insulation ANFIS structure

13.3.2 Transformer Insulation Deformation Under DER and EV Penetration

This research work also includes the time varying harmonic study of transformer under intermittent and varying nature of DER and EV. These may cause detrimental effect of transformer winding and oil significantly.

Firstly, the harmonics and temperature impact is being diagnosed from the simulation analysis and literature. The insulation status is being examined in terms of no

Fig. 13.5 Training and testing data of paper insulation using hybrid optimization

problem, possible problem and imminent problem respectively. The rules, surface plot and contour plot are shown in Figs. 13.6 and 13.7 examining severe faults in transformer insulation.

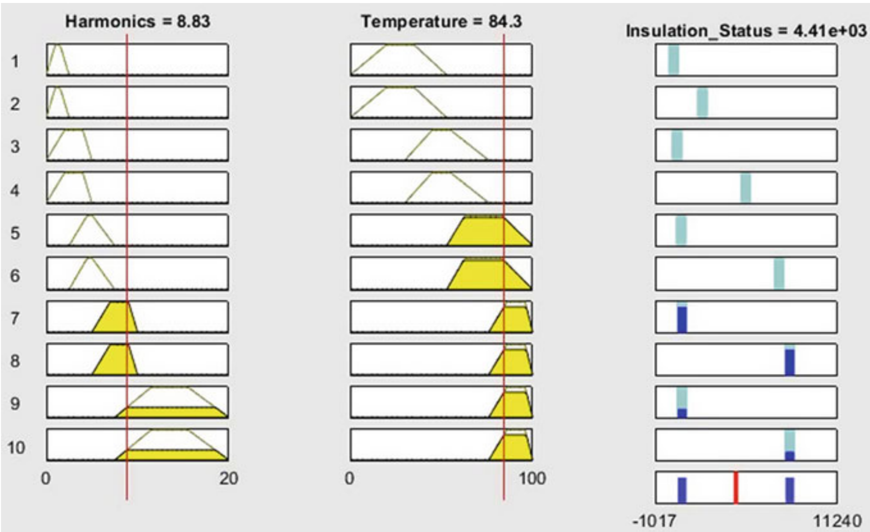

Fig. 13.6 Rules execution for transformer insulation using Takagi–Sugeno FIS

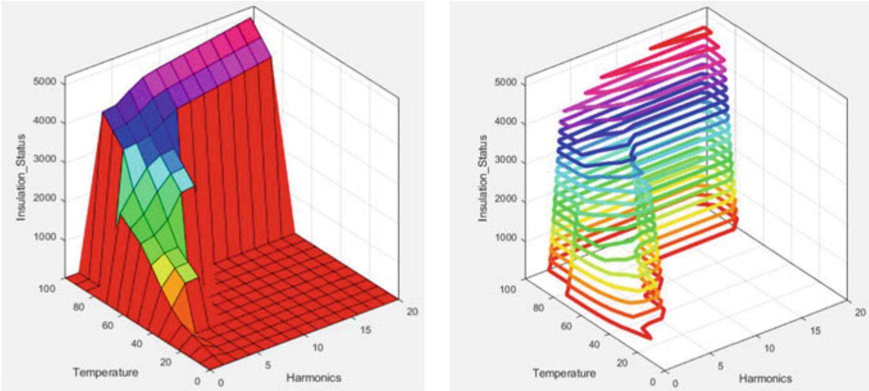

Fig. 13.7 Surface and contour plots of transformer insulation under harmonics

Furthermore, ANFIS based analysis is also done for detailed analysis of training and testing data with structure representation with training error of 0.22913 (precisely) as shown in Figs. 13.8 and 13.9 respectively. The confusion matrix and fuzzy rules implementation is demonstrated in Table 13.1 for transformer insulation analysis.

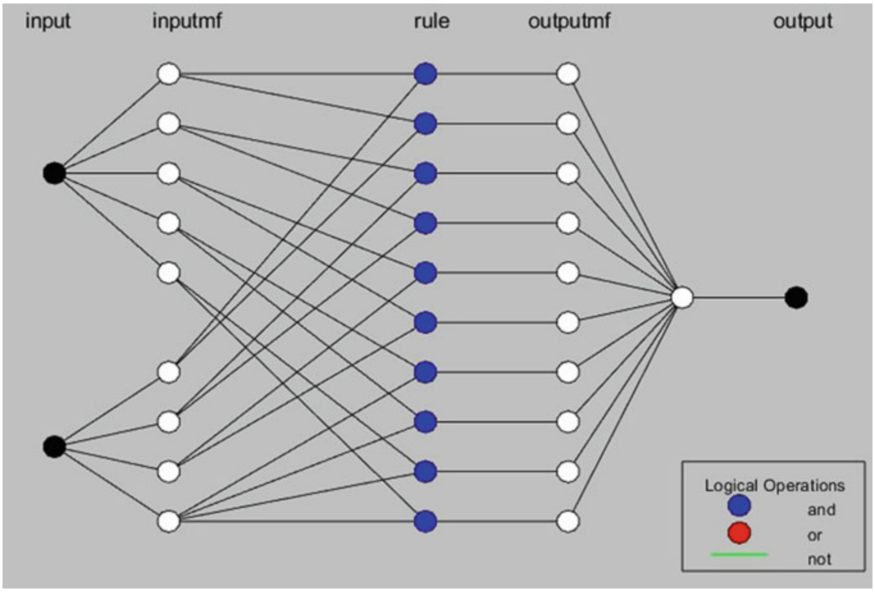

Fig. 13.8 Harmonics and temperature based transformer insulation ANFIS structure

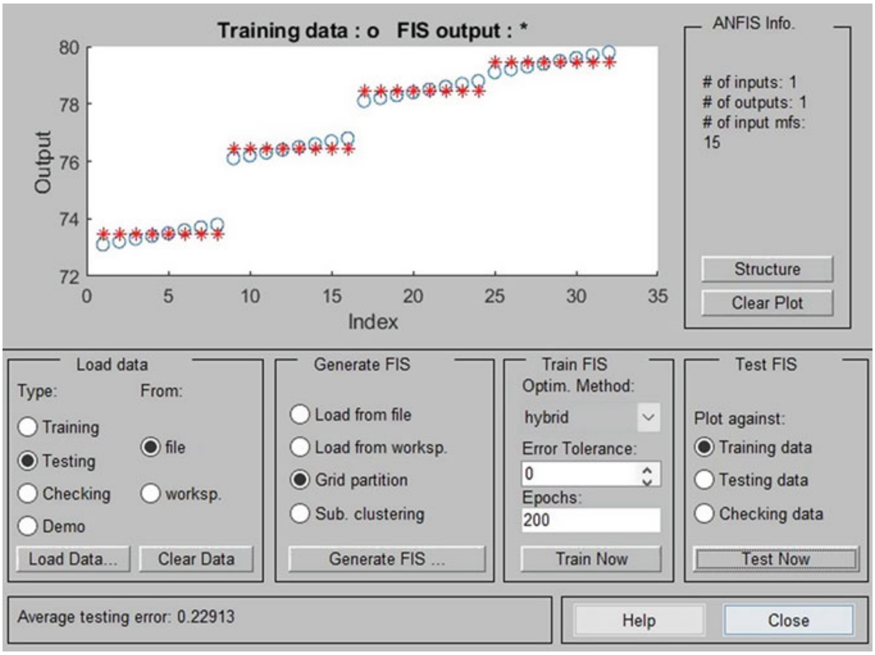

Fig. 13.9 Training and testing of harmonics and temperature using hybrid optimization

Table 13.1 Confusion matrix and fuzzy rules analysis for insulation diagnosis

Actual value		Predicted value	
	Outcomes	Positive	Negative
	Positive	True positive	True negative
	Negative	False positive	False negative
Correlation parameters	Input parameters	No. of samples	Summary
	True positive	180	185 correct
	True negative	05	
	False positive	10	15 incorrect
	False negative	05	
	Total	200	
	Accuracy	92.50%	

13.3.3 Limitations and Future Scopes of the Proposed Research Work

- Sometimes fuzzy logic can identify many errors, and complexity may increase as the number of input membership functions and related rules rises.

- Pressure, and vibration are factors that influence accuracy of proposed methodology, hence that study may useful for future scope.
- Other parameters like dissolved gases, partial discharge, corona formation in oil and paper insulation can be diagnosed under high penetration of DER and EV.

13.4 Conclusion

In this research work novel ANFIS based system is developed for transformer condition assessment in smart grid network. Impact analysis of various DER and EV on transformer insulation is discussed. Oil and paper insulation under moisture contents, IFT, harmonics and temperature rise caused due to DER and EV's with its significant impact for transformer insulation is simulated and graphically demonstrated. The novel proposed ANFIS model is more than 90% efficient and errors of less than 1% for training and testing data sets utilized for study Moreover the confusion matrix analysis is also represented in form of tabulated version so that analysis of insulation and its diagnosis can be examined under various application of input fuzzy rules and accuracy can be measured for efficiency of proposed model. Time varying harmonics can be examined better with fuzzy instead of FFT analysis for THD and TDD analysis.

References

1. Chakravorti, S., Dey, D., Chatterjee, B.: Recent Trends in the Condition Monitoring of Transformers, vol. XVI, p. 280. Springer, London (2013). ISSN 1612-1287
2. Soni, R., Mehta, B.: Review on asset management of power transformer by diagnosing incipient faults and faults identification using various testing methodologies. Eng. Failure Anal. 105634 (2021). ISSN 1350-630
3. Soni, R., Mehta, B.: Graphical examination of dissolved gas analysis by ratio methods and Duval triangle method to investigate internal faults of power transformer. Mater. Today Proc. (2022)
4. Dao, T., Phung, B.T.: Effects of voltage harmonic on losses and temperature rise in distribution transformers. IET Gener. Transm. Distrib. **12**, 347–354 (2018)
5. Soni, R., Mehta, B.: Evaluation of power transformer health analysis by internal fault criticalities to prevent premature failure using statistical data analytics approach. Eng. Failure Anal. **136**, 106213 (2022). ISSN 1350-6307
6. Soni, R., Mehta, B.: A review on transformer condition monitoring with critical investigation of mineral oil and alternate dielectric fluids. Electr. Power Syst. Res. **214**(Part B),108954 (2023). ISSN 0378-7796
7. Soni, R., Mehta, B.: Diagnosis and prognosis of incipient faults and insulation status for asset management of power transformer using fuzzy logic controller and fuzzy clustering means. Electr. Power Syst. Res. **220**,109256 (2023). ISSN 0378-7796
8. Forouhari, S., Abu-Siada, A.: Application of adaptive neuro fuzzy inference system to support power transformer life estimation and asset management decision. IEEE Trans. Dielectr. Electr. Insul. **25**(3), 845–852 (2018)

9. Sekatane, P., Jordaan, J., Bokoro, P.: Assessment of moisture content in power transformer based on traditional techniques and adaptive neuro-fuzzy interference system. In: 11th International Conference on Electrical and Electronics Engineering (ELECO), Bursa, Turkey, pp. 987–991 (2019)
10. Soni, R., Chaudhari, K.: An approach to diagnose incipient faults of power transformer using dissolved gas analysis of mineral oil by ratio methods using fuzzy logic. In: SCOPES, pp. 1894–1899 (2016)
11. Soni, R., Mehta, B.: Condition-Based Monitoring of Power Transformer with Graphical Analysis of Incipient Faults Using Fuzzy Inference Expert System. In: Chakraborty, B., Biswas, A., Chakrabarti, A. (eds) Advances in Data Science and Computing Technologies. ADSC 2022. Lecture Notes in Electrical Engineering, vol 1056. Springer, Singapore, (2023)
12. Jang, R.J.-S., Sun, C.T., Mizutani, E.: Neuro-Fuzzy and Soft Computing, A Computational Approach to Learning and Machine Intelligence. Prentice Hall, Upper Saddle River, NJ 07458 (1997)
13. Kumari, A., Patra, J., Pal, N., et al.: Impact of solar panel on the transformer performance: a case study. Iran. J. Sci. Technol. Trans. Electr. Eng. **44**, 1197–1206 (2020)
14. Li, Q., Zhao, N.: Probabilistic impact of wind energy integration on distribution transformers. Energ. Rep. **6**(Supplement 9), 491–496 (2020). ISSN 2352-4847
15. Godina, R., Rodrigues, E.M.G., Matias, J.C.O., Catalão, J.P.S.: Effect of loads and other key factors on oil-transformer ageing: sustainability benefits and challenges. Energies **8**(10), 12147–12186 (2015)

Chapter 14
Cooling High-Powered LEDs Using an Innovative Fully Automated Heat Pipe System

Arif Amin Zargar and Neeraj Tripathi

Abstract Independent cooling system consisting of a computer, heat pipe, and fan was introduced as an initial step toward enhanced control over heat dissipation from high-power LEDs. Maintaining the substrate temperatures of the LEDs within an acceptable range has been proved experimentally to increase the performance of high-power LEDs and extend their lifespan. Instead of using light from a single sun, as traditional solar cells do, multijunction concentrator cells harness the power of concentrated solar energy. Therefore, these cells generate more power with less cooling. Concentrated sunlight was used to evaluate output power (in suns) achieved by a multi-junction concentrator solar cell operating between 160 and 250 suns. The extra heat generated by the cells was dissipated using heat pipes in this project. The heat pipe's waste heat was transferred to two thermoelectric generators, which were thermally linked to the condenser. These generators produced the power that was used.

14.1 Introduction

In recent years, there has been a rise in the application of light-emitting diodes, sometimes known as LEDs, in public lighting, billboards, vehicle headlights, and traffic signals. LEDs are gradually replacing traditional light sources including fluorescent tubes and incandescent bulbs [1–4]. Some of these reasons include a longer lifespan, higher dependability, lower energy usage, faster response time, a greater variety of color possibilities, and a reduced influence on the environment. Even though modern technology has increased, more than 80% of the electric power consumed by LED devices is utilized for heat dissipation, leading to rising chip junction temperatures, even though high-power LEDs have an energy efficiency of 15–25% from electricity to light, compared to 10% in traditional lighting [5, 6]. Traditional lighting has an

A. A. Zargar (✉) · N. Tripathi
Shri Mata Vaishno Devi University, Kakryal, Katra 182320, India
e-mail: arifamin9@gmail.com

P. H. V. S. Talpa Sai et al. (eds.), *Intelligent Manufacturing and Energy Sustainability*, Smart Innovation, Systems and Technologies 372,
https://doi.org/10.1007/978-981-99-6774-2_14

energy efficiency of only 10%. Chip junction temperatures should be kept below a safe range (typically lower than 120 °C) in order to provide optimal performance and a long lifespan for the chip. There are some applications for LED lighting that demand as much as 3000 lm per lamp, which presents issues for heat management in large-scale manufacturing and widespread adoption. It has been established in multiple studies [7, 8] that an increase in junction temperature has a detrimental effect on optical efficiency, leads to luminescence wavelength drift, and reduces device lifetime. In order to continue developing and deploying high-power LEDs, it is essential to keep their temperatures precisely under control. Multiple active, passive, and hybrid cooling solutions for high-power LEDs have been developed in recent years. The LEDs are compatible with these fixes. Hsieh et al. [9] proposed micro spray cooling as a method for cooling high-power LEDs to solve the problem of thermal management. Spray cooling has been shown to be an effective method of dissipating the large heat flux produced by high-power LEDs. Liu et al. [10] used numerical simulations to analyse and make comparisons between three different microjet architectures that are used in the cooling systems of high-power LEDs. Li et al. [11, 12] created a cooling system that makes use of a thermoelectric cooler (TEC) in order to increase the heat dissipation of high-power LEDs. As a result, the system is able to cool LEDs that have a maximum power of 106.7 W. Because of the work that Li and his colleagues did, this is now an option. Deng and Liu [13] came to the conclusion that liquid metal cooling was a viable way for dissipating the heat that was produced by high-power LEDs after conducting a significant amount of study, both experimentally and theoretically. Experimentation and modelling were employed to investigate how effective a liquid active cooling system is at maintaining a consistent temperature for high-powered LEDs used in automobile headlights [14]. The ability of high-power LEDs to dissipate heat was addressed by Lu et al.'s [15, 16] invention of a heat pipe with both a flat and loop configuration. Yang et al. [17] came up with the idea for a newly produced flat polymer heat pipe, and they used a custom-built laboratory prototype to investigate the pipe's efficiency as well as its heat transfer characteristics. The pace at which heat could be dispersed was to be increased, this was the primary objective. Heat sinks made of metal fins offer a high degree of stability, but when natural convection is the only method of cooling used, their cooling effectiveness is insufficient. The heat pipe is a feasible alternative efficient technique of cooling since it has a high conductivity coefficient, low thermal resistance, and a short volume [18]. The apparatus includes a thermal insulator in addition to its evaporator and condenser components. Heat pipe integrated assemblies continue to bring in a significant number of customers [19] because they can be purchased at a reasonable cost and have a long lifespan. Nevertheless, there are a few significant downsides associated with the utilization of active cooling. If the heat is not removed, the light fixture as a whole will be rendered inoperable in the event that the fan is turned off. An LED operation needs to have a heat-pipe radiator that can automatically regulate the temperature for it to be exceptionally reliable.

14.1.1 Efficiency of Hybrid Photovoltaic/Thermoelectric Generator from a Condensate Heat Pipe

Photovoltaics (PV) have been demonstrated to be an effective, reliable, and long-lasting renewable energy source [20]. In 2020, PV electricity generation is expected to increase by 22% [21, 22]. With a 3.6% share of the world's total electricity production, it trails only hydropower and wind as the third largest renewable electricity resource [23, 24]. The rising popularity of renewable energy and the falling price of PV systems have fuelled the industry's rapid expansion in recent years [25, 26]. The use of focused solar radiation would significantly reduce the cost of operation. Because the quantity of current that is produced by CPV (Concentrator Photovoltaics) is linearly proportional to the amount of solar radiation that is incident upon it, high levels of solar radiation intensity result in a substantial amount of current being produced by CPV. At the moment, there are primarily two categories of solar concentrators available on the market: low-concentration systems, which make use of troughs or parabolic reflectors (and have a concentration ratio of up to 10X), and high-concentrator systems, which make use of Fresnel Lenses (and have a concentration ratio of 500X or more). Natural convection ventilation can be used in low-concentration systems to eliminate the need for mechanical cooling systems. Unfortunately, the CPV's operating temperature increases when subjected to strong solar radiation, which significantly lowers the voltage generated and, in turn, the output power and, ultimately, the efficiency. The optical concentration ratio will respond differently depending on the type of cooling mechanism that is used, whether it be static or dynamic must be employed to keep the working temperature of the CPV down to keep it functioning efficiently [27]. Pumping a cooling liquid (often water) through an active cooling system creates a forced flow within the CPV system, which improves the efficiency of the CPV system significantly. However, there are typically a number of issues that arise, such as leakage in the system and the increased expenses of pumping power and maintenance. Despite dynamic cooling's superior efficiency, numerous technical issues and the high cost of operation and maintenance can be avoided with static cooling. Surface anti-reflection [28] and selective coatings are two common approaches to this problem. There have been several attempts to create an efficient and successful passive cooling technology. Conventional cooling fins on the CPV's back have already dispersed the heat that accumulates there by convection and radiation [29]. In addition to passively cooling CPV cells, thermoelectric generators can be used to harvest the excess heat produced by the CPV and turn it into usable energy [30]. Passive cooling of GaInP/GaAs/Ge (gallium indium phosphide/gallium arsenide/germanium) multijunction CPVs and the harvesting of additional electrical energy may employ heat pipes linked with thermoelectric generators, as will be discussed below. This straightforward approach provides a useful method of passive cooling for CPV systems functioning in environments with moderate concentration ratios of solar radiation. The proposed technology provides an alternative to

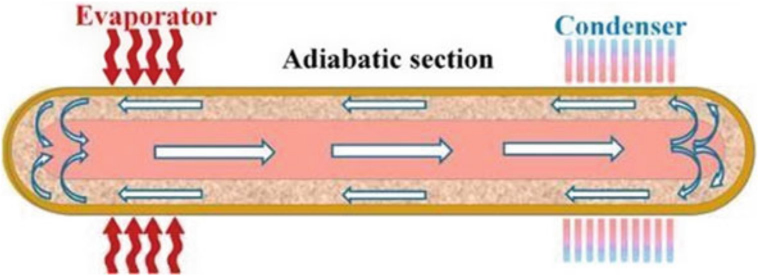

Fig. 14.1 The heat pipe circulation with a fluid

the conventional heat-fin cooling of CPVs, which is both maintenance-free and cost-effective. Due to the poor efficiency of the solar cells (about 12%), this may not be effective for one-sun solar cells.

14.1.2 Heat Pipe

In Fig. 14.1, we see a heat pipe (HP), a device that facilitates the rapid and effective transfer of heat. It's made up of a closed, vacuum-sealed tube with a solid outer surface and a porous metal (wick) layer inside. Heat transfer occurs as the working fluid alternates between liquid and vapor phases inside the heat pipe's pores [31, 32]. The evaporator end of the tube is in touch with the heated object, while the system's heat is dissipated thanks to the condenser's connection to an external heat source, such as a heat sink or fins. Between the evaporator and the condenser is a region of the tube called the "adiabatic section" because no heat is transferred between the two ends [33].

The evaporator section of heat pipes is responsible for changing the liquid in the wicking layer into a gas. As a result of the pressure difference between the two ends, the vapor is drawn to the cooler condenser section, where it condenses into a liquid and returns via the wicking layer to the evaporator. This two-phase flow will continue so long as the evaporator and condenser are at different temperatures.

14.1.3 The Cooling System's Regulatory Apparatus

An integrated microprocessor, LCD display, A/D converter, and digital temperature sensor form a small control system that can automatically regulate and safeguard electronic devices. The control system relies heavily on a single-chip computer (MCS-52), which integrates the CPU, RAM, I/O, and interrupt circuitry onto a single circuit board. The high-performance microprocessor (CMOS 8bit) in the 8052-architecture microcontroller we chose is with 8 K bytes of rewritable, non-volatile flash memory.

The microcontroller offers a low-priced and highly adaptable alternative for the control system. The MAX6675 A/D Converter takes the analog signal from the K-type thermocouple 1 and 2 that are placed on the substrate's surface and converts it into a digital signal in real-time. All aspects of the HVAC (Heating, Ventilation and Air Conditioning) system are managed by this digital signal. A DS18B20 sensor constantly checks the temperature of its surroundings.

14.1.4 Thermoelectric Generators

Thermoelectric generators (TEG) can transform heat into electricity because of the Seebeck effect. Devices of this type are simple, maintenance-free, silent, and environmentally beneficial; however, they have low efficiency in comparison to PV. Because of their solid-state construction, TEG devices boast advantages over their bulkier counterparts in terms of dependability, energy efficiency, the noise level during operation, and compactness. However, such devices are notorious for their poor thermal efficiency, which only worsen when they are subjected to uneven temperatures along their sides. As can be seen in Fig. 14.2, TEGs are made up of multiple P–N junction pairs with an inverse See beck coefficient. Thermocouples are semiconductor junctions constructed from p- and n-type semiconductor materials known for their great performance. When a temperature differential exists between the two ends of a given connection, an electric potential difference is created across those ends. A closed external load experiences current flow because of the potential difference. It is possible to boost the TEG's output power by raising heating and cooling differentials, or by series-connecting multiple TEGs.

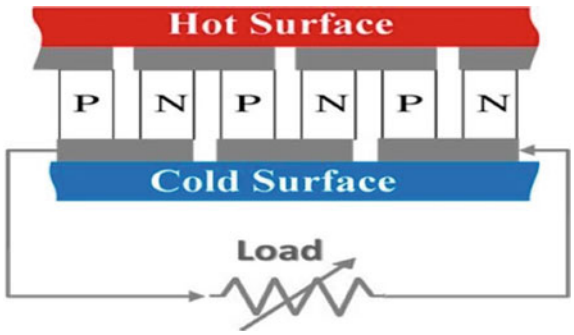

Fig. 14.2 Thermoelectric generator

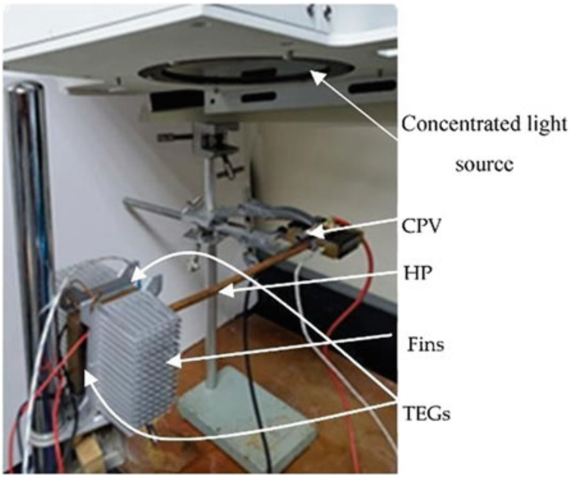

Fig. 14.3 Proposed setup of methodological layout

14.2 Numerical Investigation

14.2.1 Proposed Layout Setup

The apparatus depicted in Fig. 14.3 was utilized in this study. Three separate circuits linked the HP's GaInP/GalnAs/Ge CPV cell to the copper block evaporator. The HP's evaporator was a copper block with a hole drilled into it. One of the HP's many features is a copper block designed to safeguard the device's condenser. A TEG was connected to each copper block, with the warm side touching the block and the cold side touching the heat fins. Both the copper block that made up the CPV and the copper block that made up the hot sides of the TEGs required thermal grease for peak performance, as did the aluminium heat fins that made up the cold sides of the TEG.

The I-V characteristics of the PV cells were measured with a Keithley current source, and from there we were able to derive the cell parameters (Voc, Isc, Im, and Vm). Digital multimeters were used to measure the thermoelectric current and voltage. K-type thermocouples were used to take the readings.

Light sources with high optical concentration ratios (150 sun–260 suns) are ideal for illuminating CPV because the heat generated on the back side of the CPV is quickly and efficiently transferred to the other side via the copper block and the HP. The heat pipe transfers warmth to the hot sides of the TEG, while the heat fins cool the cold sides. Because of the temperature difference between the two sides of each TEG, thermoelectric power is produced and combined with the CPV output. In this experimental setup, detrimental heat generated by the CPV is converted into electricity using TEG elements, allowing for a more effective expansion of the CPV cell. This is accomplished by: (i) utilizing a heat pipe for the passive (no extra cost for cooling pumps, motors, etc.), quick, and effective removal of heat built up on the

CPV, which improves its efficiency. (ii) Putting that heat to work in thermoelectric generators to produce electricity. This boosts the system's overall output.

14.3 Result and Discussion

Four different setups were used to evaluate the proposed system's performance:

(i) LHP+HS (Long heat pipe + Heat sink): The CPV is linked to a 25-cm-long HP with heat sink fins thermally attached on both sides of the second copper block. In this setup, the CPV is the sole generator of electricity, no TEGs are used.

(ii) SHP+HS (Short heat pipe + Heat sink): The CPV is linked to a 15-cm-long heat pipe, and the heat sinks' fins are thermally attached directly to the two sides of the second copper block in a SHP+HS arrangement. Since the CPV is the sole generator of power in this setup, TEGs are unnecessary.

(iii) LHP+TEG+HS (Long Heat pipe + Thermoelectric generator + Heat sink), wherein the CPV is linked to the TEG via the HS. Two thermoelectric generators (TEGs) with heat sinks fins are linked to the second copper block. The combined power of the CPVs and the TEGs is the total power generated.

(iv) SHP+TEG+HS (Short heat pipe + Thermoelectric generator + Heat sink): CPV is linked to a short HP in the iv configuration (SHP+TEG+HS). Two thermoelectric generators (TEGs) with fin heat sinks are linked to the second copper block. The combined power of the CPVs and the TEGs is the total power generated. Each of the four setups is measured against the output of the classic HS Only setup, in which the CPV is hardwired to a single-fin heat sink. The temperature at the CPV is plotted versus the optical concentration ratio in Fig. 14.4 for each of the four experimental setups and the control setup (HS Only). Maximum temperatures are observed in the traditional setup with only HS, suggesting that this region of optical concentration is not optimal for CPV passive cooling. The LHP+HS configuration's CPV temperatures are second-lowest only to those of the SHP+HS and SHP+TEG+HS versions (Table 14.1).

As can be observed in Fig. 14.5, the maximum power output of the CPV system changes as the operational temperature rises. When compared to the other configurations used, the greatest output came from the LHP+TEG+HS configuration. Over 16% more power is generated compared to a regular HS Only system, and an optical concentration ratio of nearly 230 suns is achieved. Long HP also has more impact than short HP (Table 14.2).

At an optical concentration of 230 suns, the total power gains for LHP+TEG+HS, SHP+TEG+HS, LHP+HS, and SHP+HS correspondingly are 20%, 17%, 12%, and 6% respectively. This is in comparison to the total power increases for normal HS-only systems.

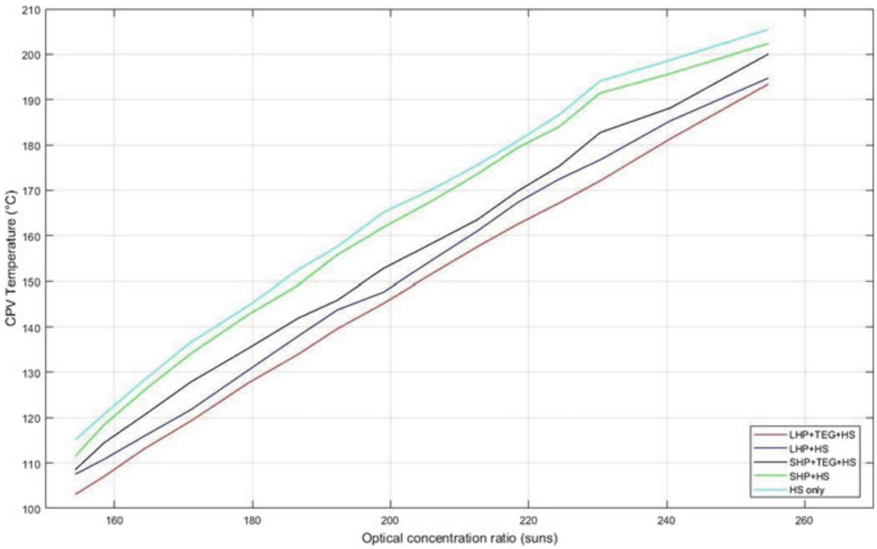

Fig. 14.4 Optical concentration ratio and CPV temperature

Table 14.1 The values of parameters, optical concentration (suns) and CPV temperature (celsius)

x (suns)	LHP+TEG+HS (y1)	LHP+HS (y2)	SHP+TEG+HS (y3)	SHP+HS (y4)	HS only (y5)
154.345	103.064	107.525	108.516	111.49	115.125
158.528	107.029	110.829	113.472	118.429	120.742
164.354	113.142	115.951	119.585	126.029	128.342
171.077	119.255	121.733	126.855	134.124	135.611
179.443	127.681	127.516	132.307	142.715	142.715
186.614	133.959	133.959	138.915	149.158	149.489
192.291	139.576	140.733	143.872	155.767	156.593
199.014	145.193	147.671	149.819	161.88	165.184
206.185	151.802	154.776	155.436	167.827	170.305
212.609	157.584	161.054	161.549	173.61	175.592
218.435	162.541	167.332	166.836	179.392	180.879
224.411	167.166	172.453	171.297	185.009	186.661
230.387	172.123	178.731	175.757	191.453	192.113
240.546	181.375	185.34	185.175	196.739	198.722
254.739	193.435	194.757	198.061	201.365	205.496

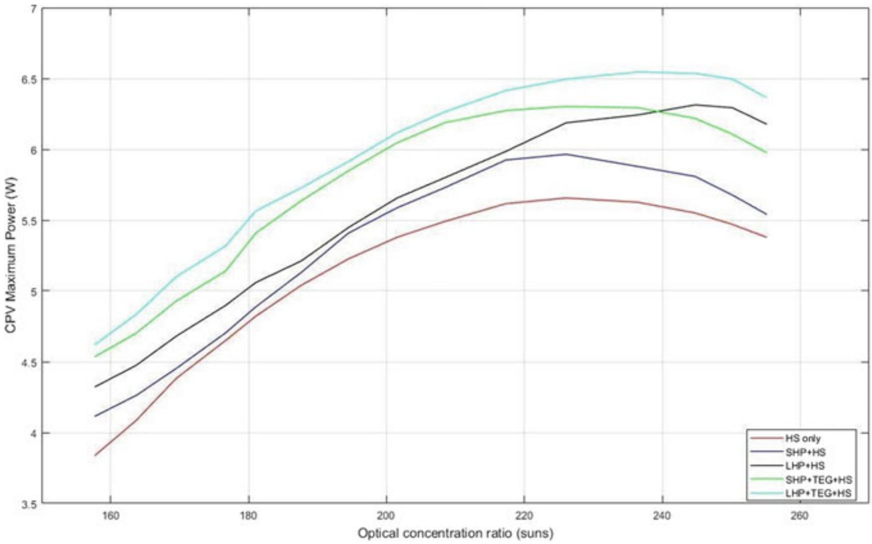

Fig. 14.5 Optical concentration ratio versus CPV's maximum power

Table 14.2 The values of the parameters, optical concentration (suns) and Maximum CPV (W)

x (suns)	HS only (y1)(W)	SHP+HS (y2)(W)	LHP+HS (y3)(W)	SHP+TEG+HS (y4)(W)	LHP+TEG+HS (y5)(W)
157.689	3.83675	4.11475	4.32199	4.53428	4.62021
163.68	4.08443	4.26134	4.47363	4.70109	4.83251
169.525	4.38265	4.39276	4.68087	4.92854	5.1004
176.685	4.65054	4.64043	4.89822	5.14084	5.31775
181.069	4.8224	4.88811	5.05996	5.40873	5.56542
187.645	5.03974	5.13073	5.2116	5.63619	5.72717
194.513	5.22676	5.44917	5.35818	5.84848	5.91419
201.527	5.3784	5.65641	5.58564	6.04561	6.11637
208.395	5.4896	5.79793	5.79793	6.18714	6.26296
217.309	5.61597	5.9243	5.98495	6.27307	6.41459
226.076	5.65641	5.96474	6.18714	6.30339	6.49547
236.451	5.62608	5.87881	6.24274	6.29328	6.54601
244.781	5.55026	5.80804	6.3135	6.21747	6.53591
250.187	5.46939	5.67662	6.29328	6.10626	6.49547
255.156	5.3784	5.54015	6.17703	5.97484	6.36405

14.4 Conclusion

The novel cooling technology that is based on heat pipes, a PWM fan, and automatic management makes it possible to use high-power LEDs without the risk of damaging the device. In this experiment, heat pipes were utilized to evacuate the cells' surplus heat in a manner that was both efficient and quick. Along with the CPV cooling system, we have also put two thermoelectric generators in the heat pipe so that we may make useful use of the heat that would otherwise be wasted. It has been determined how effective each of these four distinct cooling arrangements is. The LHP+TEG+HS configuration displays a maximum output power that is around 16% higher than that of a standard HS setup at an optical concentration ratio of 230 suns. This is the case when compared to the conventional HS arrangement. When compared to the short HP design, the long HP configuration's TEG components can produce a greater amount of output power. At an optical concentration of 230 suns, the total power increase for the LHP+TEG+HS configuration, the SHP+TEG+HS configuration, the LHP+HS configuration, and the SHP+HS configuration were 20%, 17%, 12%, and 6% respectively.

References

1. Takai, I., Ito, S., Yasutomi, K., Kagawa, K., Andoh, M., Kawahito, S.: LED and CMOS image sensor based optical wireless communication system for automotive applications. IEEE Photonics J. **5**(5), 6801418 (2013)
2. Feezell, D.F., et al.: Semipolar InGaN/GaN light-emitting diodes for high-efficiency solid-state lighting. J. Display Technol. **9**(4), 190–198 (2013)
3. Cho, J., Schubert, E.F., Kim, J.K.: Efficiency droop in light-emitting diodes: challenges and countermeasures. Laser Photonics Rev. **7**(3), 408–421 (2013)
4. Hsieh, C.C., Li, Y.H., Hung, C.C.: Modular design of the LED vehicle projector headlamp system. Appl. Opt. **52**(21), 5221–5229 (2013)
5. Yang, K.S., Chung, C.H., Lee, M.T., Chiang, S.B., Wong, C.C., Wang, C.C.: An experimental study on the heat dissipation of LED lighting module using metal/carbon foam. Int. Commun. Heat Mass Transfer **1**(48), 73–79 (2013)
6. Narendran, N., Gu, Y., Freyssinier, J.P., Yu, H., Deng, L.: Solid-state lighting: failure analysis of white LEDs. J. Cryst. Growth **268**(3–4), 449–456 (2004)
7. Narendran, N., Gu, Y.: Life of LED-based white light sources. J. Display Technol. **1**(1), 167 (2005)
8. Tang, Y., Ding, X., Yu, B., Li, Z., Liu, B.: A high-power LED device with chips directly mounted on heat pipes. Appl. Therm. Eng. **66**(1–2), 632–639 (2014)
9. Hsieh, S.S., Hsu, Y.F., Wang, M.L.: A microspray-based cooling system for high powered LEDs. Energ. Convers. Manage. **78**, 338–346 (2014)
10. Liu, S., Yang, J., Gan, Z., Luo, X.: Structural optimization of a microjet based cooling system for high power LEDs. Int. J. Therm. Sci. **47**(8), 1086–1095 (2008)
11. Li, J., Zhang, Y., Yuan, Y., Yu, H.: New applications of an automated system for high-power LEDs. IEEE/ASME Trans. Mechatron. **21**(2), 1035–1042 (2015)
12. Li, J., Ma, B., Wang, R., Han, L.: Study on a cooling system based on thermoelectric cooler for thermal management of high-power LEDs. Microelectron. Reliab. **51**(12), 2210–2215 (2011)
13. Deng, Y., Liu, J.: A liquid metal cooling system for the thermal management of high-power LEDs. Int. Commun. Heat Mass Transfer **37**(7), 788–791 (2010)

14. Lai, Y., Cordero, N., Barthel, F., Tebbe, F., Kuhn, J., Apfelbeck, R., Würtenberger, D.: Liquid cooling of bright LEDs for automotive applications. Appl. Therm. Eng. **29**(5–6), 1239–1244 (2009)
15. Lu, X.Y., Hua, T.C., Wang, Y.P.: Thermal analysis of high-power LED package with heat pipe heat sink. Microelectron. J. **42**(11), 1257–1262 (2011)
16. Lu, X.Y., Hua, T.C., Liu, M.J., Cheng, Y.X.: Thermal analysis of loop heat pipe used for high-power LED. Thermochim. Acta **493**(1–2), 25–29 (2009)
17. Yang, K.S., Yang, T.Y., Tu, C.W., Yeh, C.T., Lee, M.T.: A novel flat polymer heat pipe with thermal via for cooling electronic devices. Energ. Convers. Manage. **100**, 37–44 (2015)
18. Lu, T.J.: Thermal management of high-power electronics with phase change cooling. Int. J. Heat Mass Transf. **43**(13), 2245–2256 (2000)
19. Luo, X., Xiong, W., Cheng, T., Liu, S.: Temperature estimation of high-power light emitting diode street lamp by a multi-chip analytical solution. IET Optoelectron. **3**(5), 225–232 (2009)
20. Liu, X., Xiao, Y., Inthavong, K., Tu, J.: Experimental and numerical investigation on a new type of heat exchanger in ground source heat pump system. Energ. Effi. **8**, 845–857 (2015)
21. Xiao, C., Tian, Q., Zhou, C., Li, J., Zhu, W.: A novel cooling system based on heat pipe with fan for thermal management of high-power LEDs. J. Opt. **46**, 269–276 (2017)
22. Routhier, A.F., Honsberg, C.: Using PV and thermal energy storage to decrease carbon dioxide emissions. In: 2018 IEEE 7th World Conference on Photovoltaic Energy Conversion (WCPEC) (A Joint Conference of 45th IEEE PVSC, 28th PVSEC and 34th EU PVSEC), 2018 Jun 10, pp. 1477–1480. IEEE
23. Solar PV—Analysis. https://www.iea.org/reports/solar-pv. Accessed on 10 Dec. 2022
24. Renewable Power Generation Costs in 2020. https://www.irena.org/Publications/2021/Jun/Renewable-Power-Costs-in-2020
25. Photovoltaic cost reduction—an overview. ScienceDirect. https://www.sciencedirect.com/topics/engineering/photovoltaic-cost-reduction
26. Mariotti, S., Al Turkestani, M., Hutter, O.S., Papageorgiou, G., Major, J.D., Swallow, J., Nayak, P.K., Snaith, H.J., Dhanak, V.R., Durose, K.: Direct silicon heterostructures with methylammonium lead iodide perovskite for photovoltaic applications. IEEE J. Photovoltaics **10**(4), 945–951 (2020)
27. Zsiborács, H., Hegedűsné Baranyai, N., Vincze, A., Háber, I., Weihs, P., Oswald, S., Gützer, C., Pintér, G.: Changes of photovoltaic performance as a function of positioning relative to the focus points of a concentrator PV module: case study. Appl. Sci. **9**(16), 3392 (2019)
28. Du, B., Hu, E., Kolhe, M.: Performance analysis of water cooled concentrated photovoltaic (CPV) system. Renew. Sustain. Energ. Rev. **16**(9), 6732–6736 (2012)
29. Moiz, S.A., Alahmadi, A.N.M., Karimov, K.S.: Improved organic solar cell by incorporating silver nanoparticles embedded polyaniline as buffer layer. Solid-State Electron. **163**, 107658 (2020)
30. Moiz, S.A., Alahmadi, A.N., Aljohani, A.J.: Design of silicon nanowire array for PEDOT: PSS-silicon nanowire-based hybrid solar cell. Energies **13**(15), 3797 (2020)
31. Ahmadinejad, M., Moosavi, R.: Energy and exergy evaluation of a baffled-nanofluid-based photovoltaic thermal system (PVT). Int. J. Heat Mass Transf. **1**(203), 123775 (2023)
32. Ahmadinejad, M., Soleimani, A., Gerami, A.: The effects of a novel baffle-based collector on the performance of a photovoltaic/thermal system using SWCNT/water nanofluid. Therm. Sci. Eng. Prog. **34**, 101443 (2022)
33. Sangdot, R., Patel, H., Student, P.G.: A review on photovoltaic panel cooling using heat pipe. IJSDR **1**(5), 573–576 (2016)

Chapter 15
Coupling Code for Real-Time Simulation of a Wave Energy Converter

Kameswara Sridhar Vepa and N. Seetharamaiah

Abstract This paper discusses the fluid–structure interaction in the context of moving parts in the structure that can influence the interface between fluid and structure. A coupling code is developed that can fully couple the fluid–structure interaction using different black box solvers and, at the same time, provide a complete picture of the real-time problem. The coupling code is tested using a numerical model of a cube-shaped floating buoy subjected to a theoretical wave model of sinusoidal form. The power generated by the buoy and the power calculated by the code are in agreement with each other.

15.1 Introduction

As the focus on energy generation from ocean waves increases, wave dynamics research becomes essential [1]. One of the significant problems encountered while simulating a wave energy system is the exchange of information between wave impact on the buoy and the influence of internal mechanisms on the overall behavior [2]. Equipment like wave energy converters must stay offshore throughout life and involve many components. It is essential to study the response behavior of all these components thoroughly. However, the main obstacle faced in doing that is the lack of tools to model everything centrally. This work provides a solution to this aspect of coupling different solvers to extract the actual behavior of the floating buoy. A two-way coupling code is developed to communicate between different black-box solvers.

There are four components of this coupling code: (1) Hydrodynamic component for modeling the wave-body/structure interaction, (2) Structural component that is used to model any complex offshore structure, (3) Kinematic system simulator that simulates the dynamics of the machinery, and (4) Control component to incorporate control mechanism into the model.

K. S. Vepa (✉) · N. Seetharamaiah
Department of Mechanical Engineering, School of Technology, GITAM, Hyderabad, India
e-mail: svepa@gitam.edu

P. H. V. S. Talpa Sai et al. (eds.), *Intelligent Manufacturing and Energy Sustainability*, Smart Innovation, Systems and Technologies 372,
https://doi.org/10.1007/978-981-99-6774-2_15

A theoretical model for a wave energy converter is developed to test the code, which is then modeled numerically, and the communication between the individual solvers is tested. In the following section, communication between different modules of coupling code is explained. Later, the theoretical calculations for the loads coming onto the buoy and the expected theoretical Power generated by the model are explained.

15.2 Code Overview

Taking the kinematic and control components in the code as one component, there are three essential components viz., (i) Hydrodynamic component, (ii) Internal mechanism component, and (iii) Structural component. All three components will interact with each other using the fourth component, i.e., a model-based simulator, which most of the current wave energy converters require [3]. The hydrodynamic component can also include aerodynamic effects.

The hydrodynamic component interacts with the internal mechanism component to account for the energy transfer from the waves to the wave energy converter (WEC), and the internal mechanism component gives the input to simulate hydrodynamics about the influence of the internal mechanism of the WEC on the local wave climate [4]. The internal mechanism component provides the input to the structural component to simulate the dynamic loading conditions on the structure of the WEC. The structural component, in turn, transfers the external loading on the structure to the internal mechanism component.

The hydrodynamic component gives the input to the structural component about the loads coming onto the structure because of the prevailing hydrodynamic and/ or aerodynamic conditions. The structural component provides the movement of the WEC to the hydrodynamic component so that the effect of WEC on local wave climate is studied. The input data for the hydrodynamic component are the WEC movement along with the inertia changes because of the movement of the internal mechanism of the WEC. Input data for the structural component comes from the wave data given by the hydrodynamic component and the transient loading conditions because of the WEC operation from the internal mechanism component. Input data for the internal mechanism component are the WEC movement from the structural component and the incident wave energy from the hydrodynamic component. SPH-FE coupling is used for coupling hydrodynamics and structural components in this work. A flow chart showing the data transfer can be seen in Fig. 15.1.

SPH as a method for water wave dynamics was already studied in the works of Sigalotti and Zheng [5, 6]. Oger et al. [7] and Gong et al. [8] studied the SPH method for wedge water entry simulation. In this work, the coupling of SPH and finite elements is employed to study the response behavior of the structure as well. The kernel approximation used in this work is given by Eq. 1, where f is any arbitrary function multiplied by the kernel function over the domain Ω.

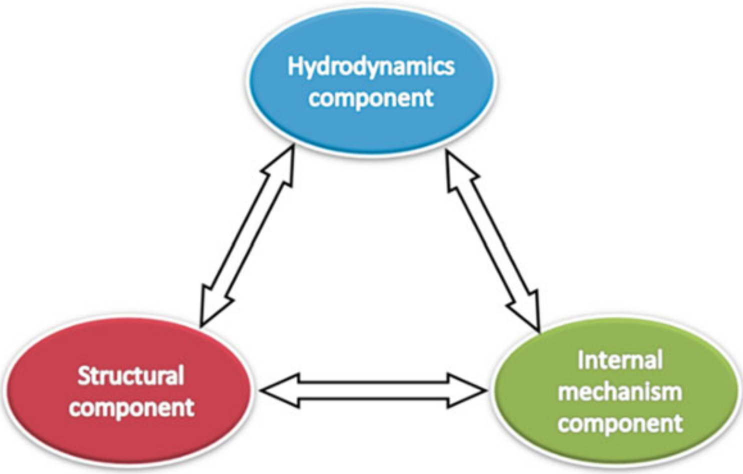

Fig. 15.1 Data flow between different components of the coupled system

$$f(x) = \int_{\Omega} f(x') \frac{1}{h^3} \begin{cases} \left(1 - \frac{3}{2}|x|^2 + \frac{3}{4}|x|^3\right) \mathrm{d}x' & for\ |x| \leq 1 \\ \frac{1}{4}(2 - |x|)^3 \mathrm{d}x' & for\ 1 < |x| \leq 2 \\ 0 & for\ 2 < |x| \end{cases} \tag{15.1}$$

where h represents the radial dimension where the kernel function is active. The choice of kernel function is such that it is always normalized, non-negative, and even for any value of $\boldsymbol{x}'$. The smoothing value decreases monotonically with the increasing distance.

Integral equations are transformed into discrete forms, and the support domain is scaled using a factor k. The particle approximation for particle i is done as shown in Eq. 2.

$$f(x_i) = \sum_{j=1}^{N} \frac{m_j}{\rho_j} f(x_j).W_{ij} \tag{15.2}$$

The kernel function $W(\boldsymbol{x}_i - \boldsymbol{x}_j, h)$ and $j = 1$ to N represents the particles surrounding particle i and are within the smoothing function field. m_j and ρ_j represents the mass and density of particle j, which is in the neighborhood of particle i. The spatial derivative of the particle approximation is done based on Eq. 3.

$$\nabla.f(\boldsymbol{x}_i) = \sum_{j=1}^{N} \frac{m_j}{\rho_j} f(\boldsymbol{x}_j).\nabla \boldsymbol{W}_{ij} \tag{15.3}$$

This SPH formulation is now used to discretize the Navier–Stokes equation, which yields a set of ODEs that are then, solved using explicit time integration. Equation 4 gives the continuity equation discretized for the SPH formulation. This equation is used for all the space indices.

$$\frac{D\rho_i}{Dt} = \sum_{j=1}^{N} m_j \left(\boldsymbol{x}_i - \boldsymbol{x}_j\right). \frac{\partial \boldsymbol{W}_{ij}}{\partial \boldsymbol{x}_i} \tag{15.4}$$

If α and β are the space indices, then the momentum equation used in the code is as shown in Eq. 5.

$$\frac{D\boldsymbol{v}_i^{\alpha}}{Dt} = \sum_{j=1}^{N} m_j \left(\frac{\boldsymbol{s}_i^{\alpha\beta}}{\rho_i \rho_j}. \frac{\partial \boldsymbol{W}_{ij}}{\partial \boldsymbol{x}_i^{\beta}} - \frac{\boldsymbol{s}_j^{\alpha\beta}}{\rho_i \rho_j}. \frac{\partial \boldsymbol{W}_{ji}}{\partial \boldsymbol{x}_j^{\beta}} \right) \tag{15.5}$$

where v represents velocity and s represents the stress tensor. Discretized energy (e) equation is given by Eq. 6:

$$\frac{De_i}{Dt} = -\frac{p_i + \Pi_{ij}}{\rho_i^2} \sum_{j=1}^{N} m_j \left(\boldsymbol{v}_i - \boldsymbol{v}_j\right) \cdot \frac{\partial \boldsymbol{W}_{ij}}{\partial \boldsymbol{x}_i^{\beta}} \tag{15.6}$$

where Π_{ij} represents artificial viscosity suggested by Monaghan [9]. It is observed that using artificial viscosity prevents penetration of particles approaching each other.

The fluid (water in this case) is modeled as weakly compressible in this code, and hence an equation of state (EOS) is used to calculate pressure based on density (Eq. 7). For water, the bulk modulus $K = 2.2.10^9$ N/m^2.

$$p = K \ln\left(\frac{\rho}{\rho_0}\right) \tag{15.7}$$

In addition, the particle movement is controlled by the differential Eq. 8. $\upsilon \cong 0.5$ is the XSPH correction recommended by Monaghan [9], which is applied to the incompressible SPH flow for smoothing the velocity among neighboring particles. However, this term is used in this code to prevent different particles (with different velocities) from occupying the exact location.

$$\frac{\mathrm{d}\boldsymbol{x}_i}{\mathrm{d}t} = \boldsymbol{v}_i + \upsilon \sum_{j=1}^{N} \frac{m_j}{\rho_j} \left(\boldsymbol{v}_i - \boldsymbol{v}_j\right) \boldsymbol{W}_{ij} \tag{15.8}$$

Modeling of the structural components is done using shell elements following the Belytschko-Lin-Tsay formulation [10], and stress–strain equations are solved using FE code. This shell element is based on the co-rotational and velocity-strain formulation. A total of two through-shell integration points are used in the model. Mindlin [11] theory of plates and shells is used to discretize the velocity of any point in the element (Eq. 9).

$$\boldsymbol{\vartheta} = \boldsymbol{\vartheta}^m - \hat{z} e_3 \times \boldsymbol{\theta} \tag{15.9}$$

where $\boldsymbol{\vartheta}^{\boldsymbol{m}}$ is the velocity of the mid-surface, $\boldsymbol{\theta}$ is the velocity vector and $\hat{z}$ is the distance along the thickness of the shell element.

The deformation $\boldsymbol{u}$ of each shell element is computed using Eq. 10 based on momentum conservation.

$$R \frac{\partial^2 \boldsymbol{u}}{\partial t^2} - \nabla . \boldsymbol{\sigma} = \boldsymbol{f} \tag{15.10}$$

where σ is the stress tensor, R is the density associated with the shell element, and f ($= -$R.g. $\hat{y}$) is the body force per unit volume. Stress and Strain tensors are associated, as shown in Eq. 11.

$$\boldsymbol{\sigma} = \boldsymbol{C} : \boldsymbol{\upsilon} \quad where\ \varepsilon = \frac{1}{2}\left[\nabla \boldsymbol{u} + (\nabla \boldsymbol{u})^T\right] \tag{15.11}$$

Since the material used is linear elastic with isotropic behavior, the values in tensor C can be deduced from two independent material constants, i.e., Young's modulus and Poisson's ratio. More than one material is used for different parts of the structural system, which are presented in the numerical model section.

A commercially available mechanism solver, Universal Mechanism (UM), is the internal mechanism component. The main program, which controls the data flow and generates the required files for the input and output, is written in a high-level technical computing software package MATLAB.

15.3 Theoretical Calculations

Research done in wave dynamics has shown that the behavior of ocean waves can be divided into six sea states, where each sea state corresponds with a certain energy level of the waves (see Table 15.1). Sea state 1 corresponds with a mellow sea or waves with low amplitude, whereas sea state 6 corresponds with a stormy sea. Because each of these sea states has different amplitudes and different wave frequencies, it is recommended to use numerical tools to simulate the power extraction. Note that, in reality, the waveforms are rarely sinusoidal.

All the parameters are determined for sea state 3. This is the sea state that occurs most frequently in the coastal region. This work uses a cube-shaped buoy with a side of 5 m for testing purposes. The buoy position amplitude z_A is calculated using the formula [3]:

$$z_A(\omega) = \frac{F_{ex,A}(\omega)}{\sqrt{\left[k - \left(m + m_{sup} + m_a(\omega)\right) \cdot \omega^2\right]^2 + \left[\left(b_{hyd}(\omega) + b_{ext}\right)\omega\right]^2}} \tag{15.12}$$

Table 15.1 Different sea states occurring on the coast

Sea state	Wave height (m)	Wave period (s)	Wave frequency (Hz)
1	0.25	4.72	0.21
2	0.75	5.04	0.20
3	1.25	5.71	0.18
4	1.75	6.53	0.15
5	2.25	7.30	0.14
6	2.75	7.92	0.13

The phase angle β_{mot} between the movement of the sea and the movement of the buoy is calculated by the formula [3]:

$$\beta_{mot} = \beta_{Fex} - \tan^{-1}\left(\frac{\left(b_{hyd}(\omega) + b_{ext}\right)\omega}{k - \left(m + m_{sup} + m_a(\omega)\right)\omega^2}\right) \tag{15.13}$$

$Z_A(\omega)$ is the real movement amplitude of the buoy in the function of the pulsation of the sea. This amplitude is bigger than the wave height H_s due to the inertia of the buoy. A positive phase angle between the movement of the sea and the buoy means that the sea movement precedes the buoy movement. These two variables are calculated using the data from De Backer's work [3].

With all the previous data, it is still not possible to calculate the buoy position amplitude and the phase angle. This is because the buoy mass m and the buoy stiffness k are still unknown.

The following formula calculates the buoy stiffness k:

$k = \rho_{sea} g A_w$ Where: A_W = waterline area = 19.63 m^2
$k = 196,421.706 \frac{N}{m}$ ρ_{sea} = density of seawater $\approx 1020 \frac{kg}{m^3}$

The values of the parameters are taken from the work of De Backer [3]:

- Added mass: $m_a = 19.5$ tons
- Hydrodynamic damping coeff.: $b_{hyd} = 7.8 \frac{tons}{s}$
- Amplitude sea force on buoy: $F_{ex,\omega} = 100$ kN
- Force phase angle: $\beta_{F,ex} = 6°$ (0.105 radians)
- External damping coefficient: $b_{ext} = 20 \frac{tons}{s}$
- Supplementary mass: $m_{sup} = 130$ tons
- Angular wave frequency (SS 3): $\omega = 1.131 \frac{radians}{s}$
- Buoy mass: m = 37,000 kg.

This gives for $z_A = 1.902$ m and for $\beta_{mot} = 42.733°$ (0.746 radians). These two variables are calculated manually and by using MATLAB.

Movement, Force, and Power at the Buoy

When all the variables are known, it is possible to calculate the movement, Force, and Power at the buoy. This work considers a hypothetical situation, so the movement and Force are sinusoidal. In reality, this is not the case since the waveform is rarely sinusoidal.

The movement of the buoy lags in relation to the sea with the phase angle β_{mot}. The movement of the sea and buoy are given by [3]:

$$\begin{aligned} z_{sea} &= H_s.\sin(\omega t) \\ z_{buoy} &= z_A.\sin(\omega t - \beta_{mot}) \end{aligned} \tag{15.14}$$

The Force that the sea carries onto the buoy lags in relation to the sea with a phase angle β_{Fex}.

$$\begin{aligned} F_{buoy} &= F_{ex,\omega}.\sin(\omega t - \beta_{Fex}) \\ F_{buoy} &= 10,000 * \sin(1.131 * t - 0.105) \end{aligned} \tag{15.15}$$

These three variables are plotted as a function of time in Fig. 15.2.

The Power that is exercised by the sea on the buoy is the product of the Force transferred by the sea and the velocity of the buoy. The buoy velocity is the derivative of the buoy displacement with respect to time. Once the Power is calculated, the energy in one wave period can be determined. Thus, the average power output can be defined.

$$\begin{aligned} z_{buoy} &= z_A.\sin(\omega t - \beta_{mot}) \Rightarrow v_{buoy} = \frac{dz_{buoy}}{dt} = z_A.(\omega.\cos(\omega t - \beta_{mot}) \\ P_{broy} &= F_{buoy} \cdot v_{buoy} = F_{ex,\omega}.\sin(\omega t - \beta_{Fex}).z_A.\omega.\cos(\omega t - \beta_{mot}) \end{aligned} \tag{15.16}$$

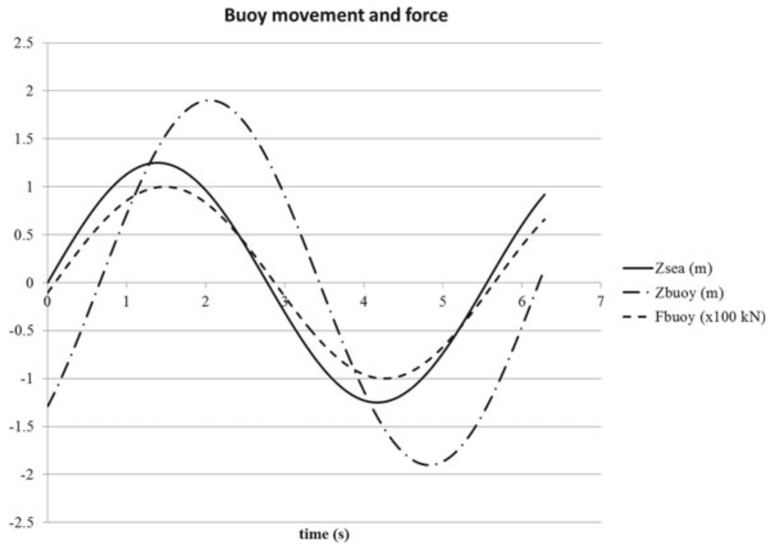

Fig. 15.2 Sea motion, force on the buoy, and displacement of the buoy

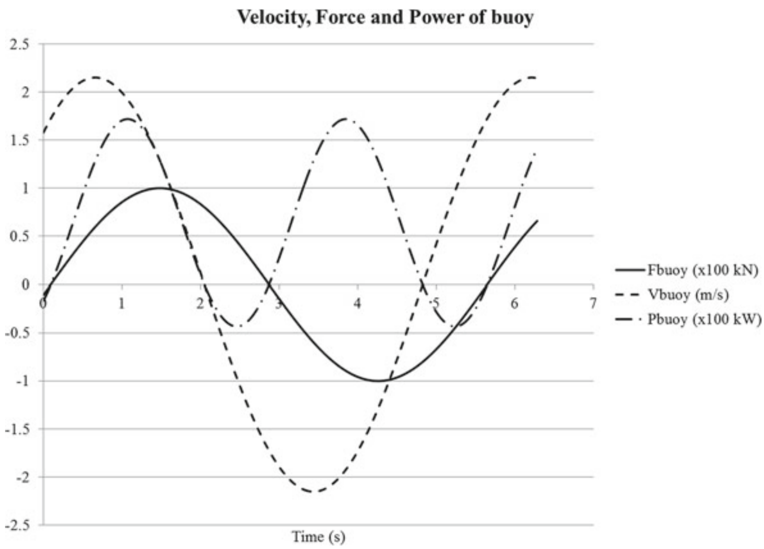

Fig. 15.3 Transversal velocity, force, and power at the buoy

Figure 15.3 illustrates the buoy's linear velocity, Force, and Power. Due to the phase angle between Force and velocity, the mean incoming Power is not equal to zero. During most part of the wave period, the sea provides energy to the buoy. During the part where the Power is smaller than zero, the buoy gives back energy to the sea.

For further research, the minimum and maximum of the Power should be known. Also, the times when these extreme values occur and the time when the Power equals zero are calculated. The extreme values occur where the derivative of the Power with respect to time is equal to zero.

$$P_{ext} \Rightarrow > \frac{\partial P_{sea}}{\delta t} = 0$$

Or:

$$\cos(2\omega t - \beta_{mot} - \beta_{Fex}) = 0$$

where, $t = \frac{k\pi}{4\omega} + \frac{\beta_{mot}}{2\omega} + \frac{\beta_{Fex}}{2\omega}$ With: $k = 1, 3, 5, \ldots$

The Power is extreme for $t_1 = 1.071$ s and $t_2 = 2.459$ s. This corresponds with $P_{max} = 171.878$ kW and $P_{min} = -43.239$ kW.

Secondly, the mean Power the buoy receives from the sea is calculated. Therefore the sea power is integrated over one period of the power course. This is half the period of one buoy course. In order to find the starting and ending point of a specific half period, the power expression has to be equalized to zero.

$$P_{buoy} = F_{ex,\omega}.\sin(\omega t - \beta_{Fes}).z_A.\omega.\cos(\omega t - \beta_{mot}) = 0$$

$$\Rightarrow \sin(\omega t - \beta_{Fex}).\cos(\omega t - \beta_{mot}) = 0$$

$\rightarrow t = \frac{k\pi}{2\omega} + \frac{\beta_{mot}}{\pi}$ or $: t = \frac{1\pi}{\omega} + \frac{\beta_{fex}}{\pi}$ with $k = 1, 3, 5, \ldots$ and $1 = 0, 1, 2, \ldots$
The Power equals zero for $t_3 = 0.093$ s, $t_4 = 2.048$ s and $t_5 = 2.871$ s.

$$\int_{t_3}^{t_5} P_{sea}\,dt = \frac{F_{ex,\omega}.\omega.z_A}{2}.\left[\int_{t_3}^{t_5} \sin(2\omega t - \beta_{Fex} - \beta_{mot})dt + \int_{t_3}^{t_5} \sin(-\beta_{Fex} + \beta_{mot})dt\right]$$
$$= \frac{F_{ex,\omega}.\omega.z_A}{2}.[\sin(-\beta_{Fex} + \beta_{mot})(t_5 - t_3)$$
$$-\frac{1}{2\omega}\cos(2\omega(t_5 - t_3) - \beta_{Fex} - \beta_{mot})\Big]$$

This gives an energy amount of 147.331 J over a one-half period of the buoy motion. Since a half period of the buoy motion lasts $\frac{2\pi}{2\omega}$ seconds or: $t_5 - t_3$. The mean Power P_{mean} is equal to:

$$P_{mean} = \frac{147,309.705.2\omega}{2\pi} = 53,033 \text{ W}$$

When applying the theoretical model described by De Backer [3]. The average theoretical absorbed Power can be calculated as follows:

$$P_{abs,av} = \frac{1}{2} b_{ext}\omega^2 z_A^2$$
$$P_{abs,av} = 46 \text{ kW} \tag{15.17}$$

15.4 Conclusions

As can be seen, this value does not vary much from the calculated value of 53 kW. The main reason for this variation is the rounding error while taking the values of m_{sup} and b_{hyd}. The theoretically determined variables show that the movement of the buoy is sinusoidal. This means that a direct attachment of the generator to a pole (representing the heaving motion of the WEC) ensures that the angular velocity of the generator is also sinusoidal around zero. In every half period of the buoy movement, the generator turning sense changes. This is detrimental to the generator's efficiency.

The maximum value of the Power is three times higher than its average output power. This means that the generator could be three times smaller if the sinusoidal power output could be flattened out to a constant power. This results in a higher efficiency and cheaper generator. So if it is possible to ensure both a unidirectional movement at the generator and a flattened generator power, the generator efficiency will be much higher.

References

1. Lindroth, S., Leijon, M.: Offshore wave power measurements—a review. Renew. Sustain. Energ. Rev. **15**(9), 4274–4285
2. Sharma, R., et al.: Challenges in computer applications for ship and floating structure design and analysis. Comput.-Aided Des.
3. De Backer, G.: Hydrodynamic design optimization of wave energy converters consisting of heaving point absorbers. UGent (2009)
4. Vanderheggen, K.: Nieuwe concepten van composiet vlotters voor opwekking van golfenergie. Universiteit Gent, Ghent (2010)
5. Sigalotti, L.D.G., et al.: A shock-capturing SPH scheme based on adaptive kernel estimation. J. Comput. Phys. **212**(1), 124–149 (2006)
6. Zheng, K., et al.: Numerical simulations of water wave dynamics based on SPH methods. J. Hydrodyn. Ser. B **21**(6), 843–850 (2009)
7. Oger, G., et al.: Two-dimensional SPH simulations of wedge water entries. J. Comput. Phys. **213**(2), 803–822 (2006)
8. Gong, K., Liu, H., Wang, B.: Water entry of a wedge based on SPH model with an improved boundary treatment. J. Hydrodyn. Ser. B **21**(6), 750–757 (2009)
9. Monaghan, J.J.: Smoothed particle hydrodynamics. Rep. Prog. Phys. **68**(8), 1703–1759 (2005)
10. Belytschko, T., Lin, J.I., Chen-Shyh, T.: Explicit algorithms for the nonlinear dynamics of shells. Comput. Methods Appl. Mech. Eng. **42**(2), 225–251 (1984)
11. Mindlin, R.D.: Influence of rotatory inertia and shear on flexural motions of isotropic, elastic plates. J. Appl. Mech. **18**, 31–38 (1951)

Chapter 16
Damage Identification on Aircraft Wing Using Convolutional Neural Network Based Pattern Recognition

M. Sucharitha, P. H. V. Sesha Talpa Sai, Subeesh Kopiyil Thazha, Mathew Thomas, Basavaraj Hunagund, and V. G. Krishna Anand

Abstract Damages to the aircraft body must be identified in order to avoid unforeseen events that could result in catastrophes if not examined properly. As most of these damages are provoked under normal working conditions, such as in this case during aircraft flight operations, rectifying these damages is nearly impractical. This work veils through a compiled report of Structural Health Monitoring (SHM) of an aircraft wing aiming at the deterioration caused throughout the entire structure of the wing which is subjected to numerous aerodynamics and mechanical constraints. The SHM report provides data which is used to study intramural Damages. Based on the investigation, the Convolutional Neural network (CNN), which is a typical algorithm of deep learning along with Recurrence graph, was chosen as the appropriate Methodology. The structural response recurrence graph can reveal details about the damage, similarity, and underlying structure. Wavelet packets are used to filter and recreate the initial structural response signal, considering the vibrational coupling between the aircraft and wing. Then, as a novel kind of damage feature, the recurrence graph of distinct damages is taken as input picture of the CNN. The findings show that this method provides added information about damage than traditional statistical pattern recognition techniques. These outcomes confirmed the proposed CNN-based model's suitability for use with additional aircraft components.

M. Sucharitha (✉)
School of Electronics Engineering, VIT-AP University, Amaravati, Andhra Pradesh, India
e-mail: deanrndmrcet@gmail.com

P. H. V. Sesha Talpa Sai
Department of Mechanical Engineering, Malla Reddy College of Engineering and Technology, Hyderabad, India

S. K. Thazha · M. Thomas · B. Hunagund
School of Mechanical Engineering, Lincoln University College, Kuala Lumpur, Malaysia

V. G. Krishna Anand
Department of Aeronautical Engineering, Malla Reddy College of Engineering and Technology, Hyderabad, India

P. H. V. S. Talpa Sai et al. (eds.), *Intelligent Manufacturing and Energy Sustainability*, Smart Innovation, Systems and Technologies 372,
https://doi.org/10.1007/978-981-99-6774-2_16

16.1 Introduction

16.1.1 Structural Health Monitoring (SHM)

SHM is a process of implementing a damage identification strategy for mechanical, civil, and aeronautical engineering infrastructure. Damage may be alterations to geometric, structural features. They cause damage to the functionality. Conventional non-destructive testing techniques are utilized to recognize and monitor these damages. But during the past few years, the majority of SHM research has focused on a more comprehensive method of assessing structural degeneration [1–3].

Damage does not necessarily mean that a system has lost all functionality; rather, it means that it is no longer performing as well as it could. As the damage advances, it will eventually get to the point where it interferes with the user's ability to utilise the system. Failure is the term used for this situation. Damage can build up gradually over a long period of time, caused by corrosion or wear and tear. Planned discrete occurrences, such as aeroplane landings, as well as unexpected natural disaster dangers can cause damage over comparatively shorter time periods as well [4].

The steps in this approach involve gathering damage-sensitive features from frequently spaced measurements of a structural or mechanical system and statistically analysing these characteristics to evaluate the system's status. SHM is utilised for quick condition screening following a severe event of earthquake or an unexpected blast loading. The goal of this testing is to deliver exact data in almost real-time on how the system will operate under these extreme conditions and how the system will hold up afterward [5].

16.1.2 Damage Identification

Aerial loss of control (LOC) has continued to be a major contributing element in deadly aviation accidents throughout the past few decades. In most LOC incidents, the aircraft deviates significantly from its nominal flight envelope as a result of external risks, technical difficulties, and pilot mistake. Safe flight envelope (SFE) is the area in the space that an aircraft can fly safely. It can be found by the controls and using the models such as kinematic and aerodynamic. In the literature, the flying envelope is defined in a variety of ways; the conventional maneuvering envelope, which is frequently utilised to minimise stall and potential structural damage, imposes rigid restrictions on the load factor and speed [6, 7].

These envelopes can be preserved as a permanent part of a system for preventing LOCs during a normal flight. However, after unexpected failures or structural damage, they might no longer be applicable since the damaged aircraft's aerodynamic characteristics would change often dramatically. For instance, when a wing is damaged, the maximum lift coefficient drops, decreasing the maximum load factor

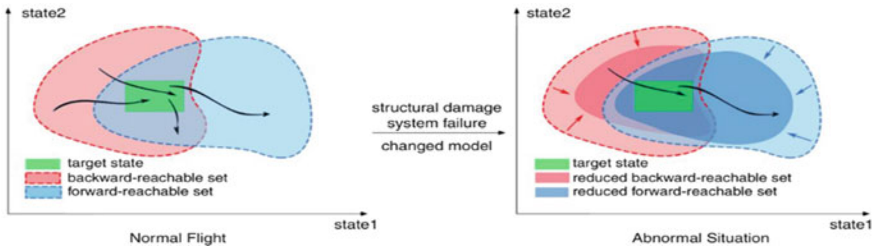

Fig. 16.1 Safe flight envelope and its modification following unexpected damage and failures

and raising the stall speed. As a result, as shown in Fig. 16.1, overall maneuvering envelope decreased because of the altered aerodynamic coefficients.

The second difficulty is of a more practical nature and arises from the extremely significant with regard to the cost of computation of a realistic aircraft model and a nonlinear reachability analysis. The so-called "curse of dimensionality" affects every present technique, making it impossible to execute them online due to the fact that they scale poorly as state-space dimension increases [8, 9].

16.1.3 Machine Learning (Neural Network Pattern Recognition)

Pattern recognition is the study of how robots can look around them, separate out interesting patterns from background patterns, and draw logical inferences about the many kinds of patterns. Despite over 50 years of work, developing a general-purpose machine pattern recognizer is still a difficult challenge. Humans are typically the best pattern recognizers, but we are still unsure of how they accomplish it.

A pattern might be a voice signal, cursive handwriting, a face, or a fingerprint image. One of the two tasks listed below may be involved in classifying or recognizing a pattern given: There are two types of classification: Unsupervised classification, which is related to clustering in that the pattern is allocated to an unnamed class, and supervised classification, which is similar to discriminant analysis in that the input pattern is recognized as a member of a predetermined class [10, 11].

16.2 Structural Health Monitoring Using Machine Learning

Damage is defined in the context of this study as modifications to the geometry, structure and material characteristics. It also affects boundary positions and system connectivity issues that may cause lower performance or total failure. The Overall study of damages involves the acquisition of all the insights related to the localization, degree of intensity and period of Occurrence of the type of damage. The available insights must now be assigned to a method which best suits our requirements and also abstracts valuable data for further evaluation. A CNN is a feedforward neural network with a deep structure and convolution calculation, can recognise images and can extract and identify features more accurately through intelligent layer-by-layer learning, which can lead to more accurate damage location and degree of damage [12].

Natural frequencies (NF's) and mode shapes (MS's) are the primary units to SHM system, which was developed utilising neural network modelling. Even if a simplified model is built according to structural features in good condition, these characteristics are used to represent the quality of the structures. The NF's and MS's that balance the damaged structure are then shown for this model with varied stiffness decreases [13].

A neural network model that outputs the locations and levels of damage is trained using the data gathered. Therefore, the suggested SHM system that simultaneously detects structural degradation and implicitly predicts how long a structure will remain functional is a neural network model. By modelling the structure with different levels of stiffness decreases, the suggested AI-based SHM system accurately detects damage sites and levels in accordance with the given data set. Updates to the simplified model, which can depict the structure's dynamic behaviour and predict its remaining performance, are also made possible by the discovered stiffness decreases [14].

Convolution layers, which use the convolution and pooling processes as well as the idea of local receiver fields to optimise image processing, layer normalisation, which uses the dropout process and other processes to improve network performance, and the fully connected layer, which is in charge of sorting, make up CNN networks. A general architecture for the CNN is shown in Fig. 16.2.

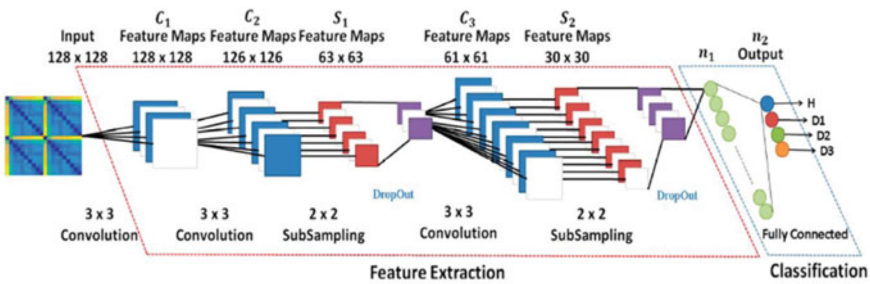

Fig. 16.2 General CNN architecture

16.3 Methodology

16.3.1 Numerical Simulation

The fourth order equation below is used to simulate the static vertical deflections, v(x), of a horizontal beam.

$$-\partial 2\partial x2(EI(x)\partial 2v\partial x2) = q(x) \tag{16.1}$$

where q(x) is any applied volume load or force, E is the modulus of elasticity, I(x) is the cross-section moment of inertia.

Basic functions with non-vanishing 2nd derivatives are sufficient due to the partial integration in finite element weak formulation. Traditionally, third order Hermite finite element is used in FEM beam simulations. The stress–strain relations for the linear elasticity physics mode can be stated as follows to represent how structural stresses develop in solid structures:

where,

$$\begin{pmatrix}\sigma_x\\ \sigma_y\\ \sigma_z\\ \tau_{xy}\\ \tau_{yz}\\ \tau_{xz}\end{pmatrix} = \frac{E}{(1+\nu)(1-2\nu)}\begin{pmatrix}1-\nu & \nu & \nu & 0 & 0 & 0\\ \nu & 1-\nu & \nu & 0 & 0 & 0\\ \nu & \nu & 1-\nu & 0 & 0 & 0\\ 0 & 0 & 0 & \frac{1-2\nu}{2} & 0 & 0\\ 0 & 0 & 0 & 0 & \frac{1-2\nu}{2} & 0\\ 0 & 0 & 0 & 0 & 0 & \frac{1-2\nu}{2}\end{pmatrix}\begin{pmatrix}\epsilon_x\\ \epsilon_y\\ \epsilon_z\\ \gamma_{xy}\\ \gamma_{yz}\\ \gamma_{xz}\end{pmatrix} \tag{16.2}$$

where E is the elastic or Young's modulus, and ν is the Poisson's ratio of the material. The strains are related to the material displacements (u, v, w) as

$$\epsilon_x = \frac{\partial u}{\partial x}, \epsilon_y = \frac{\partial v}{\partial y}, \epsilon_z = \frac{\partial w}{\partial z}, \gamma_{xy} = \frac{\partial u}{\partial y} + \frac{\partial v}{\partial x}, \gamma_{yz} = \frac{\partial v}{\partial z} + \frac{\partial w}{\partial y}, \gamma_{xz} = \frac{\partial u}{\partial z} + \frac{\partial w}{\partial x} \tag{16.3}$$

16.3.2 Image Classification Using Machine Learning

The current work instigates on the development of a machine learning algorithm to detect the anomaly in the behaviour of the aircraft wing assuming as cantilever beam, and is of isotropic with free end load. The material is homogenous and there is no anomaly in the aircraft and are perfectly structurally integrated to each other through internal members. Structural damping is considered to be negligible but however in experimental conditions, the system is conserved until elastic deformation. All Euler–Bernoulli assumptions were obeyed alongside the current assumptions.

16.3.3 Components Used

16.3.3.1 Arduino Board

The ATmega328P, heart of Arduino UNO microcontroller board, has a 16 MHz ceramic resonator, 14 digital input/output pins, a USB port, a power jack, an ICSP header, and a reset button. Its six analogue inputs can be converted into PWM outputs. All the components necessary for the microcontroller's operation are present. Other parts used are USB cable, an AC-to-DC adapter, or a power supply like a battery.

16.3.3.2 Accelerometer

Any person or object can use an accelerometer sensor to measure their acceleration in relation to their present rest frame. It is not an acceleration in coordinates. Accelerometer sensors are used in many electrical items, including phones, wearable electronics, and other gadgets. In biomedical applications, accelerometers are employed in sensors primarily for step counting, activity monitoring, motion artefact detection, and motion suppression.

16.4 Result and Discussion

16.4.1 Numerical Simulation

Following Figs. 16.3, 16.4 and 16.5 displays the images used for training has been modelled in Ansys by varying the magnitude of loading. It can be observed that there is a substantial deformation followed by deflection in the wing structure when the load is gradually increased indicating the anomaly in the structure can be expected. These images are pre-processed to machine learning algorithm which identifies the anomaly based on the classification. ANSYS structural mechanical APDL is used in the current work to model these designs.

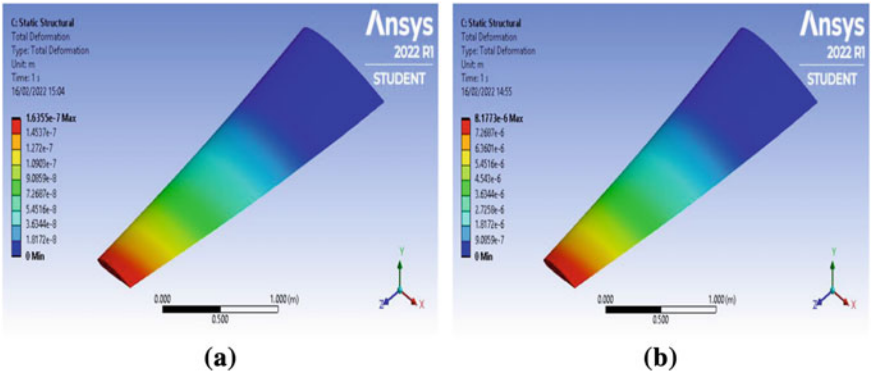

Fig. 16.3 **a** Trained dataset for deformed shape at 0.1 Pa. **b** Trained dataset for deformed shape at 5 Pa

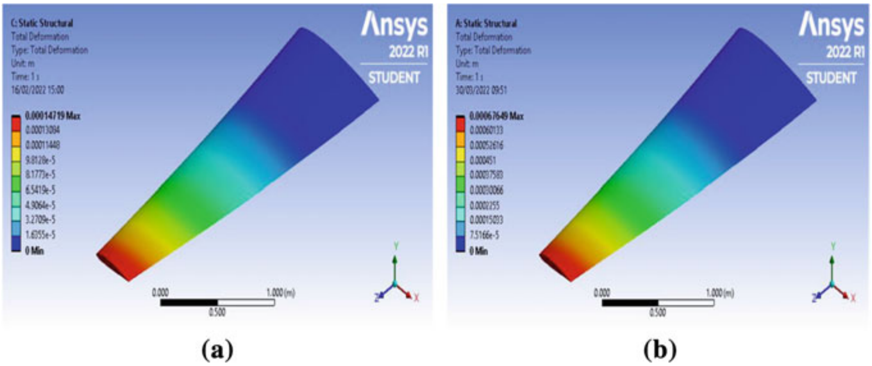

Fig. 16.4 **a** Trained dataset for deformed shape at 90 Pa. **b** Trained dataset for deformed shape at 200 Pa

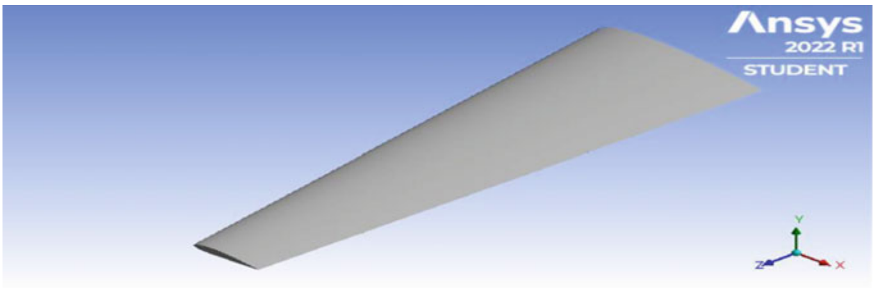

Fig. 16.5 Trained dataset for undeformed shape

16.4.2 Experimental Results

The experiments at various application of point load at the tip of the cantilever beam i.e., idealized wing, the accelerometer provided the result on x, y, z directions for acceleration. This helped us to identify the behaviour of the beam and its amplitude to relate with deformation and deflection. Following results in x, y, z directions reveal the behaviour of wing in various axes. The results are shown in Figs. 16.6 and 16.7. The comparison of training and validation losses with epochs is shown in Fig. 16.8. The plot indicate that after 6 epochs the training and validation losses convergence close to each other.

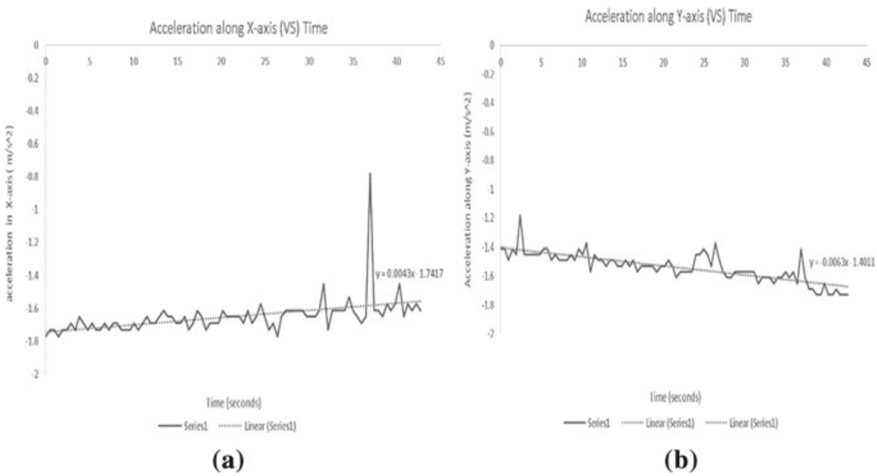

Fig. 16.6 **a** Acceleration along X-axis versus time. **b** Acceleration along Y-axis versus time

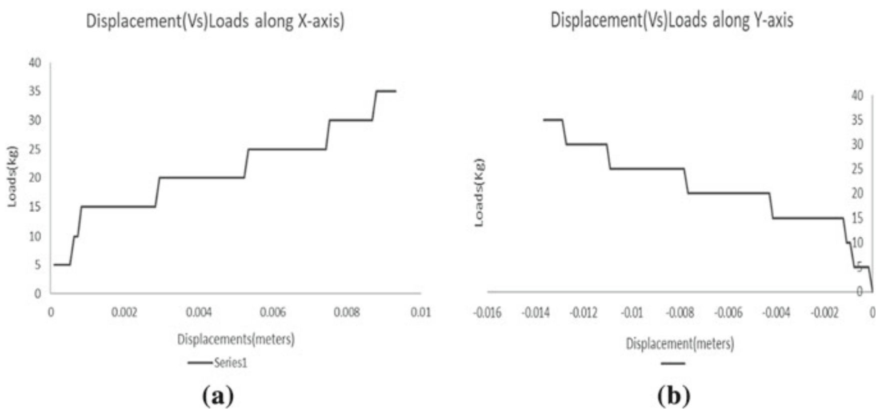

Fig. 16.7 **a** Loads versus displacement (X-axis). **b** Loads versus displacement (Y-axis)

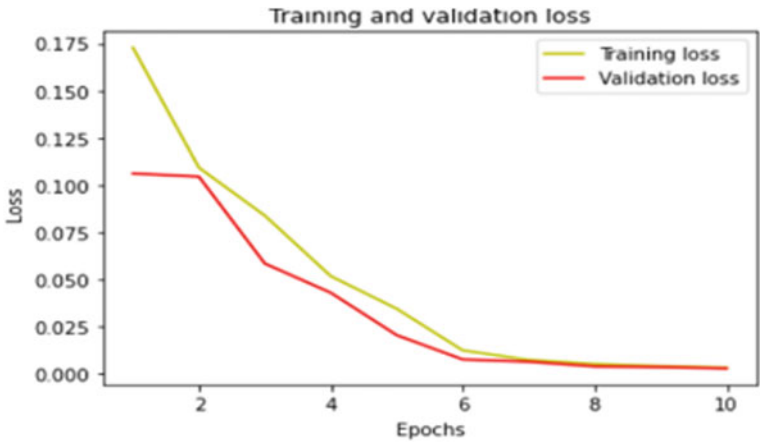

Fig. 16.8 Comparison of training and validation loss with epochs

16.5 Conclusion

Because deep learning techniques have more strong complex feature representation capabilities than other approaches, they are widely applied in the field of image processing and have produced successful results. The suggested method, which is based on a recurrence graph and CNN, can be used as a reference to identify damage to various engineering structures. The main areas of research for enhancing and popularising deep learning-based damage identification methods include developing a better deep learning neural network structure, enhancing the pooling algorithm, proposing more discriminative damage feature vectors, and conducting real-world engineering tests. The above methodology can now be used for further analysis of the aircraft wing on various mechanical constraints such uneven bending, twisting and buckling of the aircraft wing and can also be used for prediction at various aerodynamic constraints such as various angle of attack, turbulent flow etc. This proposed machine learning can be further used for various other aircraft components such as landing gears, aircraft tail, fuselage etc. which will help with the overall structural health monitoring of the aircraft.

References

1. Sohn, H., Farrar, C.R., Hemez, F.M., Shunk, D.D., Stinemates, D.W., Nadler, B.R., Czarnecki, J.J.: A Review of Structural Health Monitoring Literature: 1996–2001, p. 1. Los Alamos National Laboratory, USA (2003)
2. Sohn, H., Farrar, C.R., Hemez, F.M., Czarnecki, J.J.: A Review of Structural Health Review of Structural Health Monitoring Literature 1996–2001 (2002)
3. Lynch, J.P., Loh, K.J.: A summary review of wireless sensors and sensor networks for structural health monitoring. Shock Vibr. Dig. **38**(2), 91–130 (2006)

4. Farrar, C.R., Worden, K.: An introduction to structural health monitoring. Philos. Trans. Royal Soc. A Math. Phys. Eng. Sci. **365**(1851), 303–315 (2007)
5. Diamanti, K., Soutis, C.: Structural health monitoring techniques for aircraft composite structures. Prog. Aerosp. Sci. **46**(8), 342–352 (2010)
6. Qing, X., Li, W., Wang, Y., Sun, H.: Piezoelectric transducer-based structural health monitoring for aircraft applications. Sensors **19**(3), 545 (2019)
7. Wang, S.C.: Artificial neural network. In: Interdisciplinary Computing in Java Programming, pp. 81–100. Springer, Boston, MA (2003)
8. Abiodun, O.I., Jantan, A., Omolara, A.E., Dada, K.V., Mohamed, N.A., Arshad, H.: State-of-the-art in artificial neural network applications: a survey. Heliyon **4**(11), e00938 (2018)
9. Momoh, J.A., Button, R.: Design and analysis of aerospace DC arcing faults using fast Fourier transformation and artificial neural network. In: 2003 IEEE Power Engineering Society General Meeting (IEEE Cat. No. 03CH37491), vol. 2, pp. 788–793. IEEE (2003, July)
10. Raol, J.R.: Neural network based parameter estimation of unstable aerospace dynamic systems. IEE Proc.-Control Theor. Appl. **141**(6), 385–388 (1994)
11. Berke, L.: Application of Artificial Neural Networks to the Design Optimization of Aerospace Structural Components, vol. 4389. NASA (1993)
12. Ye, L., Su, Z., Yang, C., He, Z., Wang, X.: Hierarchical development of training database for artificial neural network-based damage identification. Compos. Struct. **76**(3), 224–233 (2006)
13. Bakhary, N., Hao, H., Deeks, A.J.: Damage detection using artificial neural network with consideration of uncertainties. Eng. Struct. **29**(11), 2806–2815 (2007)
14. Nick, H., Aziminejad, A., Hosseini, M.H., Laknejadi, K.: Damage identification in steel girder bridges using modal strain energy-based damage index method and artificial neural network. Eng. Fail. Anal. **119**, 105010 (2021)

Chapter 17
Design and Numerical Analysis of Electromagnetic Rail Gun for Defense Applications

R. Ajith Raj, P. H. V. Sesha Talpa Sai, Alimelugari Gurudutta, Ryali Venkata Nava Sarathy Prasad, Arjun Prakash Sharma, and Potnuru Srikar

Abstract This paper focus on electromagnetic rail gun and it's working. Different kinds of rail guns have been concentrated out of which electromagnetic rail gun viewed as productive. Examination of underlying mechanics of rail gun and future extent of rail gun is executed. The principal benefit of rail gun is a shot that can be pushed without utilizing any synthetics yet rather by utilizing electric flow. It utilizes electromagnetic power to send off shots which are in the middle of between the two rails. A rail gun comprises of three sections a power source, a couple of equal rails and a moving armature. A rail gun comprises of superconductive rails mounted lined up with one another with an in the middle among them and is associated with a DC supply. The shot secures speed through frightful powers made by streaming current through equal rails. The driving of rail gun is accomplished by changing over electrical energy into motor energy. The gun's overall efficiency is determined by rail gun configuration, power supply and inductance angle. In this paper rail gun is designed and cycles are performed to break down the current to launch a payload at a speed of 2000 m/s with the distance between rails as 5, 10 and 1000 cm rail length.

R. A. Raj (✉)
Department of Aerospace Engineering, Karunya Institute of Technology and Sciences, Coimbatore, India
e-mail: directorrndmrcet@gmail.com

P. H. V. Sesha Talpa Sai · P. Srikar
Department of Mechanical Engineering, Malla Reddy College of Engineering and Technology, Hyderabad, India

A. Gurudutta · R. V. N. S. Prasad · A. P. Sharma
School of Electronics and Communication Engineering, Lincoln, University College, Kuala Lumpur, Malaysia

P. H. V. S. Talpa Sai et al. (eds.), *Intelligent Manufacturing and Energy Sustainability*, Smart Innovation, Systems and Technologies 372,
https://doi.org/10.1007/978-981-99-6774-2_17

17.1 Introduction

In the late 1950's solar energy was used to provide the propulsion. This later directed towards the development of ion thrusters. These ion thrusters are now available to use. Limitations of these thrusters are low thrust. To avoid these limitations later they came up with the devices which produce high thrust. Better rocket propellants, space elevators, cannon launches from the surface of the earth, and laser launches are the four main categories for the proposed solutions. In this essay, we'll talk about gun launches. The rail gun is an electromagnetic device that uses magnetic repulsion to propel an armature down tracks at speeds of up to several thousand metres per second without the need of explosive propellants. Currently, a significant amount of fuel, space, and human endeavours are needed to launch satellites, rockets, and other spacecraft. It will require fewer human efforts and is more reliable if we use electromagnetic qualities to launch transport into space with the aid of electrical gadgets. This goal seeks to reduce the vast amount of fuel used by the space shuttle launcher by making practical use of appealing features. An initial push for high velocity vehicles is considered to be the most important part during their flight, this type of push can be obtained from various sources such as rail guns and catapult. Speaking of them rail gun is considered to be the most effective one. A Rail gun is used for launching high velocity projectiles. Usually, two metal rails that are parallel make up a rail gun. Out of various options of rail guns we have, the EM rail guns seem worthy of the further study application [1].

Two parallel, electrically conducting, extended metallic rails separated from one another by solid dielectric blocks are the distinguishing features of rail guns. A projectile is placed in an insulating space between the rails. A DC power supply's opposing terminals are connected to the rails. After passing through the first rail, which includes a metal region in the projectile or plasma intended to be directly behind the projectile, current from the power source returns through the second rail to the power source. The magnetic field created by the current passing through the armature between the rails creates a mechanical force in the rails' extended direction. The projectile is propelled along the length of the rails by the mechanical force, often reaching top speeds of around 5 km/s.

A rail gun's effectiveness is typically determined by the rail gun plan and its pulsed power supply architecture. The rail gun configuration is dependent on the rail gun fundamental parameters, such as current distribution across a rail, attractive transition thickness between the rails, temperature circulation inside the rails and armature surface, and shocking power following up on the rails. The speed of the moving armature, armature and rail calculations, rail characteristics, and armature and rail materials all have an impact on the rail gun crucial boundaries.

The electromagnetic rail gun's pulse power supply framework (PPS) is a crucial component. The PPS, for the most part, is made up of beat frame organisation modules (PFN). Skin impact is the result of the current not entering the rails and armature completely and the current thickness not being uniform along the rail cross segment when an abnormally high current value and short span beat are applied to the rail gun. Additionally, the current is distributed more closely to each conductor's outer layer. This renders the electromagnetic analysis of the rail gun incredibly perplexing. As a result, it is desirable to compute the rail gun key boundaries well in advance of continuous framework in order to gain a quantitative understanding of them. The rail material utilized in electromagnetic rail guns overall has been unadulterated copper or a composite of copper. Amalgams have been picked so that some fortifying of rails is accomplished without inordinate lessening of conductivity; in this way Cu-Zr or Cu-Cd rails have been utilized.

In plasma armature rail guns, regularly called plasma driven rail guns, an armature is normally framed by disintegrating a meager metal foil attached to the rear of, or fixed simply behind, a non-leading shot. This kind of rail gun shows incredible guarantee, both through hypothetical examinations and investigations, for accomplishing amazingly high speeds of shots.

Every charge that moves in a magnetic field experiences force, according to Lorentz's law. Consequently, the projectile is basically propelled by the magnetic field that electrons travelling down the rails emit [2]. Similar to conventional weapons, the dynamic reaction of the barrel may be an issue for EM launchers. To demonstrate the mechanical reaction of an EM barrel under static and dynamic stresses, a preliminary analysis has been carried out using a conceptually viable barrel design [3]. The inductance gradient of the rails affects the rail gun's effectiveness [4]. Projectile launching becomes more compatible and accurate while using rail guns. The risks associated with using explosives and chemical propellants are also avoided when using a rail gun [5].

17.2 Literature Review

Henry Kolm et al., has referenced that the major impediment of the rail gun is shortcoming due loss of inductively put away energy as a gag circular segment at the moment of dispatch. Different issues are regulation of the percussive powers which will more often than not blow the rails separated and the dangerous impact of high brush current thickness.

He referenced that the length of rail guns is restricted by expanding resistive and inductive misfortune. He even proposed that the rail guns can be associated in series to beat this impediment [6].

Hammon et al., has talked about the principal idea of Electromagnetic rail gun and ET gun framework. He recommended that, the volume decreases of parts can be affected in (at least one) of two different ways: lessening the size of the part at fixed evaluations or expanding the rating while at the same time keeping up with the size [7].

Fred Charles Beach has given the hypothesis behind the rail gun. He made correlation between the ordinary gun and rail gun. He has proposed that the rail gun is a decent decision because of its high shot speed, low framework weakness, low shooting signature, expanded shot time span of usability, selectable lethality, simplicity of shot stockpiling, dealing with and resupply, and negligible natural effect [8].

Ian McNab has zeroed in on the beat power framework expected to drive the gun. He has recommended that turning machines offer appealing high energy stockpiling capacity and high yield voltages. He additionally has referenced that, the assortment of assistants needed to help a turning machine, might be a huge obstruction to their presentation in circumstances like the FMBT, where weight and volume framework imperatives are troublesome and where procedure on the combat zone will pressure [9, 10].

Youthful Hyun et al., has talked about the strategy for acquiring the heap opposition of ETC gun by leading an examination. This review has demonstrated that, the heap obstruction can be assessed with an experimental technique. In order to remove the ETC gun obstacle, the surrounding characteristics of the power, the moved energy, and the time subsidiary of the current that may be obtained from the deliberate current and voltage are taken into account. This experimental methodology can be used to distinguish the time-changing framework boundaries that are hard to get with summed up framework recognizable proof strategies [11].

Bryan Mcdaniel has talked about various kinds of rail gun which can be utilized to speed up the shot with hyper speed. He determined that to work on the attractive field between the rails another rail is associated corresponding to the principal rail called increased rails. Because of this, the power following up on the shot can be expanded. He also made a correlation between the various kinds of energy took care of rail gun. He suggested that disseminated energy took care of rail gun enjoys more benefit than breech took care of rail gun as it has low inductive misfortune. He likewise has created DES rail gun utilizing PSPICE reproduction and analyzed the outcomes by directing an examination [12].

17.3 Working and Principle

According to Lorentz's law, every charge moving in a magnetic field experiences force. So basically the magnetic field emitted by electrons travelling on the rails propels the projectile.

There are many advantages and disadvantages of the rail guns developed till now. The rail launchers developed till now have short span of line compared to a conventional cannon because of rail and armature failure. They are non-axisymmetric, concentrated in the rails, and are transient because of the movement of the projectile. The discontinuity of the force causes local bending and shear stresses in the rails near the armature location. The dynamic response of the barrel might be a concern for the EM launchers just as for conventional guns. A preliminary analysis has been performed with a conceptually workable barrel design to illustrate the mechanical response of an EM barrel under static and dynamic loads.

The efficiency of rail gun depends on inductance gradient of the rails. For the past several years the inductance gradient value of rails is calculated using analytical and numerical methods. These two methods are time consuming and a simple method has to be developed to compute the 'L' value of the rails.

At the point when a current-carrying conductor is presented to a magnetic field, it encounters a power. Electric flow can be prompted in a moving transmitter when it is set in an attractive field. Fleming's Right-hand rule can be utilized to decide the course of the incited current.

It's memorable critical that these principles don't determine greatness; rather, they show the course of the three boundaries which are attractive field, current, and power when the other two boundary's bearings are known. Fleming's Right-Hand Rule is mostly pertinent to electric generators. Various significant boundaries apply to any response engine including, the particular motivation, the push, and the power prerequisites of the system.

17.4 Design of Rail Gun

Rail gun is a weapon capable of launching projectile without the usage of explosives or propellants, but, are launched at extremely high velocities, Mach 7 (at sea level) or more. Using rail guns launching of projectiles become more compatible and can achieve great accuracy. With the usage of rail gun the hazards of usage of explosives and chemical propellants are evaded as well.

The growing quantity of debris in Earth orbit poses a danger to users of the orbital environment, such as spacecraft. It also increases the risk that humans or man-made structures could be impacted when objects reenter Earth's atmosphere. During the design of a spacecraft, a requirement may be specified for the survivability of the spacecraft against Meteoroid/Orbital Debris.

The direction of the induced current can be determined using Fleming's Right-Hand Rule. The magnetic field created by a current-carrying segment is described by Biot- Savart's law. This work is focused on design of rail gun and iterations are performed to analyze the current to launch a projectile at velocity 2000 m/s with 5 and 10 cm rail distance and 1000 cm rail length as shown in Tables 17.1 and 17.2 and the schematic design of the corresponding rail gun is shown in Figs. 17.1 and 17.2.

The proposed system will assist with making sending off framework more dependable, cost-productive, and less utilization of fuel. The speed of shot can increment by utilizing curl firearm strategy and for greater dependability the rail weapon technique embedded for space launcher. The utilization of attractive field of the earth for the space transportation would upset the starting strategy of the space transport, which would thusly work on the proficiency and the unwavering quality of the starting method. The use of rail gun speed increase standards to space impetus shows critical potential. Exhibited speed increase level and speed execution of the idea are inside space impetus prerequisites. Primer framework idea assessment demonstrates that adequate push and motor mass qualities can be accomplished with as of now accessible or not so distant future innovations. As the standard of the attractive levitation

Table 17.1 Calculation of current and force at rail distance 5 cm

Current (I) Amp	Distance (D) cm	Length (L) cm	Magnetic field (B)	Force (F)	Velocity(V)
5000	5	1000	0.0002	1000	10
10,000	5	1000	0.0004	4000	40
15,000	5	1000	0.0006	9000	90
20,000	5	1000	0.0008	16,000	160
25,000	5	1000	0.001	25,000	250
30,000	5	1000	0.0012	36,000	360
35,000	5	1000	0.0014	49,000	490
40,000	5	1000	0.0016	64,000	640
45,000	5	1000	0.0018	81,000	810
50,000	5	1000	0.002	100,000	10,001
55,000	5	1000	0.0022	121,000	1210
60,000	5	1000	0.0024	144,000	1440
65,000	5	1000	0.0026	169,000	1690
70,000	5	1000	0.0028	196,000	1960
70,500	5	1000	0.00282	198,810	1988.1
70,600	5	1000	0.002824	199,374.4	1993.744
70,700	5	1000	0.002828	199,939.6	1999.396
70,711	5	1000	0.00282844	200,001.8208	2000.018208
70,800	5	1000	0.002832	200,505.6	2005.056

is under significant application for the rail route transportation and space transportation, for space explorers to go in space is in a totally effective way. The speed of a shot or rockets are expanded by rail weapon strategy with a successfully.

The magnetic field (B) is calculated by using formula shown in Eq. (17.1)

$$B = u0 * I/2 * \pi * D. \tag{17.1}$$

where, I is current.

D is the armature length and u0 is given by Eq. (17.2)

$$u_0 = 4\pi \times 10 - 7\ N/A_2 \tag{17.2}$$

Next force required is calculated by using the Eq. (17.3)

$$F = I * L * B \tag{17.3}$$

where,

I Is the Current

Table 17.2 Calculation of Current and Force at Rail distance 10 cm

Current (I) Amp	Distance (D) cm	Length (L) cm	Magnetic field (B)	Force (F)	Velocity (V)
5000	10	1000	0.0001	500	5
10,000	10	1000	0.0002	2000	20
15,000	10	1000	0.0003	4500	45
20,000	10	1000	0.0004	8000	80
25,000	10	1000	0.0005	12,500	125
30,000	10	1000	0.0006	18,000	180
35,000	10	1000	0.0007	24,500	245
40,000	10	1000	0.0008	32,000	320
45,000	10	1000	0.0009	40,500	405
50,000	10	1000	0.001	50,000	500
55,000	10	1000	0.0011	60,500	605
60,000	10	1000	0.0012	72,000	720
65,000	10	1000	0.0013	84,500	845
70,000	10	1000	0.0014	98,000	980
75,000	10	1000	0.0015	112,500	1125
80,000	10	1000	0.0016	128,000	1280
85,000	10	1000	0.0017	144,500	1445
90,000	10	1000	0.0018	162,000	1620
100,000	10	1000	0.002	200,000	2000

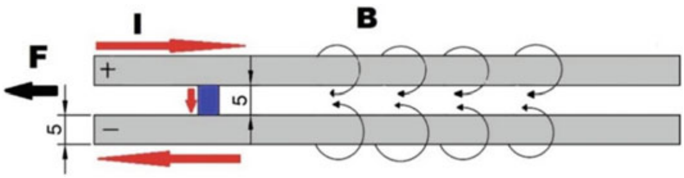

Fig. 17.1 Rail Gun with 5 cm rail distance

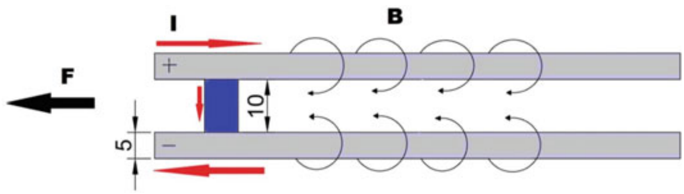

Fig. 17.2 Rail Gun with 10 cm rail distance

L Is the length of rails
B Is the magnetic field.

At last we are calculating Velocity where the projectile is ejected by using formula given in Eq. (17.4)

$$V = F/100 * m \tag{17.4}$$

Here, m is the mass of rail where m is considered as 1 kg.

17.5 Results and Discussions

Figure 17.3 represents the graph between velocity and current in x axis and y axis respectively. It is understood that when distance between rails is 5 cm 70,000 A of current is required to launch the projectile at velocity 2000 m/s.

Figure 17.4 represents the graph between velocity and current in x axis and y axis respectively. In this distance between rails is 10 cm 100,000 A of current is required to launch the projectile at velocity 2000 m/s.

Therefore it is understood that if the distance between the rails are maintained low we can achieve more velocity with less current.

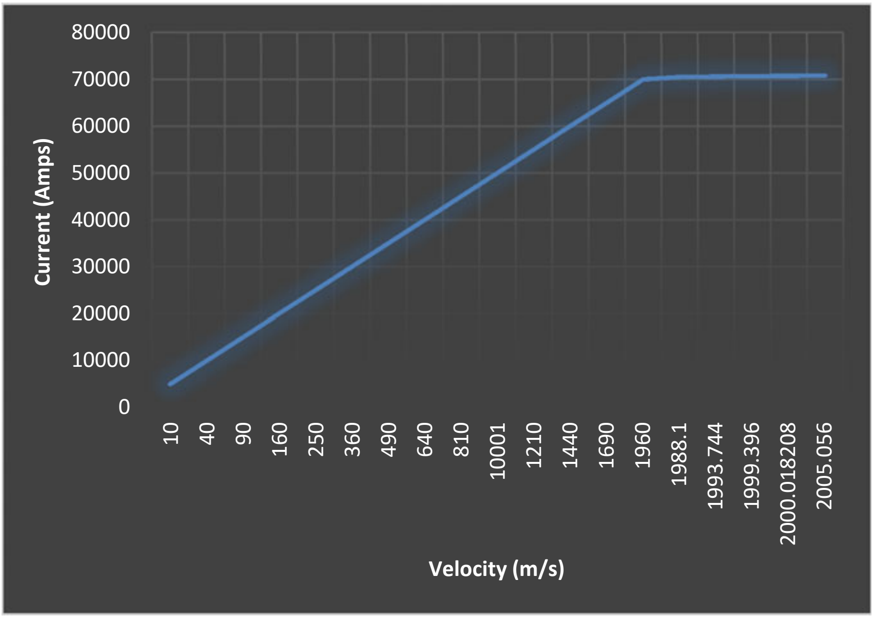

Fig. 17.3 Current versus velocity for 5 cm rail distance

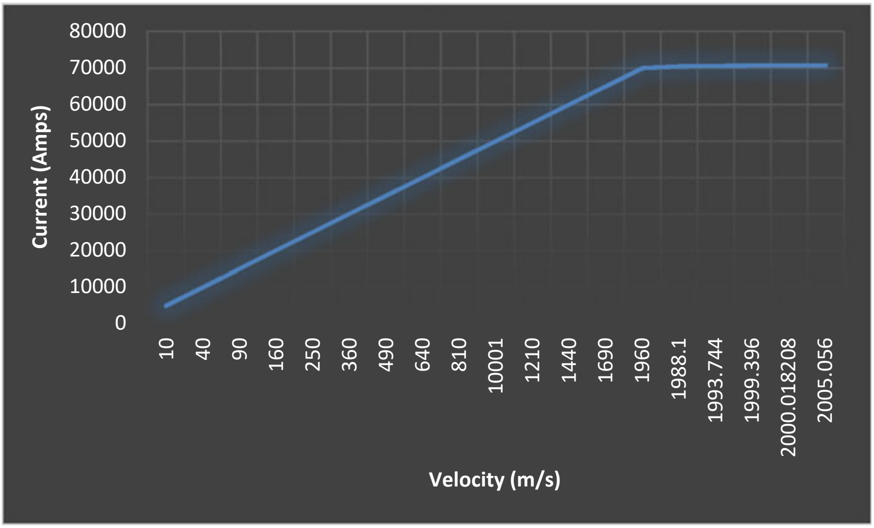

Fig. 17.4 Current versus velocity for 10 cm rail distance

17.6 Conclusion

The suggested system will make launching systems more dependable, economical, and propellant-efficient. It will help with launching off system more reliable, cost-useful, and less usage of fuel. The speed of shot can increase by using twist gun system and for more noteworthy trustworthiness the rail weapon strategy implanted for space launcher. The use of alluring field of the earth for the space transportation would agitate the beginning procedure of the space transport, which would accordingly deal with the capability and the resolute nature of the beginning strategy. The rail gun approach is a very efficient way to boost the bullet or rocket's speed. The effect of current and velocity with respect to the distance between the rails are studied in detail and the current required to launch the projectile at velocity of 2000 m/s is analyzed. This proposed of system will help to make launching system more reliable, cost-efficient, and less consumption of propellant.

References

1. McNab, I.R.: Launch to space with an electromagnetic railgun. IEEE Trans. Magn. **39**(1) January 2003
2. Wikimedia Foundation.: Lorentz Force. Wikipedia. Retrieved 19 Feb 2022 (23 Jan 2022)
3. Tzeng, J.T.: Structural mechanics for electromagnetic rail guns. In: U.S. Army Research Laboratory Weapons and Materials Research Directorate Aberdeen Proving Ground, MD 21005 (2004)

4. Keshtkar, A., Bayati, S., Keshtkar, A.: Derivation of a formula for inductance gradient using intelligent estimation method. IEEE Trans. Magn. **45**(1), 305–308 (2009)
5. Lohakare, K., Mahajan, S., Shevade, D.S.: Review Paper on Electromagnetic Railgun (EMR). AMET-2019 MITCOE, Pune, India (2019)
6. Koln, H., Mongeau, P., Williams, F.: Electromagnetic Launcher. IEEE Trans. Magnet. **16** (1980)
7. Hammon, H.G., Bhasavanich, D, Warren, F.T.: Design approaches to pulsed power drivers for electromagnetic and electro thermal gun systems. IEEE Trans. Magn. **35**(1) (1992)
8. Beach, F.C.: Design and construction of one meter rail gun. 1996 M. S. Thesis, Naval Postgraduate School. pp. 1–5, Monterey, California (1996)
9. McNab, I.R.: Minimization of the input power for a long rail gun. IEEE Trans. Magn. **39**(1) (2003)
10. McNab, I.R.: Pulsed power for electromagnetic gun. IEEE Tran. Magn. **33**, 453–460 (1997)
11. Lee, Y.-H., Park, K.-J., Jung, J.-W.: Load resistance estimation in ETC experiments. IEEE Trans. On Magn. **39**(1), 248–252 (2002)
12. Bryan McDaniel, B.S.E.E.: A multistage distributed energy bench-top electromagnetic launcher. M.S. Thesis, Naval Postgraduate School, pp. 4–6, 23–24. Monterey, California (2006)

Chapter 18
Design of Energy Efficient Reversible Full Adder and Ripple Carry Adder for Digital Computing Applications

S. Nagaraj, K. Sai Khyathi, and K. Pavansai

Abstract In VLSI (Very Large Scale Integration), reversible gates play an important role in the design of low-power circuits. Unlike conventional gates, which are irreversible and result in the loss of information, reversible gates ensure that the input information can be completely recovered from the output. Reversible gates have applications in various areas, such as quantum computing, low-power digital circuits, and cryptography. They are particularly useful in quantum computing, where the conservation of information is crucial due to the principles of quantum mechanics. Using reversible gates such as the Toffoli, Feynman, and new gates, we have constructed and studied FA and RCA in this study. To simulate and synthesize, we used ModelSim and Xilinx. The FA's and RCA's speed and area are contrasted with those of conventional gates and reversible gates. The PFA and PRCA were discovered to have produced the best results in terms of area and delay.

18.1 Introduction

The use of electronic devices has increased in today's technological era. The size of technological products used by the general public needs to be drastically decreased. Only when the interior circuit of an electronic device is optimized can the dimensions of the device be decreased. Reversible gates are fundamental building blocks in Very Large Scale Integration (VLSI) design that enable the creation of reversible logic circuits. Unlike traditional logic gates, reversible gates ensure a one-to-one mapping between their input and output states, meaning that no information is lost during computation. This property makes reversible gates particularly useful in applications such as quantum computing, low-power computing, and nanotechnology.

The concept of reversibility stems from the principle of conservation of information. In traditional computing, irreversible gates like AND, OR, and NOT gates

S. Nagaraj · K. S. Khyathi (✉) · K. Pavansai
Department of ECE, SVCET(Autonomous), Chittoor, AP 517127, India
e-mail: saikhyathi2002@gmail.com

P. H. V. S. Talpa Sai et al. (eds.), *Intelligent Manufacturing and Energy Sustainability*, Smart Innovation, Systems and Technologies 372,
https://doi.org/10.1007/978-981-99-6774-2_18

result in the loss of information due to the production of heat and entropy [1, 2]. In contrast, reversible gates aim to minimize information loss by ensuring that it is possible to determine the initial inputs uniquely from the outputs [3, 4].

Reversible gates exhibit specific characteristics that differentiate them from conventional gates [5–8]:

Information Preservation: Reversible gates do not destroy information, as the inputs can be uniquely reconstructed from the outputs. This property is crucial for applications such as quantum computing, where information loss can lead to errors and instability.

Bidirectionality: Reversible gates are bidirectional, meaning that the gate can function in both the forward and backward directions. In other words, the same gate can be used for computation as well as for the inverse computation.

Energy Efficiency: Due to their reversibility, these gates have the potential to significantly reduce power dissipation. In traditional logic circuits, irreversible gates dissipate energy as heat during computation. Reversible gates, on the other hand, enable the recovery of the energy consumed during computation, leading to energy-efficient designs.

Some commonly used reversible gates in VLSI design include the Toffoli gate (CCNOT), Fredkin gate (CSWAP), Peres gate, and Feynman gate. These gates can be combined and cascaded to implement complex reversible circuits that perform various computations without information loss.

Reversible logic has gained attention in recent years due to its potential to address the power dissipation challenge in modern computing systems. It has applications in emerging fields such as quantum computing, where reversible gates play a vital role in manipulating quantum states without losing information. Additionally, reversible logic finds applications in low-power designs for mobile devices, nanotechnology, and other areas where energy efficiency is a primary concern.

In summary, reversible gates form the basis of reversible logic circuits in VLSI design. They preserve information, enable bidirectional computation, and offer energy-efficient solutions for various applications. By harnessing the principles of reversibility, these gates open up new possibilities for efficient and reliable computing systems.

The majority of integrated circuits (IC) are adders and multipliers. By comparison, it will increase the area of an integrated circuit. If we can able to decrease the area of an adder, we can also, decrease the area of a multiplier. Firstly, the design code is in conventional and proposed reversible logic, and then finally, the proposed FA and proposed RCA are designed using the Toffoli Gate (TG), Feynman Gate (FG), and New Gate (NG). And finally, we compare the delay, area, and performance power of FA with PFA and RCA with PRCA.

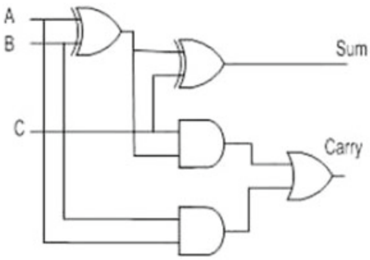

Inputs			Outputs	
A	B	C_{in}	Sum	Carry
0	0	0	0	0
0	0	1	1	0
0	1	0	1	0
0	1	1	0	1
1	0	0	1	0
1	0	1	0	1
1	1	0	0	1
1	1	1	1	1

Fig. 18.1 Full adder

18.2 Full Adder

Only two numbers can be added using the half-adder. The FA has two output stages, sum and carry, and three input states. We can implement this using AND and XOR gates (Fig. 18.1).

18.3 Ripple Carry Adder

The phases of Ripple Carry Adder's operation Each full adder takes the carry-in as an input and outputs the carry-out and the sum bit. The carry-out of an FA serves as a carry-in for its most important full adder. When carry-in is made available to the full adder, the FA is triggered. After activation, the FA begins to operate (Fig. 18.2).

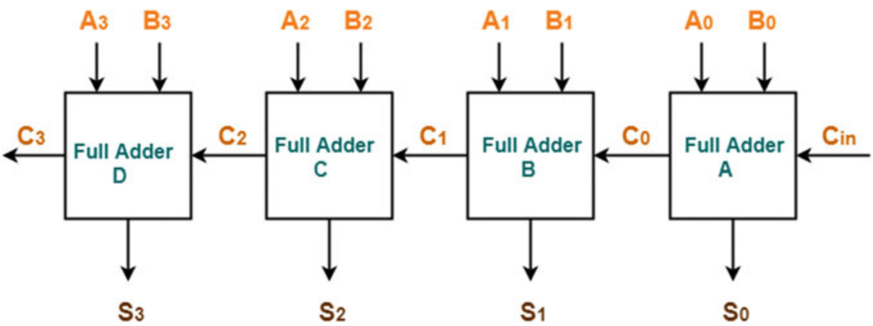

Fig. 18.2 Ripple carry adder

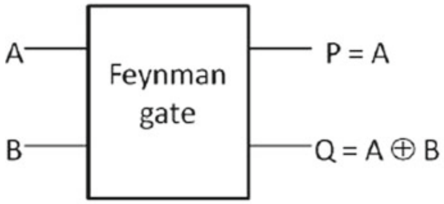

A	B	P	Q
0	0	0	0
0	1	0	1
1	0	1	1
1	1	1	0

Fig. 18.3 Feynman gate

18.4 Reversible Logic Gates

18.4.1 Feynman Gate

In the diagram below, the 2*2 FG is depicted. The CNOT Gate is another name for the FG. The input (A, B) and output (P, Q) vectors of the FG are provided, correspondingly. The FG has a Quantum Cost of 1. The Feynman Gate is employed in a 4-bit RCA in our design (Fig. 18.3).

The delay value of the conventional FG gate is 0.757 ns, and the Proposed FG is 0.761 ns. The LUTs (Area) used in the conventional and Proposed FG gates are 1. The power consumed in the convention FG is 0.082 and the proposed FG is 0.082 (Figs. 18.4 and 18.5).

18.4.2 Toffoli Gate

The 3 × 3 Toffoli is shown in the figure below. The TG's inputs (A, B, C) and outputs (P, Q, R) vectors are provided, correspondingly. The quantum cost of the TG is 5. The Toffoli gate is used in the RCA of our design. The 3 × 3 Toffoli is shown in the figure below. The Toffoli gate's inputs (A, B, C) and outputs (P, Q, R) vectors are provided, correspondingly. The quantum cost of the Toffoli gate is 5. The Toffoli gate is used in the RCA of our design (Fig. 18.6).

The Delay value of the conventional FG gate is 0.889 ns and the Proposed FG is 0.761 ns. The LUTs (Area) used in the conventional and Proposed FG gates are 1. The power consumed in the convention FG is 0.082 and the proposed FG is 0.082 (Figs. 18.7 and 18.8).

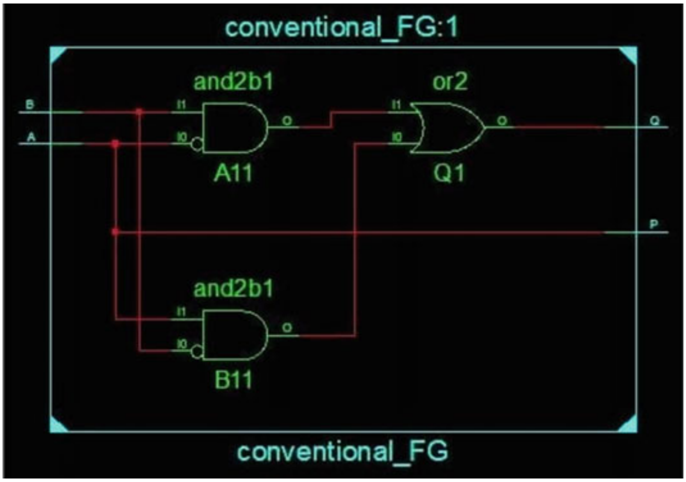

Fig. 18.4 Conventional Feynman gate

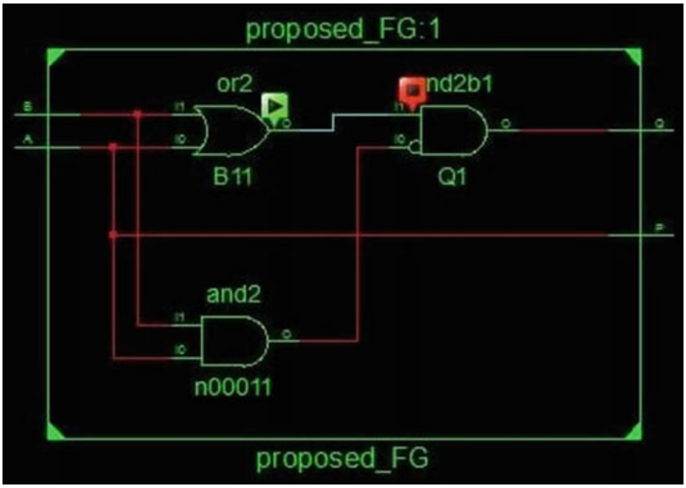

Fig. 18.5 Proposed Feynman gate

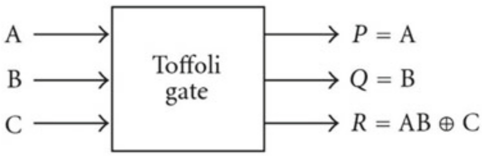

INPUT			OUTPUT		
A	B	C	P	Q	R
0	0	0	0	0	0
0	0	1	0	0	1
0	1	0	0	1	0
0	1	1	0	1	1
1	0	0	1	0	0
1	0	1	1	0	1
1	1	0	1	1	1
1	1	1	1	1	0

Fig. 18.6 Toffoli gate

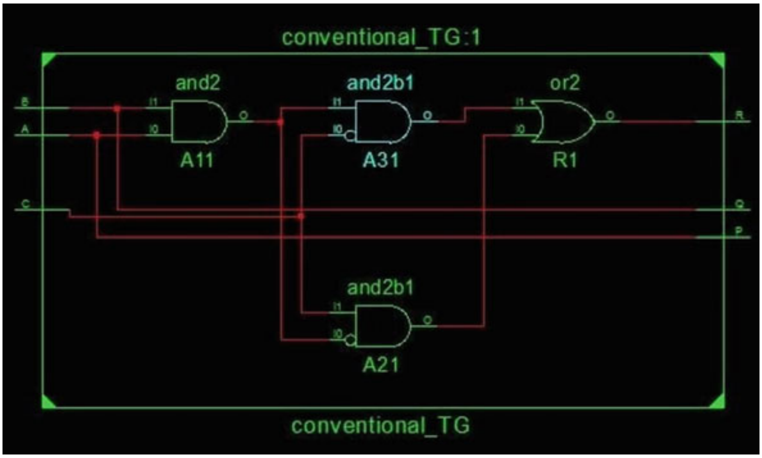

Fig. 18.7 Conventional Toffoli gate

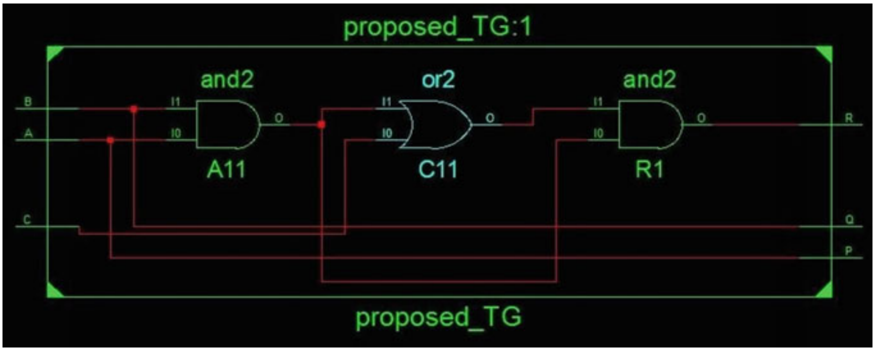

Fig. 18.8 Proposed Toffoli gate

18.4.3 New Gate

The NG is a three-way reversible gate, indicating it accepts three input signals and produces three outputs. The basic symbol of the NG reversible gate and its functional table is shown in Fig. 18.13. The internal logic diagram of the NG reversible gate using the conventional and proposed methods (Fig. 18.9).

The Delay value of the conventional NG gate is 0.893 ns and the Proposed NG is 0.761 ns. The LUTs (Area) used in the Conventional is 2 and the Proposed NG gates are 1. The power consumed in the conventional NG is 0.082 and the proposed NG is 0.082 (Figs. 18.10 and 18.11).

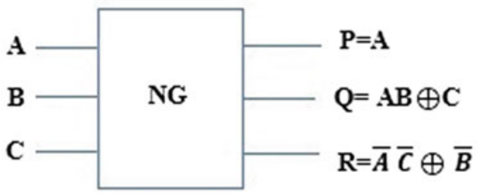

(i)

A	B	C	P	Q	R
0	0	0	0	0	0
0	0	1	0	1	1
0	1	0	0	0	1
0	1	1	0	1	0
1	0	0	1	0	1
1	0	1	1	1	1
1	1	0	1	1	0
1	1	1	1	0	0

(ii)

Fig. 18.9 New gate

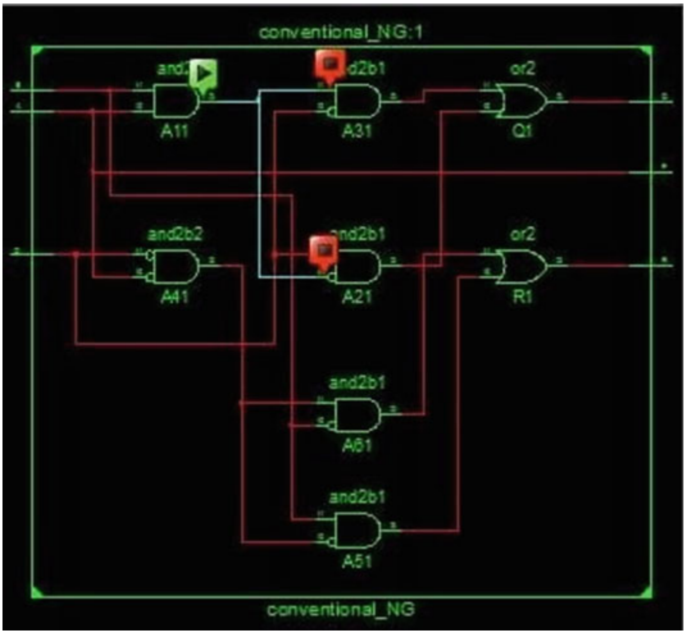

Fig. 18.10 Conventional New gate

18.5 Proposed Full Adder

Reversible logic gates can be used to create the suggested full adder's logic diagram. FG, TG, and NG.FG, TG, and NG methods improved in every aspect such as Delay, Area, and Performance Power (Figs. 18.12 and 18.13).

The Delay value of the FA is 0.893 ns and the PFA is 0.280 ns. The LUTs (Area) used in Full Adder is 2 and PFA is 1. The power consumed in the FA is 0.080 and PFA is 0.079.

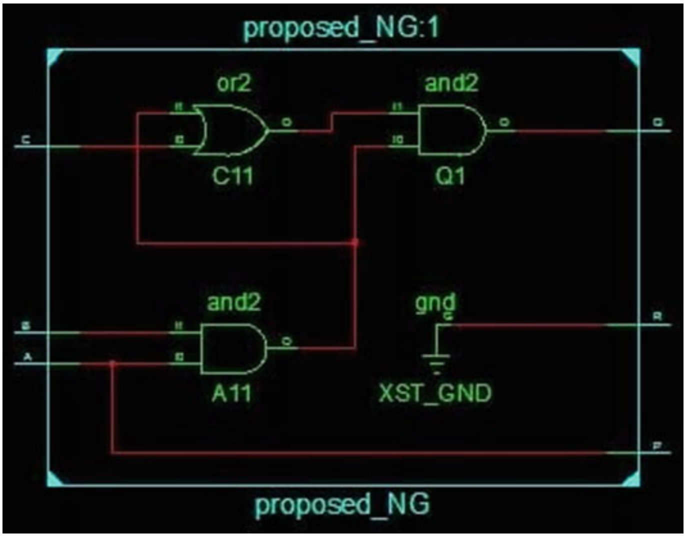

Fig. 18.11 Proposed New gate

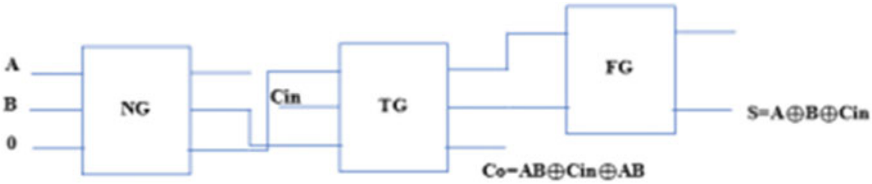

Fig. 18.12 Block diagram of FA

18.6 Proposed Ripple Carry Adder

The PRCA is 0.280 ns, and the Delay value of the RCA is 1.551 ns. RCA uses two LUTs (Area), while PRCA uses only one. The RCA and PRCA both use 0.082 watts of power.

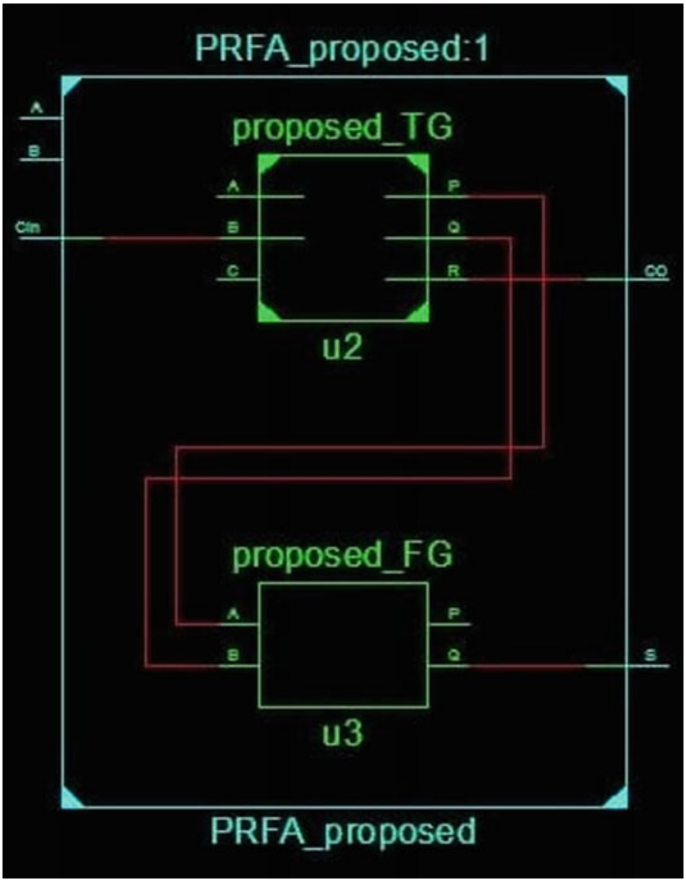

Fig. 18.13 Proposed FA

18.7 Comparision with Normal Gates and Reversible Gates

18.8 Simulation Results and Discussion

Verilog HDL was used to create all of the mentioned discussed and suggested designs, and the Xilinx Tool was used to simulate them. Tables 18.1 and 18.2 display values of the delay, area and Power from synthesis reports of the FA and RCA (Figs. 18.14 and 18.15).

Table 18.1 Comparision of FA

S. No	Ripple carry adder	Delay (nS)	Area (LUTs)	Power (mW)
1	Normal gates	0.893	2	82
2	Reversible gates	0.280	1	82

Table 18.2 Comparision of RCA

S. No	Ripple carry adder	Delay (nS)	Area (LUTs)	Power (mW)
1	Normal gates	1.551	2	82
2	Reversible gates	0.280	1	82

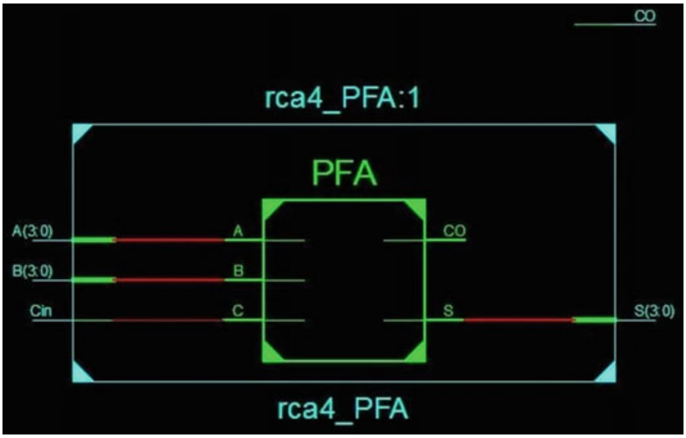

Fig. 18.14 Proposed RCA

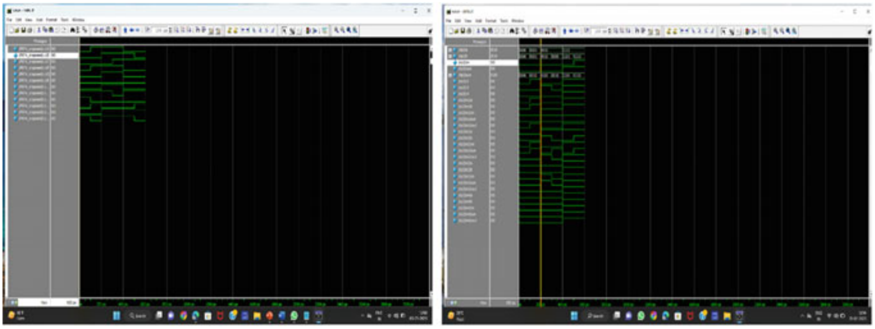

Fig. 18.15 Output waveforms of PFA and PRCA

18.9 Conclusion

In this project, we have implemented the full adder and ripple carry adder by using reversible logic gates such as the Feynman gate, Toffoli gate, and new gate. And compared the power, delay, and area between the full adder and ripple carry adder with normal gates and reversible gates using Xilinx software. The delay value for full adder using reversible gates decreased by 30% and the area decreased by 50% when compared with the normal gates. The delay value for ripple carry adder using reversible gates decreased by 16% and the area decreased by 50% when compared with the normal gates.

References

1. Jagannatha, K., Divya, D., Reddy, K. S., Desai, P.K., Sevanthi, S.: ASIC design of reversible full adder circuits. In: 2012 International Conference on Computing, Electronics and Electrical Technologies (ICCEET). Nagercoil, India (2012)
2. Pujar, J., Raveendran, S., Panigrahi, T., Vasantha, M.H., Kumar, N.: Design and analysis of energy effective reversible sense grounded full adder. In: 2019 IEEE 62nd International Midwest Symposium on Circuits and Systems (MWSCAS). Dallas, TX, USA (2019)
3. Design and implementation of 8 bit and 16 bit ALU using verilog language. **3**(2), pp. 30–34 (2018). ISSN No. 2455-2143. Online since Jun 2018 at IJEAST
4. Apra Meya, R.S., et al.: Optimized reversible. IJERA, ALU. **10**(8) (Series-V), 33–38 (Aug 2020). ISSN: 2248-9622
5. Arya, G., et al.: Performance analysis of ALU with reversible logic. IJACSE Jul–Aug (2020)
6. Reversible logic gates design and implementation of ALU and PAL. J. Eng. Sci. **11**(11), Nov (2020), ISSN 0377-9254
7. Review on design and analysis of ALU using reversible logic gates. IJRAMR **3**(2), Feb 2022 SSN (Online): 2582-7839
8. Reversible logic gates and its performances. In: Proceedings of the Second IICISC 2018. IEEE Xplore Compliant, May (2018). ISBN: 978-1-5386-0807-4

Chapter 19
Design of Low Power 11T SRAM Cell Using CNTFET Technology

Anitu Atri, Vikram Singh, and Tabassum Khurshid

Abstract With the miniaturization of CMOS technology, the conventional CMOS-based SRAM is facing several challenges, such as increased power consumption, decreased stability, and limited scalability. Carbon nanotube field-effect transistors (CNTFETs) have emerged as a promising alternative to CMOS technology due to their excellent electrical properties, including high electron mobility, low leakage current, and high mechanical strength. This paper presents a low power 11T SRAM cell using CNTFET. The proposed 11T SRAM cell is designed using P-CNTFET as header switch and an N-CNTFET as a footer with separate read circuit and is stimulated using H-Spice tool using 32 nm CNTFET Stanford model. The proposed SRAM cell is operated with the supply voltage of 0.9 V to improve read noise margin of 0.246 V and improved read delay of 0.01627 ns with a write delay of 0.0645 ns. A state of art comparison with existing with CNTFET-based 6T, 7T, 8T and 11T SRAM cells is also presented.

19.1 Introduction

Static random access memory (SRAM) is a type of volatile memory that is commonly used in microprocessors, digital signal processors, and other integrated circuits. It is a high-speed memory that uses flip-flops to store data and is often used for cache memory due to its fast read and writes times [1]. Multiple SRAM cells combined together to create larger memory structures that are capable of storing a larger amount of data. The need for faster and energy-efficient electronic devices has resulted in a reduction in the size of transistors in CMOS technology to less than 10 nm. However, this decrease in size has brought about several challenges, such as increased leakage current and reduced reliability, mainly due to the effects of quantum tunneling. To overcome these challenges, researchers have explored the use of CNTFETs as a

A. Atri (✉) · V. Singh · T. Khurshid
School of ECE, Shri Mata Vaishno Devi University, Katra, Jammu and Kashmir, India
e-mail: 21mmc001@smvdu.ac.in

P. H. V. S. Talpa Sai et al. (eds.), *Intelligent Manufacturing and Energy Sustainability*, Smart Innovation, Systems and Technologies 372,
https://doi.org/10.1007/978-981-99-6774-2_19

potential replacement for conventional CMOS transistors. CNTFETs have demonstrated superior performance in terms of speed, power consumption, and noise immunity, making them a promising alternative for future electronic devices [2]. The advancement in nanotechnology has led to the development of SRAM cells using CNTFETs [3].

In last few years, researchers have been conducting studies on SRAM cells based on CNTFETs with a focus on enhancing their stability, scalability, and reliability. Some studies have suggested innovative circuit designs for CNTFET-based SRAM cells, while others have examined the use of various fabrication methods and materials to improve their performance [4]. Some commonly used SRAM cell designs include 6T, 7T, 8T, 9T, 10T, and 11T cell, where T stands here for number of transistors used. The total number of transistors used affects the performance and other characteristics of SRAM cell which includes power consumption, read and write speed, and stability. The choice of SRAM cell type hinges on the particular specifications of the device or system that is being developed, given that each type of SRAM cell has advantages and drawbacks of their own [5]. Overall, CNTFET-based SRAM cells have the potential to provide significant improvements in performance and power consumption, making them an alternative option for future memory technologies [6].

19.2 Brief Review of CNTFET Technology

CNTFETs have been identified as a potential solution to the limitations of complementary metal–oxide–semiconductor field-effect transistors (CMOSFETs), which have been the cornerstone technology for digital integrated circuits for many years. The ongoing scaling of CMOSFETs has resulted in issues such as power consumption and leakage current, which pose significant challenges. The superior electrical properties of CNTFETs, such as high carrier mobility, low sub threshold swing, and excellent electrostatic control, make them a promising alternative. CNTFETs use carbon nanotubes, which are cylindrical structures made of Graphene sheets as shown in Fig. 19.1, with diameters of a few nanometers, as the channel material in transistors as shown in Fig. 19.2. By utilizing CNTs, it is possible to develop more energy-efficient and high-performance electronic devices that can overcome the limitations of traditional CMOS technology [7].

The chirality of CNTs also plays a crucial role in their properties. Armchair CNTs exhibit metallic behavior, while zigzag CNTs are semiconducting as shown in Fig. 1b. The type of chirality chosen for CNTFETs used in SRAM design can significantly impact the device's performance. For example, zigzag CNTFETs have shown to have better on–off current ratios compared to armchair CNTFETs, leading to better SRAM performance [9]. Therefore, the diameter and chirality of CNTs are critical factors that need to be considered in the design of CNTFETs for SRAM applications. The optimal choice of diameter and chirality can result in better device performance, leading to improved SRAM functionality [7] and can be expressed as

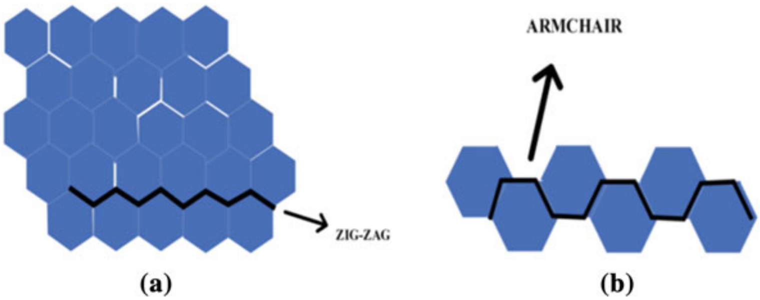

Fig. 19.1 Graphene sheet **a** Zig-Zag **b** Armchair [9]

Fig. 19.2 Structure of CNTFET [7]

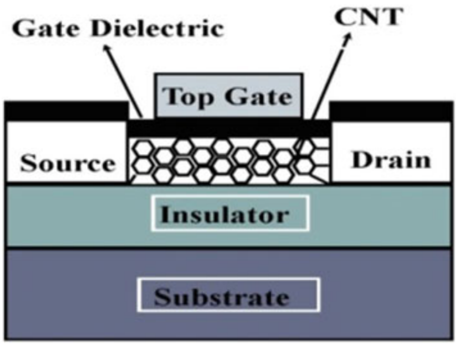

$$\text{Channel length (L)} = a\sqrt{m^2 + mn + n^2} \tag{19.1}$$

$$\text{Diameter of CNT } (\mathrm{D_{cnt}}) = \mathrm{L}/\pi \tag{19.2}$$

$$\text{Threshold voltage}(\mathrm{V_{th}}) = \frac{\mathrm{a\,V\pi}}{\sqrt{3}.\mathrm{q.Dcnt}} \tag{19.3}$$

where ‘q’ is the electron charge, $\mathrm{V\pi} = 3.033$ eV , CNT atomic distance (a) = 2.49 Å.

CNTFET sizing can be adjusted by modifying the number of carbon nanotubes used in the channel and to achieve the desired threshold voltage and current drive capability. By increasing the number of tubes, the channel width can be increased, which in turn increases the current carrying capacity of the device. This approach allows for greater flexibility in designing CNTFET-based circuits and can optimize their performance for specific applications.

19.3 Related Literature

In recent years, CNTFETs have emerged as a promising technology for developing SRAM cells with superior performance compared to traditional CMOS technology. Several studies have investigated the performance of SRAM cells utilizing CNTFETs, aiming to improve their efficiency and effectiveness. One study proposed a modified 6T structure for a CNTFET-based SRAM cell, which showed its improved write ability, read stability, and read access time when compared with the conventional 6T SRAM cells [10]. Another study proposed an asymmetric CNTFET-based SRAM cell that achieved improvement in write margin and read stability when compared with the symmetric CNTFET-based SRAM cells [11].

A hybrid SRAM cell was also proposed that utilized both CNTFETs and conventional CMOS technology, showing improved read and write performance compared to traditional CMOS-based SRAM cells [12]. Additionally, a dual-Vt CNTFET-based SRAM cell was proposed, which indicates the upgraded write-ability and read-stability when compared with the conventional CNTFET-based SRAM cells [13]. Other studies have focused on design optimizations to improve the performance of CNFET SRAM cells, such as the usage of lightly doped drain/source regions and the optimization of gate length and width [14].

Comparative analyses of different SRAM cells using traditional MOSFET and CNTFET technology have been carried out. The simulation results show that the CNTFET-based SRAM cell has better performance in terms of read signal noise margin (RSNM), write signal noise margin (WSNM), read delay (RD) and write delay (WD), while the MOSFET-based SRAM cell has better performance in terms of RD and WD. Overall, CNTFET-based SRAM cells are a promising candidate for future memory applications due to their superior performance compared to traditional MOSFET-based SRAM cells [15–17].

Furthermore, studies have investigated the impact of various CNTFET parameters such as channel length, channel diameter, and gate oxide thickness on the performance of CNTFET SRAM cells [18–24]. The Table 19.1 shows the technology road map and their advantages. Table 19.1 is illustrating the technology path for transitioning from traditional transistors to carbon nanotube field-effect transistors (CNTFETs), in addition to their benefits and drawbacks.

Therefore, CNTFET-based SRAM cells have demonstrated superior performance compared to traditional CMOS technology, making them a promising candidate for future memory applications.

19.4 Proposed 11T SRAM Cell Using CNTFET

A single bit of data can be stored in a memory cell known as a 6T SRAM cell, which is composed of six transistors organized in a certain pattern. The basic operation of a 6T SRAM cell involves using two interconnected inverters, each consisting of

Table 19.1 Comparison of CNTFET technology with other technologies

Tech	Advancements	Advantages	Limitations
CMOS	Carried on with reduction of attributes, decreased consumption of power, and enhanced performance	Continued characteristic like decrease utilization of power along with the performance enhancement	Physical barriers hinder scalability, increasing problems with manufacturing at decreased size of features
Hybrid Technology	Bringing together the conventional CMOS with CNTs to boost efficiency and reduce consumption of power	Enhanced functionality and decreased power consumption particularly when compared with standard CMOS technology	Concerns with dependability and stability, as well as difficulties with material integration and production
CNTFETs	In comparison with CMOS technology, using CNTs improves performance, consumes less power, and produces a lesser impact on the environment	Lowered power requirements, faster switching, increased device density, enhanced low-temperature performance, and reduced vulnerability to radiation-induced malfunctions	High fabrication costs, difficulties in achieving uniformity in device performance, and challenges with material integration and manufacturing

two transistors (a P-CNFET and an N-CNFET transistor) [7, 23]. The remaining two transistors serve as access transistors, which are used to control read and write operations as shown in Fig. 19.3.

The 6T SRAM works under three mode write, read and hold. In hold operation, the word line is switched off and the pass transistor enters an off state during the hold operation. The latch then safeguards the previous value all throughout this time frame. The write operation begins by setting the bit-lines to the desired values of either 0 or 1, and the word-line is activated to select the corresponding cell. This results in the voltage on one of the access transistors being higher than the voltage

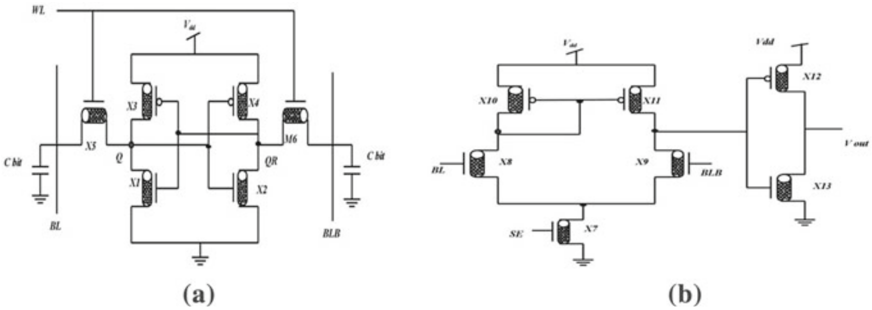

Fig. 19.3 6T SRAM using CNTFET; **b** Sense Amplifier [7]

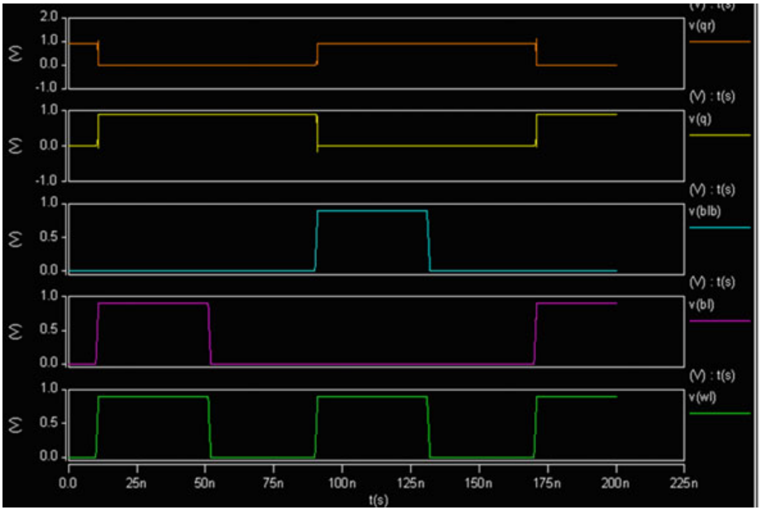

Fig. 19.4 Write operation in CNTFET based 6T SRAM

on the other access transistor. As a result, the higher voltage transistor enters the ON state, while the other remains in the OFF state. This allows for the transfer of data from the bit-lines to the storage nodes as shown in Fig. 19.4. During the read operation, the word-line is again activated, and the voltages on the bit-lines are compared. If the voltages on the bit-lines match the stored data in the cell, no operation is performed. However, if the voltages on the bit-lines do not match, the sense amplifier is activated to amplify the voltage difference and update the cell with the correct value shown in Fig. 19.5.

When a single P-CNFET or N-CNFET is added as a header switch between the latch and supply in a 6T SRAM cell using CNFETs, it can have a significant impact on the behavior and properties of the cell. A P-CNFET can be used as a switch to connect the supply voltage to the internal storage node during write operations, resulting in faster and more effective writing to the cell. However, this can also increase the write power consumption due to the additional switching activity. Alternatively, an N-CNFET can be utilized as a switch to connect the internal storage node to ground during the read operation, which can enhance read stability and reduce the read disturb issue. Moreover, the elimination of precharge circuitry with a header N-CNFET can reduce the read power consumption of the cell.

The addition of a P-CNFET or N-CNFET can improve write operation or read stability, respectively, compared to a 6T SRAM cell using only CNFETs as shown Fig. 19.6. However, it can also increase the complexity and size of the SRAM cell, which can be problematic in some cases. Furthermore, adding any additional FETs to the SRAM cell can increase the risk of leakage current and other reliability issues. The decision to add a P-CNFET or N-CNFET to a 6T SRAM cell using CNFETs depends on the specific application requirements. If the goal is to improve write operation, a

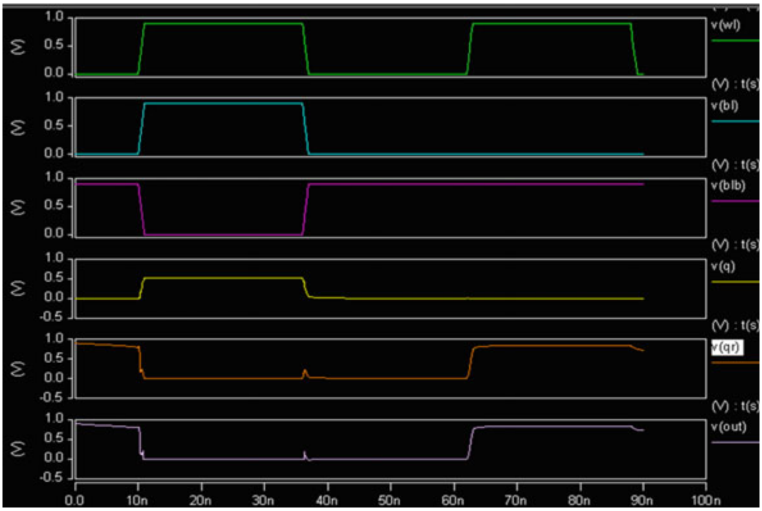

Fig. 19.5 Read operation in CNTFET based 6T SRAM

P-CNFET can be added. Likewise, if the focus is on read stability enhancement, an N-CNFET can be added. However, careful evaluation of the trade-offs and potential reliability issues are necessary for each application. Adding P-CNFET or N-CNFET between supply and latch of a 6T SRAM cell that uses CNFETs can have a significant impact on the cell's behavior and characteristics.

Reduced write power consumption can be achieved by using the P-CNFET footer as a switch for separating the internal storage node from ground during write operations. However, this may compromise the cell's write margin and reliability. Alternatively, N-CNFET footer can be used to connect the internal storage node to ground during read operations; thereby increasing read margin and reducing the read disturb issue. However, the additional switching activity may lead to an increase in read power consumption [20].

While adding footer P-CNFET or N-CNFET can improve power consumption and operation stability, it may also increase cell complexity and size, and result in leakage current and reliability issues. Choosing to add footer P-CNFET or N-CNFET depends on the specific application requirements. If reducing write power consumption is essential, a P-CNFET can be added, while an N-CNFET can be added to improve read stability. However, careful consideration of the trade-offs and potential reliability concerns are necessary for each application.

When header and footer transistors are added to a 6T SRAM using CNTFET, it becomes an 8T SRAM, which improves the stability of the cell during read and write operations. This improvement is due to reduced voltage swings, better write margin, and lower leakage. However, the use of additional transistors results in increased area, power consumption, and access time, which may not be desirable for some applications. The choice between 6 and 8T SRAM using CNTFET depends on the

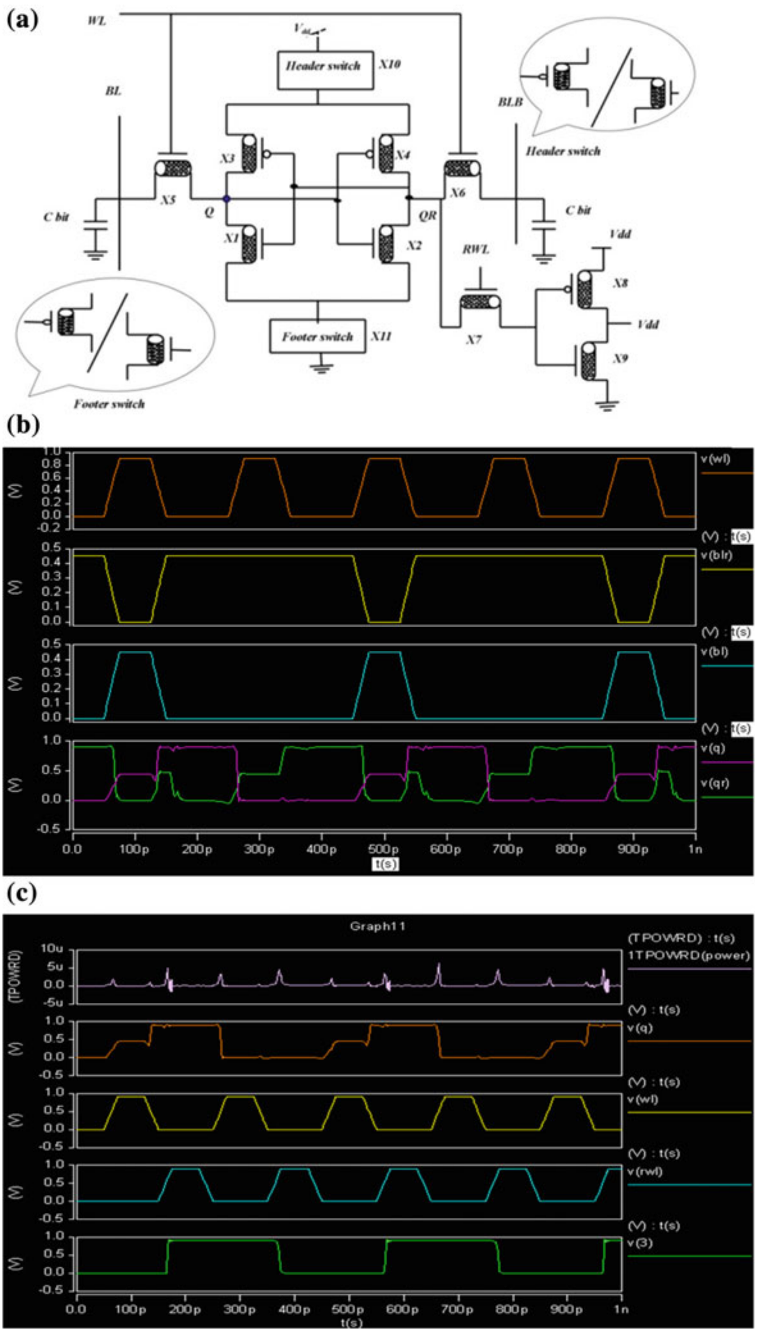

Fig. 19.6 **a** 11T CNTFET based SRAM; **b** Write operation simulation output; **c** Read operation simulation output

specific requirements of the application, such as density, power consumption, and access time [17].

In proposed SRAM cell a P-CNFET in header while an N-CNFET in footer is used, this will increase the read stability, read delay along with write delay. The 11T SRAM cell has advantages compared to a 6T SRAM cell. The header and footer transistors in the 11T SRAM cell decrease leakage current and improve the cell's stability. Moreover, a separate read circuit allows for efficient read operations without affecting write operations as shown in Fig. 19.6. Nonetheless, the more complex 11T SRAM cell has higher power consumption and larger area requirements compared to the simpler 6T SRAM cell. Ultimately, the choice between using an 11T or 6T SRAM cell using CNTFETs depends on specific design needs, performance requirements, power usage, and area trade-offs. The 11T SRAM cell has benefits like improved stability and reduced read disturb errors, but with the cost of increased complexity and overhead.

19.5 Results and Discussion

The proposed 11T SRAM designed and simulated with H-Spice tool at 32 nm technology node with supply voltage of 0.9 V and with the help of CosmoScope software waveforms for the proposed circuit are shown in Fig. 19.6 and 19.7.

It has been observed that CMOS-based 6T SRAM cell offers the lowest read and writes delay times, with values of 1.22 and 2.7 ns, respectively. It also has the lowest write noise margin of 0.07V and hold noise margin of 0.127 V. The CNFET-based 6T SRAM cells offers the lowest read and write delay times among all the CNFET-based SRAM cells, with values of 0.00472 and 0.00721 ns, respectively. It also has the highest read noise margin of 0.17 V and hold noise margin of 0.35 V. The CNFET-based 6T SRAM cell, which contains one footer and one header with a

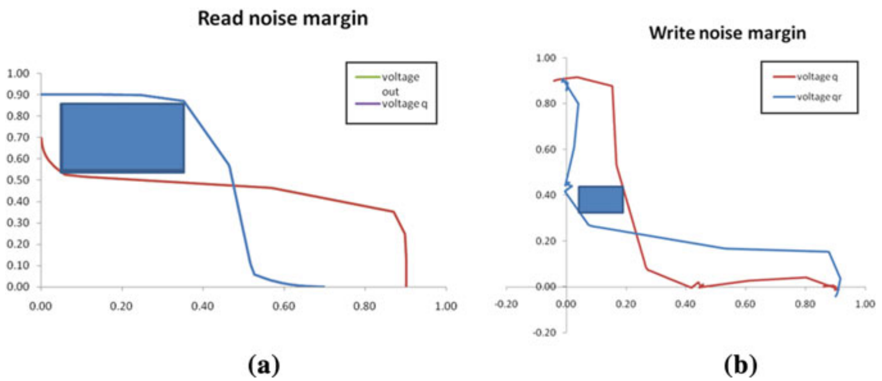

Fig. 19.7 **a** Read noise margin; **b** Write noise margin

Table 19.2 Comparison of the proposed 11T CNTFET based SRAM with existing literature

SRAM Type	RD (ns)	WD (ns)	RNM (V)	WNM (V)	HNM (V)	V_{DD} (V)	Tech (nm)	Ref
CMOS 6 T	1.22	2.7	0.012	0.07	0.127	0.9	32	[7]
CNTFET-6 T	0.00472	0.00721	0.17	0.18	0.35	0.9	32	[7]
CNTFET-6 T	0.156	0.0699	0.1473	0.143	0.140	0.33	32	[23]
CNTFET-8 T	0.119	6.11	0.1564	0.156	0.130	0.3	32	[17]
CNTFET-11 T	3.27	6.11	0.1562	0.1563	0.156	0.3	32	[25]
CNTFET-11 T	0.01627	0.0645	0.246	0.12	-	0.9	32	**This Work**

separate read circuit, provides the best read delay and noise margin performance. It offers a read delay of 0.156 ns and a read noise margin of 0.1473 V. However, it has the highest write delay of 0.0699 ns and a lower write noise margin and hold noise margin compared to other CNFET-based SRAM cells. The CNFET-based 8T and 11T SRAM cells have higher read and write delays than the 6T SRAM cells, with values ranging from 0.119 to 3.27 ns. However, they offer similar write noise margins and hold noise margins compared to the CNFET-6T SRAM cell. Our proposed model that is 11T SRAM gives us the better stability in read noise margin. In addition to read noise margin of the proposed circuit also improves in term of read and write delay which are presented in Table 19.2.

Therefore, the CMOS-based 6T SRAM cell offers the best read and writes delay performance among all the SRAM cells listed. However, the CNFET-based 6T SRAM cell offers better noise margins. The CNFET-based 6T SRAM cell containing one footer and one header with a separate read circuit provides the best read performance but worse write performance compared to other CNFET-based SRAM cells.

19.6 Conclusion

CNTFET based SRAM cell gave better device characteristics from traditional CMOS based SRAM cell. In traditional CMOS there are no separate read circuits but in the proposed 11T SRAM designed using CNTFET have separate read circuit which reduces the leakage current and improve read noise margin because of its high mobility and low leakage property. 11T SRAM CELL Based on CNTFET (6T SRAM cell contains one footer and one header with a separate read circuit). This type of 11T SRAM cell uses a separate read circuit to improve read delay, write delay and enhance stability and provides the highest level of performance and reliability. Hence the proposed 11T SRAM using CNTFET achieved the desired results in terms of reduced read delay and also write delay and improves the read noise margin for which the desired results are shown above when compared with the traditional 6T CMOS based SRAM.

References

1. Duari, C., Birla, S., Singh, A.K.: A dual port 8T SRAM cell using FinFET and CMOS logic for leakage reduction and enhanced read and write stability. J. Integrated Circuits Syst. **15**(2) (2020)
2. Kumar, H., Srivastava, S., Singh, B.: Low power, high-performance reversible logic enabled CNTFET SRAM cell with improved stability. Mater. Today Proc. **42**, 1617–1623 (2021)
3. Newar, T., Roy, T., Chowdhury, J., Das, J. K.: Design and stability analysis of CNTFET based SRAM cell. In: 2016 IEEE Students' Conference on Electrical, Electronics and Computer Science (SCEECS), pp. 1–5 (2016)
4. Elangovan, M.: A novel darlington-based 8T CNTFET SRAM cell for low power applications. J. Circ. Syst. Comput. **30**(12) (2021)
5. Saha, S., Saha, S., Chattopadhyay, S.: A comprehensive study on performance analysis of different SRAM Cells in CNTFET technology, In: 4th International Conference on Computing Methodologies and Communication (ICCMC), pp. 106–112. Erode, India (2020)
6. Devi, M., Madhu, C., Garg, N., Singh, S., Singh, P.: Design and Stability analysis of CNTFET based SRAM cell. In: Materials Science and Engineering Conference Series 2021, IOP, vol. 1033, pp. 012043 (2021)
7. Singh, P., BK, R.P.: Low power dissipation and low power consumption SRAM architecture based On 22-nm CNTFET technology
8. Lin, S., Kim, Y.B., Lombardi, F.: Design of a CNTFET-based SRAM cell by dual-chirality selection. IEEE Trans. Nanotechnol. **9**(1), 30–37 (2009)
9. Elangovan, M., Gunavathi, K.: High stable and low power 10T CNTFET SRAM cell. J. Circ. Syst. Computers **29**(10) (2020)
10. Sachdeva, A., Kumar, D., Abbasian, E.: A carbon nano-tube field effect transistor based stable, low-power 8T static random access memory cell with improved write access time. AEU-Int. J. Electron. Commun. **162** (2023)
11. Geier, M.L., McMorrow, J.J., Xu, W., Zhu, J., Kim, C.H., Marks, T.J., Hersam, M.C.: Solution-processed carbon nanotube thin-film complementary static random access memory. Nat. Nanotechnol. **10**(11), 944–948 (2015)
12. Chen, R., Chen, L., Liang, J., Cheng, Y., Elloumi, S., Lee, J., Todri-Sanial, A.: Carbon nanotube SRAM in 5-nm technology node design, optimization, and performance evaluation—Part I: CNFET Transistor Optimization. IEEE Trans. Very Large Scale Integr. (VLSI) Syst. **30**(4), 432–439 (2022)
13. Kavitha, S., Kumar, C., Fayek, H.H., Rusu, E.: Design and implementation of CNFET SRAM cells by using multi-threshold technique. In: IOP Electronics **12**, **1611**(7) (2023)
14. Mathur, N., Birla, S.: Performance evaluation and comparative analysis between traditional CNTFET based 9 T SRAM cells. In: IOP Silicon, pp. 1–13 (2022)
15. Elangovan, M., Gunavathi, K.: Effect of CNTFET parameters on novel high stable and low power 8T CNTFET SRAM cell. Trans. Electr. Electron. Mater. **23**(3), 272–287 (2022)
16. Srinivasu, B., Sridharan, K.: Low-power and high-performance ternary SRAM designs with application to CNTFET technology. IEEE Trans. Nanotechnol. **20**, 562–566 (2021)
17. Saiphani Kumar, G., Singh, A., Raj, B.: Design and analysis of a gate-all-around CNTFET-based SRAM cell. J. Comput. Electron. **17**, 138–145 (2018)
18. Kumar, H., Srivastava, S., Khosla, P.K., Singh, B.: High stable and energy efficient emerging nanoscale CNTFET SRAM cells using circuit level low power techniques. In Silicon **2022**, 1–13 (2022)
19. Elangovan, M., Karthickeyan, D., Arul Kumar, M., Ranjith, R.: Darlington based 8T CNTFET SRAM cells with low power and enhanced write stability. Trans. Electr. Electron. Mater. **23**(2), 122–135 (2022)
20. Shrivastava, Y., Gupta, T.K.: Design of compact reliable energy efficient read disturb free 17T CNFET Ternary S-RAM cell. IEEE Trans. Dev. Mater. Reliab. **21**(4), 508–517 (2021)

21. Kanhaiya, P.S., Lau, C., Hills, G., Bishop, M.D., Shulaker, M.M.: Carbon nanotube-based CMOS SRAM: 1 kbit 6T SRAM arrays and 10T SRAM cells. IEEE Trans. Electron Dev. **66**(12), 5375–5380 (2019)
22. Aparna, R.C.S.C.J.I.J.: A study of different SRAM cell designs. Int. J. **9**(3), 303–309 (2021)
23. Bala, S., Khosla, M.: Design and performance analysis of low-power SRAM based on electrostatically doped tunnel CNTFETs. J. Comput. Electron. **18**, 856–863 (2019)
24. Valluria, A., Musala, S.: Comparative analysis of CNTFET based SRAM cells. ECS Trans. **107**(1), 19177 (2022)
25. Singh, J., Mohanty, S.P., Pradhan, D.K., Singh, J., Mohanty, S.P., Pradhan, D.K.: Single-ended SRAM Bitcell design. Robust SRAM Des. Anal. 57–82 (2013)

Chapter 20
Designing of Photovoltaic System Using Matlab

Neha Kumari and Harpreet Kaur Channi

Abstract Solar PV facilities are needed to meet rising power demand, fossil fuel depletion, and environmental concerns. Land for solar PV will always be scarce. Renewable green energy must be encouraged to fulfil future energy demand. Solar PV is the most popular DER for many reasons. Using MATLAB, the authors analyse the Single-Phase Solar Photovoltaic Rooftop System. New grid synchronisation methods analyse output current characteristics. Floating solar photovoltaic panels provide more electricity and are energy-efficient and convenient. The report reviews past FPV implantation attempts. The paper uses MATLAB to model a 200 W PV Module. Floating solar panels were developed because land was costly, especially in agricultural regions where it was needed for crop growth. These ideas use sturdy pontoons to install solar panels at various angles. Submergible arrays of values and layered thin-film PV are two alternatives for maritime and big lacustrine situations. This article examines floating PV technologies, design possibilities, and India's FPV future.

20.1 Introduction

The usage of renewable energy has lately grown significantly all around the world. One of India's finest possibilities for obtaining sustainable Energy is solar electricity. The modern solar energy sector is intriguing. Solar Energy has increased dramatically over the past 10 years due to declining PV module production costs [1]. FPVs are solar panels attached to a structure that floats over water, typically a lake or reservoir (FPV). Below Fig. 20.1 is a floating photovoltaic system. The first 20 plants, each with a few hundred KWp capacity, were assembled between 2007 and 2013 [2]. Electricity installed is expected to increase from 3 GW in 2020 to 10 GW by 2025.

Solar Energy helps to alleviate the lack of electricity on the linked grid. The need for power in our country will continue to grow. Building a PV power plant requires

N. Kumari (✉) · H. K. Channi
Department of Electrical Engineering, Chandigarh University, SAS Nagar, Mohali, Punjab, India
e-mail: nehasingh030903@gmail.com

P. H. V. S. Talpa Sai et al. (eds.), *Intelligent Manufacturing and Energy Sustainability*, Smart Innovation, Systems and Technologies 372,
https://doi.org/10.1007/978-981-99-6774-2_20

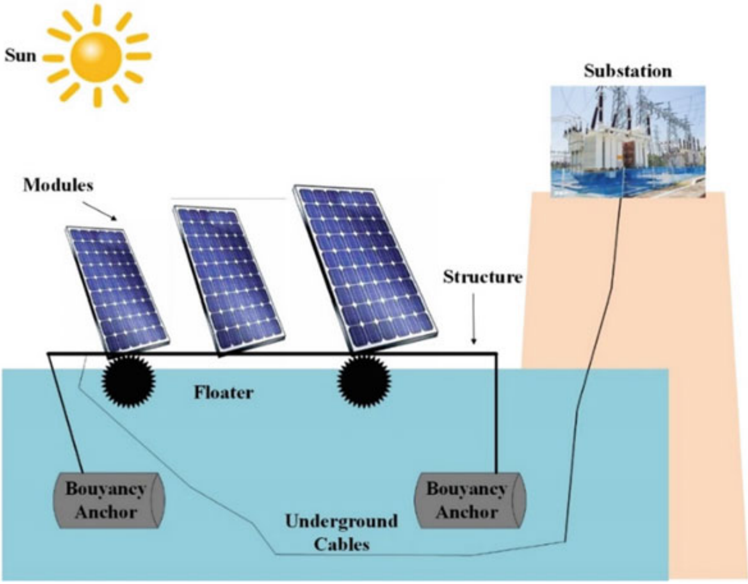

Fig. 20.1 Diagram of floating photovoltaic system

a sizable amount of land, which is extremely difficult for a highly populated region like Bangladesh. Bangladesh has a vast coastline region, lakes, ponds, and reservoirs that might be used for the solar energy project rather than requiring land. FPV power plant installation requires large coastal areas, including 57 principal rivers, which will be advantageous. FPV systems have been built worldwide since solar energy is a significant sustainable power plant. Given massive reservoir areas, numerous canals, and rivers, floating PV power plants provide a novel concept to the electrical generating industry [3]. The first small-scale and commercial FPV systems were established in Japan in 2007 and California in 2008, respectively, during the 2000–2010 decade. It took until 2013 for installations more prominent than 1 MWp to be constructed. The overall capacity of FPV hit 2 GWp at the end of 2019. There will likely be 62 GWp of FPV worldwide by 2030. Currently, Asia controls 87% of the world's FPV capacity.

20.1.1 Working

A solar power generator placed on the water is known as floating solar. They're set up on a sturdy platform. Pontoons act as the floats for the floating PV. Power converters, anchoring systems, transformers, PV modules, cables, etc., are among the parts that make up an FPV system.

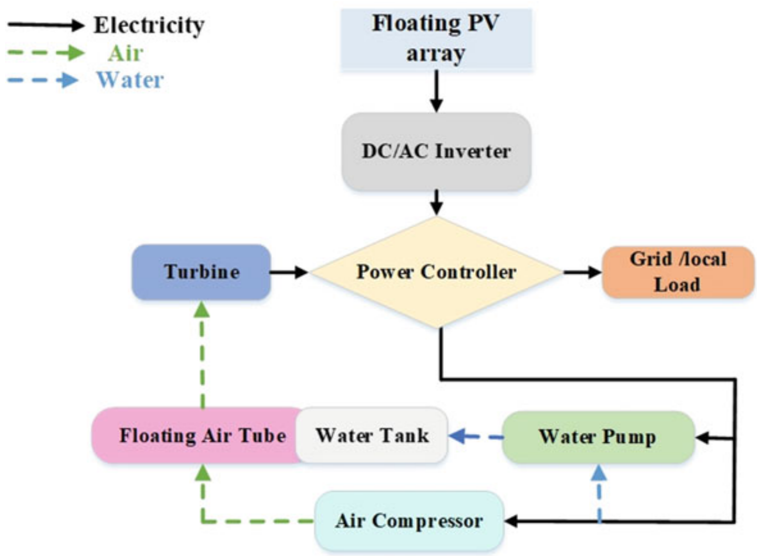

Fig. 20.2 Block diagram of FPV system

On the deck of the pontoons are the PV modules installed. The anchoring method that employs mooring lines ensures they are kept in a static condition for proper operation. The combiner, which is situated adjacent to the module, combines all of the transmissions obtained from the numerous module installed on the pontoon. The central inverter, connected to the multiple arrays from the plant and floats on a separate pontoon, accepts it next. Finally, Energy is transferred due to its being linked to the transformer (Fig. 20.2).

20.1.2 Factors Affecting the Development of the FPV System

- No land occupancy: The most apparent benefit of PV plants that float is that they don't take up any real estate at all, except for the tiny sizes of their electrical infrastructure [4].
- Tracking: The most apparent benefit of floating PV plants is that they don't need space other than the tiny footprints required by their electrical infrastructure [5].
- Installation and decommissioning: Compared to land-based plants, floating PV plants are more compact, easier to maintain, and easier to build and decommission. The primary aspect is that their installation may be completely reversible since no permanent structures are present, such as the foundations utilized for a land-based plant.
- Water conservation and quality: Water evaporation may be decreased by partially covering water basins. Climatic factors and the fraction of the plant area covered

Table 20.1 Data of floating solar projects in the future in India

Floating projects	State	Rated value (MW)
Omkareshwar reservoir	Madhya Pradesh	600
Ramagundam reservoir	Telangana	100
Getalsud dam project	Jharkhand	100
Kayamkulam PROJECT	Kerala	92
Rihand dam	Uttar Pradesh	50

both affect this outcome. This is a significant benefit in dry conditions like some areas of India since it prevents around 30% of the evaporation of the covered area [6].

- Environmental control: Algal blooms, a significant issue in developed nations, could be lessened. Deploying active systems in conjunction with partial basin covering may mitigate light pollution from the surface. Industrial pollution of a water basin presents management challenges that go beyond those addressed by simple insurance [7]. Table 20.1 shows the Future Solar Power Floating Projects in India.

20.2 Literature Review

Chowdhury et al. [8] suggested floating PV systems minimize water body evaporation. Kaptai, Rangamati, needs a floating PV power plant. Kaptai FPV produces project forecasts for panel position, solar energy system efficiency, surface area, financial and environmental advantages, and moving PV power plant energy production. Liu et al. [9] examined the advancement of PV technology, the power production efficacy of floating PV systems, and their potential and benefits in China. Nagananthini et al. [10] evaluated the FPV thin film technique. FPV technology development considers land value in urban and agricultural environments. Water-cooling solar panels in FPV-based systems boosts electricity generation. Light film technology is one of the best FPV energy extraction technologies. It may also benefit future massive FPV systems.

Kumar et al. [11] presented offshore PV, FPV, and design and construction methodologies. The FPV's output power, lifespan, and investment cost rely on its design. Economic and environmental assessments are needed for rapid growth and investment in FPV systems. Environmental and economic effects of floating PV systems were examined. .Shatil et al. [12] investigated building floating solar panels at Chalan Beel, Natore, and Rajshahi. The scientists compared the surface-mounted and hovering panels' output power and cost throughout the trial. The floating panel energy conversion costs 0.57 cents/kWh, comparable to other nations.

Hafeezet et al. [9] tested a gliding solar power plant near an urban lake and compared it to a soil-based photovoltaic system. SAM was used to conduct techno-economic research in Pakistan. The technological inquiry calculates FPV water reduction efficiency and monitors real-time temperature fall.

Farrar et al. [13] examined water and power use in desert Jordan. Many FPV systems use an irrigation reservoir. A 300 kWp FPV system with a fixed tilt saved water, Energy, money, and CO_2. Standard floating PV outperformed ground-mounted and FPV with monitoring and active condensation. The proposed method reduced greenhouse gas emissions by 141TCO_2 and had an 8.4-year system payback—Choi et al. [14] measured solar array local pressure. Economic research reduced manufacturing costs. When the wind blew from the side, the left and right columns' sheltering effect lowered the center of the solar panel array's drag and lift coefficients by 45–86%. These findings made it possible to switch floating body core components to cheaper materials, reducing manufacturing costs by 19% for a 2.5 MW system (20*30). Lopez et al. [15] examined the practicality of solar PV floating strategies in Spain, a nation with plenty of water and thermal Energy. We employed ecological spatial data and geographical data for standard, artificial, and significantly modified freshwater bodies to estimate energy production.

20.3 Designing a Model of 200 W PV Module in MATLAB

Designing of 200 W solar (PV) module in MATLAB software is performed.

A collection of PV cells is realized via the PV Array building block. Each string in the array comprises modules linked in series, while the columns are connected in parallel. You may use this building element to simulate predefined PV modules and those from the NREL System Advisor Model.

To simulate the varying I-V features of the modules as a function of irradiance and temperature, the PV Arrays module is a five-parameter model consisting of an illuminating current source (I_L), a diode, a pair of resistance (R_s), and a shunt resistance (R_{sh}) (Figs. 20.3 and 20.4).

The equations that define the diode I-V characteristics for a single module are given below (Tables 20.2 and 20.3; Figs. 20.5, 20.6, 20.7 and 20.8).

$$I_d = I_o\left[exp\left(\frac{Vd}{VT}\right) - 1\right] \tag{20.1}$$

$$V_{T=\frac{kT}{q}} * nI * N_{cell} \tag{20.2}$$

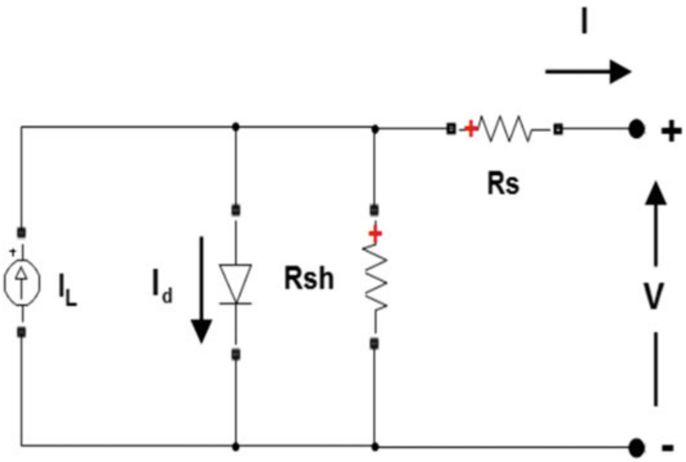

Fig. 20.3 Model of PV array module

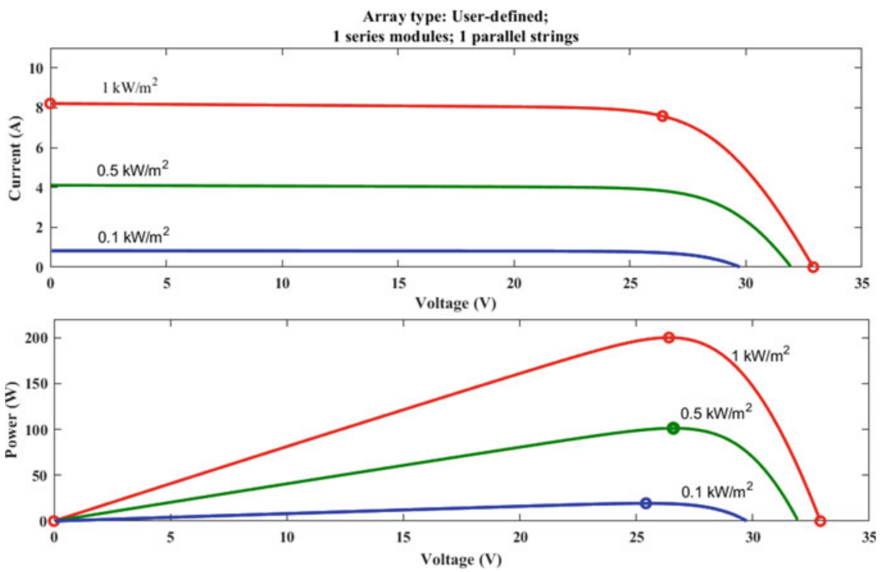

Fig. 20.4 Graph of current–Voltage and power–Voltage characteristics

20.3.1 Indian FSPV Projects for the 2019–2020 Budget Year

For a project using 4 MW of photovoltaic panels and 2 MW/1 MWh of batteries, Sun Power Energy Supplier will be presented with an award in November 2020. The duration of the Contract for the business's electricity requirements is set at 25 years. In India, a cutting-edge solar water storage system is expected to reduce yearly carbon

Table 20.2 Parameters used

I_d	Diode current (A)
V_d	Diode voltage (V)
I_0	Diode voltage (V)
nI	Diode ideality factor
k	Boltzmann constant = $1.3806e^{-23}$ J.K^{-1}
q	Electron charge = 1.6022* 10^{-19} C
T	Cell temperature (K)

Table 20.3 Rating of 200 W solar PV module

Parameter	Rated value
Related power (P_{mp})	200 W
Voltage at maximum power (V_{mp})	26.4 V
Current at maximum power (I_{mp})	7.58 A
Open circuit voltage (V_{oc})	32.9 V
Short circuit current (I_{sc})	8.21 A
Total number of cells in series (N_s)	54
Total number of cells in parallel (N_p)	1

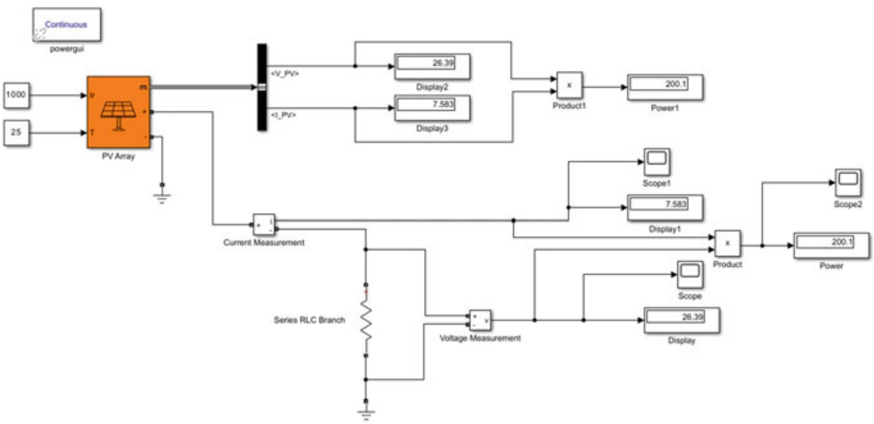

Fig. 20.5 The 200 W PV module model shown

dioxide emissions by 8111 tonnes [16]. Rihand Dam in Uttar Pradesh will host a 150 MW drifting solar power project in the 2019–20 fiscal year, according to SECI's green light. The winning bidder (UPPCL) has a contract to Acquire Power with both SECI and Uttar Pradesh Power Company Limited. A 20 MW peak solar power plant that includes a 60 MWh storage facility is now being developed. To power the Getalsud Dam in Jharkhand, SECI is constructing generating electricity from the sun with a capacity of 150 MW. The Uttarakhand reservoir Baur will serve as the site of

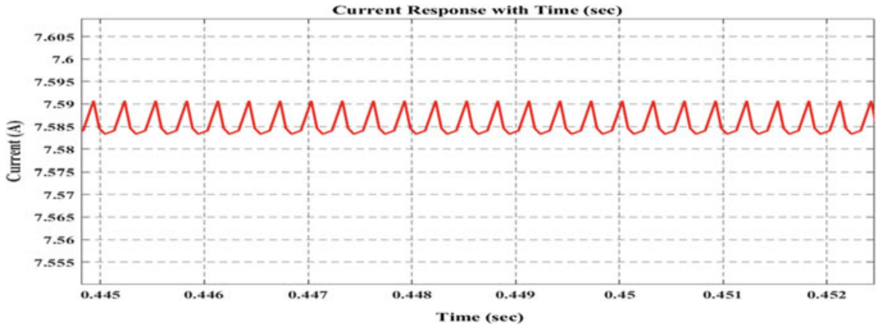

Fig. 20.6 Response of current

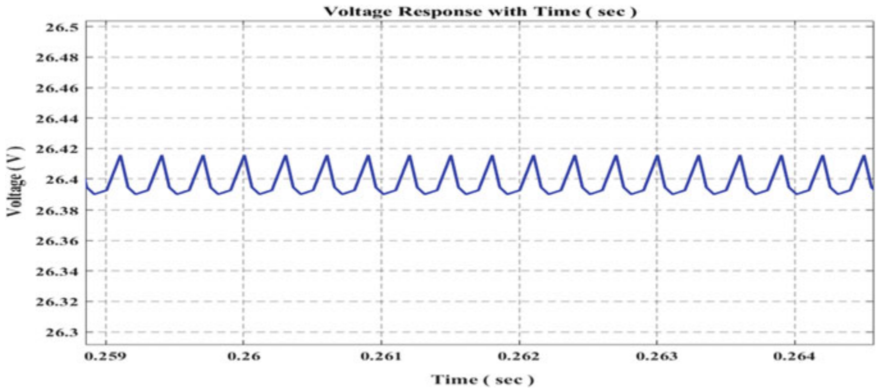

Fig. 20.7 Response of voltage

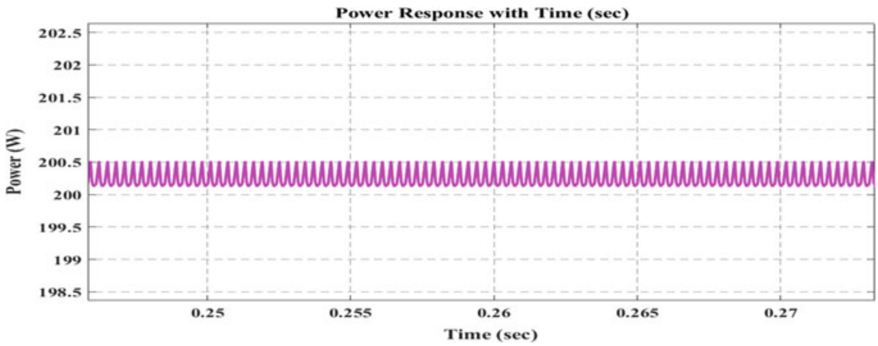

Fig. 20.8 Response of power

a 200 MW solar power facility that SECI plans to construct. 50 photovoltaic arrays with an overall generation of 40,000 MW will be built as part of the Energy from the Sun Park Project by 2021–2022 [16].

20.4 Comparative Studies

The Kaptai floating PV power plant in Rangamati is skilled at forecasting variables such as panel location, solar array efficiency, available surface area, financial advantages, and ecological benefits. The production of the plant's total Energy is fully modeled as a consequence [16]. Floating solar panel installations were researched for their potential at Chalan Beel, Natore, and Rajshahi. Electrical parameters like output power and cost are also assessed to compare ground-mounted and floating panels. The analysis concluded that the movable panel arrangement had a fair energy conversion cost of 0.57 cents/kWh compared to other countries. The giant FPV energy plant in the world is being built in South Korea next to Saemangeum, an estuary tidal flat on the Yellow Sea coast. The 2.1 GW floating solar farm is part of the 3 GW massive renewable energy project in the Yellow Sea off South Korea's coast—worth one million families. According to estimates, the 150 MW Huainan solar farm, which is now the largest movable solar farm in operation globally, will outperform the project's generation capacity by a factor of 14. [17]. A 320 MW FPV power plant was constructed in two stages by Hangzhou Fengling Electricity Science Technology in the Chinese province of Zhejiang. The second phase, which has a capacity of 120 MW, was finished in April 2020, and the first phase, with a total capacity of MW, was completed in 2017. On an NTPC reservoir at Kayamkulam near Alappuzha, Kerala, Tata Power Solar plans to build a 105 MW floating photovoltaic project.

20.5 Conclusions

This study discussed the feasibility of using FPV systems to generate Energy from freshwater sources in various settings. Solar PV power plants need a considerable amount of land, which is difficult to come by in densely populated areas like Bangladesh. Bangladesh's vast coastline, lakes, ponds, and reservoirs may be employed in place of land to construct a solar project. Floating solar panels were primarily motivated by the land premium, especially in agricultural regions where land is more valuable for cultivation. This paper highlighted the importance of FPV. The PV panels of current projects are installed in various horizontal and slanted configurations on a sturdy pontoon construction. The scope of future Solar Power Floating Projects in India has also been discussed in this paper.

References

1. Feldman, D., Barbose, G., Margolis, R., Bolinger, M., Chung, D., Fu, R., Seel, J., Davidson, C., Darghouth, N., Wiser, R.: Photovoltaic system pricing trends: historical, recent, and near-term projections 2015 edition (2015)
2. Trapani, K., Redón Santafé, M.: A review of floating photovoltaic installations: 2007–2013. Prog. Photovoltaics Res. Appl. **23**(4), 524–532 (2015)
3. Rahman, M.W., Mahmud, M.S., Ahmed, R., Rahman, M.S., Arif, M.Z.: Solar lanes and floating solar PV: New possibilities for source of energy generation in Bangladesh. In: 2017 Innovations in Power and Advanced Computing Technologies (i-PACT), pp. 1–6. IEEE (2017)
4. Tina, G.M., Cazzaniga, R., Rosa-Clot, M., Rosa-Clot, P.: Geographic and technical floating photovoltaic potential. Therm. Sci. **22**(Suppl. 3), 831–841 (2018)
5. Cazzaniga, R., Cicu, M., Rosa-Clot, M., Rosa-Clot, P., Tina, G.M., Ventura, C.: Floating photovoltaic plants: performance analysis and design solutions. Renew. Sustain. Energy Rev. **81**, 1730–1741 (2018)
6. Feldman, D., Barbose, G., Margolis, R., Bolinger, M., Chung, D., Fu, R., Seel, J., Davidson, C., Darghouth, N., Wiser, R.: Photovoltaic System Pricing Trends. Historical, Recent, and Near-Term Projections (No. NREL/PR-6A20-64898). National Renewable Energy Lab.(NREL), Golden, CO (United States) (2015)
7. Trapani, K., Millar, D.L.: Floating photovoltaic arrays to power the mining industry: a case study for the McFaulds lake (Ring of Fire). Environ. Prog. Sustain. Energy **35**(3), 898–905 (2016)
8. Chowdhury, R., Aowal, M.A., Mostafa, S.M.G., Rahman, M.A.: Floating solar photovoltaic system: An overview and their feasibility at kaptai in rangamati. In: 2020 IEEE International Power and Renewable Energy Conference, pp. 1–5. IEEE (2020)
9. Liu, L., Wang, Q., Lin, H., Li, H., Sun, Q.: Power generation efficiency and prospects of floating photovoltaic systems. Energy Procedia **105**, 1136–1142 (2017)
10. Nagananthini, R., Nagavinothini, R., Balamurugan, P.: Floating photovoltaic thin film technology—a review. Intell. Manuf. Energ. Sustain. Proc. ICIMES **2019**, 329–338 (2020)
11. Kumar, M., Niyaz, H.M., Gupta, R.: Challenges and opportunities towards the development of floating photovoltaic systems. Sol. Energy Mater. Sol. Cells **233**, 111408 (2021)
12. Shatil, A.H., Saha, S., Ahmed, K.F., Hasan, A.S., Rahman, S.I.: Design and comparison of floating solar panel for Chalan Beel. In: 2022 International Conference on Advancement in Electrical and Electronic Engineering (ICAEEE), pp. 1–4. IEEE (2022)
13. Farrar, L.W., Bahaj, A.S., James, P., Anwar, A., Amdar, N.: Floating solar PV to reduce water evaporation in water stressed regions and powering water pumping: Case study Jordan. Energy Convers. Manage. **260**, 115598 (2022)
14. Choi, S.M., Park, C.D., Cho, S.H., Lim, B.J.: Effects of wind loads on the solar panel array of a floating photovoltaic system–Experimental study and economic analysis. Energy **256**, 124649 (2022)
15. López, M., Soto, F., Hernández, Z.A.: Assessment of the potential of floating solar photovoltaic panels in bodies of water in mainland Spain. J. Clean. Prod. **340**, 130752 (2022)
16. Nandal, V., Kumar, R., Singh, S.K.: Barriers identification and analysis of solar power implementation in Indian thermal power plants: an interpretative structural modeling approach. Renew. Sustain. Energy Rev. **114**, 109330 (2019)
17. Pathipooranam, P. (2022). An enhancement of the solar panel efficiency–A comprehensive review. Front. Energ. Res. 1090

Chapter 21
Development of a Pellet Rotation System for Automated Visual Inspection

B. Yeswanthkumar Reddy, K. Govardhan Reddy, and R. Hussain Vali

Abstract Nuclear power plants use uranium fuel, consisting of solid ceramic pellets of cylindrical shape with 18 mm diameter and 14 mm height, which are manufactured by various metallurgical processes. The pellets are placed on specially designed trays after grinding and pellet washing operations. These pellets are manufactured in large quantities and must confirm very stringent quality requirements usually prevalent in nuclear engineering applications. As part of quality checks on the fuel pellets, the operators manually check defects like fits, cracks, etc. occurring on the cylindrical surface. With the help of a machine vision system, the pellets were inspected by turning each pellet in its location itself while observing its surface for defects. The main equipment involves transferring system of pellets, a pellet rotation system, a vision system, a pellet retrieval system, and a system of rejection and recirculation of defective pellets. This paper mainly deals with the pellet rotation system. The design equipment has the provision to receive 5 pellets at 80 mm pitch, such that the axis of all the pellets is in the horizontal plane. They are rotated in their position in steps of 30 degrees such that in 12 steps the entire cylindrical surface will cover precisely. The cameras of the vision system were placed above each pellet with proper illumination. The programmable logic controller is used to control the pneumatic cylinders with proper intervals of time to accept or rejection of the pellet by the vision system.

Please note that the LNCS Editorial assumes that all authors have used the western naming convention, with given names preceding surnames. This determines the structure of the names in the running heads and the author index

---

B. Y. Reddy
Mechanical Department, JNTUA College of Engineering Pulivendula, Pulivendula 516390, India
e-mail: yeswanth.basireddy@gmail.com

K. G. Reddy (✉)
BSH Department, Vigan Institute of Management and Technology for Women, Hyderabad, India
e-mail: gova305@gmail.com

R. H. Vali
Department of Mechanical Engineering, Malla Reddy College of Engineering and Technology, Hyderabad, India

P. H. V. S. Talpa Sai et al. (eds.), *Intelligent Manufacturing and Energy Sustainability*, Smart Innovation, Systems and Technologies 372,
https://doi.org/10.1007/978-981-99-6774-2_21

21.1 Introduction

Nuclear power is the fourth-largest source of electricity in India after thermal, hydroelectric, and renewable sources of electricity. Nuclear power is generated by bombarding Uranium with neutrons, which release a tremendous amount of energy. This radioactive material is made in the form of pellets by processes like pre-compaction, granulation binder, lubricant admixing, final compaction, sintering, centreless grinding, washing, etc. These pellets after metallurgical processes were placed on the specially designed trays. Before using these pellets directly in the tubes of the nuclear reactor, they have to undergo quality checks for defects like fits, cracks, etc. occurring on the cylindrical surface. These quality checks were performed manually by the operators and it is very critical to find the interval voids present in the pellet and the time for inspection is also very high. To avoid these problems an automated visual inspection is implemented to increase the accuracy of finding internal voids and reduce the inspection time. The automated visual inspection is done by rotating the pellet in equal steps such that it should cover the total surface area of the pellet. This paper deals with the pellets rotation system along with the automated inspection.

21.2 Development of Pellet Rotation System

The pellets for the inspection are transferred to the rotation system. In order to inspect the surface of the pellets they are rotated with constant speed and should be free from vibrations or disturbances. The pellets are rotated at an angle of 30° in 12 steps such that the entire pellet surface is covered. In order to rotate the body there must be a support for rotating the pellet. The support for rotation of the pellet can be done by two methods.

1. Gripping support
2. Rigid support.

Griping support causes inconvenience for inspection because it is not possible for inspecting the area under the grip and also there will be the cause of disturbances like vibrations created by the support. Rigid support will be easy in both rotating and inspecting the pellet without any disturbance. So a rigid support is best suited for a pellet rotation system.

21.2.1 Rotating a Body

In order to rotate a cylindrical pellet there must be an external cylindrical rotating body. If the pellet is in contact with the rotating body then the pellet automatically rotates in the anti-clockwise direction by considering the following conditions.

- The roller surface must be smooth and it should not affect the surface of the pellet
- The roller must be in a cylindrical shape so that it will be easy to inspect the surface of the pellet
- There should not be any heat developed between the contact surfaces of the pellet and the roller.

To rotate the roller, there must be external devices to rotate. The pellets are rotated by the two actuation methods. One is electrical actuation in which the stepper motors are used, and the other method is a mechanical actuation system in which the rotation is done by using rack and pinion mechanisms.

21.2.2 Electrical Actuation System

If the electrical actuation system is used the pellets must be rotated as shown in Fig. 21.1. The rotating shaft of the stepper motor is connected to a long shaft on which the rotating discs are mounted. The other end of the shaft is rigidly supported to the fame of the setup. As the pellets cannot be stable on the disc a frame is arranged on the top of the rotating disc. The support has a V-shaped gap in order to make the pellet in contact with the disc. The whole setup is shown in Fig. 21.2.

The stepper motor has its own advantages and disadvantages but from the point of view, it has the following disadvantages.

- There will be a slip present between the surfaces of the pellet and the roller
- There is a cause of the rise in temperature of the motor
- The rupture between the roller and pellet causes the formation of powder, which affects the pellets in the inspection process
- Due to the continuous running of the motor, there will be the formation of errors in the angle of rotation.

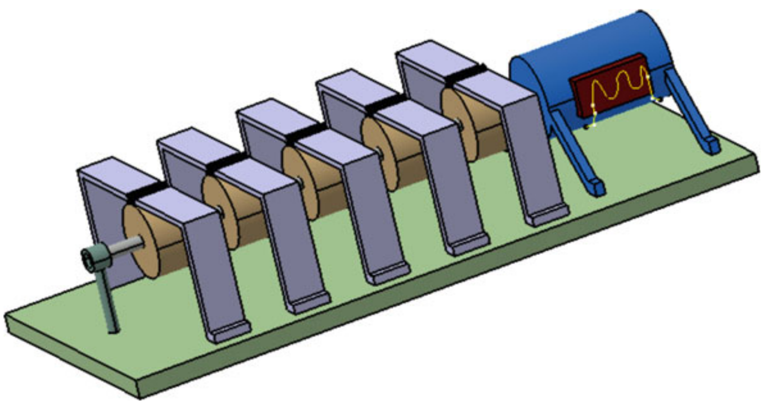

Fig. 21.1 Arrangement of stepper motor for pellet rotation

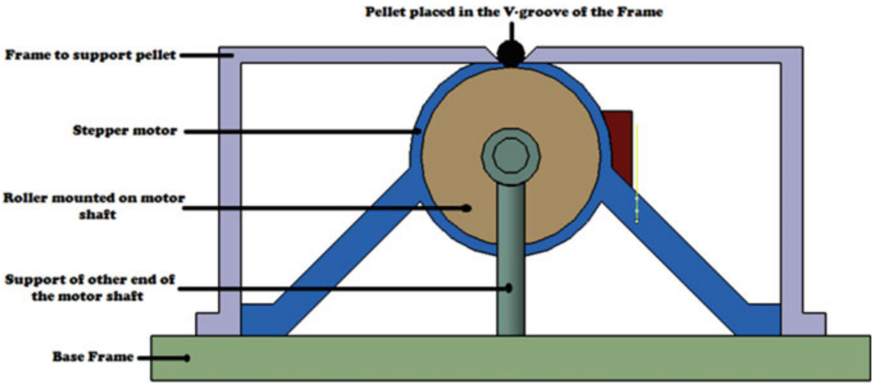

Fig. 21.2 Elements in electrical pellet rotation system

Because of all these disadvantages, the stepper motor is not considered and the mechanical actuation with the help of pneumatics cylinders is preferred for the pellet rotation system.

21.2.3 Mechanical Actuation System

If the rotation system runs with the help of mechanical parts, then it is said to be a mechanically operated rotation system. In this method, the pellet is rotated by using two rollers. The concept of pneumatics is applied to the rotation of the roller [1]. The principle of rack and pinion along with high compressed air of about 6 bars is used for the rotation of the pellet. The counterparts used in this system are

- Rollers
- Rack and Pinion
- Pneumatic cylinders
- Solenoid valves
- Programmable Logic Controller
- Rigid Frame for supporting mechanical Parts.

The selection of the counterparts depends on the design of the roller. Depending on the size of the roller the pinion is selected. The roller is designed as follows:

Length of the pellet	$L = 18$ mm
Radius of the pellet	$R = 7$ mm
Diameter of the pellet	$D = 14$ mm
Circumference of the pellet	$\pi D = 43.96$ mm
Angle for one step	$\theta = 30^{o}$
Number of steps for one revolution	$N = 12$

Rack movement for one step $L_2 = 3.1416$ mm
Pitch circle diameter of the roller P = 15 mm.

The linear displacement of the rack is converted to the angular displacement of the roller. Since the pellet is in contact with the roller, the pellet also rotates simultaneously with the same speed of the roller. The angle of the roller for one step ‘Θp’ can be found with the following relation

$$\frac{\pi}{\pi.P} = \frac{\theta p}{360}$$
$$\theta p = \frac{360}{P}$$

Substituting the value of P_d in the above equation we get

$$\theta p = \frac{360}{15} = 24^{\circ}$$
$$Arc\,length\,of\,the\,roller = \frac{d}{2}\theta p\frac{\pi}{180}$$

where ‘d’ is the diameter of the roller

$$Arc\,distance\,per\,step = \frac{\pi d}{12} = \frac{14\pi}{12} = Arc\,length\,of\,roller$$
$$\frac{14\pi}{12} = \frac{d}{2}\theta p\frac{\pi}{180}$$

Substituting the value of Θp we get

$$d = 17.5\,\text{mm}.$$

Therefore the roller is designed with the obtained value of ‘d’.

The rack has teeth on its horizontal surface and makes the pinion rotate. The pinion or gear has teeth with the same pitch as the rack. The linear motion of the rack makes the pinion rotate at a fixed point. The angle of the pellet depends on the angle of rotation of the roller. The rack and pinions were not designed separately and were selected from the catalogs in order to reduce the design time and manufacturing cost of the parts. The selection depends on the displacement of the rack for one step and the length of the rack. Figures 21.3 and 21.4 contain the technical specifications of the rack and pinion in the catalog.

Pneumatic cylinders are also known as air cylinders which produce force, often in combination with movement powered by compressed air or gas. Once actuated the compressed air enters into the tube at one end of the piston and imparts force on the piston. Consequently, the piston becomes displaced by the compressed air. These pneumatic cylinders are of different types but for the function of application,

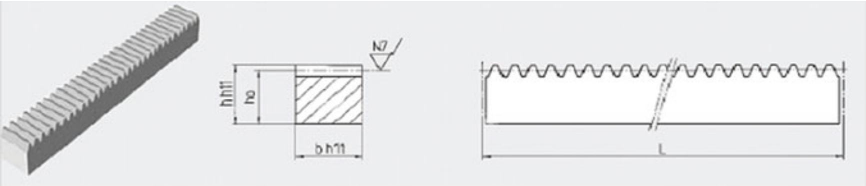

Part No	P	Module	L	z	b	h	ho	Fp	Pf	m (Kg)
124101	3.141	1.0	251.33	80	15	15	14.00	0.046	-0.05/-0.33	0.41
124102	3.141	1.0	499.51	159	15	15	14.00	0.062	-0.05/-0.33	0.82
124103	3.141	1.0	999.03	318	15	15	14.00	0.095	-0.05/-0.33	1.65
124104	3.141	1.0	1998.05	636	15	15	14.00	0.160	-0.05/-0.33	3.30

Fig. 21.3 Selection of rack from the catalog

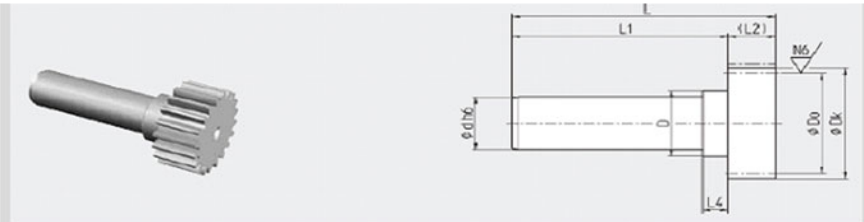

Part No	P	Module	z	D	Dk	D_0	D	L	L_1	L_2	L_4	J	m (Kg)
201020	3.142	1.0	20	12	22.0	20.0	16	70	55	15	2.5	3	0.09
201025	3.142	1.0	25	12	27.0	25.0	16	70	60.5	9.5	2.5	4	0.09
201116	4.712	1.5	16	12	27.9	24.9	16	90	70	20	4.5	7	0.14

Fig. 21.4 Selection of pinion from the catalog

a double-acting pneumatic cylinder is selected. The maximum displacement of the pneumatic cylinder is equal to rack movement for one step.

The power for the pneumatic cylinders is controlled by the solenoid valves. These valves are electromechanical switches used for controlling or changing the state of the valve. The operation of a solenoid valve is the same as a light switch typically controls the flow of the air, whereas the light switch controls the flow of electricity. Whenever the solenoid gets the signal it changes the position of the valves for the required functioning. For rotation of the pellet, a two-way two-position direction control valve is used and it is controlled by a solenoid.

The signal to the solenoid valve is given by the programmable logic controller (PLC), which is a digital computer used for the automation of industrial processes. These PLCs are designed for multiple inputs and output arrangements. The main difference from computers is that PLCs are armored for severe conditions and have

Fig. 21.5 Programmable logic controller

the facility for extensive input/output arrangements. Figure 21.5 shows the S7 1200 PLC from Siemens.

Programmable Logic Controller works with the help of ladder logic. The process of automation of any system was structured with the help of ladder diagrams. Since the programming of PLC using logic is simple and that is the reason for selecting a PLC instead of Microcontrollers and Microprocessors.

21.3 Working of Pellet Rotation System

The pellets after metallurgical processes will be sent to the pellet rotation system where these pellets are rotated for quality inspection. The pellets are arranged orderly in specially designed trays. Using a mechanized system for pellet transfer from trays to the rotation system, they are placed in between the two rollers. The rollers are cylindrical bodies that are screwed on the other side of the pinion. The systematic arrangement of the rack, pinion, rollers, and pneumatic cylinders is shown in Fig. 21.6. The mechanism mainly works on engaging and disengaging the rack with a pinion to rotate the pellet on the rollers. The number of rollers used in this system is ten which can rotate five pellets at a time with two pneumatic double-acting cylinders. The ends of the rollers are bolted with pinions. A single rack can rotate the pinions and simultaneously the rollers.

The cylinder-1 shown in Fig. 21.6 can engage and disengage the rack with pinion. The cylinder-2 is connected to the cylinder—1 and can move the rack linearly and the pinion to rotate. The nuclear power plant generates a high amount of heat in which water in the reactor is converted to steam. After utilizing the steam for power generation it is directed for automation purposes. This is one of the reasons for selecting pneumatics in a mechanical rotation system instead of an electrical rotation system. The steam after treatment is regulated to 6 bar pressure which is sufficient for the pellet rotation system.

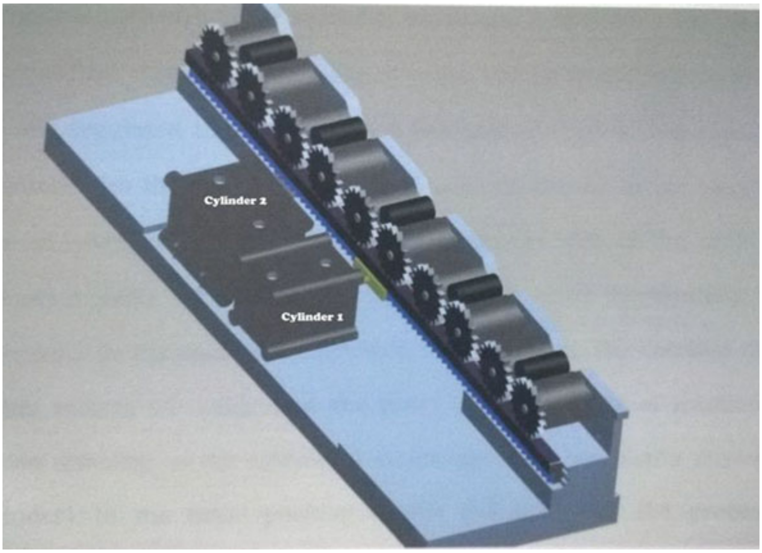

Fig. 21.6 Systematic arrangement of elements for a pellet rotation system

The pneumatic cylinders have a connection with two solenoids. These solenoids control the movement of the cylinders automatically. The solenoid control valves have 2way 4 ports. The solenoids are energized with the logic used in the Programmable logic controller. The line diagram of the arrangement of cylinders and solenoids is shown in Fig. 21.7

The filtered, regulated, and lubricated air enters into the solenoid valves s_1 and s_3 resulting in the rack engaging and move horizontally. After one step rotation of the pinion, the rack disengages and reverts back to the original position due to energizing of s_2 and s_4. This continues for 6 steps to complete one rotation of the pellet. One forward movement of the rack makes the roller rotate at an angle of 30°.

21.4 Automated Visual Inspection

The system consists of a fuel pellet rotating mechanism, where the pellets are placed on rollers to facilitate pellet rotation around its longitudinal axis. A Charge Coupled Device (CCD) camera with a 1/3-inch sensor size and 410,000 pixels was used for image grabbing [1]. LED white light was used for illumination. One camera is used to digitize the surface of the pellet. CCD camera and fuel pellet rotation are controlled through software developed in Lab View [2]. The software processes all the grabbed images to construct a single image of the unwrapped pellet surface. Algorithms are developed to enhance the image quality, determine the region of interest; convert to a binary image subsequently identify and localize various predefined defects [3]. The

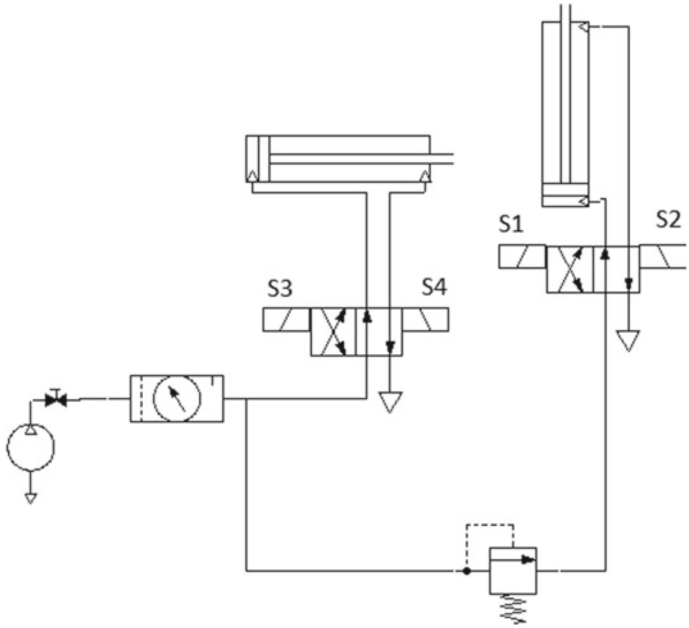

Fig. 21.7 Line diagram of the cylinders and solenoids

software stores the digitized images along with the analyzed defects in the database. The images are taken after the 30° rotation of the pellet. The images stored in the database are shown in Fig. 21.8. If the camera detects the crack, the rejection system dismisses the pellet and is again sent to the recycling process. If there is no crack found in the pellet, the tray contacting the inspected pellets is sent for further processing. The whole process is programmed and controlled by the PLC. This process is carried out continuously.

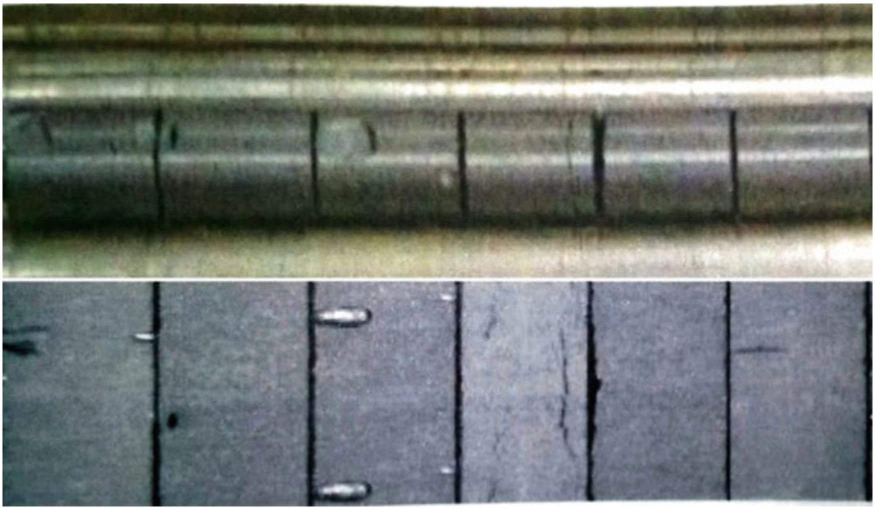

Fig. 21.8 Images of the inspected pellets in the database

21.5 Conclusion

The pellet rotation system and inspection system are implemented and comparatively better ones. The main input parameter is a huge amount of force for the actuation of cylinders. The improper selection of components like racks and pinions from the catalog may increase the cause of errors and malfunctioning of the system. The actuation of the pellet rejection system, when the defects are found, is completely dependent on the algorithm. This is a very simple operating machine for inspecting of nuclear fuel pellets. This principle is implemented in any type of visual inspection.

References

1. Anand, M.S., et al.: Development of a system for simultaneous rotation of multiple stacks of uranium dioxide pellets. In: Advanced Manufacturing and Materials Science: Selected Extended Papers of ICAMMS 2018. Springer International Publishing (2018)
2. Kantor, C.A.: Design and Development of an Automated Pellet Inspection System for Nuclear Fuel Pellets. University of Ontario Institute of Technology (Canada) (2015)
3. Aguirre, F., Domingo, A.: ENUSA (Empresa Nactional del Uranio S. A.) 'Spain, "Fuel pellets automatic visual inspection". In: 15th World Conference on Non-Destructive Testing—Materials Characterization and Testing (2000)

Chapter 22
Development of Conceptual Model for the Introduction Stage of Lean Intelligent Manufacturing Using Simulation Model Based on the Identification of the Appropriate Technologies of Industry 5.0

A. Mohammed Faisal, L. Karthigeyan, and G. Suresh

Abstract Industry 5.0 is the improved version of Industry 4.0 with human participation. However, all the technologies from Industry 4.0 are used in Industry 5.0 as enablers with human participation. Due to limitations such as more time consumption for humans and huge investment at operational level, the introduction stage of lean intelligent manufacturing is too difficult to understand the appropriate technologies of Industry 5.0. So, the simulation can be used as technology of Industry 5.0 to develop the conceptual model for the introduction stage of the lean intelligent manufacturing. Therefore, it is to develop a conceptual model for the introduction stage of lean intelligent manufacturing based on the simulation model to provide insights how to identify the appropriate technologies of Industry 5.0. A real-time case approach of a manufacturing enterprise is analyzed using the simulation models based on the value stream mapping (VSM) to develop the conceptual model of lean intelligent manufacturing. According to the simulation analysis, the traditional lean manufacturing can be transformed to lean intelligent manufacturing based on the technologies of Industry 5.0. VSM, 5S, Kaizen and Kanban are the appropriate lean techniques that are linked to the appropriate technologies of Industry 5.0 such as Industrial Internet of Things (RFID, sensors), Simulation, Big Data Analytics (Descriptive,

A. M. Faisal (✉)
Rajalakshmi School of Business, Chennai, India
e-mail: a.mohd.faisal@gmail.com

L. Karthigeyan
Confederation of Indian Industry (CII)—Institute of Logistics, Chennai, India
e-mail: l.karthigeyan@cii.in

G. Suresh
Department of Mechanical Engineering, Rajalakshmi Institute of Technology, Chennai, India

P. H. V. S. Talpa Sai et al. (eds.), *Intelligent Manufacturing and Energy Sustainability*, Smart Innovation, Systems and Technologies 372,
https://doi.org/10.1007/978-981-99-6774-2_22

Predictive and Prescriptive Analytics) and Cloud Computing (Storage). So, traditional lean manufacturing is transformed into lean intelligent manufacturing due to linking the lean techniques with the technologies of Industry 5.0.

22.1 Introduction

The term “Industry 5.0” first appeared in Michael Rada’s article “From Virtual to Physical” in the year of 2015 based on the human-centered technology with the waste prevention from virtual to realistic environment [1]. Because researchers and practitioners have different perspectives on what Industry 5.0 is, there is no consensus on its definitions [2]. Industry 5.0 is the improved version of Industry 4.0 [3] with human participation. Industry 5.0 is future upgraded revolution of Industry 4.0 that includes all the technologies of Industry 4.0 (Table 22.1) will be an enabler for Industry 5.0 because technology of Industry 5.0 has chronologically been developed based on technology of Industry 4.0 with the human participation [3]. Some unique technologies of Industry 5.0 are smart additive manufacturing, cobots, cyber physical cognitive systems, edge computing (EC) and future 6G systems [4] and 5G, 4D printing, cloud storage platform and Holography are improved version of Industry 4.0’s technology [5].

The concept of lean manufacturing emphasizes the reduction of waste to shorten lead times based on the lean thinking [8]. Lean manufacturing has been recognized as a valuable manufacturing philosophy to eliminate the waste leads to improve the value stream processes [9] for manufacturing a product [10]. VSM is a simple mapping technique that can help to understand the manufacturing process for introduction of lean principles and wastages for flow of information as well as material based on the value stream process for waste elimination [11]. VSM, a technique that is closely related to lean manufacturing [12], is frequently used in conjunction with

Table 22.1 Industry 4.0’s technologies applicable to Industry 5.0

Technology	References
Cyber physical system	[2–4, 6, 7]
Big data analytics	
Additive manufacturing	
Autonomous robotics	
Industrial internet of things	
Simulation	
Augmented reality	
Cloud Computing	
Computer Aided Designing (CAD)	[4]
Nanotechnology	[4]
Electric Vehicles	[6]

manufacturing process improvement to detect wasteful states in the manufacturing process based on the current (as-is) and future (to-be) mapping that create plans to get rid of them. The conceptual model for the introduction stage of lean manufacturing can be designed using VSM based on the current (as-is) and future (to-be) mapping.

Due to limitations such as more time consumption for humans and huge investment at operational level, the lean manufacturing is too difficult to implement at the introduction stage. Traditional lean manufacturing can be transformed to lean intelligent manufacturing based on the technologies of Industry 5.0 that can be observed as a possible solution and an enabler for such limitations [5, 6]. Manufacturers can develop a more economical and sustainable manufacturing process that optimizes productivity while limiting waste for the enhancement of worker abilities in the lean intelligent manufacturing process by combining these two supplemental concepts, such as Industry 5.0 and lean manufacturing. Simulation is one of Industry 5.0 technologies that is getting more and more sophisticated to understand the virtual ambience of manufacturing. For instance, Industry 5.0 technologies like simulation can be utilized to improve the knowledge and abilities of human workers in line with the principles of lean intelligent manufacturing. Manufactures can test and assess new concepts and procedures using the vigorous technology of simulation before putting them into practice in the real world. This could lead to the development of a more effective and environmentally friendly manufacturing process that is advantageous to both producers and consumers.

Simulation is used with real-time case approach aims to circumvent the limitations such as more time consumption for humans and huge investment at operational level for the introduction phase of lean intelligent manufacturing. The current and future models of VSM can be tested and assessed using the simulation to understand the lean intelligent manufacturing to identify the appropriate technologies of Industry 5.0 before putting them into practice in the real world. The conceptual model for the introduction stage of lean intelligent manufacturing can be developed using simulation analysis based on the current and future models of VSM. Therefore, it is to develop a conceptual model for the introduction phase of lean intelligent manufacturing based on the simulation models to provide insights how to identify the appropriate technologies of Industry 5.0.

22.2 Method

The conceptual model for the introduction stage of lean intelligent manufacturing can be designed using simulation analysis based on the current and future models of VSM. So, simulation is used with real-time case approach of the current and future static models to understand the introduction phase of lean intelligent manufacturing in a virtual technology before putting them into practice in the real world. The following stages are followed based on a manufacturing real-world case approach to develop the conceptual model for the introduction phase of lean intelligent manufacturing for Industry 5.0 (Fig. 22.1).

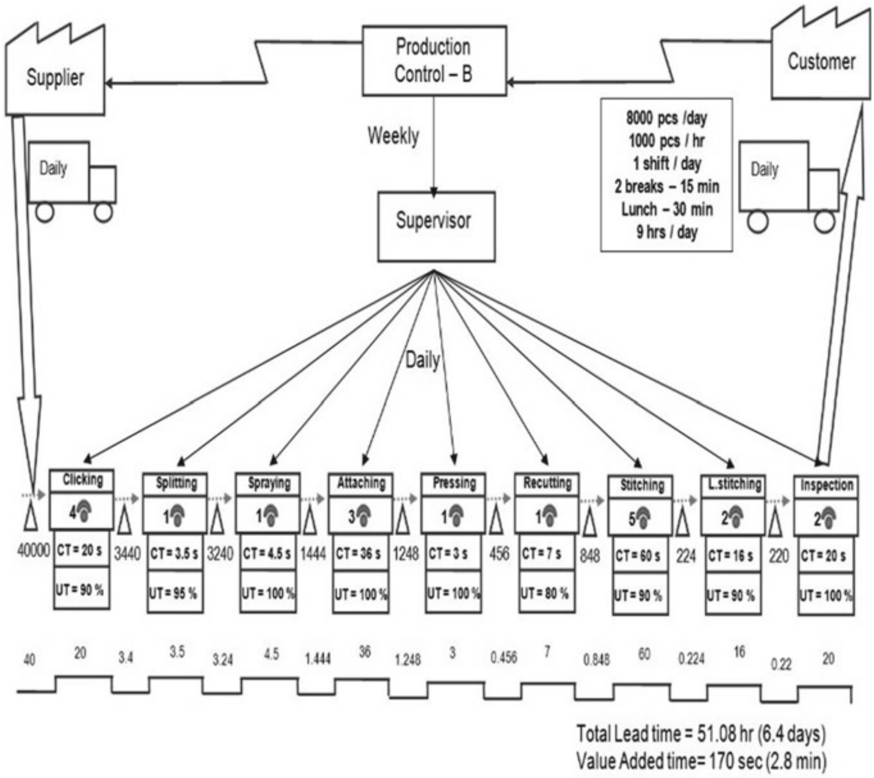

Fig. 22.1 Current-State static model using VSM

- Current-State static model is developed using VSM.
- Future-State static model is developed using VSM.
- Current-State model is simulated based on VSM.
- Future-State model is simulated based on VSM.

Current-state static model is mapped using VSM based on the process data such as time for processing, inventory between the process, workers for each process and uptime (UT) of machine. Future-state static model is mapped using VSM (Fig. 22.2) based on the lean variables.

The dynamic model of the simulation is done as follows [13–17]:

- Process information is collected based on the VSM.
- Chi Square test is used to identify distributions for the process variable that is important for simulation.
- Arena simulation software serves to model and analyze a model.
- A pilot model of the current-state mapping is simulated to find the following variables.

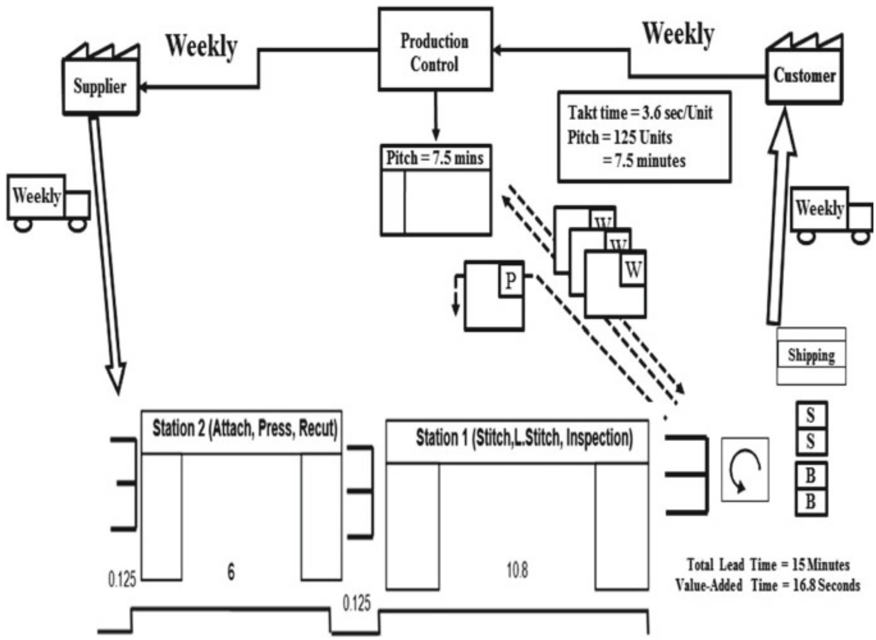

Fig. 22.2 Future-state static model using VSM

- Warm-up duration.
- Simulation runs.
- Number of replications.

- The future-state model is developed for the experiments.
- The future-state model is analyzed to understand the following variables.
  - Takt time.
  - Pitch.
  - Number of processes.
  - No. of inspection.
  - Number of Kanban System.
- Mean throughput (unit per day) is measured to understand the dynamic simulation model based on both states of VSM.

22.3 A Simulation Analysis Based on the VSM

ABC Company is a small enterprise that produces goods such as purses, mobile straps, and wallets. The lean technique such as VSM is selected for the introduction stage to understand the traits of goods manufacturing company and their distinctive requirements. Based on the high customer demands, mobile strap is selected as product for simulation analysis. The following stages are followed for simulation analysis to develop the conceptual model for the introduction phase of lean intelligent manufacturing for Industry 5.0.

- Current-State static model is developed using VSM.
- Future-State static model is developed using VSM.
- Current-State model is simulated based on VSM.
- Future-State model is simulated based on VSM.

Current-state static model is mapped using VSM based on the process data such as time for processing, inventory between the process, workers for each process and uptime (UT) of machine (Fig. 22.1). Future-state static model is mapped using VSM (Fig. 22.2) based on the lean variables such as Takt-time, pitch, the quantity of processes, inspections, and Kanban cards (Table 22.2).

Current-state dynamic model is developed for a push type of inventory model. It consists of the elements for input as Create, set of Processes and output as Dispose (Fig. 22.3). The pilot simulation model is experimented based on the following variables. The confidence interval method showed that 30 replications were statistically significant at 5% level for the simulation experiments of VSM.

- Cycle time for nine processes: suitable distributions—Uniform, Weibull, Normal and Triangular.
- Simulation runs—400 h per week due to weekly delivery to the customer.
- No. of replications—5.
- Warm-up duration—8 h.

Future-State dynamic model is developed for a pull type of inventory model. It consists of the two Arena Workstation templates [18] for the processing and output

Table 22.2 Lean variables and its level for each state of VSM

Dynamic simulation models	Inventory model	Variables				
		Takt time	Pitch	No. of process	No. of inspection	No. of Kanban
Current-state	Push	4	0	7	3	0
Future-state	Pull	3.6	125	5	1	3

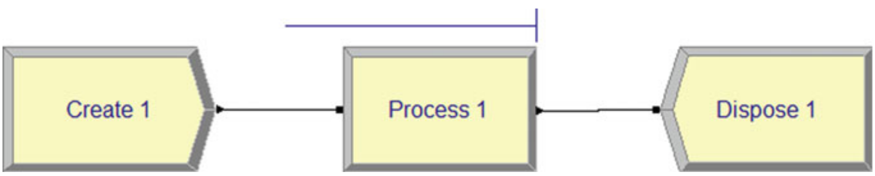

Fig. 22.3 Current-state dynamic model using simulation

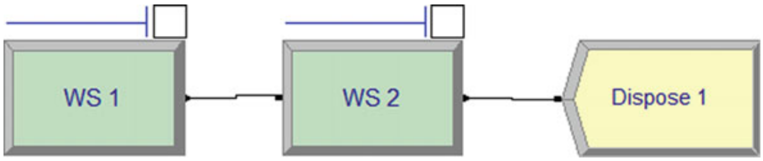

Fig. 22.4 Future-state dynamic model is developed based on VSM using simulation

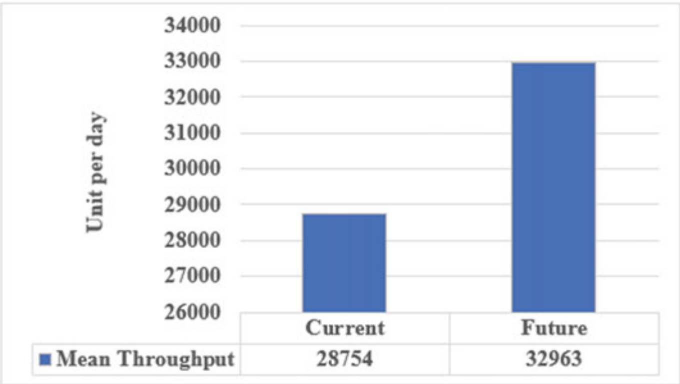

Fig. 22.5 Mean Throughput of each state of VSM based the simulation

as Dispose (Fig. 22.4). The lean variables and their level (Table 22.2) are used for understanding the future-state simulation model. While understanding the analysis of the simulation model based on the future state static model of VSM, there was an increase in mean throughput that shows the future state static model of VSM could increase the level of performance due to the implementation of lean intelligent manufacturing (Fig. 22.5).

22.4 Conceptual Model for Identifying the Appropriate Technologies of Industry 5.0 Based on the Lean Intelligent Manufacturing

One of the Industry 5.0 technologies utilized with real-time case approach is simulation that circumvents the limitations such as more time consumption for humans and huge investment for the introduction phase of lean intelligent manufacturing at operational level. The current and future static models of VSM are tested and assessed using the simulation to understand the lean intelligent manufacturing before putting them into practice in the real world. VSM is not only used as a technique for simulation analysis but also as a plan of implementation based on the selection of appropriate lean techniques such as 5S, Kaizen and Kanban. In order to fully comprehend the analysis of the simulation model based on the future state static model of VSM, an increase in mean throughput was seen, which demonstrates how the future state static model of VSM may be able to improve performance as a result of the adoption of lean intelligent manufacturing by the selection of appropriate lean techniques. VSM, 5S, Kaizen and Kanban are the appropriate techniques that are linked to the appropriate technologies of Industry 5.0. So, traditional lean manufacturing is transformed into lean intelligent manufacturing due to linking the lean techniques with the technologies of Industry 5.0.

The simulation is not only used for analysis but also noticed as an important technology of Industry 5.0 for the development of a conceptual model for the introduction stage of lean intelligent manufacturing because limitations such as more time consumption for humans and huge investment at the operational level are solved. So, the conceptual model of lean intelligent manufacturing for introduction stage is easy to recognize the appropriate technologies of Industry 5.0 based on the simulation analysis of VSM. The conceptual model for the introduction stage of lean intelligent manufacturing is designed using simulation analysis based on the current and future models of VSM with the appropriate technologies of Industry 5.0 and lean techniques for the introduction stage (Fig. 22.6). The conceptual model suggests that Industrial Internet of Things (RFID, sensors), Simulation, Big Data Analytics (Descriptive, Predictive and Prescriptive Analytics) and Cloud Computing (Storage) are the appropriate Industry 5.0 technologies for implementation of lean intelligent manufacturing based on the simulation analysis of the current and future models of VSM. VSM, 5S, Kaizen and Kanban are the appropriate techniques that are linked to the appropriate technologies of Industry 5.0 such as Industrial Internet of Things (RFID, sensors), Simulation, Big Data Analytics (Descriptive, Predictive and Prescriptive Analytics) and Cloud Computing (Storage).

22.5 Conclusion

This simulation study showed that the conceptual model is developed with the appropriate technologies of Industry 5.0 and lean techniques to understand the implementation of lean intelligent manufacturing at the introduction stage in a virtual ambience before putting them into practice in the real world. The simulation is not only used for analysis but also noticed as an important technology of Industry 5.0 for the development of a conceptual model for the introduction stage of lean intelligent manufacturing because limitations such as more time consumption for humans and huge investment at the operational level are solved. Industrial Internet of Things (RFID, sensors), Simulation, Big Data Analytics (Descriptive, Predictive and Prescriptive Analytics) and Cloud Computing (Storage) are considered as the appropriate technologies for Industry 5.0 to develop the model of lean intelligent manufacturing at the introduction stage based on the simulation analysis of the current and future models of VSM. VSM, 5S, Kaizen and Kanban are the appropriate techniques that are linked to the appropriate technologies of Industry 5.0 such as Industrial Internet

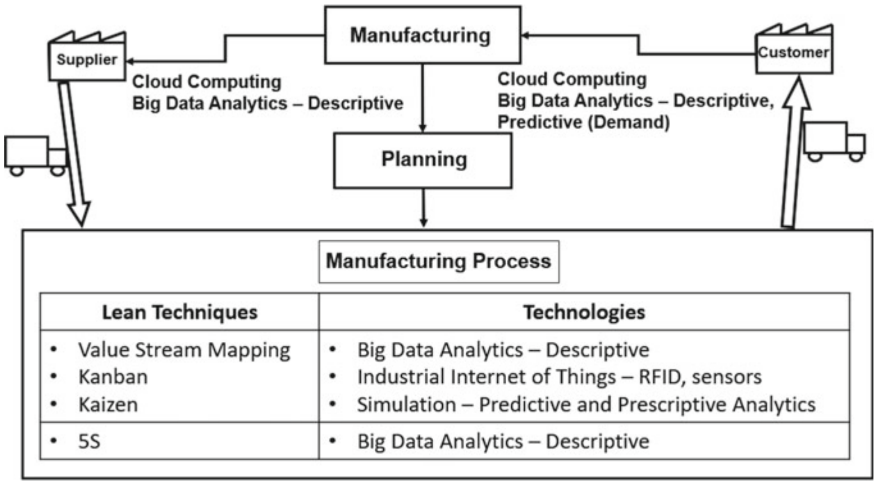

Fig. 22.6 Conceptual model for introduction of the lean intelligent manufacturing due to linking the lean techniques with the technologies of Industry 5.0

of Things (RFID, sensors), Simulation, Big Data Analytics (Descriptive, Predictive and Prescriptive Analytics) and Cloud Computing (Storage). So, traditional lean manufacturing is transformed into lean intelligent manufacturing due to linking the lean techniques with the technologies of Industry 5.0. The conceptual model of lean intelligent manufacturing for introduction stage is easy to recognize the appropriate technologies of Industry 5.0 based on the lean techniques. Future case studies will be encouraged to determine the best-suited technologies of Industry 5.0 and to add additional lean techniques to build the empirical model.

References

1. Rada, M.: From virtual to physical. https://michael-rada.medium.com/industry-5-0-definition-6a2f9922dc48 (2015)
2. Kumar, R., Gupta, P., Singh, S., Jain, D.: Human empowerment by industry 5.0 in digital era: analysis of enablers. In: Phanden, R.K., Mathiyazhagan, K., Kumar, R., Paulo Davim, J. (eds.) Advances in Industrial and Production Engineering. LNME, pp. 401–410. Springer, Singapore (2021)
3. Maddikunta, P., Pham, Q., Prabadevi, B., Deepa, N., Dev, K., Gadekallu, T., Rukhsana Ruby, R., Liyanage, M.: Industry 5.0: a survey on enabling technologies and potential applications. J. Ind. Inf. Integr. **26**, 100257 (2015)
4. Khan, M., Haleem, A., Javaid, M.: Changes and improvements in Industry 5.0: a strategic approach to overcome the challenges of Industry 4.0. Gr. Tech. Sust. **1**(2), 100020 (2023)
5. Mora, E., Gaiardelli, P., Resta, B., Powell, D.: Exploiting lean benefits through smart manufacturing: a comprehensive perspective. In: Lödding, H., Riedel, R., Thoben, K.D., von Cieminski, G., Kiritsis, D. (eds.) Advances in Production Management Systems. The Path to Intelligent,

Collaborative and Sustainable Manufacturing. IFIP AFCT, vol. 513, pp. 127–134. Springer, Cham (2017)
6. Moraes, A., Carvalho, A.M., Sampaio, P.: Lean and Industry 4.0: a review of the relationship, its limitations, and the path ahead with Industry 5.0. Mac. **11**(4), 443 (2023)
7. Demir, K.A., Doven, G., Sezen, B.: Industry 5.0 and human-robots co-working. Procedia Comput. Sci. **158**, 688–695 (2019)
8. Womack, J.P., Jones, D.T.: Lean Thinking: Banish Waste and Create Wealth in Your Corporation. Simon & Schuster, New York (1996)
9. Hines, P., Rich, N.: The seven value stream mapping tools. Int. J. Ope. Prod. Manag. **17**(1), 46–64 (1997)
10. Womack, J., Jones, D.T., Roos, D.: The Machine That Changed the World. Rawson Associates, New York (1990)
11. Rother, M., Shook, J.: Learning to See. The Lean Enterprise, USA (1999)
12. Shah, R., Ward, P.T.: Lean manufacturing: context, practice bundles, and performance. J. Operat. Manag. **21**(2), 129–149 (2003)
13. Faisal, A.M.: Data analytics based prescriptive analytics for selection of lean manufacturing system. In: 6th IEEE International Conference on Inventive Computation Technologies, pp. 464–466 (2021)
14. Baykoc, O.F., Erol, S.: Simulation modeling and analysis of a JIT production system. Int. J. Prod. Eco. **55**, 203–212 (1998)
15. Faisal, A.M., Ravi, A.G.: Simulation modeling and analysis for the implementation of total quality management using value stream mapping in Labour-intensive small and medium-sized enterprises. In: 2nd IEEE International Conference on Trends in Electronics and Informatics, pp. 1442–1444 (2018)
16. Altiok, T., Melamed, B.: Simulation Modelling and Analysis with Arena. Elsevier Inc., London (2007)
17. Faisal, A.M.: Predictive simulation modeling and analytics of value stream mapping for the implementation of lean manufacturing: a case study of small and medium-sized enterprises (SMEs). In: 2nd IEEE International Conference on Intelligent Computing and Control Systems, ICICCS, pp. 582–585 (2018)
18. Treadwell, M.A., Herrmann, J.W.: A Kanban module for simulating pull production in Arena. In: Winter Simulation Conference, pp. 1413–1417. Florida (2005)

Chapter 23
DSP Based Inbuilt Active PFC Battery Charger

Sisir, Satyavir Singh, and Bharath

Abstract It has been observed that the Electric vehicles production is increasing rapidly as it will be a substitute for the usage of fossil fuels. The objective is to minimize usage of fossil fuels to reduce pollution as well as the cost of refueling the vehicle with efficient and reliable chargers. The Charging of an Electric Vehicle is still an open problem regarding its performance. Hence, the charging technologies and their improvements can be tailored by increasing the efficiency of battery charging and adjustable charging voltages. A DSP controller-based off-board battery charger with a three-stage AC-DC charger is presented in the study. To serve it, a step-up AC-DC converter with power factor correction for line regulation and a full-bridge phase-shifted DC-DC converter is placed in the circuit with a transformer and a full bridge rectifier at the output end. The addressed scheme is having external feedback from the battery to a DSP controller that senses battery voltage and charges the battery accordingly. The presented simulated and hardware results are verified and compared to conventional chargers. The results are attaining the charging efficiency up to 94% at different voltage levels.

23.1 Introduction

Electric cars (EVs) and hybrid EVs (HEVs) have developed into significant numbers in recent years due to environmental regulations. The main part of EVs are batteries, which required to be highly efficient to store the energy. Lithium-ion (Li-ion) batteries are having several benefits including high power and energy density, high charging and discharging rate, low self-discharge, minimal memory effect, etc. Li-ion batteries have been widely used in electric vehicles (EVs) to replace NiCd, and lead-acid batteries [1]. The life of secondary batteries will be prolonged by a good battery charger that uses appropriate charging methods and provides safe charging state. A

Sisir · S. Singh (✉) · Bharath
Department of Electrical and Electronics Engineering, SRM University, Amaravati, Andhra Pradesh, India
e-mail: satyavir.s@srmap.edu.in

P. H. V. S. Talpa Sai et al. (eds.), *Intelligent Manufacturing and Energy Sustainability*, Smart Innovation, Systems and Technologies 372,
https://doi.org/10.1007/978-981-99-6774-2_23

number of studies have been done to develop the concept of DSP Based Chargers. DC-DC Converter Based on a series inverter and a multi-stage current driven rectifier to the active balance charger for lithium ion series batteries are presented in [2]. Off-Board Charger Systems with unidirectional power flow are reviewed in [3]. Off-board chargers are designed to be separate from the vehicle and can be used for charging at home, in public charging stations, or in another suitable locations. They are typically more powerful than on-board chargers and can charge the battery at higher rates, which can reduce charging times. Off-board chargers can also be designed for bidirectional power flow, which allows the battery to inject energy back to the grid and enabling vehicle-to-grid (V2G) applications.

On-board chargers are integrated into the vehicle and are typically limited in power rating due to weight, space and cost. However, they can simplify connectivity issues and reduce hardware battery requirements. This work will be extended in our research and we will focus on analyzing the load capacity and infrastructure of plug-in electric vehicles and hybrids. The charger topology is said to be capable of power factor correction and voltage and current regulation without additional components [4]. Such a mechanism greatly increases the potential of the electric car charging industry and its endless possibilities. Because this technology adapts to the vehicle connected to it and it is safe to reach new user voltages.

The charging infrastructure is categorized into different levels based on the power rating and charging time required. Level 1 charging (convenience charging) typically uses a standard household outlet and provides a low power rating of up to 1.4 kW. Level 2 charging (primary charging) provides a higher power rating of up to 19.2 kW and requires a dedicated charging station. Level 3 charging (fast charging) provides a very high power rating of up to 350 kW and can charge the battery up to 80% in around 30 minutes. Level 3 charging stations are typically located along highways and in public locations. Hence, charger systems can be categorized into off-board and on-board types with unidirectional or bidirectional power flow. Different power levels of charging infrastructure are available, and roadbed charging is a promising technology for the future. The optimal charging system and infrastructure for a specific application depend on several factors, including the type of vehicle, battery, and charging requirements.

Efficient and reliable battery chargers are essential for ensuring optimal charging times and battery life, which are key factors for EV adoption and customer satisfaction. A good battery charger should have high power density, low cost, and low volume and weight. To achieve this, the charger's design should take into account various components, control, and switching strategies. The charger control algorithms are implemented using different technologies, such as analog controllers, microcontrollers, digital signal processors, and specific integrated circuits. The choice of technology depends on the charger's rating, cost, and type of converters. To ensure compliance with standards, various regulations limit the allowable harmonic and DC current injection into the grid, such as IEEE-1547 [5], SAE-J2894 [6], IEC1000-3-2 [3], and the U.S. National Electric Code (NEC) 690 [7]. As a result, EV chargers are usually designed to comply with such standards.

This paper is organized as follows: introduction in first section and subsequently in Sects. 23.2 and 23.3 battery chargers for EVs, Chargers Topologies are reviewed respectively. In Sect. 23.4 Model setup of DSP based charger is presented. In the next section result and analysis have been carried out and at the end conclusion of the work is given.

23.2 Battery Chargers for Electric Vehicles

Battery chargers for electric vehicles (EVs) are devices that are used to replenish the energy stored in the battery of an electric vehicle. There are several types of EV chargers available, ranging from slow chargers to fast chargers, and the type of charger will depend on specific use and needs. There are the most common types of battery chargers for electric vehicles:

- Level-1 Chargers: These are the slowest chargers available, and they typically use a standard 120-V household level 1 chargers might take up to 20 h to fully charge EV, they are most effective when used overnight.
- Level-2 Chargers: These chargers require a 240-V outlet, comparable to those used for an electric dryer or stove, and are faster than Level 1 chargers. Most EVs may be fully charged using level 2 chargers in 4 to 8 hours.
- DC Fast Chargers: The EV battery may be completely recharged by one of these chargers, which is the fastest charging up to 80% in just 30 minutes. DC fast chargers are perfect for anyone who need to quickly charge their EV while on the go and are frequently available at public charging stations.

When choosing a battery charger for your EV, it's important to consider your daily driving habits and the distance you typically travel. This will help you determine which charger is best suited for your needs. Additionally, it's important to ensure that the charger you choose is compatible with your specific EV model [8].

There are several charging protocols that can be considered for maximizing the expected battery cycle life within a fixed charging time and state of charge (SOC)

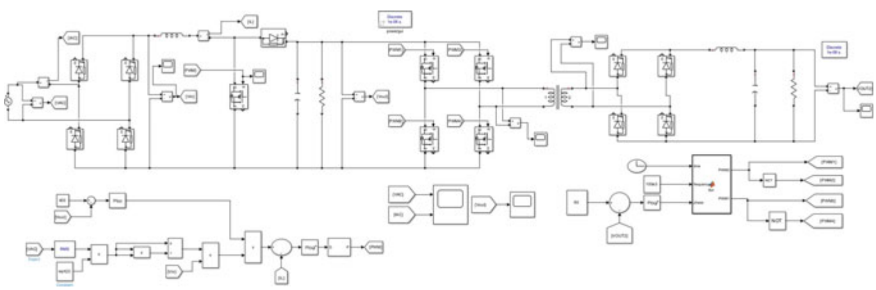

Fig. 23.1 Simulation model of DSP based inbuilt charger

range. One possible approach is to use a multistage charging protocol that involves controlling the charging current and voltage at different stages of the charging cycle. The basic working of this charger involves typically three stages, first-an AC supply, EMI filter, Bridge rectifier, second—PFC IC,Boost converter, H-Bridge circuit and third—a current transformer, DSP-IC, Full bridge rectifier and a battery at the output end as shown in Fig. 23.2.

23.3 Chargers Topologies

For both single-phase and three-phase chargers, there are several topologies or schemes, among them half-bridge and full-bridge topologies [3]. Half-bridge topologies have fewer components and lower cost, but have high component stress, while full-bridge systems have more components and higher cost, but lower component stress. Full-bridge systems also require more pulse-width modulation inputs, which increases the complexity and cost of the control circuits [1]. Other topologies include basic bidirectional circuits for chargers and single phase bidirectional half-bridge chargers. A three-phase full-bridge bidirectional device that connects to a DC-DC converter [9].

23.4 Model Setup of DSP Based Charger

A digital signal processing (DSP) is implemented in a DSP-based inbuilt active power factor correction (PFC) battery charger to control the charging process and correct the charger's power factor. By lowering the amount of energy lost during the charging process, active PFC technology contributes to the charger's increased efficiency. This is accomplished by modifying the charger's input voltage and current to meet the needs of the battery being charged. The charger can thus increase the energy that is supplied through the battery while lowering the amount of energy wasting as heat. The DSP technology used in these chargers allows for precise control over the charging process, which helps to ensure that the battery is charged safely and efficiently. The charger can monitor the battery's With the help of the DSP technology found in these chargers, the charging procedure can be precisely controlled, assisting in making sure the battery is charged effectively and safely. To avoid overcharging or undercharging, the charger can measure the voltage and current levels in the battery and govern the charging rate accordingly. Second feature of DSP-based inbuilt active PFC battery chargers is their ability to handle a wide range of input voltages and frequencies. This makes them ideal for use with a variety of power sources, including generators and solar panels. In summary, the DSP-based inbuilt active PFC battery chargers are an efficient and reliable charging solution for a variety of battery-powered devices, including electric vehicles, backup power systems, and renewable energy storage systems.

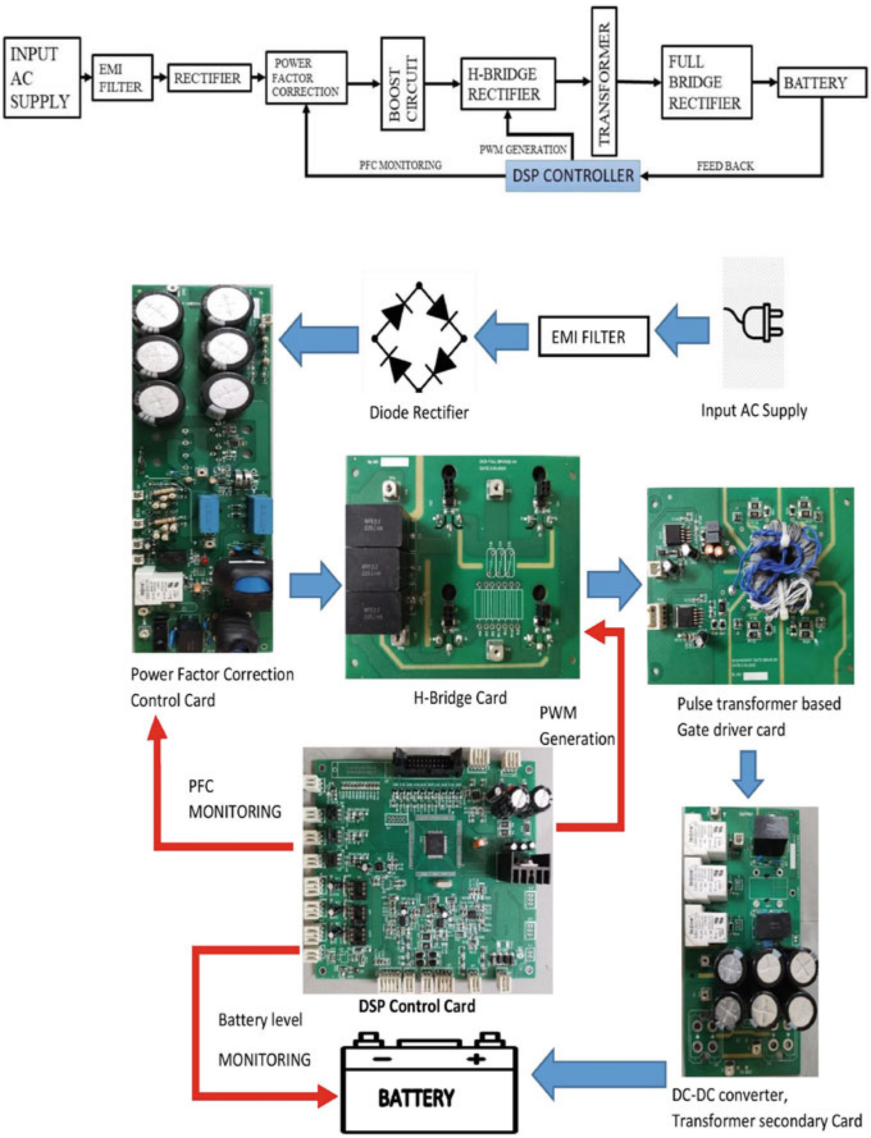

Fig. 23.2 Charger block-diagram and Hardware arrangement

The addressed charger topology for PFC rectification offers the following characteristics:

- The topology can be simply designed for the single-phase version (for off- board EV charging). It operates in G2V (Grid to vehicle) mode.

- It substantially improves the harmonic profile by synthesising three levels at the line voltage.
- All other capacitor voltages are automatically balanced; there is no need for any complicated control techniques; only the output voltage must be balanced.
- It functions in boost mode and has an output voltage range of 12–48 V.
- Operate in continuous conduction mode to eliminate requirement of bulky filters.

A continuous mode DSP based charger is used to provide a PWM control signal to operate a switching device in an AC-DC conversion. DC power supply is giving to a battery model. The power electronics component and DSP processor along with components are shown in Fig. 23.2. The digital signal processing technology is constantly evolving to improve the structure, data, and instructions that can be accessed separately. By taking use of this, the process can be completed much more quickly. The DSP is faster at multi-processing than the typical controller since it has a separate hardware multiplier which increases performance [10]. The charger model for the simulation is presented in Fig. 23.1 with simulink blocks. The charger model for the addressed topology is presented in Fig. 23.2 with block-diagram along with hardware components. Power factor without Correction as shown in Fig. 23.3 and corrected pf presented in Fig. 23.4, to reduce the harmonic distortion of the input current waveform with the goal to improve the efficiency of power delivery. To match the input voltage waveform in an active PFC, a boost converter modifies the input current waveform, resulting in a near unity power factor as shown hardware result in Fig. 23.5. PFC reduces the reactive power consumption of the charger and improves efficiency, especially at low line voltages. DSP based active PFC battery charger incorporates this technique to improve the efficiency of the charging process as shown in Fig. 23.6 and hardware result shown in Fig. 23.7. The charger uses a digital signal processor to manage and control the charging process while performing active power factor correction as shown in Fig. 23.8, additional protocols are maximizing the expected battery cycle life within a fixed charging time and SOC range include pulse charging, fast charging and controlled charging.

23.5 Result and Analysis

To serve the objective of sustainable and efficient charger, the response is observed under input voltage regulation, active pf correction, battery monitoring, charging control, safety features and output voltage regulation.

In input voltage regulation, the charger regulated the input voltage to ensure that it is within the appropriate range for charging the battery as shown in Figs. 23.6 and 23.7. Hence the voltage has been controlled to prevent damage to the battery and ensure safe operation. In active power factor correction, charger performed corrected active power factor results in improved efficiency of the charging process as seen in Figs. 23.4 and 23.5. It can be seen the input voltage waveform and adjusting the input current waveform using a boost converter and control circuit. In battery

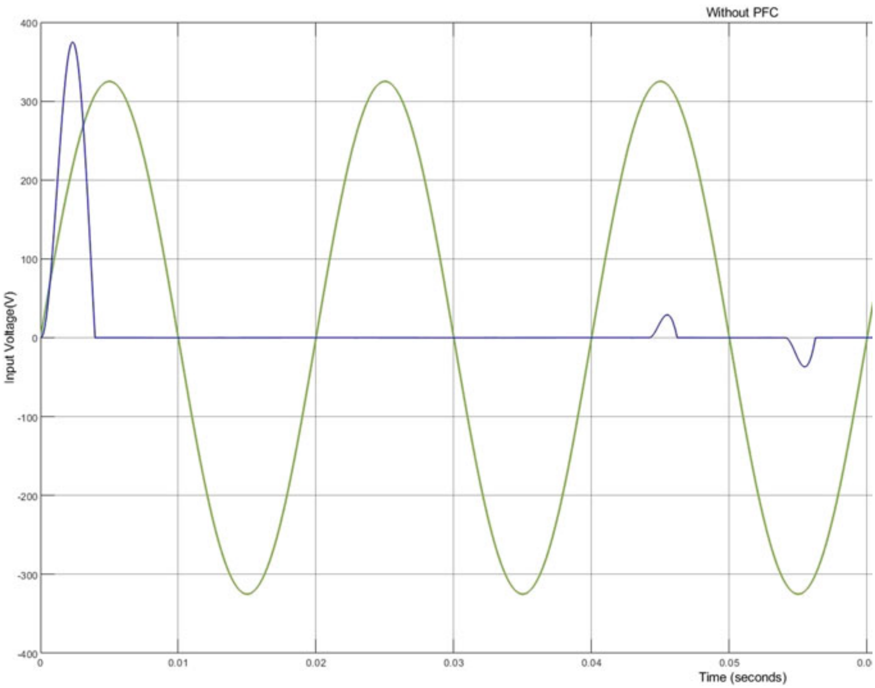

Fig. 23.3 Charger input without power factor correction

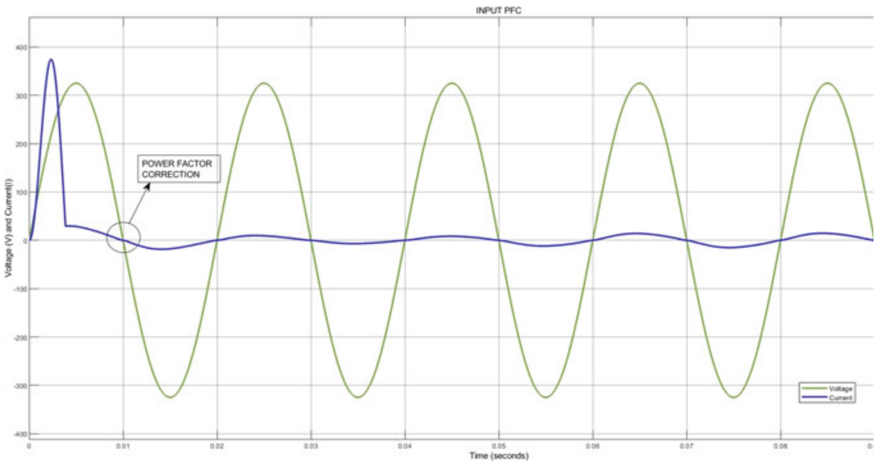

Fig. 23.4 Charger input with power factor correction

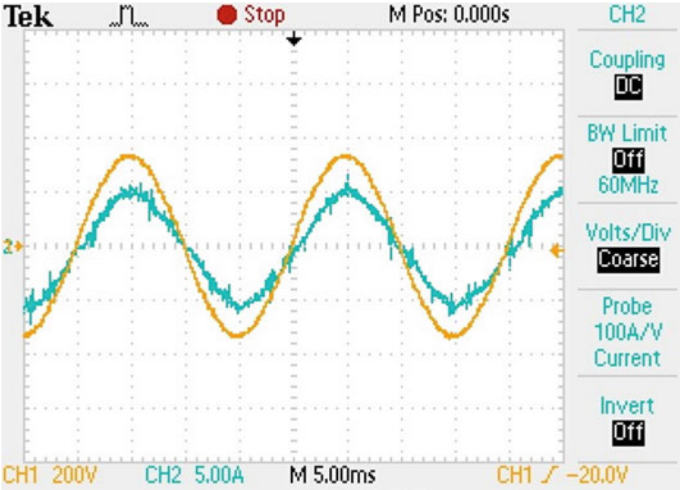

Fig. 23.5 Hardware input power factor corrected: Yellow-voltage, blue-current

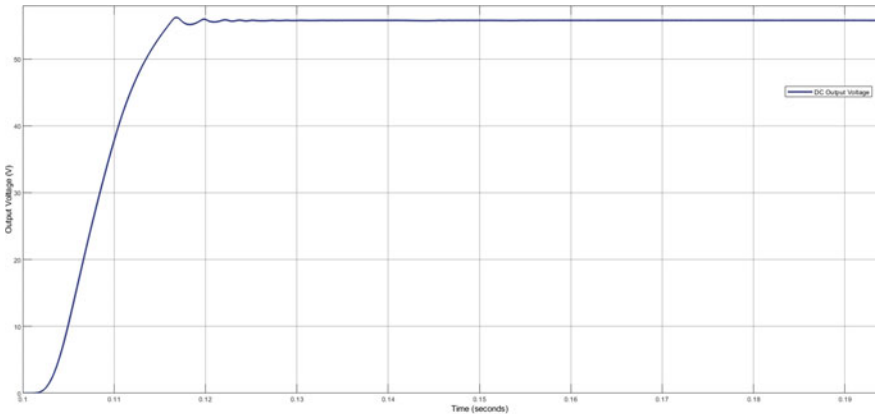

Fig. 23.6 Constant DC output voltage

monitoring, charger monitors the battery's state of charge and condition. This is typically carriedout with sensors which measures the battery's voltage, current and temperature. In Charging control, charger controlled it's process and involve adjusted charging voltage and current to ensure battery safely and efficiency.

Safety features had charger with over-voltage protection, over-current protection and temperature monitoring, to prevent damage to the battery with safe operating condition. Output voltage regulation, regulates the output voltage within the appropriate range for the device to be connected for charging. An AC main supply is passed through an EMI filter to reject the noise or the magnetic interference from

Fig. 23.7 Hardware constant DC output voltage

Fig. 23.8 Output voltages ranges for three line input voltages

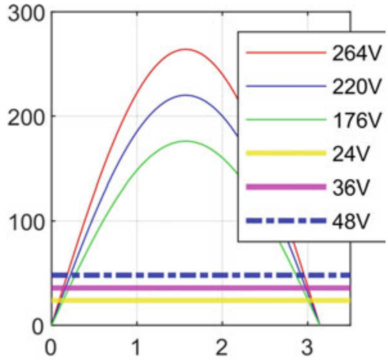

the input supply. Further fed to a full wave bridge rectifier, the output of the rectifier is boosted using a boost circuit with active PFC control in order to extract the maximum power for higher efficiency. The PFC controller used is UCC28180 Texas to make for a longer life. Thus obtained DC voltage (390 V) is stepped down using a H-Bridge DC-DC conversion. Here the H-Bridge DC-DC conversion involves the transformer circuit for isolation between input and output, along with a diode rectifier. The DSP-Controller monitors the input voltage, input current, DC-Bus voltage, Output voltage, Output current and drives the H-Bridge with a precise PWM control with a digital PID controller. Hence, topology meets the requirement of providing the output voltage to charge battery at range of voltages between 12 V, 24 V, 36 V and 48 V with a maximum current of 50 A.

23.6 Conclusion

DSP-based charger is providing advanced control and monitoring of the charging process, resulting in improved efficiency, accuracy, and safety compared to traditional chargers. The advanced digital signal processing techniques with DSP—based charger can deliver fast and reliable charging performance as well as protecting the battery from damage and ensuring long-term sustainability. The built-in power factor correction improves its efficiency. DSP based charger is very useful for range of electric vehicle battery charging topologies. The battery charging cost has been minimized as compared to the existing battery chargers and the charging time is reduced to practical level. DSP based chargers are very efficient and available for battery banks of various voltage levels: 12V, 36V and 48V.

References

1. Lin, F.-J., Huang, M.-S., Yeh, P.-Y., Tsai, H.-C., Kuan, C.-H.: Dsp-based probabilistic fuzzy neural network control for li-ion battery charger. IEEE Trans. Power Electron. **27**(8), 3782–3794 (2012)
2. Farahani, G.: Dc–dc series-resonant converter with multi-stage current-driven for balance charger of series-connected lithium-ion batteries. IET Power Electron. **14**(5), 992–1007 (2021)
3. Yilmaz, M., Krein, P.T.: Review of battery charger topologies, charging power levels, and infrastructure for plug-in electric and hybrid vehicles. IEEE Trans. Power Electron. **28**(5):2151–2169 (2012)
4. Shi, C., Tang, Y., Khaligh, A.: A single-phase integrated on-board battery charger using propulsion system for plug-in electric vehicles. IEEE Trans. Veh. Technol. **66**(12), 10899–10910 (2017)
5. IEEE Standards Board.: IEEE Standard for Interconnecting Distributed Resources with Electric Power Systems: 1547–2003. IEEE
6. Alam, M.S., Ahmad, A., Khan, Z.A., Rafat, Y., Chabaan, R.C., Khan, I., Al-Shariff, S.M.: A bibliographical review of electrical vehicles (xevs) standards. SAE Int. J. Altern. Powertrains 7(1):63–98 (2018)
7. Daly, J.M.: Changes in the 2002 national electrical code. IEEE Trans. Ind. Appl. **38**(4), 974–980 (2002)
8. Hassoune, A., Khafallah, M., Mesbahi, A., Nouaiti, A., Bouragba, T.: Experimental implementation of a smart battery charger for electric vehicles charging station. Int. J. Power Electron. Drive Syst. **11**(4), 1689 (2020)
9. Neira, S., Pereda, J., Rojas, F.: Three-port full-bridge bidirectional converter for hybrid dc/dc/ac systems. IEEE Trans. Power Electron. **35**(12), 13077–13084 (2020)
10. Jianning, L.: The design of dsp electric vehicle charging power supply. Veh. Dyn. **1**(1) (2017)

Chapter 24
Effect of Rotor Tip and Stator Hub Clearance on Aero Performance in Axial Flow Compressors for Aero Gas Turbine Engines

Manjunath S. Dalbanjan and Niranjan Sarangi

Abstract Gas turbine engines are widely used as power plants. Absence of reciprocating and rubbing parts in gas turbine engine helps in lower consumption of lubrication oil and provides higher power to weight ratio with high reliability, apart from reduction in balancing and vibration problems. Turbine inlet temperature and efficiency of components are two main factors which are responsible for gas turbine engine performance. Compressor is one of the main component which directly influences the efficiency of the gas turbine engine. The tip clearance causes leakage of flow which interacts with the main passage flow and the wall boundary layer region causing performance deterioration in compressors. The efficiency and compressor operating envelop gets impacted with the tip leakage flow. In this study, a steady state analysis has been carried out to understand the combined effect of radial clearance on rotor and the stator hub on the aerodynamic performance of intermediate stage axial flow compressor through three dimensional viscous analysis using ANSYS CFX-19.2. The analysis was carried out for 30 different tip and hub clearance configurations varying from 0 to 6% of rotor tip axial chord. Out of 30 configurations only 11 combination of hub and tip clearance were selected meeting the design requirement of surge margin. The study concluded that out of 11 configurations, the combination having 1.5% rotor tip clearance and 3.0% stator hub clearance resulted into higher efficiency of 3%, higher pressure ratio of 4% and surge margin improvement from 15 to 18.3% a gain of about 22%. It is also observed that the stator performance is better with hub clearance for the configuration under investigation.

M. S. Dalbanjan (✉) · N. Sarangi
DRDO-GTRE—Gas Turbine Research Establishment, Bengaluru, India
e-mail: manju131@gmail.com

Visvesvaraya Technological University, Belagavi, Karnataka, India

P. H. V. S. Talpa Sai et al. (eds.), *Intelligent Manufacturing and Energy Sustainability*,
Smart Innovation, Systems and Technologies 372,
https://doi.org/10.1007/978-981-99-6774-2_24

24.1 Introduction

The axial flow compressors are preferred choice mainly for gas turbine power plants and specifically in aircraft applications. The performance of the compressor dictates the operating envelope of the gas turbine engines. Achieving a wide operating range and maximize efficiency of compressor poses a challenging task to the designer. The operating range in axial flow compressor is defined by choke point and stall point within which the compressor can perform efficiently. The tip leakage flow has certain effect on the operating range which will significantly effects the performance of the compressor. Various methodology were studied to understand the tip leakage flow physics due to radial clearance at the tip and hub of rotor and stator blades respectively by Donghyun [1]. Mitesh et al. [2] presented the effect of casing treatment for stability enhancement of a single stage transonic axial flow compressor. For higher tip gap the trailing edge separation was dominated and was responsible for compressor stalling. Baojie et al. [3] showed that the formation of tip leakage vortex makes the flow unstable and initiate the stalling process with loss in performance. Subbaramu et al. [4] investigated the effect of radial clearance and rotor solidity on the secondary flow interaction in a compressor stage. The study showed that increase in radial clearance will reduce the stall margin and efficiency. Gong et al. [5] showed that due to presence of tip gap, the leakage vortex was observed at the downstream of the blade row and flow disturbance near the tip. Xicheng et al. [6] studied various linearly variable radial gaps and uniform tip gaps by using numerical methods. The results showed there is considerable effect on the performance of the compressor due to various tip gap configuration. Songtao [7] observed at the design condition, the leaked flow travels through blade passage and interrupts the flow on the adjacent blade. At choke and stall condition tip circulation moves downstream along streamwise direction causing flow turbulence and large wakes. John et al. [8] showed the loss in the flow rate measurement in a multi stage axial flow compressor due to tip leakage flow. The study showed that the loss in the flow measurement is to the tune of 7% due to the reverse flow caused by tip leakage on the suction surface of blade. Most of the studies are limited to radial clearance for the rotor alone the combined effect of radial clearance on rotor as well as stator is not studied in detail. The emphasis of this study is to evaluate the combined effect of radial tip clearance on rotor and hub clearance on stator on aerodynamic performance of an intermediate stage axial flow compressor.

24.2 Methodology

The steady state 3D CFD analysis is carried out to study the combined effect of tip clearance at the rotor and hub clearance at the stator on the aerodynamic performance parameters using Ansys CFX 19.2. The computational methodology followed for the analysis process is explained below.

24.2.1 CFD Code Validation Study

Computational fluid dynamics (CFD) has emerged as a most powerful tool for determining the flow physics inside the casing for turbo machinery applications. Prior to testing of the actual components complete evaluation of the design can be done using CFD. A careful validation should be done with the standard test case before adopting any CFD software. Hence an assessment of Ansys CFX tool was carried out to check the suitability of the tool for the turbo machinery application. For assessment of the CFD tool used in this study, a validation study was done by considering NASA stage 37 test case. It is a single stage transonic compressor and the details of geometry and boundary conditions are mentioned in the paper by Reid and Moore [9]. A detailed analysis is carried out using Ansys 19.2 CFD tool by Dalbanjan and Sarangi [10] and the outcome of analysis is compared with experimental results of NASA stage 37. The study showed pressure ratio and massflow are within 1% error band, but efficiency is predicted slightly higher compared to test data. The comparison of CFD analysis and experimental data is shown in the Figs. 24.1 and 24.2.

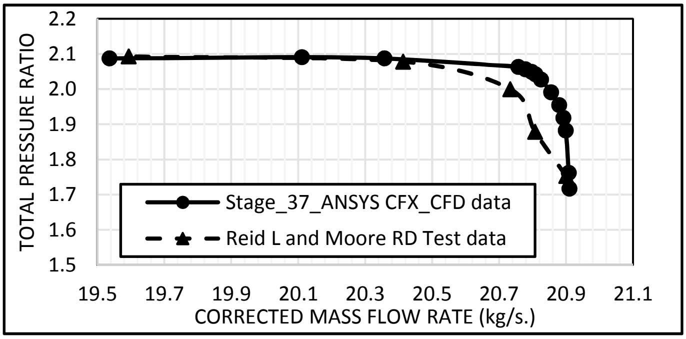

Fig. 24.1 Mass flow rate versus pressure ratio for NASA stage 37

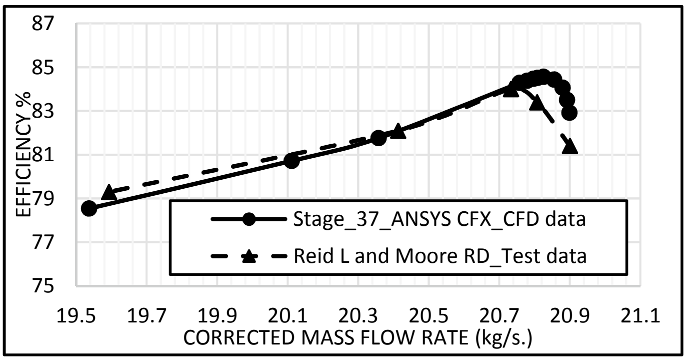

Fig. 24.2 Mass flow rate versus efficiency for NASA stage 37

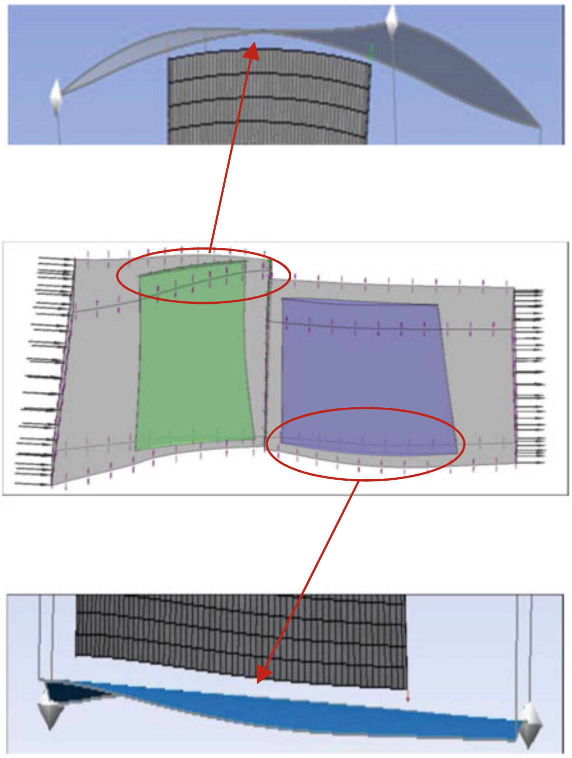

Fig. 24.3 Rotor tip clearance. Geometric model of rotor and stator domain. Stator hub clearance

24.2.2 *Solid Modeling of Blade Geometry in Flow Domain*

A 3D geometric modeling using the 3D modeling software is carried out. The geometric model consists of inlet and outlet domain, rotor blade and stator blade. The domain at inlet and outlet is extended so that the flow at inlet of rotor and outlet of stator is developed and settled. Single rotor and stator domain is considered for analysis so that the computational time can be reduced. The next step is to discretize the entire domain in to number of elements. Figure 24.3 shows the rotor and stator geometric model. Figure 24.3 shows the rotor tip clearance and stator hub clearance respectively.

24.2.3 *Grid Generation and Grid Convergence Study*

Grid independence or convergence study ensures the results are independent of mesh size. Grid independence study is carried out by considering four different grid size configurations. H- type topology is selected for flow domain and near blade surface O- type topology is used. In the tip and hub clearance region around 10 elements with

Fig. 24.4 Mesh domain for rotor and stator

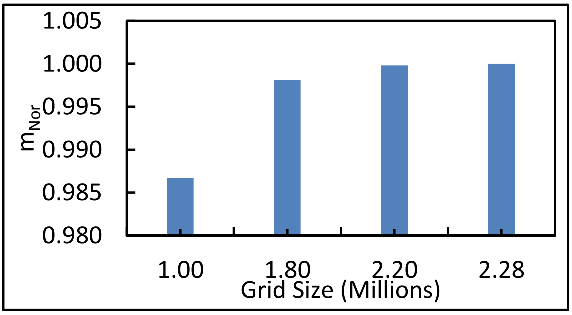

Fig. 24.5 Grid size versus normalised massflow rate

proper interface alignment and non matching grid topology is considered. The mesh distribution is done circumferential, stream and span wise direction on the rotor and stator blade surface, but near casing wall higher grid density is used to maintain y + < 2. Minimum angle is kept less than 165 degree whereas maximum angle and determinant value is greater than 20 degree and 0.6 respectively is maintained to achieve required grid quality. For the analysis k-ω with SST turbulence viscosity model along with high resolution turbulence numeric and advection scheme is selected. Mesh for both rotor and stator stage domain is generated as shown in Fig. 24.4. Grid independence study is performed to arrive at the final grid size. Four different cases is considered by varying number of grids in rotor and stator domain and their performance parameters are shown in Figs. 24.5 and 24.6. It can be seen that from the case-2 onwards the variation in performance parameters are negligible. Thus for further analysis case-3 is selected with grid size of 2.20 million elements.

24.2.4 Boundary Condition

Selection and application of appropriate boundary condition plays crucial role to achieve the reliable analysis results. At inlet total pressure and total temperature is

Fig. 24.6 Grid size versus normalised total pressure ratio

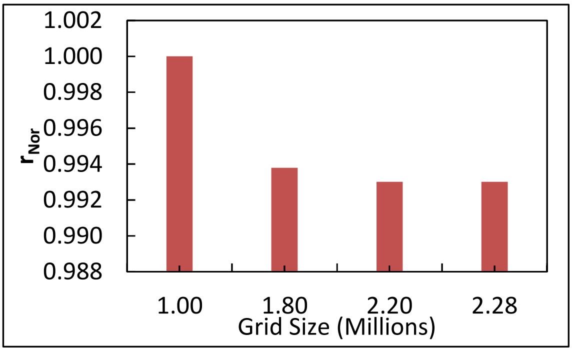

applied, at the interface between rotor and stator stage mixing model is selected. The static back pressure is applied at the stator exit. No slip wall boundary condition at blade hub and casing is specified.

24.2.5 Solution Methodology

Various combination of tip and hub clearance values ranging from 0 to 6.0% of rotor tip chord is analyzed. A total of 30 different combinations are considered for analysis. 11 Combinations out of 30 are selected which were meeting design surge margin requirement. The 11 combinations are shown in Table 24.1. The simulation is carried out using Ansys CFX-19.2 solver. Compressor characteristics are generated by keeping the speed constant and at the stator outlet increasing the static back pressure. Near stall point the static back pressure is increased in smaller steps of 1 kPa and the residual convergence level for all the parameters is specified as 1×10^{-6}.

24.3 Results and Discussion

The simulation is carried out at design speed and the constant speed characteristics are generated for various tip and hub clearance. Figure 24.7 shows the corrected mass flow rate versus total pressure ratio for various combination of tip and hub clearance configuration from 0 to 6.0% of rotor tip chord. It can be seen that the zero % clearance is giving highest mass flow due to absence of tip leakage flow. However the presence of circular vortex at the hub and tip of rotor in the flow passage causes the total pressure ratio to drop. Thus the zero clearance may not be the ideal or best performing condition. The results obtained shows that the combination having rotor tip clearance of 1.5% and stator hub clearance of 3.0% yields maximum performance parameters like pressure ratio and efficiency and wider operating envelope. It is also

Table 24.1 Showing tip and hub clearance for rotor and stator

Sl. No	Rotor tip clearance (%)	Stator hub clearance (%)	Case name
1	0.0	0.0	R0.0 + S0.0_%RCLR
2	1.5	0.0	R1.5 + S0.0_%RCLR
3	1.5	1.5	R1.5 + S1.5_%RCLR
4	1.5	3.0	R1.5 + S3.0_%RCLR
5	3.0	3.0	R3.0 + S3.0_%RCLR
6	3.0	4.5	R3.0 + S4.5_%RCLR
7	3.0	6.0	R3.0 + S6.0_%RCLR
8	4.5	4.5	R4.5 + S4.5_%RCLR
9	4.5	6.0	R4.5 + S6.0_%RCLR
10	6.0	3.0	R6.0 + S3.0_%RCLR
11	6.0	6.0	R6.0 + S6.0_%RCLR

seen that the massflow and pressure ratio deteriorates as the rotor and stator clearances are increased. The drop in massflow is around 1%, but the gain in peak pressure ratio from (0,0) clearance to the (1.5%, 3%) i.e. the combination of 1.5% tip clearance in rotor and 3% hub clearance in stator is 4.0%.

Figure 24.8 shows corrected mass flow rate versus efficiency. It is observed that for all the possible combination, the case of rotor tip clearance of 1.5% and stator hub clearance of 3.0% gave maximum efficiency compare to zero tip and hub clearance. The efficiency with the zero clearances is lower by 3 points due to formation of circular vortex at the hub and tip region creating higher losses. Further increase in the tip clearance, drop in efficiency by 6 points is observed.

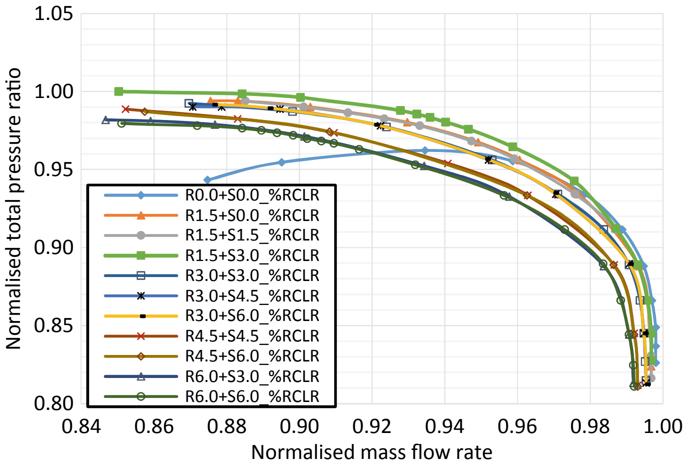

Fig. 24.7 Normalised corrected mass flow rate versus total pressure ratio

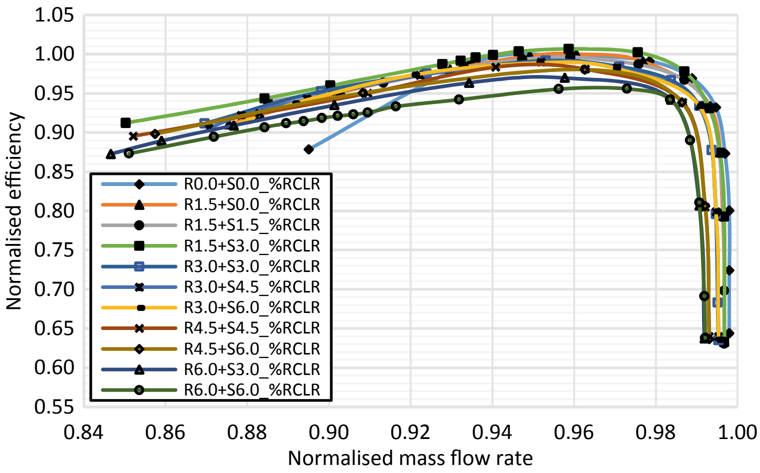

Fig. 24.8 Normalised corrected mass flow rate versus efficiency

Figure 24.9i shows variation of normalised total pressure versus normalised span for the rotor and stator blade for three different configuration i.e. R0 + S0%, R1.5 + S3.0% and R6.0 + S6.0% at design point. From the rotor plot it can be observed that up to 50% of blade span, there is no difference of total pressure. However after 50% span improvement in total pressure was observed for the R1.5 + S3.0% case. This higher total pressure helps to get better pressure ratio for the stage. Figure 24.9ii shows variation of normalised total pressure versus normalised span of the stator. The plot shows the stator tip is affected by the rotor tip clearance swirl flow and the hub clearance effect is not significant as compare to rotor tip clearance. The average total pressure for case R1.5 + S3.0% is higher compare to R0 + S0% and R6.0 + S6.0% configuration. The tip leakage vortex is up to 10% of span for the R6.0 + S6.0% configuration. This is the reason for lower efficiency at the higher tip clearance.

Figure 24.10i plot shows spanwise variation of relative Mach number at rotor exit at design point for the tip clearance of various configuration. It is observed from the plot that at the tip Mach number shows higher value for R1.5 + S3.0% compare

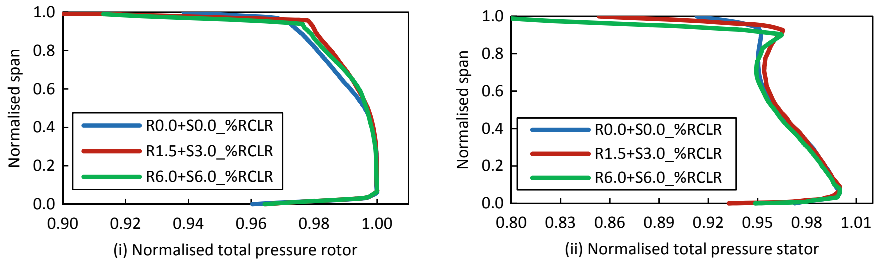

Fig. 24.9 Variation of total pressure across span of the **i** rotor and **ii** stator

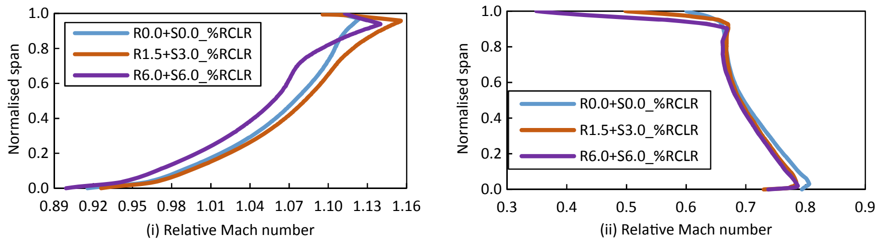

Fig. 24.10 Spanwise variation of relative Mach No. **i** rotor exit and **ii** stator exit

to R6.0 + S6.0% combination. The rise in the relative tip Mach no is 3% compare to R0.0 + S0.0% condition. Figure 24.10ii shows spanwise variation of relative Mach number at stator exit at design point for the tip and hub clearance of various configuration. It is observed from the plot that at the hub Mach number is reduced for R1.5 + S3.0% compare to R0.0 + S0.0% combination. The reduction in the relative Mach number is 2.5% compare to R0.0 + S0.0% condition.

Figure 24.11i shows the blade loading plot for rotor at mid span for the tip and hub clearance of various configuration for design point. Rotor is performing better up to 60% of span but due to higher tip clearance the drop in static pressure is observed. Figure 24.11ii shows the blade loading plot for stator at mid span for the tip and hub clearance of various configuration at design point. The effect of tip and hub clearance is not very dominant on the blade loading parameters of stator. The blade loading is more or less uniform throughout the stator blade and is performing as designed.

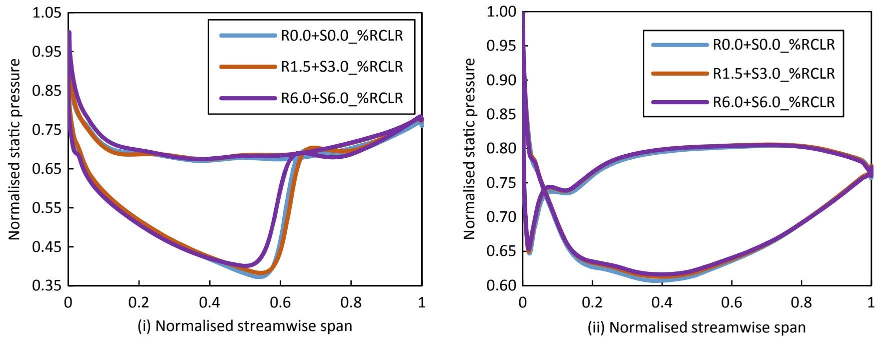

Fig. 24.11 Blade loading plot for i rotor and ii stator at mid span

24.4 Conclusions

A 3D steady state viscous CFD analysis is carried out to investigate the sensitivity of tip and hub clearance on the aerodynamic performance of a intermediate single stage axial flow compressor using ANSYS CFX 19.2. The analysis is carried out for 30 different tip and hub clearance configuration varying from 0 to 6% of rotor tip axial chord. Out of 30 configurations only 11 combinations of hub and tip clearance are selected which were meeting the design requirement of surge margin. Out of 11 configurations the combination having rotor tip clearance of 1.5% and stator hub clearance of 3.0% yields 3% higher efficiency, 4% higher pressure ratio and surge margin improvement from 15 to 18.3% offering gain of 22%. The study also showed that the stator performs better if hub clearance is provided and helps to improve efficiency without disturbing the blade loading. The characteristics plots like corrected mass flow rate versus pressure ratio and corrected mass flow rate versus efficiency are generated for various tip and hub clearances at design speed. The study concluded that the zero tip clearance is not yielding higher pressure ratio and highest efficiency. It is also observed that the rotor tip clearance plays a dominant role compared to stator hub clearance in improving or deteriorating the engine performance.

References

1. Donghyun, Y.: Progress in large-eddy simulation of a rotor tip clearance flow. In: 12th Annual DOD HPCMP User Group, Conference, Austin, TX (2002)
2. Goswami, M., Alone, D., Inoue, M., Kuroumaru, M., Yoshida, S., Minami, T., Yamada, K. Furukawa, M.: Flow behavior in a single stage transonic axial flow compressor with diminishing to large rotor tip clearances in the presence of axisymmetric circumferential grooved casing treatment. In: Proceedings of the Asian Congress on Gas Turbines, ACGT2016-03, IITB, Mumbai, India (2016)
3. Liu, B., Yu, X., Wang, H., Liu, H., Jiang, H., Chen, M.: Evolution of the tip leakage vortex in an axial compressor rotor. In: Proceedings of ASME turbo Expo GT2004-53703, Power for Land, Sea, and Air, June 14–17. Vienna, Austria (2004)
4. Subbaramu, S., Nagpurwala, Q.H., Varpe, M., Narahari, H.K.: Effect of tip leakage and secondary flow interaction on the performance and stability of a transonic axial compressor stage. In: Proceedings of the Asian Congress on Gas Turbines, ACGT2016–133, IITB, Mumbai, India (2016)
5. Gong, H.L., Je, H.B.: A numerical study on the structure of tip clearance flow in a highly forward swept axial–flow fan. In: Proceedings of ASME FEDSM (2002)
6. Jia, X., Wang, Z., CAI, R.: Numerical investigation of different tip gap shape effects on aerodynamic performance of an axial–flow compressor stator. In: Proceedings of ASME TURBO EXPO 2001, New Orleans, Louisiana, USA, 2001-GT-0337 (2001)
7. Songtao, W., Zhongqi, W.: The tip and hub leakage flow of a repeated two stage compressor. In: Proceedings of ASME TURBO EXPO 2002, Amsterdam. The Netherlands, GT-2002–30437 (2002)
8. Trevor John, W., Susan Prahst, P.: 3-D digital piv measurements of the tip clearance flow in an axial compressor. In: Proceedings of ASME TURBO EXPO 2002. Amsterdam, The Netherlands, GT-2002–30643 (2002)

9. Reid, L., Moore, R.D.: Design and overall performance of four highly loaded high speed inlet stages for an advanced high pressure ratio core compressor. In: NASA TP 1337 (1978)
10. Dalbanjan, M.S., Sarangi, N.: An effect of tip clearance on aero performance in axial flow compressors for aero gas turbine engines. In: Int. J. Mech. Prod. Eng. Res. Dev. **9**(4), 769–776 (2019)

Chapter 25
Efficiency Enhancement and Energy Optimization in Alloy Steel Drilling: An Experimental and Statistical Analysis

Ardamanbir Singh Sidhu, Raman Kumar, Sehijpal Singh, and Harpreet Kaur

Abstract This study optimizes and model's active energy consumption ($\ddot{A}EC_{m/c}$) during drilling. The experiments were performed using ST52.3 alloy steel with a coated solid carbide drill. The Taguchi approach was employed to design the experiments using an orthogonal array (OA) to explore the critical factors influencing the process. The experiments were conducted using a vertical milling centre machine on cylindrical samples. The outcomes exhibited that the feed rate had the highest percentage contribution to $\ddot{A}EC_{m/c}$, followed by the peck length. A response surface quadratic model (RSM) was developed to predict the $\ddot{A}EC_{m/c}$ based on the experimental. Optimizing the drilling parameters resulted in a significant improvement of 47.5% in $\ddot{A}EC_{m/c}$ compared to the parameters commonly used in the industry. The developed model and optimization approach can aid in improving energy efficiency, reducing energy costs, and enhancing sustainability in the alloy steel during drilling operations.

25.1 Introduction

Reducing energy use and creating effective processes are paramount in the manufacturing and machining industries [1]. Drilling operations, a crucial step in many sectors, including the construction, aerospace, and automotive industries, frequently demand a lot of energy. Therefore, reducing energy use during drilling operations is essential to cut costs, boost productivity, and encourage sustainable practices [2].

A. S. Sidhu · R. Kumar (✉) · S. Singh
Department of Mechanical and Production Engineering, Guru Nanak Dev Engineering College, Ludhiana, Punjab 141006, India
e-mail: sehgal91@yahoo.co.in

H. Kaur
Department of Electrical Engineering, Chandigarh University, Mohali, Punjab 140413, India
e-mail: harpreet.ee@cumail.in

P. H. V. S. Talpa Sai et al. (eds.), *Intelligent Manufacturing and Energy Sustainability*, Smart Innovation, Systems and Technologies 372,
https://doi.org/10.1007/978-981-99-6774-2_25

The efficiency of the energy model in optimizing machine settings for drilling processes was noted by Bi and Wang [3]. According to the simulation findings, the optimization might save 67% of the energy required for the drilling operation. The competitiveness of a firm can be increased by increasing energy efficiency. Kant and Sangwan [4] provided a prediction and optimization model based on combined RSM and GA to estimate energy usage. The findings were found to be accurate to within 4%. Using the model to choose machine tools depending on energy consumption can help various industrial businesses. The value of sustainability in machining procedures was covered by Kant and Sangwan [4]. According to the inquiry, near-dry machining was possible using micro-hole textured cutting inserts to improve tribological qualities. Chen et al. [5] suggested a simulation-based technique that used a virtual machine tool to improve the machining conditions and lower energy consumption. The outcomes revealed that the optimization lowered the machine tool's overall energy usage by 13%. Ramba et al. [6] examined three drilling optimization models based on several factors. The 28% improvement is produced using the rate of penetration model.

According to Chen et al. [5], the real-time drilling productivity forecasting and optimizing approach has high diagnostic accuracy and is very successful at optimizing. It also has an improved energy model with the greatest precision and the least error. A unique method for optimal drilling parameters was proposed by Ramba et al. [6] using the best drilling settings lowered input power by about 7.5%. The machining variables were optimized, and by monitoring low specific cutting energy, a clean surface, and a substantial material removal rate, the possible best solutions may be identified [7]. Bhushan [8] emphasized optimizing cutting parameters in machining processes to increase energy economy. The ideal cutting settings were established using optimization techniques like RSM and the Taguchi method. Researchers can use these tools to identify ideal settings to model the links between cutting parameters and performance indicators.

Tebaldo et al. [9] studied the effect of cutting speeds on tool life, surface finish, and machining costs under different environmental conditions while turning Inconel 718 on a CNC lathe with coated cemented carbide tools. Faga et al. [10] experimented with machining Ti-6Al-4 V with different cooling systems. They studied the effect on human health, tool life, coolant utilization, cutting forces, power demand, and surface quality. Gaitonde et al. [11] applied RSM to develop models for machining power, roughness, specific cutting force, and tool wear while steel turning in the cut and machining time depth. Abhang and Hameedullah [12] applied RSM to make power consumption models of a different order while turning EN-31 steel on the lathe machine. It was stated how much energy was needed to make a Ti6Al4V item printed using EBM. According to the evaluation of the machining phase, the depth of cut and spindle speed should be maintained as high as feasible to minimize the energy usage of this phase [13]. To increase the sustainability of machining, cutting energy consumption must be decreased [14]. Manufacturing companies that use energy waste reduction measures may significantly reduce emissions while assuring they function within energy usage restrictions. Industry energy consumption makes up 50% of worldwide energy [15].

Due to its great strength and endurance, alloy steel is frequently used in industrial applications that require durable materials. However, because of its hardness and toughness, drilling alloy steel presents unique difficulties and requires more energy. Enhancing process effectiveness and minimizing energy waste in alloy steel drilling processes may be accomplished by optimizing drilling parameters and estimating energy consumption [16].

However, despite the significance of energy consumption in drilling operations, there is a lack of comprehensive studies addressing the optimization and modelling of active energy consumption, specifically in the context of drilling alloy steel.

The Taguchi approach, a commonly used design optimization tool, provides a systematic methodology for identifying essential variables that affect process performance [17]. By utilizing OAs and signal-to-noise ratios, the Taguchi method allows for efficient exploration of parameter combinations to determine the optimal levels that lead to improved process outcomes. Response surface modelling techniques provide mathematical models to predict and optimize the response variables based on the experimental data. This research aims to optimize and model the $\text{ÄEC}_{m/c}$ during drilling operations in alloy steel. Manufacturers can reduce energy costs, minimize environmental impact, and enhance operational efficiency by optimizing the drilling parameters. The insights gained from this study can serve as a footing for future research and practical implementation, leading to improved drilling practices and energy-efficiency drilling strategies in the alloy steel industry.

25.2 Materials and Methods

25.2.1 Description of the Experimental Setting

The trials were carried out at Industry Auto International in Ludhiana, Punjab, India. They entailed utilizing a coated solid carbide drill to drill ST52.3 alloy steel. Low-carbon manganese steel ST52.3 is well recognized for its ability to be welded, good impact resistance, and adaptability to extremely cold temperatures. This type of steel has a machinability similar to mild steel and is available in untreated and normalized forms. Solid carbide drills from Namoh Toolings were chosen for their precision, productivity, and operational safety. The exact drill had an external cooling system and a TiAIN coating. These drills were conducted on an airport component called Blickle. Cylindrical specimens of the ST52.3 material were used in the studies to guarantee generalizability, having 56 mm diameter and 77 mm length. According to the L-27 trial plan, three 16 mm diameter holes were in each cylindrical component. A vertical milling centre (VMC) BFW/V-4 with BT-40 standards was the equipment utilized for drilling. A power logger (HIOKI make) was utilized to measure active power and multiplied with drilling time to get active energy consumption $\text{ÄEC}_{m/c}$.

25.2.2 Experiment Design

The Taguchi tactic is widely utilized for designing experiments with OA because it can efficiently identify critical factors that impact operations while minimizing time and resource requirements. This approach is less sensitive to noise and uncontrolled parameters. Genichi Taguchi developed a robust method for experimental design, and two commonly employed techniques are the signal-to-noise ratio (Š/Ň) and OA [18]. The key quality factor in this study was "the smaller, the better." The "smaller-is-better" category of the Š/Ň ratio was used because it was preferable to minimize the average percentage deviation from the goal value $\ddot{A}EC_{m/c}$. The tests used an OA design matrix L-27 with 27 trials and three levels of control dimensions. The input variables comprised the feed-in rate (mm/rev.) at levels 0.12, 0.16, and 0.22, the peck length (mm) at levels 5, 10, and 15, and the drill point angle (degrees) at levels 120, 130, and 140. The spindle speed (rpm) at levels 1000, 1200, and 1400 was also included. The trials were planned using Minitab software, considering research, suggestions from tool suppliers, and pertinent drilling operations literature.

25.3 Optimization of $\ddot{A}EC_{m/c}$ for Drilling of ST 52.3

The experimental design and the average value of the $\ddot{A}EC_{m/c}$ obtained after three repetitions are presented in Table 25.1. The Š/Ň ratio value was calculated for average repetition, considering lower values to be better.

The active energy consumption of the machining operation, tracked from the beginning to the end, is represented by the parameter $\ddot{A}EC_{m/c}$. Subtracting the beginning value from the end value yields active energy consumption, especially during milling. As an alternative, the active energy consumption may be calculated using the average active power consumption. In the experiments following the L-27 OA Taguchi design, measurements were taken for $\ddot{A}EC_{m/c}$. A total of 27 experiments were performed, and the results were plotted in Fig. 25.1, illustrating the means and Š/Ň ratios of $\ddot{A}EC_{m/c}$. The objective of the experiments was to minimize $\ddot{A}EC_{m/c}$, therefore considering the "smaller, the better" option. The findings revealed that increasing spindle rpm, feed rate, and peck length decreased in $\ddot{A}EC_{m/c}$. As these factors increased, the machining operation was completed in less time, resulting in lower active energy consumption. It indicated that the third level of A, B, and C, and the second level of D, resulted in the minimum consumption of $\ddot{A}EC_{m/c}$. As a result, the optimal combination for minimizing $\ddot{A}EC_{m/c}$ was determined as A-3 (1400 rpm), B-3 (0.22 mm/rev.), C-3 (15 mm), and D-2 (130°). Implementing these specific factor levels led to an optimum value of $\ddot{A}EC_{m/c}$, which amounted to 0.021 kWh.

Table 25.1 $ÄEC_{m/c}$ for each set of experiments and Š/Ň ratios

Exp. No	Speed (A)	Feed (B)	Peck length (C)	Point angle (D)	$ÄEC_{m/c}$ (kWh)	Š/Ň ratio
1	1	1	1	1	0.045	26.9357
2	1	1	2	2	0.040	27.9588
3	1	1	3	3	0.037	28.6360
4	1	2	1	2	0.038	28.4043
5	1	2	2	3	0.034	29.3704
6	1	2	3	1	0.034	29.3704
7	1	3	1	3	0.036	28.8739
8	1	3	2	1	0.034	29.3704
9	1	3	3	2	0.029	30.7520
10	2	1	1	1	0.040	27.9588
11	2	1	2	2	0.036	28.8739
12	2	1	3	3	0.034	29.3704
13	2	2	1	2	0.034	29.3704
14	2	2	2	3	0.030	30.4576
15	2	2	3	1	0.030	30.4576
16	2	3	1	3	0.031	30.1728
17	2	3	2	1	0.029	30.7520
18	2	3	3	2	0.023	32.7654
19	3	1	1	1	0.040	27.9588
20	3	1	2	2	0.034	29.3704
21	3	1	3	3	0.032	29.8970
22	3	2	1	2	0.033	29.6297
23	3	2	2	3	0.028	31.0568
24	3	2	3	1	0.029	30.7520
25	3	3	1	3	0.030	30.4576
26	3	3	2	1	0.026	31.7005
27	3	3	3	2	0.021	33.5556

25.3.1 Analysis of Variance (ANOVA) for ÄECm/c

ANOVA statistical technique for determining When using an ANOVA, you may examine the variance within and between groups to see if the variations in means are statistically significant [1]. The fundamental principle of ANOVA is to divide the overall variability seen in a data set into two parts: the variability between groups and the variability within groups. There may be disparities in the means of the groups being compared if the variance between groups is noticeably more remarkable than the variation within groups [19]. Table 25.2 summarizes the ANOVA results for the means of $ÄEC_{m/c}$ in the drilling operations and Table 25.3 for the Š/Ň ratios.

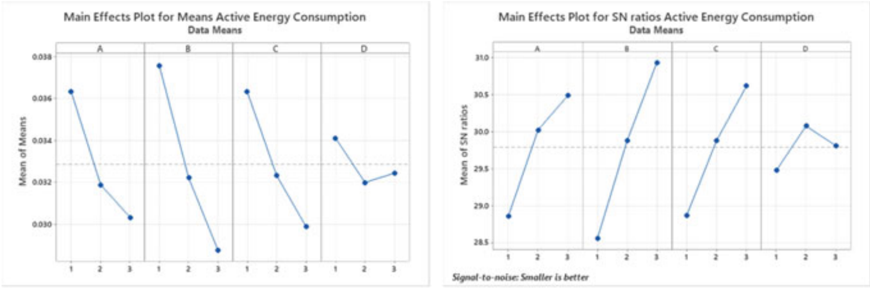

(a) (b)

Fig. 25.1 Graphs for **a** means and **b** Š/Ň ratios of ÄEC$_{m/c}$

Table 25.2 ANOVA for Means of ÄEC$_{m/c}$

Source	DoF	Seq SS	Adj MS	Adj MS	F	p	PC
A	2	0.000175	0.000175	0.000087	76.00	0.000*	23.240
B	2	0.000352	0.000352	0.000176	153.32	0.000*	46.746
C	2	0.000191	0.000191	0.000095	82.97	0.000*	25.365
D	2	0.000022	0.000022	0.000011	9.71	0.013*	2.921
A × B	4	0.000004	0.000004	0.000001	0.90	0.517	0.531
A × C	4	0.000002	0.000002	0.000001	0.52	0.728	0.265
A × D	4	0.000001	0.000001	0.000000	0.13	0.966	0.132
Inaccuracy	6	0.000007	0.000007	0.000001			0.800
Total	26	0.000753					100

Table 25.3 ANOVA for Š/Ň ratios of ÄEC$_{m/c}$

Source	DoF	Seq SS	Adj MS	Adj MS	F	p	PC
A	2	12.7522	12.7522	6.3761	26.38	0.001*	22.459
B	2	25.6433	25.6433	12.8217	53.05	0.000*	45.163
C	2	13.9751	13.9751	6.9876	28.91	0.001*	24.613
D	2	1.6424	1.6424	0.8212	3.40	0.103	2.891
A × B	4	0.8835	0.8835	0.2209	0.91	0.512	1.556
A × C	4	0.3423	0.3423	0.0856	0.35	0.833	0.603
A × D	4	0.0891	0.0891	0.0223	0.09	0.981	0.157
Inaccuracy	6	1.4500	1.4500	0.2417			2.558
Total	26	56.7780					100

The ANOVA results presented in Table 25.2 for the means indicate that the percentage contribution (PC) of the feed rate to $\ddot{A}EC_{m/c}$ was the uppermost at 46.74%, then the peck length at 25.36%, spindle rpm at 23.24%, and point angle at 2.92%. The remaining percentage accounts for the inaccuracy (0.80%). In Table 25.3, the ANOVA results for the Š/Ň ratios of $\ddot{A}EC_{m/c}$ show that the feed rate has the highest percentage contribution at 45.16%, followed by the peck length at 24.61%, spindle rpm at 22.46%, and point angle at 2.89%. The remaining percentage represents inaccuracy (2.56%). The feed rate is the most critical variable for $\ddot{A}EC_{m/c.}$ The point angle, however, does not significantly impact the response $\ddot{A}EC_{m/c}$ for means, although it does for Š/Ň ratios. Additionally, the interactions between factors A × B, A × C, and A × D do not significantly affect the $\ddot{A}EC_{m/c}$ for means and Š/Ň ratios.

25.3.2 Response Surface Model (RSM) of $\ddot{A}EC_{m/c}$

The primary objective of RSM is to create a mathematical model that illustrates how the response variable varies when the explanatory factor values change. The connections between the variables may be deduced from this model, along with forecasts and response variable optimization [20]. RSM is beneficial when there is a complicated and nonlinear connection between the response variable and the explanatory factors. It enables the investigation of the curvature and the interactions between the variables [21]. Equation (25.1) represents the developed RSM for $\ddot{A}EC_{m/c}$ in drilling operations. The coefficients of determination are presented in Table 25.4.

The coefficient of determination for the developed for $\ddot{A}EC_{m/c}$ indicates a strong fit for the model in predicting $\ddot{A}EC_{m/c}$. ANOVA analysis was employed to validate the $\ddot{A}EC_{m/c}$ model; the results are presented in Table 25.5.

$$\begin{aligned}\ddot{A}EC_{m/c} = {} & 0.06415 - 0.00778A - 0.00528B - 0.00444C - 0.00453D \\ & + 0.001444A^2 + 0.000944B^2 + 0.000778C^2 + 0.000806D^2 \\ & - 0.000500A \times B - 0.000944B \times C \end{aligned} \tag{25.1}$$

Table 25.4 Coefficient of determination for $\ddot{A}EC_{m/c}$

Response	R-Sq (%)	Quadratic full	Linear and square	Linear and interactions	Linear	Selected model and terms included	
$\ddot{A}EC_{m/c}$	R-Sq	99.37	98.14	97.22	93.99	99.25	Linear, A^2, B^2, C^2, D^2, A × B, B × C
	R-Sq. (pred)	96.96	95.82	94.01	90.68	97.77	
	R-Sq. (adj)	98.74	97.32	96.19	92.89	98.78	

Table 25.5 ANOVA for ÄECm/c RSM model

Source	DoF	Adj SS	Adj MS	F	P
Model	10	0.000748	0.000075	211.82	0.000
Linear	4	0.000713	0.000178	505.05	0.000
A	1	0.000162	0.000162	458.91	0.000
B	1	0.000347	0.000347	982.19	0.000
C	1	0.000187	0.000187	529.42	0.000
D	1	0.000018	0.000018	49.66	0.000
Square	4	0.000025	0.000006	17.43	0.000
A × A	1	0.000013	0.000013	35.46	0.000
B × B	1	0.000005	0.000005	15.16	0.001
C × C	1	0.000004	0.000004	10.28	0.006
D × D	1	0.000003	0.000003	8.82	0.009
2-Way Interaction	2	0.000008	0.000004	11.83	0.001
A × B	1	0.000003	0.000003	8.50	0.010
B × C	1	0.000005	0.000005	15.16	0.001
Error	16	0.000006	0.000000		
Total	26	0.000753			

The Pareto chart, revealed in Fig. 25.2, aids in evaluating the importance and size of the input variables to the output variable, $\ddot{A}EC_{m/c}$. It offers a graphic depiction of the impact of each input component on ECm/c, listed from highest to lowest. A reference line (shown in red) is displayed in the graph to denote statistically significant input variables. Bars are deemed statistically significant when they pass this reference line. The feed rate (B) has the maximum contribution to $\ddot{A}EC_{m/c}$, followed by the peck length (C), spindle RPM (A), and point angle (D), respectively. The quadratic effects of A^2 come next, followed by the 2-way interaction BC, the quadratic effect B^2, C^2, D^2, and the 2-way interaction AB.

25.3.3 *Confirmatory Experiments and Parameters Used in the Industry*

Taguchi verification experiments, also known as confirmation experiments, are conducted to validate the results obtained from a Taguchi design of experiments and further evaluate the optimized process's robustness [17, 22]. In this case, the Minitab software utilized the Taguchi technique to predict the response variable, $\ddot{A}EC_{m/c}$. Since the optimum value of $\ddot{A}EC_{m/c}$ has been achieved at levels A-3, B-3, C-3, and D-2, which are the same as those used in experiment number 27, and experiment number 27 was repeated three times, separate validation experiments were not

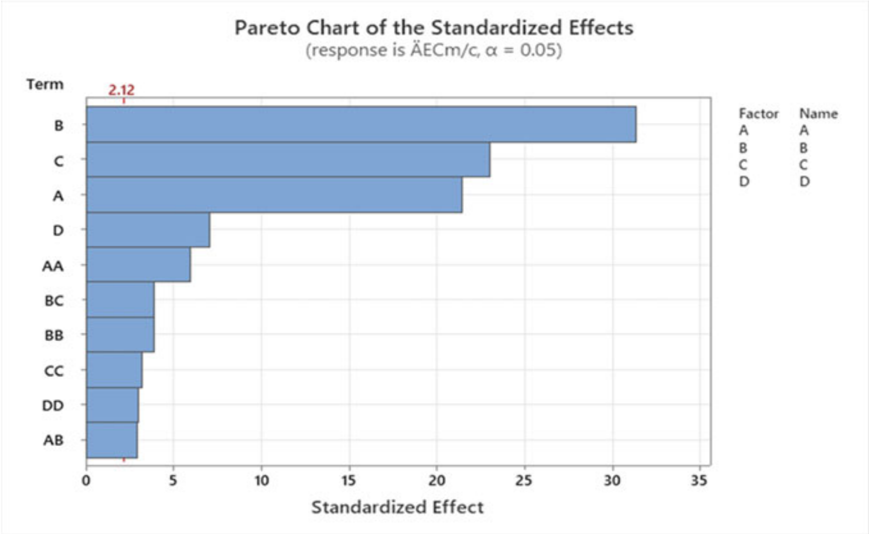

Fig. 25.2 Pareto graph for $\text{ÄEC}_{m/c}$

conducted to confirm the optimal results of $\text{ÄEC}_{m/c}$. It is also evident that the RSM can accurately forecast $\text{ÄEC}_{m/c}$ for drilling ST52.3 alloy steel with a 95% confidence level.

In the industrial setting, the drilling parameters utilized are spindle speed (A) of 1050 rpm, feed (B) of 0.12 mm/rev., peck length (C) of 10 mm, and point angle (D) of 140°. At these parameters, an observed $\text{ÄEC}_{m/c}$ value of 0.048 kWh was recorded. It is noteworthy that at the optimal drilling parameters, there is a significant 47.5% enhancement in $\text{ÄEC}_{m/c}$ compared to the drilling parameters employed in the industry.

25.4 Conclusions

The active energy consumption in ST52.3 alloy steel during drilling operations has been explored using the Taguchi approach and RSM. The Taguchi method facilitated the identification of critical input factors that significantly affect the active energy consumption ($\text{ÄEC}_{m/c}$) in the drilling process. ANOVA and Pareto analysis determined that feed, peck length, and spindle RPM had the most substantial influence on $\text{ÄEC}_{m/c}$. The developed RSM model provided a reliable representation and exhibited high levels of determination (R-Sq.), indicating a strong fit to the experimental data. The verification experiment confirmed the accuracy of the obtained optimum parameters, as they aligned with the levels that yielded the lowest $\text{ÄEC}_{m/c}$. The results indicated a significant improvement in $\ddot{A}EC_{m/c}$ of 47.5% compared to the industry-standard drilling parameters, demonstrating the effectiveness of the optimization process. This study provides valuable insights into optimizing and modelling the active energy consumption in alloy steel drilling operations. By considering the identified influential factors and utilizing the developed models, manufacturers can enhance drilling efficiency and reduce energy consumption, improving productivity and cost savings. Further research can focus on exploring additional factors and refining the optimization process for other machining operations or materials.

References

1. Kumar, R., Bilga, P.S., Singh, S.: An investigation of energy efficiency in finish turning of en 353 Alloy Steel. In: 28th CIRP Conference on Life Cycle Engineering, LCE 2021. Elsevier B.V. (2021)
2. Chandel, R.S., Kumar, R., Kapoor, J.: Sustainability aspects of machining operations: a summary of concepts. Mater. Today Proc. **50**, 716–727 (2022)
3. Bi, Z.M., Wang, L.: Optimization of machining processes from the perspective of energy consumption: a case study. J. Manuf. Syst. **31**(4), 420–428 (2012)
4. Kant, G., Sangwan, K.S.: Prediction and optimization of machining parameters for minimizing power consumption and surface roughness in machining. J. Clean. Prod. **83**, 151–164 (2014)
5. Chen, X., et al.: Real-time prediction and optimization of drilling performance based on a new mechanical specific energy model. Arab. J. Sci. Eng. **39**(11), 8221–8231 (2014)
6. Ramba, V., et al.: Optimization of drilling parameters using improved play-back methodology. J. Petrol. Sci. Eng. **206**, 108991 (2021)
7. Nguyen, T.-T.: Prediction and optimization of machining energy, surface roughness, and production rate in SKD61 milling. Measurement **136**, 525–544 (2019)
8. Bhushan, R.K.: Optimization of cutting parameters for minimizing power consumption and maximizing tool life during machining of Al alloy SiC particle composites. J. Clean. Prod. **39**, 242–254 (2013)
9. Tebaldo, V., di Confiengo, G.G., Faga, M.G.: Sustainability in machining: "eco-friendly" turning of Inconel 718. Surface characterization and economic analysis. J. Clean. Prod. **140**, 567–1577 (2017)
10. Faga, M.G., et al.: Technological and sustainability implications of dry, near-dry, and wet turning of Ti-6Al-4V alloy. Int. J. Precis. Eng. Manuf. Green Technol. **4**(2), 129–139 (2017)
11. Gaitonde, V.N., et al.: Machinability investigations in hard turning of AISI D2 cold work tool steel with conventional and wiper ceramic inserts. Int. J. Refract Metal Hard Mater. **27**(4), 754–763 (2009)
12. Abhang, L., Hameedullah, M.: Power prediction model for turning EN-31 steel using response surface methodology. J. Eng. Sci. Technol. Rev. **3**(1), 116–122 (2010)
13. Cozzolino, E., et al.: Energy consumption assessment in manufacturing Ti6Al4V electron beam melted parts post-processed by machining. Int. J. Adv. Manuf. Technol. **125**(3), 1289–1303 (2023)
14. Li, J., et al.: Tough-brittle transition mechanism and specific cutting energy analysis during cryogenic machining of Ti–6Al–4V alloy. J. Clean. Prod. **383**, 135533 (2023)
15. Pantazis, D., et al.: A design of experiments cyber-physical system for energy modelling and optimization in end-milling machining. Robot. Comput. Integ. Manuf. **80**, 102469 (2023)
16. Sidhu, A.S., Singh, S., Kumar, R.: Optimization and modelling of active power consumption of ST52.3 alloy steel during a drilling operation. Mater. Today Proc. **50**, 1999–2006 (2022)

17. Singh, S., et al.: Aluminum metal composites primed by fused deposition modeling-assisted investment casting: hardness, surface, wear, and dimensional properties. Proc. Inst. Mech. Eng. Part L J. Mater. Des. Appl. **236**(3), 674–691 (2022)
18. Channi, A.S., et al.: Tool wear rate during electrical discharge machining for aluminium metal matrix composite prepared by squeeze casting: a prospect as a biomaterial. J. Electrochem. Sci. Eng. **13**(1), 149–162 (2023)
19. Sidhu, A.S., et al.: Prioritizing energy-intensive machining operations and gauging the influence of electric parameters: an industrial case study. Energies **14**(16), 4761 (2021)
20. Goyal, K.K., et al.: A soft computing-based analysis of cutting rate and recast layer thickness for AZ31 alloy on WEDM using RSM-MOPSO. Materials **15**(2), 635 (2022)
21. Gelis, K., Akyurek, E.F.: Entropy generation of different panel radiator types: design of experiments using response surface methodology (RSM). J. Build. Eng. **41**, 102369 (2021)
22. Krishnaiah, K., Shahabudeen, P.: Applied Design of Experiments and Taguchi Methods. PHI Learning Pvt. Ltd (2012)

Chapter 26
Efficient and Cost-Effective Renewable Energy Integration of Photovoltaic and Hydro in Rural India Using HOMER Pro: A Case Study of Chupki, Punjab

Harpreet Kaur, Raman Kumar, Pulkit Kumar, Swapandeep Kaur, Krishna Kant Dixit, and Hemant Sharma

Abstract This study attempts to supply renewable energy efficiently and cost-effectively. Photovoltaic (PV) and hydro energy potential in Chupki, India, is examined using HOMER Pro v3.14. 161 homes can receive continuous energy from a hybrid renewable energy system (HRES). Optimized PV modules, hydro turbines, converters, and batteries make up the optimal HRES. The top four configurations were selected based on net present cost (NPC) and cost of energy production (COE). The optimal HRES configuration includes a 1510 kW solar array, 1059 kW hydro turbine, 3874 kWh lithium-ion batteries, and a 482 kW converter, achieving 100% renewable energy integration. The optimal HRES was evaluated for economic, technical and renewable energy factors. The findings and optimized HRES configuration can

H. Kaur · P. Kumar
Department of Electrical Engineering, Chandigarh University, Mohali, Punjab 140413, India
e-mail: harpreet.ee@cumail.in

P. Kumar
e-mail: pulkit10001@ieee.org

R. Kumar (✉)
Department of Mechanical and Production Engineering, Guru Nanak Dev Engineering College, Ludhiana, Punjab 141006, India
e-mail: sehgal91@yahoo.co.in

S. Kaur
Department of Electrical Engineering, Guru Nanak Dev Engineering College, Ludhiana, Punjab 141006, India

K. K. Dixit
Department of Electrical Engineering, GLA University, Mathura, India
e-mail: krishnakant.dixit@gla.ac.in

H. Sharma
Department of CSE, IES College of Technology, Bhopal, India
e-mail: hemant.sharma@iesbpl.ac.in

P. H. V. S. Talpa Sai et al. (eds.), *Intelligent Manufacturing and Energy Sustainability*, Smart Innovation, Systems and Technologies 372,
https://doi.org/10.1007/978-981-99-6774-2_26

serve as a basis for similar initiatives in other rural regions, facilitating the transition towards renewable energy sources and enhancing energy access and reliability.

26.1 Introduction

In February 2023, India's renewable energy capacity, excluding big hydro and nuclear projects, was 122 Giga Watts (GW), according to the Central Electricity Authority (CEA) monthly report [1]. This was a 15% rise from February 2022 but 30% short of the central government's 175-GW objective for 2022. India's energy consumption rate falls to third, utmost position in the world, and it is ranked fourth in the world for the total capacity of renewable energy, comprising large hydro, wind, and solar power, according to the REN21 Renewables 2022 global status report [2, 3]. At COP (Conference of Parties) 26, the government increased its 2030 non-fossil fuel energy ambition to 500 GW. This has been proven to be the world's greatest renewable energy growth strategy [4]. In the last 8.5 years, non-fossil fuel capacity has expanded 396% to 178.79 GW (including big hydro), accounting for 43% of its overall capacity (as of May 2023) [5]. The capacity of solar energy is 66.7 GW as of May 2023, rising 24.4 times in 9 years. The capacity of renewable energy sources, particularly huge hydro, has expanded by 128% since 2014 [6].

India aims to lower its carbon intensity by 45% by the end of the decade, install 50% renewable power by 2030, and reach net-zero carbon emissions by 2070. India wants five million tons of renewable hydrogen by 2030, which is supported by 125 GW of renewable energy. India has authorized fifty-seven 39.28 GW of solar plants, and wind energy will have found 30 GW of offshore locations by 2030. India has 168.96 GW of renewable energy capacity, including 82 GW under implementation and 41 GW under bidding. Figure 26.1 shows renewable energy share in GW in India.

26.2 Literature Survey

By optimizing the operational techniques of HRES incorporating hydro, solar, and wind energy sources, it is possible to enhance resource utilization efficiency without requiring additional investments [7]. A case study was conducted in China's upper Yellow River region, where a large-scale hydro-solar-wind HRES was implemented. Compared to a standard operating policy, the findings revealed that the optimal operating rules for the complementary operation of the hydro-solar-wind HRES resulted in a significant increase in energy production and a higher guaranteed rate. Specifically, energy production improved by 5.2%, while the guaranteed rate saw a 4% increase [8]. Wind-solar-hydro hybrid systems were studied due to the depletion of non-renewable energy sources in the Chinese Yalong River basin. Wind-solar-hydro

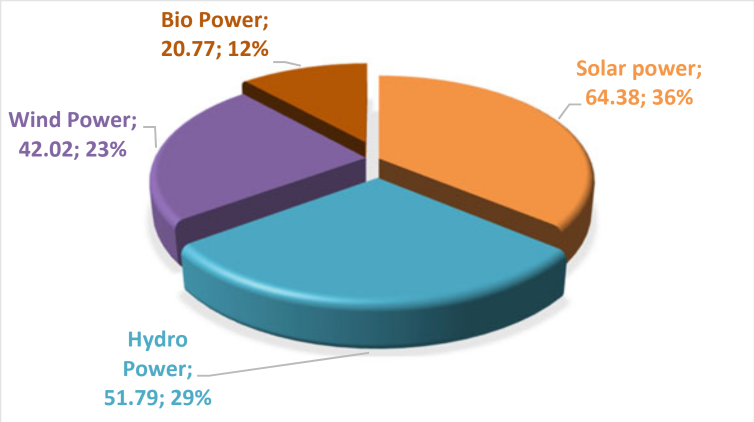

Fig. 26.1 Renewable energy share in GW in India

experimental base used the optimum operation model and simulation-estimation approach [9].

The variability and unpredictability of energy resources pose challenges for energy management in HRES [10]. Bhayo et al. [11] addressed these challenges by investigating the integration of a hybrid PV battery system with a pump-hydro-storage system. The study explicitly explored the utilization of rainfall potential and assessed the probabilities of power supply loss under varying conditions [11]. HRES efficiently combines several renewables and optimizes a hybrid system, including pumped hydro storage, cascade hydropower, run-of-river hydropower, and solar plants [12]. A standalone HRES was examined and optimized for a 3.032 kWh/day dwelling unit with integrated solar PV batteries, collected rainwater, and pumped-hydro storage [13]. According to Homa et al. [14], research on the hybrid solar and hydro system may be able to fulfil utility demands with a single integrated system and resolve operational problems with energy systems that only use one energy source. Solar PV may become the cheapest renewable energy due to its falling cost. Solar PV and hydropower, a reliable regulating power source, may make long-distance transmission electricity affordable. Based on the hydro-solar hybrid power's installed capacity ratio, the reservoir's regulating capacity can be accessed [15]. System stability is threatened by the increasing growth of solar and wind generation, which are unpredictable and intermittent. Sayed et al. [16] proposed a grid-connected hybrid power system that fully exploits hydro, solar, and wind power sources.

The global energy landscape is transforming sustainable and renewable energy sources. However, the efficient and cost-effective renewable energy supply remains challenging, particularly in rural areas. This study aims to address this problem by exploring the potential of an HRES that combines PV and hydro energy in Chupki, Punjab, India. It aims to develop an optimized HRES configuration that efficiently meets 161 households' energy needs. The study examines the feasibility and cost-effectiveness of the proposed HRES by evaluating NPC and COE.

26.3 Materials and Methods

Figure 26.2 depicts the process that is involved in designing the HRES approach. The software program, HOMER Pro v3.14, has been used to optimize the HRES consisting of PV and hydro. The methodology comprises reviewing the literature on HRES and problem formulation, identifying the study area and collecting relevant information, and calculating load and resource assessment. The next step includes designing and simulating HRES, followed by optimization, and in the last step, a discussion of results, implications, vital conclusions and future scope.

26.3.1 Study Location

The chosen location is the Chupki village, which can be found in Punjab, Ludhiana district, India, at coordinates 30.796950 N and 75.837717 E. Details regarding the investigated area are provided in Fig. 26.3. It is accessible through the bypass route canal from Ludhiana. Chupki power station's vertical-axis semi-Kaplan turbines and induction generators run on a syphon inflow mechanism. Although the power plant alone has two hydraulically powered gates to manage water release, the primary canal has three electrically controlled gates that send water into the diversion channel for power generation. Gearboxes and turbines are linked to vertical alternators. Air circuit breakers and 11-kV step-up transformer link the electricity generated to a low-tension bus bar. The site was chosen primarily because getting further data and the actual load was convenient. A survey was conducted for all 161 homes having a population of 967 in the research area of 164 hectares to gather information on energy use.

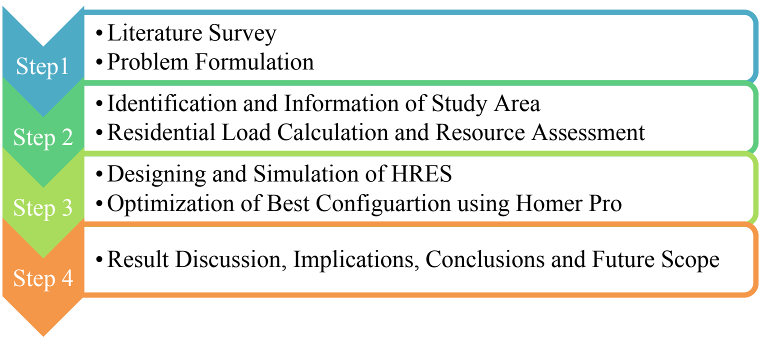

Fig. 26.2 Hybrid system designing and optimization methodology

Fig. 26.3 Location of Chupki Village Alamgir, Punjab, India

26.3.2 Data Collection and Load Profile

Table 26.1 provides information on the power ratings and energy consumption of gadgets typically used in 161 households during the summer and winter of 2022. It includes the number of gadgets in a home and the power rating of the gadget in Watts. The total power rating for all the gadgets in a household is calculated by multiplying the rating by the number of gadgets.

The utilization time in hour/day is the average number of hours the gadget is used per day during the specified season. Load in kWh/day is the energy consumption of the gadget per day calculated by multiplying the total rating by the utilization time and converting it to kilowatt-hours (kWh) by dividing by 1000. The daily load average for one family is 13.3 kWh/day in summer and 10.144 kWh/day in winter. The daily load average for 161 households is 2141.3 kWh/day in summer and 1633.184 kWh/day in winter. Energy consumption is more in summer than in winter. Residential load profiles for both weekends and weekdays for summer and winter are shown in Fig. 26.4. The peak load is observed in July, and the minimum load demand is in January.

Description of load estimation includes the average daily energy demand of 1887.2 kWh/day, indicating the typical energy consumed over 24 h, and is a crucial metric for estimating overall energy requirements and planning. The average load is 78.64 kW, and the peak load is 400.86 kW. The load factor, at 0.2, signifies the ratio of the average load to the peak load. The time-step variability is 20%, the percentage of load fluctuation from one-time step to the next.

Table 26.1 Electric load calculations for the 161 residential households

Gadget	Count in each house	Rating (W)	Total rating (W)	Summer		Winter	
				Utilization time (hour/day)	Load (Wh/day)	Utilization time (hour/day)	Load (Wh/day)
CFL	4	24	96	10	960	14	1344
Ceiling fan	3	54	162	20	3240	0	0
Water pump	1	750	750	5	3750	4	3000
Electric iron	1	1000	1000	1	1000	1	1000
Television	1	100	100	3	300	3	300
Washing machine	1	450	450	1	450	2	900
Refrigerator	1	150	150	24	3600	24	3600
	Daily load average for one family (kWh/day)				13.300		10.144
	Daily load average for 161 households (kWh/day)				2141.300		1633.184

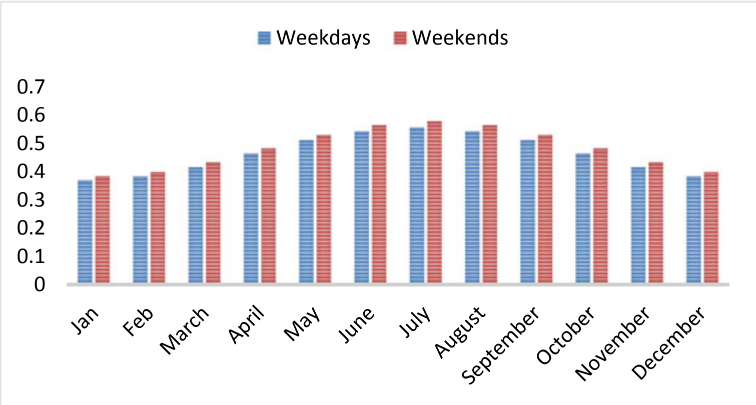

Fig. 26.4 Residential load profile

26.3.3 Resource Assessment

It has been determined that resources are available in the form of solar radiation (kWh/m^2/day) and canal stream flow in litres per second. The selected area has a reasonable amount of water available and receives enough irradiation from the sun. This is the reason why this site is adopted for HRES performance analysis. Figure 26.5 shows the computed daily average solar radiation and clearness index for 2022. These values are 5.18 kWh/m^2/day and 0.6, respectively. The average stream flow of the Chupki Canal may be seen in Fig. 26.6, with a value of 7.95 L per second on average.

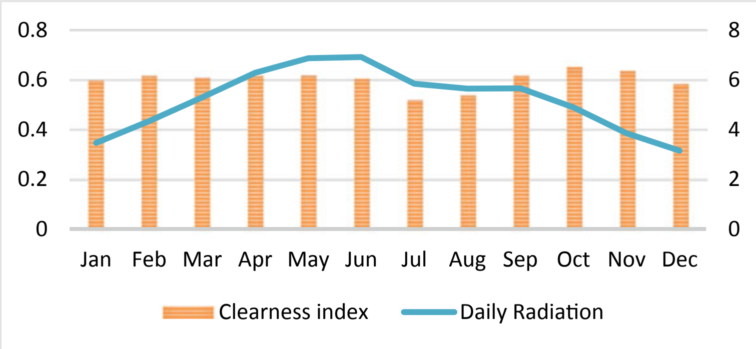

Fig. 26.5 Global horizontal irradiance: clearness index and daily radiation of Chupki

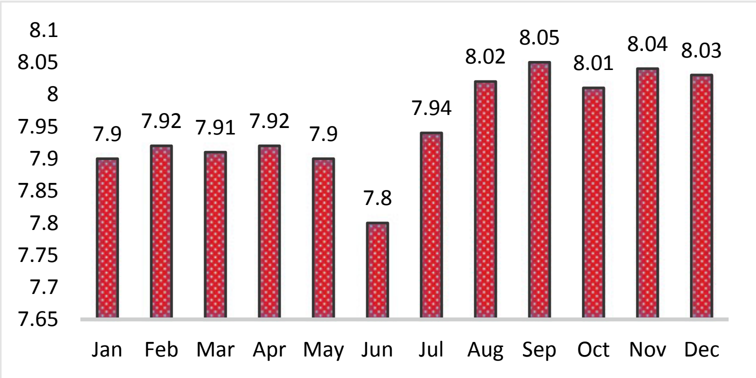

Fig. 26.6 Stream flow of hydro source in litres per second

26.4 Hybrid System Designing and Simulation

The design, simulation, and modelling process for HRES was completed using the HOMER Pro. The HRES consists of PV and hydro energy. The graphical representation of an HRES is shown in Fig. 26.7. For financial calculations, the design considers several constraints, including an 8% interest rate and a 2% inflation rate. The dispatch strategy chosen is cycle charging, ensuring optimal utilization of renewable energy sources. With an annual capacity shortage of 0%, the HRES is designed to meet the complete electricity demand. The system's components have a projected lifetime of 25 years, ensuring long-term sustainability. These constraints collectively influence the economic feasibility and operational aspects of the HRES in providing an uninterrupted and sustainable energy supply in the rural region. The proposed HRES comprised a solar array with a capacity of 1510 kW, a hydro turbine with a capacity of 1059 kW, 3874 lithium-ion batteries with a capacity of 1 kWh, and a converter with a power output of 482 kW.

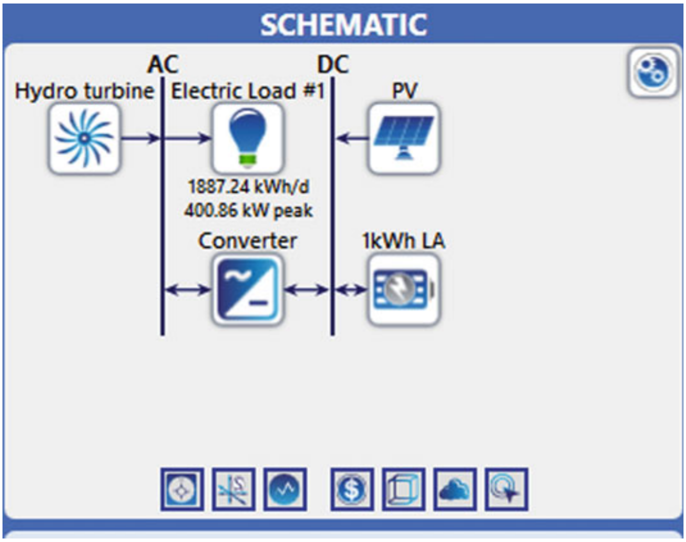

Fig. 26.7 Schematic diagram of a hybrid system

PV and hydro were considered throughout the planning and modeling stages of HRES since they are the resources readily accessible in the selected location. The PV module, hydro turbine, converter, and battery with the static standard will make up the HRES that has been suggested. An optimization process was conducted to enhance the suggested HRES further to determine the most suitable configuration. Each combination of factors, including PV rating, hydro turbine rating, battery capacity, and converter rating, was individually optimized for every system category. This meticulous approach aimed to identify the optimal HRES configuration. The optimization process yielded a total of 1610 potential solutions, out of which 704 were found to be viable, while the remaining 906 were not feasible. From the pool of practical alternatives, the four most favorable combinations of PV, hydro turbine, battery, and converter ratings were selected, considering both technical and economic aspects. These top four configurations were applied to obtain a single, optimal solution that best met the desired criteria. Consequently, the optimization process resulted in a refined HRES design by analyzing many possible solutions and narrowing them down to the most promising options. Table 26.2 provides an overview of the four distinct permutations that were chosen.

The four cases of HRES have corresponding configurations and performance metrics. HRES configuration consists of PV capacity in kW, battery capacity in kWh, hydro turbine capacity in kW, and converter rating in kW for each case. These values represent the optimized sizes of the components used in the HRES. NPC is the total cost of the HRES over its lifetime, considering the initial capital cost and operational costs discounted to present value. It is measured in US dollars ($). COE signifies the average cost of producing one unit of energy (kWh) from the HRES. It

Table 26.2 Simulation and optimization outcomes

HRES	PV (kW)	Battery (kWh)	Hydro Turbine (kW)	Converter (kW)	NPC ($) (M)	COE ($)
Case 1	1510	3874	1059	482	14.9	1.68
Case 2	1560	3986	1059	501	15.1	1.69
Case 3	1510	4243	1059	702	15.1	1.70
Case 4	1510	4819	1059	482	15.2	1.71

is calculated by dividing the NPC by the total energy generation over the system's lifetime. The COE values for each case are denoted in $ per kWh. The performance and cost-effectiveness of each HRES configuration can be assessed by comparing the values.

For instance, Case 1 has a PV capacity of 1510 kW, a battery capacity of 3874 kWh, a hydro turbine capacity of 1059 kW, and a converter rating of 482 kW. Its NPC is 14.9 million $, and the COE is 1.68 $ per kWh. Similarly, the other cases (Case 2, Case 3, and Case 4) have different configurations and corresponding NPC and COE values. These metrics help evaluate the economic viability and efficiency of the HRES configurations, aiding in selecting the most suitable option based on cost and energy production factors.

By comparing the COE of Case-1's optimal HRES compared to previous research. It has been determined that the optimized configuration in this study is superior or highly competitive compared to similar arrangements. The COE of the current PV and hydro HRES is exceptionally low at 1.68 $ per kWh, in contrast to the COE of 613.801 $ per kWh for the bio and hydro HRES in the same Chupki Village, Alamgir, Ludhiana [17]. These findings highlight the significant cost advantages of the optimized PV and hydro HRES proposed in this study. The remarkably low COE demonstrates the potential for achieving highly efficient and cost-effective energy production in Chupki Village. The current HRES configuration is a financially favorable and economically competitive solution compared to alternative renewable energy configurations.

26.5 Implications, Conclusions and Future Scope

26.5.1 Implications

This study has significant implications for renewable energy implementation in rural areas, particularly in emerging nations. An HRES, such as the one proposed in Chupki, can achieve a sustainable and continuous energy supply. The findings showcase the feasibility and cost-effectiveness of integrating PV and hydro energy sources to meet the energy demand of rural communities. The optimized HRES configuration serves as a model for similar regions, enabling the efficient utilization of renewable resources and reducing dependence on conventional energy sources.

26.5.2 Conclusions

The primary objective of this study is to develop and optimize HRES to fulfil the energy needs of 161 typical dwellings in a rural area of Punjab, India. Different HRES off-grid techniques were analyzed from a technological, economic, and ecological perspective, considering the area's existing resources. The optimal PV and hydro-based renewable energy off-grid setup was identified.

The study concludes that the HRES utilizing PV and hydro energy is a viable and effective solution for providing sustainable electricity in Chupki, Punjab, India. The optimized HRES configuration, consisting of a solar array, hydro turbine, batteries, and converter, demonstrated efficient energy generation with 100% renewable integration. Based on the simulation and optimization results, it has been determined that the optimal configuration for the HRES consists of a 1510 kW PV capacity, a 3874-kWh battery capacity, a 1059 kW hydro turbine capacity, and a 482 kW converter rating. This configuration demonstrates an NPC of 14.9 million USD and a COE of 1.68 USD per kWh. The findings of this study indicate that the HRES implemented in Chupki can serve as a successful model for other rural areas seeking to transition to renewable energy sources. By adopting a similar approach, these regions can effectively harness the potential of renewable energy and contribute to the sustainable development of their communities.

26.5.3 Future Scope

The study opens up several avenues for future research and development in renewable energy. Further investigations can explore additional variables and optimization techniques to enhance the HRES configuration. Integrating energy storage technologies and smart grid solutions can improve the system's reliability and stability. Moreover, conducting long-term monitoring and performance analysis of the implemented HRES in Chupki can provide valuable insights for system optimization and efficiency improvements. Additionally, similar studies can be performed in different geographical locations to assess the feasibility and adaptability of the proposed HRES model in diverse rural settings.

References

1. Singh, U., Rizwan, M., Malik, H., García Márquez, F.P.: Wind energy scenario, success and initiatives towards renewable energy in India—a review. Energies **15**, 2291 (2022)
2. Lal, S.R.S., Herbert, G.M.J., Arjunan, P., Suryan, A.: Advancements in renewable energy transition in India: a review. Energy Sour. Part A Recov. Utiliz. Environ. Effects 1–31 (2022)
3. Kumar, R., Channi, H.K.: A PV-biomass off-grid hybrid renewable energy system (HRES) for rural electrification: design, optimization and techno-economic-environmental analysis. J. Clean. Prod. **349**, 131347 (2022). https://doi.org/10.1016/j.jclepro.2022.131347
4. Pandey, R.S., Shukla, S.: Perspective of G20 along with India's cultural values. Knowl. Res. Multidisc. J. **1**, 59–70 (2023)
5. Rauf, A., Nureen, N., Irfan, M., Ali, M.: The current developments and future prospects of solar photovoltaic industry in an emerging economy of India. Environ. Sci. Pollut. Res. **30**, 46270–46281 (2023)
6. Colenbrander, S., Vaze, P., Vikas, C., Ayer, S., Kumar, N., Vikas, N., Burge, L.: Low-carbon transition risks for India's financial system. Glob. Environ. Chang. **78**, 102634 (2023)
7. Kaur Channi, H., Singh, M., Singh Brar, Y., Dhingra, A., Gupta, S., Singh, H., Kumar, R., Kaur, S.: Agricultural waste assessment for the optimal power generation in the Ludhiana district, Punjab, India. Mater. Today Proc. **50**, 700–708 (2022). https://doi.org/10.1016/j.matpr.2021.04.481
8. Li, Y., Ming, B., Huang, Q., Wang, Y., Liu, P., Guo, P.: Identifying effective operating rules for large hydro–solar–wind hybrid systems based on an implicit stochastic optimization framework. Energy **245**, 123260 (2022). https://doi.org/10.1016/j.energy.2022.123260
9. Cheng, Q., Liu, P., Xia, Q., Cheng, L., Ming, B., Zhang, W., Xu, W., Zheng, Y., Han, D., Xia, J.: An analytical method to evaluate curtailment of hydro–photovoltaic hybrid energy systems and its implication under climate change. Energy **278**, 127800 (2023)
10. Shu, X., Kumar, R., Saha, R.K., Dev, N., Stević, Ž, Sharma, S., Rafighi, M.: Sustainability assessment of energy storage technologies based on commercialization viability: MCDM model. Sustainability **15**, 4707 (2023)
11. Bhayo, B.A., Al-Kayiem, H.H., Gilani, S.I., Khan, N., Kumar, D.: Energy management strategy of hybrid solar-hydro system with various probabilities of power supply loss. Sol. Energy **233**, 230–245 (2022)
12. Chen, C., Liu, H., Xiao, Y., Zhu, F., Ding, L., Yang, F.: Power generation scheduling for a hydro-wind-solar hybrid system: a systematic survey and prospect. Energies **15**, 8747 (2022)
13. Bhayo, B.A., Al-Kayiem, H.H., Gilani, S.I., Ismail, F.B.: Power management optimization of hybrid solar photovoltaic-battery integrated with pumped-hydro-storage system for standalone electricity generation. Energy Convers. Manage. **215**, 112942 (2020)
14. Homa, M., Pałac, A., Żołądek, M., Figaj, R.: Small-scale hybrid and polygeneration renewable energy systems: energy generation and storage technologies, applications, and analysis methodology. Energies **15**, 9152 (2022)
15. Melamu, M.T.: Modelling and Control of Hybrid Photovoltaic and Micro-Hydro System. Cape Peninsula University of Technology (2021)
16. Sayed, E.T., Olabi, A., Elsaid, K., Al Radi, M., Semeraro, C., Doranehgard, M.H., Eltayeb, M.E., Abdelkareem, M.A.: Application of artificial intelligence techniques for modeling, optimizing, and controlling of desalination systems powered by renewable energy resources. J. Clean. Prod. **413**, 137486 (2023)
17. Amritpal Singh, A.S.: Analysis of power generation from biogas and mini hydro grid using homer software. Int. Res. J. Eng. Technol. **8**, 1–6 (2021). https://www.irjet.net/archives/V8/i5/IRJET-V8I5855.pdf

Chapter 27
Emerging Power Quality Challenges due to Integration of Renewable Energy Sources in AC/DC Microgrids

Sumalatha Kalakotla and Cheena Korra

Abstract Renewable energy becomes a key contributor to our modern society, but their integration to power grid poses significant technical challenges. (1) Voltage and frequency fluctuations are caused by non-controllable variability of RES. (2) Harmonics, which are caused due to power electronic devices. This suggested hybrid distribution system consists of solar and wind energy sources that must be linked to the grid at a Point of Common Coupling in order to optimize system performance (PCC). Both solar and wind systems use simple Maximum Power Point Tracking (MPPT) algorithms to achieve maximum power under all-weather situations. To maintain the correct voltage at the DC link, a diode clamped multilevel inverter is used. It is controlled by a fuzzy logic controller (FLC) based on vector control methods. The results show that FLC outperforms traditional PI controllers in terms of enhancing the step response of the de link voltage. The paper consists of existing approaches to improve power quality. Furthermore, even when combined with injected active power from a solar-wind hybrid power system, this control methods potently maintains constant grid voltage and also maintain power factor as unity, independent of climatic conditions.

S. Kalakotla (✉) · C. Korra
Department of Electrical and Electronics Engineering, KU College of Engineering and Technology, Kakatiya University Campus, Warangal, India
e-mail: sumalathakala@kakatiya.ac.in

C. Korra
e-mail: korrachinna@kakatiya.ac.in

C. Korra
Department of Electrical and Electronics Engineering, University College of Engineering, Kakatiya University, Kottagudem, India

P. H. V. S. Talpa Sai et al. (eds.), *Intelligent Manufacturing and Energy Sustainability*, Smart Innovation, Systems and Technologies 372,
https://doi.org/10.1007/978-981-99-6774-2_27

27.1 Introduction

Energy is the basic input of life. Among all the different forms of energy, Electricity plays a key role. Today, meeting the world's constant increase in energy demand is a major concern. Furthermore, the rapid depletion and exhaustibility of existing energy sources has necessitated a thorough examination of renewable energy sources (RES) as another source of energy [1, 2]. Among renewable energy sources, solar photovoltaic (PV) and wind power have gained a lot of attention and are considered to be the most rising electricity-producing power technologies [3]. Massive turbines with a large power capacity can be used to harness WE. PV energy has also demonstrated significant potential as a promising power source because it is renewable, overall, clean and unbound, and can be created without toxic contamination [4].

Both of these renewable energy sources, however, have some shortcomings due to their irregular character and reliance on ecological variables such as differences in solar radiance intensity and speed of the wind [5]. The results demonstrated the value of MPPTs in extracting the best potential output power from hybrid systems during changes in the environment. Furthermore, because no reactive power is added, hybrid systems perform well at unity power factor [6]. The Double Fed Induction Generator (DFIG) is frequently utilized due to advantages such as tough construction, active and reactive power regulation, and the ability to obtain maximum power [7]

MPPT algorithms are employed on both solar and wind systems to extract the greatest feasible output power from hybrid systems during changes in atmospheric conditions [8, 9]. The potency of the hybrid system control method is assessed under various situations, such as solar irradiance fluctuation and wind speed change [10, 11]. These changes lead to voltage and frequency fluctuations which affects the power quality and it is discovered that the control techniques efficiently keep the grid voltage constant [12–14].

27.2 Integration of Renewable Energy Sources

Figure 27.1 shows the hybrid power system layout, which includes a PV station and a wind farm that are located in various locations but are connected via transformers to a Point of Common Coupling (PCC) bus. The PV station is made up of several PV modules that are coupled in series and parallel. An incremental conductance MPPT method is used to harvest maximum power from a PV array at various levels of solar irradiation. The DC/DC boost converter steps up the output, and the DC power is converted to AC by the DC/AC inverter. The wind farm's second component is a Doubly Fed Induction Generator (DFIG), which is led by a big wind turbine. Grid side converter and Rotor Side Converter are two converters featured in DFIG. The former is used to keep the DC bus voltage constant, while the latter is utilized to get the most out of wind turbines. Furthermore, when wind speeds fluctuate, a modified MPPT technique that is based on mechanical power evaluation captures

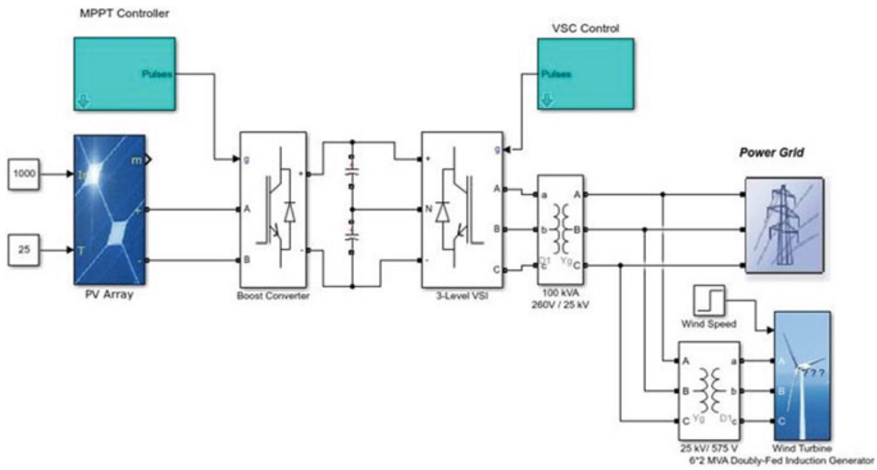

Fig. 27.1 Integration of solar and wind systems

the maximum power. It is very essential to maintain the unity power factor in the power system, with active power being transferred to the grid via transformers and transmission lines. A 260 V/25 kV A/Y transformer connects the PV array to the grid, while a 25 kV/575 V Y/A transformer connects the wind turbine to the grid.

27.3 PV Systems

27.3.1 PV Cell Model

The PV cell consists of one or two layers of a semiconducting material usually silicon. When sunlight falls on the cell, it creates an electric field across the layers causing electricity to flow.

PV cells are now widely employed in a variety of applications, including grid-connected systems, distant buildings, satellites, and traffic-related equipment outdoors. As shown in Fig. 27.2, the basic construction of a solar PV cell comprises of a semiconductor p–n junction and numerous components. Ip is the photoelectric current with a current source when diode 'D' is coupled in anti-parallel with the current source, as shown in Fig. 27.2. Shunt capacitance, C, and shunt resistance, R, appear in practical applications, as do series resistance, R, and series inductance, L.

Fig. 27.2 PV Cell with electrical components

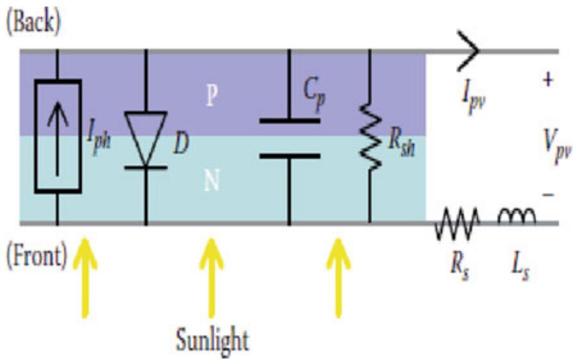

27.3.2 PV Operating Characteristics

As can be seen in Fig. 27.3, C_L values for the wing configuration are marked as increasing trend up to 18° AOA and then, it decreases for further increase in angle of attack. In specific, TLE with 2VG performed better at 18° AOA and the corresponding C_L value is 0.91. On the other hand, TLE with 4VG performed better at 18° AOA with C_L value of 0.85 in comparison with TLE and VG alone wing configurations. TLE with 2VG gave and 50% improvement in C_L in comparison with base plain wing configuration. Moreover, as can be seen in Fig. 27.3, the TLE with 2VG attachments perform well at stall condition comparison with other wing configurations.

The two key parameters that determine PV cell operation characteristics and power generation are solar irradiance, indicated as ‘G’ (W/m^2), and temperature,

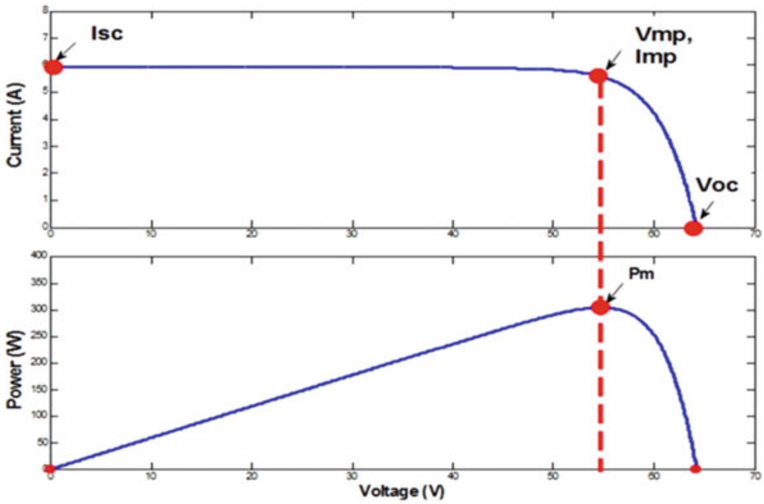

Fig. 27.3 PV operating characteristics

designated as ‘T’ (C). The relationship between the two parameters and the PV operating characteristics is mathematically model.

Apply Kirchhoff’s law to ideal photovoltaic model, we will get the relation as shown below,

$$I_{pv} = I_{ph}\,(G,\ T) - I_d\left(T, V_{pv}\right)$$

By using the above relation, a curve is drawn between voltage and current as shown below A curve is drawn between voltage versus power as shown above.

27.3.3 Incremental Conductance MPPT Technique

Maximum power point tracking (MPPT) or sometimes just power point tracking (PPT), is a technique used with variable power sources to maximize energy extraction as conditions vary. The technique is most commonly used with photovoltaic (PV) solar systems, but can also be used with wind turbines, optical power transmission and thermophotovoltaics. MPPT is the process of adjusting the load characteristic as the conditions change.

27.3.4 Fuzzy Logic Controller

L.A. Zadeh introduced fuzzy logic method in 1965. He observed that the classical set theory focusses on precision instead of easy and efficient controlling techniques. It is a significant problem-solving method. It came into existence mostly in 1980’s and early 1990. It is a superset of crisp logic. In contrast to classical set, the elements in the fuzzy set have definite degree of membership.

Fuzzy logic is similar to human decision making with its ability to work from fuzzy data and find precise outcome. Classic logic has two states (ex: 0 or 1 or true or false). This requires huge understanding of a system, exact equations and precise values. Whereas fuzzy logic is a continual form of logic (ex: 0, 0.1, 0.2…0.9, 1 or bad, very bad, poor, good etc.). Fuzzy sets depend on certain rules. Rule base is the most significant requirement for the fuzzy logic system. That certain-rules consists of If–Then rules. First, the fuzzy sets and membership functions are stated. Then the If–Then rules are decided for that particular control. These rules control the output on input.

If–Then rules includes two parts: (1) Antecedent and (2) Consequence or Conclusion.

If statement is the Antecedent and Then statement is the Consequence. (Ex: If the fan is fast, then decrease the speed.)

Operations:

Consider two fuzzy sets (A, B), such that A, B $\epsilon \cup$, where, $\cup$ is the Universe of Discourse. Main operations are:

1. Complement
2. Intersection.
3. Union.
1. COMPLEMENT: Complement of a fuzzy set with membership function is given as:

$$\mu^{-} = 1 - \mu_A(x)$$

2. INTERSECTION: There are common elements in both fuzzy sets A and B. it is denoted by A ∩ B. The membership function is given as:

$$\mu_{A \cap B}(x) = \mu_A(x) \cap \mu_B(x)$$

3. UNION: It contains all the elements present in both the fuzzy sets A and B. It can be written as A + B or A ∪ B. The membership function is given as:

$$\mu_{A \cup B}(x) = \mu_A(x) \cup \mu_B(x)$$

Fuzzy logic is a basic control system that depends on the degree of its input state. Its output depends on both the input state and rate of change of this state. It works as per the commands given by humans. This system internally converts these rules to their mathematical equivalent equations.

Advantages of fuzzy control:

This system is a robust system where no precise inputs are required. It is flexible and allow changes. This provides solutions to complex problems. Do efficient work even under noisy inputs. This is very simple user interface. In this controller, high precision sensors are not required and also fast microprocessors are not required. This logic system has a simple structure and easily constructed. If feedback system fails, it can be easily reprogrammable. It operates well in highly non-linear system also. It is efficient and require less data. It is a natural way of expressing unknown information. Developing rule base is easier than optimizing the parameters for PID controller.

Disadvantages:

Regular upgrades are required. It is completely dependent on human intelligence and expertise. These controllers cannot recognize machine learning or neural networks.

Implementation of fuzzy logic:

It maps the input to an output in a very efficient manner. Mapping can be easily controlled without much complex knowledge about the process. Steps to be performed are:

1. Study the rule base system and the system can be controlled by applying the operator.
2. Concept of membership functions and linguistic variables are to be understood.
3. Analyze the power system to be controlled and determine the state variables, which examined as input to the system.
4. To get the required control in the process, make an understanding as how to control the state variables.
5. Form the rule base for the linguistic variables of inputs and outputs.
6. Advance the membership function to make the control more productive.
7. Now check the results after integrating the fuzzy controller into the plant.

Architecture of fuzzy logic control

This is a cutting-edge technology that is mostly employed in the electricity system. The implementation of FLC is simple and quick. As a result, FLC can be used for both linear and non-linear systems. Figure depicts the FLC procedure, which has two inputs (error and change in error) and one output (current reference). FLC takes numerical inputs from Fuzzy Inference System (FIS), by using appropriate rules, it generates mathematical output, and then this mathematical output is given back to the FLC system just like a feedback system. This process is called as defuzzification process (Fig. 27.4).

Fuzzification—The role of fuzzifier is to convert the values 0 and 1 called as crisp values into the values between 0 and 1 including them also called as fuzzy set. It is the most important step in the system is to obtain state variables. After stating the variables, they are sent to fuzzification block to fuzzify the inputs. The numerical inputs have to be converted to fuzzy linguistic variables by fuzzy rule base rules. This process of converting state variable into linguistic variable is called fuzzification process. The linguistic variables comprise of state error, the rate of change of state error.

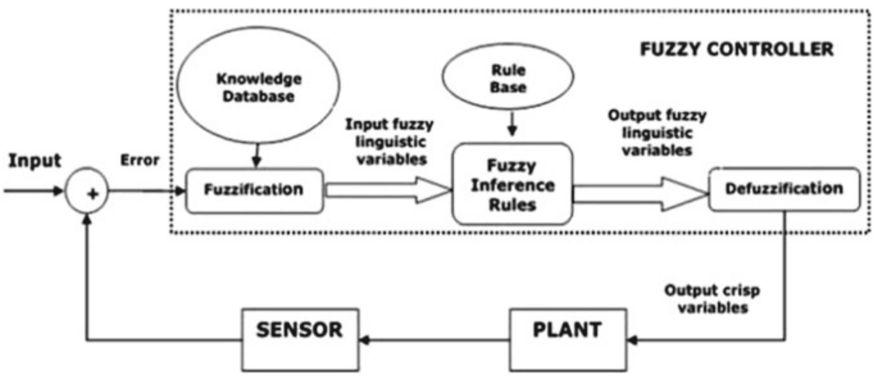

Fig. 27.4 Architecture of fuzzy logic control

Membership function is defined as the graphical representation of degree of belonging of an element to the fuzzy set. Membership functions can be triangular, trapezoidal, gaussian and bell shaped membership functions.

Fuzzy Knowledge Base—It stores the knowledge about all the input–output fuzzy relationships. It also has the membership function which defines the input variables to the fuzzy rule base and the output variables to the plant under control.

Fuzzy Rule Base—It gives information about how the mathematical operations are performed.

Fuzzy Rule Inference—It acts as a kernel of any FLC. Basically, it simulates human decisions by performing approximate reasoning. Fuzzy inference is designed using two methods.

1. Mamdani method.
2. Sugeno method.

Defuzzification—The role of defuzzifier is to convert the fuzzy values into crisp values getting from fuzzy inference engine. The inverse of fuzzification is known as defuzzification. There are three different methods of this process. They are:

1. Centre of gravity method.
2. Bisector of area method.
3. Mean of minimum method.

Working of fuzzy logic system:

The fuzzy logic system works based on fuzzy rules which are obtained by a person who works on it. Fuzzy logic controller has two inputs such as error (e) and change in error (Δe).

Δe e	N	Z	P
N	N	N	Z
Z	N	Z	P
P	Z	P	P

Where, Z is zero, P is positive, N is negative.

This DC link controller's main goal is to keep the voltage constant. The reference value and actual value of voltages at the de-link are compared. If they are not equal then the difference between them called as error signal is sent back to the FLC controller. This FLC controller will adjusts the voltage at the dc-link. The output of the FLC controller is known as the direct-axis of reference current, with I denoting the inner current controller.

27.4 Wind Energy Conversion System

The performance of the modified wings and the plain wing are evaluated, and the findings show that the TLE and VG wings performed marginally better than the conventional plain wing model. The results obtained for TLE with 2VG and TLE with 4VG wing models indicate that the performance is not significantly different with each other. However, both models performed better than the standard plain wing model. C_L/C_D ratio of the wings with TLE with 4VG and 2VG plain wing configurations are better at 18° angle of attack.

Wind power is generated by wind power plants. It consists of wind blades, wind turbine, double fed induction generator which converts wind energy into electrical energy.

Wind first hits a turbine-blades, causing them to rotate and turn the turbine connected to them. Turbine converts kinetic energy to rotational energy, by moving a shaft which is connected to a generator, which in turn produces electrical energy through electro magnetism.

Characteristics of wind energy system

Let us assume that the wind reaches the turbine at a constant velocity, with uniform attributes (temperature and density), and without any disturbances, to understand how a wind turbine works and what its features are. The power coefficient of a real wind turbine can be defined as the power extracted by the wind turbine multiplied by C. A wind turbine's real power P is calculated as follows:

$$P_m = C_p\left(\frac{1}{2}\rho A v_w^3\right) = \frac{1}{2}\rho\pi R^2 v_w^3 C_p(\lambda, \beta) \quad (27.1)$$

ρ—air density; R—Wind turbine's blade radius; V—speed of the wind; C, changes according to the wind speed, turbine blades and the rotational speed of the turbines. Thus, the power coefficient denoted as C, is represented as a function of blade pitch angle β and tip-speed ratio λ (Fig. 27.5).

27.4.1 Mechanical Power Measurement-Based Modified MPPT Technique

Maximum—power is extracted from the wind turbine at the rotor's ideal rotational speed. By detecting the best rotational speed during wind speed variations, the MPPT method recovers maximum power from the wind turbine. While most MPPT strategies focus on wind turbine parameters and wind speed, flaws in wind turbine modelling and sensor inaccuracy would influence the MPPT technology's performance. The research suggests utilising a modified MPPT control technique to

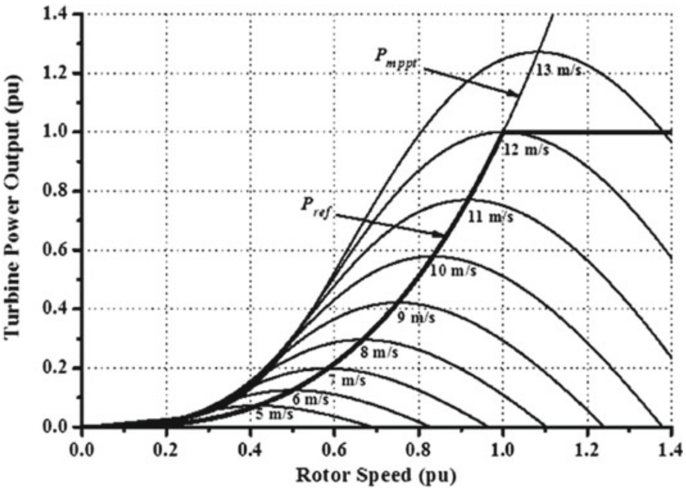

Fig. 27.5 Characteristics of wind energy system

establish the best rotation speed based on mechanical power measurement. Figure depicts the MPPT strategy flow chart, with the following steps discussed:

i. First, the MPPT control establishes the fundamental values for mechanical power (P) and rotational speed (…).
ii. The real mechanical power is then estimated using the MPPT method to determine the suitable rotation speed ().
iii. The best rotational speed is usually 1.2 p.u. while the mechanical power (P) is greater than 0.75 p.u. which corresponds to the maximum wind energy capacity (9 MW).
iv. Determines the ideal rotational speed if the mechanical power (P) is less than 0.75 p.u.

Without sensing wind turbulence, the enhanced MPPT technique easily specifies the best rotational speed for calculating maximum power.

Power quality issues:

Power electronic converters are the heart of renewable energy system. These devices are responsible for harmonic injection in the system. Operation of these converters highly dependent on quality of voltage signal. To improve power quality of RES's different measures are taken. Due to non-controllable variability of renewable energy sources, we observe voltage and frequency fluctuations such as voltage sag, voltage swell, voltage flickering. And harmonics occur due to power electronic devices. These can be compensated by using various FACTS devices. Here, we use Unified Power Quality Conditioner. It has many advantages compared to other FACTS devices. It compensates real power, reactive power and apparent power also.

UPQC: Unified power quality conditioner

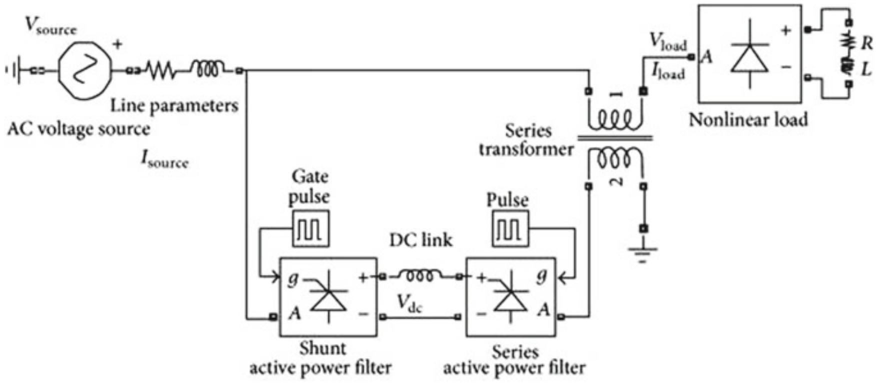

Fig. 27.6 Unified power quality conditioner

See Fig. 27.6.

Working principle

UPQC consists of front-end converter, D-STATCOM, DVR, filter, and DC link. The front-end converter is protected by direct voltage restorer, which compensates the voltage fluctuations. And load is compensated by using D-STATCOM. Both D-STATCOM and DVR are voltage source inverters, which are connected using DC link. Here, as both load and voltage are compensated, real and reactive power are also gets compensated.

27.5 Conclusion

This paper discusses the integration of renewable energy sources into a microgrid with power quality improvement features, with an emphasis on Indian conditions. As the fossil fuels are depleting and also due to increase in population, there is urge of electricity. In order to satisfy the customer's demand, integration of renewable energy sources is done. Estimation of solar irradiance using regression analysis with different meteorological and geographical parameters, as well as estimation of wind power using an intelligent approach, economic feasibility of grid-connected hybrid Energy Systems, analysis and design of a Sustainable microgrid primarily powered by renewable energy sources with dynamic performance improvement, and flexible hybrid system power quality improvement using advanced fuzzy current and voltage-controlled techniques.

References

1. Liang, X.: Emerging power quality challenges due to integration of renewable energy sources. In: Proceedings of 2016 IEEE Industry Applications Society (IAS) Annual Meeting, Portland, OR, USA (2016)
2. Wei, W., Liu, F., Mei, S., Hou, Y.: Robust energy and reserve dispatch under variable renewable generation. IEEE Trans. Smart Grid **6**(1), 369–380 (2015)
3. Liu, C., Botterud, A., Zhou, Z., Du, P.: Fuzzy Energy and reserve co optimization with high penetration of renewable energy. IEEE Trans. Sustain. Energy **8**(2), 782–791 (2017)
4. Konda, S.R., Panwar, L.K., Panigrahi, B.K., Kumar, R., Member, S.: A multiple emission constrained approach for self-scheduling of GENCO under renewable. CSEE J. Power Energy Syst. **3**(1), 63–73 (2017)
5. Shadmand, M.B., Balog, R.S.: Multi-objective optimization and design of photovoltaic-wind hybrid system for community smart DC microgrid. IEEE Trans. Smart Grid **5**(5), 2635–2643 (2014)
6. Fernandez, E.F., Cruz, F.A., Mallick, T.K., Sundaram, S.: Effect of spectral irradiance variations on the performance of highly efficient. IEEE J. Photovolt. **5**(4), 1150–1157 (2015)
7. Mahmoudi, N., Shafie-khah, M., Saha, T.K., Catalão, J.P.S.: Customerdriven demand response model for facilitating roof-top PV and wind power integration. IET Renew. Power Gener. **11**(9), 1200–1210 (2017)
8. Gibson, K., Cole, I.R., Goss, B., Betts, T.R., Gottschalg, R.: Compensation of temporal averaging bias in solar irradiance data. IET Renew. Power Gener. **11**, 1–7 (2017) (213)
9. Wang, B., Kong, Q., Liu, W., Yang, L.T.: On efficient utilization of green energy in heterogeneous cellular networks. IEEE Syst. J. **11**(2), 846–857 (2017)
10. Khondekar, M.H., Ghosh, D.N., Ghosh, K., Bhattacharjee, A.K.: Complexity in solar irradiance from the earth radiation budget satellite. IEEE Syst. J. **9**(2), 487–494 (2015)
11. Shah, A.S.B.M., Yokoyama, H., Kakimoto, N.: High-precision forecasting model of solar irradiance based on grid point value data analysis for an efficient photovoltaic system. IEEE Trans. Sustain. Energy **6**(2), 474–481 (2015)
12. Burgess, P., Vahdati, M., Essah, E.: Investigation of the accuracy of historical irradiance products and interannual variability of solar irradiance using met office ground data. IET Renew. Power Gener. **9**(5), 405–411 (2015)
13. Galleano, R, Results of the fifth international spectroradiometer comparison for improved solar spectral irradiance measurements and related impact on reference solar cell calibration. IEEE J. Photovolt. **6**(6), 1587–1597 (2016)
14. Mani, A.: Handbook of Solar Radiation Data for India. Allied Publishers, New Delhi (1980)
15. Bucksteeg, M., Niesen, L., Weber, C.: Impacts of dynamic probabilistic reserve sizing techniques on reserve requirements and system costs. IEEE Trans. Sustain. Energy **7**(4), 1408–1420 (2016)

Chapter 28
Evaluation of Mechanical Properties in Friction Stir Welding of Aluminium AA6061 with Various Tool Pin Profiles at Different Process Parameters

P. S. S. S. Raghavendra, Manish Kumar Singh, K. Aruna Prabha, Ch. Naveen Reddy, M. S. Srinivasa Rao, and B. V. R. Ravi Kumar

Abstract The friction stir welding (FSW) process is used in various industries, which includes railways, marine, aerospace, automotive to join copper, aluminum, and magnesium alloys. It is used to combine two similar or dissimilar plates. Different tool pin profiles such as triangular tool, square tool, taper threaded cylindrical tools and cylindrical grooves tool are used at different process parameters and friction stir welding is performed on Aluminium AA6061 plates. Testing of the weldments is done to find tensile, yield strengths, elongation, hardness, and energy absorbed by the weldments. The impact of different tool pin profiles while welding with different process parameters on the mechanical properties of the weldments are evaluated. Destructive and non-destructive tests are conducted on the weldments and based on results it was observed that square tool performed more efficiently followed by cylindrical grooves tool.

P. S. S. S. Raghavendra · M. K. Singh · K. Aruna Prabha (✉) · Ch. N. Reddy · M. S. S. Rao · B. V. R. Ravi Kumar
Department of Mechanical Engineering, VNR Vignana Jyothi Institute of Engineering and Technology, Hyderabad 500090, India
e-mail: arunaprabha_k@vnrvjiet.in

Ch. N. Reddy
e-mail: naveenreddy_ch@vnrvjiet.in

M. S. S. Rao
e-mail: srinivasarao_ms@vnrvjiet.in

B. V. R. Ravi Kumar
e-mail: rajaravikumar_bv@vnrvjiet.in

P. H. V. S. Talpa Sai et al. (eds.), *Intelligent Manufacturing and Energy Sustainability*, Smart Innovation, Systems and Technologies 372,
https://doi.org/10.1007/978-981-99-6774-2_28

28.1 Introduction

Friction Stir Welding (FSW) is a solid-state welding process that involves the joining of materials without the need of a filler material or external heat source which is one of the main criteria to differentiate FSW from conventional welding processes [1]. FSW was invented in 1991, at The Welding Institute (TWI) in Cambridge England [1]. The FSW process involves a rotating tool which is plunged into the joint between the two pieces of material to be joined. The tool creates frictional heat, softening the material and causing it to deform. The rotating tool then moves along the joint line, stirring the softened material together and creating the bond. Some advantages of FSW over traditional welding techniques include strong and high-quality welds [1].

28.2 Methodology

The methodology followed is mentioned in Fig. 28.1.

AA 6061 Aluminium alloy and H13 tool steel were chosen as work piece material and tool material respectively. The HRC value of the tool material is 60. For deciding

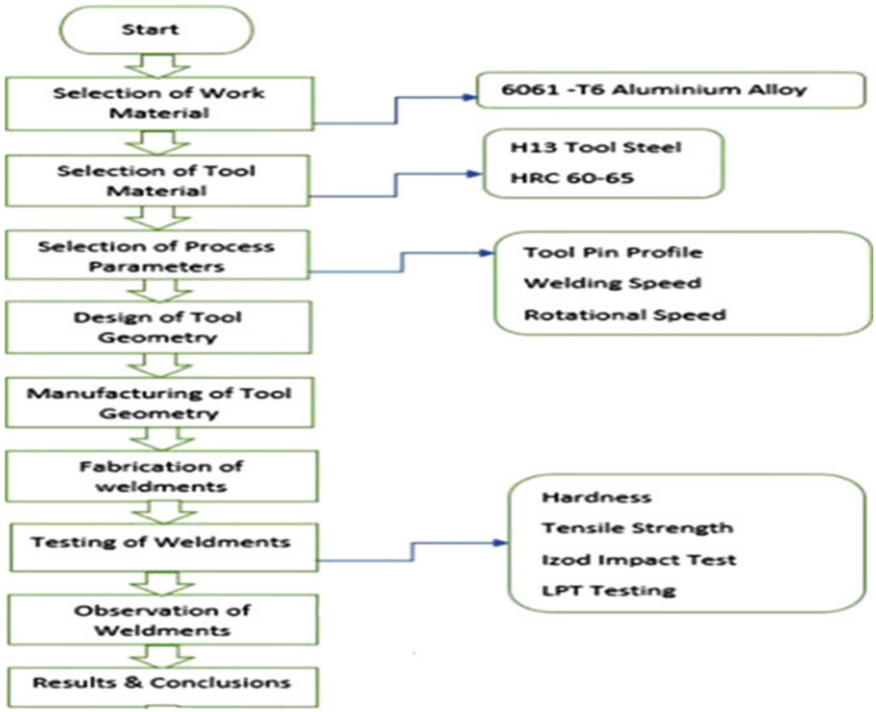

Fig. 28.1 Methodology of FSW [2]

out the best tool pin profile the process parameters which were chosen out to perform the experiment process are axial force, welding speed, rotational speed, and tilt angle. The design of tool geometry was done in CATIA V5 software. The tool pin profiles which were designed are square tool, cylindrical grooves tool, triangular tool, and taper threaded cylindrical tool. With the help of tool pin profiles, weldments were welded by following the friction stir welding process. UTM, Rockwell Hardness testing, Izod impact test and LPT testing were performed on the weldments to observe the weldments and determine the optimum tool pin profile out of the tools which were designed [3].

28.3 Experimentation and Materials

28.3.1 CATIA Design and Manufacturing of Tool Pin Profiles

The FSW tool pin profiles designed for the experimentation process are square tool, cylindrical grooves tool, taper threaded cylindrical tool, triangular tool as seen in Fig. 28.2. The below mentioned tools are used for performing friction stir welding and after the welding process is done, the efficiency of these tools were compared based on the results of destructive and non-destructive testing which were conducted on the weldments. The different components of tool pin profiles such as pin, shoulder, collar, and shank were designed and using CATIA V5 software. The dimensions of these tool pin profiles such as pin length, length and diameter of shoulder, length, and diameter of collar and finally the dimensions of shank were maintained to be constant as distinct dimensions of tool pin profiles can also show an impact on the efficiencies of the tools.

The choice of the geometry of various tool pin profiles was based on various factors. The pin length was chosen based on the thickness of the work piece material. The pin length should be more than the half of the work piece thickness and less than the total thickness of the work material. The empirical relation of 3:1 is followed for the ratio of the shoulder length to the collar length. The empirical relation of 3:1 is followed for the ratio of the shoulder diameter to the pin diameter/side. The collar diameter should be made greater than the shoulder diameter to withstand the load through the axial force. The shank length and shank diameter dimensions were provided based upon the friction stir welding machine model: FSWB-10-300 setup.

28.3.2 Process Parameters and Materials

The welding process parameters which were considered for performing the welding process are axial force, welding speed, rotational speed, and tilt angle. Four different

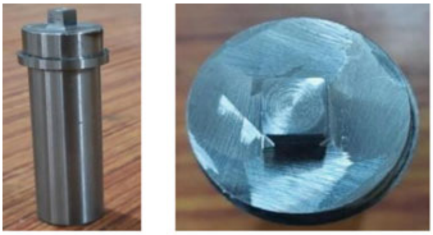

(a) Square Tool

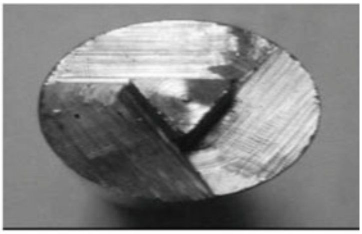

(b) Triangular Tool

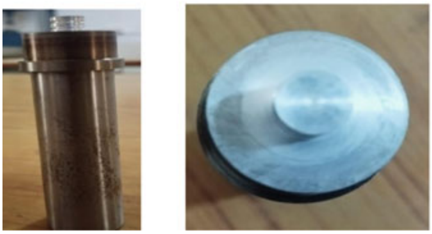

(c) Cylindrical Grooves Tool

(d) Taper Threaded Cylindrical Tool

Fig. 28.2 Tool pin profiles

sets of process parameters are considered with distinct values in each set except tilt angle as shown in the table below. The reason to vary all the process parameters is to observe the impact of each individual process parameter on the tool pin profiles [4] and to finally decide which tool pin profile is proved to be more efficient after being impacted by each individual process parameter. The work materials which are to be welded are Aluminium 6061 plate [150 mm × 100 mm × 6 mm] dimensions. Non-consumable tool tips of triangular, square, taper threaded cylindrical and distorted octahedral profiles are made of H13 tool material all manufactured and turned using lathe machine. The machine setup is turned on, and the tool is enabled to plunge onto metal plates along the joint line as the spindle rotates. The FSW welding is done on Friction Stir Welding (FSW) Machine Model: FSWB-10-300.

AA6061 aluminium alloy contain magnesium and silicon as its major alloying elements. This AA6061 aluminium alloy has Mg (1.049%), Mn (0.092%), Ti (0.027%), Zn (0.09%), Fe (0.601%), Si (0.609%), Cu (0.26%), Cr (0.105%), Al (97.167%). The testing method which was used to identify the chemical composition of AA6061 aluminium alloy was ASTM E 1251-2017a. The equipment which was used for performing this test was optical emission spectrometer SPECTROMAXX. The choice of the set of process parameters were based on the experimentation process. The load which was selected are 5, 6, 7, and 8 kN. The Welding speed which was selected are 30, 50, 70, and 90 mm/min. The rotational speed which was preferred are 800, 1000, 1200, 1400 rpm. For every set of process parameters, the value of load, welding speed and rotational speed was varied with a constant rate to determine the optimal tool pin profile for every set of process parameters. There are 4 different set of process parameters and out of which it will be determined that which set of process parameters is the best for the different tool pin profile.

28.4 Testing

28.4.1 UTM Testing

A universal testing machine is a mechanical testing apparatus used to determine the physical properties of materials such as tensile strength, compressive strength, and flexural strength. The strength which was used in this experimentation process is tensile strength. This is a test to measure the maximum tensile load that a material can with- stand without breaking. It is used to determine the tensile strength, yield strength and elongation of a material. The tensile strength testing is conducted only on weld nugget zone to determine the strength of the weldment [5]. The test procedure or standard used for conducting UTM is 100 kN. The force measurement accuracy of this setup is 0.5%. The displacement resolution of the setup is 0.01 mm. The ASTM standard specimens for testing are ASTM E8. The method of testing was as per ASME SEC IX.

28.4.2 Macro-Hardness Testing

Macro-hardness testing is a non-destructive method which is used to determine the hardness of a material. Under a specific load, the depth of penetration of an indentor into the material is being measured. Regular macro-hardness is applied when the surface area is large and indentation is deep. Superficial macro-hardness is applied when the surface area is large, but penetration is shallow. The macro hardness testing is conducted only on weld nugget zone to determine the hardness of the weldments. The indentor which had been chosen to perform Rockwell hardness test is hard steel ball (1/16″ dia). The major load which was applied to perform this test was 100 kg. It is also commonly used in the medical, automotive, and aerospace industries to test the hardness of materials used in critical applications [6, 7].

Overall, Rockwell hardness testing is a fast, reliable, and accurate method for measuring the hardness of materials and it is an essential tool for ensuring the quality and safety of products made from these materials.

28.4.3 Izod Impact Testing

The Izod impact test is a mechanical procedure for determining a material's impact resistance, particularly for plastics and metals. The test entails striking a specimen with a pendulum so that the energy needed to break the specimen can be measured. The Izod test is conducted only on the weld nugget zone to determine the energy absorbed by the weldments [8]. While performing the Izod impact test, a specimen is clamped vertically and struck with a pendulum. The specimen is struck by the pendulum while it freely swings from a fixed height. The height to which the pendulum rises after impact serves as a gauge for the energy absorbed by the specimen. The test is done numerous times, and the average of the outcomes is used to determine the material's Izod impact strength [8].

The maximum impact energy that can be absorbed by the specimen, while performing an Izod impact test is 170 J. The angle of drop of the pendulum is 90°. The specimen's position resembles the cantilever beam's position. It is commonly used in consumer goods, automotive, and aerospace [8].

28.4.4 Liquid Penetrant Testing (LPT)

In friction stir welded aluminum alloys, surface-breaking flaws can be found via LPT, or liquid penetrant testing. In this non-destructive testing procedure, a liquid penetrant is applied to the material's surface, allowed to infiltrate into any surface flaws or fractures, and then the surplus penetrant is removed. Next, a developer is used to highlight any places where the penetrant has seeped into a flaw. The test procedure or standard used for conducting LPT is ASTM E 165. The penetrant which was used in LPT is SKL-Sp1 and the developer which was used is SKD-S2. The inspection method used in this LPT is Type II which talks about visible penetrate. The type of removable used to remove the penetrant is solvent removable. The testing was conducted at room temperature and 100% weld surface was tested. The dwell time is of 15 min and the developing time is of 10 min. The pre and post cleaning methods used were Magnaflux and spot-check SKC 1 To perform LPT on friction stir welded Aluminum alloys, the equipment and materials which were used are Penetrant, Cleaner, Developer, UV lamp, Applicators, safety equipment [9].

LPT can be an effective method for detecting surface-breaking defects in friction stir welded alloys of aluminium. However, it is important to follow the specific procedures and requirements of the inspection to ensure accurate and reliable results. All test results are presented in Table 28.1.

Table 28.1 Tensile strength, Macro-hardness and Izod Impact Results of weldments fortified using various tool pin profiles

Process parameters 1, 2, 3, 4	Tool pin profile	Results		
		Tensile strength (MPa)	HRB (Rockwell B Scale)	Energy absorbed (J)
Process parameter 1 Axial force: 510 kgf Welding speed: 0.5 mm/s Speed of rotation: 13.33 rps Tilt angle: 0°	Square tool	109.4	62.33	12
	Cylindrical grooves tool	66.7	56.33	6
	Triangular tool	52.3	41.33	4.5
	Taper thread tool Cylindrical tool	38.0	40.66	1.5
Process parameter 2 Axial force: 610 kgf Welding speed: 0.8 mm/s Speed of rotation: 16.66 rps Tilt angle: 0°	Square tool	85.6	59.66	12
	Cylindrical grooves tool	67.8	45.66	8
	Triangular tool	56.2	42.66	6
	Taper threaded Cylindrical tool	26.8	23.33	2
Process parameter 3 Axial force: 710 kgf Welding speed: 1.2 mm/s Speed of rotation: 20 rps Tilt angle: 0°	Square tool	74.1	66.33	6
	Cylindrical grooves tool	68.7	60.66	5
	Triangular tool	62.7	42.33	3.5
	Taper threaded Cylindrical tool	56.8	32.66	3
Process parameter 4 Axial force: 810 kgf Welding speed: 1.5 mm/s Speed of rotation: 23.33 rps Tilt angle: 0°	Square tool	97.6	62.33	10
	Cylindrical grooves tool	66.6	54.33	7

(continued)

Table 28.1 (continued)

Process parameters 1, 2, 3, 4	Tool pin profile	Results		
		Tensile strength (MPa)	HRB (Rockwell B Scale)	Energy absorbed (J)
	Triangular tool	59.3	44.33	5.5
	Taper threaded Cylindrical tool	21.0	40.66	4.5

28.5 Results and Discussions

28.5.1 UTM Test

It is observed that AA 6061 friction stir welded alloys had maximum tensile strength when welded using square tool tip profile because square tool tip has a large contact area with the material when compared to other tools which allows for more efficient heat transfer [8] and plastic deformation during welding [9]. This leads to better grain refinement and increased strength in the weld [10–12]. It was also observed that the alloys had minimum tensile strength when welded using taper threaded cylindrical tool pin profile because taper threaded cylindrical tool has least contact area with the material when compared to other tools which allows for less efficient heat transfer [8] and plastic deformation during welding [9] as seen in Fig. 28.3. This leads to poor grain refinement and reduces strength in the weld [13, 14].

The UTM graph shows that the tensile strength of the square tool was the best followed by cylindrical grooves tool for every set of process parameters. For square tool, at process parameter 3 the values were minimum (74.1 Mpa) and at process parameter 1 the values were maximum (109.4 Mpa). In square tool, there was a gradual decrease in the value at process parameter 2, process parameter 3, but there was an increase in value at process parameter 4. For cylindrical grooves tool, there

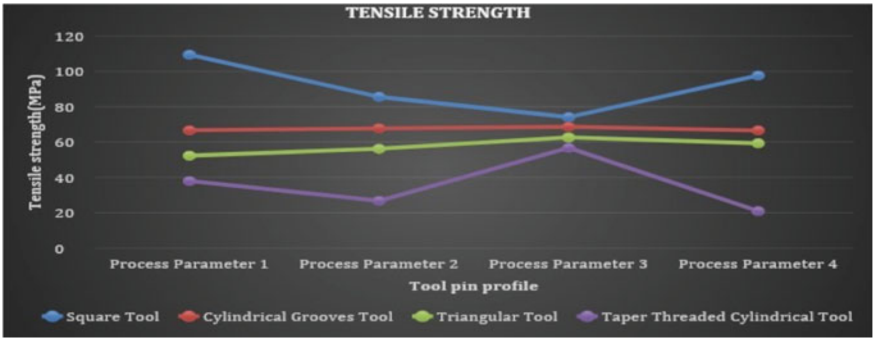

Fig. 28.3 Graph 1: Tensile strength testing results obtained by using different tool pin profiles at different process parameters

was not much fluctuations in terms of tensile strength values. Even for triangular tool, there was not much fluctuations in terms of tensile strength values, but it was the third best tool.

For taper threaded cylindrical tool, at process parameter 3 the values were maximum (56.8 Mpa) and at process parameter 4 the values were minimum (21 Mpa). In taper threaded cylindrical tool, there was a decrease in value of tensile strength for process parameter 2 compared to process parameter 1, but there was a sudden increase in the value at process parameter 3 and for process parameter 4 it had shown the least value.

28.5.2 Macro-Hardness Test

It is observed that AA 6061 friction stir welded alloys had maximum hardness when welded using square tool pin profile because square tool has a more gradual and smooth shape and as the tool is not having any sharp corners it reduces the amount of material displacement during FSW [8, 9]. Because of the smooth and gradual shape of the tool it is having better ability to trap and distribute the aluminum oxide particles that are generated during FSW, which leads to increase in hardness of the material. It was also observed that the alloys had minimum hardness when welded using taper threaded cylindrical tool pin profile because of the threads which interrupts the welding process as the chips get glued to the threads during welding because of which the material does not gets deformed uniformly and grooves will be formed on either of the sides of weldments which results in reduction of hardness of the weldment as seen in Figs. 28.4 and 28.5.

Rockwell hardness test graph shows that the macro-hardness of the square tool was the best followed by cylindrical grooves tool for every set of process parameters. For

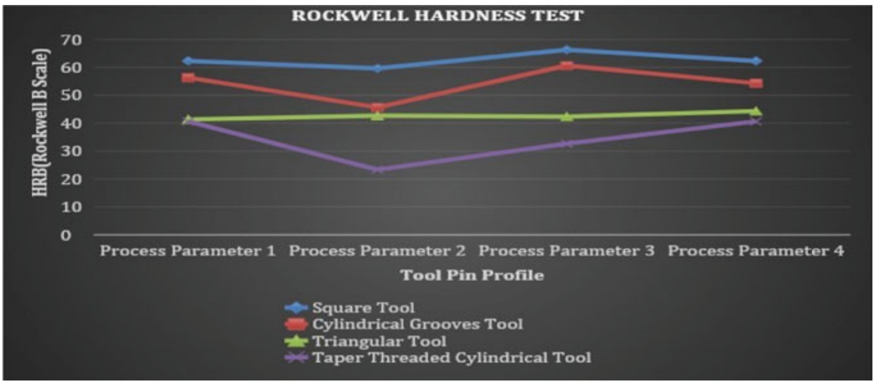

Fig. 28.4 Graph 2: Macro-hardness testing results obtained by using different tool pin profiles at different process parameters

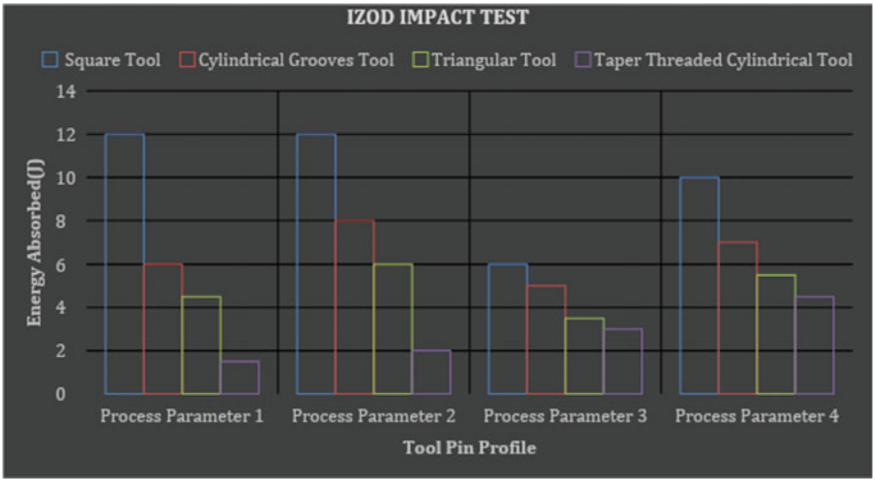

Fig. 28.5 Graph 3: Izod impact testing results obtained by using different tool pin profiles at different process parameters

square tool, there were no major fluctuations in terms of hardness, but the maximum hardness value was obtained at process parameter 3 (66.33). For cylindrical grooves tool, at process parameter 3 the values were maximum (60.66) and at process parameter 2 the values were minimum (45.66). In cylindrical grooves tool, there was a gradual decrease in the value at process parameter 2, but there was an increase in value at process parameter 3. For triangular tool, there was not much fluctuations in terms of hardness values. For taper threaded cylindrical tool, at process parameter 4, process parameter 1 the values were maximum (40.66) and at process parameter 2 the values were minimum (23.33). In taper threaded cylindrical tool, there was a decrease in value of hardness for process parameter 2 compared to process parameter 1, but there was a gradual increase in the value at process parameter 3 and process parameter 4.

28.5.3 Izod Impact Test

It is observed that friction stir welded alloys had maximum energy when welded using square tool pin profile because square tool pin profile provides a better combination of material flow, frictional heating [8] and mixing of the material during FSW process [9]. The better combination of flow of material and mixing of the material can be justified by the results of LPT testing conducted on AA 6061 welded alloys. It was also observed that the alloys had minimum energy when welded using taper threaded cylindrical tool pin profile because taper threaded cylindrical tool pin profile provides reduced material flow, reduced frictional heating [8] and poor mixing of the material during FSW pro- cess [9]. The reduced material flow and poor mixing of the material can be justified by the results of LPT testing conducted on AA 6061 welded alloys. The results of LPT testing had revealed that because of surface defects such as voids and tunnels in the welding zone there was no proper mixing of material which had led to decrease in the energy of welded alloys.

The Izod Impact test graph shows that the energy absorbed values of the square tool was the best followed by cylindrical grooves tool for every set of process parameters. For square tool, at process parameter 3 the values were minimum (6 J) and at process parameter 1, process parameter 2 the values were maximum (12 J). In square tool, there was a gradual decrease in the value at process parameter 3, but there was an increase in value at process parameter 4. For cylindrical grooves tool, at process parameter 2 the values were maximum (8 J) and at process parameter 3 the values were minimum (5 J). In cylindrical grooves tool, there was a gradual increase in the value at process parameter 2, but there was a decrease in value at process parameter 3. For triangular tool, at process parameter 3 the values were minimum (3.5 J) and at process parameter 2 the values were maximum (6 J). For taper threaded cylindrical tool, at process parameter 1 the values were minimum (1.5 J) and at process parameter 4 the values were maximum (4.5 J). In taper threaded cylindrical tool, there was a gradual increase in the value from process parameter 2 to process parameter 4.

28.6 Conclusions

Destructive and non-destructive tests are conducted on friction stir weldments of Aluminium AA6061 alloys. From tests conducted such as tensile test, Izod impact test for determining the energy absorbed and rockwell hardness test for determining the hard- ness of the weldments square tool pin profile FSW weldments has proved to be more efficient followed by cylindrical grooves tool in the aspect of tensile strength, hard- ness, and resistance. The friction stirs welding process which was done using distorted octahedral tool resulted in improper welding of workpiece. The welding is said to be improper if grooves are formed on the center line of weldment and defects such as voids, cracks and porosity are observed in weld nugget zone this was detected by LPT test.

References

1. Jeff Defalco.: An Introduction to Friction Stir Welding, the Fabricator, 15 September (2009)
2. De Filippis, L.A.C., Serio, L., Facchini, F., Mummolo, G., Ludovico, A.D.: Prediction of the vickers microhardness and ultimate tensile strength of AA5754 H111 friction stir welding butt joints using artificial neural network. Materials **9**, 915–915 (2016)
3. Kesharwani, R.: Comparison of microstructure, texture, and mechanical properties of the SQ and thread pin profile FSW joint of AA6061-T6 with Al_2O_3 particle reinforcement. Mater. Today Commun. **33,** 104785 (2022)

4. Aruna Prabha K., Prasad P., Prasad B.S.: Effect of tool rotational speed on mechanical properties of aluminium alloy 5083 weldments in friction stir welding. Mater. Today Proc. **5**, 18535–18543 (2018)
5. Dinaharan I., Chung-Hyun, G.: Effect of material location and tool rotational speed on microstructure and tensile strength of dissimilar friction stir welded aluminum alloys. Arch. Civil Mech. Eng. **12**(4), 446–454 (2012). https://doi.org/10.1016/j.acme.2012.08.002
6. Yazdanshenas, A., Goh, C.-H.: Rockwell hardness testing on an aluminum specimen using finite element analysis. SSRG Int. J. Mech. Eng. **7**(4), 1–10 (2020)
7. Dhalia, K., Jain, N.: Testing of material strength of brass mixed with aluminum metal. Int. J. Sci. Technol. Manage. **8**(2), 1–5 (2021)
8. Kumar, N.N., Vamshi, G.: Study of weld defects in aluminium 2014 T6 alloy using liquid penetrant and correlating with radiography films. Int. J. Sci. Res. Dev. **7**(9), 197–200 (2019)
9. Selvamani, S.T., Umanath, K., Palanikumar, K.: Heat Transfer Analysis during Friction Stir Welding of Al6061-T6 Alloy. Research Gate (2011)
10. Rathinasuriyan, C., Muniamuthu, S., Mystica, A., Kumar, V.S.: Investigation of heat generation during submerged friction stir welding on 6061-T6 aluminum alloy. Mater. Today **46**, 8320–8324 (2021)
11. Patil, S.K.: A critical review on microstructure and hardness of aluminum alloy 6061 joints obtained by friction stir welding-past, present, and its prospects. Mater. Today Proc. 2023, 75–78 (2022)
12. Bahrami, M.: On the role of pin geometry in microstructure and mechanical properties of AA7075/SiC nano-composite fabricated by friction stir welding technique. Mater. Des. **53**, 519–527 (2014)
13. Su, J.Q.: Microstructure evolution during FSW/FSP of high strength aluminum alloys. Mater. Sci. Eng. A **405**, 277–286 (2005)
14. Moghaddam, M.: Characterization of the microstructure, texture and mechanical properties of 7075 aluminum alloy in early stage of severe plastic deformation. Mater. Char. **119**, 137–147 (2016)

Chapter 29
Experimental and Numerical Analysis of Flow Acoustics Over Different Co-annular Nozzle Shapes

R. Sarweswaran, A. Muthuram, S. Seralathan, T. S. Abzal, K. Vinay Kumar Joseph, and P. Kishore

Abstract Co-annular or coaxial nozzles are normally used in the aircraft exhaust nozzles for various applications such as noise reduction, mixing enhancement, thrust vectoring, infrared signatures, etc. This paper investigates the flow acoustics of three different co-annular nozzle geometries such as base circular nozzle, circle-chevron and chevron-circle nozzle with the various parameters such as acoustic power level, sound pressure level and velocity magnitude. The computational analysis has been done with the three nozzles for a pressure of 60 psi at the inlet and experimental analysis with various pressures such as 70, 80, and 90 psi. Based on the investigations it is observed that the co-annular nozzle circle-chevron nozzle shows better mixing enhancement and noise reduction compared to other nozzle shapes.

29.1 Introduction

Flow acoustics in aircraft exhaust nozzles is an important aspect of aircraft design and performance. The exhaust nozzle plays a crucial role in controlling the flow of exhaust gases from the aircraft engines and has a significant impact on noise generation and thrust efficiency. Co-annular nozzle is a type of nozzle that has two separate exhaust streams. Normally, the turbofan engine itself act as a co-annular device with bypass duct. The inner stream contains high temperature flow produced from the combustion chamber by the combustion of fuel and oxidizer. The outer stream is cooler gas at ambient temperature that comes from the axial fan of turbofan engine. Similarly,

R. Sarweswaran · A. Muthuram · S. Seralathan (✉) · T. S. Abzal · K. V. K. Joseph · P. Kishore
Department of Aeronautical Engineering, Hindustan Institute of Technology and Science, Chennai, Tamilnadu 603103, India
e-mail: siva.seralathan@gmail.com

A. Muthuram
Department of Aerospace Engineering, SRM Institute of Science and Technology, Kattankulathur, Chengalpattu 603203, India

P. H. V. S. Talpa Sai et al. (eds.), *Intelligent Manufacturing and Energy Sustainability*, Smart Innovation, Systems and Technologies 372,
https://doi.org/10.1007/978-981-99-6774-2_29

the co-annular nozzle also has a primary flow surrounded by the secondary flow. Compared to the early system studies, it is significantly quieter. It is also quieter than comparable convergent nozzles under many circumstances. The co-annular nozzle produces a reduction in noise due to the rapid velocity decay. The noise reaches the maximum at the end of potential core generated from the jet in convergent nozzle where there is a high velocity, and the velocity decays at a relatively slow rate. In contrast, there is a very faster decay rate in case of co-annular nozzle as secondary stream is being acted upon by both the primary flow and the outer ambient air. The co-annular nozzle also does not incur any thrust losses. The acoustical advantage related to the interaction between the two jets can be revealed by comparing the noise characteristics of different and previously existing co-annular nozzles. The Chevron nozzle acts as the best passive control noise reduction device. Mixing jet noise benefit is one of the significant characteristics of the co-annular nozzle. It helps in attenuation of the jet noise and reduces the infrared signature (IR). For reducing the noise, potential core length of jet must be reduced. The alterations in the co-annular nozzle can enhance or modify the mixing process which does not require any additional power or energy source. This type of control is called 'passive control'. With the modification of nozzle geometry, the mixing can be altered by enhancing the interaction between the jets.

29.2 Literature Survey

The influence of secondary jet on the primary one at supersonic and high subsonic Mach number was studied by Papamoschou [1] and enhancement of mixing with high velocity secondary jet, specifically supersonic. Zaman and Papamoschou [2] also reported a similar work with co-annular. Regardless of the operational settings of the central jet, the enhancement of mixing in the surrounding jet was observed across exit Mach number in the range of 0.8 to 1.20. Srinivasarao et al. [3] looked at how Mach number affected co-flowing jets that were under expanded, appropriately expanded, and supersonic up to a nozzle pressure ratio (NPR) of 7. Zaman and Dahl [4] studied numerically and experimentally a two-stream nozzle to recognize the sources of tones and search solutions. The modifications were done in various parameters such as inner nozzle lip thickness, varying the geometry and length of the inner nozzle duct and lip-to-lip distance between the inner and outer nozzles for investigating the source. The tones were eliminated by using a leading-edge treatment of the struts via disruption of the vortex shedding. Tide and Srinivasan [5] experimentally studied the influence of chevrons like number of chevrons and chevron penetration in chevron nozzles. Acoustic measurements, for instance, broadband shock noise, acoustic power, directivity, spectra, and overall sound pressure level were taken over a extent of nozzle pressure ratios ranging from subcritical to under expansion. Shadowgraph images of the shock-cell structure of jets from different chevron nozzles were acquired for a range of nozzle pressure ratio. The findings demonstrated that for low and medium nozzle pressure ratios, a higher chevron count with a lower level of penetration produced the best noise reduction. The numerical studies were carried out by Muthuram et al. [6] with the help of a validated steady 3D density-based k-omega SST turbulence model with improved wall functions. It was concluded that the best option for acoustic power level attenuation with momentum thrust benefits was chevron cap with tapered tip creating expansion waves at the chevron nozzle exit.

Thanigaiarasu et al. [7] used both planar laser-induced fluorescence and particle image velocimetry to study confined, turbulent coaxial jets in a non-axisymmetric co-flow. The results showed that the introduction of a coaxial stream affected the inner jet and reduced mixing with the surrounding co-flow. The effect was amplified as the coaxial jet's momentum flow ratio increased synthetic jets perpendicular to the mainstream as utilized by Shankar et al. [8] to experimentally examine the mixing enhancement of coaxial jets. PIV and hot wire anemometers were used to measure coaxial jet parameters like turbulence intensity, Reynolds shear stress, radial velocity, streamwise velocity and vorticity. Besides, it was discovered that the momentum coefficient was the most important factor in enhancing jet mixing.

Hence, this numerical analysis focuses on the mixing and flow acoustics of co-annular nozzles by modifying the nozzle geometry with various primary and secondary nozzle combinations. The circle-circle nozzle is taken as a reference case to compare the flow acoustics of other two nozzles.

29.3 Methodology

29.3.1 Computational Setup

The computational model is done using Solidworks software and the computational simulation is carried out using ANSYS Fluent software [9]. The dimensional details and three-dimensional models of all the three nozzles namely base circular nozzle, circle-chevron and chevron-circle nozzle are shown in Figs. 29.1 and 29.2. Circle-chevron or outer chevron nozzle indicates the primary (inner) circular nozzle with chevron nozzle as secondary one (outer) and chevron-circle or inner chevron indicates the primary chevron nozzle with the secondary circular nozzle. The k-ε realizable turbulence model is used. The number of nodes and elements used for the three models in these investigations are listed in Table 29.1.

29.3.2 Experimental Setup

The experimental analysis is carried out by using an anechoic chamber of size 100 cm × 80 cm × 80 cm and ARDUINO UNO controller, condenser microphone sound

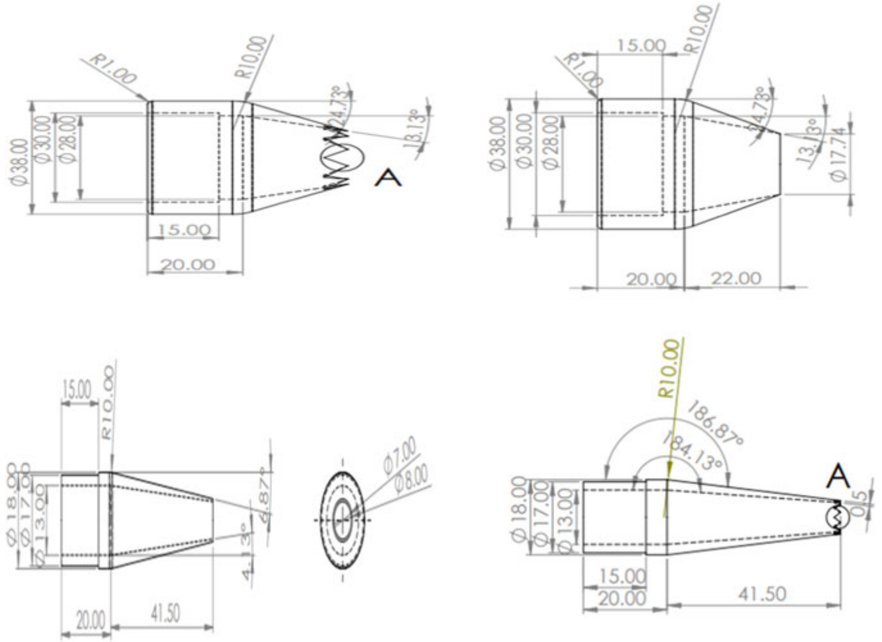

Fig. 29.1 Longitudinal cross-section of the inner and outer nozzles

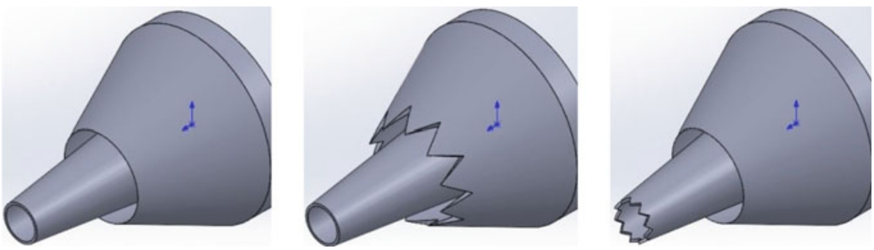

Fig. 29.2 3D model of co-annular nozzles (circle-circle, circle-chevron, and chevron-circle)

Table 29.1 Number of nodes and elements for the three co-annular nozzles

Nozzles	Nodes	Elements
Base nozzle	125,537	1,094,224
Inner chevron nozzle	210,204	1,094,224
Outer chevron nozzle	207,292	1,079,753

sensor, ARDUINO IDE software is used to collect the sound pressure level of co-annular nozzles. The three co-annular nozzles namely the circle-circle, circle-chevron and chevron-circle nozzles made up of stainless steel are shown in Fig. 29.3. Base co-annular circle-circle nozzle (without any chevrons) is used as reference to compare the remaining two nozzles. The chevron used as both inner and outer nozzle has a count of eight. The experimental setup used for this analysis is shown in Fig. 29.4. In experimental analysis, the main aim is to find the sound pressure level (dB) of each co-annular nozzle at different pressure variations of 70, 80 and 90 psi.

The sound pressure level (SPL) is found by using a condenser microphone sound sensor connected to an Arduino board which is programmed to collect analog data SPL from the sound sensor and data acquisition system has been used to extract the data. The whole process is carried inside the acoustic chamber which is used to avoid the noise from outside and to run the experiments without any disturbances. The condenser microphone sound sensor is the main component which is to collect the sound pressure level values in decibel units per second from programmed code which is already uploaded in Arduino UNO board.

Fig. 29.3 Fabricated three co-annular nozzles (circle-circle, circle-chevron, and chevron-circle)

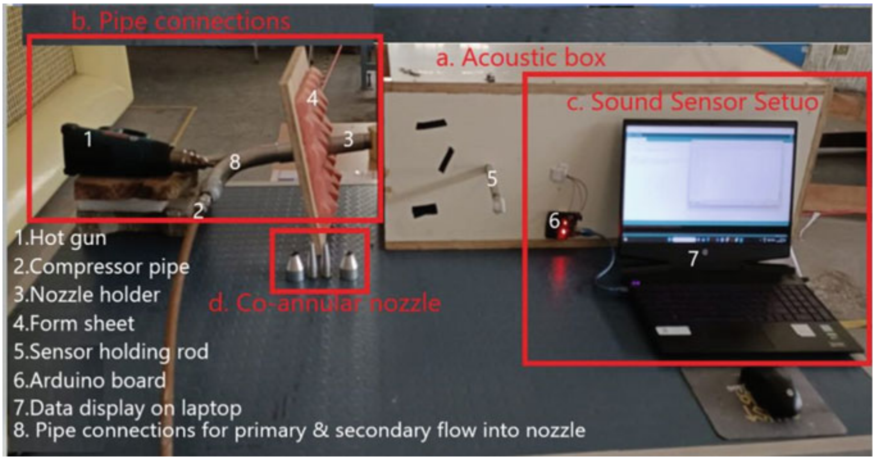

Fig. 29.4 Experimental setup

29.4 Results and Discussion

Researchers and engineers use computational fluid dynamics simulations and experimental techniques to understand and optimize the flow behavior and acoustic performance of exhaust nozzles. The outcome of this simulation is to find the co-annular nozzle that gives low acoustic power level without compromising on outlet flow efficiency.

The velocity magnitude contours of the three co-annular nozzles are shown in Figs. 29.5, 29.6, and 29.7. The velocity magnitude is larger near the nozzle exit for both primary and secondary nozzles and it reduces downstream as the evolution of jet occurs. The potential core length is the nozzle exit Mach number which prevails up to certain distance. The potential core length is less if jet decays at a faster rate and vice versa. As can be seen in these figures, it is observed that the potential core length is small in case of circle-chevron nozzle compared to other two nozzles. This shows that the interaction between the jets from the primary nozzle and secondary nozzle is more and stronger in case of circle-chevron. The chevrons in the secondary nozzle breakdown the large coherent structures to small ones which results in a large mass entrainment and promoting turbulence and mixing. This controls the evolution of noise arising from the circle nozzle.

There are four shear layers for the jets emanating from the co-annular nozzles: two inner shear layers and two outer shear layers. The shear layers emanating from the interface of primary-secondary and secondary-ambient can be seen in Figs. 29.5,

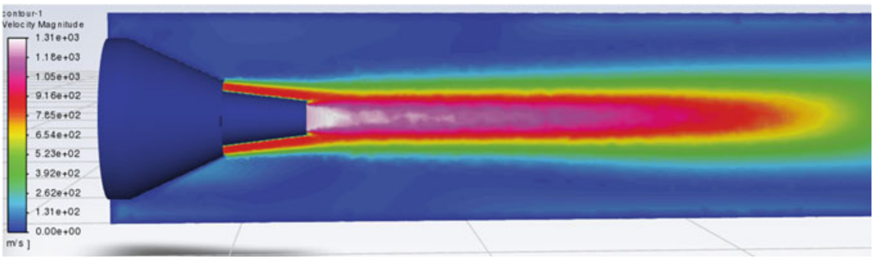

Fig. 29.5 Velocity magnitude contour of base circle-circle nozzle

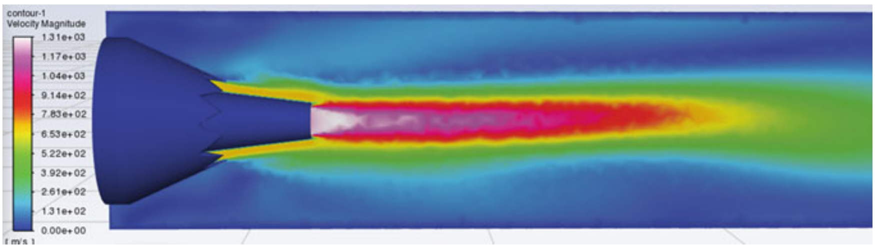

Fig. 29.6 Velocity magnitude contour of circle-chevron nozzle

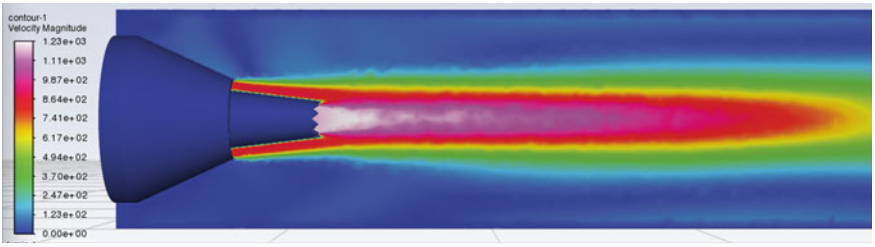

Fig. 29.7 Velocity magnitude contour of chevron-circle nozzle

29.6, and 29.7. The interaction happens between inner and outer shear layers. There is also interaction between the outer shear layer and the ambient. There is a mass entrainment of ambient fluid across the outer shear layer of the secondary chevron nozzle in circle-chevron nozzle as seen in Fig. 29.6. This is more than the entrainment caused by the chevron in chevron-circle nozzle as the fluid between the inner shear layer of primary chevron nozzle and secondary circular nozzle is limited. The inner potential core from the primary nozzle is bounded by the potential core generated by the secondary nozzle. At the end of potential core, the jet tends to behave like a single jet. The mixing process creates large-scale turbulent structures, known as 'jet plumes' that propagate sound waves and generate noise.

The acoustic power level in an aircraft exhaust nozzle refers to the amount of sound energy radiated by the exhaust gases passing through the nozzle. It is a measure of the noise generated by the engine exhaust system. The acoustic power level is typically quantified using decibels (dB) or sound pressure levels (SPL). To estimate the acoustic power level, researchers use various techniques such as computational fluid dynamics (CFD) simulations and experimental measurements. CFD simulations involve solving the equations of fluid dynamics and acoustics to predict the flow behavior and noise generation in the exhaust nozzle. The acoustic power level contours of the three co-annular nozzles are shown in Figs. 29.8, 29.9, and 29.10. As can be seen in these figures, it is evident that the acoustic power level is less in case of circle-chevron nozzle compared to other two nozzles.

Also, the acoustic power level from both primary and secondary nozzle emerges as a single in Fig. 29.9 which leads to a decrease in sound. The chevron nozzle's

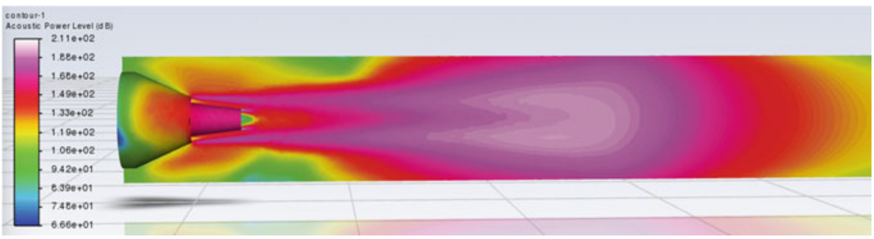

Fig. 29.8 Acoustic power level of circle-circle nozzle

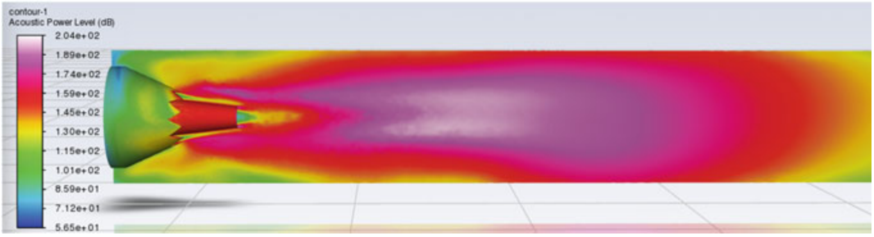

Fig. 29.9 Acoustic power level of circle-chevron nozzle

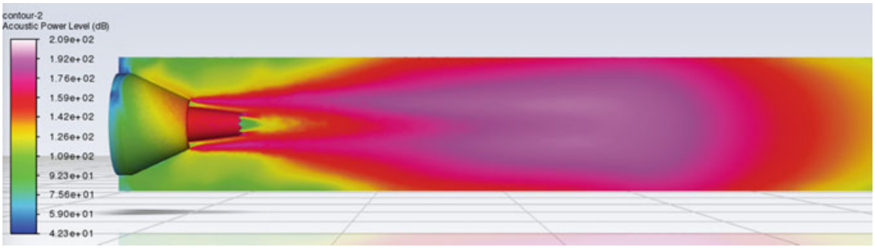

Fig. 29.10 Acoustic power level of chevron-circle nozzle

jagged edges may cause more turbulence to enter and exit the shear layers. Therefore, it can aid in the two jets' mixing [10]. As the mixing is improved, the noise greatly reduces as the jet decays faster due to this mixing. The area between the inner shear layer and the outer shear layer is important as there is momentum and energy transfer.

Sound pressure level, on the other hand, is a measure of the sound pressure at a particular location. Sound pressure level (SPL) versus time is a graphical representation of the variations in sound pressure over a specific period. It provides a visualization of the temporal changes in sound intensity or loudness. In this experimental work, three co-annular nozzles are tested with the primary and secondary flow of 70, 80, and 90 psi pressures. Acoustic power level reading is collected by using sound sensor in terms of sound pressure level (dB). The sound pressure levels such as 70, 80 and 90 psi plotted against time for the various nozzles are shown in Figs. 29.11, 29.12, and 29.13.

In a sound pressure level versus time graph, the x-axis typically represents time, while the y-axis represents the sound pressure level in decibels (dB). The graph shows how the sound pressure level fluctuates over time, indicating the presence of sound events, their intensity, and duration. The variation of pressure profoundly influences the sound pressure level in the three co-annular nozzles. Chevrons are used to minimize the sound at the exit of the jet engine. For 70 psi, the reduction in sound pressure level is more which is around 5%. The turbulence generated by the circle-chevron or outer chevron nozzle affects the characteristics in the initial merging region which precedes the intermediate region. In the circle-chevron nozzle, the secondary jet protects the primary jet in such a way that the noise level is greatly

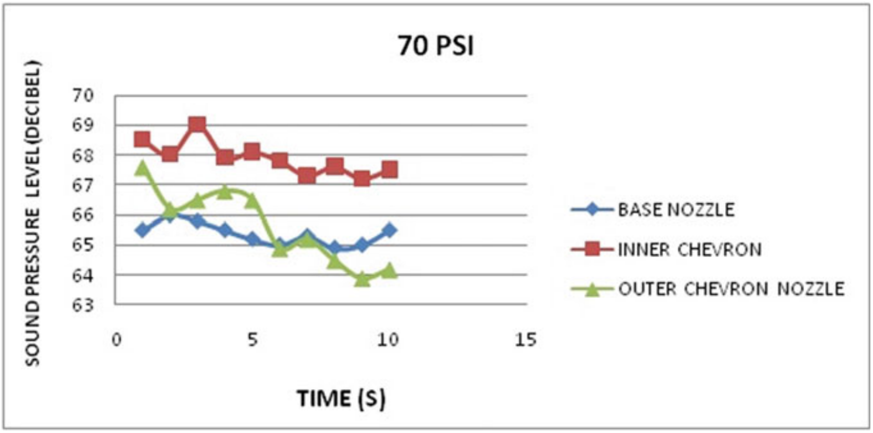

Fig. 29.11 Sound pressure level at 70 psi versus time

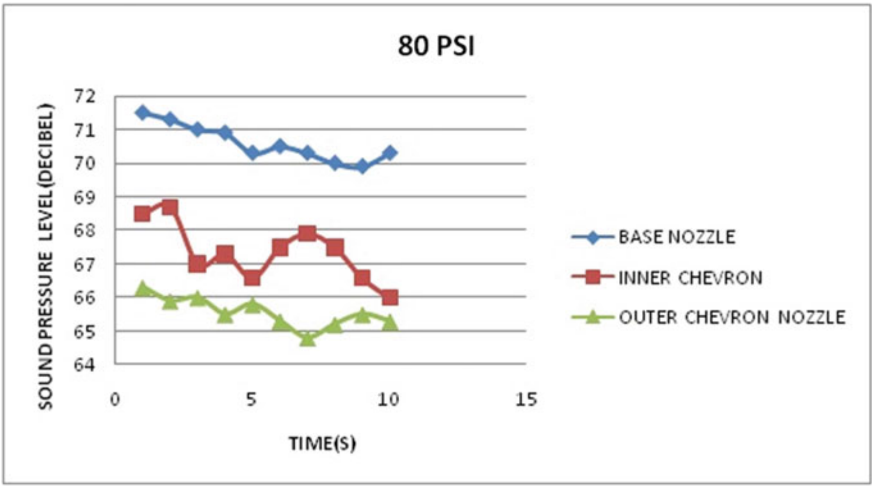

Fig. 29.12 Sound pressure level at 80 psi versus time

reduced. As the pressure increases, there is a rapid decrease in acoustic power level in the near-field region and 5–6% noise reduction in seen in circle-chevron compared to other two nozzles. But in the case of chevron-circle nozzle, the secondary jet decreases the development rate of the primary shear layer and lengthens the primary potential core of the jet. To reduce the acoustic power level in aircraft exhaust nozzles, design strategies focus on optimizing the nozzle geometry, reducing turbulence, coherent structures, and promoting mixing between the exhaust gases and the ambient air.

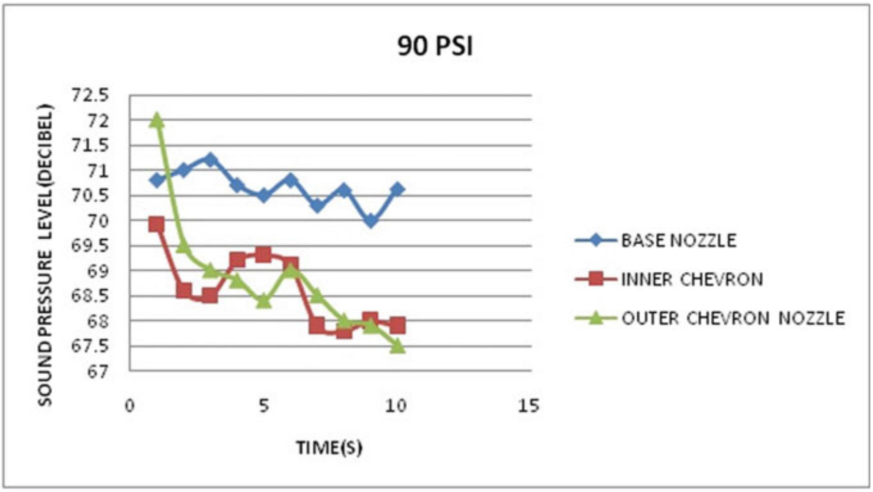

Fig. 29.13 Sound pressure level at 90 psi versus time

29.5 Conclusion

Based on the computational results, the potential core length in the case of circle-chevron nozzle is lesser than other nozzles. This is due to the better mass entrainment between the fluids of inner shear layer, outer shear layer and the ambient. Hence, there is a rapid decay of the jet which is due to the result of mixing enhancement caused by the chevrons in the secondary nozzle. This leads to a reduction of noise in case of circle-chevron nozzle. These are observed from the velocity magnitude and acoustic power level contour plots obtained.

Sound pressure level is obtained through experimental investigations from the sound sensor and plotted against time. It is concluded from the graph that there is a decrease in noise for circle-chevron nozzle. Therefore, the circle-chevron is best for noise reduction and mixing compared with base nozzle. It is evident that the acoustic power level reduces up to 5–10 dB in circle-chevron nozzle as compared with other nozzles. Also, there is a rapid decrease in acoustic power level in the near-field region and 5–6% noise reduction in seen in circle-chevron compared to other two nozzles. This work also shows that the nozzle geometry has a greater impact on both mixing and acoustic characteristics in a co-annular jet. The potential core length reduction causes a change in the flow acoustics and finally leads to noise reduction.

References

1. Papamoschou, D.: Mixing enhancement using axial flow. In: Proceedings of the 38th Aerospace Sciences Meeting and Exhibit, 2000-0093 (2000). https://doi.org/10.2514/6.2000-93
2. Zaman, K.B.M.Q., Papamoschou, D.: Study of mixing enhancement observed with a co-annular nozzle configuration. In: Proceedings of the 38th Aerospace Sciences Meeting and Exhibit, 2000-0094 (2000). https://doi.org/10.2514/6.2000-94
3. Srinivasarao, T., Lovaraju, P., Rathakrishnan, E.: Characteristics of co-flow jets from orifices. Int. J. Turbo Jet Eng. **31**(2), 141–148 (2013). https://doi.org/10.1515/tjj-2013-0040
4. Zaman, K.B.M.Q., Dahl, M.D.: Noise and spreading of subsonic coannular jets—comparison with single equivalent jet. AIAA J. **45**(11), 2661–2670 (2007)
5. Tide, P.S., Srinivasan, K.: Effect of chevron count and penetration on the acoustic characteristics of chevron nozzles. Appl. Acoust. **71**(3), 201–220 (2010)
6. Muthuram, A., Thanigaiarasu, S., Divvela, R., Ethirajan, R.: Nozzle geometry effect on twin jet flow characteristics. Int. J. Turbo Jet Eng. **39**(4), 525–532 (2022)
7. Thanigaiarasu, S., Shankar, R.N., Rathakrishnan, E.: Influence of bypass ratio on subsonic and correctly expanded sonic coflowing jets with finite lip thickness. Proc. Inst. Mech. Eng. Part G J. Aeros. Eng. **233**(7), 2536–2548 (2018). https://doi.org/10.1177/0954410018782511
8. Shankar, R.S., Thanigaiarasu, S., Elangovan, S., Rathakrishnan, E.: Coflowing jet control using lip thickness variation. Int. J. Turbo Jet Eng. **38**(3), 289–302 (2021). https://doi.org/10.1515/tjj-2018-0024
9. Muthuram, A., Venkat Raman., S, Kavikumar, K., Seralathan, S., Sathish, S., Anita, M.: Computational investigation of jet mixing enhancement by CD nozzle with arc tabs. In: Proceedings of the International Conference on Power, Energy, Control and Transmission Systems (ICPECTS), Chennai, pp. 1–6 (2022)
10. Zaman, K.B.M.Q., Bridges, J.E., Fagan, A.F., Miller, C.J.: Tones encountered with a coannular nozzle and a method for their suppression. AIAA J. **56**(5), 1922–1929 (2018)

Chapter 30
Experimental Investigations on Aerodynamics Parameters of Combined Tubercles with Vortex Generator on NACA 0015 Wing Airfoils

Abhishek Badampudi, Pavankalyan Avilala, Mohanashouri Patnam, Saravanan Periasamy, Sankaralingam Lakshmanan, Seralathan Sivamani, and Saranya Kanagarajan

Abstract The basic airfoil is made to enhance its post-stall performance at stall conditions compared to pre-stall conditions. Thus, the focus of this study is to combine vortex generators and leading-edge tubes to increase the airfoil's L/D ratio in the post-stall phase. The tubercles like (Spherical Leading-edge Tubercles) SLET and (Triangular vortex generator) TVG were chosen for this study based on the performance reported in earlier research. The wing model with SLET and TVG combination pair are investigated experimentally for varied angle of attack from 0° to 24°. The modified combination in wing improved the coefficient of lift for various angles of attack and in the post stall conditions. This is due to TLE and VG's streamwise vortices that occurs and stagnate around the surface for a longer period, thereby delaying flow separation and lowering pressure drag nearer to the wing models trailing edge.

30.1 Introduction

Boundary layer effects on separation plays a critical role in flow separation and significantly affects the fluid flows performance in many technological applications and plays a key part in how well the body being exposed to the flow behavior. Low Reynolds number flows are one where separation bubbles detrimental impacts

A. Badampudi · P. Avilala · M. Patnam · S. Periasamy · S. Lakshmanan · S. Sivamani (✉)
Department of Aeronautical Engineering, Hindustan Institute of Technology and Science, Chennai, Tamilnadu 603 103, India
e-mail: siva.seralathan@gmail.com

S. Kanagarajan
Department of Physics, Government College of Engineering, Thanjavur, Tamilnadu 613 001, India

P. H. V. S. Talpa Sai et al. (eds.), *Intelligent Manufacturing and Energy Sustainability*, Smart Innovation, Systems and Technologies 372,
https://doi.org/10.1007/978-981-99-6774-2_30

are most prominent. Lift enhancement attachments are incorporated to a wing to compensate mentioned parameters.

Despite its enormous size and weight, the humpback whale (Megaptera Novaeangliae) can spin and jump with great precision [1]. Humpback whales possess protuberances in flippers, which may account for their impressive motions. The authors reasoned that if this trait could be applied to a wing, its attributes might be enhanced. 'Tubercle Effect' is the name given to this effect. The stall area of a redesigned wing emerges at a higher angle of attack than it does in an unmodified wing thereby increasing efficiency. As a result, sinusoidal tubercles are made available in the aircraft wing. In comparison with sinusoidal Tubercle Leading Edge (TLE) and airfoil without TLE, spherical TLE showed a modest improvement [2].

A small fin-like device called a 'Vortex Generator' (VG) is fitted on the lifting surface to delay stalling and decrease the flow separation aerodynamically. As a result, different results might be predicted, including improved aerodynamic behavior like steep climbs, larger capacity, and stall speeds along with unfavorable inferior effects such as a cruising speed decrement, icing as well if not properly placed or proportioned [3]. There are many different types of VGs like vane, triangular, rectangular, etc. Rectangular VGs are mostly commonly used. The location of VGs in the aircraft wing design from the leading edge to the rotor blades and it is found in a variety of applications like blade root, fuselage surface and wind turbine blades.

Vortex generators and other lift-enhancing devices are fitted to the wing [4]. Recent research has shown that TLEs, in addition to VGs, can also create beneficial streamwise vortices that induce delaying separation flows [5]. Many conflicting views on the performance of other TLE's with sinusoidal and spherical, but it is found that spherical TLE outperformed sinusoidal TLE [2]. There is also debate over the specifications for the TLE's size in spherical are resolved by testing using the trial-and-error method [6]. Additionally, there are conflicting views on the best shape, type, and performance of VGs. The rectangular and triangular VG's performance are analyzed in low Reynolds numbers [7, 8]. The idea of TLE + VG in the airfoil emerged with improved aerodynamic performance compared to base plain airfoil [9]. TLE's and VG's main job is to produce streamwise vortices in counter-rotating direction.

The leading-edge inserts significantly improve the performance of aircraft at low to high 'α' (angle of attack) due to creation of a high level-swirl vortex that helps to keep the flow attached on top surface of wing's and allows the wing to generate lift beyond the stall condition. Even though the VGs behave like tiny winglets and perform similar functions to the TLE, these create small, induced tip vortices shaped like spiral impinging on the boundary layer and airflow on the top surface of the wing. The produced vortices associate with energy levels of high to low layers and assisting boundary layer's flow to resist the negative pressure gradient level for a quite longer duration and postponing the stall.

The main objective is to combine TLE and VGs on upper surface wing to produce vortices and help to delay the bubble separation and improvement in stall angle yields to higher aerodynamic efficiency of wing configuration. According to reports from prior years on lift enhancement devices, TLE and VGs both perform better than the standard airfoil on their own. Based on extensive research on the passive devices, it appears that all delay separation impinges on individual bubbles. The crucial aim is to combine the TLE's and VG's performance into single form in the modified wing and compare it to base wing. Based on research into this concept, it is discovered that this combination has already been used on the cambered NACA 4415 airfoil [10, 11]. The symmetrical wing airfoil geometry is chosen because the cambered airfoil geometry is already tested, and the results are already known. Thus, the NACA 0015 is used for this study to sketch the parametric analysis of TLE's and VG's [12, 13].

Therefore, the objective of this work is to investigate the idea of TLE with VG positioned on a wing with symmetric cross-sectional airfoil based on influential parameters chosen through pervious research work [14, 15]. In this study NACA 0015 is chosen as the base airfoil and experiments are performed for TLE and VGs with different combinations at varied angle of attacks from 0° to 24°. By adding Tubercles and Vortex Generators, they are positioned in the leading-edge portion of the wing to postpone the stall effects.

30.2 Experimental Investigation

To accommodate constraints, the model is fabricated in wood to get the good surface finish to observe the flow over different wing configurations. VG with Delta vane are positioned on wing top surface with 26 pressure ports insertions and painted to ensure smooth surface [16–18]. These 26 pressure ports are placed over the upper and lower surfaces of a wooden model with proper attachment to clamp the wing model in the wind tunnel test section at the specified angle of attack with a fixture attached to it. A sheet of aluminium with a thickness of 2 mm is used for the creation of the vortex generator, and it was divided into four equal pieces. The model has the vortex generators attached and the finished airfoil with leading edge tubercles and vortex generators is shown in Fig. 30.1.

The wing model is mounted in a wind tunnel. Tubes of size 0.8 mm diameter are used to connect the ports to the inline manometer. The test section speed is calibrated with the help of inline manometers to ensure accuracy and standardizing the benchmarks. When the model is positioned at zero angle of attack, the wind tunnel is operated at 10 m/s, and the manometer is allowed to stabilize before readings of the variables, as well as static pressure and dynamic pressure are recorded. The same process is followed till the angle of attack (AOA) is 24° with a gap of 3°. A spreadsheet with the collected data is created, and the coefficient of pressure (C_P) is calculated [19].

$$C_n = \frac{1}{C}\int \left(C_{pl} - C_{pu}\right)dx \tag{30.1}$$

where C_p is the coefficient of pressure

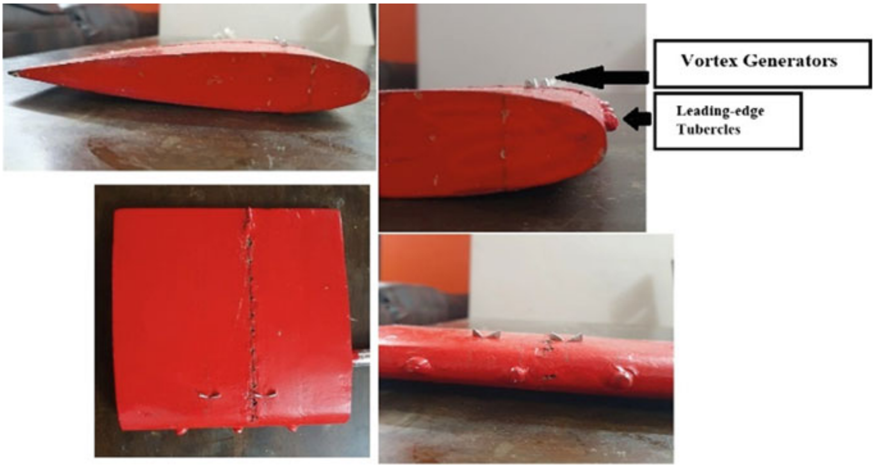

Fig. 30.1 TLE's with VG wing configuration

$$C_l = C_n cos \propto - C_a sin \propto \quad (30.2)$$

where α is the angle of attack in degrees

The above stated Eqs. (30.1) and (30.2) are used for the calculations of coefficient of lift (C_L) and the values are tabulated in Table 30.1. Figure 30.2 shows the wing with attachments during different angles of attacks from 0° to 24°.

Table 30.1 C_L values for various wing configurations

α (degrees)	Plain	TLE	VG	TLE and 2VGs	TLE and 4VGs
0	0	0	0	0	0
3	0.1	0.14	0.18	0.2	0.18
6	0.22	0.28	0.32	0.35	0.34
9	0.31	0.37	0.41	0.47	0.44
12	0.43	0.51	0.58	0.62	0.59
15	0.59	0.64	0.69	0.74	0.69
18	0.72	0.82	0.85	0.91	0.87
21	0.643	0.673	0.71	0.74	0.69
24	0.61	0.64	0.68	0.72	0.64

Fig. 30.2 Different AOA of the wing with attachments

30.3 Results and Discussion

The fabricated wing configurations are tested in wind tunnels from 0° to 24° angle of attacks in steps of 3°. The pressure port values are acquired through inline manometer for all angles of attack (AOA). The C_L values for all wing configurations are calculated using the Eq. (30.2) and values of ratio between C_L and C_D are listed in Table 30.2. Figure 30.3 shows the variations of C_L with different angles of attacks. As can be seen in Fig. 30.3, for all the wing configurations the C_L values are linearly increasing up to AOA 18°. Further increase in the angle of attack leads to variations in the coefficient of lift values and the C_L value tends to decrease due to stall effects.

As can be seen in Fig. 30.3, C_L values for the wing configuration are marked as increasing trend up to 18° AOA and then, it decreases for further increase in

Table 30.2 Aerodynamic parameters for all the wing configurations

Wing configurations	C_L/C_D	$\Delta C_L/C_D$
Base wing	2.79	–
TLE's attached	2.53	– 9.40%
VG attached	2.36	– 15.38%
TLE with 2VG attached	3.33	19.50%
TLE with 4VG attached	3.22	15.00%

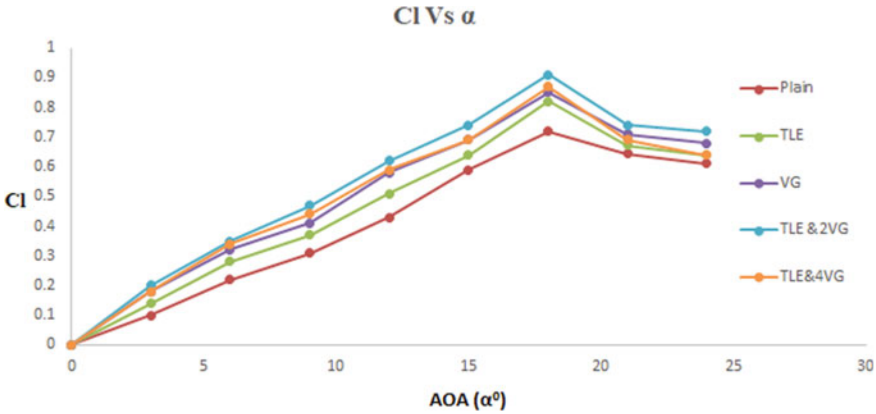

Fig. 30.3 C_L Vs α for wing configurations

angle of attack. In specific, TLE with 2VG performed better at 18° AOA and the corresponding C_L value is 0.91. On the other hand, TLE with 4VG performed better at 18° AOA with C_L value of 0.85 in comparison with TLE and VG alone wing configurations. TLE with 2VG gave and 50% improvement in C_L in comparison with base plain wing configuration. Moreover, as can be seen in the Fig. 30.4, the TLE with 2VG attachments perform well at stall condition comparison with other wing configurations.

As mentioned in Table 30.2, the C_L/C_d ratio are calculated using Eq. (30.2) and it is observed that the wings with TLEs with 2VGs and TLEs with 4VG has the difference in C_L/C_d ratio of 19.5% and 15% with reference to base plain wing respectively at AOA 18°. The experimental C_L values as depicted in Fig. 30.3 recorded the maximum magnitude of C_L as 0.7201 at angle of attack (AOA) 18°. The greatest value of C_L of 0.7201 seen at 18° and further increase in angle of attack, C_L start to decrease. The critical angle of attack at which the C_L is greatest is AOA 18° decreasing trend of C_L begins in further increasing the angles of attack.

Figure 30.4 displays the wing model of TLE with 2VG till the stall angle at AOA 18° for experimental investigations and the same at 21° AOA in computational studies. The trend observed both in experimental investigations and numerical analysis are similar with decrease in lift gradually beginning at 18° AOA onwards in

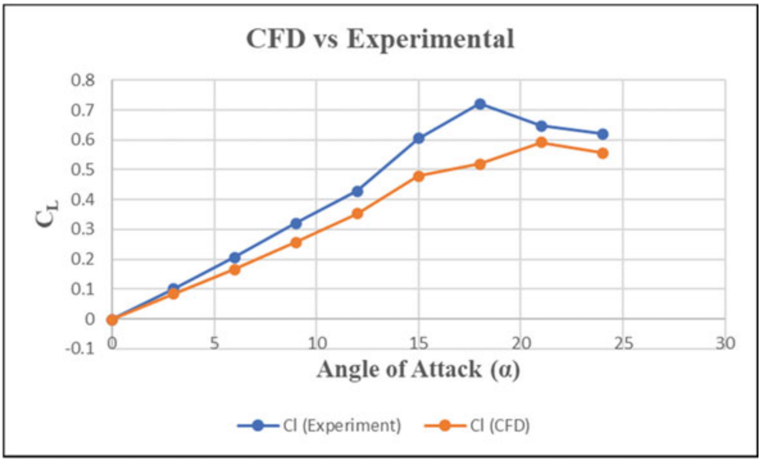

Fig. 30.4 C_L Vs α of wing model with TLE and 2VGs

experimental case whereas the same commences at 21° AOA in case of computational study. This phenomenon occurs due to chordwise vortices induced by TLE with VG, which promotes the sticking flow effects on surface to be lengthier, ensuring separation delay which are sinking the pressure drag formation near the wing trailing edge.

Figure 30.5 shows the variations of C_L with various plain wing models with TLE, 2VGs and 4VGs. As can be seen in Fig. 30.6, at angle of attack $\alpha = 21°$, the plain wing begins to stall and in case of TLE + 2VGs, the stall occurs at $\alpha = 18°$. But TLE + 4VGs, it is observed that the stall pattern is similar to that of plain wing model. The wing with 2VGs is found to be enough to increase the performance rather than using 4VGs.

Figure 30.6 shows the variations of C_D with various plain wing models with TLE, 2VGs and 4VGs. As can be observed in Fig. 30.7, at angle of attack $\alpha = 18°$, the plain wing starts to increase the drag compared to VG fitted wings. A similar drag trends is observed for 2VGs and 4VGs fitted wings. A significant drag reduction is observed before 15°. Therefore, it is noticed that plain wing starts to increase the drag after certain AOA but not the wing with TLE and 2VGs or 4VGs. Moreover, the wing with 2VGs is found to be good enough to decrease the drag rather than 4VGs.

The variations of C_L/C_D are shown in Fig. 30.7. At angle of attack $\alpha = 15°$, plain wing starts to reduce in L/D ratio in comparison with VG fitted wings. The L/D ratio for 2VGs and 4VGs fitted wings are slightly higher than plain wing and it is seen with significant L/D ratio beyond 15° onwards. Moreover, it is noticed that at certain AOA the plain wing starts to show a decrease L/D ratio but not the wing with TLE and 2VGs or 4VGs. Furthermore, the wing with 2VGs is observed to be enough to give the expected L/D performance rather than 4VGs. Table 30.3 lists the C_L/C_D behavior of various wings considered in this study.

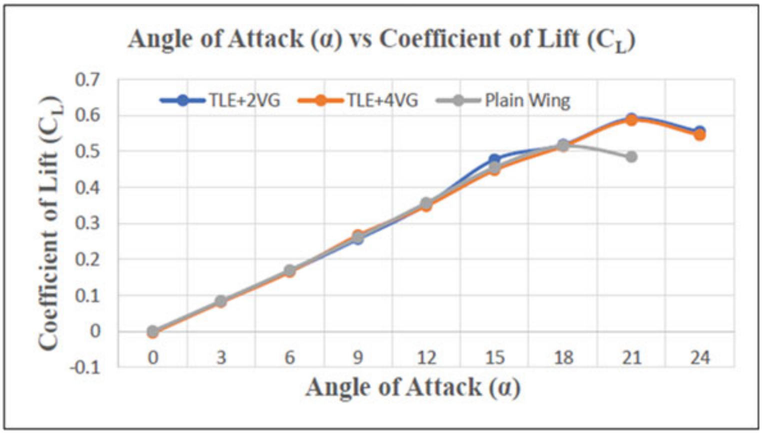

Fig. 30.5 C_L Vs α of plain wing model with TLE, 2VGs and 4VGs

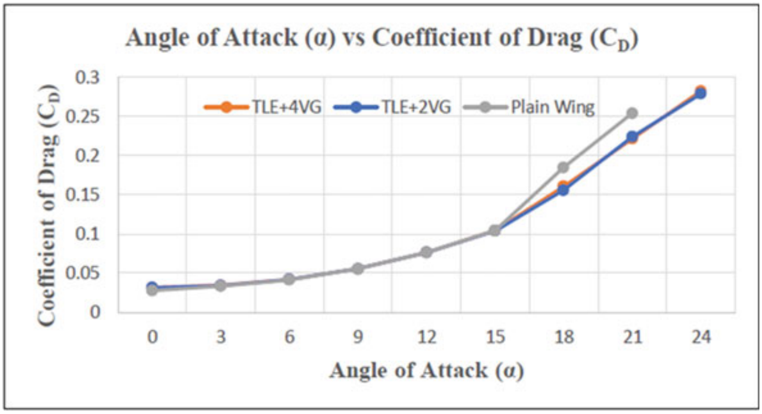

Fig. 30.6 C_D Vs α of plain wing model with TLE, 2VGs and 4VGs

It is clear that after certain AOA, the plain wing starts to stall but it is delayed with wings with TLE having 2VGs or 4VGs. The stall for the wing with TLE with 2VGs or 4VGs occurs at α = 21°. Table 30.3 shows the behavior at these two angles of attack for better comprehension. At 18° angle of attack, wing with TLE and 2VGs as well as TLE and 4VGs performs 19.50 and 15.00% better in comparison with plain wing. But, at 21° angle of attack, wings with TLE and 2VGs as well as TLE with 4VGs outperformed plain wing but gives a similar performance to that of 2VGs. Thus, wings with TLE + VGs are enough to increase the aerodynamic performance rather than 4VGs.

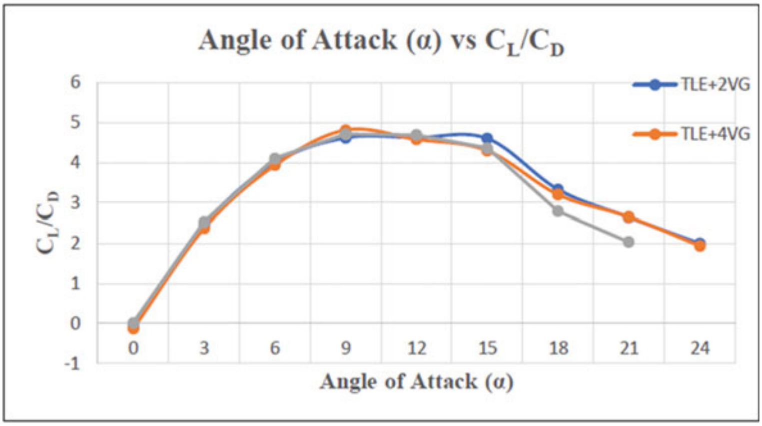

Fig. 30.7 C_L/C_D Vs α of plain wing model with TLE, 2VGs and 4VGs

Table 30.3 C_L/C_D behavior

Air foil model	α = 18°		α = 21°	
	C_L/C_D	$\Delta C_L/C_D$	C_L/C_D	$\Delta C_L/C_D$
Plain wing	2.78862	–	2.02636	–
Wing with TLE	2.53656	– 9.40%	2.17410	6.80%
Wing with VG	2.35974	– 15.38%	2.14267	5.43%
Wing with TLE + 2VG	3.33306	19.50%	2.64168	23.29%
Wing with TLE + 4VG	3.20562	15.00%	2.64803	23.48%

30.4 Conclusion

The performance of the modified wings and the plain wing are evaluated, and the findings show that the TLE and VG wings performed marginally better than the conventional plain wing model. The results obtained for TLE with 2VG and TLE with 4VG wing models indicate that the performance is not significantly different with each other. However, both models performed better than the standard plain wing model. C_L/C_D ratio of the wings with TLE with 4VG and 2VG plain wing configurations are better at 18° angle of attack.

The experimental analysis proves that TLE + 2VG wing configurations yields better C_L value compared to other wing configurations. C_L of TLE + VG improved with increase in angle of attack till 18°, but the decline in C_L is noticeably smooth rather than sharp. After the stall angle, the C_L would drastically decrease for any wing profile. The inclusion of TLE and VG in the wing configuration caused streamwise vortices that helped the flow to adhere on the surface for a longer duration, and postponing the flow separation yields thereby minimizing pressure drag on the wing trailing edge. This phenomenon guarantees the improved performance of the TLE

+ VG which are inserted wing at post-stall regime, where lift is lost gradually and smoothly rather than abruptly. Further numerical studies are needed to determine the drag effects while adding the inserts at leading edge, and VG at different wingspan locations to identify the performance post stall performance.

References

1. Fish, F.E., Lauder, G.V.: Passive and active flow control by swimming fishes and mammals. Ann. Rev. **38**, 193–224 (2006)
2. Aftab, S.M.A.: Numerical and experimental study of leading-edge tubercles with vortex generators on NACA 4415 airfoil. Ph.D Thesis (2017)
3. Kristy, L.H.: Effect of leading-edge tubercles on airfoil performance. Ph.D, Thesis (2012)
4. Sudhakar, S., Venakata Krishnan, L., Ramesh, O.N.: The Influence of Leading-Edge Tubercles on Airfoil Performance at Low Reynolds Numbers. AIAA, SciTech Forum (2020)
5. Syed Mohammed Aminuddin Aftab, Srinivasa Murthy, P.: Comparative of vortex generator orientation on wing surface considering delta vortex generators. Appl. Mech. Mater. **225** (2012)
6. Fouatih, O.M., Medale, M., Imine, O., Imine, B.: Design optimization of the aerodynamic passive flow control on NACA 4415 airfoil using vortex generators. Eur. J. Mech. B Fluids **56**, 82--96 (2016)
7. Aftab, S.M.A., Ahmad, K.A.: CFD study on NACA 4415 airfoil implementing spherical and sinusoidal tubercle leading edge. PLoS ONE **12**(11), e0188792 (2017)
8. Calle, O.L.: Preliminary study of the vortex generators in ultralight aircraft (2015)
9. Chellin, S., Uriate, A., Martinez, P., Fernandez, U., Losu lbarra, L.: Modeling of vane-type vortex generators and study on airfoil aerodynamic performance. Energies **13**(10), 2423 (2020)
10. Kumar, R., Architha, N., Deodhar, R., Tejas, N., Menon, R.: Analytical testing of vortex generators with an airfoil profile. IJERT NCETESFT **8** (2020)
11. Fouatih, O.M., Medale, M., Imine, O., Imine, B.: Design optimization of the aerodynamic passive flow control on NACA 4415 airfoil using vortex generators. Eur. J. Mech. B/Fluids **56** (2016).
12. Hares, H., Mebarki, G., Brioua, M., Naoun, M.: Aerodynamic performances improvement of NACA 4415 profile by passive flow control using vortex generators. J. Serbian Soc. Comput. Mech. **13**, 17–18 (2019)
13. Sahin, I., Acir, A.: Numerical and experimental investigations of lift and drag performances of NACA 0015 wind turbine airfoil. Int. J. Mater. Mech. Manuf. **3**(1), 22–25 (2015)
14. Johari, H., Henoch, C.W., Custodio, D., Levshin, A.: Effects of leading-edge protuberances on airfoil performance. AIAA J. **45**(11), 2634–2642 (2007)
15. Huang, J.B.: Study of control effects of vortex generators on a supercritical wing. Sci. China Technol. Sci. **53**, 2038–2048 (2010)
16. Součková, N., Simurda, D., Popelka, L.: Control of boundary layer separation on flapped airfoil with low-profile vortex generator. Colloquium Fluid Dynamics Institute of Thermo-Mechanics, Prague (2009)
17. Zhang, M., Wang, G., Xu, J.: Experimental study of flow separation control on a low-Re airfoil using leading-edge protuberance method. Exp. Fluids **55**(4), 1–13 (2014)
18. Miklosovic, D.S., Murray, M.M., Howle, L.E.: Experimental evaluation of sinusoidal leading edges. J. Aircr. **44**(4), 1404–1408 (2007)
19. Shan, H., Jiang, L., Liu, C., Love, M., Marines, B.: Numerical study of passive and active flow separation control over a NACA0012 airfoil. Comput. Fluids **37**, 975–992 (2008)

Chapter 31
Fabrication and Characterization of Carbon Nano Tube Reinforced with Alumina Matrix Material

Yemmani Suresh Babu, Syed Altaf Hussain, and B. Durga Prasad

Abstract Carbon nano tube (CNT) reinforced with alumina (Al_2O_3) were fabricated by using spark plasma sintering process with a so-gel technique. The distribution of CNT's within Al_2O_3 can be obtained by mixing the reinforcement material with matrix material of Al_2O_3 sol gel condenses as a result. The mixed consisting gel of Al_2O_3/CNT, was calcined into after being dried Al_2O_3/CNT composite powders. The composite of Al_2O_3/CNT were spark plasma sintered into CNT reinforcement and alumina matrix material. Due to more evenly distributed CNT tubes in the sharing loads, the composite's toughness has increased. All at once coefficient of thermal expansion are decreases by increasing the reinforced material in alumina, it can be with standing at very high temperature, similarly reducing the wear behavior of composite material.

31.1 Introduction

Since its discovery in 1991 new technological possibilities provided by CNT opportunities for overcoming the limitations of traditional materials. Because of its outstanding characteristics, including as great modulus of elasticity, flexibility, density, and strong electrical conductivity, carbon nano-tubes might be employed as reinforcement for composite materials [1–4]. CNT reinforced polymer matrix nano-composite have made advances in recent years, showing a considerable improvement in mechanical properties over monolithic materials. CMC's and MMC's, on the other hand, have seen relatively little progress. Because of a strong van der Waals attraction, carbon nanotubes prefer to clump together. As a result, avoiding carbon nanotube

Y. S. Babu (✉) · B. Durga Prasad
Department of Mechanical Engineering, Jawaharlal Nehru Technological University Anantapur, Ananthapuramu, Andhra Pradesh, India
e-mail: yemmanisuresh@gmail.com

S. A. Hussain
Department of Mechanical Engineering, Rajeev Gandhi Memorial College of Engineering and Technology, Nandyal, Andhra Pradesh, India

P. H. V. S. Talpa Sai et al. (eds.), *Intelligent Manufacturing and Energy Sustainability*, Smart Innovation, Systems and Technologies 372,
https://doi.org/10.1007/978-981-99-6774-2_31

agglomeration during the process of nano-tubes reinforced MMCs or CMMC's is difficult. Various efforts have been made to develop Al_2O_3/CNT nano-composites. However, the Al_2O_3/CNT nanocomposite that has been created so far has mechanical properties that are significantly lower than planned. The insertion of CNT as reinforcement enhanced fracture toughness in most cases, while it decreased hardness or strength in others. The aggregation of reinforcement is weak contact in between Al_2O_3/CNT. Due to its relatively high hardness (15–22 GPa), good oxidation resistance, and chemical stability with iron or steel, alumina is one of the most commonly used ceramic materials [5]. As a result of its weak fracture toughness, however, applications have been limited. As a result, several attempts has been made to create harder alumina by adding nano-scale second phases or a novel sintering technique like sintering process [6]. That is, In order to boost the alumina fracture toughness, CNTs are utilised as reinforcements. The sol–gel approach utilized to distribute CNTs uniformly in an alumina matrix by trapping scattered the gel network's CNTs. CNT reinforced Al_2O_3 matrix was tested for fracture toughness and hardness.

31.2 Methodology

31.2.1 Sol–Gel Technique for Producing Al_2O_3/CNT

Fabricating carbon nano-tube reinforced alumina composite. As an alumina precursor, Al (OBus)3 or aluminium tri-sec-butoxide was used. MCNT's with a diameter of 15–30 nm, a length of 10–50 m, and a density of 1.6 g/cm^3 were manufactured by CVD employing an alumina-supported catalyst. The Yoldas technique [7, 8], which involves the Aluminium hydroxide (AlOOH) is hydrolyzed and peptized, was used to make alumina sol. During the process, CNT in suspension were dispersed in ethanol, presented with alumina sol. CNT volume fractions were kept constant at 1, 3, 5, 7 and 9%. The gel of CNT and alumina was dried at 350° for 6 h. In order to create the CNT/Al_2O_3 composite powders, gel powder was calcined 1 h at 1250 °C with a 10 Pa hoover as shown in Fig. 31.1.

31.2.2 Nano-Composites with CNT Reinforcement in an Al_2O_3 Matrix Are Consolidated and Characterized

Spark plasma sintering was used to consolidate the calcinated CNT/Al_2O_3, which allows a powder compact that will be sintered using Joule heat and spark plasma produced by a powerful electric current delivered through the compact. Given that the surface oxides of powders are easily removed by the spark plasma produced during the spark plasma sintering process, the powder compact may be sintered at a

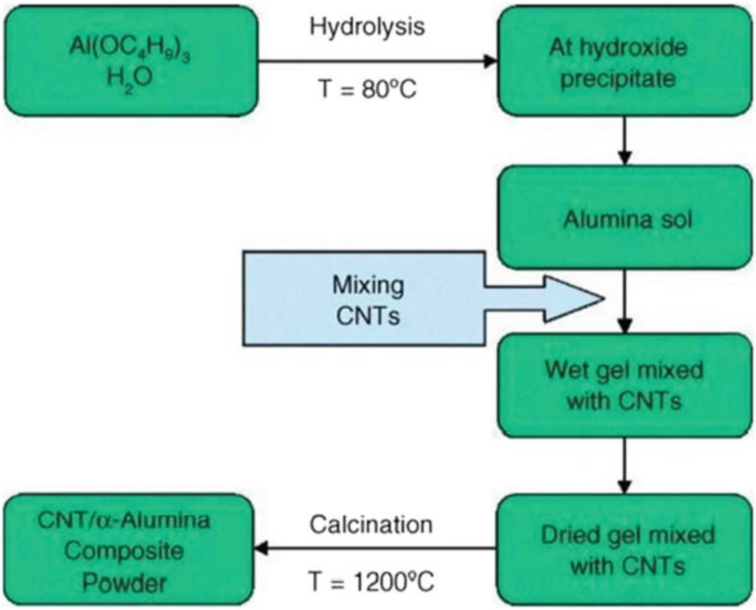

Fig. 31.1 Schematic diagram for the sol–gel manufacturing method for powdered alumina composites enhanced with CNT's

lower temperature than traditional sintering.. Calculated CNT/Al_2O_3 powders were put into a graphite mould, then sintering at 1650 °C for 5 min under a pressure of 25 MPa was performed. To eliminate carbon dispersed from the graphite mould, CNT/Al_2O_3 were sintered using spark plasma and annealed for six hours at 1000 °C. Al_2O_3/CNT nano-composite's hardness was assessed the length of the fracture was measured to determine the fracture toughness using the Vicker's indentation test with a load of 9.8 N. of the crack that was produced.

31.3 Results and Discussion

The ethanol's distributed carbon nano-tube is introduced to enhance the CNT in the Al_2O_3 matrix to alumina sol. Figure 31.2 represents the deformation observed in Plate 1 after the impact simulation. The projectile penetrated the plate completely at a velocity of 1142 m/s. It is observed that the maximum deformation is 41.414 mm. Figure 31.3 provides a visual representation of the deformation seen in Plate 1 after the impact simulation. The largest deformation measured is 41.414 mm, and the maximum deformation takes place at $1.2e^{-4}$ s. With respect to Plate 2, maximum deformation is observed as 41.503 mm at a velocity of 1131.5 m/s. It is observed that Plate 2 is completely penetrated at a velocity of 1131.5 m/s. Figure 31.4 provides a

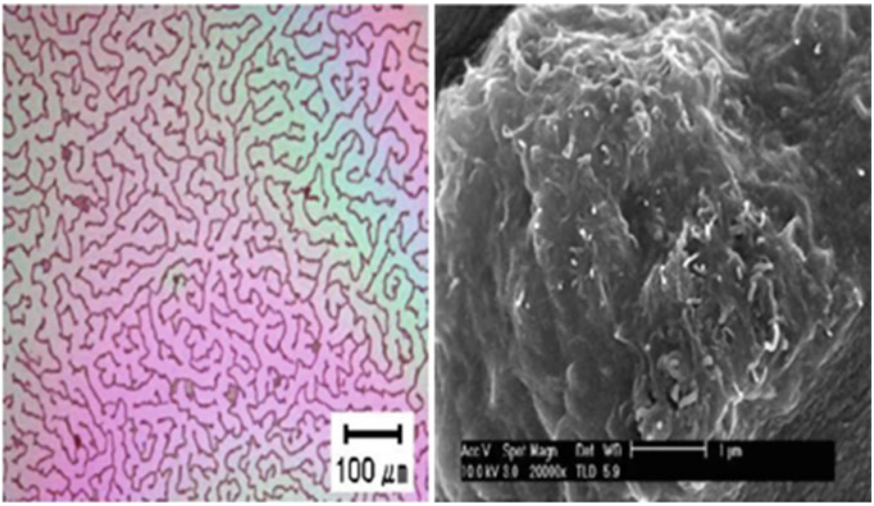

Fig. 31.2 The micrographs of Al_2O_3/CNT. **a** Microstructure of dried gel and **b** SEM analysis of calcinated Al_2O_3/CNT composite powders

visual representation of the deformation seen in Plate 2 after the impact simulation. The largest deformation measured is 41.503 mm, and the maximum deformation takes place at $1.3e^{-4}$ s. With respect to Plate 3, the maximum deformation observed is 45.289 mm at a velocity of 1139.5 m/s. Plate 3 got completely penetrated at a velocity of 1139.5 m/s. Figure 31.5 provides a visual representation of the deformation seen in Plate 3 after the impact simulation. The largest deformation measured is 45.289 mm, and the maximum deformation takes place at $1.3e^{-4}$ s.

The carbon nanotube/alumina mixed gel was dried from the alumina sol, as illustrated in Fig. 31.2a, which exhibits optical micrographs of dried Al_2O_3/CNT. The CNT are found to be uniformly disseminated inside the dried powders, with no agglomeration, in developed composites show that CNT's were implanted homogeneously within alumina powder Fig. 31.2b. Figure 31.3 shows that the, calcination of an alumina gel, alumina was produced. The Al_2O_3/CNT nanocomposite was made by sintering the composite powders together with spark plasma. Regardless of the volume percentage of carbon nanotubes, the relative density of Al_2O_3/CNT nanocomposite ranges from 99.5 to 100%. The microstructures of the Al_2O_3/CNT nano composite were studied using a SEM analysis. Figure 31.4 depicts the cracked surface of an alumina nanocomposite reinforced with carbon nanotubes that was made using the sol–gel method and sintered using spark plasma. The fracture surface of the CMC's showed the pulled-out carbon nanotubes. It demonstrates that the interface between Al_2O_3/CNT is tightly bound, and that when loading, a large amount of load is transferred from the matrix to carbon nanotubes.

When the carbon nanotube weight percentage reaches 3.3%, however, some carbon nanotubes cluster on the broken surface of the Al_2O_3/CNT of developed composite, as seen in Fig. 31.4.

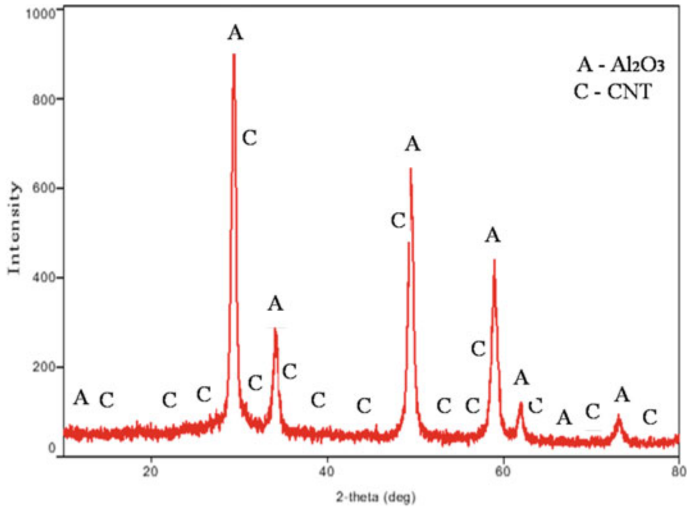

Fig. 31.3 XRD analysis of Al_2O_3/CNT

The mechanical characteristics of Al_2O_3/CNT nano-composites generated by sol–gel and sintering with spark plasma are shown in Fig. 31.5. The hardness of a produced composite rises as the CNT volume percentage rises. This contradicts recent findings that found that the hardness of produced composite diminishes as the volume percent of CNT increases [10]. It is primarily due to differences in carbon nanotube dispersion within the matrix and reinforcement interfacial strength. Because matrix material was agglomerated in prior studies, load distributed from the matrix to the reinforcement material could not be high [9–12]. The reinforcement material were disseminated inside the alumina grains and strengthened to the matrix, are observed in Fig. 31.4. As a consequence, it is possible to effectively transfer loads from the matrix to reinforcement, and CNT significantly load distributed and increasing the hardness of developed composite. This is also seen in CNT polymer nano-composites, where the strength is increased by about tenfold by adding carbon nanotubes to the polymer matrix [13]. When compared to monolithic alumina, the resistance to fracture reinforced material and matrix material was improved. The fracture toughness of Al_2O_3/CNT nanocomposite with 3 wt.% of CNT was 10% higher than monolithic matrix material. The fracture toughness reduces marginally when the wt.% of CNT is increased, but it remains greater than monolithic alumina. As demonstrated in Fig. 31.4, this is mostly attributed to the nanocomposites' remaining pores between clumped-together carbon nanotubes. The crack bridging action of CNT can explain the toughening mechanism in produced composite material by the sol–gel technique. The crack bridging action is substantially supported during fracture propagation by the CNT that on Fig. 31.4e, bridge the two crack surfaces. As demonstrated in a Al_2O_3/CNT nano-composite having a particular percentage of reinforcement

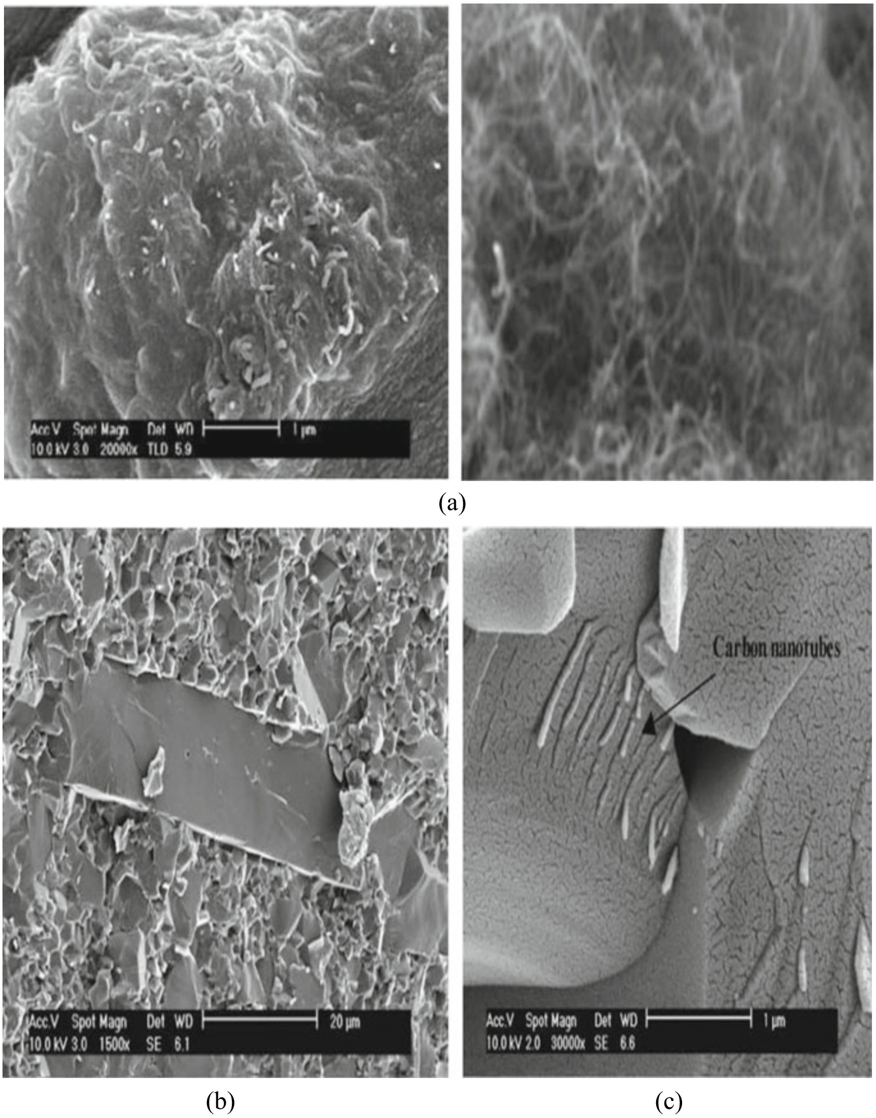

Fig. 31.4 The micrographs of CNT reinforced Al_2O_3 matrix composite powders. **a** Graphs of Al_2O_3/CNT composite powders. **b**–**e** The volume fraction of CNT, **f**–**h** pure Al_2O_3, **i** 1% of CNT, **j** 3% of CNT, **k** 5% of CNT, **l** 7% of CNT and **m** 9% of CNT

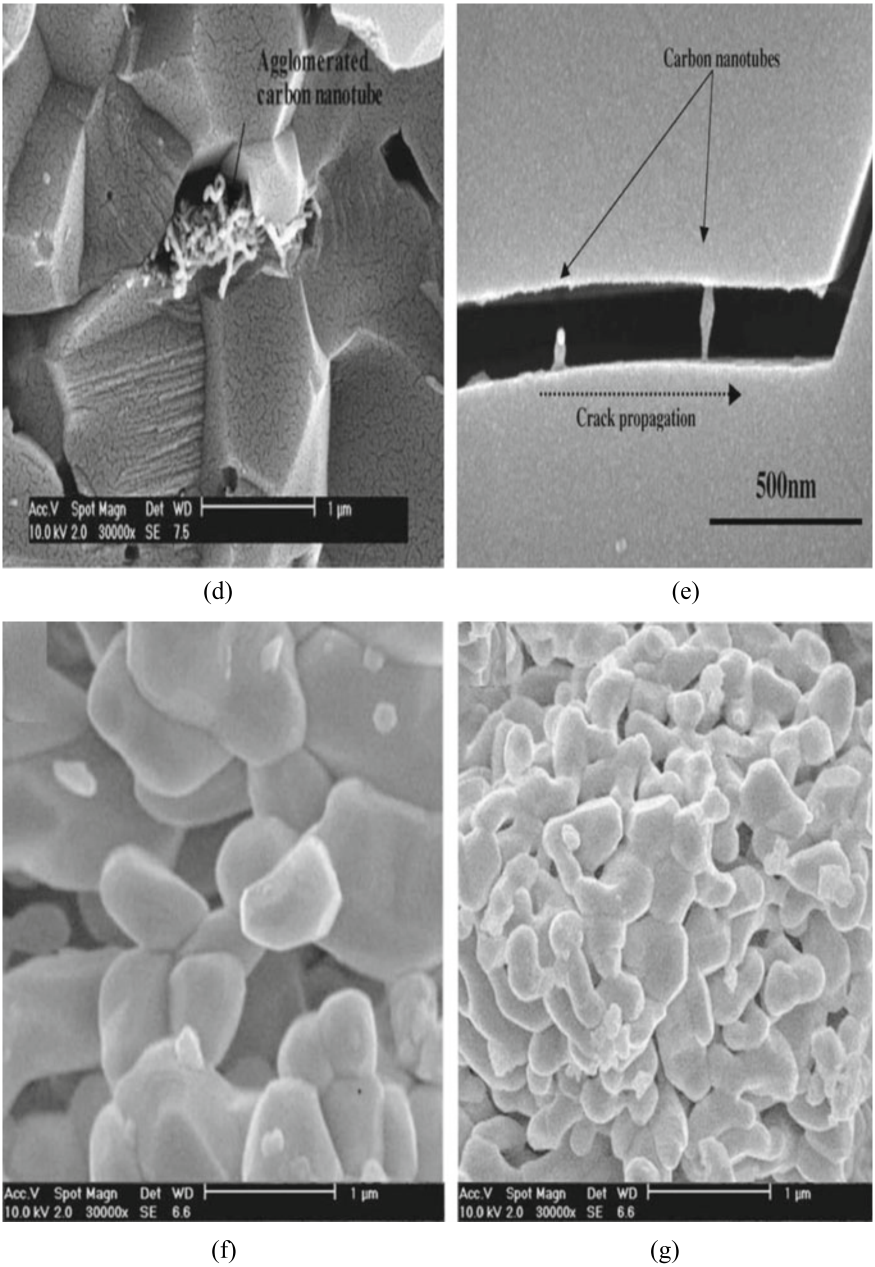

Fig. 31.4 (continued)

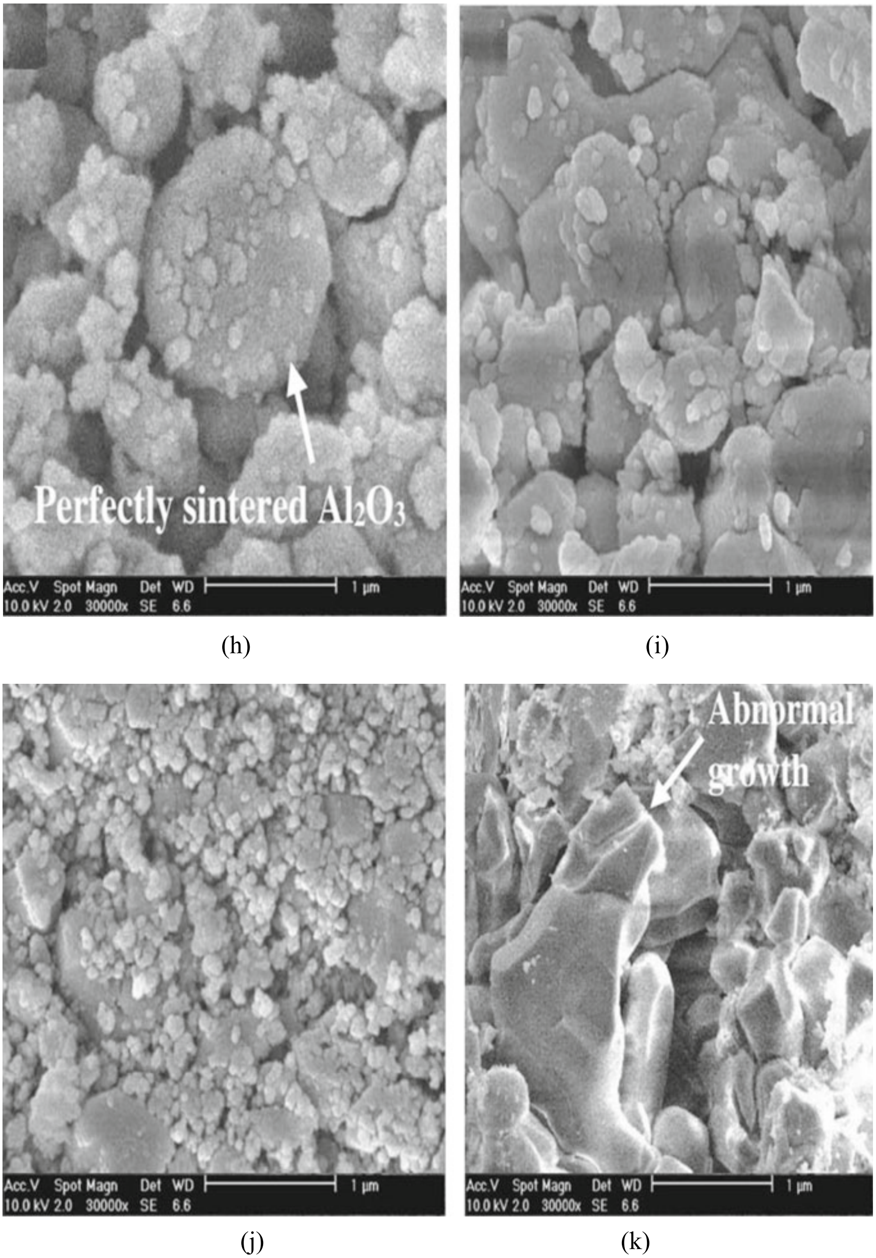

Fig. 31.4 (continued)

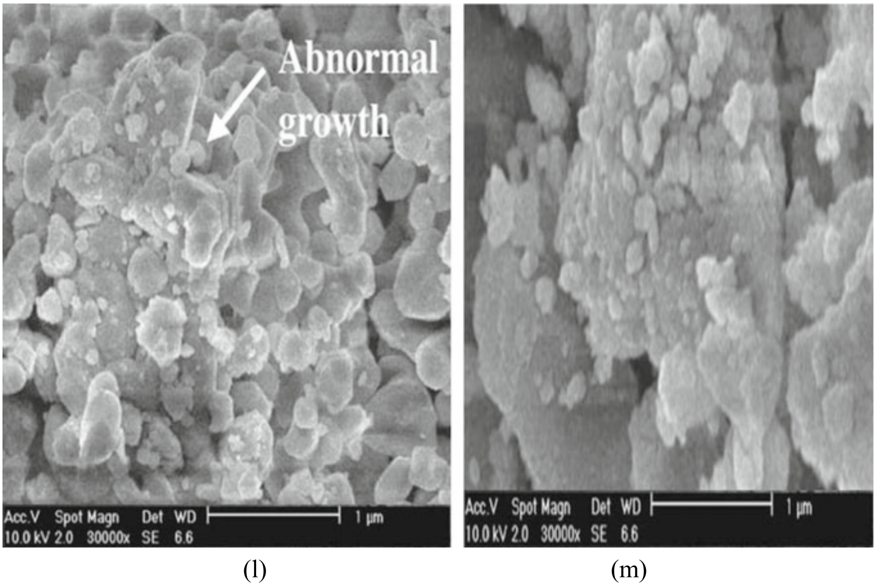

Fig. 31.4 (continued)

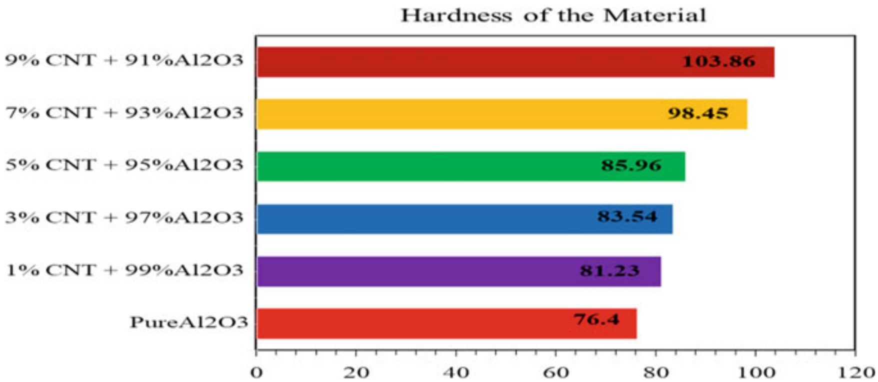

Fig. 31.5 Variation of Hardness by varying wt.% of CNT in Al_2O_3 matrix material

material, the fracture weakens as a result of a reduction in the CNT crack-bridging action.

31.4 Conclusion

The sol–gel technique was used to produce a Al_2O_3/CNT nanocomposite with improved hardness, which was then sintered by spark plasma. In a carbon nanotube/alumina nanocomposite, the carbon nanotubes were uniformly disseminated inside the alumina matrix. The toughness of Al_2O_3/CNT nanocomposites was improved by increasing the carbon nanotube volume percentage. The percentage of CNT transmission between the Al_2O_3/CNT provides the basis for the strengthening process. Toughening is directly pertaining to the CNT's role in crack bridging during the development of composite cracks.

References

1. Iijima, S.: Helical microtubules of graphitic carbon. Nature **354**(6348), 56–58 (1991). https://doi.org/10.1038/354056a0
2. Falvo, M.R., Clary, G.J., Taylor, R.M., II., Chi, V., Brooks, F.P., Jr., Washburn, S., Superfine, R.: Bending and buckling of carbon nanotubes under large strain. Nature **389**, 582–584 (1997). https://doi.org/10.1038/39282
3. Lee, R., Kim, H., Fischer, J., et al.: Conductivity enhancement in single-walled carbon nanotube bundles doped with K and Br. Nature **388**, 255–257 (1997). https://doi.org/10.1038/40822
4. Kim, P., Shi, L., Majumdar, A., McEuen, P.L.: Thermal transport measurements of individual multiwalled nanotubes. Phys. Rev. Lett. **87**(21), 215502 (2001). https://doi.org/10.1103/PhysRevLett.87.215502
5. Riedel, R.: Handbook of ceramic hard materials, p. 649. Wiley, Germany (2000)
6. Carlsson, M., Johnsson, M., Pohl, A.: Preparation and characterization of alumina based TiNn and SiCn composites. MRS Online Proc. Libr. **740**, 66 (2002). https://doi.org/10.1557/PROC-740-I6.6
7. Yoldas, B.E.: Alumina sol preparation from alkoxides. Ceram. Bull **54**, 289–290 (1975)
8. Yoldas, B.E.: Alumina gels that form porous transparent Al_2O_3. J. Mater. Sci. **10**, 1856–1860 (1975). https://doi.org/10.1007/BF00754473
9. Chertihin, G.V., Andrews, L., Taylor, P.R.: Reactions of pulsed-laser-evaporated Al with C and C_2H_2 infrared spectra and CASSCF calculations for AlC, Al_2C, Al_2C_2, and AlC_2H. J. Am. Chem. Soc. **116**(8), 3513–3518 (1994). https://doi.org/10.1021/ja00087a043
10. Zhan, G.-D., Kuntz, J.D., Wan, J., Mukherjee, A.K.: Single-wall carbon nanotubes as attractive toughening agents in alumina-based nanocomposites. Nat. Mater. **2**(1), 38–42 (2002). https://doi.org/10.1038/nmat793
11. Peigney, A.: Composite materials: tougher ceramics with nanotubes. Nat. Mater. **2**(1), 15–16 (2003). https://doi.org/10.1038/nmat794
12. Flahaut, E., Peigney, A., Laurent, C., Marlière, C., Chastel, F., Rousset, A.: Carbon nanotube-metal-oxide nanocomposites: microstructure, electrical conductivity and mechanical properties. Acta Mater. **48**(14), 3803–3812 (2000). https://doi.org/10.1016/s1359-6454(00)00147-6
13. Mamedov, A.A., Kotov, N.A., Prato, M., Guldi, D.M., Wicksted, J.P., Hirsch, A.: Molecular design of strong single-wall carbon nanotube/polyelectrolyte multilayer composites. Nat. Mater. **1**(3), 190–194 (2002). https://doi.org/10.1038/nmat747

Chapter 32
Flow Prediction Models for a Mini Hydroelectric Power Station

Brayan A. Bonilla, Luigi O. Freire, and Carlos I. Quinatoa

Abstract In this paper, a comparison between two systems implemented in Jupyter Notebook with the Python computation kernel is presented. They use machine learning to predict the flow rate. The models were trained and evaluated using data from the year 2022. The first system uses the ARIMA method and shows an error of 4.55% in flow prediction. A high similarity is observed between the actual and predicted flow curves for each month. The second system uses the RNA-GRU method and shows a MAPE error of 4.62% in the flow prediction. As with ARIMA, there is a significant resemblance between the actual and predicted flow curves for each month. These graphs allow us to evaluate the average errors of the forecasts. In this case, it is evident that the ARIMA method has a lower error compared to the GRU method. This paper demonstrates the ability of both systems implemented in Jupyter Notebook to predict the flow rate.

32.1 Introduction

The stochastic nature of inflowing flows in hydroelectric generation in Ecuador necessitates the use of forecasting models for efficient operation. Various statistical models have been proposed, but the effectiveness of Artificial Intelligence-based forecasting models, particularly neural networks incorporating evolutionary algorithms, stands out due to their satisfactory results [1]. Hydrograph and multiple regression methods are utilized to determine the volume inflow of rivers. A mathematical model is derived

B. A. Bonilla (✉) · L. O. Freire · C. I. Quinatoa
Technical University of Cotopaxi, Latacunga, Ecuador
e-mail: brayan.bonilla4225@utc.edu.ec

L. O. Freire
e-mail: luigi.freire@utc.edu.ec

C. I. Quinatoa
e-mail: carlos.quinatoa7864@utc.edu.ec

P. H. V. S. Talpa Sai et al. (eds.), *Intelligent Manufacturing and Energy Sustainability*, Smart Innovation, Systems and Technologies 372,
https://doi.org/10.1007/978-981-99-6774-2_32

for the ratio between the volume of water and the total volume, enabling the prediction of machine shutdowns and startups. This prediction capability facilitates accurate forecasts of future shutdowns, depending on the type of deduction performed [2]. The models to predict monthly flows have been given from the analysis of historical records which were adjusted and evaluated from the performance of the same, the results were appropriate to show and estimate inflows, the regulation of these allows greater energy production in a coordinated operation [3]. The historical record base is taken directly from the Colombian electric company, so that statistical techniques will be used to create a reliable database of the monthly flow of the Cauca river valley, developing prediction models of monthly mean flows using statistical methods and linear and non-linear approaches [4]. The historical data obtained pertain to each day in 5 years prior to the prediction, for which a basic monthly flow rate for each month is obtained to avoid distorting the water curve, and then these models and tools are examined to evaluate their validity in the estimation [5].

In Ecuador, where neural networks are used to predict the water level and the water reservoir level in hydroelectric plants only have less than 50% of successful cases due to the high noise of the signal it sends, unique prediction models are needed according to their geographic location [6]. The use of various algorithms to predict different aspects of hydroelectric power plants is widely used to evaluate the influence of ANN training on the reservoir prediction of a hydroelectric dam, indicating that it can perform projections of up to 48 h and improve energy production planning [7]. Various models are employed for flow rate production, with the most commonly used ones being Artificial Neural Networks, Adaptive Neuro-Fuzzy Networks, Singular Spectral Analysis, Structural Model, and Physical Model. These models can be applied within different time windows, ranging from one to twelve months. Software tools enable the inclusion of macro climatic variables relevant to the respective terrains [8]. Focusing the prediction model through algorithms and variable control of either a virtual system or physical system should focus on the accuracy of the flow prediction to maintain an adequate level of control system usage [9]. The prediction of variables using the ARIMA method is widely used lately since it is an autoregressive model that can be included in several systems, in this case variables related to water, such as its flow rate or indirectly through meteorological variables [10]. Therefore, the flow prediction modeling implementation and specification is given by different methods such as ARIMA, ANNs, as they present a multilayer perceptron that helps to solve problems that are not linear and can be fully connected or only locally connected and are functional for this purpose [11].

Although other prediction models mention that they have been built using stochastic and neural techniques, no detailed training is provided on the provenance and representativeness of these data, nor a detailed evaluation of the effectiveness of each. It is not shown how the results of stochastic techniques and neural networks were compared, nor are specific performance metrics presented to support the claim that both approaches are feasible alternatives [12].

The objective of this study is to compare and evaluate the performance of prediction models for estimating water flows used in electric power generation. For this purpose, GRU (Recurrent Gated Units) and ARIMA (AutoRegressive Integrated

Moving Average) algorithms will be implemented in the Illuchi 2 mini-hydroelectric power plant. These algorithms will be validated and contrasted using historical data in order to determine their effectiveness. Prediction models.

32.2 Problem

The project is based on generating two prediction models for mini hydroelectric power plants in Ecuador, for this has been taken as a reference the mini power plant Illuchi 2 located in the province of Cotopaxi in the canton Latacunga, This is done through the use of mathematical models and training of neural networks through a record of historical data from 2018 to 2021 that gives a total of 1400 data, which are taken daily because it allows to have an accurate record of the amount of water passing through the plant in a period of time, to comply with legal requirements of the INEN 59: 2012 and ensure proper, sustainable operation of the plant and in turn validate its effectiveness with actual data obtained in the year 2022 and their respective percentage of error.

The ARIMA model is chosen for this project as it determines the orders of differentiation, autoregression, and moving average. The autocorrelation function (ACF) and the partial autocorrelation function (PACF) were used alongside historical flow data to identify suitable orders. This allowed for the adjustment of the model to the training data and the generation of flow forecasts.

On the other hand, the GRU model is utilized to organize historical flow data in a temporal sequence. It divides the data into training, validation, and test sets. The model's structure consists of multiple layers with GRU units. The configuration includes values such as (MSE), (MAE), and (SGE). Once trained, the model can take a temporal sequence as input and provide corresponding actual flows as output. It has the capability to learn from non-linear patterns and capture complex dependencies (Fig. 32.1).

ARIMA

This model was used because we have historical flow data that exhibit linear and seasonal patterns, which are provided by the electric company ELEPCO S.A. ARIMA is specially designed to capture linear trends and seasonal components.

Thus, ARIMA is a linear model that fits best with linear relationships and has sufficient historical data to estimate the model parameters, since a significant amount of past figures is required to make accurate estimates.

An ARIMA process (p, q) is expressed:

$$\tilde{z}_t = \phi_1 \tilde{z}_{t-1} + \phi_2 \tilde{z}_{t-2} + \cdots + \phi_p \tilde{z}_{t-p} + a_t - \theta_1 a_{t-1} - \theta_2 a_{t-2} - \cdots - \theta_q a_{t-q} \tag{32.1}$$

The expression can be reduced using the delay operator:

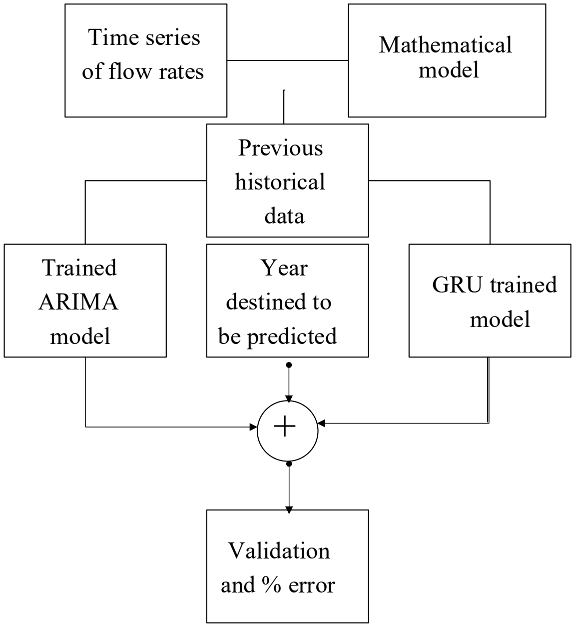

Fig. 32.1 Project structure

$$(1 - \phi_1 B - \cdots - \phi_p B^p)\tilde{z}_t = (1 - \theta_1 B - \cdots - \theta_p B^p)a_t \tag{32.2}$$

$$\phi_p(B)\tilde{z}_t = \theta_q(B)a_t \tag{32.3}$$

where the roots of $\phi p(B) = 0$ are outside the unit circle for the process to be stationary and the process will be invertible if those of $\theta q(B) = 0$ are. In addition, it must be satisfied that $\phi p(B)$ and $\theta q(B)$ have no common roots. Failure to meet this condition results in $zt = at$ and the process would be white noise.

A method used to combat the non-stationary behavior of some time series. It consists of assuming that the trend evolves over time and if we subtract each value of the series with the previous value it will be free of the trend [13, 14].

Gated Recurrent Unit (GRU)

The chosen model, GRU, captures non-linear trend relationships and complex data patterns with its depth of processing. It is recurrent and can recall long-term information in the flow data. GRU has been proven to outperform the basic version of LSTM in certain applications. It also serves as an optimization of LSTM, reducing the number of parameters. Unlike LSTM, GRU does not have a dedicated memory unit.

The equation for the update gate is as follows:

$$u_t = \sigma(W_u h_{t-1} + W_u x_t + b_u) \tag{32.4}$$

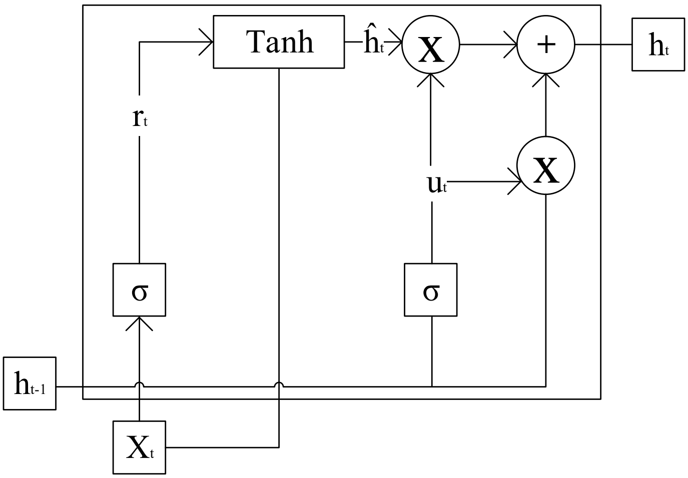

Fig. 32.2 Representation of the GRU cell and its internal operations

that of the reset gate:

$$r_t = \sigma(W_r h_{t-1} + W_r x_t + b_r) \tag{32.5}$$

This reset gate is to be combined with the previous state ht − 1 and the tanh function is applied to determine which information is to be reset:

$$\hat{h}_t = \tanh(W_h h_{t-1} r_t + W_h x_t + b_h) \tag{32.6}$$

Finally, the use of an exponential mean allows us to combine the above result with the previous state:

$$h_t = u_t \quad \hat{h}_t + (1 - u_t) \quad h_{t-1} \tag{32.7}$$

GRU, like LSTM has a matrix of weights for each type of gate, where Wu are the weights for the update gate, Wr the weights for the reset gate and Wh the weights of the combination of the update with the current input. In Fig. 32.2, we can see the visual representation of the operations on a single cell [15].

32.3 Development

Figure 32.3 shows the steps used to follow up the project in general.

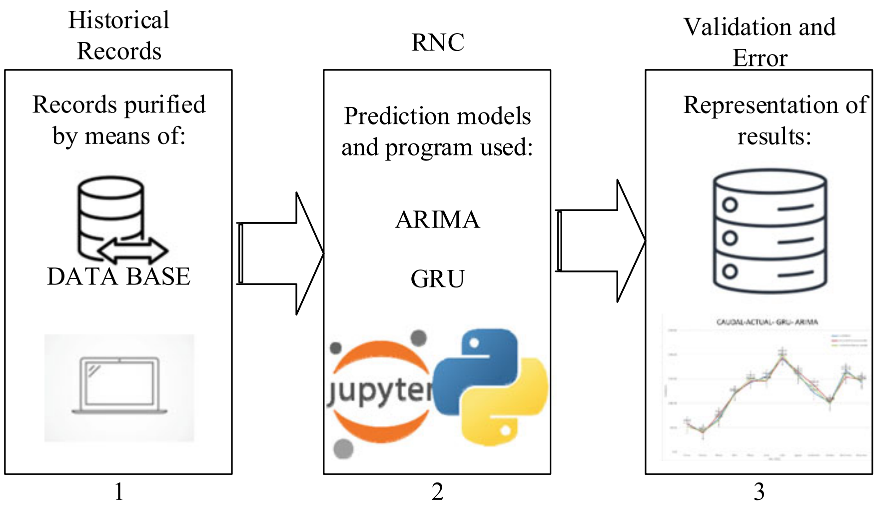

Fig. 32.3 Steps for information processing

32.3.1 Results

Table 32.1 the forecast was made using the ARIMA method and its respective errors were calculated to determine the behavior of the flow demand in the year 2022, where it is observed that the model is feasible since it has an error of 4.55%.

Figure 32.4 shows the behavior of the curves of the real flow rate and the flow rate predicted with the ARIMA model, where a high similarity between the curves and their distortion in each month of the year 2022 can be better appreciated.

The forecast was made using the RNA-GRU method and its respective errors were calculated to determine the behavior of the flow demand in the year 2022, where it is observed that it is adequate since it has a MAPE error of 4.62% (Table 32.2).

Figure 32.5 shows the behavior of the curves of the real flow rate and the flow rate predicted with the RNA-GRU model, where a high similarity between the curves and their distortion in each month of the year 2022 can be better appreciated.

An analysis was performed in Fig. 32.6. Comparing the results of the two prediction methods with the actual flow data, the ARIMA mathematical model implemented in Jupyter Notebook with Python achieved the most accurate prediction with a mean absolute percentage error of 4.55%. In contrast, the RNA-GRU model resulted in an error of 4.62%. As mentioned earlier, an error below 5% is considered acceptable. The flow curve throughout 2022 can be visualized by comparing it with the predicted data for all twelve months of the year.

Table 32.1 Flow forecasting for ARIMA model power generation

S. No.	Month	Caudal actual	ARIMA forecasted demand	Error abs.	Error % abs.	∑ Error abs.	MAD	Error nor.	∑ Error nor.	TS
1	January	578.47	521.37	57.09981	**9.87**	57.099812	57.1	57.09981	57.099812	**1**
2	February	430.36	417.77	14.41061	**3.57**	71.511042	35.8	– 14.41061	42.689204	**1.2**
3	March	691.18	650.89	40.29442	**5.83**	111.80484	37.3	40.29442	82.983621	**2.2**
4	April	1219.64	1197.33	22.3042	**1.83**	134.10904	33.5	22.3042	105.28782	**3.1**
5	May	1427.80	1506.96	79.16282	**5.54**	213.27186	42.7	– 79.16282	26.124998	**0.6**
6	June	1546.68	1460.34	86.33988	**5.58**	299.61174	49.9	86.33988	112.46487	**2.3**
7	July	1917.73	2007.05	89.32245	**4.66**	388.93418	55.6	– 89.32245	23.142426	**0.4**
8	August	1592.61	1545.63	46.98155	**2.95**	435.91573	54.5	46.98155	70.123976	**1.3**
9	September	1206.95	1291.34	84.38708	**6.99**	520.30281	57.8	– 84.38708	– 14.263103	**– 0.2**
10	October	1019.81	984.27	35.54144	**3.49**	555.84425	55.6	35.54144	21.278338	**0.4**
11	November	1629.48	1629.48	43.71936	**2.61**	599.56361	54.5	43.71936	64.997697	**1.2**
12	December	1430.08	1454.82	24.73657	**1.73**	624.30018	52.0	– 24.73657	40.26113	**0.8**
				SUMA%	**54.66%**					
				n	**12**					
				MAPE	**4.55%**					

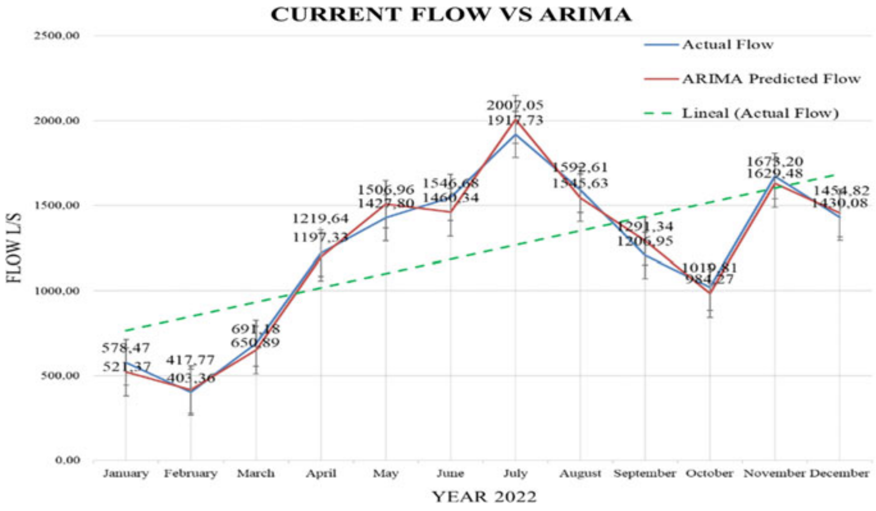

Fig. 32.4 REAL-ARIMA flow behavior

32.3.2 Discussion

The ARIMA method was used to forecast the flow demand in 2022, resulting in an error of 4.55%. The predicted flow closely resembled the real flow, exhibiting similar variations each month. Comparing the predictions of both methods with the actual flow, the ARIMA model achieved a more accurate forecast with an average absolute percentage error of 4.55%, while the RNA-GRU model had an error of 4.62%. Since a value below 5% is considered acceptable, it can be concluded that the analysis and validation were appropriate. Furthermore, the flow curve throughout 2022 demonstrated a similar pattern of growth and reduction compared to the forecasted data for all 12 months.

32.4 Conclusions

It is essential to scale the data during the training of the flow models to avoid affecting the different values used. In our approach, using the RMSprop training technique with a training ratio of 80% and validation of 20% on the GRU network, we achieved a closer approximation to the real data.

Both the ARIMA model and the RNA-GRU model proved to be effective in predicting flow rates for mini hydroelectric power plants, with errors below 5% when compared to the real values measured in the year 2022. Specifically, the ARIMA model presented an error of 4.55%, while the RNA-GRU model showed an error of 4.62%.

Table 32.2 Flow forecasting for power generation model RNA-GRU

S. No.	Month	Actual flow	Forecasted demand GRU	Error abs.	Error % abs.	$\sum$ Error abs.	MAD	Error nor.	$\sum$ Error nor.	TS
1	January	578.47	572.25	6.216408	**1.07**	6.2164084	**6.2**	6.216408	6.2164084	1
2	February	403.63	388.41	14.94376	**3.70**	21.16017	**10.6**	14.94376	21.16017	2
3	March	691.18	763.14	71.95531	**10.41**	93.115477	**31.0**	− 71.95531	− 50.795137	− 1.6
4	April	1219.64	1187.11	32.52755	**2.67**	125.64303	**31.4**	32.52755	− 18.267586	− 0.6
5	May	1427.08	1453.38	25.58154	**1.79**	151.22457	**30.2**	− 25.58154	− 43.849124	− 1.5
6	June	1546.68	1456.88	89.80176	**5.81**	241.02632	**40.2**	89.80176	45.952633	1.1
7	July	1917.73	1940.91	23.17939	**1.21**	264.20571	**37.7**	− 23.17939	22.773246	0.6
8	August	1592.61	1635.51	42.89923	**2.69**	307.10494	**38.4**	− 42.89923	− 20.125983	− 0.5
9	September	1206.95	1369.04	162.0861	**13.43**	469.19108	**52.1**	− 162.0861	− 182.21212	− 3.5
10	October	1019.81	1029.38	9.574716	**0.94**	478.7658	**47.9**	− 9.574716	− 191.78684	− 4
11	November	1673.20	1544.17	129.0295	**7.71**	607.79533	**55.3**	129.0295	− 62.7573	− 1.1
12	December	1430.08	1486.75	56.67534	**3.96**	664.47068	**55.4**	− 56.67534	− 119.43264	− 2.2
				SUMA	**55.40%**					
				n	**12**					
				MAPE	**4.62%**					

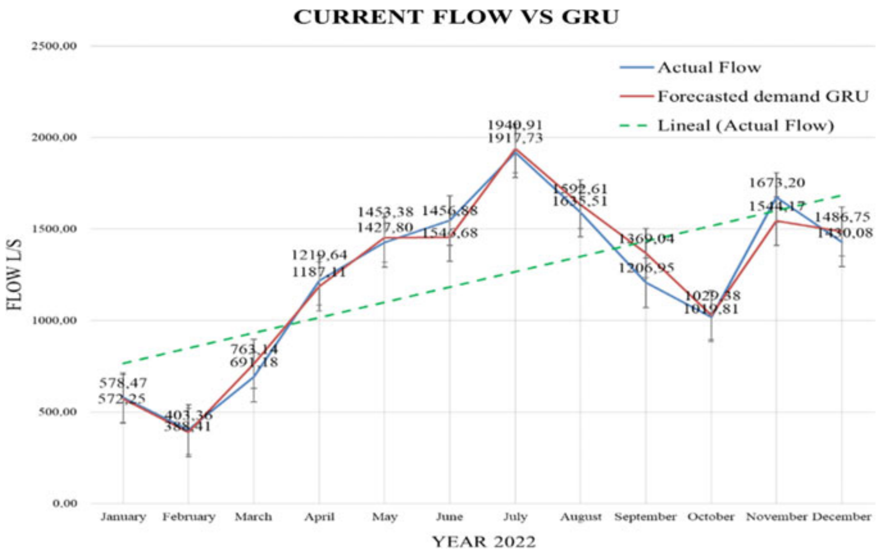

Fig. 32.5 REAL-GRU flow behavior

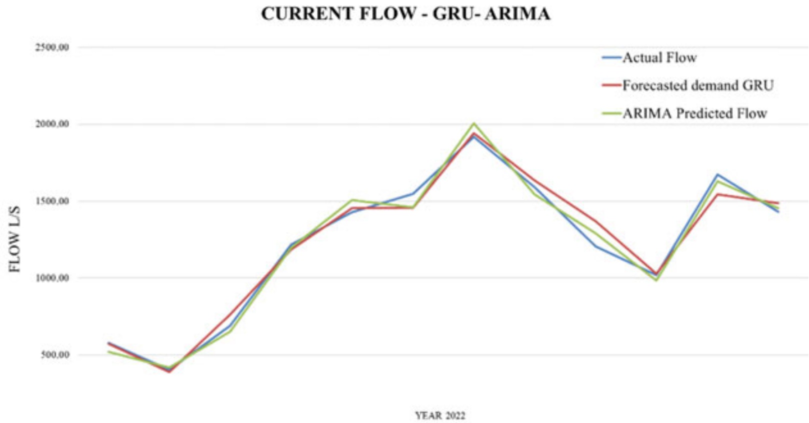

	January	February	March	April	May	June	July	August	September	October	November	December
Actual Flow	578,47	403,36	691,18	1219,64	1427,80	1546,68	1917,73	1592,61	1206,95	1019,81	1673,20	1430,08
Forecasted demand GRU	572,25	388,41	763,14	1187,11	1453,38	1456,88	1940,91	1635,51	1369,04	1029,38	1544,17	1486,75
ARIMA Predicted Flow	521,37	417,77	650,89	1197,33	1506,96	1460,34	2007,05	1545,63	1291,34	984,27	1629,48	1454,82

Fig. 32.6 Behavior of the predicted flow demand compared to its actual demand

The feasibility of the Illuchi 2 mini-hydroelectric power plant project relies on selecting a reliable prediction model and utilizing trustworthy historical data. Our research precisely assesses the impact of the ARIMA and RNA-GRU models. These models interpret trend, seasonality, and randomness in the flow time series while adapting to diverse patterns and characteristics. This guarantees reliable and accurate outcomes, facilitating efficient management of the Illuchi 2 mini-hydroelectric power plant.

In future research work, it is recommended to explore other prediction models and advanced machine learning techniques that can further improve the accuracy of water flow estimation. These actions will optimize power generation and strengthen the management of the Illuchi 2 mini-hydroelectric power plant.

References

1. Hinojosa, V.H.: «Cenace,» 2008 [Online]. Available at: https://revistaenergia.cenace.gob.ec/index.php/cenace/article/view/268. Accessed 17 Feb 2023
2. Alcázar Montero, J.: «ResearchGate,» 07 2007 [Online]. Available at: https://www.researchgate.net/publication/46314616_El_Metodo_del_Caudal_Basico_para_la_determinacion_de_Caudales_de_Mantenimiento_Aplicacion_a_la_Cuenca_del_Ebro. Accessed 19 Feb 2023
3. Sugastti Medina, C.A., Arce Encína, A.S.: «Universidad Nacional del Este,» 2020 [Online]. Available at: http://servicios.fpune.edu.py:8080/jspui/handle/123456789/1062. Accessed 17 Feb 2023
4. Carvajal Escobar, Y., Correa, G., Matilde Muñoz, F.: «Redalcy,» 2007 [Online]. Available at: https://www.redalyc.org/pdf/2311/231120826008.pdf. Accessed 18 Feb 2023
5. Gonzalez, H., Piedrahita, J., Castrillón, O.: «Scielo,» 10 2020 [Online]. Available at: https://www.scielo.cl/scielo.php?script=sci_arttext&pid=S0718-07642020000500215. Accessed 17 Feb 2023
6. Olmedo, D.E., Ambato Hernandez, J., Asqui Santillán, G.E.: «Researchgate,» 2018 [Online]. Available at: https://www.researchgate.net/publication/329440607_MODELAMIENTO_BASADO_EN_REDES_NEURONALES_ARTIFICIALES_PARA_LA_PREDICCION_DE_RECURSOS_HIDRICOS_EN_UNA_CENTRAL_HIDROELECTRICA. Accessed 17 Feb 2023
7. Chafla, E., Asqui Santillán, G., Paucar, J., Olmedo Vizueta, D.: «Espoch,» 07 2019 [Online]. Available at: http://perspectivas.espoch.edu.ec:8081/index.php/RCP_ESOCH/article/view/20/57. Accessed 18 Feb 2022
8. Velásquez, J.D., Smith, R., Cebalos, A., Correa, P., Goez, C., Hernandez, O., Salazar Velasquéz, L.F., Zapata, E.C.: «Universidad Nacional de Colombia,» 09 2004 [Online]. Available at: https://www.researchgate.net/profile/Juan-Velasquez17/publication/255786858_Modelos_de_prediccion_de_caudales_parar_el_sector_electrico_Colombiano/links/00b7d520ae94206147000000/Modelos-de-prediccion-de-caudales-parar-el-sector-electrico-Colombiano.pdf. Accessed 17 Feb 2023
9. Freire, L.O., Bonilla, B.A., Corrales, B.P., Villarroel, J.L.: «Springer,» 30 04 2023. [Online]. Available at: https://doi.org/10.1007/978-981-19-8493-8_47. Accessed 12 May 2023
10. Aguado Rodríguez, J.G., Castro Popoca, M., Quevedo Nolasco, A., Arteaga Ramirez, R., Vázquez Peña, A.M., Zamora Morales, P.B.: «Scielo,» 02 2016 [Online]. Available at: https://www.scielo.org.mx/scielo.php?script=sci_arttext&pid=S14053195201600010001. Accessed 15 May 2023
11. Gomez Vargas, E., Alvarez Pomar, L., Obregon Neira, N.: «iiisci,» 2012 [Online]. Available at: https://www.iiisci.org/journal/PDV/risci/pdfs/HCA987UD.pdf. Accessed 12 May 2023
12. Sugastti Medina, C.A., Arce Encina, A.S., Panadero, W.: «FPUNE SCIENTIFIC,» 17 05 2023 [Online]. Available at: http://servicios.fpune.edu.py:83/fpunescientific/index.php/fpunescientific/article/view/248. Accessed 29 May 2023
13. Seminario Gastelo, J.G.: «Universidad de Piua,» 05 2012 [Online]. Available at: https://pirhua.udep.edu.pe/bitstream/handle/11042/4986/ING_2106.pdf?sequence=1&isAllowed=y. Accessed 30 Apr 2023

14. Gonzáles Casimiro, M.P.: «Sarriko,» 14 05 2014 [Online]. Available at: https://addi.ehu.es/handle/10810/12492. Accessed 30 Apr 2023
15. Nanclares Rodríguez, F.J.: «Uam,» 06 2021 [Online]. Available at: https://repositorio.uam.es/bitstream/handle/10486/700024/nanclares_rodriguez_francisco_javier_tfg.pdf?sequence=1. Accessed 10 May 2023

Chapter 33
Geothermal Gradient in India—Comparison and Current Status

Parminder Singh and Harpreet Kaur Channi

Abstract The increasing population and development of cities in India have increased the demand for energy in recent years. India has to improve its infrastructure to make the most use of the available energy sources if it wants to expand continuously. While there is an important ascent in the applications of renewable energy resources, namely solar energy using photo voltaic cells and wind energy using windmills, geothermal resources like heat springs, hot water geysers, hot water springs, and hot water reservoirs remain one of the resources that are still being scouted and exploited. This paper explains the importance of understanding geothermal gradient and its significance. It also reviews the ongoing geothermal projects in India and provides insight into the current status and the detailed methodology for calculating geothermal gradient and provides valuable information about the economic and environmental benefits of GHG reduction. The government, researchers, and academics may use this report as a reference to encourage a higher share of renewable energy both in India and elsewhere in the world.

33.1 Introduction

Geothermal energy is renewable. Geothermal originates from Greek geo (Earth) and thermal (heat). It's renewable since the Earth's core recharges it.

As depicted in Fig. 33.1, the Earth's core rocks retain thermal energy from slow radioactive decay of minerals and rocks. Iron-nickel alloys and other elements form Earth's deepest layer. The inner core's surface temperature is 5430 °C, comparable to the sun. The uppermost layer of the Earth's core contains liquid iron and nickel alloys, and its temperature varies between 4500 and 5500 °C. As we move toward the mantle and then towards the crust of Earth, the temperature varies significantly from 1000 to 3500 °C for the mantle and 20 °C for the crust, as shown in Fig. 33.2 [1]. The

P. Singh · H. K. Channi (✉)
Chandigarh University, Mohali, Punjab 140413, India
e-mail: harpreetchanni@yahoo.in

P. H. V. S. Talpa Sai et al. (eds.), *Intelligent Manufacturing and Energy Sustainability*, Smart Innovation, Systems and Technologies 372,
https://doi.org/10.1007/978-981-99-6774-2_33

Fig. 33.1 Earth's interior

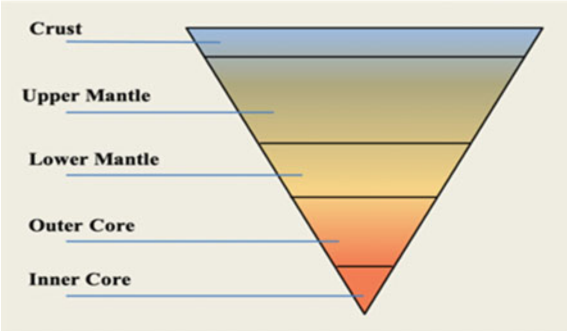

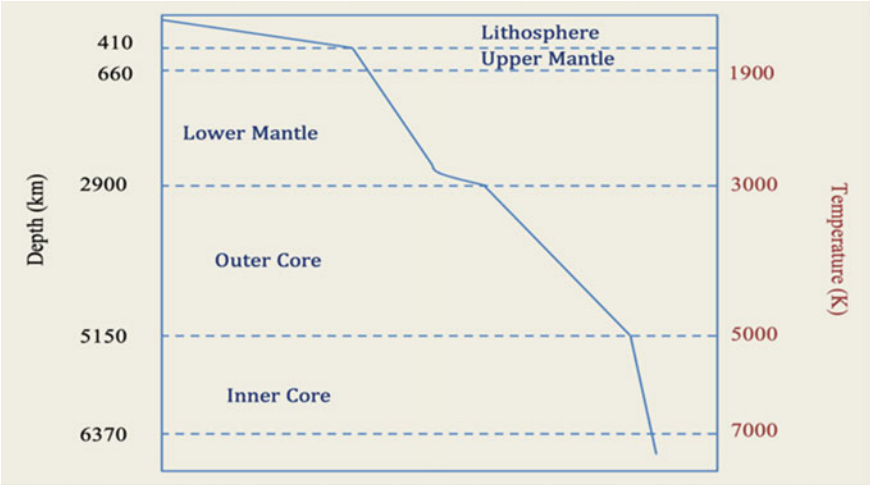

Fig. 33.2 Temperature variation of earth

difference in temperature between the Earth's core and crust allows thermal energy to flow continuously from the inner core to the Earth's crust. Geothermal Gradient refers to the depth-dependent Earth's core temperature. Figure 33.3 shows heat energy flow from the core's deepest parts to the crust's shallower sections through geothermal gradient [2].

33.2 Literature Survey

Jia et al. [3] introduced a butted BHE approach that accurately predicts the large profundity on a level plane. It may help BHE frameworks use geothermal energy effectively by providing perspective. Xu et al. [4] analyzed temperature logs in the Erlain Basin, shedding light on the structural context of the eastern CAOB. Cioffi et al.

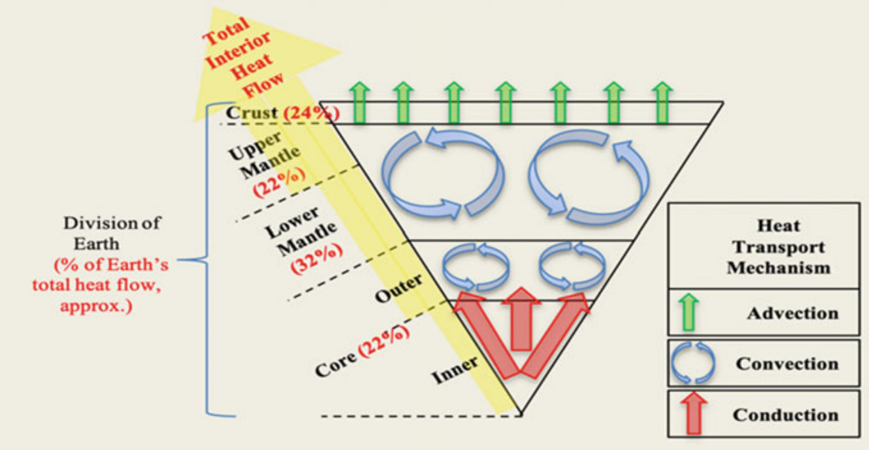

Fig. 33.3 The process of advection, convection and conduction inside Earth's core and mantle

[5] investigated that intracontinental deformation in the inner Borborema Province was consistent until roughly 530–525 Ma. Hu et al. [6] showed that significant metasomatism of residual melts and liquids before magmatism enhanced the mantle material that generated dioritic magmas. Madon et al. [7] studied thermal conductivity in oil/gas wells and drill holes in the Malay Basin. These studies contribute to understanding the geology and structures of their respective regions. Melouah et al. [8] developed a geothermal model for Triassic regions using integrated analysis techniques. Their multidisciplinary approach enhanced understanding of heat transfer and reservoir engineering. Anene et al. [9] studied geothermal gradients in the Eastern Niger Delta, noting a non-linear relationship between temperature and depth. Recent advancements in nanotechnology have unveiled the ability of nanoparticles, including CuO, TiO_2, Al_2O_3, and Ag, when suspended in water, to enhance the rate and efficiency of heat transfer. The authors conducted a comprehensive assessment of the application of nanotechnology in closed geothermal heat pumps and heat exchangers, providing a thorough evaluation in their published works [10, 11]. The researchers demonstrated that the Ni/Zeolite catalyst they synthesized possessed a granular shape and exhibited crystalline characteristics, along with enhanced surface area and pore volume measuring 80.661 $m^2\ g^{-1}$ and 0.123 cc g^{-1}, respectively. Moreover, they achieved the highest biodiesel yield of 89.4% by incorporating 3% w/w of the Ni/Zeolite catalyst at an operating temperature of 60 °C. Additionally, the researchers examined the catalyst's reusability and found that after three cycles, the biodiesel yield decreased to 73.3% [12, 13]. A Case study of Manuguru, India—The Godavari geothermal field in India is one of the locations where different geothermal fluids and groundwaters may occur. The groundwaters in the area are also near neutral (pH: 6.6–7.5) and have surface temperatures of 24–28 °C, whereas the geothermal waters in the area have a temperature range of 30–55 °C. Thermal logging in a borewell with a depth range of 50–1000 m reveals that the geothermal gradient and heat flow in the

Manuguru area are higher than the regional norm, ranging from 22.5 to 105.5 °C/km 83 to 388 mW/m^2, respectively. As a result, the Godavari Valley's Manuguru geothermal zone can produce 3584 MWe of electricity through the Organic Rankine Cycle (ORC) [14]. A case study in Iran. In non-volcanic basins like the Zagros, Kopet-Dagh, central Persian Gulf, Qom, and Moghan regions, average geothermal gradients are estimated to be 21 °C/km, 31.5 °C/km, 26.7 °C/km, 30 °C/km, and 25 °C/km; close to volcanic sites like the Sabalan stratovolcano, and they are estimated to be 149 °C/km [15].

33.3 Geothermal Energy in India

India possesses vast potential for the successful extraction and utilization of geothermal energy across a range of sectors. Based on the positioning and movements of the Indian subcontinent tectonic plate, the Indian continent has been identified to contain seven distinct geothermal provinces. These regions have been classified as the Sonata geothermal region, Sohana geothermal region, Godavari geothermal region, Gujarat-Rajasthan geothermal region, Himalaya geothermal region, Western geothermal region, and Mahanadi geothermal region. Each province represents a unique geological setting with specific characteristics and geothermal resource possibilities. Recognizing these distinct geothermal regions provides valuable insights into the geothermal energy potential and aids in the strategic planning and development of geothermal projects in India. The existence of geothermal resources like hot water springs and water geysers across India results from the movement of tectonic plates. This evidently points to geothermal geysers and reservoirs at the foothills of the Himalayas and other seismic-prone areas. According to the Geological Survey of India, approximately 340 hot springs are within Indian boundaries. Out of these 340 thermally anomalous regions, only 31 are examined, and shallow drilling has been done in only 16 of 340 [16–18].

Public sector investments must be increased at the Central and State Government levels since power is the most important infrastructure. Given the enormity of the sector development needed, a sizable portion of the investment must also come from the private sector. In the past, only high-temperature resources could generate electricity from geothermal energy. Still, thanks to binary heat exchange technology and other new technologies applied at different stages of the power generation process, generating electricity even from resources with moderate temperatures is possible. Geothermal energy has a significant potential for providing heat and electricity while emitting few pollutants. Recent discoveries in nanotechnology reveal that nanoparticles suspended in water, such as CuO, TiO_2, Al_2O_3, and Ag, can improve the heat transfer coefficient and rate. They gave a complete evaluation of the application of nanotechnology in closed geothermal heat pumps and heat exchangers in their article. Most geothermal springs in Indian territories have surface temperatures ranging from 37 to 90 °C, making them ideal for direct heat applications.

The Himalayan (Puga, Chhumathang), Saharan (Puga, Chhumathang), Cambay Basin, Son-Narmada-Tapi (SONATA) lineament belt, West Coast, Godavari Basin, and Mahanadi Basin are the seven geothermal provinces into which these springs are divided. Puga Valley and Chhumathang in Jammu and Kashmir, Manikaran in Himachal Pradesh, Jalgaon in Maharashtra, Tapovan in Uttarakhand, and Tattapani in Chhattisgarh are a few of the notable geothermal resources. One of the promising geothermal sites in India is Puga Valley in Ladakh from the data shown in Table 33.1, which has a temperature range of 30–84°C and a depth of borehole ranging from 28.5 to 384.7 m. The site has been studied extensively, and it has been found that it has significant potential for power generation and other industrial applications as shown in Fig. 33.4. Another geothermal site located in Ladakh is Chhumathang, which has a temperature range of 30–87 °C and a borehole depth of 20–221 m. The site has the potential to generate electricity and can also be used for space heating and cooling, greenhouses, and fish farming. In Himachal Pradesh, the Manikaran geothermal site has a temperature range of 28–96 °C and a borehole depth of 21–636 m. This site has already been utilized for power generation and can also be used for direct-use applications like heating, bathing, and cooking. Similarly, the Tapoban geothermal site in Uttarakhand has a temperature range of 30–65 °C and a borehole depth of 291–728 m. This site has been evaluated for its potential to generate power and can also be used for space heating, agriculture, and industrial processes. Moving to Maharashtra, Unharve, Tural, and Barkeshwar are three promising geothermal sites, with temperatures ranging from 40 to 72 °C and borehole depths ranging from 50 to 800 m. These sites have the potential for direct use in heating, bathing, and greenhouses, as well as for power generation and industrial applications. While some sites like Takshin in Arunachal Pradesh, Jarkem in Meghalaya, and Garampani in Assam have not been fully evaluated, they still hold promise for future geothermal exploration and development.

The Indian government has set an ambitious target of achieving 10 GW of geothermal energy production by 2030. However, due to the nascent stage of geothermal extraction in India, attaining this milestone poses significant challenges. This study utilizes literature analysis and questionnaire-based surveys to identify barriers and obstacles hindering the utilization of geothermal energy in India. These barriers encompass the conception of geothermal reservoirs, theoretical heat energy estimation, determination of extractable electricity, and selection of suitable extraction techniques. Overcoming these barriers necessitates meticulously structured analysis and dedicated research focused on the efficient extraction of geothermal energy.

33.4 Methodology

The possibility of a hot water spring or geyser being used as a geothermal energy source depends on numerous factors such as the geothermal gradient of the site, flow rate of fluid from the geothermal spring, temperature of the fluid, depth of the

Table 33.1 Comparison of depth and temperature of geothermal sites

Geothermal site name	Location of the field	The temperature of the reservoir (°C)	Depth of Borehole (m)
Puga Valley	Ladakh	30–84	28.5–384.7
Chhumathang	Ladakh	30–87	20–221
Manikaran	Himachal Pradesh	28–96	21–636
Tapoban	Uttarakhand	30–65	291–728
Tatta Pani	Chhattisgarh	50–98	100–620
Anhoni-Samoni	Madhya Pradesh	32–45	585
Unharve	Maharashtra	72	50–500
Tural	Maharashtra	54	50–600
Barkeshwar	Maharashtra	40–70	770–800
Takshin	Arunachal Pradesh	52	NA
Jarkem	Meghalaya	46	NA
Garampani	Assam	54	NA

borehole, the specific heat of the reservoir, the porosity of the rocks and classification of the rocks at the site [18] (Fig. 33.5).

Calculating the geothermal gradient of a selected location is a various-step procedure to be followed thoroughly to obtain the exact amount of geothermal potential of the particular location. The unit of measurement for the geothermal gradient is expressed as degrees Celsius per meter (°C/m). The geothermal gradient, also known as the thermal gradient, of a particular location is determined by two essential factors. Firstly, it depends on the depth of the borehole or crack, indicating the vertical distance from the surface. Secondly, it relies on the temperature difference between the surface and the bottom of the borehole or crack. These two parameters play a crucial role in quantifying the rate at which temperature changes with increasing depth beneath the Earth's surface. Generally, calculating the geothermal gradient of an active geothermal region can be categorized into seven distinct stages. However, estimating time consumption and capital investment is not very effective in generalizing the process for every stage, and these parameters vary from one region to another. Geothermal gradient (G) mathematically can be defined as shown in Eq. 33.1,

$$G = \Delta T/\Delta D. \tag{33.1}$$

where ΔD is the depth of the crack or borehole, and ΔT is the difference in the temperature [7].

The temperature variation is caused by the varying geothermal gradient across all these geothermal sites. The site with a high geothermal coefficient will have more temperature difference as we move into more depth, whereas, for a location with a low geothermal coefficient, the temperature variation will be minor as we move into

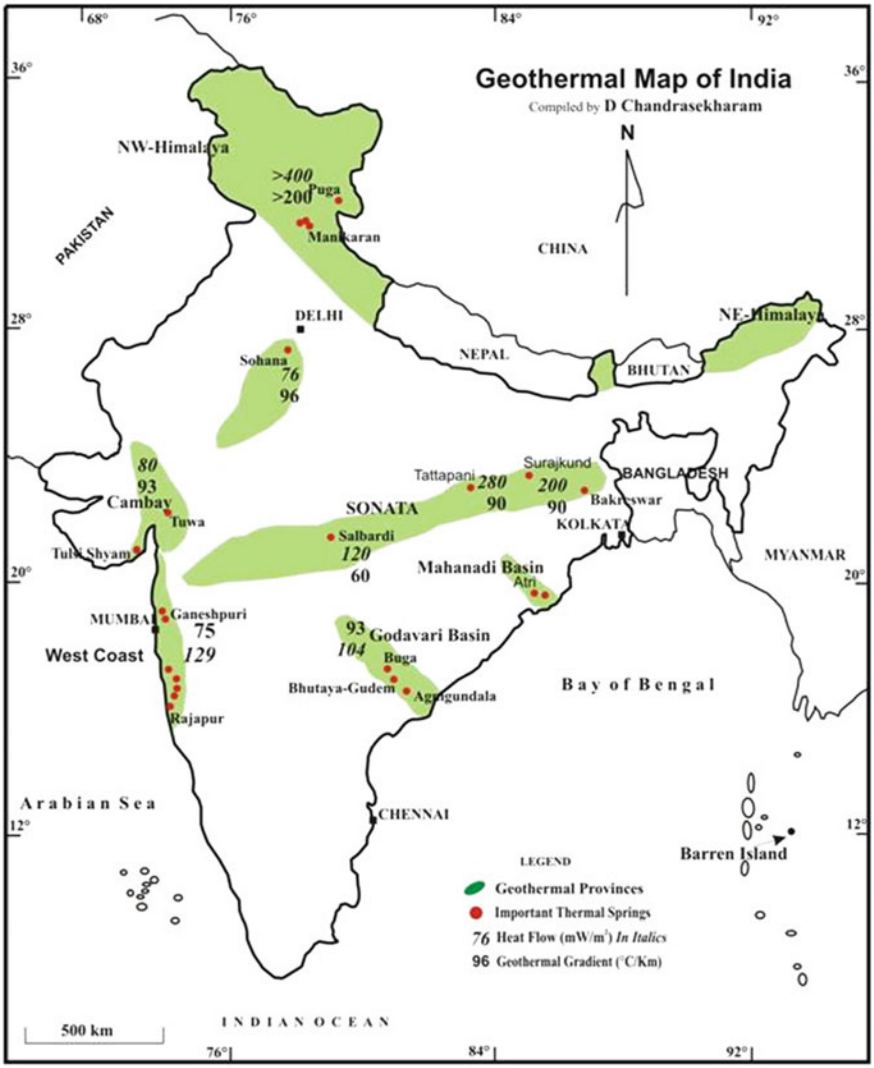

Fig. 33.4 Geothermal regions in India and their locations [16]

more depth. The geothermal gradient of Puga Valley in Jammu and Kashmir is shown below. The data are assembled from three distinct locations within Puga Valley to understand the variation of geothermal gradient within an active geothermal region. The geothermal gradient from Puga Valley at location 1 using temperature gradient and depth of borehole is calculated as shown below in Eq. 33.2,

$$G = (40 - 0)/(100 - 0) = 0.04\,^{\circ}\mathrm{C/m}. \tag{33.2}$$

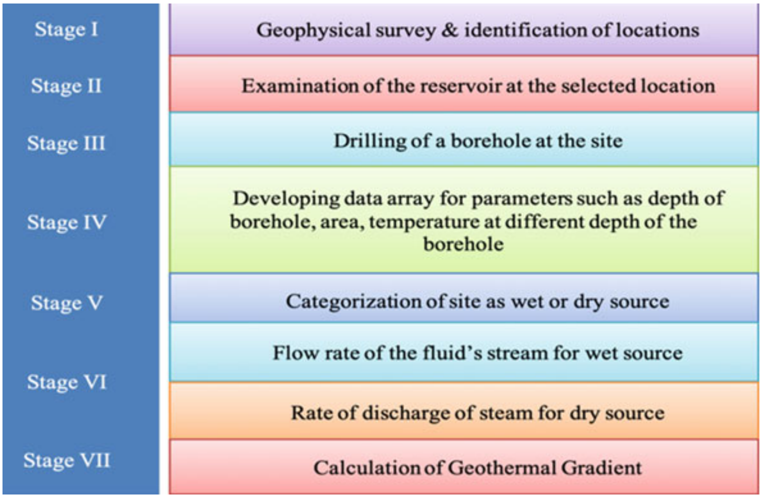

Fig. 33.5 Seven stage methodology chart

Similarly, the gradients for location 2 and location 3 are calculated as 0.58°c/m and 0.59°c/m, respectively as shown in Fig. 33.6. In the same manner, the geothermal gradient for each site is calculated, taking data from different locations on a single site to be more accurate. The calculated geothermal gradient for most active geothermal locations lies within the estimated geothermal gradient. The selected area's temperature gradients and an average temperature chart against the depth of the borehole were finally computed at each location once all of the specified points had been assessed. The gradient calculated is the average of at least two locations within the geothermal areas. Table 33.2 shows the comparison of the estimated and calculated geothermal gradient at selected areas [16, 18–25].

33.5 GHG Emission Analysis Using RETscreen

As the world continues to grapple with the effects of climate change, it is becoming increasingly clear that we need to shift to cleaner and more sustainable forms of energy. An in-depth analysis was conducted utilizing the powerful RETscreen software to quantify the extent of greenhouse gas (GHG) emission reductions achievable through the implementation of a geothermal power plant. The results revealed an impressive reduction rate of 92% in GHG emissions. This outcome not only highlights the considerable environmental benefits associated with geothermal energy but also underscores its potential for bolstering financial incentives provided by governments in the form of subsidies tied to carbon emission levels from renewable power plants (Fig. 33.7).

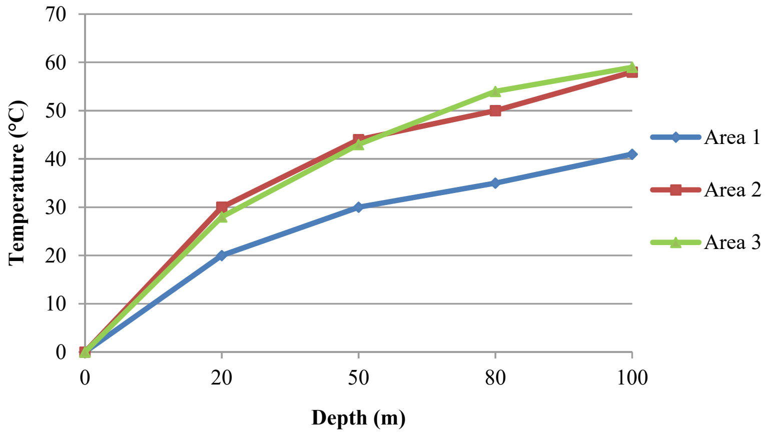

Fig. 33.6 The varying geothermal gradient with depth in Puga Valley

Table 33.2 Geothermal gradients: estimations versus calculations

Geothermal site	Estimated gradient (°C/m)	Calculated gradient (°C/m)
Puga Valley	0.35–2.5	0.40–0.59
Chhumathang	0.7–2.5	0.79–1.23
Manikaran	0.09–0.11	0.097–0.099
Tapoban	0.04–0.06	0.047–0.621
Tatta Pani	0.11–0.15	0.144–0.192
Anhoni-Samoni	0.059	0.0598
Unkeshwar	NA	0.1141
Salbardi	NA	0.1022

Geothermal power plants hold immense promise in the battle against climate change due to their capacity to generate electricity without releasing harmful GHG emissions. The reduction of carbon emissions resulting from the adoption of geothermal energy is a pivotal factor in curbing the escalating temperatures of the Earth's atmosphere, a phenomenon directly linked to global warming and its adverse consequences. Governments worldwide recognize the pressing need to transition to cleaner energy sources, and in support of this transition, they offer substantial subsidies and incentives to renewable power plants based on their carbon emission reduction potential. Geothermal power plants, with their exceptional emission reduction rate of 92%, are particularly well-positioned to attract significant financial backing. This influx of funds not only benefits the power plant operators but also helps to drive the expansion and development of geothermal infrastructure, fostering a more extensive and robust renewable energy sector.

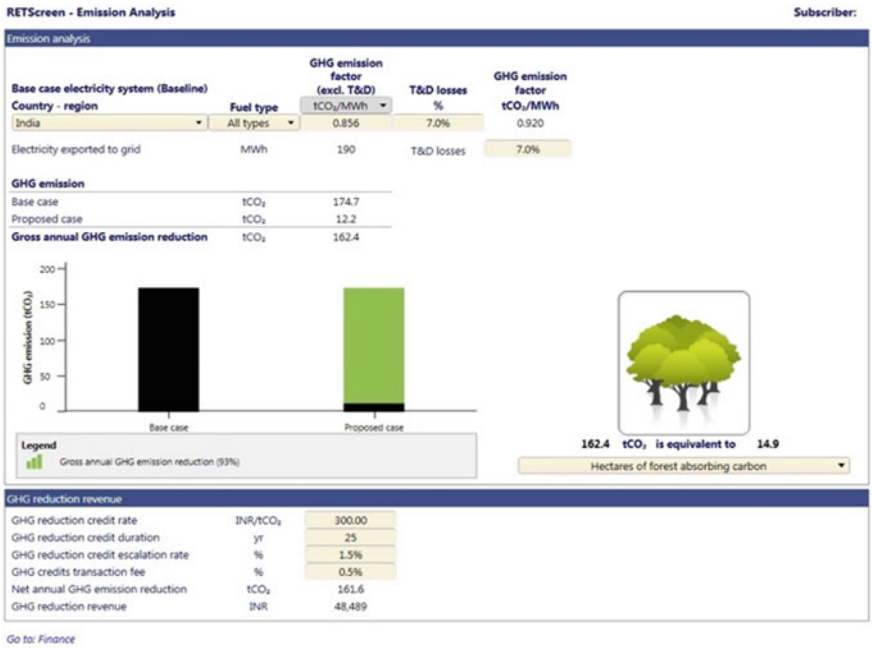

Fig. 33.7 GHG emission analysis

33.6 Conclusion

Based on a comprehensive analysis of diverse geothermal sites in India, it can be conclusively determined that the calculated geothermal gradient falls within the estimated range for the majority of these sites. However, it is noteworthy that no available data on the geothermal gradient exists for the Unkeshwar and Salbardi locations. Consequently, employing the discussed techniques, the geothermal gradient values for Unkeshwar and Salbardi have been successfully determined as 0.1141 °C/m and 0.1022 °C/m, respectively. The results also revealed an impressive reduction rate of 92% in GHG emissions in comparison to other non-renewable based power plants. These findings unequivocally underscore India's vast potential for Geothermal Energy. Efficient utilization of this potential resource represents a momentous stride towards realizing India's vision of a zero-carbon-emitting and eco-friendly nation. India can drive towards its developmental goals at an accelerated pace, surpassing earlier expectations.

References

1. Exploring the Earth Using Seismology—Incorporated Research Institutions for Seismology. http://surl.li/hdwoq. Accessed 14 Sept 2022
2. Modeling the Interior of the Earth Using Seismic Waves. http://surl.li/hdwot. Accessed 14 Sept 2022
3. Jia, G.S., Ma, Z.D., Xia, Z.H., Wang, J.W., Zhang, Y.P., Jin, L.W.: Investigation of the horizontally-butted borehole heat exchanger based on a semi-analytical method considering groundwater seepage and geothermal gradient. Renew. Energy **171**, 447–461 (2021). https://doi.org/10.1016/j.renene.2021.02.129
4. Xu, W., et al.: Geothermal gradient and heat flow of the Erlian Basin and adjacent areas, Northern China: geodynamic implication. Geothermics **92**, 102049 (2021). https://doi.org/10.1016/j.geothermics.2021.102049
5. Cioffi, C.R., Meira, V.T., Trindade, R.I.F., Lanari, P., Ganade, C.E., Gerdes, A.: Long-lived intracontinental deformation associated with high geothermal gradients in the Seridó Belt (Borborema Province, Brazil). Precambrian Res. **358**, 106141 (2021). https://doi.org/10.1016/j.precamres.2021.106141
6. Hu, Y., Liu, S., Fu, J., Sun, G., Gao, L., Guo, R.: Neoarchean-early Paleoproterozoic granitoids, the geothermal gradient and geodynamic evolution in the Hengshan Terrane, North China. Craton Gondwana Res. **94**, 143–163 (2021). https://doi.org/10.1016/j.gr.2021.03.004
7. Madon, M., Jong, J.: Geothermal gradient and heat flow maps of offshore Malaysia: some updates and observations. Bull. Geol. Soc. Malaysia **71**, 159–183 (2021). https://doi.org/10.7186/bgsm71202114
8. Melouah, O., Eldosouky, A.M., Ebong, E.D.: Crustal architecture, heat transfer modes and geothermal energy potentials of the Algerian Triassic provinces. Geothermics **96**, 102211 (2021). https://doi.org/10.1016/j.geothermics.2021.102211
9. Anene, C.Z., Frank, C., Odumodu, R., Nfor, B.N.: An analysis of the variable geothermal gradients in the eastern coastal swamp of the Niger delta, Nigeria. COOU J. Phys. Sci. **4**(1) (2021) [Online]. Available at: www.coou.edu.ng. Accessed 14 Sept 2022
10. Vali Rajammagari, H., Wani, M.M.: Experimental analysis of the effect of zinc oxide nano additive diesel-ethanol blend on the performance and emission characteristics of a variable compression ratio diesel engine at various compression ratios (2022). https://doi.org/10.1080/10916466.2022.2154790
11. Rajammagari, H.V., Mohmad, M.W.: The effect of mixed nanoadditive-blended diesel–water emulsion on the performance, combustion, and emission characteristics of a DI diesel engine. Heat Transf. **49**(6), 3531–3548 (2020). https://doi.org/10.1002/HTJ.21786
12. Hussain Vali, R., Marouf Wani, M.: Optimal utilization of ZnO nanoparticles blended diesel-water emulsion by varying compression ratio of a VCR diesel engine. J. Environ. Chem. Eng. **8**(4), 103884 (2020). https://doi.org/10.1016/J.JECE.2020.103884
13. Hussain Vali, R., et al.: Optimization of variable compression ratio diesel engine fueled with zinc oxide nanoparticles and biodiesel emulsion using response surface methodology. Fuel **323**, 124290 (2022). https://doi.org/10.1016/J.FUEL.2022.124290
14. Singh, H.K., Chandrasekharam, D., Minissale, A., Raju, N.J., Baba, A.: Geothermal potential of Manuguru geothermal field of Godavari valley, India. Geothermics **105**, 102545 (2022). https://doi.org/10.1016/j.geothermics.2022.102545
15. Kelishami, S.B.A., Rezaei, M., Mohebian, R.: A new approach to estimate and delineate the geothermal gradient of Iran. Geothermics **103**, 102428 (2022). https://doi.org/10.1016/j.geothermics.2022.102428
16. Chandrasekharam, D.: Geothermal energy resources of India: past, present and future scenarios. In: World Geothermal Congress, pp. 24–29 (2005)
17. Chandrasekharam, D.: Geothermal energy resources for developing countries. J. Bundschuh—Google Books. http://surl.li/hdwno. Accessed 14 Sept 2022
18. Gupta, M.L., Sharma, S.R., Drolia, R.K., Singh, S.B.: Subsurface thermal conditions of Puga valley hydrothermal field, Himalaya, India. J. Geophys. Geophys. **54**(1), 51–59 (1983)

19. Shanker, R., Thussu, J.L., Prasad, J.M.: Geothermal studies at Tattapani hot spring area, Sarguja district, central India. Geothermics **16**(1), 61–76 (1987). https://doi.org/10.1016/0375-6505(87)90079-4
20. Yadav, K., Sircar, A.: Geothermal energy provinces in India: a renewable heritage. Int. J. Geoherit. Park **9**(1), 93–107 (2021). https://doi.org/10.1016/j.ijgeop.2020.12.002
21. Bhatia, S.C.: Geothermal energy resources and its potential in India. Adv. Renew. Energy Syst. **I**, 389–402 (2014). https://doi.org/10.1016/b978-1-78242-269-3.50015-2
22. General, F.: Geothermal as Energy Source for Remote Areas, pp. 1–9 (1995)
23. Sarolkar, P.B.: Exploration strategy for hot springs associated with Gondwana coalfields in India. Coalfields and Lignite Occurrences of in World, pp. 25–29 (2010)
24. Masum, M.: Int. Res. J. Geol. Min. **4**(6), 163–175 (2014). https://doi.org/10.14303/irjgm.2014.026
25. Sarolkar, P.B.: Geothermal energy in India: poised for development. In: Proceedings—43rd Workshop on Geothermal Reservoir Engineering, pp. 1–4 (2018) [Online]. Available at: http://surl.li/hdwns. Accessed 14 Sept 2022

Chapter 34
Hardness and Wear Studies of AA 7075-B_4C-Gr Composite Produced by Stir Casting Technique

G. Venkateswarlu and T. Madhavi

Abstract Traditional monolithic materials aren't always able to combine strength, stiffness toughness, and density well. Composites are the most promising materials of current research because they have the potential to overcome these drawbacks and satisfy the constantly growing demands of contemporary technology. In current research, stir casting is used to fabricate the AA 7075-B4C-Gr composite. The matrix of AA 7075 alloy, which may be used for space, aviation, and automotive components at high temperatures, was reinforced with boron carbide (B_4C). The mechanical properties in terms of hardness and wear test were carried out on AA 7075-B_4C–Gr composite. The sample of AA7075 alloy was also casted and tested for comparison.

34.1 Introduction

Composites are artificial materials formed of one or more discontinuous phases that are in close proximity to one another and have a discernible interface. These are multifunctional material systems that provide properties that cannot be obtained from separate phases. Composites are also specifically designed to be economical, effective in terms of properties and application focused. The continuous phase is referred to the "matrix" but the phase in discontinuous is often tougher and stronger than the continuous phase and is referred to as the "reinforcement". The reinforcement helps the matrix overall mechanical qualities while allowing it to take on the correct shape and support the majority of an applied load. Reinforcement reduces density while increasing strength, stiffness, wear resistance and temperature resistance. Composites are often divided into two groups based on the nature of the reinforcement and the kind of matrix material. Ceramic matrix composites (CMCs), metal matrix composites (MMCs), and organic matrix composites (OMCs) are all included in the

G. Venkateswarlu · T. Madhavi (✉)
Department of Mechanical Engineering, Sree Chaitanya College of Engineering, Karimnagar, Telangana, India
e-mail: madhavi.nvr@gmail.com

P. H. V. S. Talpa Sai et al. (eds.), *Intelligent Manufacturing and Energy Sustainability*, Smart Innovation, Systems and Technologies 372,
https://doi.org/10.1007/978-981-99-6774-2_34

first categorization (MMCs). Polymer matrix composites (PMCs) and carbon matrix composites are often included when the phrase "organic-matrix composite" is used. The second group is based on the kind of reinforcement used, including woven composites, laminated composites, continuous fibre, and whiskers. Polymer Matrix Composites (PMCs) contain a sin system and strengthening fibres like aramid and glass fibres. These composites include low densities, excellent corrosion resistance, low thermal conductivities and low electrical conductivities. Applications include sports items, hulls, channels, and boats. These composites are produced using the easily-up and spray methods, as well as the filament winding in Gan pultrusion method. Ceramic Matrix Composites (CMCs) include a ceramic matrix reinforced with short fibres or whiskers of B_4C and SiC, etc. Ceramic matrix composites stand out for their low conductivity, high temperature resistance, high stiffness, chemical stability and crystalline or amorphous architectures. But these composites have limited applicability due to high processing costs and the need for extensive infrastructure. Metal Matrix Composites (MMCs) compose of Al, Mg alloy as matrix and B_4C and SiC as reinforcement. Frequently ceramics are used to strengthen the matrix. MMCs display a mix of ceramic (high strength and hardness with load bearing capability) and metallic (toughness and formability) features. These materials are specially designed to meet specific needs, such as a decrease in density or an increase in stiffness, yield strength, or ultimate tensile strength, which translates to better specified qualities. Early research was conducted employing fibre reinforcement for process development. Short fibre, particle, and whisker reinforced composites are used because of their isotropy, high production costs, and little secondary processing. Particles are commonly employed Due to their superior specific modulus, strength, and wear resistance, which provide a large performance boost over unreinforced alloys while also being cheap cost, excellent workability, and durable. Early research was conducted employing fibre reinforcement for process development. Short fibre, particle, and whisker reinforced composites are used because of their isotropy, high production costs, and little secondary processing. Sunil Ratna Kumar et al. [1] The study involved enhancing the mechanical properties of aluminum by incorporating reinforcement material such as titanium carbide (TiC), silicon carbide (SiC), aluminum oxide (Al_2O_3), titanium dioxide (TiO_2), and tin (Sn) into its matrix. In comparison to conventional methods, the in-situ approach of strengthening the aluminum matrix with a ceramic phase, specifically titanium carbide (TiC), is highly preferred. In the present study, an aluminum-copper (Al-Cu) alloy, specifically the 2014 Aluminum alloy series, was utilized as the matrix material. The in-situ technique was employed to incorporate TiC reinforcement into the alloy during the experiment. In comparison to Al-4.5%Cu alloy, the developed Al-0.5%Cu/10%TiC Metal Matrix Composite (MMC) material demonstrates greater yield strength, ultimate strength, and hardness. According to reports, the yield and ultimate tensile strengths increased by roughly 15% and 24%, respectively. Ratnam et al. [2] investigated the microstructures and mechanical properties. The characteristics of ultrafine grained (UFG) and coarse grained (CG) Al7075 alloys, along with their alterations resulting from heat treatment via equal-channel angular pressing (ECAP) processing and natural ageing, can be discussed. Their research showed that the UFG samples' micro hardness, ultimate strength, tensile yield strength,, and natural ageing all exceeded those of the CG samples by 103%, 35%, and 48%, respectively, following the testing. Their research demonstrates that extreme plastic deformation may greatly enhance the mechanical characteristics of age-hardening Al alloys. According to a journal paper by Hanji [3] published in Waterstones, the aluminium matrix may be enhanced by adding reinforcement made of hard ceramic particles as SiC, Al_2O_3, B4C, etc. By adding B4C particles to the 7075Al matrix, an attempt is made to improve the mechanical qualities of AMCs, such as their tensile strength and hardness. Analysis was done on the microstructure and mechanical characteristics of the manufactured AMCs. The 105 size B4C was selected Based on the outcomes of the tensile strength test conducted on the metal matrix composites with different particle sizes. They came to the conclusion from the microstructure study that increasing the grain size and material weight will boost tensile strength. Al7075-TiB2 in-situ composite was explored by Keshavamurthy et al. [4]. In their study, the researchers employed stir casting technology and utilized master alloys composed of Al-10%Ti and Al-3%Br. They conducted various analyses including microstructure analysis, microhardness tests, grain size investigations, and tensile tests on both the matrix alloy and the composite material. TiB2 particles are distributed rather uniformly throughout the alloy's matrix microstructure. The composite's average grain size was less than that of the unreinforced alloy. Al7075-TiB2 composite has much greater micro hardness, ultimate tensile, and yield strength than unreinforced alloy. For MMCs B4C, SiC, Al_2O_3 and Gr are the commonly preferred particulate reinforcements. The addition of ceramic particulates to the composite material significantly enhances its ability to withstand abrasion [5]. Baradeswaran et al. [6] conducted research on the mechanical properties of a hybrid metal matrix composite consisting of Al7075/Al2O/graphite. They discovered that as the weight percentage of the ceramic phase increased, there was a corresponding increase in hardness, compression strength, and flexural strength of the composite material. Mohanavel et al. [7] conducted a study to examine the microstructure and mechanical properties of an alloy and composites. Their research focused on examining the reinforcement capabilities of Al_2O_3/Gr when incorporated into the parent alloy. The study focused on analyzing the microhardness, tensile strength, and flexural strength of the materials.

34.2 Materials and Method

34.2.1 Materials

In the current investigation, Aluminum 7075 was chosen as the matrix material, and its chemical composition can be found in Table 34.1 and reinforcements used in this study are B_4C and Gr. Alloy 7075 is the benchmark for a lightweight, cost-effective material with medium-to-high strength. Aluminum 7075 possesses notable

Table 34.1 AA7075 chemical composition

Elements	Zn	Mg	Cu	Si	Fe	Mn	Cr	Al
wt%	5.6–6.1	2.1–2.5	1.2–1.6	0.5	0.5	0.5	0.5	Rest

Table 34.2 Properties of Al 7075

Properties	310 MPa
Tensile strength	276 MPa
Shear strength	207 MPa
Fatigue strength	96.5 MPa
Elastic modules	68GPa
Poisson's ratio	0.33
Elongation	12–17%

structural strength, toughness, excellent surface finish, commendable corrosion resistance to atmospheric and seawater environments, favorable machinability, as well as weldability [8]. Mechanical properties of Aluminium 7075 are shown in Table 34.2. Processing of Al 7075 matrix done by Liquid state process includes ultrasonic assisted castings, stir casting, and squeeze casting. Solid state process includes high energy ball milling, FSP, and Powder metallurgy. Boron carbide, with a chemical formula approximately B4C, is an exceptionally hard ceramic and covalent material made of boron and carbon. It finds wide-ranging applications in bulletproof vests, tank armor, engine sabotage powders, and various industrial uses due to its exceptional hardness and strength. With a Vickers hardness exceeding 30 GPa, boron carbide is recognized as one of the hardest materials currently known, ranking just below cubic boron nitride and diamond in terms of hardness. Mechanical properties of boron carbide are shown in Table 34.3. Graphite, formerly known as plumbago, is a crystalline form of carbon where its atoms are arranged in a hexagonal structure. It occurs naturally in this configuration and is considered the most stable form of carbon under standard conditions. At high pressures and temperatures, graphite transforms into diamond. Graphite finds applications in the manufacturing of pencils and lubricants. It exhibits excellent heat and electrical conductivity, making it valuable in electronic devices like electrodes, batteries, and solar panels. Table 34.4 provides information about the mechanical properties of graphite.

34.2.2 Method of Fabrication of Composite

The stir casting process is favored for producing metal matrix composites due to its affordability, suitability for mass production, simplicity, ability to achieve conformal shaping, and ease of controlling the composite structure. These advantages make it

Table 34.3 Mechanical properties of boron carbide

Property	Value
Density (g/cm^3)	2.52
Hardness (Knoop 100 g) (kg mm^{-2})	2900–3580
Melting point (°C)	2445
Fracture toughness	2.9–3.7 MPa
Young's modulus	450–470
Electrical conductivity	140
Thermal conductivity	30–42

Table 34.4 Mechanical properties of graphite

Property	Value
Bulk density (g/cm^3)	1.3–9.5
Porosity (%)	0.7–53
Modulus of elasticity (GPa)	15-Aug
Compressive strength (MPa)	20–200
Flexural strength (MPa)	6.9–100
Thermal conductivity (W/m K)	25–470
Specific heat capacity (J/kg K)	710–830
Electrical resistivity (Ω m)	5×10^{-6} to 30×10^{-6}

a widely used technique in the production of metal matrix composites. The experimental setup for stir casting primarily consisted of an electric furnace and a stirrer. The furnace had a maximum working temperature of 1000 °C. Fine scraps of AA7075 were used as the starting material. These scraps were placed in the furnace and heated to a temperature slightly higher than 600 °C, causing them to transform into a semi-liquid state. Following the heating of the AA7075 scraps to a semi-liquid state, preheated reinforcement materials are introduced into the mixture. Mechanical stirring is then carried out at a rotation speed of 150 rpm. Once the aluminum matrix metal composite (AMMC) reaches a liquefied state with the reinforcement evenly dispersed, it is poured into cylindrical molds. The poured material is then compressed to achieve the desired shape. Based on the findings from the literature review, four samples were prepared, and their compositions are outlined in Table 34.5. The schematic representation of the stir casting setup can be found in Fig. 34.1 while the process of stir casting is depicted in Fig. 34.2.

Table 34.5 Composition of sample

Sample	Al 7075 (wt%)	B4C (wt%)	Gr (wt%)
I	96	2	2
II	94	4	2
III	92	6	2
IV	90	8	2

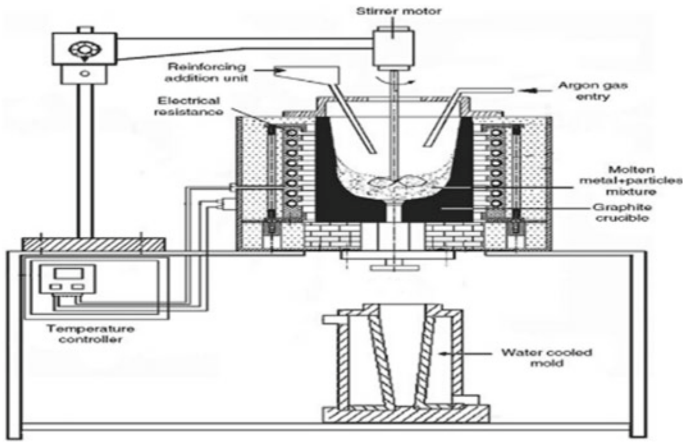

Fig. 34.1 Schematic representation of the stir casting setup

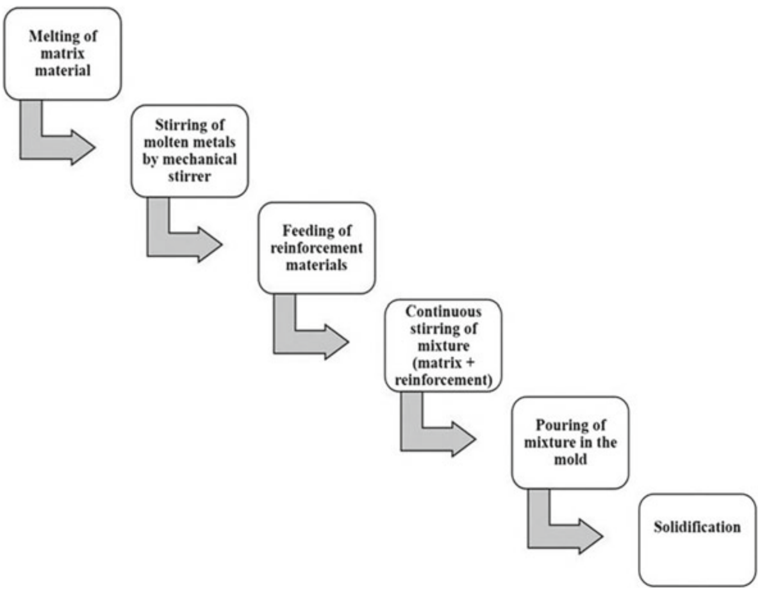

Fig. 34.2 Process of stir casting

34.2.3 Hardness

Hardness is a characteristic that quantifies a material's resistance to deformation or changes in shape. It refers to the ability of a material to withstand wear, tear, scratching, abrasion, and cutting forces, thus determining its resistance to these processes. Materials that are harder exhibit greater resistance to cutting and shaping compared to softer materials. The increased hardness makes it more challenging to modify or alter the shape of harder materials. Harder materials often tend to be more brittle, meaning they have limited flexibility and are prone to shattering or fracturing rather than undergoing significant deformation or bending. The Vickers hardness test was introduced as an alternative to the Brinell method for measuring the hardness of materials. It was developed in 1921 by Robert L. Smith and George E. Sandland at Vickers Ltd. The Vickers hardness test offers a reliable and widely used technique for assessing the hardness of various materials. The Vickers hardness test is frequently considered more user-friendly compared to other hardness testing methods. This is because the calculations involved in the Vickers test are not influenced by the size of the indenter, and the same indenter can be employed for all materials regardless of their hardness. A Vickers hardness tester, used for conducting the Vickers hardness test, can be observed in Fig. 34.3.

34.2.4 Heat Treatment

Heat treatment is a manufacturing process employed to modify the physical and, in some cases, chemical properties of a material. It is most commonly applied in metallurgy. Heat treatment involves subjecting a material to controlled heating or cooling, often to extreme temperatures, in order to achieve the desired outcome, such as hardening or softening the material. By carefully controlling the heating and cooling process, the material's structure and properties can be precisely altered to meet specific requirements. Heat treatment encompasses various techniques, including annealing, case hardening, precipitation strengthening, tempering, carburizing, normalizing, and quenching. These techniques involve specific heating and cooling processes that are intentionally carried out to alter the properties of the material. It's worth noting that heating and cooling can also occur unintentionally during other manufacturing processes, such as hot forming or welding. While these incidental heating and cooling processes may have some effect on the material's properties, the term "heat treatment" specifically refers to intentional heating and cooling processes aimed at achieving desired property modifications. In heat treatment the material was heated up to the recrystallize temperature, then the product was dipped into the different medium like the water and oil etc.

Fig. 34.3 Vickers hardness tester

34.2.5 Wear Test

Wear resistance refers to the capacity of a material, such as stone, to withstand and endure various external forces that it encounters during its service life. These forces can include abrasion, edge cutting, impact, and other forms of wear. The wear resistance of a material is a critical characteristic that determines its durability and longevity in practical applications. The wear tests were conducted on aluminum (Al7075) alloy and aluminum (Al7075) + nano B_4C and Gr MMCs as per The ASTM

G99-95 standard was utilized for conducting a computerized pin-on-disk wear test at room temperature, employing a data acquisition system integrated with the test rig. which was used to evaluate the wear behavior of the aluminum (AL7075) alloy and aluminum (AL7075) + nano B_4C and Gr MMCs The sliding wear test was performed on the toughened steel disc (En-32) with a hardness of 60 HRC and a surface roughness (Ra) of 0.5 pm, as depicted in Fig. 34.4. The test samples for sliding wear were machined to a nominal diameter of 8 mm and a gauge length of 30 mm. Sliding wear is induced by sliding the test samples over a rotating disc during the wear test. The disc, with a diameter of 120 mm, is connected to a DC motor capable of rotating at a speed of 1000 rpm. To apply the desired load to the test sample, a steel wire and pulley arrangement is utilized, allowing the addition of dead weight of up to 200 N. This setup facilitates the evaluation of the material's resistance to sliding wear under controlled conditions. The test sample is securely mounted onto the fixture and positioned at a specific track diameter. The track diameter can be modified according to the specific sample and testing conditions as needed. The testing machine is equipped with a controller that allows for the manipulation of various sliding wear parameters. These parameters include sliding velocity, applied load, and testing duration, providing flexibility in customizing the testing conditions for each sample. The experiments were conducted, and upon completion of the designated time, measurements of wear in microns and frictional force in Newton were recorded. Tests were conducted on samples at 1 kg load and at distance of 200, 400 and 600 mts respectively on all samples.

Fig. 34.4 Wear test machine

34.3 Results and Discussion

34.3.1 Hardness

Samples tested by Vickers hardness tester and hardness values are shown in Table 34.6 and in Fig. 34.5.

Hardness of specimens after heat treatment and quenching in water are shown in Table 34.7. Graph of hardness values is shown in Fig. 34.6.

Hardness of specimens after heat treatment and quenching in oil are shown in Table 34.8. Graph of hardness values is shown in Fig. 34.7.

Table 34.6 Vickers hardness values of samples

Sample	Trial 1			Trail 2			VHN
	D1	D2	VHN	D1	D2	VHN	
I	78	88	290	67	76	296	293
II	67	76	302	87	87	306	304
III	89	76	325	67	67	326	325.5
IV	87	86	340	79	57	345	342.5

Fig. 34.5 Graph for hardness

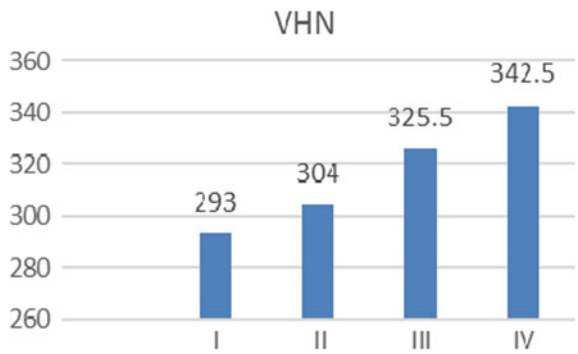

Table 34.7 Hardness values of water samples

Sample	Trial 1			Trail 2			VHN
	D1	D2	VHN	D1	D2	VHN	
I	87	79	310	89	96	312	311
II	76	67	323	98	94	345	334
III	68	89	344	98	93	343	343.5
IV	59	67	357	96	92	356	356.5

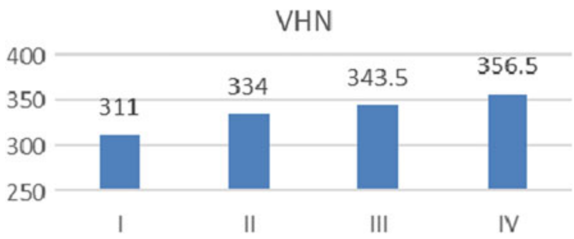

Fig. 34.6 Graph for hardness of water quenched samples

Table 34.8 Hardness values of oil quenched samples

Sample	Trial 1			Trail 2			VHN
	D1	D2	VHN	D1	D2	VHN	
I	78	88	290	67	76	296	293
II	67	76	302	87	87	306	304
III	89	76	325	67	67	326	325.5
IV	87	86	340	79	57	345	342.5

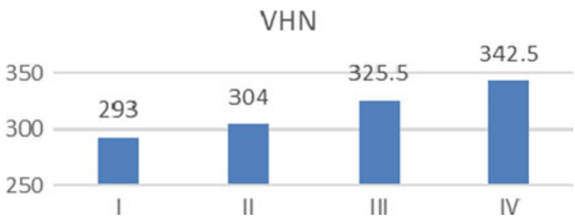

Fig. 34.7 Graph for hardness of oil quenched samples

34.3.2 Wear Test

Wear tests was conducted on samples at 1 kg load and at distance of 200, 400 and 600 mts respectively on all samples. Results of wear test at 1 kg load and 200 mts are shown in Table 34.9 and Fig. 34.8.

Results of wear test at 1 kg load and 400 mts are shown in Table 34.10 and Fig. 34.9.

Results of wear test at 1 kg load and 600 mts are shown in Table 34.11 and Fig. 34.10.

Table 34.9 Wear at 1 kg load and 200 mts

Sample	Initial weight	Final weight	Loss of weight
I	14.434	14.434	0.074
II	13.667	13.667	0.068
III	14.355	14.355	0.063
IV	14.445	14.445	0.056

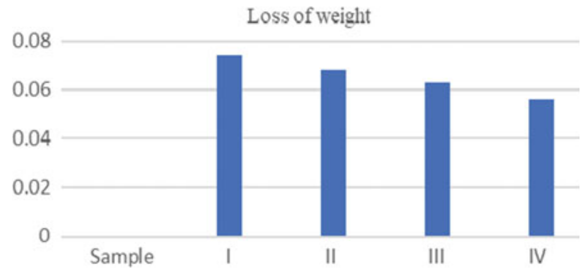

Fig. 34.8 Graph Wear at 1 kg load 200 mt

Table 34.10 Wear at 1 kg load and 400 mts

Sample	Initial weight	Final weight	Lose of weight
I	14.464	14.464	0.089
II	13.567	13.567	0.081
III	14.345	14.345	0.079
IV	14.434	14.434	0.071

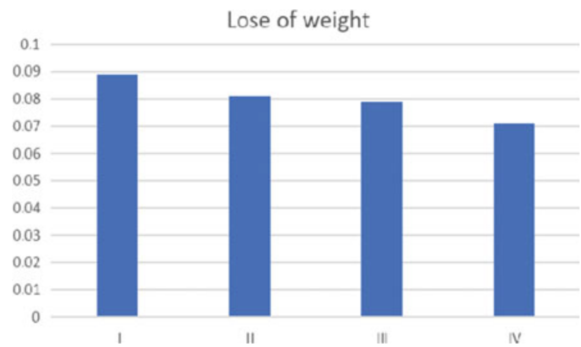

Fig. 34.9 Wear at 1 kg load and 400 mts

Table 34.11 Wear at 1 kg load and 600 mts

Sample	Initial weight	Final weight	Lose of weight
I	14.575	14.575	0.913
II	15.675	15.675	0.89
III	14.786	14.786	0.785
IV	14.567	14.567	0.657

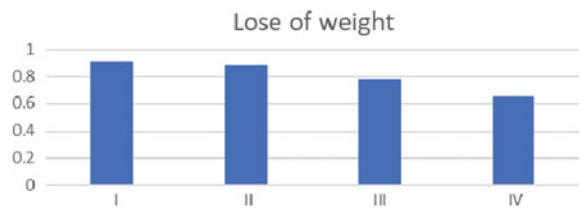

Fig. 34.10 Wear at 1 kg load 600 mts

34.4 Conclusion

1. Stir casting was used to create the AL7075-B4C-gr metal matrix composite materials, which were then extruded.
2. Both the Gr (graphite) and B4C (boron carbide) particles are uniformly dispersed throughout the matrix alloy. This means that the distribution of these particles is uniform and consistent throughout the entire matrix material, ensuring their effective reinforcement and potential enhancement of the material's properties.
3. The micro hardness of the metal matrix composite material made of AL7075-B4C-Gr is greater than that of the matrix material.
4. As the percentage of reinforcement increased, there was a corresponding increase in the hardness of the material. This indicates that higher reinforcement percentages lead to greater hardness in the composite material. The reinforcing particles contribute to the strengthening of the matrix material, resulting in an overall increase in hardness.
5. The heat-treated samples exhibited higher hardness compared to the non-heat-treated samples. This suggests that the heat treatment process resulted in an improvement in the hardness of the material. Additionally, among the heat-treated samples, those that were water quenched demonstrated higher hardness than the ones that were oil quenched. This indicates that the choice of quenching medium can influence the hardness of the material, with water quenching leading to a greater increase in hardness compared to oil quenching.
6. As the percentage of reinforcement is increased and the distance is decreased, the wear rate tends to decrease. This correlation suggests that increasing the reinforcement and minimizing the spacing between reinforcements can enhance the material's resistance to wear.

References

1. Sunil Ratna Kumar, K., et al.: Evaluation of mechanical behaviour of powder metallurgy-processed aluminium self lubricating hybrid composites with B4 C and Gr additions. IJRMET **6**(1), 120–127 (2015)
2. Ratnam, Ch., Sunil Ratna Kumar, K.: Corrosion behavior of powder metallurgy processed aluminum self-lubricating hybrid metal matrix composites with B4C and SIC and Gr additions. SSRG-IJME **4**, 279–290 (2017)
3. Hanji, A., Siddeshkumar, N.G., Ravindranath, V.M., Shivashankar, G.S.: Study on corrosion behavior of heat-treated hybrid metal matrix composites reinforced with B4C and SIC and graphite particles. J. Mater. Sci. Mech. Eng. **2**(9), 41–46 (2015)
4. Keshavamurthy, R., Mageri, S., Raj, G.: Microstructure and mechanical properties of Al7075-TiB_2 in-situ composite. Res. J. Mater. Sci. **1**(10), 6–10 (2013). ISSN: 2320-6055
5. Veeresh Kumar, G.B., Rao, C.S.P., Selvaraj, N.: Mechanical and tribological behavior of particulate aluminum metal matrix composites. J. Miner. Charact. Eng. **10**(1), 59–91 (2011)
6. Baradeswaran, A., Perumal, A.E.: Study on mechanical and wear properties of Al 7075/Al_2O_3/graphite hybrid composites. Compos. B Eng. **56**, 464–471 (2014)

7. Mohanavel, V., et al.: Mechanical behaviour of hybrid composite (AA6351 + Al_2O_3 + Gr) fabricated by stir casting method. Mater. Today: Proc. **4**(2), 3093–3101 (2017)
8. Singh, S.C.E., Selvakumar, N.: Effect of milled B4C nanoparticles on tribological analysis, microstructure and mechanical properties of Cu–4Cr matrix produced by hot extrusion. Arch. Civ. Mech. Eng. **17**, 446–456 (2017)

Chapter 35
Investigations on the Influence of Stacking Sequence on the Mechanical Properties of Kevlar/Jute Composite Laminates

A. R. S. Nikhil Aanandhan, M. Ashwin, V. Sriram, G. Gokul Sree, J. Jensin Joshua, and S. Seralathan

Abstract At present, aircraft and automobile manufacturers are primarily focusing on weight reduction to protect ecosystems by consuming less energy. Introduction of low-density materials is the main approach for weight reduction. As a result, the industry is replacing steel with composite materials. The focus of this study is to investigate the Kevlar-jute composite mechanical properties namely, modulus of elasticity, flexural strength, tensile strength, impact strength, and weight. The Kevlar and jute composite is made using an epoxy matrix. Compression moulding and vacuum infusion are used to create test samples. The results showed that adding Kevlar to jute fibre composites significantly improve the characteristics of the resultant hybrid composites. Flexural strength is strongly impacted by the stacking process based on the location of the Kevlar plies. The stacking sequence has no impact on the tensile characteristics of Kevlar and Jute fibre for the same relative weight fraction. The ratio of Kevlar to jute enhances tensile strength, flexural strength, impact energy, strain energy, and decreases specimen weight.

35.1 Introduction

The reduction of weight is the primary focus of vehicle manufactures in the current environmentally conscious world to save natural resources and save energy. The introduction of superior material design, and improved assembling forms are primarily responsible for weight reduction. With the emergence of composite materials, it became extremely simple to reduce segment weight while preserving solidity and

A. R. S. Nikhil Aanandhan · M. Ashwin · V. Sriram · G. Gokul Sree · J. Jensin Joshua · S. Seralathan (✉)
Department of Aeronautical Engineering, Hindustan Institute of Technology and Science, Chennai, Tamilnadu 603103, India
e-mail: siva.seralathan@gmail.com

P. H. V. S. Talpa Sai et al. (eds.), *Intelligent Manufacturing and Energy Sustainability*, Smart Innovation, Systems and Technologies 372,
https://doi.org/10.1007/978-981-99-6774-2_35

load bearing capability. Composite materials have an increasingly variable strain energy storage capacity and a high solidity to weight ratio. Although they are not always more practical than their steel counterparts, composite materials offer more opportunities for significant weight savings. The impact of stacking progression on the pliable, adaptable modulus, and flexural characteristics of Kevlar-Jute surface reinforced epoxy composites was studied by Bhanupratap [1]. The qualities of the newly created blend composites were improved by Kevlar and Jute fibers joining. The main effect of stacking gathering (viz., changing the context in which Kevlar was used) was on the flexural quality. Layering gathering had no impact on the adaptability of fibers made of Kevlar and Jute that were similar in relative weight. The proportion of Kevlar to Jute created the material's tractable, flexural quality, influence imperativeness, strain imperativeness, and reduced the specimen's weight. More the use of Kevlar reduced the use of epoxy and reduced the cost of the specimens. Bhargav and Suresh Babu [2] concentrated on evaluating the mechanical characteristics of a composite made of Jute fiber and nanotubes. Better mechanical qualities were demonstrated by the three-layer jute fiber's inflexibility and 6% volume filler piece was made of nanotubes. The carbon nanofiller redesigned the composite's flexibility by including carbon atoms. Significant progress was made in the flexural nature of the composite in the 6% volume division of carbon nano filler. Due to the agglomeration of nano tube filler in the composite, flexural quality increased by up to 8% when nano tube filler was added. At 6% volume division of carbon nano filler, the impact nature of the composite improved, and other test models furthermore revealed around proportionate estimation of test specimen. Due to its desirable characteristics, such as high tensile strength and low density, Kevlar fiber was used as a reinforcement in laminate materials and was a good option for defense utility items like bulletproof armors [3]. Laminates reinforced with natural fibers had the advantages over their synthetic equivalents [4]. Due to the ability to have their properties tailored, hybrid laminates that used both natural and synthetic fibers as reinforcement materials were becoming more popular in a variety of applications, including building construction, automobile and locomotive panels, aircraft structures and marine parts [5].

Numerous researchers have investigated the type of fibers, its length, orientation, and stacking patterns influencing the ability of the fiber to maintain desirable properties while being subjected to various types of loads [6]. Jute fiber is regarded as one of the most promising materials among natural fibers due to its widespread commercial availability in the requisite form at a reasonable price. Composites made from jute have shown promising outcomes in several low loads bearing structural and non-structural applications [7]. In this regard, research was to determine the effect on mechanical characteristics of hybrid composites by the hybridization of jute fabric with E-glass or carbon textiles. Zhang et al. [8] examined several jute/glass laminate combinations by assessing tensile, flexural, and interlaminar shear characteristics as performance indicators. To take advantage of the reduced cost of jute while significantly boosting the laminates' resistance to moisture absorption, the impact of hybridization was examined. According to Bandaru et al. [9], composites reinforced with banana and jute fibers had a greater tensile and flexural strengths than composites reinforced with only one natural fiber. The mechanical characteristics of sisal, jute, and glass fiber reinforced polyester composites were studied by Zheng et al. [10]. The authors concluded that sisal-jute fiber may be utilized as an alternative material for glass fiber reinforced polymer composites. The impact of hybridizing jute fabric with E-glass fabric and the layering order on the mechanical characteristics of woven jute-glass fiber reinforced hybrid composites were investigated by Zhang et al. [11]. The authors concluded that the composite created with E-glass fabric at extreme layers had the highest interlaminar shear strength and tensile strength. Nevertheless, the composite with a fabric stacking sequence of glass-jute-glass-jute had the highest flexural strength [12].

The focus of this present study is to determine the impact strength of the Kevlar-jute composite. The current composites environment calls for low weight, extremely strong, and stiff composites that are primarily reinforced with natural fibers due to their higher stiffness and strength relative to synthetic fibers and lower density. Kevlar's primary characteristic is its increased elongation to failure, which makes Kevlar composites more impact resistant. The capacity of jute to tolerate vibrations brought on by an external impediment is the material's key characteristic [13].

Thus, the objective of this study is to examine the mechanical characteristics of a Kevlar and jute fiber composite material. The structural behavior of the Kevlar/jute composite laminate, as well as its tensile strength, stiffness, impact resistance, and fracture toughness are assessed to check its viability as a viable engineering material.

35.2 Materials and Methods

Kevlar is an aramid polymer fiber that is both extremely strong and heat resistant as shown in Fig. 1a. Poly-paraphenyleneterepthalmide is a chemical compound with strong polyamides as its fundamental functional groups. Aramid fibers, a synthetic material primarily utilized in aerospace and military applications for ballistic-rated body armor fabric and ballistic composite products, is robust and heat-resistant. The Kevlar fiber used in this present study weighs 200 GSM (grams per square meter). The fundamental benefit of Kevlar is that it has a greater elongation to failure characteristic, which tends to make composite materials stronger.

The bast family of plant fibers includes the long, silky, and lustrous fiber known as jute. Jute is primarily used in this study as it is resistance to torsional vibrations upon impact as seen in Fig. 1b. Jute is widely accessible, and due to its advantages as a natural fiber, including its strength, stiffness, and low density, it is frequently utilized in a variety of applications. Jute is a versatile material that works well in compression molding due to its special qualities which includes low-thermal conductivity and heat insulation. Jute is organic and biodegradable, making it environmentally beneficial. Jute fibers have a reputation for being robust, coarse, and environmentally benign.

In this study, LY556 is the type of resin and HY951 is the type of hardener used. Due to its superior mechanical performance compared to most other resin types and resistance to environmental deterioration, epoxies are almost exclusively used in the aviation and marine industries. A chemical compound with the name epoxy

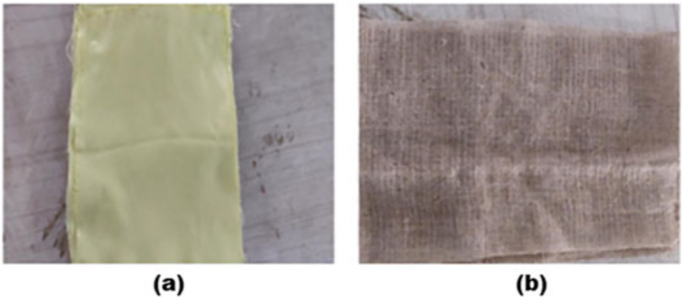

Fig. 35.1 **a** Kevlar fiber and **b** Jute fiber

refers to two previously chemically bound carbon atoms and an oxygen atom. The name 'alpha-epoxy' refers to the three-member ring structure of the simplest epoxy. The most frequent kind of hardeners used with epoxy resin that has been cured at room temperature are polyamines. These are organic molecules having two or more amine groups. All hardeners are blends of amido amines and aliphatic polyamines. The reactivity of the hydrogen atoms in amines has a major impact on the epoxy system's cure time. For every 100 parts of epoxy and hardener combined, the ratio of two materials should be followed. The combination of LY556 and HY951 results in a laminate with high water resistance and very little cure shrinkage, making the laminates of this epoxy dimensionally stable and essentially stress-free.

The fabrication is executed through vacuum infusion process for the first two plates and compression molding technique for third plate. Specimen formation is done based on the ASTM Standard. Figure 2a represents the vacuum infusion process used to manufacture composite plates. Figure 2b represents the compression molding setup used for molding the composite plates. In this study, three specimen strips of the following proportions are chosen. The Plate 1 viz., Kevlar-Kevlar-jute-jute-jute-Kevlar-Kevlar (k-k-j-j-j-k-k) of dimensions 3.0 mm thick, 60.0 mm width, and 200.0 mm in length as shown in Fig. 3a, Plate 2 viz., Kevlar-Kevlar-jute-jute-jute-jute-Kevlar-Kevlar (k-k-j-j-j-j-k-k) of dimensions 3.50 mm thick, 60.0 mm width, and 200.0 mm in length as shown in Fig. 3b, and Plate 3 viz., Kevlar-Kevlar-jute-jute-Kevlar-Kevlar (k-k-j-j-k-k) of dimensions 2.80 mm, 60.0 mm width, and 200.0 mm in length as shown in Fig. 3c is used in the present investigations.

35.3 Results and Discussion

The weight fraction is computed using Eq. (35.1).

$$W_f = \frac{Weight\ of\ fiber}{Total\ weight\ of\ composite} * 100 \tag{35.1}$$

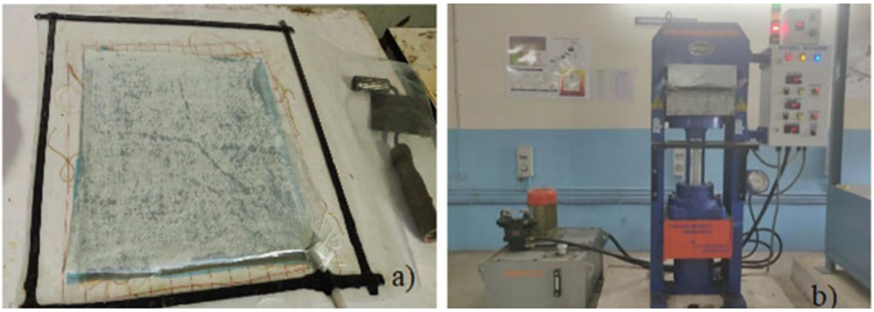

Fig. 35.2 **a** Vacuum infusion process and **b** compression molding setup

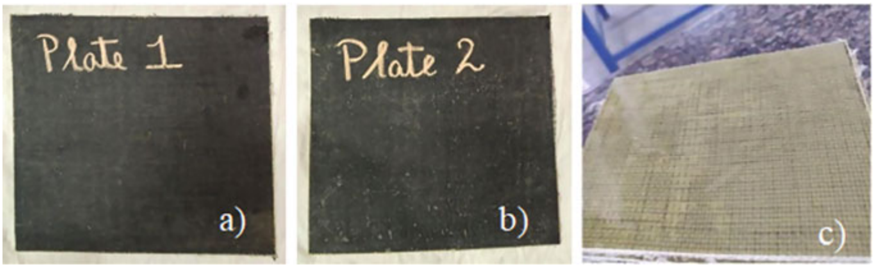

Fig. 35.3 **a** Plate 1—Kevlar-Kevlar-jute-jute-jute-Kevlar-Kevlar, **b** plate 2—Kevlar-Kevlar-jute-jute-jute-jute-Kevlar-Kevlar and **c** plate 3—Kevlar-Kevlar-jute-jute-Kevlar-Kevlar

Table 35.1 shows the values for the tensile strength and young's modulus of Kevlar, jute, and epoxy materials. Table 35.2 represents the weight fraction of composite of Plate 1 having four Kevlar and three jutes, Plate 2 with four Kevlar and four jute and Plate 3 having four Kevlar and two jutes. W_J, W_K and W_E are the weight of Jute, weight of Kevlar and weight of epoxy respectively.

The volume fraction of composite is computed using Eq. (35.2)

$$V_F = \frac{\frac{W_J}{\rho_J} + \frac{W_{CF}}{\rho_{CF}}}{\frac{W_J}{\rho_J} + \frac{W_{CF}}{\rho_{CF}} + \frac{W_E}{\rho_E}} \tag{35.2}$$

Table 35.1 Mechanical property of specimen strips

Material	Mechanical property		
	Density (g/cm^3)	Tensile strength (MPa)	Young's modulus (GPa)
Epoxy	1.3	54	3.61
Kevlar	1.47	378.78	60
Jute	1.4	59.80	30

Table 35.2 Weight fraction of composite

	Weight (N)	Weight fraction of composite			$W_J + W_K + W_E$
		W_{JUTE}	W_{KEVLAR}	W_{EPOXY}	
Plate 1	%	27	23	50	100
	Gram	96	80	176	352
Plate 2	%	30	23	47	100
	Gram	128	80	208	416
Plate 3	%	22	27	51	100
	Gram	64	80	144	288

Table 35.3 lists the volume fraction of composite materials V_E, V_K, V_J representing the volume fraction of epoxy, Kevlar, jute, and composite respectively. In the case of a two-phase composite, the modulus of elasticity for the upper limit and lower limits is estimated using the formulae as shown in Eqs. (35.3) and (35.4) respectively. Table 35.4 lists the modulus of elasticity of the composite plate 1, plate 2 and plate 3. ASTM C469 standard is followed for evaluating the modulus of elasticity.

$$E_c(u) = E_J V_J + E_K V_K + E_E V_E \tag{35.3}$$

$$E_c(L) = \frac{(E_J V_J + E_K V_K)E_E}{(V_J + V_K)E_E + V_E(E_J + E_K)} \tag{35.4}$$

Tensile strength of the composite is estimated using Eq. (35.5)

$$\sigma_C = \sigma_J V_J + \sigma_K V_K + \sigma_E V_E \tag{35.5}$$

Table 35.3 Volume fraction of composite

	Volume fraction		
	V_E	V_K	V_J
Plate 1	0.18	0.21	0.609
Plate 2	0.172	0.17	0.658
Plate 3	0.32	0.23	0.24

Table 35.4 Modulus of elasticity of the composite

Plate	Modulus of elasticity of composite in GPa	
	Upper bound, $E_C(u)$	Lower bound, $E_C(L)$
Plate 1	31.519	1.03588
Plate 2	30.560	2.51173
Plate 3	28.1552	3.1230

Table 35.5 lists the tensile strength of composites and as can be observed, Plate 3 has the highest tensile strength which may be due the stacking sequence of the plate and Plate 2 has the lowest value for tensile strength. ASTM D638 standard is referred for performing the tensile strength.

The strain of the composite is calculated using Eq. (35.6)

$$\varepsilon_C = \varepsilon_J = \varepsilon_K = \varepsilon_E \tag{35.6}$$

Table 35.5 lists the total elongation of composite and Plate 3 is higher compared to other plates. This may be due to the stacking of jute layers in the composite plate and Plate 2 has the lowest elongation which may the due the stacking sequence of Kevlar laminate in the composite plate.

The overall load on composite is computed by Eq. (35.7)

$$F_C = A_C \times \sigma_C \tag{35.7}$$

Force ratio of reinforcement and matrix is computed using Eq. (35.8)

$$\frac{F_R}{F_M} = \frac{E_R V_R}{E_M V_M} \tag{35.8}$$

Table 35.5 Tensile strength, elongation, tensile load, and strain energy of composite

		Plate 1	Plate 2	Plate 3
Tensile strength of composite	Tensile of strength epoxy, σ_E (MPa)	54	54	54
	Tensile of strength Kevlar, σ_K (MPa)	378.78	378.78	378.78
	Tensile of strength jute, σ_J (MPa)	59.80	59.80	59.80
	Total tensile strength of composite, σ_C (MPa)	125.68	112.55	130.71
Elongation of composite	Total elongation of composite	0.003987	0.003682	0.004642
Tensile load on composite	Area, A_c (mm^2)	300	350	300
	Total load, F_c (N)	37.704	39.39	39
	Load on each, F_E (N)	7.42	5.259	5.92
	Load on each, F_K (N)	11.426	13.426	17.71
	Load on each, F_J (N)	18.852	20.695	16.37
Strain energy of composite	Area, A_c (mm^2)	300	350	300
	Total load, F_c (N)	37.04	39.39	39
	Modulus of elasticity, E (GPa)	31.519	30.560	28.1552
	Strain energy, U (mJ)	2.2551	2.175	2.701

Force on each particulate can be calculated by using Eq. (35.9)

$$F_C = F_M + F_R \tag{35.9}$$

Table 35.5 lists the different values of tensile load and strain energy of the composite plates. The work done is stored as elastic strain energy ‘U’ and it is computed using Eq. (35.10)

$$U = \frac{P^2 L}{2EA} \tag{35.10}$$

As can be seen in Table 35.5, Plate 3 has favorable mechanical properties when compared to the other plates. This may be because of its k-k-j-j-k-k even number of stacking sequence, while the other two plates may have fewer mechanical properties because of their k-k-j-j-j-k-k and k-k-j-j-j-j-k-k stacking sequence in which it uses more numbers of jute laminates.

Figures 35.4, 35.5 and 35.6 depict the tensile strength, modulus of elasticity and total elongation of various composites taken up in this study. As can be seen in the Figure, combining Kevlar and jute fibers in the k-k-j-j-k-k stacking sequencing can result in higher tensile strength and modulus of elasticity. First, Kevlar fibers are recognized for their great strength and stiffness, which may considerably contribute to the composite laminate’s overall mechanical qualities. When jute fibers recognized for its toughness and impact resistance are mixed, the resulting composite material can demonstrate an equilibrium of strength and toughness, making it suited for a variety of applications. Second, the k-k-j-j-k-k stacking sequence uses alternating layers of Kevlar and jute fibers to assist disperse the load and decrease the concentration of stress in the composite laminate. Because the force is distributed uniformly throughout the material, this might result in higher tensile strength and modulus of elasticity. Third, when the qualities of the different fibers are combined, the Kevlar/Jute composite laminate can demonstrate a synergistic effect. Therefore, as these qualities are combined, it produces a composite material with better mechanical properties than each material alone.

Because of their combination of high toughness, strength, and even load distribution, the k-k-j-j-k-k stacking sequence of Kevlar and jute fibers, i.e., Plate 3, results in a composite material with greater tensile strength and modulus of elasticity.

35.4 Conclusion

Experimental investigations are carried out on the impact of stacking order on the mechanical properties of Kevlar-Jute fabric reinforced epoxy composites. Based on the investigations, the findings of this investigation are listed below.

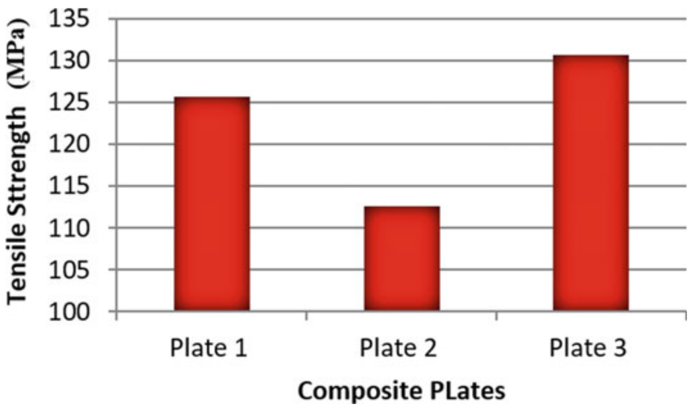

Fig. 35.4 Tensile strength for various composite plates

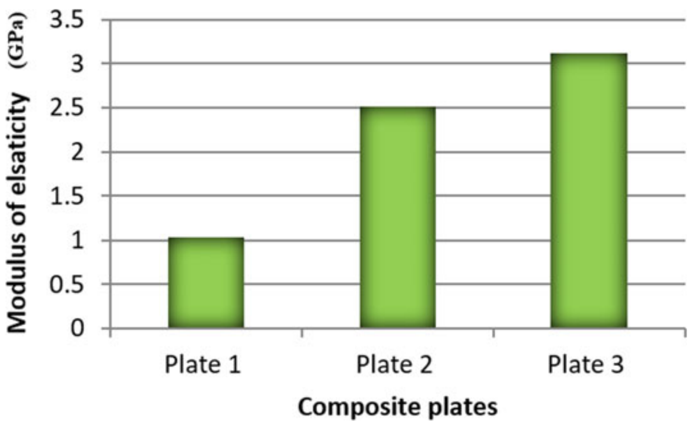

Fig. 35.5 Modulus of elasticity for various composite plates

- Characteristics of the resultant hybrid composites improve by the addition of Kevlar to jute fiber composites.
- Tensile strength is strongly impacted by the stacking sequence which modifies the location of the Kevlar ply.
- Stacking sequence has minimal impact on the tensile characteristics of Kevlar and jute fiber for the same relative weight fraction.
- Kevlar to jute ratio boosts tensile and strain energy while lowering specimen weight.
- By lowering the epoxy percentage and increasing the Kevlar percentage, the cost of the specimen is decreased.
- Composite Plate 3 tensile load is 5% higher than Plate 1 and 12% higher than Plate 2.

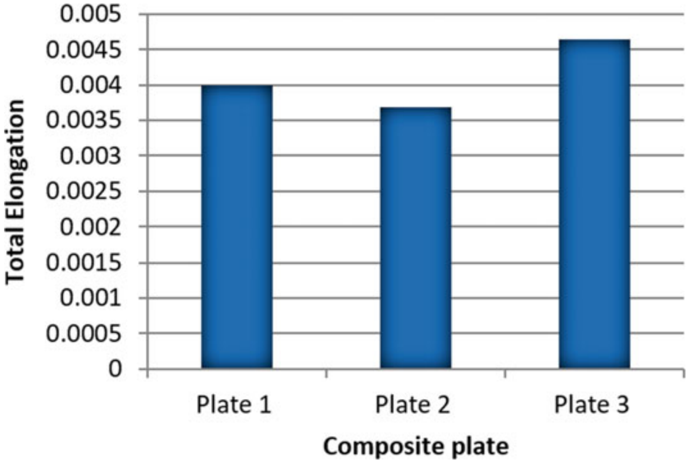

Fig. 35.6 Total elongation for various composite plates

- Composite Plate 3 had an elasticity modulus that is 63% higher than that of Plate 2 and 41% higher than that of Plate 1.
- Plate 3 strain energy is 42% higher than Plate 1 and 35% higher than Plate 2.
- Plate 3 weighs 78% less than Plate 2 and 44% less than Plate 1.

References

1. Bhanupratap, R.: Jute/Kevlar fibre reinforced epoxy composites: a dynamic mechanical study. Mater. Today Proc. **22**(4), 3145–3151 (2020)
2. Bhargav, M., Suresh Babu, V.: Experimental investigation of fiber orientation effect on mechanical and erosive wear performance of TiO_2 filled woven jute fiber based epoxy composites. Mater. Today Proc. **44**(1), 2167–2622 (2021)
3. Sangilimuthukumar, J., Thiagamani, S.M.K., Kumar, C.M., Krishnasamy, S., Arpitha, G.R., Mayakannan, S.: Erosion characteristics of epoxy-based jute, kenaf and banana fibre reinforced hybrid composites. Mater. Today Proc. **64**(1), 6–10 (2022)
4. Shaari, N., Jumahat, A.: Unhole and open hole compressive behaviours of hybrid Kevlar/glass fibre reinforced silica nanocomposite. Mater. Res. Express **5**(6), 065009 (2018)
5. Kabir, R.B., Ferdous, N.: Kevlar—the super tough fiber. Int. J. Text. Sci. **1**(6), 78–83 (2012)
6. Masoumi, M., Mansoori, H., Dastan, T., Sheikhzadeh, M.: Intralayer hybridization of triaxially braided composite lamina using carbon and basalt fibers: experimental and numerical study. Compos. Struct. **267**, 113896 (2021)
7. Swolfs, Y., Gorbatikh, L., Verpoest, I.: Fibre hybridization in polymer composite: a review. Compos. A Appl. Sci. Manuf. **67**, 181–200 (2014)
8. Zhang, J., Chaisombat, K., He, S., Wang, C.H.: Hybrid composite laminates reinforced with glass/carbon woven fabrics for lightweight load bearing structures. Mater. Des. **36**, 75–80 (2012)
9. Bandaru, A.K., Mittal, V.K., Ahmad, S., Bhatnagar, N.: Influence of hybridization on in-plane shear properties of 2D & 3D thermoplastic composites reinforced with Kevlar/basalt fabrics. Polym. Test. **61**, 396–403 (2017)

10. Zheng, Y., Sun, Y., Li, J., Limin, L., Chen, L., Liu, J., Tian, S.: Tensile response of carbon-aramid hybrid 3D braided composites. Mater. Des. **116**, 246–252 (2017)
11. Zhang, C., Binienda, W.K., Goldberg, R.K., Kohlman, L.W.: Meso-scale failure modeling of single layer triaxial braided composite using finite element method. Compos. A Appl. Sci. Manuf. **58**, 36–46 (2014)
12. Wehrkamp-Richter, T., De Carvalho, N.V., Pinho, S.T.: Predicting the non-linear mechanical response of triaxial braided composites. Compos. A Appl. Sci. Manuf. **114**, 117–135 (2018)
13. Kurşun, A., Şenel, M., Enginsoy, H.M.: Experimental and numerical analysis of low velocity impact on a preloaded composite plate. Adv. Eng. Softw. **90**, 41–52 (2015)

Chapter 36
Modelling and Simulation of Electric Vehicle-to-Load (V2L) Configuration Using MATLAB

Pulkit Kumar and Harpreet Kaur Channi

Abstract In the field of electric vehicles, connecting the entire EV market can offer users various links, such as vehicle-to-grid (V2G), vehicle-to-home (V2H), vehicle-to-building (V2B), vehicle-to-vehicle (V2V), and vehicle-to-load (V2L). The deterioration of battery storage systems used for specific areas within extra discharge modes is inevitable. Thus, this model uses MATLAB/Simulink to distribute battery energy to varied loads. The suggested model tests the battery deterioration model using a standard driving cycle and varied load structure to study battery charging and discharging cycles. The proposed solution uses electric vehicles with this circuitry to drive general house loads during long power outages, trips, and cyclone-damaged power infrastructure.

36.1 Introduction

Due to fossil fuel pollution and rising oil costs, electric automobiles have become more real than futuristic [1–3]. After so many hurdles in harnessing renewable or green energy to fulfill the natural world's rapidly expanding energy demands, a paradigm change is needed [4–8]; as per the future demand at many places, Electric vehicles can deliver energy to many locations in which it is not currently available. In the current scenario, the researchers recognized and decided to bring their efforts to make strategies and implement different technologies to achieve smart integration of Electric Vehicles with the traditional power grid [to building V2B (Vehicle to Building), one the term 'vehicle to vehicle' (V2V)], Vehicle to Grid, V2G, to home (V2H), and with lesser extent using an electric vehicle to run the desired load, i.e. Vehicle to Load (V2L) to improve the quality of the power needed to be delivered [9].

P. Kumar · H. K. Channi (✉)
Department of Electrical Engineering, Chandigarh University, SAS Nagar, Mohali, Punjab, India
e-mail: harpreetchanni@yahoo.in

P. Kumar
e-mail: pulkit10001@ieee.org

P. H. V. S. Talpa Sai et al. (eds.), *Intelligent Manufacturing and Energy Sustainability*, Smart Innovation, Systems and Technologies 372,
https://doi.org/10.1007/978-981-99-6774-2_36

Some authors have given their considerations about V2L that applications like Vehicle to Everything (V2X) can act as a clustering of different generations [10]. V2L systems can enable power transmission so Electric vehicles can be replaced with traditional Synchronous Power Generators to power the other isolated loads [11]. Many EVs can allow Vehicle to Premise Technology for E-mobile Hospitality without data or load coordination. According to research and technological advances, lithium-ion batteries will power various load sites with vehicle autonomy. SOC, temperature, C-rate, and DOD may cause V2L to deteriorate batteries prematurely. Overcharging and expiry reduce battery health (SOH) [12]. SOH The rate of deterioration might be defined by various factors such as DOD, SOC, and temperature constraints. The primary thing is the C-rate during regular usage and charge storage [13].

36.2 Literature Review

V2L issues fixed. The author suggested a Just-in-time smart grid to improve battery life, characteristics, and electric vehicle use [14]. Closed-loop battery deterioration control is rare in V2L research [15]. V2L research requires battery charging [16]. Electric cars use the author's V2L devices. These treatments cannot reduce lithium-ion battery degradation. Few articles have addressed V2G system degeneration, and no V2L systems exist. They are needed for EV grid-based virtual synchronous generators and early battery depletion. MATLAB/Simulink is used to build electric vehicle-system load power flow in this study [17]. Electric vehicles reduce fossil fuel use and carbon emissions. Electric car research. Environmental impacts of EV research. Gas cars pollute more than EVs. According to studies, EVs' environmental impact depends on many factors, including charging electricity. Lifetime EV emissions may be high. They are researching EV adoption. EV use and purchase were examined. The cost usually deters EV adoption. Charging infrastructure, range anxiety, and perceived irritation have been studied [18]. EVs with grids. Balance grids with EVs. Chargers and intelligent grids are required. Transportation evaluations concluded. Oil imports and energy security may decrease with EVs. Traffic and urban air may improve. Electric fields. EV adoption depends on pricing, charging infrastructure, and user attitudes. EV transportation effects and strategies need more study. More electric car research [19]. EVs impress academics. Power electronics, motors, and EV batteries. Another issue is chargers. Charge EVs. Economy charger. Knowledge of EVs is abundant—research EV uptake and transportation integration [20]. EVs reduce fuel and pollution. EVs reduce greenhouse gas emissions and improve air quality, attracting academics, politicians, and the public [21]. This literature review covers EV history, technology, commercialization, and environmental consequences. ICEs win. Battery technology and ecological concerns rekindled EV excitement. Performance and range EVs began with the 2008 T Roadster. Rechargeable EV batteries. Lithium-ion batteries dominate EVs [22]. EVs need public and private charging infrastructure. EV chargers pollute. Cleaner EVs. They're solar. Fossil fuels restrict EVs' environmental advantages. Government subsidies and battery and charging infrastructure have grown the EV sector. Electricity source affects EV ecological benefits. Improve EV range using sustainable energy and battery solutions [23].

36.2.1 Problem Formulation and Novelty of Work

Power electronics applications use PI and PR current controllers for current control, but they differ in handling steady-state error or system resonances. Unlike the PI controller, which regulates current based on error and integral action, the PR controller adds a resonant term to cancel resonances and achieve zero steady-state error at the resonant frequency. The specific requirements and features of the system under control determine which option is best. In our proposed work, we have used a PR current controller to remove the resonance and steady-state error occurring while using the traditional methodology of current controlling using PI current controllers (Fig. 36.1).

36.3 Methodology

In today's power networks, linear loads are the primary harmonic generation source, which can quickly deteriorate the power quality and create resonant problems in the whole system. Rectifiers and inverters are the major applications for delivering power in power electronics systems and are one of the primary reasons for power quality degradation. The overall performance of this converter circuitry can be judged based on the harmonics reference generation systems and current controlling techniques.

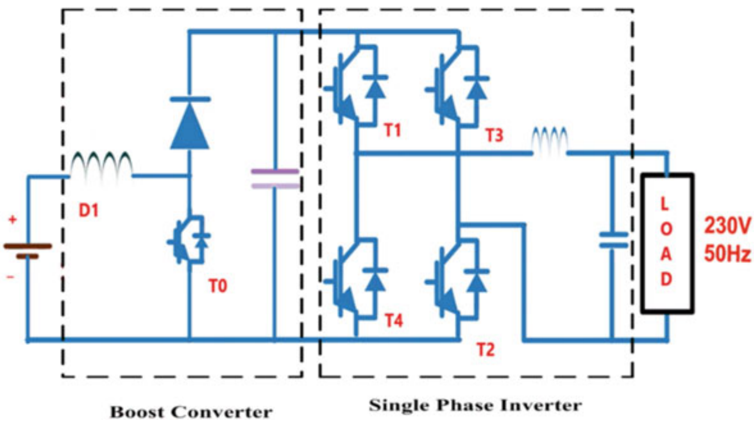

Fig. 36.1 Schematic diagram of the proposed system

For the controlling part, the conventional controller named PI (Proportional Integral) control was easily implemented; however, due to several drawbacks, they can't track the references of non-directional current values without the error. Thus Proportional Resonant converters are introduced as they have infinite gain at nearly zero steady-state error and have a better response in time domain analysis.

36.3.1 Controller Topology

The system's block diagram with a PR current controller is shown in Fig. 36.2. The three central block systems in the image are the controller, inverter, and filter blocks. The reference value of current, I_i^*, has been compared with the current taken at the output I_i after completing the process of Filtering out the ripples. The work taken out will be the following error that will serve as input for the controller. According to the illustration above, the controller PR value of $G_{Pr}(S)$ will be represented by:

$$G_{Pr}(S) = K_P + K_I \frac{S}{S^2 + W_0^2} \tag{36.1}$$

where K_P is the proportional gain term, K_I is the integral gain value, and W^0 is the resonant frequency component which will provide the infinite value of gain at the frequency of the system at a value written as W^0, which will not be coming again and again after any phase shift and gain. The value of K_P.

The term shows the system's dynamics, for instance, gain and phase margins. It was utilizing its bandwidth. Despite all, the unlimited gain is causing stability issues to arise. As a result, the proposed controlling system will be developed for less-than-ideal conditions, hence introducing the damping system [24]. It is shown in (36.2) below;

$$G_{Pr}(S) = K_P + K_I \frac{2_{wc}s}{s^2 + 2_{wc}s + W_0^2} \tag{36.2}$$

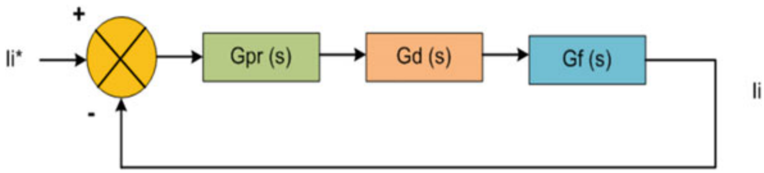

Fig. 36.2 Block diagram of PR controller based inverter system

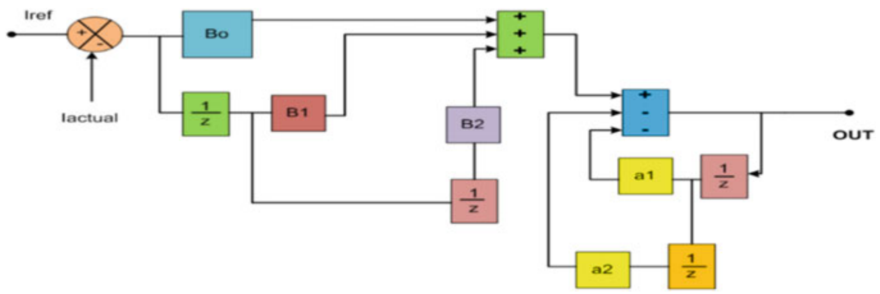

Fig. 36.3 Controller topology system's parameters

36.3.2 Proportional Integral

The control deviation of a PI controller is the discrepancy between the supplied value yd(t) and the actual output value y(t)

$$Error(t) = Y_d(t) - Y(t) \tag{36.3}$$

The law of control says that:

$$u(t) = K_p\left[Error(t) + \frac{1}{T_1}\int_0^t Error(t)dt + T_D \cdot Error(t)/dt\right] \tag{36.4}$$

the transfer function of Eq. (36.2) will be

$$\boldsymbol{G}(\boldsymbol{s}) = \frac{\boldsymbol{U}(\boldsymbol{s})}{\boldsymbol{E}(\boldsymbol{s})} = \boldsymbol{K}_{\boldsymbol{p}} \cdot \left(1 + \frac{1}{\boldsymbol{T}_{\boldsymbol{s}} \cdot \boldsymbol{s}} + \boldsymbol{T}_{\boldsymbol{D}} \cdot \boldsymbol{s}\right) \tag{36.5}$$

Here $\boldsymbol{K}_{\boldsymbol{p}}$ is the constant of proportionality, and Ts represents the time constant of integration and $\boldsymbol{T}_{\boldsymbol{D}}$ is the time constant of differential [25] (Fig. 36.3).

36.4 Proposed Methodology for Inverter Applications

The Inverter systems are the primary and essential source for power generation methods. In contrast, the number of inverter systems connected to the grid fluctuates in numbers. The three-phase Inverter controlling techniques in a study compensate for the unbalanced loads. The Proportional Resonant Controller's effectiveness has improved and has been used by many researchers in some articles. Controlling the injected harmonics within a particular range in the inverters is crucial for reducing the power supply quality's worst consequences. Due to having the superior transient response to conventional PI regulating methods subjected to load disturbances and

Table 36.1 Comparative analysis of PI and PR controller

Parameters	PI (proportional integral)	PR (proportional resonance)
Working principle	The difference between the reference current and the actual observed current serves as the basis for the PI current controller's operation	To attain zero steady-state error and eliminate steady-state oscillations brought on by system resonances
Steady-state error	The PI controller can remove the steady-state error. The integral term continuously modifies the controller output to minimize the error as it integrates the error over time	It eliminates the impact of resonances by adding the resonant term, leading to zero error in steady-state at the resonant frequency
Resonant frequency response	The PI controller does not explicitly address resonant frequency response	The PR controller is specifically designed to address resonant frequency response
Complexity and tuning	Different compensators or filters can be needed to deal with system resonances	The proportional gain, integral gain, and resonance frequency are tuned to tune the PR controller and improve system performance
Resonant peak amplification	The PI controller has no reliable methods to enhance or reduce resonant peaks	Depending on the desired control results, the PR controller can be set to either accentuate or suppress resonant peaks [27]

for achieving better performances using a harmonic compensation technique, the PR controllers, too [26] (Table 36.1).

36.5 Simulation Results

A 2 kW Vehicle to Load power flow Inverter System is designed in the proposed system. The benefit of the suggested work is that MATLAB/Simulink is used to produce the results using the PR-based Controlling technique. As a result, an EV was able to serve as both a backup power supply like an Inverter for a home during uneven power cuts and if the power is interrupted due to heavy damage of power lines due to cyclones (Table 36.2).

In the output waveforms, there is an analysis taken that as the load increases, the current requirement of the system also increases as per that Inverter Load Voltage and Inverter Current with various load profiles, i.e. 250 W to 2 kW, is studied. Figure 36.4 shows the reference value of dc voltage, i.e. 400 V, and it follows the path accordingly. In contrast, Fig. 36.5 shows the Inverter output voltage, which is perfectly regulated at 230 V. Figure 36.6 shows the load voltage profile of the inverter with different loads varying from 250 to 2000 W, as the simulation model is designed to deliver power to 2000 W of load efficiently. Whereas in Fig. 36.7, the load current profile

Table 36.2 Model specifications

Sr. No.	Parameter	Values
1	Output supply voltage	240 V AC
2	Frequency	50 Hz
3	Input inductance	20 mH
4	Output inductance	2 mH
5	Switching frequency	10 kHz
6	Battery potential	160 V
7	Output capacitor	5 uF
8	DC converter capacitor	5600 uF
9	Filtering capacitance	5.2 uF
10	Rated power	2 kW

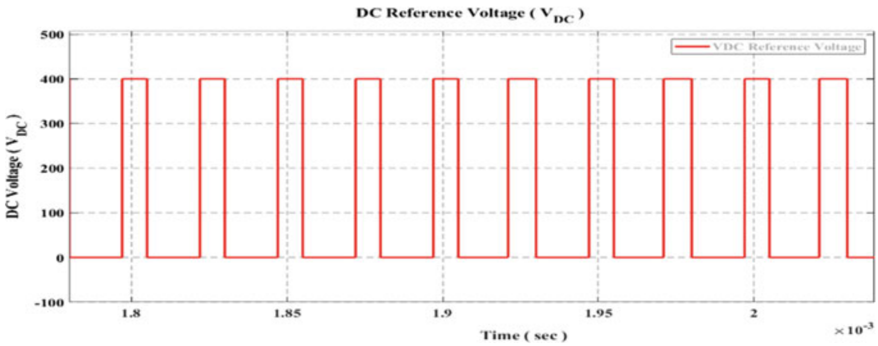

Fig. 36.4 DC reference voltage

of the different loads the different load has an additional current requirement. As the load demand increases, the system's current value requirement also increases.

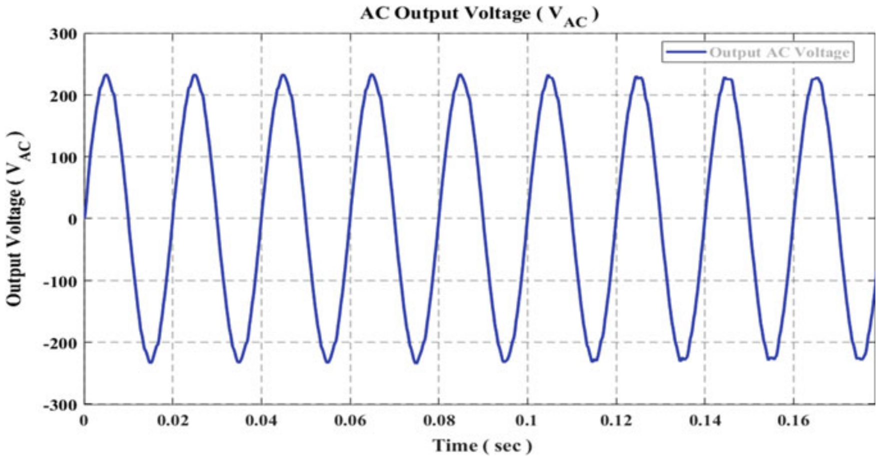

Fig. 36.5 AC output voltage

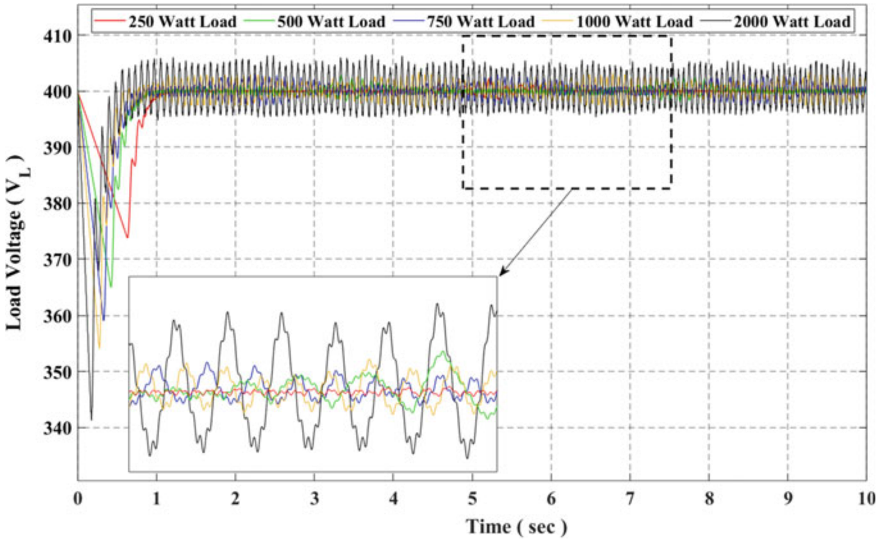

Fig. 36.6 Inverter load voltage with different load profiles

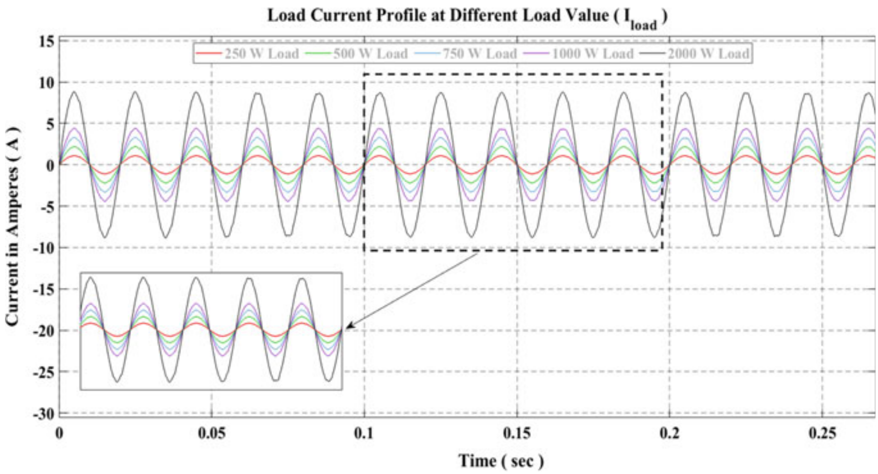

Fig. 36.7 Load current profile at different load values

36.6 Conclusion

The proposed methodology of Using the Proportional resonant controller in the replacement of traditional PI-based controllers. The main aim of using PR based controller is to reduce the fundamental error in the value of current, as well as the harmonic content in the inverter is reduced as such, the harmonics order of 3rd, 5th, and 7th are reduced to some extent, and the Total THD of the proposed system has come around 1.14%. At last, the conclusion of the work shows the advantage of using the Proportional Resonant Controller for Inverter System Applications in Vehicle To Load energy power flow.

References

1. Austin, M., Lefevre, R.: In the new energy revolution, electrical vehicles become reality. IEEE Transp. Electrif. eNewslett. **9** (2013)
2. Boulanger, A.G., Chu, A.C., Maxx, S., Waltz, D.L.: Vehicle electrification: status and issues. Proc. IEEE **99**(6), 1116–1138 (2011)
3. Machura, P., Li, Q.: A critical review on wireless charging for electric vehicles. Renew. Sustain. Energy Rev. **104**, 209–234 (2019)
4. Choi, W., Lee, W., Sarlioglu, B.: Reactive power compensation of grid-connected inverter in vehicle-to-grid application to mitigate balanced grid voltage sag. In: Proceedings of the 2016 IEEE Power and Energy Society General Meeting, PESGM 2016, pp. 1–5. IEEE (2016)
5. Rahman, M.A., Islam, M.R.: Diferent control schemes of entire microgrid: a brief overview. In: Proceedings of the 3rd International Conference on Electrical Engineering and Information Communication Technology (ICEEICT), pp. 1–6. IEEE (2016)

6. Noorul Ameen, A., Suresh, S.: Design of bi-directional power converter for vehicle-to-grid capability of reactive power compensation. In: Proceedings of the 2nd International Conference on Trends in Electronics and Informatics (ICOEI), pp. 1336–1340. IEEE (2018)
7. Tian, Z., Tu, L., Tian, C., Wang, Y., Zhang, F.: Understanding battery degradation phenomenon in real-life electric vehicle use based on big data. In: Proceedings of the 3rd International Conference on Big Data Computing and Communications (BIGCOM), pp. 334–339. IEEE (2017)
8. Ansean, D., Garcia, V.M., Gonzalez, M., et al.: Lithium-ion battery degradation indicators via incremental capacity analysis. IEEE Trans. Ind. Appl. (2019)
9. Tompson, A.W.: Economic implications of lithium ion battery degradation for Vehicle-to-Grid (V2X) services. J. Power. Sources **396**, 691–709 (2018)
10. Ahmadian, A., Sedghi, M., Elkamel, A., Fowler, M., Aliakbar Golkar, M.: Plug-in electric vehicle batteries degradation modeling for smart grid studies: review, assessment and conceptual framework. Renew. Sustain. Energy Rev. **81**, 2609–2624 (2018)
11. Rechkemmer, S.K., Zang, X., Zhang, W., Sawodny, O.: Empirical Li-ion aging model derived from single particle model. J. Energy Storage **21**, 773–786 (2019)
12. Tang, X., Wang, Y., Zou, C., Yao, K., Xia, Y., Gao, F.: A novel framework for Lithium-ion battery modeling considering uncertainties of temperature and aging. Energy Convers. Manag. **180**, 162–170 (2019)
13. Balasundaram, M., Ramar, V., Yap, C., Li, L., Tay, A.A.O.: Palani Balaya Heat loss distribution: impedance and thermal loss analyses in $LiFePO_4$/graphite 18650 electrochemical cell. J. Power. Sources **328**, 413–421 (2016)
14. Zhang, J., Yan, J., Liu, Y., Zhang, H., Lv, G.: Daily electric vehicle charging load profiles considering demographics of vehicle users. Appl. Energy **274**, 115063 (2020)
15. Zhu, J., Yang, Z., Mourshed, M., Guo, Y., Zhou, Y., Chang, Y., Wei, Y., Feng, S.: Electric vehicle charging load forecasting: a comparative study of deep learning approaches. Energies **12**(14), 2692 (2019)
16. Rahman, S., Khan, I.A., Khan, A.A., Mallik, A., Nadeem, M.F.: Comprehensive review & impact analysis of integrating projected electric vehicle charging load to the existing low voltage distribution system. Renew. Sustain. Energy Rev. **153**, 111756 (2022)
17. Yi, T., Zhang, C., Lin, T., Liu, J.: Research on the spatial-temporal distribution of electric vehicle charging load demand: a case study in China. J. Clean. Prod. **242**, 118457 (2020)
18. Amara-Ouali, Y., Goude, Y., Massart, P., Poggi, J.M., Yan, H.: A review of electric vehicle load open data and models. Energies **14**(8), 2233 (2021)
19. Zhang, X., Chan, K.W., Li, H., Wang, H., Qiu, J., Wang, G.: Deep-learning-based probabilistic forecasting of electric vehicle charging load with a novel queuing model. IEEE Trans. Cybern. **51**(6), 3157–3170 (2021)
20. Zheng, Y., Shao, Z., Zhang, Y., Jian, L.: A systematic methodology for mid-and-long term electric vehicle charging load forecasting: the case study of Shenzhen, China. Sustain. Cities Soc. **56**, 102084 (2020)
21. Zhang, X., Chan, K.W., Li, H., Wang, H., Qiu, J., Wang, G.: Deep-learning-based probabilistic forecasting of electric vehicle charging load with a novel queuing model. IEEE Trans. Cybern. **51**(6), 3157–3170 (2020)
22. Arya, Y.: Effect of electric vehicles on load frequency control in interconnected thermal and hydrothermal power systems utilizing CF-FOIDF controller. IET Gener. Transm. Distrib. **14**(14), 2666–2675 (2020)
23. Wang, H., Nagayama, T.: Response spectrum model of vehicle dynamic load for the prediction of bridge vibration level due to single vehicle-passage. Eng. Struct. **260**, 114180 (2022)
24. Le Floch, C., Belletti, F., Moura, S.: Optimal charging of electric vehicles for load shaping: a dual-splitting framework with explicit convergence bounds. IEEE Trans. Transp. Electrif. **2**(2), 190–199 (2016)
25. Swief, R.A., El-Amary, N.H., Kamh, M.Z.: Optimal energy management integrating plug in hybrid vehicle under load and renewable uncertainties. IEEE Access **8**, 176895–176904 (2020)

26. Li, C., Zhao, R., Wang, D., Cai, W., Yu, C., Gu, Y., Zhang, Q.: Optimal spatio-temporal scheduling for electric vehicles and load aggregators considering response reliability. Electr. Power Syst. Res. **162**, 183–193 (2018)
27. Zahedmanesh, A., Muttaqi, K.M., Sutanto, D.: Direct control of plug-in electric vehicle charging load using an in-house developed intermediate control unit. IEEE Trans. Ind. Appl. **55**(3), 2208–2218 (2019)

Chapter 37
Modelling, Simulation and Analysis of a High-Speed Wing of the UAV

Abinaya Balaji, L. Sankaralingam, P. Saravanan, K. Saranya, S. Seralathan, and S. Sathish

Abstract This paper investigates a high-speed experimental wing for an unmanned aerial vehicle (UAV) using software like CATIA, HYPERMESH, and NASTRAN. The analysis includes modal, static structural, and buckling analysis using NASTRAN. The wing of UAV is made of Glass fiber reinforced polymer (GFRP) composite. The result from this study meets the standard allowable parameters for stress, strain, displacement, failure index and buckling factor during 2g maneuver at a velocity of 120 m/s. The modal analysis results showed that the connections are perfect and there are no free components. The linear static structural analysis gave the values which are within the allowable limits. The failure index is found to be 0.16 and the buckling factor is 1.267 which indicates that the structure is resistant to buckling.

37.1 Introduction

UAVs or drones are used in a variety of applications including military, construction, medical, parcel delivery, search and rescue, wireless communication, and aerial surveillance. Its usage is increasing due to advancements in technology like the internet of things (IoT), 5G, and B5G. In the defense sector, UAVs play a crucial role in surveillance missions, and they are included in the defense strategies of several nations. UAVs are affordable, dependable, and multifunctional. Earlier, the literature reviews highlighted the importance of modal, static structural, and buckling analysis in determining the structural stability of the UAV [1, 2]. The UAV chosen in this study is a target drone designed using software CATIA and Altair HYPERMESH for FEM modeling and stability analysis [3]. The wing's primary components are

A. Balaji · L. Sankaralingam · P. Saravanan · S. Seralathan (✉) · S. Sathish
Department of Aeronautical Engineering, Hindustan Institute of Technology and Science, Chennai, Tamilnadu 603103, India
e-mail: siva.seralathan@gmail.com

K. Saranya
Department of Physics, Government College of Engineering, Thanjavur, Tamilnadu 613001, India

P. H. V. S. Talpa Sai et al. (eds.), *Intelligent Manufacturing and Energy Sustainability*, Smart Innovation, Systems and Technologies 372,
https://doi.org/10.1007/978-981-99-6774-2_37

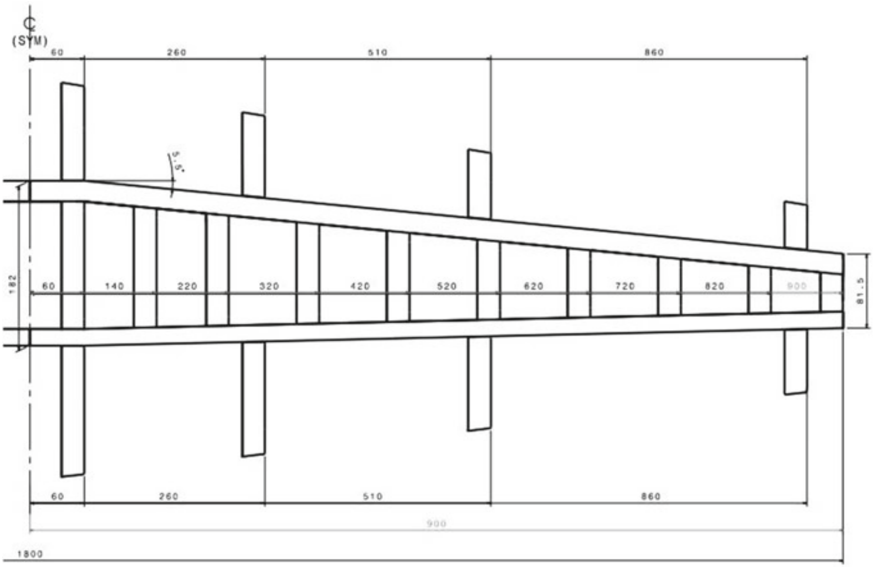

Fig. 37.1 Location of spars and ribs in the wing

spars, ribs, and skin, with spars serving as the principal structural member [4]. The skin of the UAV design modeled here is made up of a composite material [5]. It is a semi-monocoque construction. The location of spars and ribs of the wing model is shown in Fig. 37.1. The wing design is taken from the previous design models of UAVs like DRDO ABHYAS and DRDO LAKSHYA. The numbers of ribs are calculated by upsizing the number of ribs present in the previous model of DRDO ABHYAS and Table 37.1 lists the wing design specifications.

Table 37.1 Wing design specifications

Wingspan (b)	1800 mm
Wing semi-span	900 mm
Root chord length	500 mm
Tip chord length	220 mm
Airfoil	NACA 64 A 008
Taper ratio	0.40
Weight of the wing	5 kg
Aspect ratio (AR)	5
Wing plan form area (S)	0.648 m^2

The objective of the present study is to conduct FEA analysis namely, Modal analysis, Linear static structural analysis and Buckling analysis on the designed wing of the UAV during 2g maneuver at a velocity of 120 m/s.

37.2 Geometric Modelling of the Wing

Geometric modelling of wing design is an iterative process that involves calculating the number of internal components such as ribs and spars, which is based on the results obtained from the FEA [6–8]. In this design, four iterations of geometric design are done using the CATIA software, which includes part design, assembly, and wire frame and surface design modules [7, 9]. The wing profile is generated from the NACA 64 A 008 airfoil. The wing profile is shown Fig. 37.2. The number of spars used in this wing are two i.e., a multi-spar construction. The material assigned for the spars is a composite material. The thickness of the front spar is taken as 1.75 mm and the thickness of the rear spar is taken as 1.50 mm. The numbers of ribs modeled are 36 and it is classified into leading edge or front ribs, central or mid ribs and trailing edge or rear ribs.

All the ribs are made up of composite material and the thickness of the ribs are taken as 1.25 mm. Table 37.2 lists the type and number of ribs used for this construction.

Figure 37.3 shows the leading-edge rib and trailing edge rib and mid rib. The skin designed follows a semi-monocoque construction. The material given for the skin is a composite material and the skin thickness is taken as 2 mm overall except the parts covering ribs where it is maintained as 1.50 mm. Figure 37.4 depicts the skeleton of the wing.

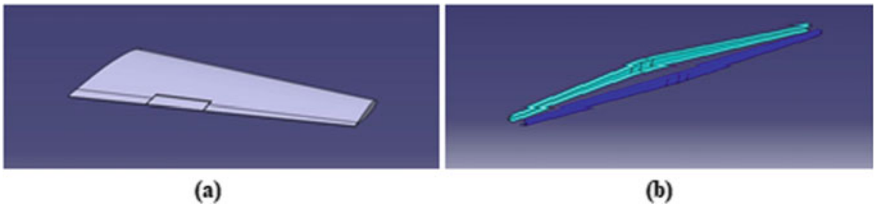

Fig. 37.2 **a** Wing profile generated from the aero foil. **b** Front and rear 'C' section spars

Table 37.2 Types and number of ribs

Type of ribs	No. of ribs
Leading edge ribs	8
Mid ribs	20
Trailing edge ribs	8

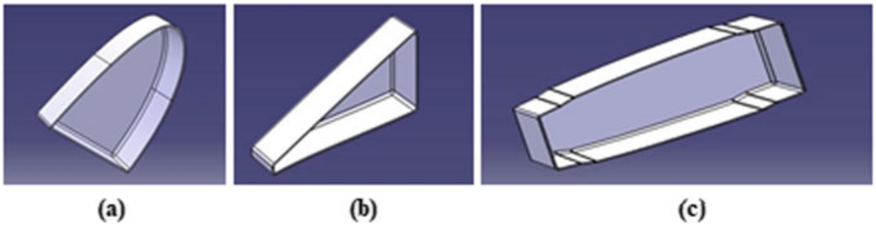

Fig. 37.3 **a** Leading edge rib. **b** Trailing edge rib. **c** Mid rib

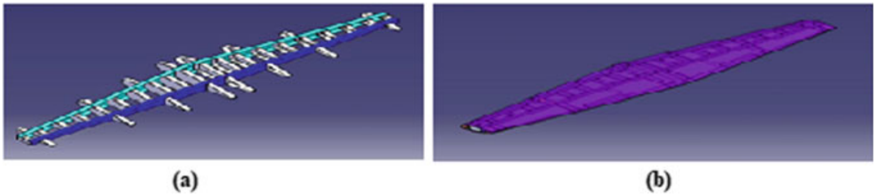

Fig. 37.4 **a** Skeleton of the wing. **b** Complete geometric model of the wing

37.3 Finite Element Modelling of the Wing

Finite element method (FEM) and finite element analysis (FEA) are highly effective techniques in engineering applications. FEM is a numerical method used to address engineering issues, making it easy to handle complicated geometry, material qualities, boundary, and load conditions. FEA is a powerful design tool to analyze different design situations and determine the best design using parametric design studies. The FEM's numerical analytical technique is suitable for a wide range of engineering issues and is developed in the aerospace sector to investigate the stress on aircraft structures. It subsequently developed into the matrix analysis approach utilized in airplane design, and many organizations created FEA algorithms for various applications after the development of underlying theory and principles.

Finite element modelling of the wing design in this study is done using Altair HYPERWORKS software. The CAD model of the wing is imported into HYPERMESH and meshed using CQUAD4 and CTRIA3 surface elements, with attention given to mesh quality metrics such as skewness, Jacobian, warpage, and aspect ratio. Material properties are assigned to each component and connections between skin, spar and ribs are modeled using CBUSH connections at the bolt attachment points. Figure 37.5 shows the FEM model of the wing without skin.

The wing material is chosen as GFRP (Glass Fiber Reinforced Polymer) composite. Several materials, including aluminum alloy, titanium alloy, and various types of composites with different lay-up orientations and thickness combinations are evaluated with the objective to identify the best combination of qualities to achieve optimal strength and stiffness while minimizing the weight and cost. Based on this, GFRP is determined to be the most suitable material for this wing, as it exhibited

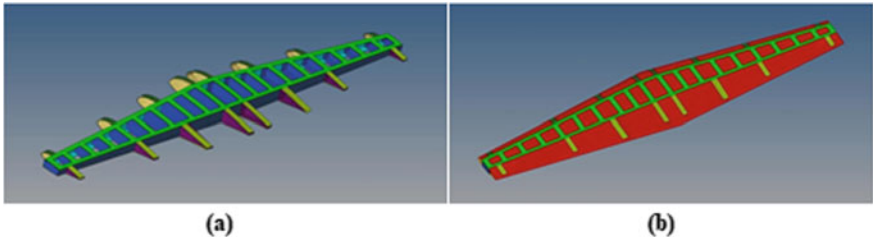

Fig. 37.5 **a** FEM model of the wing without skin (isometric view). **b** Complete FEM model of the wing (top skin-isometric view)

excellent characteristics for the present application. All the three primary components of the wing, namely the spars, ribs, and skin, are made of Glass fabric S2/34 300 GSM (GFRP). Table 37.3 provides detailed information on the material properties of this GFRP. Loads on the wing design are calculated using aerodynamic forces, vehicle inertia, control system actuators, and armaments. Initially, the UAV is assumed to be rigid to calculate the effects of aerodynamic forces. Based on the previous model tests, load interpolation principles are determined. Loads are interpolated for the wing based on the loads given to the reference UAV, DRDO ABHYAS. The investigations are carried out using NASTRAN software.

Table 37.3 Stacking sequence assigned and material properties assigned

Stacking sequence		
Component	Sequence followed	No. of plies
Front spar	45/0/0/45/0/0/45	7
Rear spar	45/0/0/45/0/0/45	7
Leading edge ribs	45/0/0/45	4
Centre ribs	45/0/0/45	4
Trailing edge ribs	45/0/0/45	4
Top skin	45/0/0/45	4
Bottom skin	45/0/0/45/0/45	0
Leading edge interface	45/0/45/45/0/45	6
Trailing edge interface	45/0/45/45/0/45	6
Material properties		
E1	18,000 MPa	
E2	18,000 MPa	
NU12	0.2	
G12	2750 MPa	
G1Z	2750 MPa	
G2Z	2750 MPa	
RHO	2^{e-6}	

Shear force and torque are given at the quarter chord point of the wing, and a total of 140 single point loads (viz., 70 on each side) are assigned. The aerodynamic data used is based on the vortex lattice method, and the air load for the wing during 2g maneuver at a velocity of 120 m/s is considered.

37.4 Results and Discussion

Three types of analysis are carried out for this wing namely, Modal analysis, Linear static structural analysis and Buckling analysis.

37.4.1 Modal Analysis

Modal analysis is a prerequisite for linear static structural analysis. There are two primary reasons for conducting a modal analysis. One is to check the connections between the elements and next is to find the natural frequency of each mode and to get the mode shapes. When a FREE run is given i.e., without any constraints, the first six degree of freedoms will be the standard—three translational and three rotational motions (U_x, U_y, U_z, θ_x, θ_y, θ_z) where there won't be any natural frequencies and the mode shapes. From the seventh mode, mode shapes will be obtained. When FORCED run is given viz., constraints at certain points, the mode shapes will be appearing from the first mode itself. In this study, a FORCED run is given as the wing will be connected at the fuselage and the single point constraints (SPCs) are given at the four points of the part of the wing where it will be connected to the fuselage. The total number of modes shapes computed are 15. The type of first four mode shapes are symmetrical bending mode with 51.0 Hz, local mode with 68.8 Hz, global mode with 106.4 Hz, and local mode with 125.9 Hz.

Figure 37.6 shows the mode shape 1. As can be seen in the Figure, Mode 1 shows a pure symmetrical bending. The frequency with which it happens is 51.90 Hz. The wing is bent upwards at the tips towards 'Z' direction depicting a maximum displacement of 34 mm. Mode 2 shows a local mode. The frequency with which the wing is deforming at the center towards 'Z' direction with a displacement of 15 mm. Figure 37.7 shows the mode shape 3 which is a global mode. The frequency with which it is happening is 106.4 Hz. The wing is deforming at the center towards 'Z' direction with a displacement of 28 mm. Mode 4 shows a local mode and the frequency with which it happens is 125.9 Hz. The wing is deforming at the trailing edge part of the wing towards the root in 'Z' direction with maximum displacement of 224 mm.

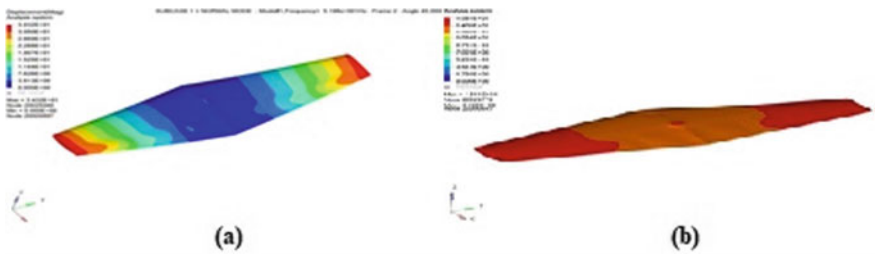

Fig. 37.6 Mode shape 1—symmetrical bending mode, mode shape 2—local mode

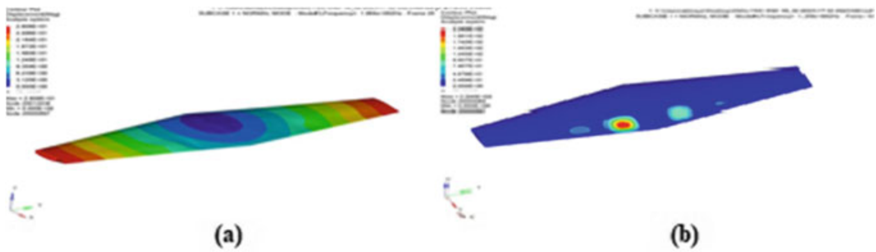

Fig. 37.7 Mode shape 3—global mode, mode shape 4—local mode

37.4.2 Linear Static Structural Analysis

Linear static structural analysis is performed to determine the structural tendency of a three-dimensional wing without time mobility. This type of analysis is useful for analyzing the wing quickly as it does not rely on time motion. The relationship between applied forces and displacements is linear in this type of analysis, which is applicable to structural issues where stresses remain within the material's linear elastic range. The stiffness matrix of the model is constant, and solving time is relatively quick compared to a nonlinear analysis. Therefore, a linear static analysis is often used as an initial estimate before performing a complete nonlinear analysis. From linear static structural analysis, the following results have been obtained.

Displacement Contour Plot. When deformation comes to picture, few results can be expected from both static structural as well as modal analysis. Spars are the parts of the wing that are most heavily loaded and sustain tremendous stresses which causes the wing to twist and curl while ribs prevent the wing from buckling. Figure 37.8a illustrates the entire extreme distortion occurring at the wing tip while only minor deformation is developed at the root. The maximum total deformation observed is 5.40 mm.

Stress in 'X' (tensile) direction and stress in 'X' (compressive) direction. As can be seen in Fig. 37.8b, the tensile stress in the composite laminate placed in the 'X'

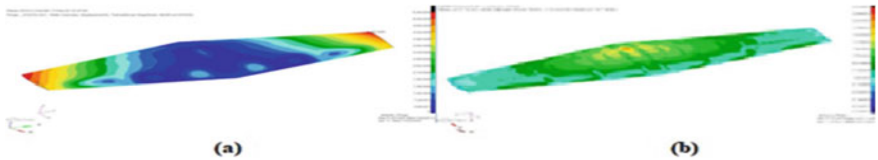

Fig. 37.8 **a** Total displacement. **b** Stress in 'X' (tensile) direction

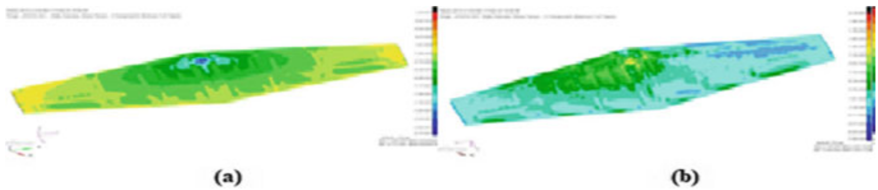

Fig. 37.9 **a** Stress in 'X' (compression) direction. **b** Stress in 'Y' (tensile) direction

direction is 25.1 MPa. Similarly, the compressive stress in the composite laminate placed in 'X' direction is 27.70 MPa (refer Fig. 9a).

Stress in 'Y' (tensile) direction and stress in 'Y' (compressive) direction. Tensile stress in the composite laminate placed in 'Y' direction is 21.40 MPa (refer Fig. 9b). The results of the compressive stress in the composite laminate placed in 'Y' direction is 23.5 MPa as shown in Fig. 37.10a.

Stress in 'XY' (tensile) direction and strain in 'X' (tensile) direction. The stresses acting in the composite in 'XY' direction is 7.17 MPa as shown in Fig. 10b. The tensile strain in the composite laminate placed in 'X' direction as shown in Fig. 37.11a is 1460 μƐ.

Strain in 'X' (compressive) direction. Figure 37.11b illustrates the compressive strain in the composite laminate placed in 'X' direction as 1570 μƐ.

Strain in 'Y' (tensile) and Strain in 'Y' (compressive) directions. Figure 37.12 shows the tensile strain in the composite laminate placed in 'Y' direction as 1380 μƐ, whereas the compressive strain in the composite laminate placed in 'Y' direction is 1450 μƐ.

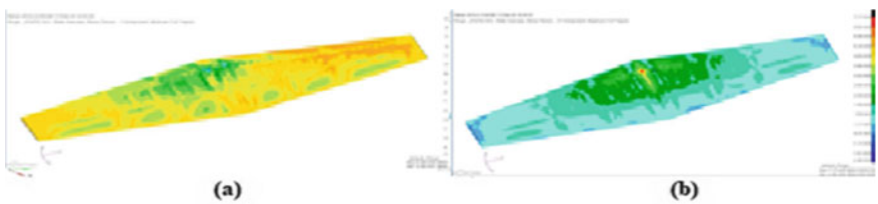

Fig. 37.10 **a** Stress in 'Y' (compression) direction. **b** Stress in XY (tensile) direction

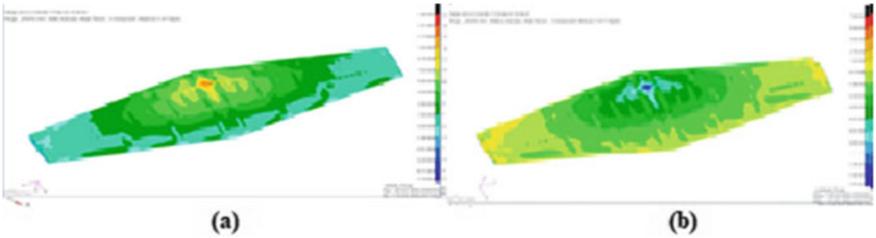

Fig. 37.11 **a** Strain in 'x' (tensile) direction. **b** Strain in x (compression) direction

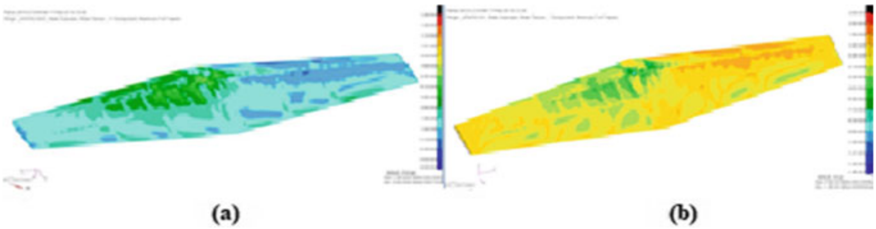

Fig. 37.12 **a** Strain 'Y' (tensile) direction. **b** Strain in 'Y' (compression) direction

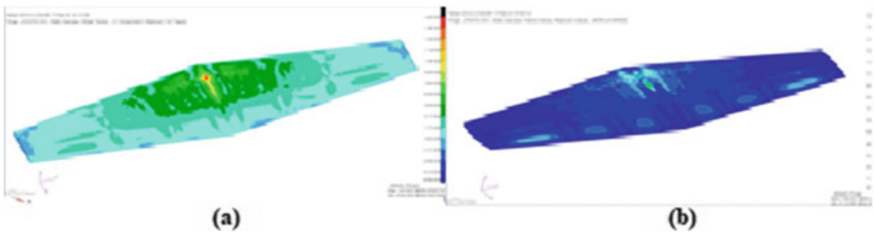

Fig. 37.13 **a** Strain in 'XY' direction. **b** Failure index

Strain in 'XY' direction. As can be seen in Fig. 37.13a, the strain acting in the composite in 'XY' direction is 1630 $\mu\varepsilon$.

Failure Index. The composite failure index contour is shown in Fig. 37.13b. UAVs wing composite laminates do not fail with respect to Tsai Wu theory and the failure index is observed as 0.16.

37.4.3 Buckling Analysis

Buckling analysis is used to estimate the critical buckling load of the structures. Generally, a linear type of analysis is followed. The analysis can be carried out either before or after the structure has been preloaded as the initial stage of a comprehensive study of an unloaded structure. In most cases, buckling is employed to calculate the critical buckling loads of rigid structures. Buckling factor plays a very vital role in buckling analysis. Based on the buckling factor, only the results will be predicted. The buckling load factor is the ratio of the buckling loads to the applied loads. The buckling factor obtained from the buckling analysis is 1.26. Figure 37.14 depicts the buckling factor and the area at which it is subjected to buckling the most.

In the modal analysis, the results showed that the connections are perfect and there are no free components. The linear static structural analysis gave the values which are within the allowable limits and the standard values of GFRP composite is given in Table 37.4 based on a coupon test. This clearly indicates that the structure is safe. The buckling analysis gives the buckling factor as 1.2627 which indicates that the structure is resistant to buckling as the structure buckles only at 126 times the load.

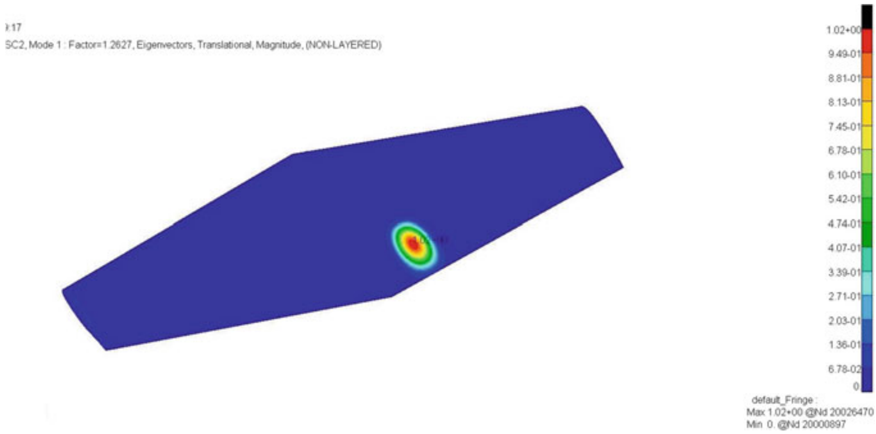

Fig. 37.14 Buckling factor

Table 37.4 Allowable of a bi-directional GFRP composite

Tensile stress (X_t)	101 MPa
Compressive stress (X_c)	150 MPa
Tensile stress (Y_t)	101 MPa
Compressive stress (Y_c)	150 MPa
Shear stress (XY)	25 MPa
Tensile strain ($\mu\varepsilon$)	5000 MPa
Compressive strain ($\mu\varepsilon$)	6000 MPa
Shear strain ($\mu\varepsilon$)	20,000 MPa

37.5 Conclusion

Modal analysis, Linear static structural analysis and Buckling analysis are performed on the designed wing of the UAV during 2g maneuver at a velocity of 120 m/s. Based on the investigations, it is observed that the structure is meeting all the design criteria. The values obtained like stress, strain, buckling factor and failure index are within the range of the respective ultimate values and allowable limits. Moreover, the wing composite laminates do not fail with respect to Tsai Wu theory and the failure index is found to be 0.16. Buckling analysis gives the buckling factor as 1.267 indicating that the structure is resistant to buckling.

References

1. Wang, B.H., Wang, D.B., Ali, Z.A., Ting Ting, B., Wang, H.: An overview of various kinds of wind effects on unmanned aerial vehicle. Meas. Control **52**(7–8), 731–739 (2019)
2. Balmer, G.R.: Modelling and Control of a Fixed-wing UAV for Landings on Mobile Landing Platforms. Degree Project in Systems Engineering, KTH Royal Institute of Technology, Stockholm, Sweden (2015)
3. Priyambodo, T.K., Majid, A.: Modeling and simulation of the UX-6 fixed-wing unmanned aerial vehicle. J. Control Autom. Electr. Syst. **32**, 1344–1355 (2021)
4. Panagiotou, P., Giannakis, E., Savaidis, G., Yakinthos, K.: Aerodynamic and structural design for the development of a MALE UAV. Aircr. Eng. Aerosp. Technol. **90**(7), 1077–1087 (2019)
5. Panagiotou, P., Fotiadis-Karras, S., Yakinthos, K.: Conceptual design of a blended wing body MALE UAV. Aerosp. Sci. Technol. **73**, 32–47 (2018)
6. Escobar-Ruiz, A.G., Lopez-Botello, O., Reyes-Osorio, L., Zambrano-Robledo, P., Amezquita-Brooks, L., Garcia-Salazar, O.: Conceptual design of an unmanned fixed-wing aerial vehicle based on alternative energy. Int. J. Aerosp. Eng. **2019**, Article ID 8104927 (2019)
7. Panagiotou, P., Kaparos, P., Salpingidou, C., Yakinthos, K.: Aerodynamic design of a MALE UAV. Aerosp. Sci. Technol. **50**, 127–138 (2016)
8. Hussain Vali, R., Marouf Wani, M.: Optimal utilization of ZnO nanoparticles blended diesel-water emulsion by varying compression ratio of a VCR diesel engine. J. Environ. Chem. Eng. **8**(4), 103884 (2020)
9. Panagiotou, P., Kaparos, P., Yakinthos, K.: Winglet design and optimization for a MALE UAV using CFD. Aerosp. Sci. Technol. **39**, 190–205 (2014)

Chapter 38
Net Zero Energy Building: A Case Study of Jaisalmer

Bhavana Kushwah and Harpreet Kaur Channi

Abstract Due to the increased concentration of greenhouse gases, our ecosystem faces severe global warming and climate change challenges. Conventional energy resources have been incredibly exhausted in developing and maintaining the infrastructure for housing and industries over the past few decades. To meet the continuous demand of the energy sector, it is now crucial to explore the possibilities of renewable energy sources and sustainable infrastructures. Making buildings with net zero demand is one such goal. Net zero energy buildings (NZEBs) can meet their energy demands. NZEBs are a necessity within the context of growing urbanization in India. Technological advantages in solar energy, geothermal heating, and wind turbines can achieve net zero energy status. In the present paper, we are reviewing the NZEB's facts about their implementation and sustainability in the country. We are carefully examining one of the NZEBs, named Rajkumari Ratnavati School in Jaisalmer, as a case study from multiple NZEB standards perspectives. The present study attempts to cover the essential aspects of NZEBs with examples like Rajkumari Ratnavati School.

38.1 Introduction

Zero-energy buildings generate more energy than they need. Zero-energy structures create energy. This means you can utilize the building's electricity for nothing and reduce your electricity costs. It is not surprising that the Earth's resources are swiftly running out while the planet experiences climate change, given the toll that global pollution has on the environment [1]. During additional energy production, the amount of Greenhouse gases starts increasing drastically and harms the environment. Globally buildings account for 33% of Greenhouse gas emissions. Adequate light air, hot water availability, and air conditioning conditions are necessary for comfortable

B. Kushwah · H. K. Channi (✉)
Department of Electrical Engineering, Chandigarh University, Mohali, Punjab 140413, India
e-mail: harpreet.ee@cumail.in

P. H. V. S. Talpa Sai et al. (eds.), *Intelligent Manufacturing and Energy Sustainability*, Smart Innovation, Systems and Technologies 372,
https://doi.org/10.1007/978-981-99-6774-2_38

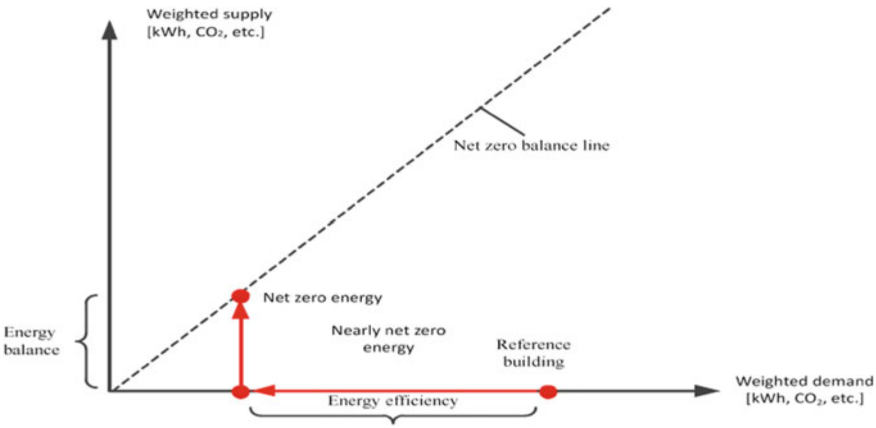

Fig. 38.1 Graph representing the path towards a Net Zero Energy Building (Net NZEB), with the nearly and variants [4]

conditions in any building, but the demand for additional energy increases due to these facilities [2].

The green building council of India, the global green build council, and USAID created a NZEB green grading system. NZB in India aspires to cut net energy usage by 40–50% and emissions by 30% relative to the national average. Near-zero energy buildings create almost as much energy as they need. Its utility influences each building's energy needs. According to their intended use, buildings fall into one of three groups. They are:

- Commercial
- Public
- Residential.

According to the following reasoning, this is unique due to its grid link. In places where just connecting to a grid is impractical, buildings are often not fed to the network, as seen in Fig. 38.1. These ZEBs are categorized as autonomous or independent ZEBs [3]. On the opposite hand, the three categories into which ZEBs that connect to the grid are divided are as follows.

38.1.1 Net Plus or Positive Energy Building

Positive Energy Excellent buildings have favourable energy balances. The structure produces less energy than it consumes, and any surplus is fed back into the grid.

38.1.2 Nearly Zero Energy Building (nZEB)

"Nearly zero energy building" refers to a ZEB with nearly zero energy balance that is connected to the grid (nZEB). It can be concluded from this that the energy generated slightly outweighs the energy used.

38.1.3 Net Zero Energy Building (NZEB)

"Net Zero Energy Building" is the term used to describe a ZEB with zero energy balance (NZEB). Energy is equally produced and consumed in that scenario [4].

The current words could be retained and incorporated into a quantifiable scale or gradually phased out.

- Zero energy $\approx$ 100% energy efficient
- Nearly zero $\approx$ 90% or higher
- Plus, fuel $\approx$ over 100%.

38.2 Literature Review

ZEB was introduced by Paul Torcellini, Shanti Pless, and Michael Deru et al. (2006). Whether energy changing and transformation accounting are acceptable to fulfil a ZEB objective and examine the pros and cons of four well-known definitions: net-zero sites energy, source energy, energy costs, and emissions. This study demonstrates the ZEB definition's significant definitional differences and design implications [5]. Peter O. Akadiri et al. (2012) discussed a theoretical foundation for applying sustainable concepts in the construction industry was produced. The approach being given contains elements of human evolution, cost benefits, and resource conservation. In the literature, each principle includes techniques and procedures [6]. Amir Hosein Ghaffarian Hoseini et al. (2013) analyzed the order to produce eco-cities that are more effective and environmentally friendly; this article examined the significant developments in intelligent building design. This study also focuses on actual and practical implementations of designing structures with zero energy consumption. Reviewing new theories, approaches, performances, and obstacles in creating zero-energy intelligent buildings (ZEIB) is particularly emphasized [7]. Elena Petrova et al. (2014) discussed the aim of creating structures that use zero energy or almost zero, which will be built on Polytechnic University's campus. The project's innovation is an integrated approach to the dwelling design independent of urban networks [8].

Eleni S. Vergini et al. (2015) proposed the ZEB concept and described a way to simulate its operation, classify ZEBs, and define the factor. ZEB's successful operation depends on power management and intelligent control, which enhance its functionality and lower its usage. For issues with many parameters, where quantitative analysis and calculations have a challenging or occasionally impossible solution, the fuzzy cognition maps (FCMs) method is applicable [9]. Rizwan Bashir et al. (2017) presented that Smart buildings that can link to the Internet of Things are becoming increasingly common. Using SLR to identify the issues and possible solutions, information from all these investigations was analyzed. Academics and professionals will use this study paper to do additional development [10].

Joud Al Dakheel et al. (2020) discussed the notion and properties of these structures to help create nearly Zero-Energy Buildings and to detect potential problems with intelligent retrofit applications. An environmental restoration idea for existing buildings has also been developed. The second part of the study examines the current Key Performance Indications for evaluating the performance and objectives of intelligent buildings [11]. Paul A. Torcellini and Sammy Houssainy et al. (2020) presented the efficient alignment of renewable power or stored with building loads examined in this research using straightforward measures. Using better data and analytic methodologies, this process will become more insightful in building design aspects, such as the usage of dynamic loads and best resource management [12]. Mr. Nitin U Thakare1, Mr. Utkarsh Manwar, et al. (2020) discussed that the buildings significantly impact the level of global energy feasting, using up about 40% of all energy and becoming a significant energy-consuming part of the worldwide structure. Y. Li, et al. (2020) analyzed using case studies of two demonstration projects, this study examined the technical viability of net zero energy buildings in China's summer heat and warm, winter temperature zone. Data on the energy usage of case buildings are obtained through simulation and real-site measurement [13]. The findings indicate that in addition to traditional energy-saving methods, the sudden realization of net zero energy buildings also must focus on reforming an energy system and integrating information technologies. Dongsu Kim, et al. (2022) examined technological improvements in ecological and energy systems that may be useful to intelligent homes and buildings. To achieve optimal functionality and energy-efficient performance, this review research focused on an overall view of creating and implementing power intelligent infrastructure techniques, such as energy-management systems, renewable power systems, and current information intelligent technologies [14].

Fig. 38.2 Location of The Rajkumari Ratnawati school, Jaisalmer [18]

38.3 The Rajkumari Ratnavati Girls School

38.3.1 History and Location

Rajasthan is the least literate state in India, with a female literacy rate of just 53%, despite having 56,507,188 residents and the third-largest population in the country [15]. In rural places like Jaisalmer, where female literacy rates are as low as 35.5%, and women are primarily responsible for household chores, 80% of Rajasthan's population resides. According to reports, 26.8% of Indian girls are wed off before they reach legal maturity. From kindergarten to class 10, the school will educate 400+ girls on average. They will pick up reading and writing skills and acquire regionally specific traditional abilities [16].

Location:	Jaisalmer, Rajasthan
Coordinates:	26° N, 70° E
Occupancy type:	Academic campus
Typology:	New construction
Climate type:	Hot and dry desert
Project area:	35,600 m^2
Grid connectivity:	Grid connected

"Ratnavati," the Jaisalmer princess, is the school's moniker. Maharawal Ratan Singh's daughter. Figure 38.2: Rajkumari Ratnavati Girl's School, an Indian jewel. Sam and Dunes is a tourist attraction 40 km from Jaisalmer's rural Thar desert. Northern Indian town Kanoi lies a few km from this sand desert. This village's new school [17, 18].

38.3.2 Structure Design and Sustainability

Its architecture is distinctive, "an oval-shaped building situated out in the center of the desert." The school's oval geometry represents the power of women. Due to the harsh environment, the team focused on sustainable elements and organized the oval-shaped form. The energy usage of a structure is significantly influenced by the architecture of the building [19]. The Rajkumari Ratnavati Girls' School's architectural features in Rajasthan were created using an integrated design methodology across three stages. The three phases—Passive design, Active design, and Renewable Design—explained below all contributed to buildings having net-zero energy use [20].

38.4 Passive Design Strategies

Passive buildings work "on their own." Climate-based passive design methods govern comfort by orienting the built environment (plan, section) [21]. Passive design options use free solar energy, unfettered airflow for cooling, and shade—natural or architectural—to moderate heat. The composite zone's Rajkumari Ratnavati Girl's School in Jaisalmer was designed passively.

38.4.1 Orientation

Figure 38.3 illustrates how the architects uniquely created the school as an ellipse that can resist temperatures up to fifty degrees Celsius. Western style and native materials blended well to block excessive sunshine. This contemporary school exemplifies eco-friendliness. It is built in a futuristic modern. The building also looks minimalist. Additionally, the traditional architecture of Rajasthan has also been used in it. This is a sustainable building [22].

Fig. 38.3 Oval shape of Rajkumari Ratnawati School, Jaisalmer [17]

38.4.2 Building Material

School walls are made of three layers. Which are local yellow sandstone, marble, and lime plaster. Regional craftspeople made it by hand. The building's inside walls are lime plastered, which insulates them. Construction has taken advantage of the local sandstone, which offers protection from the day's intense heat and warmth at night. To make space for ventilation [23].

38.4.3 Ventilation

The building is designed in a way that does not require air conditioning. Instead, traditional architecture is used in the construction so that the ones used to build it will keep it cool. All these things improve air circulation, and the temperature of the building remains cool inside. Windows and jaalis add to cross ventilation. This structure has solar panels on its roof that produce power. It also has a rainwater harvesting system inside with a 3.5 lakh liter capacity. It is a wholesome package of sustainability and eco-friendliness. To make this project possible, the money came through charitable donations; this is an NGO [24]

$$\text{CITTA} = \text{health} + \text{education} + \text{economic development}$$

This is a non-profit organization, CITTA. Its founder is Michael Daube. The supervisor of this project is Chahat Jain. The architect of this building is Diana Kellogg. The founder of the contractor Karim Khan implemented this plan and made it possible in real life. It was Manvendra who had contributed the land to build this school [25]. Diana Kellogg and Karim Khan coordinated, and local labor was employed for this project. Finally, this building was completed within one year. 400 girls would be given free education in this school [26].

38.4.4 GYAAN Centre: A Unique Trifecta of Architecture

The academy is one of the three structures in the "Gyaan Center" complex. "As shown in Fig. 38.4."

- Currently, just one building stands, although the Gyaan Center is the name of the entire project. In total, three structures will be constructed. The remaining two buildings are still under construction.
- The Medha Hall-In one of the buildings. The Medha Hall area includes a library, a museum, a venue for performances, and an art gallery showcasing regional handicrafts like textiles. The women could pick up traditional needlework and weaving skills. Through Medha Hall, CITTA India will provide a medium for

Fig. 38.4 Gyaan Centre [17]

items made by local women to reach national and international markets for gainful employment.

- The GYAAN Centre aims to empower isolated Kanori women through education and independence.The GYAAN Centre helps rural Kanoi women achieve education and independence.
- At Gyaan Center, tie up with several designers and schools like Anita Dogre, NID Ahmedabad school, and Sabyasachi Mukharji. They will provide the marketplace and the market. Architectural Digest's annual ranking of the top names in design, the AD100, was given to the school. Table 38.1 presents the list of Net-zero Energy Buildings in India [27, 28].

38.4.4.1 Advantages of Zero Energy Building

- A decrease in net monthly living expenses.
- Increased resale value.
- Enhanced living comfort.
- Increased dependability.
- Long-term affordability.
- Protection from future energy price increases.
- Be environmentally friendly.
- Reduced carbon emissions.
- Sustainable building.

38.4.4.2 Disadvantage of Zero Energy Building

- A more outstanding upfront payment.
- A lack of technical expertise.
- The need for more recent, superior technologies.

Table 38.1 List of India's NZEB

Building name	Location	Area	EPI (kWh/ m^2/y^2)	Occupancy type	Active strategies	Passive strategies
1. SIERRA'S e facility Green Office Building	Coimbatore, Tamil Nadu, India	2322.55 m^2	56.2	Office	1. Air-conditioning 2. Indoor air quality 3. Artificial lighting and controls 4. Water efficiency 5. Energy monitoring	1. Climate responsive design 2. Landscaping and water efficiency
2. Jaguar Headquarters	Manesar, Haryana	48,000 m^2		Corporate and manufacturing	1. Site layout and planning 2. Climate responsive design 3. Form and massing 4. Facade and envelope 5. Biophilic design	1. Cooling systems 2. Conventional cooling systems 3. Radiant cooling systems 4. VRF indoor/outdoor system 5. Heat pump system 6. Ventilation system 7. Water efficiency 8. Lighting design
3. Unnati Office	Greater NOIDA, Uttar Pradesh	3740 m^2	60	Office	1. Lighting design 2. Optimized energy systems/HVAC system 3. Indoor air quality 4. Metering and monitoring 5. Commissioning	1. Orientation 2. Landscaping 3. Daylighting 4. Ventilation 5. Building envelope and fenestration

(continued)

Table 38.1 (continued)

Building name	Location	Area	EPI (kWh/ m^2/y^2)	Occupancy type	Active strategies	Passive strategies
4. Avasara Academy	Lavale, Pune	11,148 m^2		Academic	1. Passive 2. Ventilation 3. Design	1. Site layout and planning 2. Facade, envelope and climate 3. Responsive massing 4. Daylighting
5. CEPT, A Living Laboratory	Ahmedabad	498 m^2	58	Office and educational	1. HVAC technologies 2. Lighting design	1. Orientation 2. Daylighting
6. Indra Paryavaran Bhawan Ministry of Environment and Forest (MoEF)	New Delhi	9565 m^2	44	Office and educational	1. Lighting design 2. Optimized energy systems/HVAC system 3. Geothermal heat exchange system	1. Orientation 2. Landscaping 3. Daylighting 4. Ventilation building 5. Envelope and fenestration 6. Materials and construction techniques

(continued)

Table 38.1 (continued)

Building name	Location	Area	EPI (kWh/m^2/y^2)	Occupancy type	Active strategies	Passive strategies
7. Akshay Urja Bhawan	HAREDA, Panchkula, Haryana	5100 m^2	30	Office-public	**1.** Ventilation and cooling	1. Orientation 2. Daylighting 3. Ventilation 4. Building envelope 4. Construction materials and techniques
8. Eco Commercial Building (ECB) Bayer Material Science	Noida	891 m^2	72	New construction	1. Lighting design 2. Optimized energy systems 3. HVAC system 4. Indoor air quality 5. Commissioning	1. Orientation 2. Landscaping 3. Daylighting 4. Ventilation 5. Building envelope and fenestration 6. Materials and constructions techniques

- Inadequate awareness and resistance to change.
- Inconsistent methods for appraisal and valuation.

38.5 Conclusion

Zero energy structures are living spaces that adapt to the demands and lifestyles of their people. Intelligent technology can be used to create "zero energy buildings," these "energy buildings" will offer a measurable and sizeable return on investment. The Jaisalmer sandstone used to construct the Rajkumari Ratnavati Girl's School was hand-carved locally by skilled artisans. For Kellogg, the community needed to be represented in a structure created for the community. Locally available materials were used to construct infrastructure, which lowered carbon emissions. Kellogg also added a photo voltaic canopy on the roof to offer cooling when temperatures approached 50 °C (120 F degrees). The jalis and canopy keep the heat out, and the structure's elliptical form also contributes to sustainability by generating a cooled airflow panel.

References

1. Torcellini, P., Pless, S., Deru, M., Crawley, D.: Zero energy buildings: a critical look at the definition (No. NREL/CP-550-39833). National Renewable Energy Lab. (NREL), Golden, CO (United States) (2006)
2. Akadiri, P.O., Olomolaiye, P.O.: Development of sustainable assessment criteria for building materials selection. Eng. Constr. Archit. Manag. (2012)
3. GhaffarianHoseini, A., Dahlan, N.D., Berardi, U., GhaffarianHoseini, A., Makaremi, N.: The essence of future smart houses: from embedding ICT to adapting to sustainability principles. Renew. Sustain. Energy Rev. **24**, 593–607 (2013)
4. Desideri, U., Asdrubali, F. (eds.): Handbook of Energy Efficiency in Buildings: A Life Cycle Approach. Butterworth-Heinemann (2018)
5. Vergini, E.S., Groups, P.P.: A review on Zero Energy Buildings and intelligent systems. In: 2015 6th International Conference on Information, Intelligence, Systems, and Applications (IISA), July, pp. 1–6. IEEE (2015)
6. Perlova, E., Platonova, M., Gorshkov, A., Rakova, X.: Concept project of zero energy building. Procedia Eng. **100**, 1505–1514 (2015)
7. Bashir, M.R., Gill, A.Q.: IoT enabled smart buildings: a systematic review. In: 2017 Intelligent Systems Conference (IntelliSys), Sept, pp. 151–159. IEEE (2017)
8. Ramesh, G.: A Review on Smart Buildings
9. Alanne, K., Sierla, S.: An overview of machine learning applications for smart buildings. Sustain. Cities Soc. **76**, 103445 (2022)
10. Aguilar, J., Garces-Jimenez, A., R-Moreno, M.D., García, R.: A systematic literature review on the use of artificial intelligence in energy self-management in smart buildings. Renew. Sustain. Energy Rev. **151**, 111530 (2021)
11. Pinto, G., Wang, Z., Roy, A., Hong, T., Capozzoli, A.: Transfer learning for smart buildings: a critical review of algorithms, applications, and future perspectives. Adv. Appl. Energy, 100084 (2022)

12. Huseien, G.F., Shah, K.W.: A review of 5G technology for smart energy management and smart buildings in Singapore. Energy AI **7**, 100116 (2022)
13. Panchalingam, R., Chan, K.C.: A state-of-the-art review on artificial intelligence for Smart Buildings. Intell. Build. Int. **13**(4), 203–226 (2021)
14. Khandelwal, R., Jain, R., Gupta, M.: Case study: India's first net-zero energy building—Indira Paryavaran Bhavan. Int. J. Sci. Technol. Res. **9**(11), 353–357 (2020)
15. Hasan, A., Mohamed, A., Mohamed, H.: Net-and nearly-zero energy buildings: a review of the definitions and case studies. In: Proceedings of the Sixth International Conference on Heating, Ventilation and Airconditioning, HVAC, Tehran, Iran (2015)
16. Yang, D., Yin, H.: The energy conversion efficiency of a novel hybrid solar system for photovoltaic, thermoelectric, and heat utilization. IEEE Trans. Energy Convers. **26**(2), 662–670 (2011)
17. Akadiri, P.O., Chinyio, E.A., Olomolaiye, P.O.: Design of a sustainable building: a conceptual framework for implementing sustainability in the building sector. Buildings **2**(2), 126–152 (2012)
18. Rajkumari Ratnavati Girl's School. In: Wikipedia, The Free Encyclopedia. https://en.wikipedia.org/w/index.php?title=Rajkumari_Ratnavati_Girl%27s_School&oldid=1125688190. Accessed 25 Dec 2022
19. https://goo.gl/maps/b3zCpyYvyPcBTiWH6. Accessed 25 Dec 2022
20. Ren, X., Li, C., Ma, X., Chen, F., Wang, H., Sharma, A., Gaba, G.S., Masud, M.: Design of multi-information fusion-based intelligent electrical fire detection system for green buildings. Sustainability **13**(6), 3405 (2021)
21. Nadeem, M.W., Goh, H.G., Hussain, M., Hussain, M., Khan, M.A.: Internet of Things for green building management: a survey. In: Role of IoT in Green Energy Systems, pp. 156–170. IGI Global (2021)
22. Yang, B., Lv, Z., Wang, F.: Digital twins for intelligent green buildings. Buildings **12**(6), 856 (2022)
23. Debrah, C., Chan, A.P.C., Darko, A.: Green finance gap in green buildings: a scoping review and future research needs. Build. Environ. **207**, 108443 (2022)
24. Rana, A., Sadiq, R., Alam, M.S., Karunathilake, H., Hewage, K.: Evaluation of financial incentives for green buildings in the Canadian landscape. Renew. Sustain. Energy Rev. **135**, 110199 (2021)
25. Razmjoo, A., Nezhad, M.M., Kaigutha, L.G., Marzband, M., Mirjalili, S., Pazhoohesh, M., Memon, S., Ehyaei, M.A., Piras, G.: Investigating smart city development based on green buildings, electrical vehicles, and feasible indicators. Sustainability **13**(14), 7808 (2021)
26. Zhao, X., Pan, W.: The characteristics and evolution of business model for green buildings: a bibliometric approach. Eng. Constr. Archit. Manag. (2021)
27. Kong, F., He, L.: Impacts of supply-sided and demand-sided policies on innovation in green building technologies: a case study of China. J. Clean. Prod. **294**, 126279 (2021)
28. Saha, S., Hiremath, R., Sanjay, P.: Barriers to adoption of green buildings—a review. Cardiometry **22** (2022)

Chapter 39
Numerical Simulations of the Cutting Forces in an End Milling Process with Process Damping, Tool Runout and Variable Pitch Effects

C. Trivikrama Raju, S. Jakeer Hussain, and G. Yedukondalu

Abstract Milling cutters with runout, process dampening, and variable pitch did not solve milling difficulties because they did not address the regenerative chatter mechanism. When the phase difference between two waves varies from tooth to tooth, it throws off the regeneration process. The focus of this study is on devising a quick and accurate technique to quantify these influences during end milling. To enhance production quality and process stability while decreasing tool wear and machining costs, these methods may be included into an adaptive model for managing cutting force. The simulation results show that the cutting forces in end milling are small as compared to conventional scale cutting. In this study, an alternative process damping model has been presented for end milling based on an equivalent viscous damping approach. Furthermore, the technique is used to investigate how different tool geometries affect stability tendencies in variable pitch milling. Some novel phenomena are shown and discussed for certain parameter combinations.

39.1 Introduction

Major technological advances have been achieved in the field of high-speed machining (HSM). Better spindle designs allow for speeds of 30k and higher in micro-milling. Increasing the spindle speed and depth of cut during machining increases the rate of material removal. Nevertheless, high speed machining at larger depths of cut is hindered by the chatter phenomenon, which results in machining process to

C. Trivikrama Raju · G. Yedukondalu
Department of Mechanical Engineering, Koneru Lakshmaiah Education Foundation, Vaddeswaram, Guntur, India

S. Jakeer Hussain (✉)
Department of Mechanical Engineering, Mother Teresa Institute of Science and Technology, Sathupally, India
e-mail: jakeershaik786@gmail.com

P. H. V. S. Talpa Sai et al. (eds.), *Intelligent Manufacturing and Energy Sustainability*, Smart Innovation, Systems and Technologies 372,
https://doi.org/10.1007/978-981-99-6774-2_39

be instable leading to unsatisfactory finish of the surface and potentially destroying the life of the cutting tool and work pieces. Driven by the current needs of highly automated production, the recognition of higher-productive, higher-quality, low-cost milling necessitates the concern of exact cutting force and chatter models. These days, the primary instruments used in manufacturing are stability lobe diagrams, which visually distinguish stable cutting circumstances from unstable or chatter ones. Using the tool point frequency response function (FRF), tool geometry, cutting factors, and cutting force coefficients, Altintas and Budak [1] demonstrated the models necessary to forecast the stability lobes. Several studies on the milling process parameters related to the chatter studies have been the subject of a number of previous research, including those by Altintas and Weck [2], Bravo et al. [3], Gagnola et al. [4] and Tanga et al. [5] inverse analysis of the self-excited chatter vibration has been recently reported, and it has been used by Suzuki et al. [6] to build a novel method for calculating the transfer function. The accuracy of the SLD was refined by Raphael et al. [7], who also investigated how the spindle's electronic position and velocity affected SLD accuracy. Lin and Tu [8], Jiang and Zhang [9], Penga et al. [10], Cao et al. [11], Gao and Meng [12] and a few more publications deal with the design of end mill spindles and identify the design elements that largely affect the stability lobe diagrams of these tools. Effects such as bearing preload on the tip of the tool frequency responses were studied by the Ozturk et al. [13]. Preload and spindle speed were shown to have a correlation in the examined instance. A dynamic model of high-speed motorised spindles was investigated by Liu and Chen [14]. To conduct a design sensitivity analysis, a design flowchart is drawn up. In the past, academics have attempted to optimise the milling process by taking a number of variables into account. To improve machining performance, Altintas [15] used simulated annealing and a genetic algorithm, two artificial computing approaches. Experimental investigations verify the combined use of the two methods. In order to foretell the cutting forces in an end milling operation, Jalili Saffar and Razfar [16] created a 3D modelling of the cutting forces are optimised using a genetic algorithm approach and then verified experimentally. Mathematics modelling the interaction between machining dynamics and material behaviour was developed by Palanisamy et al. [17]. The cutting process settings and tool vibration levels are optimised to save machining time using a robust GA approach. Using particle swarm optimization, Hsieh and Chu [18] created a generative tool path in a five axis milling machine using PSO algorithm. Using proactive and well-informed PSOs improves search efficiency. The harmony search (HS) technique was proposed by Zarei et al. [19] to determine face-milling parameters. The optimal depth of cut, feed rate, and cutting speed are achieved by a series of passes using a variety of machining settings in order to minimise the total cost of manufacturing.

Whereas optimum machining studies related to the cutting process is considered as a function of the geometric parameters of the integrated spindle tool unit are only few presented by the previous authors. In the current study, we aim to acquire the best cutting process conditions of the end milling process by taking into account a few critical parameters of the spindle-tool unit and the corresponding flexible body dynamics. End-milling studies with the currently available parametric conditions confirm the accuracy of the machining process.

39.2 Modeling of Cutting Force Simulations

The workpiece is supposed to be stiff, whereas the tool is assumed to be flexible. Cutting process stability evaluation requires consideration of both tool geometry and machining requirements. The parameter like angle between each tooth, teeth numbers, helix angle of the tool, diameter of the tool and run-out are all part of the tool geometry. Spindle speed, axial depth of cut, feed per tooth, and entry/exit angles (a function of radial immersion) are required machining requirements. As b and $h(\phi_j)$ increase in the axial direction, the tangential and radial components of the linear cutting force operating on tooth j increase accordingly.

$$F_{t,j}(\phi) = K_t bh(\phi_j) \tag{39.1}$$

$$F_{r,j}(\phi) = K_r F_{t,j}(\phi) = K_r K_t bh(\phi_j) \tag{39.2}$$

where tangential shearing (Kt) and normal shearing (Kr) both contribute to the overall flute coefficient. Both the tangential and normal force components are projected onto the fixed (x, y) coordinate frame in the following ways:

$$F_{x.j} = -F_{t.j} \cos\phi_j - F_{r.j} \sin\phi_j \tag{39.3}$$

$$F_{y.j} = +F_{t.j} \sin\phi_j - F_{r.j} \cos\phi_j \tag{39.4}$$

By adding the sum across all the teeth (flutes), the total cutting forces may be calculated using the following closed-form expressions:

$$F_x(\phi) = \sum_{j=1}^{N_t} F_{x,j}; \quad F_y(\phi) = \sum_{j=1}^{N_t} F_{y,j} \tag{39.5}$$

39.2.1 Effects of Process Damping

Energy is dissipated in a process when a cutting tool's relief angle interacts with preexisting vibrations on the surface of the machined workpiece. Turning and milling are two processes where process damping has received a lot of attention from researchers. It happens when the cutter's flank touches with the imprinted vibrations on the cutting process. It may slow down the machining process and affect the dynamic cutting forces.

At the lower speeds of the spindle, the stability of the end milling are spaced closely and the chatter-free depths of cut are shown to decrease significantly. Fortunately, the chip width that may be used at low spindle speeds can be increased because to the process damping effect. The damping force for the milling force (F_d) is denoted by a 90°-phase shift with respect to the displacement, is of the negative sign to velocity component. Based on this information, the process damping force is described as the viscous damping force

$$F_d = -C\frac{b}{V}\dot{y} \tag{39.6}$$

Here, we define the y-direction process damping force and it is considered as the function of the velocity of the cutter ($\dot{y}$), cutting speed (v), width of the chip (b) and damping coefficient (C). The time-dependent cutting force direction is a major challenge in establishing an analytical solution for milling stability. The average force direction is considered together with the average tooth angle of the cut (f_{avg}). A time-independent or self-sufficient system may be built using this method. Initially, μ_x and μ_y are used to project the force in X and Y directions then, finally, the results are projected on to the normal of the surface. The milling process's stability lobe boundaries may be calculated using the following equations:

$$b_{lim} = \frac{-1}{2K_s \mathrm{Re}(H_{or})N_t^*} \tag{39.7}$$

$$\frac{f_c}{\Omega N_t} = j + \frac{\varepsilon}{2\pi} \tag{39.8}$$

$$N_t^* = \frac{\phi_e - \phi_s}{360/N_t} \tag{39.9}$$

$$\varepsilon = 2\pi - 2\tan^{-1}\left(\frac{\mathrm{Re}[H_{or}]}{\mathrm{Im}[H_{or}]}\right) \tag{39.10}$$

$$H_{or} = \mu_x H_x + \mu_y H_y \tag{39.11}$$

where, count of the teeth is represented as N_t, H_{or} is considered as oriented frequency response at the tool tip, j = 0, 1, 2, … is the lobe number, force angle (β) in degrees. The process damping force may be easily used for both vertical and horizontal milling operations. In Fig. 39.1, n represents the surface normal direction, which is used to establish the geometry for the up-milling operation.

The n-axis damping force of a process is projected onto the x-axis as

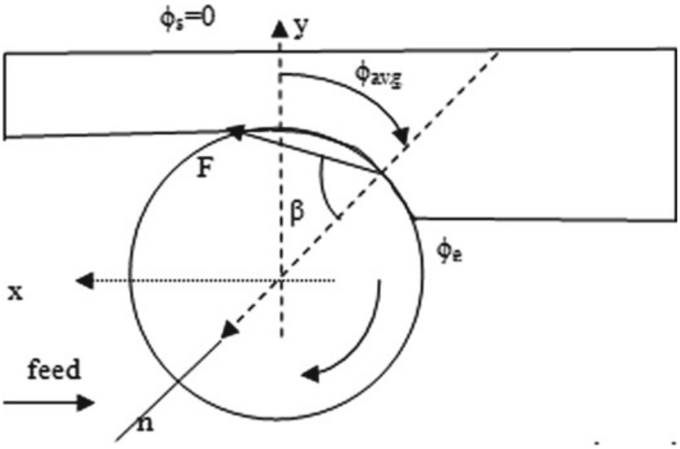

Fig. 39.1 Up-milling geometry based on the average tooth angle

$$F_x = F_d \cos(90 - \phi_{avg}) = -\left(C\frac{b}{V}\cos\left(90 - \phi_{avg}\right)\right)\dot{n} \tag{39.12}$$

The damping force of a process is projected onto the x-axis as

$$F_x = -\left(C\frac{b}{V}\cos^2\left(90 - \phi_{avg}\right)\right)\dot{x} \tag{39.13}$$

Therefore, the revised damping for x- and y-axis stability calculations is:

$$c_{new,x} = c_x + \left(C\frac{b}{V}\cos^2\left(90 - \phi_{avg}\right)\right) \tag{39.14}$$

$$c_{new,y} = c_y + \left(C\frac{b}{V}\cos^2\left(180 - \phi_{avg}\right)\right) \tag{39.15}$$

The damping values in the x and y directions are produced for down milling using the same method as outlined for up milling.

$$c_{new,x} = c_x + \left(C\frac{b}{V}\cos^2\left(\phi_{avg} - 90\right)\right) \tag{39.16}$$

$$c_{new,y} = c_y + \left(C\frac{b}{V}\cos^2\left(180 - \phi_{avg}\right)\right) \tag{39.17}$$

39.2.2 Tool Run-Out and Cutting Force Modelling

When a mechanical system is in motion, tool run-out occurs when the tool is not perfectly aligned with the axis of rotation. The effect of the tool run-out is a serious problem in the machining process that may arise from a number of different sources, including misalignment between the tool holder and spindle, incorrect radial tooth location on the cutter, inaccurate tool dimensions, thermal tool deflection, improper tool and holder balance, and so on. As a result, the tool is subjected to unequal stresses across its cutting teeth at all times. Chip thickness varies as the tool rotates. The cutting forces were determined by the cutting geometry that was inserted into the workpiece, and the cutting forces were related to the uncut chip thickness using empirical formulae. The Eccentricity called as the run-out distance and the run cut angle (λ) characterize radial run-out. A circular approximation of the cutting tool's path allows us to use the following formula to get the chip thickness, which accounts for tool run-out.

$$h_j(\phi_j) = f_t \sin(\phi_j) + h_{ro}^j \tag{39.18}$$

Here we describe the chip thickness variation caused by run-out in cutting edge j as

$$h_{ro}^j = \rho_j - \rho_{j-1} \tag{39.19}$$

The cutting edge with run-out is the difference between the calculated and actual radii of each flute, which causes a shift in the cutting load. Run-out causes a difference between the nominal radius and the real radius, which is the radius along which the flute actually travels.

The effective radius variation along the cutting edge is not a significant factor when working with the tiny values of depth of cut and helix angle examined in this study, therefore the tool run-out is appropriately described by the difference between the actual and nominal trajectories for each flute. Cutting forces in the X and Y directions may be derived from the resolution of the tangential and radial forces, as the particular cutting force is a function of these three forces and the chip thickness along the cutting edge.

$$\begin{Bmatrix} F_{x,j}(\phi_j) \\ F_{y,j}(\phi_j) \end{Bmatrix} = \begin{bmatrix} -\cos(\phi_j) & -\sin(\phi_j) \\ \sin(\phi_j) & -\cos(\phi_j) \end{bmatrix} \begin{Bmatrix} F_{t,j} \\ F_{r,j} \end{Bmatrix} \tag{39.20}$$

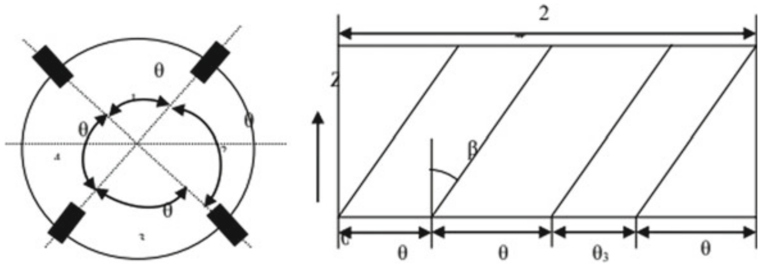

Fig. 39.2 Edge inclination on the end mill cutter's rim

39.2.3 Cutting Force Modelling Considering the Influence of Pitch

In most cases, it is believed that the cutter's teeth are evenly spaced (i.e., have a consistent tooth pitch) throughout its rim. When milling tough materials, it's common practice to use a tool with a variable pitch end mill. Mills with a tunable pitch angle may also have a tunable helix angle. Figure 39.2 depicts how the feed per tooth of a variable pitch tool changes as a function of the tooth angle θi (degrees).

The feed per tooth ratio is evaluated as given below

$$f_{t,variable} = \left[\frac{f_{t,mean} \times \theta_i \times N_t}{360^\circ} \right] \quad (39.21)$$

where $f_{t,mean}$ is the mean feed per tooth and N_t is the number of teeth.

39.3 Results and Discussions

Using the information in Table 39.1, a Matlab programme depicts the stability lobe diagram of the frequency response function of the tool tip.

Coefficients of the system's modal and cutting modes are listed in Table 39.1.

Table 39.1 System's modal parameters and cutting force coefficeints

Cutting tool parameters	Numerical values
Cutting stiffness in X and Y directions	2.1×10^8 N/m
Natural frequency ($\omega_x = \omega_y$)	2056 Hz
Damping ratio ($\xi_x = \xi_y$)	0.01
Diameter of the tool	12 mm
Specific cutting pressure (K_s)	750 N/mm^2
Total tooth of the cutter (N_t)	4

To examine the impact of process damping with these updates to the classical model, a MATLAB programme is constructed. The radial immersion ratio of 50% is used in the numerical analysis. With the data obtained from finite element analysis approach, the frequency responses are arrived and it is further utilized to plot the stability areas for the up-milling operation are displayed. Stability charts for varying the process damping constant from zero (no process damping) to the highest value ($C = 6.5 \times 10^5$ N s/m) are shown in Fig. 39.3. The average steady depth of cut is found to rise from 0.04 to 0.3 mm when the process is dampened.

In order to simulate the cutting force, modal parameters, the tool shape, and machining requirements must be provided. Each mode of the tool in the x and y axes has its own set of modal characteristics, which include its stiffness, damping ratio, and natural frequency. In Fig. 39.4, we see the results of a time-domain simulation of a milling model with two degrees of freedom, both with and without the influence of process damping. When the process damping effect is included into the model, it is shown that the x and y levels of tool displacements decrease. In addition, it offers the constant tool displacements that are crucial for a consistent cut.

A tool with a 12 mm diameter is used to demonstrate the impact of run-out. Run-out is typically measured along the feed direction. For the case of a run-out offset of 10 μm, simulations are performed in the time domain both with and without run-out effects, as shown in Fig. 39.5. The cutting process is modelled in two dimensions, and all spindle-tool system characteristics are taken into account.

The amounts of tool displacement are shown to rise as run-out increases throughout the cutting process. The cutting pressures experienced by the virtual

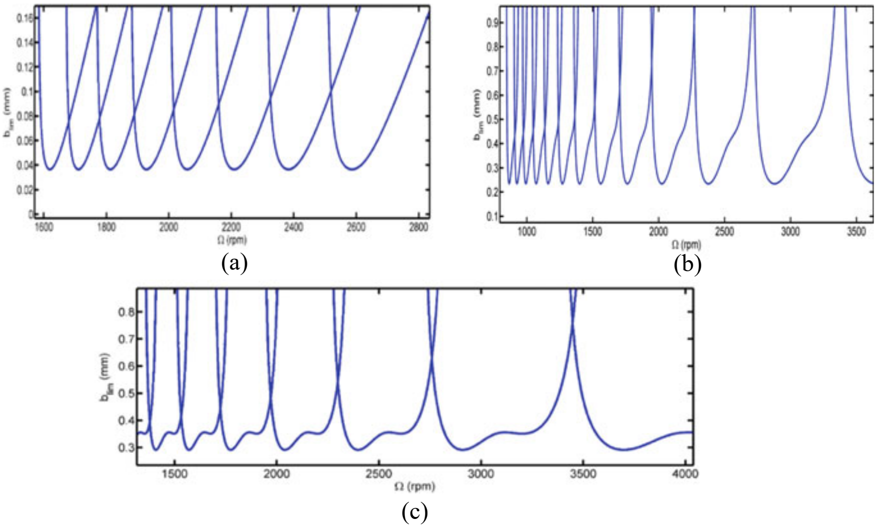

Fig. 39.3 Analytical stability lobe diagrams. **a** In the absence of process dampening, **b** in the presence of process dampening with C = 6.5 × 104 N s/m, **c** in the presence of process dampening with $C = 6.5 \times 10^5$ N s/m

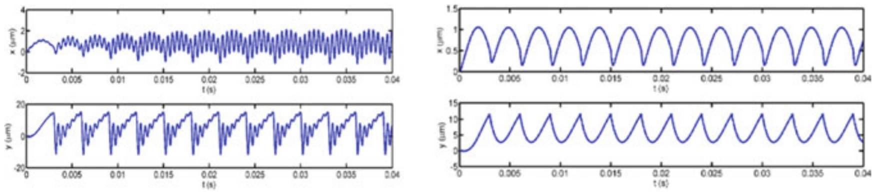

(a) (b)

Fig. 39.4 Vibrations from the cutter at a depth of 1 mm and spindle speed of 3000 rpm. **a** In the absence of process dampening, **b** presence of process dampening with C = 6.5 × 10^5 N s/m

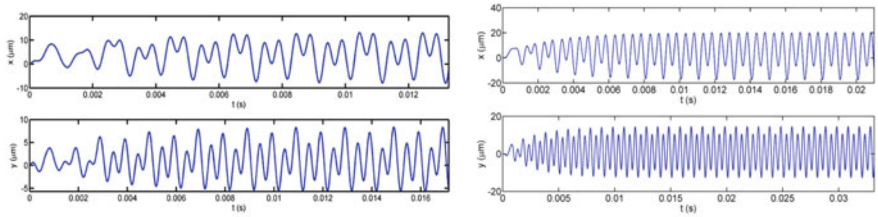

(a) (b)

Fig. 39.5 Run-out correction levels for tool displacements. **a** In the absence of run-out, **b** in the presence of run-out

tool for run-out values of 10 and 25 μm are shown in Fig. 39.6. As can be seen in Fig. 39.6, the cutting forces for each flute vary by just a little amount (10–12 μm). Cutting forces may be detected with significant amplitude in the variations in load of the chip at each tooth is shown in Fig. 39.6b, leading to unacceptable vibration levels of the tool as cutting progresses.

Using a tool with variable pitch spacing [0 95 180 275] degrees and with equal pitch [0 90 180 270] degrees for two different axial depths of cut, Fig. 39.7 displays the observed resulting forces with a 25% immersion of the radial cut in up-milling of aluminum alloy. It is seen that the forces fluctuate non-linearly due to the varied

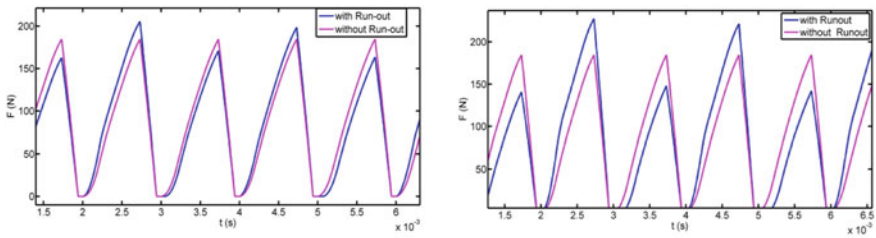

(a) (b)

Fig. 39.6 Force variations as a result of tooth wear. **a** With a run-out of 10 μm, **b** with a run-out of 25 μm

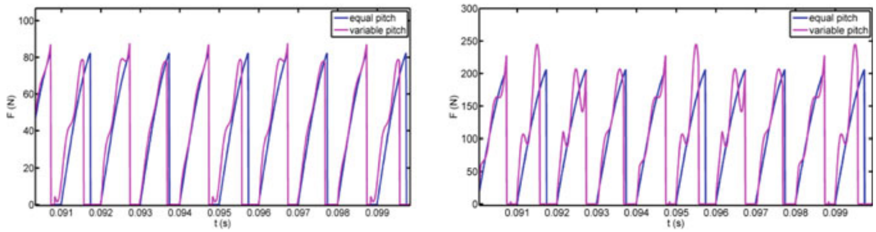

(a) (b)

Fig. 39.7 Variable-pitch time-domain simulation at 25% radial immersion. **a** Cutting depth = 1 mm, **b** cutting depth = 2.5 mm

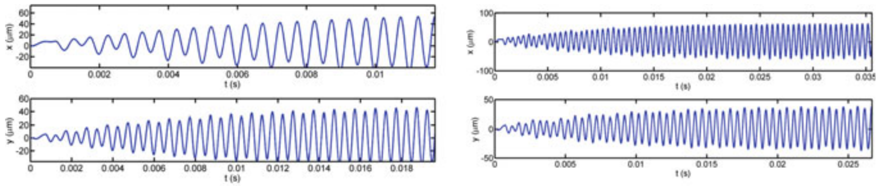

(a) (b)

Fig. 39.8 Vibration levels of tools at 1 mm depth of cut. **a** With the same pitch, **b** with different pitch

pitch as the axial depth of the cut raised from 1 to 2.5 mm, the cutting forces also have been raised significantly.

At an axial depth of cut as 1 mm example with as equivalent and varied pitch of the tool, the cutting tool displacement values are achieved as illustrated in Fig. 39.8. The cutting tool's variable pitch clearly raises the displacement levels of the tool dramatically.

39.4 Conclusions

As a result, evaluating the cutting process's stability demands an ideal selection of cutting tool settings with regard to those factors. Errors in machining may arise from a number of different factors, including tool run-out, tool deflection, workpiece displacements, and variable pitch end mills. There are situations when the procedure fails despite having a well-designed spindle and tool. The aforementioned calculations allow one to determine the maximum allowable tool run-out in terms of spindle dimensions. For the proposed spindle-tool configuration, tools with variable pitches are also permitted for use during machining to achieve the greater stable depth of cuts. In an integrated spindle-tool spindle system, the damping force at the interface regions such as collet and tool, chuck and the collet are having a major impact on the system's stability, process damping has an effect analogous to that of the internal damping. In order to guarantee the steadiness of the cutting process, the findings shown that the proposed approach may be utilized for accurate assessment of tool run-out, process damping, and variable pitch effects.

References

1. Altintas, Y., Budak, E.: Analytical prediction of stability lobes in milling. Ann. CIRP **44**, 357–362 (1995)
2. Altintas, Y., Weck, M.: Chatter stability of metal cutting and grinding. CIRP Ann. Manf. Technol. **53**, 619–642 (2004)
3. Bravo, U., Altuzarra, O., Lopez de Lacalle., L.N., Sanchez, J.A., Campa, F.J.: Stability limits of milling considering the flexibility of the workpiece and the machine. Int. J. Mach. Tools Manf. **45**, 1669–1680 (2005)
4. Gagnola, V., Bouzgarrou, B.C., Raya, P., Barra, C.: Model-based chatter stability prediction for high-speed spindles. Int. J. Mach. Tools Manf. **47**, 1176–1186 (2007)
5. Tanga, W.X., Songa, Q.H.: Prediction of chatter stability in high-speed finishing end milling considering multi-mode dynamics. Int. J. Mach. Tools Manuf **209**, 2585–2591 (2009)
6. Suzuki, N., Kurata, Y., Kato, T., Hino, R., Shamoto, E.: Identification of transfer function by inverse analysis of self-excited chatter vibration in milling operations. Precis. Eng. **36**, 568–575 (2012)
7. Raphael, G.S., Reginaldo, T.C.: A contribution to improve the accuracy of chatter prediction in machine tools using the stability lobe diagram. J. Manuf. Sci. Eng. ASME. **136**, 021005–021007 (2014)
8. Lin, C.W., Tu, J.F.: Model-based design of motorized spindle systems to improve dynamic performance at high speeds. J. Manuf. Process. **9**, 94–108 (2007)
9. Jiang, S., Zheng, S.: Dynamic design of a high-speed motorized spindle-bearing system. J. Mech. Des. ASME **132**, 0345011–0345015 (2010)
10. Penga, Z.K., Jackson, M.R., Guo, L.Z., Parkin, R.M., Meng, G.: Effects of bearing clearance on the chatter stability of milling process. Nonlinear Anal. Real World Appl. **11**, 3577–3589 (2010)
11. Cao, H., Holkup, T., Altintas, Y.: A comparative study on the dynamics of high speed spindles with respect to different preload mechanisms. Int. J. Mach. Tools Manuf **57**, 871–883 (2011)
12. Gao, S.H., Meng, G.: Research of the spindle over hang and bearing span on the system milling stability. Arch. Appl. Mech. **81**, 1473–1486 (2011)
13. Ozturk, E., Kumar, U., Turner, S., Schmitz, T.: Investigation of spindle bearing preload on dynamics and stability limit in milling. Int. J. Mach. Tools Manuf **61**, 343–346 (2012)
14. Liu, J., Chen, X.: Dynamic design for motorized spindles based on an integrated model. Int. J. Adv. Manuf. Technol. **71**, 1961–1974 (2014)
15. Altintas, Y.: Modeling approaches and software for predicting the performance of milling operations at Mal-Ubc. Mach. Sci. Technol.: Int. J. **4**, 3445–3478 (2000)
16. Jalalli Saffar, R., Razfar, M.R.: Simulation of end milling operation for predicting cutting forces to minimize tool deflection by genetic algorithm. Mach. Sci. Technol.: Int. J. **14**, 81–101 (2010)
17. Palanisamy, P., Rajendran, I., Shanmugasundaram, S.: Optimization of machining parameters using genetic algorithm and experimental validation for end-milling operations. Int. J. Adv. Manuf. Technol. **32**, 644–655 (2007)
18. Hsieh, H.T., Chu, C.H.: Improving optimization of tool path planning in 5-axis flank milling using advanced PSO algorithms. Robot. Comput.-Integr. Manuf. **29**, 3–11 (2013)
19. Zareia, O., Fesanghary, M., Farshi, B., Saffar, J., Razfar, R.M.R.: Optimization of multi-pass face-milling via harmony search algorithm. J. Mater. Process. Technol. **209**, 2386–2392 (2009)

Chapter 40
Optimization of Blade Geometry for Two Bladed Savonius Wind Turbine

S. Naga Kishore, U. V. Sujala, Mohammad Sikindar Baba, and K. Srinivasa Chalapathi

Abstract Savonius wind turbine (SWT) is an attractive power generation system due to its special qualities such as simplicity, reliability, very low noise production and best substitute for power generation of domestic applications at low wind regions. Performance test of savonius wind turbines always helps for analysing designs, optimizing parameters and for the maintenance of new plants in better way. The present paper discusses an experimental investigation on the performance of two bladed SWT having 1 m height and 1 m chord length installed in DBS Institute of Technology, Kavali (14.913°N, 79.992921°E) based on blade geometry. For performance testing, savonius rotor is initially operated at four different overlap (0.3, 0.4, 0.5 and 0.6 m) values on conventional arrangement (blade arc angle as 180°) and later employed five blade arc angles (180°, 185°, 190°, 195° and 200°) for operation. The optimum values of overlap ratio and blade arc angle are identified to achieve maximum performance. The range of tip speed ratio (TSR) from 0.4 to 0.69 is taken based on the availability of wind speed (8–40 km/h) during the period from 1st April 2022 to 30th October 2022.

Nomenclature

A	Rotor cross sectional area (m^2)
a	Shaft diameter (m)
C	Chord length (m)
C_m	Torque coefficient
C_P	Power coefficient
D	Rotor diameter (m)
e	Overlap (m)

S. Naga Kishore (✉) · M. S. Baba · K. Srinivasa Chalapathi
Department of ME, Anurag University, Hyderabad, Telangana, India
e-mail: nagakishore.surisetty@gmail.com

U. V. Sujala
Department of EEE, DBS Institute of Technology, Kavali, Andhra Pradesh, India

P. H. V. S. Talpa Sai et al. (eds.), *Intelligent Manufacturing and Energy Sustainability*, Smart Innovation, Systems and Technologies 372,
https://doi.org/10.1007/978-981-99-6774-2_40

H	Rotor height (m)
I	Rotor moment of inertia (Kg m^2)
m	Mass of air (Kg)
n	Shaft speed (rpm)
N	Blades number
P	Wind power (Watts)
P_a	Actual power (Watts)
R	Rotor radius (m)
T	Theoretical torque (Nm)
T_a	Actual torque (Nm)
V	Wind velocity (m/s)

Greek Symbols

ρ	Air density (Kg/m^3)
α	Rotor angular acceleration (1/s^2)
ω	Angular velocity (1/s)
β	Overlap ratio
θ	Angle extended to blade tip

Abbreviations

SWT	Savonius wind turbine

40.1 Introduction

One of the best renewable energy sources is wind energy due to its all-time availability with free of cost. Vertical axis wind turbines have special advantages such as omnidirectional, self-starting, low noise, more reliable and no need of yaw mechanism compared to horizontal axis wind turbine. Especially, savonius wind turbines are useful for low or unstable wind speed regions where power is not available properly and can be mounted on rooftops, ground for generating electricity, pumping water and grinding grain [1–3].

There are different design parameters (Area swept by the rotor blades, aspect ratio, overlap ratio, number of blades and geometric shape of the blades) which effect performance of savonius wind turbine [4]. Rise in aspect ratio decreases tip losses and increases power coefficient [5, 6]. The preferable value of aspect ratio ranges between 1.5 and 2 where maximum performance can be achieved [7]. It was proved from studies for savonius rotors that two blade arrangement is more efficient at same operating conditions than three blade arrangement due to reduction in drag surfaces and reverse torque which are caused to increase net torque coefficient and power coefficient [8–10]. Specially, overlap ratio is another important design parameter which influences coefficients of torque and power [11]. From the different observations [8, 12] of performance of two bladed savonius rotors, coefficients of torque and power increase up to an optimum value of overlap ratio and later reduction takes place. Generally, the optimum value of overlap ratio ranges between 0.2 and 0.3 in savonius plants [13].

Setiawan et al. [14] conducted an experimental study for evaluating performance on savonius water turbine which has rotor diameter of 0.4 m and height of 0.4 m by changing overlap ratio. In this study, different overlap ratios (0, 0.05, 0.1, 0.15, 0.2, 0.25 and 0.3) were selected and checked performance parameters. The best result in performance with a value of 62.83% as power coefficient was obtained at overlap ratio of 0.2. Mohammad et al. [15] investigated the effect of overlap ratio and blades position on SWT having rotor diameter of 0.33 m. Power and torque coefficients were analysed at different tip speed ratios (from 0.1 to 0.95) by varying overlap ratios in horizontal direction (from 0 to 0.4) and in vertical direction (from −0.2 to +0.2). From experimental investigations, the maximum performance was obtained in the plant at TSR of 0.7 on every overlap ratio. The optimum values of overlap ratio were obtained in horizontal direction as 0.15 and vertical direction as −0.1. Roy and Saha [16] presented a work on the effect of overlap ratio for SWT. The investigations on static torque coefficient were carried out at four free stream velocities (5.57, 6.96, 8.35 and 10.44 m/s) different angular and positions (from 0° to 360°) and different overlap ratios (0, 0.05, 0.1, 0.15, 0.2, 0.25 and 0.3). From the observations of rotation cycle, negative torque values were obtained in 2nd and 4th quarter. The maximum torque values were obtained at optimum value of overlap ratio of 0.2 and static torque was increased with speed. Maximum value of torque coefficient was achieved at velocity of 10.44 m/s. The recent works of different authors on the performance of two blade SWT at different overlap ratios on conventional arrangement (180° as blade arc angle) are mentioned in Table 40.1.

Blade geometry in which especially arc angle extended to tip is another influencing factor for performance. Because, this angle helps to create better force on the blade through entrance width. The optimum value of tip extension angle is needed for giving maximum performance and identified a range between 180° and 195° in savonius plants from previous studies [11, 25–28]. Akhlaghi and Ghafoorian [25] worked out to evaluate performance of savonius turbine having two blade arrangement with 30 mm as overlap. Authors selected three blade arc angles such as 150°, 180° and 200° for testing the performance and verified that 180° is best one for maximum power and torque coefficient. Al-Faruk and Sharifan [11] conducted works on optimization and comparison for conventional and swirling savonius wind tunnel. Authors focused different configurations such as open & closed top end, blade arc angle range (180°, 190°, 195° and 200°) and overlap ratio range (0.15, 0.2, 0.25 and 0.31). Authors investigated that arc angle of 195° at overlap ratio of 0.2 was given best performance on closed top end. Mao and Tian [28] designed a savonius turbine rotor for which three

Table 40.1 Comparison of the maximum power coefficient at different overlap ratios for a two bladed SWT at conventional arrangement

Investigation	Year	Rotor dimensions (H × D) m × m	TSR at C_{pmax}	Overlap ratio range	C_{pmax}
Setiawan et al. [14]	2021	0.4 × 0.4	0.6946	0, 0.05, 0.1, 0.15, 0.2, 0.25	0.5309
Tjahjanaa et al. [17]	2021	0.4 × 0.4	0.526	0.1, 0.125, 0.2	0.138
Kurniawan et al. [18]	2020	0.4 × 0.4	0.34	0.1, 0.15	0.12
Rahim and Milad [19]	2019	N/A × 0.1955–0.2645	0.8	0, ±0.1, ±0.2, ±0.3	0.27
Mohammad et al. [15]	2019	N/A × 0.33	0.7	−0.4 to +0.4	0.185
Tania et al. [20]	2018	0.18 × 0.18	1.05	0.15, 0.2, 0.25, 0.3	0.3
Alom and Saha [21]	2017	N/A × 0.61	0.8	0, 0.1, 0.15, 0.2, 0.25, 0.3	0.34
Du [22]	2016	0.2 × 0.18–0.224	0.45	0, 0.1, 0.24	0.036
Konrad and Krzysztof [23]	2015	0.154 × 0.2	0.7	0, 0.075, 0.15, 0.225, 0.3	0.19
Akwa et al. [24]	2012	N/A × 1	1.25	0, 0.15, 0.3, 0.45,0.6	0.3161
Current work	2023	1 × 1.4–1.7	0.69	0.161, 0.2343, 0.3166, 0.41	0.189

TSR Tip speed ratio, C_{pmax} Maximum power coefficient, *N/A* Not available

arc angles (150°, 160°, 170°, 180°, 190°, 200°) on blade were tested for identifying best performance. Arc angle of 160° was given best power coefficient which was 28.36 and 8.36% more than conventional arrangement.

In this paper, the performance of SWT is tested at two design parameters such as overlap and blade arc angle. The optimum value for best performance was identified for the range of overlap (0.3, 0.4, 0.5 and 0.6 m) and blade arc angle (180°, 185°, 190°, 195° and 200°). The savonius plant was fabricated at DBS Institute of Technology, Kavali, Andhra Pradesh, India, for unstable wind regions.

40.2 Experimental Setup

The savonius wind turbine was fabricated in DBS Institute of technology, Kavali, Andhra Pradesh, India, with the design specifications mentioned in Table 40.2. Turbine rotor is contained two blades made up of a galvanized iron (GI) sheet which is curved in semi-circular shape. The top and bottom portions of rotor are completely

Table 40.2 Rotor specifications

Parameter	Value
Rotor height (m), H	1
Chord length (m), C or d	1
Shaft diameter (cm), a	2.5
Blade thickness (mm), t	1.026
Number of blades, n	2
Overlap distance (m), e	0.3, 0.4, 0.5 and 0.6
Angle extended to tip (°), θ	180°, 185°, 190°, 195° and 200°
Wind speed range (km/hr)	from 8 to 40

closed with GI sheet to obtain more power coefficient [11]. Bevel gear system is used to transfer power from vertical (rotor) shaft to horizontal (main) shaft. The main shaft speed ratio is maintained as 1:15 with gear box. The two ends of DC (Direct current) generator are coupled to main shaft and battery. Digital anemometer is used for the wind speed measurement, digital DC tachometer is used for shaft rotational speed and multimeter is used for voltage and current measurement. The line diagram of front view and top views of savonius rotor, experimental setup at DBS Institute of Technology, Kavali, (14.913°N, 79.992921°E) and energy transformation in the setup are shown in Fig. 40.1.

It was noticed from the observations at setup that wind velocities in a day reach maximum values during the period from 2.00 to 5.30 p.m. The recorded wind velocities are varied from 8 to 40 km/h during period (1st April 2022 to 30th October 2022) of investigation.

Figure 40.2 represents overlap (e) and angle extended to blade tip (θ). In this work, the overlap (e) is varied with values such as 0.3, 0.4, 0.5 and 0.6 m from which overlap ratios are obtained as 0.161, 0.2343, 0.3166 and 0.41. The range of extended angle (θ) at tip is considered as 0°, 5°, 10°, 15° and 20° from which the arc angles are reached as 180°, 185°, 190°, 195° and 200°. The optimum value of overlap and arc angle is predicted based on maximum power availability. The performance of savonius rotor contains coefficients of torque and power which can be estimated by equations shown in Table 40.3.

40.3 Results and Discussion

40.3.1 Effect of Overlap

Initially, the observations were taken during the day period (8.30 a.m.–5.30 p.m.) at different overlap ratios on conventional savonius rotor (arc angle 180°). It was observed from the experimental investigations that overlap ratio played an important

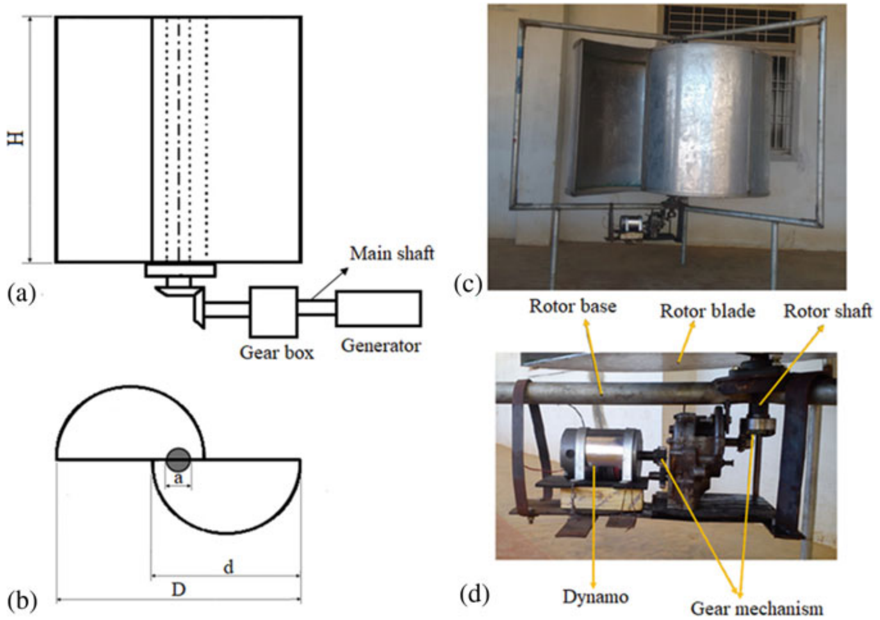

Fig. 40.1 **a** Line diagram of front view of Conventional savonius rotor. **b** line diagram of top view of conventional savonius rotor. **c** Photograph of SWT at DBS Institute of Technology, Kavali. **d** Photograph of energy transformation in setup

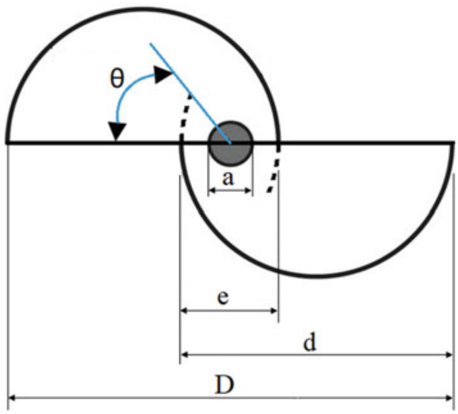

Fig. 40.2 Blade geometry of savonius rotor with overlap and tip extension angle

role on the performance parameters of two bladed SWT. The effect of overlap ratio (0.161, 0.2343, 0.3166 and 0.41) on torque and power coefficients are described.

Figure 40.3 shows that the relation between torque coefficient and TSR at different overlap ratios. At all overlap ratios, the values of torque coefficient decreased when TSR increased. But, at same TSR, the maximum values of torque coefficients were obtained at overlap ratio of 0.2343 as shown in Fig. 40.3. The maximum torque

Table 40.3 Parameters used for performance evaluation of two bladed SWT [8]

Performance parameter	Equation	Equation number
Tip speed ratio (TSR)	$TSR = \frac{\omega R}{V}$	(1)
Theoretical torque (T)	$T = \rho R^2 H V^2$	(2)
Actual torque (T_a)	$T_a = I\alpha$	(3)
Torque coefficient (C_m)	$C_m = \frac{T_a}{T}$	(4)
Theoretical power (P)	$P = \frac{mV^2}{2} = \frac{\rho A V^3}{2}$	(5)
Actual power (P_a)	$P_a = T_a \omega$	(6)
Power coefficient (C_p)	$C_p = \frac{P_a}{P}$	(7)
Blade overlap ratio (β)	$\beta = \frac{e-a}{D}$	(8)

coefficient was identified in this work as 0.42 which was observed on TSR of 0.4521 at overlap ratio of 0.2343.

The power coefficient values which were evaluated at different tip speed ratios by varying overlap ratio are shown in Fig. 40.4. It was observed that the power coefficient was increased with TSR. Particularly, maximum values of power coefficient were obtained at the overlap ratio of 0.2343 on same tip speed ratio compared to other values of overlap ratio. The maximum power coefficient was identified in this work as 0.189 which was observed on TSR of 0.69 at overlap ratio of 0.2343.

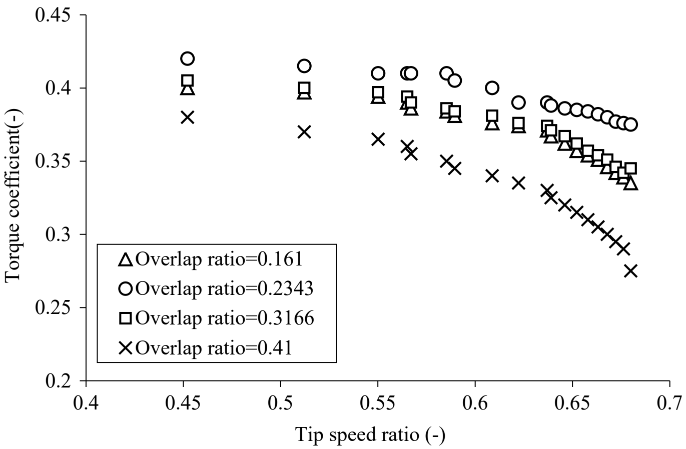

Fig. 40.3 Effect of TSR on torque coefficient at different overlap ratios

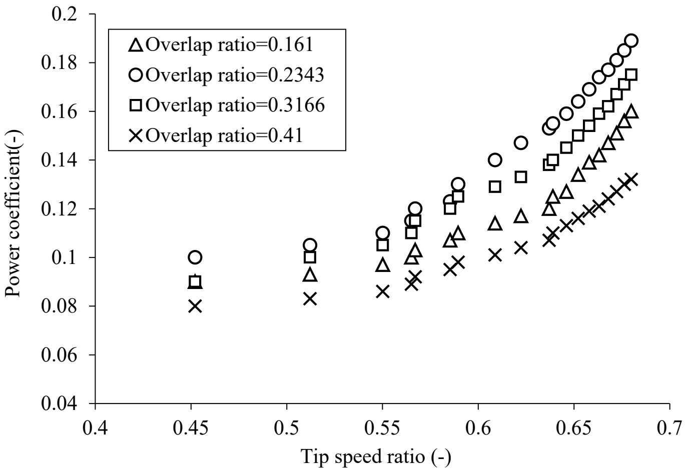

Fig. 40.4 Effect of TSR on power coefficient at different overlap ratios

40.3.2 Effect of Blade Arc Angle

After identification of optimum overlap, the further investigation was conducted on different arc angled for getting best performance. Figures 40.5 and 40.6 show the relation between torque and power coefficient and different tip speed ratios at optimum overlap ratio as 0.2343 (overlap as 0.4 m) and different arc angles. From the investigations, the maximum values were generated at 190° than other angles. Power coefficient was gradually increased till the blade angle reached to 190° and later decreased. Because, the rise in arc angle decreases the air entrance width which increases air flow velocity and creates powerful swirling motion on the blade. The reduction in power coefficient was observed when arc angle crossed 190° due to higher mass flow rate and mass moment of inertia which are caused for air flow blockage. At 190°, the power coefficient was 5.18% higher than conventional arrangement (180°). Hence, 190° was considered as optimum arc angle.

40.4 Conclusions

The motto of this work is to generate and utilize power with effective blade geometry of savonius rotor for domestic applications of rural electrification in low wind regions. For that, performance parameters were investigated on SWT (1 m as rotor height and 1 m as chord length) which was fabricated in DBS institute of Technology, Kavali (14.913°N, 79.992°E) by varying four values of overlap (0.3, 0.4, 0.5 and 0.6 m) and five arc angles (180°, 185°, 190°, 195° and 200°) at different tip speed ratios. The conclusions from the experimental observations are listed below.

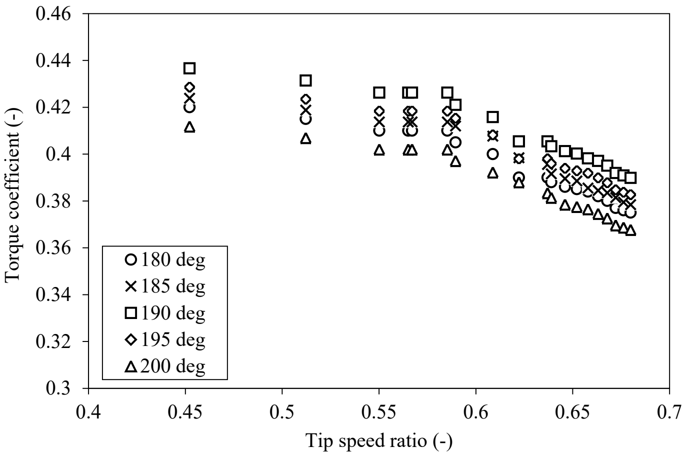

Fig. 40.5 Effect of TSR on torque coefficient at different arc angles

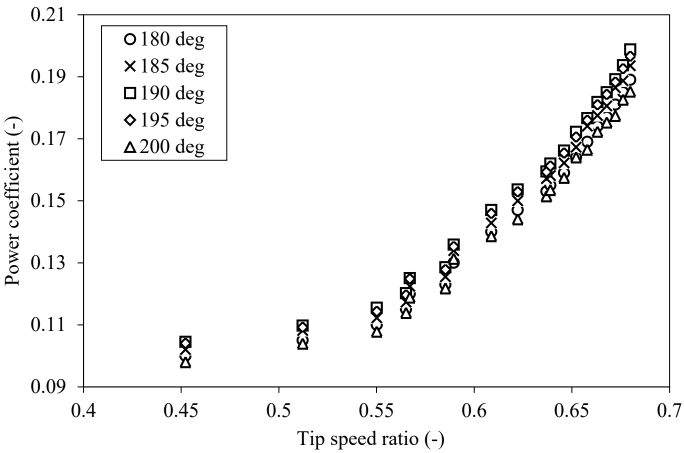

Fig. 40.6 Effect of TSR on power coefficient at different arc angles

- It can conclude from experimental observations that the power coefficients increase with overlap ratio and arc angle, reach maximum at certain values and later decrease with further rise.
- In conventional arrangement (arc angle as 180°), the maximum power and torque coefficients (0.189 and 0.42) were achieved at the overlap value of 0.4 m which was given overlap ratio as 0.2343 compared to other values of overlap (0.3, 0.5 and 0.6 m).
- At optimum overlap distance (0.4 m), the optimum blade arc angle was investigated as 190° where maximum power coefficient (0.1988) and torque coefficient (0.437) were generated than other angles (180°, 185°, 195° and 200°).

References

1. Jian, C., Kumbernuss, J., Linhua, Z., Lin, L., Hongxing, Y.: Influence of phase-shift and overlap ratio on Savonius wind turbine's performance. J. Solar Energy Eng. **134**, 0110161–0110169 (2012)
2. Roy, S., Ujjwal, K.S.: Computational study to assess the influence of overlap ratio on static torque characteristics of a vertical axis wind turbine. Proc. Eng. **51**, 694–702 (2013)
3. Douak, M., Aouachria, Z., Rabehi, R., Allam, N.: Wind energy systems: analysis of the self-starting physics of vertical axis wind turbine. Renew. Sustain. Energy Rev. **81**(1), 1602–1610 (2018)
4. Salazar-Marín, E.A., Rodríguez-Valencia, A.F.: Design, assembly and experimental tests of a Savonius type wind turbine. Sci. Tech. **24**(3), 397–407 (2019)
5. Sobczak, K.: Numerical investigations of an influence of the aspect ratio on the Savonius rotor performance. J. Phys. Conf. Ser. **1101**, 012034 (2018)
6. Kumar, A., Saini, R.P.: Performance parameters of Savonius type hydrokinetic turbine—a review. Renew. Sustain. Energy Rev. **64**, 289–310 (2016)
7. Zemamou, M., Aggour, M., Toumi, A.: Review of Savonius wind turbine design and performance. Energy Proc. **141**, 383–388 (2017)
8. Mahmoud, N.H., El-Haroun, A.A., Wahba, E., Nasef, M.H.: An experimental study on improvement of Savonius rotor performance. Alex. Eng. J. **51**, 19–25 (2012)
9. Pamungkas, S.F., Wijayanto, D.S., Saputro, H., Widiastuti, I.: Performance 'S' type Savonius wind turbine with variation of fin addition on blade. IOP Conf. Series Mater. Sci. Eng. **288**, 012132 (2018)
10. Unsakul, S., Sranpat, C., Chaisiriroj, P., Leephakpreeda, T.: CFD-based performance analysis and experimental investigation of design factors of vertical axis wind turbines under low wind speed conditions in Thailand. J. Flow Control Measurement Visual. **5**, 86–98 (2017)
11. Al-Faruk, A., Sharifian, A.: Geometrical optimization of a swirling Savonius wind turbine using an open jet wind tunnel. Alex. Eng. J. **55**, 2055–2064 (2016)
12. Vivien, S.D., Zharfan, F., Bambang, A.D., Nur, I.: Numerical study of Savonius wind turbines with standard and batch-profile blade variations. AIP Conf. Proc. **2187**, 0200411–0200417 (2019)
13. Albani, A., Ibrahim, M.Z.: Preliminary development of prototype of Savonius wind turbine for application in low wind speed in Kuala Terengganu-Malaysia. Int. J. Sci. Technol. Res. **2**(3), 102–108 (2013)
14. Setiawan, P.A., Indarti, R., Ariwiyono, N., Yuwono, T., Widodo, W.A.: An experimental study of overlap ratio effect to Savonius water current turbine by using Myring equation for $n = 1$. J. Phys: Conf. Ser. **1764**, 012198 (2021)
15. Mohammad, E., Rouzbeh, S., Rezvan, A., Mostafa, S.S.: Numerical investigation of the Savonius vertical axis wind turbine and evaluation of the effect of the overlap parameter in both horizontal and vertical directions on its performance. Symmetry **11**, 821 (2019)
16. Roy, S., Saha, U.K.: Review of experimental investigations into the design, performance and optimization of the Savonius rotor. Proc. Inst. Mech. Eng. Part A J. Power Energy. **227**, 528–542 (2013)
17. Tjahjanaa, D.D.D.P., Arifin, Z., Suyitno, S., Juwana, W.E., Prabowo, A.R., Harsito, C.: Experimental study of the effect of slotted blades on the Savonius wind turbine performance. Theor. Appl. Mech. Lett. **11**, 100249 (2021)
18. Kurniawan, Y., Tjahjana, D.D.D.P., Santoso, B.: Experimental study of Savonius wind turbine performance with blade layer addition. J. Adv. Res. Fluid Mech. Thermal Sci. **69**(1), 23–33 (2020)
19. Rahim, H., Milad, M.: Effects of inward and outward overlap ratios on the two-blade Savonius type of vertical axis wind turbine performance. Int. J. Green Energy **16**(15), 1485–1496 (2019)
20. Tania, R., Florin, R.L., Adriana, I.V.D., Roxana, M., Ancuta, A., Florin, D.: Experimental investigation on the influence of overlap ratio on Savonius turbines performance. Int. J. Renew. Energy Res. **8**(3), 1791–1799 (2018)

21. Alom, N., Saha, U. K.: Arriving at the optimum overlap ratio for an elliptical-bladed Savonius rotor. In: Proceedings of ASME Turbo Expo 2017: Turbomachinery Technical Conference and Exposition. Paper No: GT2017–64137. ASME (2017).
22. Du, Y.: An orthogonal Savonius-type wind turbine: design and experiments. M.Sc. Thesis. Case Western Reserve University (May 2016).
23. Konrad, K., Krzysztof, S.: Computational assessment of the influence of the overlap ratio on the power characteristics of a Classical Savonius wind turbine. Open Eng. **5**, 314–322 (2015)
24. Akwa, J.V., Alvesda Silva Júnior, G., Petry, A.P.: Discussion on the verification of the overlap ratio influence on performance coefficients of a Savonius wind rotor using computational fluid dynamics. Renew. Energy **38**(1), 141–149 (2012)
25. Akhlaghi, M., Ghafoorian, F.: Investigation of arc angle rotor blade variations effect of Savonius vertical axis wind turbine on power and torque coefficients using a 3D modeling. Renew. Energy Res. Appl. **4**(1), 13–19 (2023)
26. Nadhief, M.I., Prabowoputra, D.M., Hadi, S., Tjahjana, D.D.D.P.: Experimental study on the effect of variation of blade arc angle to the performance of Savonius water turbine flow in pipe. Int. J. Mech. Eng. Robot. Res. **9**(5), 779–783 (2020)
27. Alit, I.B., Sri Andyani, I.A., Mirmanto: Effect of overlapping ratio, blade shape factor, and blade arc angle to modified rotor Savonius performances. Int. J. Appl. Eng. Res. **13**(1), 411–416 (2018)
28. Mao, Z., Tian, W.: Effect of the blade arc angle on the performance of a Savonius wind turbine. Adv. Mech. Eng. **7**(5), 1–10 (2015)

Chapter 41
Optimizing Electrical System Performance with Machine Learning: An Analysis of Algorithms

Salava V Satyanarayana and Pillalamarri Madhavi

Abstract The analysis of large amounts of data received from dispatch centers is crucial for the electrical industry, retrieved from various electrical systems such as generation, transmission, and distribution are analyzed using control systems like SCADA and HMI without human intervention. However, to meet the industry 4.0 standards, automation of every system is essential. This can be achieved by integrating the data into the Internet of Things (IoT) with adequate cybersecurity measures. In this regard, this paper proposes the use of intelligent predictive data analysis to optimize the operational maintenance of electrical systems in the future. The research analyzes the recent and historical data using several state electrical utility data files. In order to examine the available data, supervised machine learning algorithms are used, and the analysis of anticipated data is used to assess each algorithm's accuracy.

41.1 Introduction

To reduce human intervention, Electrical Systems retrieve enormous amounts of data from various sources such as Generation, Consumption, and Transmission [1]. Automation of data unification is crucial for various sectors, and security concerns must be taken into consideration to enhance technology. However, linking each file to one another may result in complexities during interfacing with the cloud. As the supply and demand of power increase rapidly, systematic monitoring and controlling of data are essential. Conventionally, Supervisory Control and Data Acquisition (SCADA) is used for data analysis in the electrical system. The primary goal of

S. V. Satyanarayana (✉) · P. Madhavi
Department of Electrical and Electronics Engineering, Hyderabad Institute of Technology and Management, Hyderabad, Telangana, India
e-mail: pshve2011@gmail.com

P. Madhavi
e-mail: madhavipillalamarry@gmail.com

P. H. V. S. Talpa Sai et al. (eds.), *Intelligent Manufacturing and Energy Sustainability*, Smart Innovation, Systems and Technologies 372,
https://doi.org/10.1007/978-981-99-6774-2_41

automation is to improve the efficiency of the electrical system without any data loss, similar to a smart system. This data analysis is useful for future purposes such as Energy Management Systems (EMS) and future electric markets with control algorithms. Various tools and methods are used for analyzing big data to achieve transparency during transferring and interconnecting of the system, which is adaptable for real-time applications. Feedback data can be fed back to optimize appropriate decision-making algorithms without errors and disturbances [2]. Integration of regulatory frameworks with all systems leads to more efficient outcomes.

Industry 4.0 requires the integration of artificial devices with physical systems to execute tasks without human intervention. However, one of the major challenges is the economic challenge [3], as many devices need to be amalgamated with the systems. Big data analytics has several significant applications, including demand-side management, consumption at the utility side, power generation through various sectors, and predicting load-side demand [4]. It can also predict short-term solar power and help manage renewable energy sources for efficient energy management.

Artificial Intelligence (AI) has been making significant contributions to the power grid sector in recent years. It has enabled the development of more efficient, reliable, and sustainable power grids. AI algorithms and techniques are being applied in various aspects of the grid, including generation, transmission, distribution, and consumption. One of the primary applications of AI in the power grid is demand-side management. With the help of machine learning algorithms, AI can predict future energy demands accurately, enabling grid operators to adjust the energy supply accordingly. This helps to balance the load on the grid [5], preventing blackouts or brownouts. Another application of AI in the power grid is in the optimization of power generation. AI algorithms can analyze historical data to predict future energy demand [6] and optimize energy production to meet the demand. This reduces the reliance on fossil fuels, resulting in a more sustainable and environmentally friendly power grid. AI is also being used to improve the efficiency of the grid by detecting and resolving faults in real-time. With the help of AI algorithms, grid operators can identify potential issues and take corrective actions to prevent power outages or other disruptions.

Overall, the integration of AI in the power grid has tremendous potential to revolutionize the way we produce, distribute, and consume energy. It enables a more efficient, reliable, and sustainable power grid [7], which benefits both the consumers and the environment. The use of AI in the electrical industry improves asset reliability, enables effective energy management, and supports the integration of renewable energy sources. With sophisticated systems and decision-making abilities, it equips utilities, operators, and customers to handle the changing problems in the electrical business. For load forecasting, AI methods like time series analysis and neural networks are applied. To effectively estimate future load profiles, these algorithms examine past load data, weather trends, and other pertinent aspects. Utility companies benefit from accurate load forecasts for efficient resource allocation, scheduling, and grid management.

41.2 Machine Learning Algorithms

The effective analysis of a massive amount of data, whether structured or unstructured, is crucial for any system. To achieve this, various machine learning techniques need to be incorporated to classify and solve the problem within a specific time frame. Real-time data analysis [8] manually is complex and impractical as it often contains raw data that is irrelevant to the system. Supervised and unsupervised learning techniques can be used to train and classify the data sets, resulting in efficient and accurate output predictions. Big data analytics is the process of drawing important conclusions and data from enormous and intricate datasets. Due to their ability to automate analysis, pattern identification, and prediction activities, machine learning algorithms are essential to big data analytics. The choice of an acceptable algorithm is influenced by the nature of the problem, the properties of the data, and the desired results. Applications of Machine Learning Algorithms are Fraud Detection, health care and monitoring, Energy Management, Natural language processing social media, and Marketing. These are just a few of the numerous uses for machine learning algorithms. Machine learning is probably going to find more uses as the discipline develops, helping to boost technology and decision-making in a variety of industries.

Supervised Machine Learning

This is the most commonly used learning approach that involves testing and training data sets. The input data is trained first, data should be split as a training data set and test dataset, and then it should be tested using different algorithms to ensure better prediction. Classification and regression are two ways data can be divided. Classification involves mapping labeled input to labeled output, whereas regression involves mapping labeled input to continuous output. The algorithms used in this approach are Support Vector Machine (SVM), Decision Tree, Random Forest, and Naive Bayes. Linear and Logistic algorithms are used under regression.

In supervised learning, the objective is to create a model that can generalize from the labeled training data and produce precise predictions or classifications for hypothetical or a priori events. The steps that commonly make up the procedure are as follows:

Data collection: A labeled dataset is gathered, with each instance being linked to both the input attributes and the output labels for which they are intended. Two sets—a training set and a test/validation set to make up the dataset.

Extraction and selection of relevant features from the input data: Relevant features are extracted from the input data or chosen depending on how well they predict the target variable. To enhance the performance of the model, features can be combined or transformed using feature engineering approaches.

Model training: Using the training set and the chosen algorithm, the model discovers the underlying patterns and connections between the input features and output labels. Iterative parameter adjustments are made to the model to reduce prediction errors.

Model Evaluation: The performance of the trained model is evaluated using the test/validation set. Accuracy, precision, recall, F1 score, and area under the ROC curve (AUC-ROC) are examples of common evaluation metrics.

Model tuning: If the performance of the model is unsatisfactory, the algorithm's hyperparameters can be changed to enhance performance. Prior to training, hyperparameters are set to control how the learning algorithm behaves.

Prediction/Inference: After the model has been trained and assessed, it may be used to predict or classify previously unobserved fresh data by incorporating the discovered patterns into the input features.

It serves as the foundation for numerous practical applications, including spam identification, picture recognition, medical diagnosis, and language translation.

Unsupervised Machine Learning

In this approach, unlabeled data sets are analyzed with reference to the previous one, and proper predictions are made by clustering data. This technique is used to identify patterns in data sets that are not properly labeled or classified as per the requirement. K-Means clustering is an essential algorithm used under unsupervised data. Exploratory data analysis, data preprocessing, feature engineering, and data visualization frequently make use of unsupervised learning methods. Even when the actual labels or results are unclear, they can reveal underlying structures and offer insightful analyses of the data. Unsupervised learning's main objective is to identify inherent structures or groupings in the data without the aid of labels or prior knowledge. Algorithms for unsupervised machine learning are employed in several applications across numerous industries. Listed below are a few typical applications for unsupervised machine learning algorithms like clustering, video analysis, Natural language processing, and data preprocessing.

41.3 Analyzing the Electrical Data Using Machine Learning Algorithms

The diagram depicts the workflow for predicting electricity usage trends across different states over the years (Fig. 41.1). This involves analyzing labeled data using supervised machine learning algorithms, which will enable the prediction of future electricity consumption patterns with safe and secure [9]. The analysis will provide insights into the projected power usage of different states in the upcoming year, and the accuracy of the predictions from each algorithm (Logistic Regression, Decision Tree Classifier, Random Forest classifier, Naïve Bayes, and Support vector Machine) will be evaluated to determine the best-performing method. With this approach, the prediction will be easy with an effective supervised machine algorithm.

From the figures, using Python libraries like Pandas or NumPy to import and work with datasets in a code cell within the notebook (Figs. 41.2, 41.3). It consists

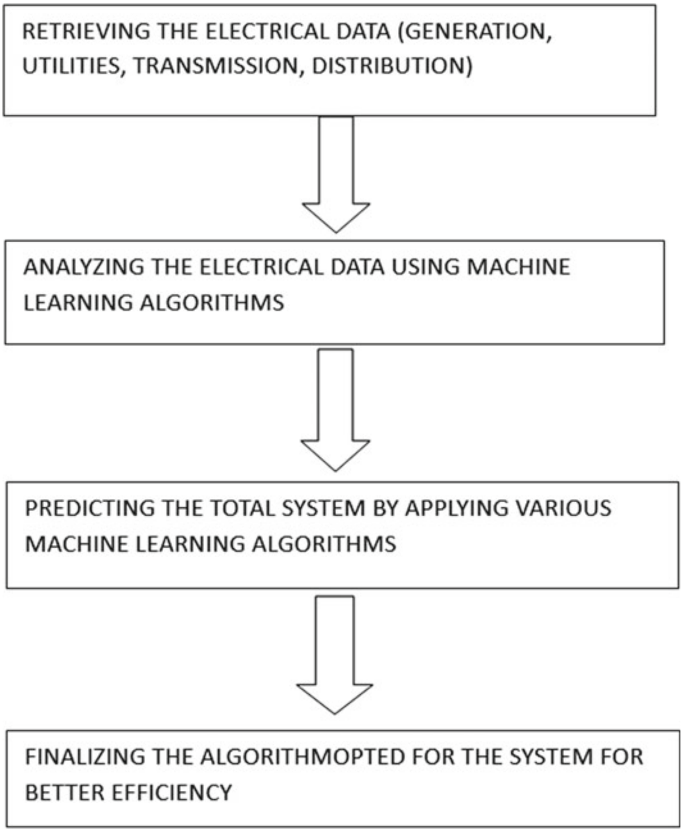

Fig. 41.1 Flow of analyzing the data using different machine algorithms

of two methods to import datasets using libraries, they are: importing a dataset from a local file (local disk) and importing a dataset through a URL. Depending on the CSV file (Consumption of electricity by various states), libraries like pandas (Provide data structures like Data Frames and Series that make it simple to handle, clean up, and preprocess structured data. Pandas are frequently used to perform operations on datasets such as data cleansing, filtering, grouping, merging, and transformation), NumPy (Offers support for sizable matrices and multidimensional arrays, as well as a range of mathematical operations to effectively work with these arrays. Linear algebra, numerical computations, and data manipulation all frequently include the use of NumPy.), and seaborn (It offers a complex interface for designing eye-catching and educational statistical visuals. Heatmaps, violin plots, and pair plots are just a few of the complex visuals that Seaborn makes easier to create).

The above figures clearly represent the accuracy of different supervised Machine Learning Algorithms to predict the state-wise utilizing power from generating

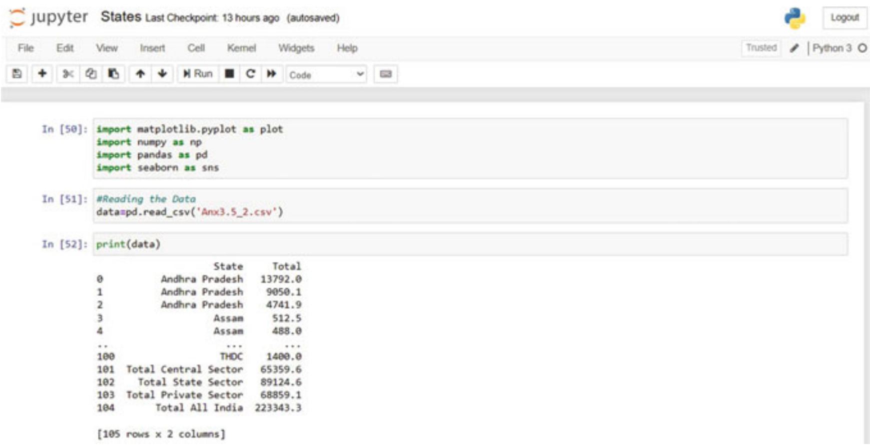

Fig. 41.2 Imported utility file for different states

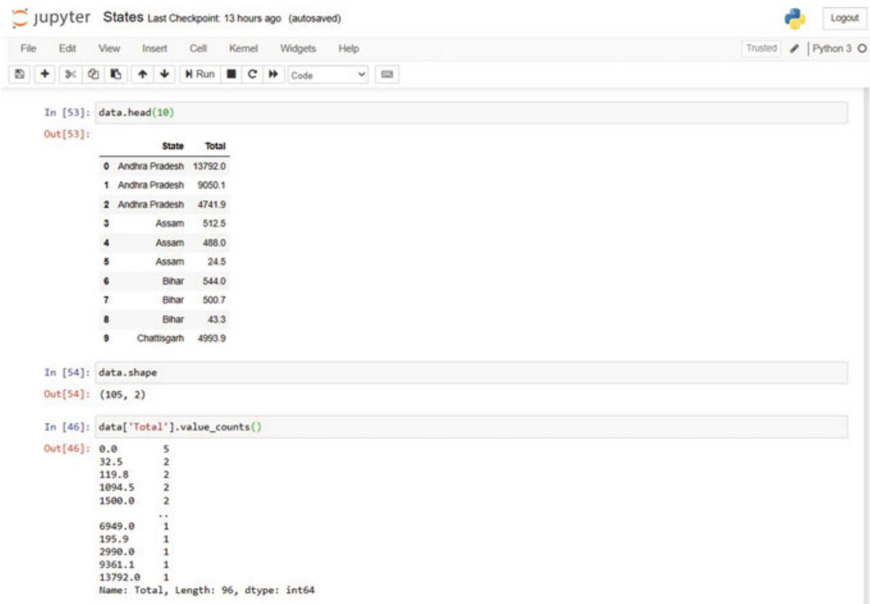

Fig. 41.3 Retrieving the data from the data set

sources like Hydro, Thermal-Steam, Thermal-Diesel, Thermal-gas, Nuclear, Renewable and overall consumption (Figs. 41.4, 41.5, 41.6).

The objective is to predict future data associated with the "Consumption of various states" data file, utilizing machine learning algorithms such as Logistic Regression, which uses previous years' data to estimate future data which gives an accuracy of

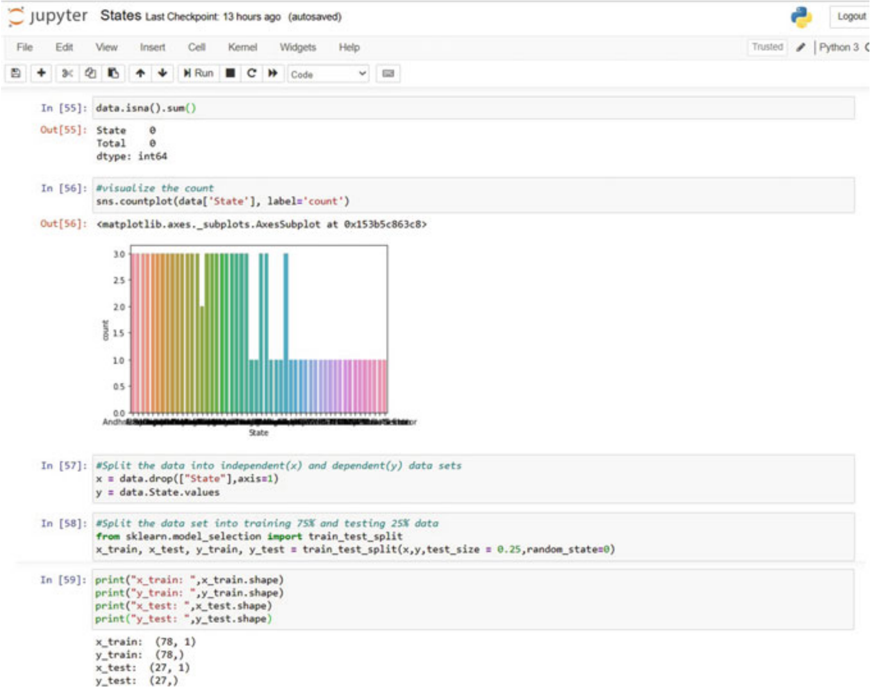

Fig. 41.4 Graphical representation of data using Matplotlib and training the data

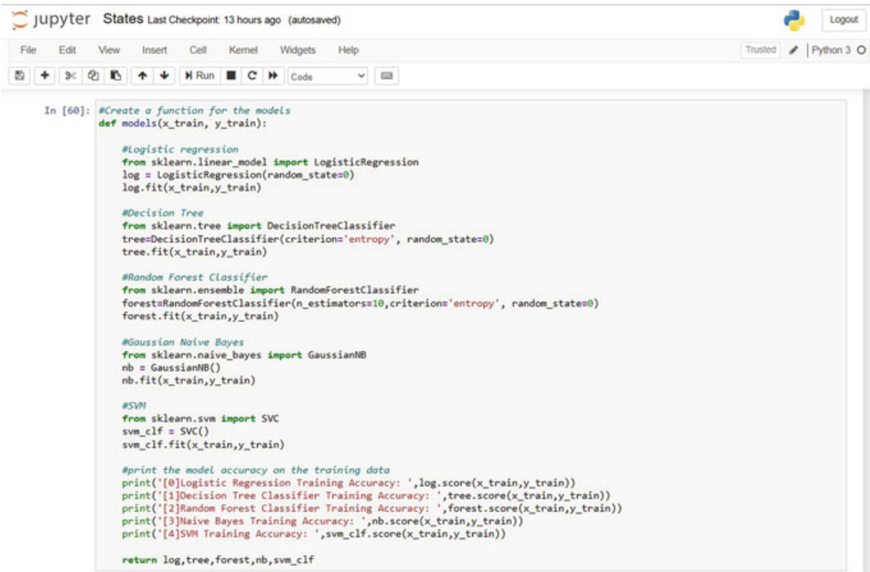

Fig. 41.5 Testing the data set for different supervised machine learning algorithms

```
In [61]: #Getting all the models
model = models(x_train,y_train)

C:\Users\Madhu\anaconda3\lib\site-packages\sklearn\linear_model\_logistic.py:940: ConvergenceWarning: lbfgs failed to converge
(status=1):
STOP: TOTAL NO. of ITERATIONS REACHED LIMIT.

Increase the number of iterations (max_iter) or scale the data as shown in:
    https://scikit-learn.org/stable/modules/preprocessing.html
Please also refer to the documentation for alternative solver options:
    https://scikit-learn.org/stable/modules/linear_model.html#logistic-regression
  extra_warning_msg=_LOGISTIC_SOLVER_CONVERGENCE_MSG)
[0]Logistic Regression Training Accuracy:  0.01282051282051282
[1]Decision Tree Classifier Training Accuracy:  0.9358974358974359
[2]Random Forest Classifier Training Accuracy:  0.8333333333333334
[3]Naive Bayes Training Accuracy:  0.47435897435897434
[4]SVM Training Accuracy:  0.16666666666666666
```

Fig. 41.6 Accuracy for the different algorithms

0.012, and Decision Tree Classifier, which determines accuracy based on specific decisions made through probability conditions given a data set, i.e., 0.935, Random Forest Classifier, which calculates the probability for one to all by combining all decisions which give an accuracy of 0.833, Naïve Bayes Classifier, which applies Bayes theorem to calculate the probability of each class to output the main class which gives an accuracy of 0.474, and Support Vector Machine, which defines functions according to hyperplanes [10] which gives an accuracy of 0.166. By implementing the sci-kit learn approach in SVM, provides accurate predictions that can be made with higher efficiency with more accuracy.

41.4 Conclusion

By utilizing Machine Learning algorithms, predictions can be made for future years based on a given dataset. In the case of the aforementioned dataset, different algorithms yielded a different accuracy, which indicates Decision Tree Classifier can be used and followed by a Random Forest Classifier to calculate power consumption for various states' predictions for upcoming years. As a result, it can be concluded that utilizing Machine Learning Algorithms simplifies data analysis and enhances the accuracy of predictions for electrical systems.

References

1. Shawkat, M.I.F., et al.: Application of machine learning techniques for power system analysis. Int. J. Electr. Power Energy Syst. (2019). https://doi.org/10.1016/j.ijepes.2019.03.018
2. Chakraborty, S., et al.: Machine learning techniques for electrical load forecasting: a review. IEEE Trans. Power Syst. (2019). https://doi.org/10.1109/TPWRS.2018.2884176
3. Mirjalili, H., et al.: Application of machine learning techniques for fault diagnosis in electrical power systems: a review. Renew. Sustain. Energy Rev. (2020). https://doi.org/10.1016/j.rser.2020.110160
4. Li, F., et al.: Machine learning approaches for fault diagnosis in electrical machines: a review. IEEE Trans. Industr. Electron. (2020). https://doi.org/10.1109/TIE.2020.2975459

5. Kavousi-Fard, K.E., et al.: Machine learning for the analysis of electrical grid data: a review. Renew. Sustain. Energy Rev. (2020). https://doi.org/10.1016/j.rser.2020.110261
6. Rani, B.K., et al.: Application of machine learning algorithms for wind turbine condition monitoring: a review. J. Clean. Prod. (2021). https://doi.org/10.1016/j.jclepro.2021.127617
7. Alshehri, A.M., et al.: Machine learning-based approach for fault detection and diagnosis in photovoltaic systems. Renew. Energy (2019). https://doi.org/10.1016/j.renene.2019.03.050
8. Shafie-khah, M.J., et al.: Machine learning for anomaly detection in smart grid communication networks. Sustain. Cities Soc. (2020). https://doi.org/10.1016/j.scs.2020.102563
9. Zhu, B., et al.: A review of machine learning for cybersecurity applications in the electric power industry. Electric Power Syst. Res. (2021). https://doi.org/10.1016/j.epsr.2021.107130
10. Madhavi, P., Satyanarayana, S.V.: Data Analysis of electrical systems using machine learning algorithms. In 2022 First International Conference on Artificial Intelligence Trends and Pattern Recognition (ICAITPR), Hyderabad, India pp. 1–4 (2022). https://doi.org/10.1109/ICAITPR51569.2022.9844178.

Chapter 42
Performance Analysis of a Parabolic Trough Collector

Harvinder Singh and Harpreet Kaur Channi

Abstract TRNSYS® software simulates a parabolic trough collector (PTC) with a phase change material (PCM) solar water heating system. The simulation predicts hot water supply during morning and evening peak demand. The main heat transfer fluid (HTF) in PTC is lauric acid (LA), whereas the secondary HTF is water. The research simulates a medium-temperature, concentrated parabolic trough collector without solar tracking. TRNSYS® simulation components have been fully explored utilizing a Type 1245 parabolic trough collector with a Type 533 horizontal storage tank with heat exchangers, which meets home and industrial hot water needs. The storage tank is vertically stratified to adjust the HTF temperature from the collector. The findings indicated that LA, with a thermal conductivity of 0.862 kJ/h-mK, gives a peak energy gain of 17,600 kJ/h in February and 4000 kJ/h in July, and a 950 F temperature increase for Chandigarh, India. The city's weather yields 24% yearly collector efficiency.

42.1 Introduction

Due to population expansion, technology, and contemporary lifestyles, worldwide energy consumption is growing. Since the 1960s, fossil fuels have depleted and destroyed the environment [1]. Therefore, renewable energy researchers and scientists are working hard to find new energy sources [2]. Globally, solar energy is plentiful. Due to its sustainability and environmental friendliness, solar energy is a better alternative energy source. If 0.1% of solar energy, or 1.08 × 1014 kW, is captured using a 10% efficient solar energy conversion system, 3 TW of energy may be obtained, four times the worldwide installed capacity [3]. The food and petrochemical sectors may utilize this thermal energy to fuel Rankine cycles in "solar thermal" power plants. 398 °C thermal energy is available from parabolic troughs. The maximum temperature is limited by thermal oil's rapid degradation around

H. Singh · H. K. Channi (✉)
Department of Electrical Engineering, Chandigarh University, Mohali, Punjab 140413, India
e-mail: harpreetchanni@yahoo.in

P. H. V. S. Talpa Sai et al. (eds.), *Intelligent Manufacturing and Energy Sustainability*, Smart Innovation, Systems and Technologies 372,
https://doi.org/10.1007/978-981-99-6774-2_42

398 °C. However, 500 °C fluids are in development. A linear parabolic reflector transmits solar energy onto an absorber pipe in PTC systems. The absorber pipe generates steam for a steam turbine. 30,000 m^2/MW and 3.9–4.5 m^3/MWh of water are needed for PTCs.

8% of power output goes to large plant operation and maintenance. PTCs are straightforward to employ with TES and backup systems [4]. This lets the facility run at night and in bad weather. Thus, peak demand dispatch ability is ensured by steady-state, full-load energy production [5]. Chandigarh is India's port city with the most residences. Solar water heating saves electricity in homes. To alleviate SDHWS difficulties for Chandigarh residents, a parabolic trough collector is modeled in TRNSYS® software using LA PCM as HTF and storage material. This primary HTF heats cold water from a smaller HTF. Heat is removed by the secondary HTF and given to the end-user load at setpoint temperature [6]. The study's objective was to solar water heating system viability. For a 10-person shared unit, the study provides SDHW at 400 °C.

42.2 Types of Solar Collectors

Several solar collector types are shown in Fig. 42.1 and will be addressed more below:

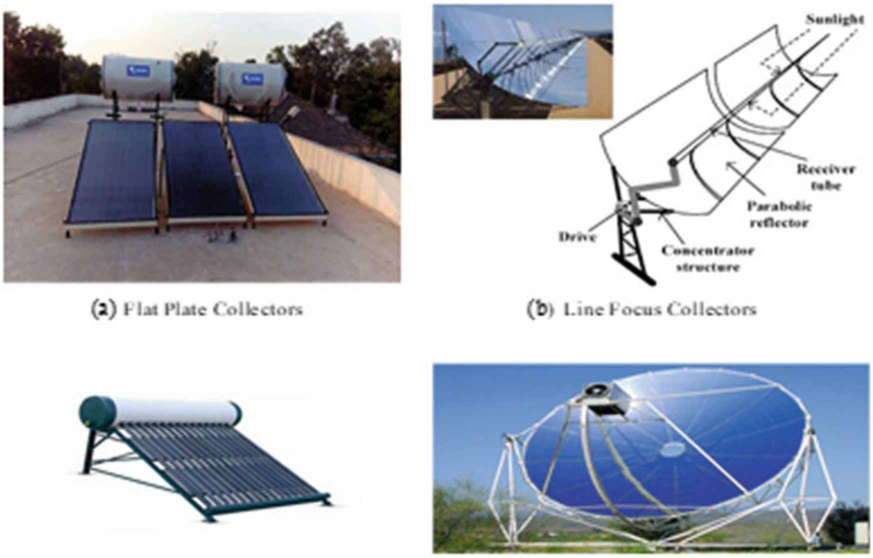

(a) Flat Plate Collectors
(b) Line Focus Collectors
(c) Evacuated Tube Collectors
(d) Parabolic-Dish Collectors

Fig. 42.1 Types of solar collector

- Flat Plate Collectors

Flat plate collectors are the most prevalent. Glass-covered metal boxes with black absorber plates. These copper or aluminum plates transmit well. Instead of black paint, heat-absorbing coatings may cover these absorber panels. Renewable Energy Sources chose parabolic trough collection and absorber tube sizes. Water operates. The experimental arrangement is closed-circuit [7].

- Evacuated Tube Collectors

Vacuum tube solar water heaters use evacuated tubes. Its heating pipe contains many parallel, clear glass tubes. Vacuum tubes heat water. Sunlight powers these vacuum tubes. Tubes limit heat loss [8].

- Line Focus Collectors

Target line solar collectors, often called parabolic troughs, heat water or air by collecting heat on an absorber plate. Thus, enormous solar thermal power plants use them to create steam. Water flows over this trough. Reflecting material directs sunlight onto this central pipe system. Pivot troughs capture solar energy by tracking the sun [9].

- Point Focus or Parabolic-Dish Collectors

Point focus large parabolic collectors reflect. The absorber plate concentrates sun energy like other solar collectors. Stirling engines want to heat self-use parabolic dishes. Sun tracking optimizes collecting and cooperating PV modules. The need to examine long-term machine performance and prospects to improve optical efficiency or cut costs by adopting new reflectors and absorbent materials pushed the change in viewpoint [10].

42.3 Literature Review

To simulate the turbulent flow in a parabolic solar collector tube, Moradi et al. [11] used two spring insert samples with different pitch ratios (P/D = 0.22, 0.44) and a defined cross-section [12]. Another researcher said this study focused on decreasing Therminol VP1 cracking and heat loss in parabolic trough concentrators [11]. Pourmoghadam and Kasaeian [13] tested PTC-powered solar multi-generation systems—performance assessment and solar assistance capacity optimization.

Allauddin et al. [14] examined how changing the absorber tube's inner wall shape affects PTC performance. It used an absorber tube geometry with circumferential inclined ribs [14]. Dutt et al. [15] designed and tested a parabolic flat plate solar collector for water-closed circulation at 12, 15, and 18 LPM. A parabolic trough collector receiver tube with elliptical dimpled fins of different elliptical ratios (ER = 0.66–1.66) was examined by Pazarlıoğlu et al. [16]. This study introduced a triangular solar air collector (TSAC) by Jiang et al. [17]. TSAC may be coated with insulating material (TSAC_1), transparent cover plate (TSAC_2), or double transparent cover plate (TSAC_3) to adapt to varied climates [17].

Nagappan et al. [18] examined a serially linked solar-powered ejector refrigeration system. For the same specification, the ejector system utilized 2.475 kW less power than the traditional refrigeration system [18]. A unique parabolic trough array solar water heater system was tested by Madadi Avargani et al. [19]. In full tracking mode, a tilt accuracy mistake of 6° reduces thermal efficiency by 10%, whereas an azimuth accuracy error of 20° does not [19]. Benhadji Serradj et al. [20] showed that CSP plants might reduce greenhouse gas emissions during electricity generation and meet considerable energy demand.

42.4 Methodology

Figure 42.2 shows the absorption system systematic evaluation of the parabolic trough collector, flat plate, and evacuated tube solar collectors used to produce heat for space heating, domestic hot water, or cooling. The steady-state thermal analysis evaluates how constant thermal hundreds impact a system or factor. It covers literature review, resource assessment, resource assessment sources, solar collector metrological data collecting, temperature and humidity data for a specific location, and resource assessment tool size calculation due to July's lower ambient temperature and the collection's bigger temperature differential, higher in a year. Project work is organized in this system flow chart diagram. Work is the failed goal.

- Feasibility study of solar collector for the water heating system at the proposed home.

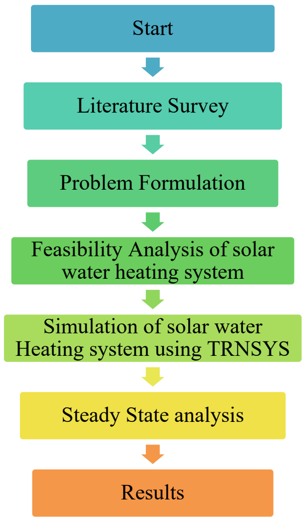

Fig. 42.2 Methodology flow chart

- Designing, modeling, and simulation of solar hot water system using the TRNSYS Software.

The following methodology is used to achieve the above objective, as shown in Fig. 42.2. The lower ambient temperature lowers the PTC's intake temperature, causing a greater temperature differential and raising the collector's thermal efficiency. The city's weather provides an average yearly efficiency of 26%.

42.5 Parameters of a Parabolic Trough System

- Overall Heat Loss Coefficient

The receiver tube loses some heat to the environment. Heat loss depends on convective, conductive, and radiative coefficients. Performance evaluation requires calculating the machine's estimated heat loss coefficient. Higher warmth loss coefficients indicate lesser warmth resistance and efficiency.

- Heat Removal Factor

If the whole receiver was at fluid intake temperature, the heat removal issue would reveal the ratio of the genuine beneficial electrical advantage to the good strength advantage. The input and outflow fluid temperatures, the tube's size, and other factors determine it. Heat-removal components' value depends on machine performance. The machine's heat removal charge should be lower.

- Collector efficiency factor

Every collector design has a constant collector efficiency component, and fluid follows the flow rate. This compares real beneficial strength increase to what would happen if the fluid temperature at the receiver tube surface were attained.

- Thermal efficiency

Every collector design has a constant collector efficiency component, and fluid follows the flow rate. This compares real beneficial strength increase to what would happen if the fluid temperature at the receiver tube surface were attained.

42.6 Site Selection and Load Estimation

India has favourable conditions for solar energy generation because to its 300–350 sunny days and 1500–2000 sunshine hours per year. This study replicates Chandigarh at its actual coordinates of 30°44′14′N–76°47′14′E. Chandigarh, a major port, has an annual average of 2,400 h of sunlight, with January seeing the most and July seeing the least. The development and improvement of a theoretical model calls for the use

Table 42.1 Optimum tilt angle in Chandigarh

January	February	March	April	May	June
26°	30°	26°	16°	8°	8°
July	August	September	October	November	December
8°	12°	20°	30°	26°	24°

of interpolations. Parameters are necessary for models. Complicating lab settings might include run time, social, and budgetary concerns, and compromises. Building and simulating natural systems is the job of simulation modelling tools. There are 160.642 square metres of open space.

Table 42.1 shows the optimum tilt angle in Chandigarh from Jan to Dec. They are very important for solar collector direction; likewise, 1-year data are displayed. With modern heat pumps or water storage heating systems, domestic hot water (DHW) has become popular. However, we're more acquainted with it than we think. Hot water needs in liters/day (250 LPD) and required temperature (40 °C) in Chandigarh. This is daily hot water consumption on Winter day in the home. There are four members and they are using hot water in winter 150 Littre per day. Every day in the kitchen, we use 10 L in a day. This depends upon how it is temperate and the member; this is not fixed and depends upon the sun. When the sun mot was coming than using an Electricity approx. Solar 1 kwh make unit 4, and unit combustion is 10 unit. Every day in the kitchen, 10 L is used a day. Bathing takes 30–50 gallons every day. 250 L solar water heaters are perfect for 3–4 person families.

42.7 Simulation

The three essential components of the finite element modeling approach are pre-processing, answer processing, and submit processing, as shown in Fig. 42.3. With the APPAL command /PREP, the pre-processor is dedicated to starting this portion of the model generation procedure. For the pre-processor, FORTRAN is programmed to enable the use of complex thermal principles to handle the entire set of parameters, including geometries and thermal hundreds. Following the pre-processing phase, we start the response phase using the /SOUL and resolve commands.

42.7.1 TRNSYS® Simulation Model

There are two loops in the TRNSYS® simulation model. The first loop is made up of. Heat Transfer Fluid pump, Phase Change Material stored in tank Parabolic Trough Collector, and a different control and switch the pump on and off. In 2nd loop is made up of heat coils, a flow diverter, and a water draw forcing function to simulate

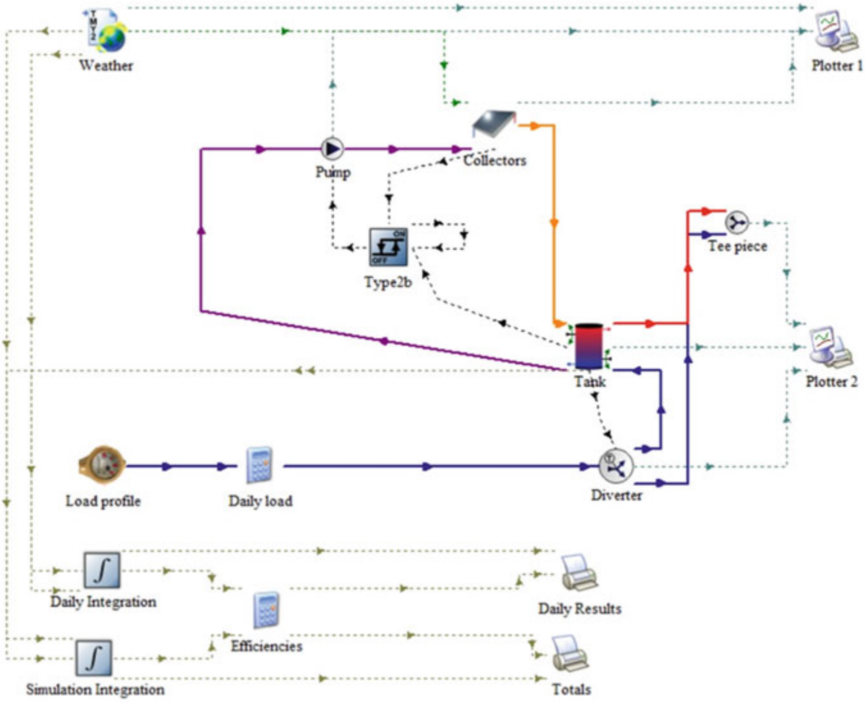

Fig. 42.3 Simulation model

the system. The energy from the sun is captured by the first loop utilizing phase change material, which is then stored in the Lightning Arrester Parabolic Trough Collector. The heated water is delivered to the outlet, which extracts the stored energy. Figure 42.2 displays TRNSYS' environment's system components. The following is a full description of each element. This simulation uses the Parabolic Trough Collector (Type 1245) from the library of basic TESS solar thermal collectors. In concentrated PTC without sun track settings is the type 1245 Phase Change Material. The absorber and Heat Transfer Fluid is housed in an evacuated glass tube behind an outside reflecting concentrator. The end user can adjust the flow rate via the collector to keep the outlet temperature constant. A system is linked to the storage Tank. Solar arrays are made up of Heat Transfer Fluid concentrators used in this System.

42.7.2 Pump

HTF is pumped and drawn by two system components. Type 110 variable-speed pumps provide liquid PCM to the collector. FCT is forced into the storage tank heat exchanger by type 14b water pull. The pulse code modulation flow rate is 500 kg/h

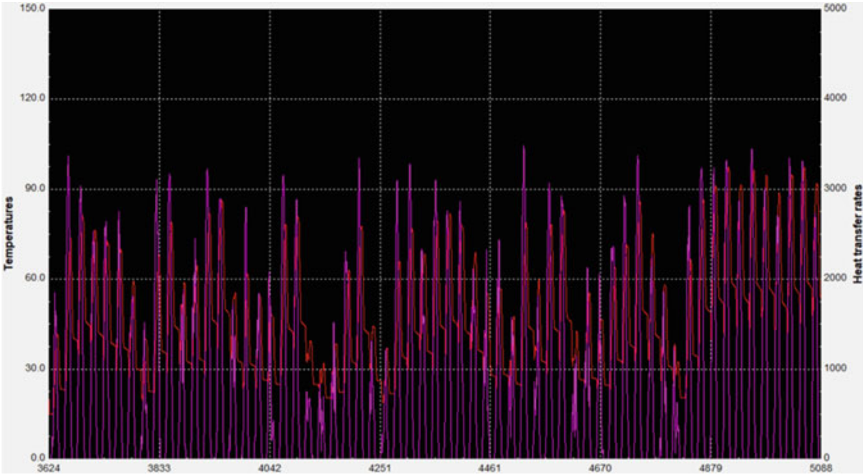

Fig. 42.4 HTF mass flow rate for February

to keep the HTF temperature below Lauric acid degradation. Speed pump controlled via the differential controller. The pump activates when the PTC's input and output temperatures differ by 200 °C.

42.7.3 Tee Piece Connector and Diverter

A tempering valve and flow mixer provide hot water. Type 11b tempering valve, flow diverter with temperature control. The temperature-controlled flow diverter distributes water to the tank according to the hot water leaving the top and the cold water entering. A flow mixer blends hot and cold water to deliver hot water to the hot shower output. Figure 42.4 depicts the tempering valve action.

42.7.4 PCM Horizontal Storage Tank

The energy storage fluid is contained in immersed heat exchangers that are part of the stored tank component, a fixed volume in the tank. Water flowing through heat exchanger coils reacts as LA PCM material used to fill the tank. This component lets the user choose between three heat exchangers: serpentine, tube, and coiled. The user specifies that this system uses heat exchangers and storage tank fluids.

42.8 Steady State Analysis

A steady-state thermal analysis determines how constant thermal hundreds affect a system or factor. We often conduct a controlled country study before doing a brief thermal research for setting up beginning circumstances. After all short findings, a consistent country evaluation is the first phase of a brief thermal examination. We employ this steady-state thermal analysis to determine temperatures, thermal gradients, warmth drift prices, and warmth fluxes in an item or a system that may be caused by thermal loads that are constant across time.

- Convection
- Solar radiation
- The charge for heat flow
- Heat flux
- Costs of heat production
- Persistent temperature challenges

42.9 Results and Discussion

The Chandigarh SDWH simulation is examined. This simulation used TRNSYS to simulate family data. This family of five uses 250 L. Water. Capacity = 50 people × 5 = 250 L. Feb, July, and Dec are simulated. Figures 42.4, 42.5 and 42.6 show February, July, and December PTC intake, exit, LA mass flow rate, and beam radiation data. PTC's entry temperature is above 350 °C, LA's transition temperature, but its output temperature is well below 3000 °C, LA's degradation temperature. The graph shows the mass flow rate of HTF turned ON with a 200 °C difference between Parabolic's intake and exit temperatures through the collector. Figures 42.4, 42.5 and 42.6 are useful. February and December provide 19,660 and 17,000 kJ/h, respectively. July's useable energy gain was 5047 kJ/h, lower than the previous two months. The energy gain numbers for February, July, and December may be justified by the radiation values of 1023, 520, and 936 W/m^2. Heat loss in the absorber tube reduces efficiency and energy gained. Reduce ambient temperatures reduce the PTC's input temperature, increasing the temperature difference and the collector's thermal efficiency. The city's weather averages 26% efficiency.

42.10 Conclusion

This simulation of a full-filament system is carried out with the help of the TRNSYS® program. Employed PCM material was utilized to store heat, and a Type 1245 Parabolic collector component and a Type 533 horizontal tank with a heat exchanger were used. Using LA thermal properties allows for simulating heat transfer fluids

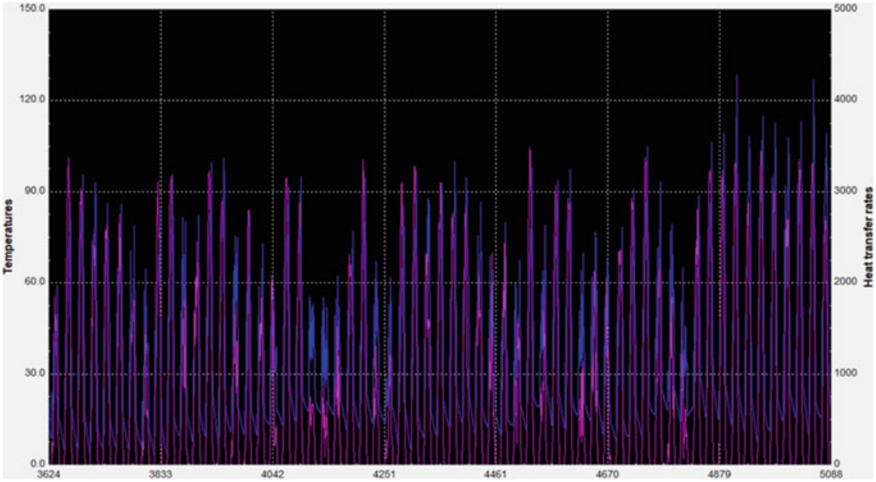

Fig. 42.5 HTF mass flow rate for July

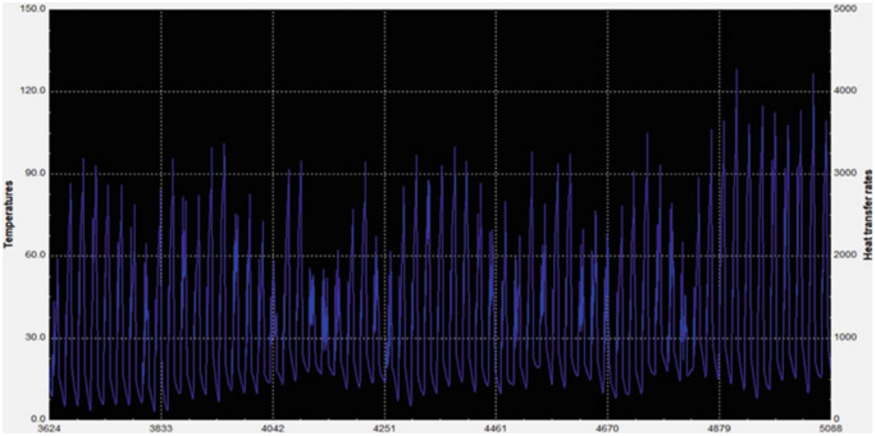

Fig. 42.6 HTF mass flow rate for December

in Parabolic via collection tanks. Fill the tank with hot water. Because less beam radiation hits this area during July, the temperature at the PTC output is lower than during the other two months. The collector's efficiency improves in July as a direct consequence of the region's lower ambient temperature during the month of July and a bigger temperature differential throughout the collection. This leads us to conclude that the thermal efficiency is improved when the incoming air temperature is lowered. Because the existing system is employed to fulfill residential SDHW needs, the temperature at the entry of the Parabolic through collector cannot be decreased by using many heat exchangers. The findings indicate that using PCM for storage makes it feasible to distribute hot water even at ungodly hours, such as early in the morning or late at night, when doing so traditionally would be challenging with buildings. As a consequence of this, we can conclude that natural systems use more units.

References

1. Baqir, M., Channi, H.K.: Analysis and design of solar PV system using Pvsyst software. Mater. Today Proc. **48**, 1332–1338 (2022)
2. Kumar, R., Channi, H.K.: A PV-biomass off-grid hybrid renewable energy system (HRES) for rural electrification: design, optimization and techno-economic-environmental analysis. J. Clean. Prod. **349**, 131347 (2022)
3. Kaur, H., Kaur, I.: Optimization and control of hybrid renewable energy systems: a review. Cogn. Inf. Soft Comput. Proc. CISC **2019**, 483–500 (2020)
4. Pandey, S., Channi, H. K.: Roof top solar installation: a case study. TEST Eng. Manage. Scopus **2020**, 15629–15633 (2020)
5. Channi, H.K.: Techno economic feasibility analysis of solar PV system in Jammu: a case study. In: Solar Cells-Theory, Materials and Recent Advances. IntechOpen (2021)
6. Channi, H.K., Kaur, I.: EROI analysis of 2 KW PV system. In: Intelligent Computing in Engineering: Select Proceedings of RICE 2019, pp. 665–671. Springer Singapore (2020)
7. Geete, A.: Performance analyses of coal-fired thermal power plant using parabolic solar collectors for feed water heaters. Aust. J. Mech. Eng. **20**(2), 332–343 (2022)
8. Büker, M.S., Parlamış, H., Alwetaishi, M., Benjeddou, O.: Experimental investigation on the dehumidification performance of a parabolic trough solar air collector assisted rotary desiccant system. Case Stud. Therm. Eng. **34**, 102077 (2022)
9. Saray, J.A., Heyhat, M.M.: Modeling of a direct absorption parabolic trough collector based on using nanofluid: 4E assessment and water-energy nexus analysis. Energy **244**, 123170 (2022)
10. Subramaniam, B.S.K., Sugumaran, A.K., Athikesavan, M.M.: Performance analysis of a solar dryer integrated with thermal energy storage using PCM-Al2O3 nanofluids. Environ. Sci. Pollut. Res. **29**(33), 50617–50631 (2022)
11. Moradi, H., Mirjalily, S.A.A., Oloomi, S.A.A., Karimi, H.: Performance evaluation of a solar air heating system integrated with a phase change materials energy storage tank for efficient thermal energy storage and management. Renew. Energy **191**, 974–986 (2022)
12. Bhandari, K.P., Collier, J.M., Ellingson, R.J., Apul, D.S.: Energy payback time (EPBT) and energy return on energy invested (EROI) of solar photovoltaic systems: a systematic review and meta-analysis. Renew. Sustain. Energy Rev. **47**, 133–141 (2015)
13. Pourmoghadam, P., Kasaeian, A.: Economic and energy evaluation of a solar multi-generation system powered by the parabolic trough collectors. Energy **262**, 125362 (2023)
14. Allauddin, U., Rafique, M.U., Malik, O., Rashid, O., Waseem, A., King, P., Karim, M., Almond, H.: Investigation of the thermo-hydraulic performance of a roughened parabolic trough collector. Appl. Therm. Eng. **219**, 119523 (2023)
15. Dutt, N., Kumar, R., Murugesan, K.: Experimental performance analysis of multi-parabolic flat plate solar collector. In: Emerging Trends in Mechanical and Industrial Engineering: Select Proceedings of ICETMIE 2022 (pp. 159–172). Singapore: Springer Nature Singapore (2023)
16. Pazarlıoğlu, H.K., Ekiciler, R., Arslan, K., Mohammed, N.A.M.: Exergetic, energetic, and entropy production evaluations of parabolic trough collector retrofitted with elliptical dimpled receiver tube filled with hybrid nanofluid. Appl. Therm. Eng. **223**, 120004 (2023)
17. Jiang, Y., Zhang, H., Zhao, R., Liu, Z., Wang, Y., You, S., Wu, Z., Wei, S.: Thermal and optical performance analysis of triangular solar air collectors and regional applicability in China. Sol. Energy **249**, 288–300 (2023)

18. Nagappan, B., Devarajan, Y., Kariappan, E.: Performance analysis of sustainable solar energy operated ejector refrigeration system with the combined effect of Scheffler and parabolic trough collectors to lower greenhouse gases. Environ. Sci. Pollut. Res. **29**(32), 48411–48423 (2022)
19. Madadi Avargani, V., Divband, M.: Performance evaluation of a solar water heating system with glass-covered parabolic trough concentrators, under different system tracking modes. J. Therm. Anal. Calorim. **147**(7), 4873–4888 (2022)
20. Benhadji Serradj, D.E., Sebitosi, A.B., Fadlallah, S.O.: Design and performance analysis of a parabolic trough power plant under the climatological conditions of Tamanrasset, Algeria. Int. J. Environ. Sci. Technol. **19**(4), 3359–3376 (2022)

Chapter 43
PLL Based Photovoltaic System of LCL Three-Phase Grid Connected Inverter with and Without SVPWM Technique

Naga Surya Kiran Rayavarapu and Chandra Sekhar Obbu

Abstract A photovoltaic (PV) system uses the sun's energy to produce electricity in an endless supply. PV systems are integrated with traditional residential and commercial electrical systems to satisfy the consumer side's electrical energy needs. This paper explains power conversion stages between PV panel to three phase utility grid. PV panel requires a power interfacing circuit to make electric isolation and maximize the voltage with adjusted duty cycle. Power interfacing circuit with a dc link will deliver the power to three phase utility grid by connecting three phase voltage source inverter (VSI). However, semiconductor switching in inverter cause harmonics. Such harmonics can be suppressed by using LCL type grid connected filter. Meanwhile for VSI, a phase locked loop (PLL) based algorithm and a current control feedback technique is employed in the circuit with the help of Direct-Quadrature (dq) theory and PWM techniques like Space vector pulse width modulation (SVPWM) and Sinusoidal pulse width modulation (SPWM). Simulation results are carried out for active power injection from PV panel to the constant three phase utility grid.

43.1 Introduction

Over the past few years, the demand for PV systems has been continuously rising due to a number of causes like cost reduction, government incentives, energy security, environmental concerns and technological advancements. PV systems are installed in outdoor environments and exposed to various weather conditions, temperature and partial shading results voltage fluctuations. In such cases a conventional DC–DC converters with fixed duty cycle are failed to draw maximum power. This paper presents a specified power interfacing circuit with adjusted duty cycle. An isolated

N. S. K. Rayavarapu (✉) · C. S. Obbu
Department of Electrical Engineering, National Institute of Technology Delhi, New Delhi, India
e-mail: 212231005@nitdelhi.ac.in

C. S. Obbu
e-mail: obbuchandra@nitdelhi.ac.in

P. H. V. S. Talpa Sai et al. (eds.), *Intelligent Manufacturing and Energy Sustainability*, Smart Innovation, Systems and Technologies 372,
https://doi.org/10.1007/978-981-99-6774-2_43

DC–DC converter improves PV system efficiency in terms of maximizing the power and voltage by adapting suitable MPPT algorithm like Perturb and observe (P and 0) and Incremental conductance algorithm (INC). PV systems can produce high voltages and currents, when it is subjected to a fault or malfunction, like as a short circuit, excessive heat or sparks can be generated. During maintenance or in the event of grid outage utility workers are trying to repair the grid. To protect the utility grid, equipment's and utility workers from electric socks, electrical fires, PV system demands isolation. An Isolated transformer is required for to provide isolation between input to output of the DC-DC converter. A high-power electronic converter circuit, such as a three-phase VSI or current source inverter (CSI) [1], is necessary to operate the utility grid [2, 3]. For inverter fixed dc voltage is obtained from DC link with lower ripple voltage. However, power converters include semiconductor switches. Such switching transients introduce rapid change in the output voltage or current, causing distortions in the waveform. These distortions manifest as harmonic components, which are the integer multiples of fundamental frequency of the system (typically grid frequency). Due to these harmonics voltage and current faces power quality issues. Such harmonics are suppressed by most commonly used LCL type grid connected filter. For grid synchronization with a three phase AC utility grid, a technique called PLL algorithm is required. For to control active power flow from the PV system, a specially employed current control feedback scheme has been proposed in dq frame theory [4]. Additionally, for to drive the VSI this paper presents two PWM schemes known as SPWM and SVPWM for block diagram (Fig. 43.4).

43.2 Solar PV Module

Solar PV modules or panels are a type of power generator that transform solar energy into electrical current. Solar cells are the smallest part in solar PV system. The power endless source generated from selected PV system deliver to the consumer in various power conversion stages. The PV system at highest irradiance levels, will produce more current and power. At Standard test conditions (STC), Power and voltage curve of PV module is shown in the Fig. 43.1. In the proposed model under STC parameter of PV module are mentioned in the Table 43.1. Various power converters and controlled mechanism discussed in the following sections.

43.3 Isolated DC–DC Converter

Conventional DC–DC converters [5, 6] may not be able to efficiently convert the low and variable voltages in the PV module in satisfying the load requirements. A power interfacing circuit is required to extracts maximum power from PV panel with adjusted duty cycle [7] and additionally isolation is required to protect from faulty conditions and during maintenance. To address these issues isolated DC-DC

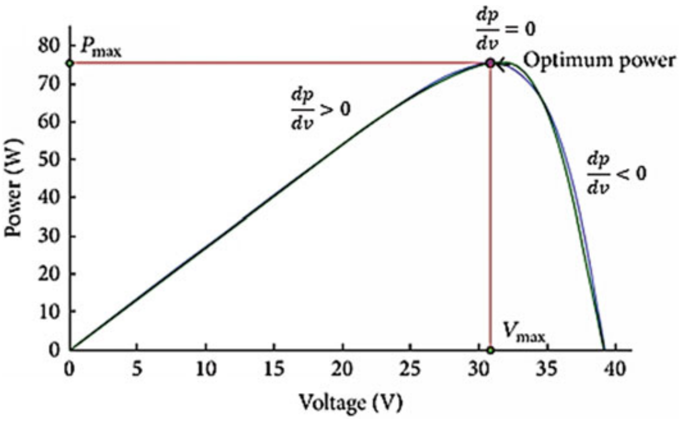

Fig. 43.1 Power and voltage (pv) curve for solar panel

Table 43.1 Parameters of PV module

Parameters name	Symbol	Value
Maximum power	*Pmpp*	213.15 W
MPP voltage	*Vmpp*	29 V
MPP current	*Impp*	7.35 A
Irradiance	*Irad*	1000 W/m^2
Temperature	T	25°C
Open circuited voltage	*Voc*	36.3 V

converter with input capacitor [8] is proposed in this paper. In primary side of the isolated converter consists of a full bridge configuration of power switches, typically comprised of four switches (e.g., transistors or MOSFETs). These switches are connected parallel with input voltage source. The complete bridge's switching action can be done for applied input voltage from transformer primary winding. On the secondary side of the transformer winding has a center tapped. The two ends of the secondary winding are connected to the rectifier circuit or output filter. The center tap of the secondary winding is typically connected to the common ground reference for both the input and output sides. When the primary switches are turned on and off in a specific sequence, the input voltage is modulated. This action induces an alternating magnetic field in the transformer, which is coupled to the secondary winding. The centre tap of the secondary winding provides a reference point, ensuring the electrical isolation between input and output.

43.4 Incremental Conductance Algorithm (INC)

P & O and INC [9] are two effective and simple tracking MPPT algorithms. INC [10] does not require any knowledge of the PV array model or parameters, which simplifies the control system design and makes it more flexible for different PV array types and configurations. A floating voltage is provided by the P & O algorithm, which always rounds up to the maximum voltage. The maximum voltage is precisely established via in incremental conductance technique. When using INC, the controller continuously monitors changes in the voltage and current of PV array. PV panel power is described in the Eq. 43.1.

$$P = V.I \tag{43.1}$$

Differentiate Eq. 43.1 with respect to voltage attains Eq. 43.2.

$$\frac{1}{V}\frac{\Delta P}{\Delta V} = \frac{I}{V} + \frac{\Delta I}{\Delta V} \tag{43.2}$$

when slope is 0, Eq. 43.2 rewritten as Eq. 43.3 denotes the maximum power point condition at saddle point named as optimum power shown in Fig. 43.1.

$$\frac{\Delta I}{\Delta V} = -\frac{I}{V} \tag{43.3}$$

Similarly, slope may negative or positive, Eq. 43.2 can be rewritten as Eq. 43.4 or 43.5.

$$\frac{\Delta I}{\Delta V} < -\frac{I}{V} \tag{43.4}$$

$$\frac{\Delta I}{\Delta V} > -\frac{I}{V} \tag{43.5}$$

The logic behind INC algorithm implemented in the flow chart as shown in the Fig. 43.2 that loop never terminates until it reaches to MPP.

$$V_{ref} = V_{mpp} \tag{43.6}$$

Equation 43.6 defines the operating point under STC. Maximum power point (MPP) changes with respect to change in weather conditions. Therefore, algorithm always tracks the new voltage either decrease or increasing to one perturb voltage value ΔV at new MPP condition (Fig. 43.3).

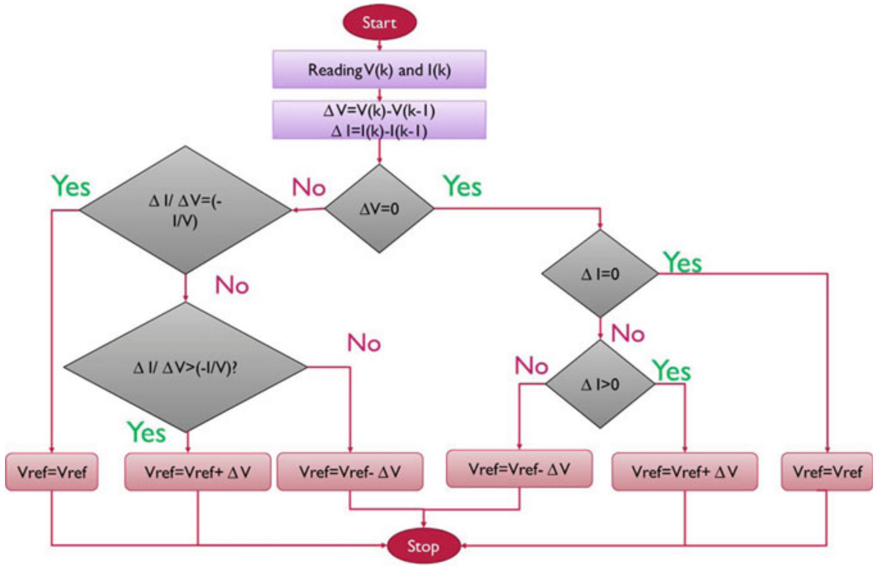

Fig. 43.2 Incremental conductance algorithm flow chart

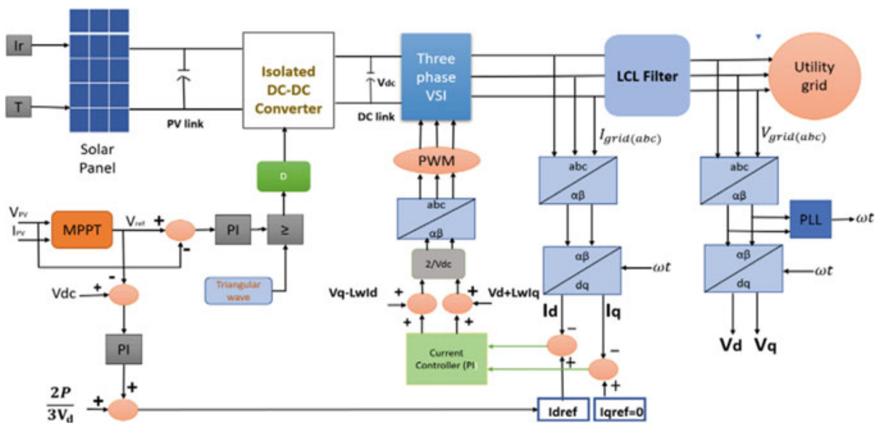

Fig. 43.3 Block diagram for PLL based PV of system LCL three phase grid connected inverter

43.5 DC Link

Generally DC link buffers the voltage. The output power of three phase utility grid can be resolved into two components by expanding the Eq. 43.7 into Eq. 43.8. First term indicates active power and other is the power consumed by capacitor DC link [11]. The maximum value of DC link capacitor can be calculated by considering in terms of apparent power (S) is given as Eq. 43.9.

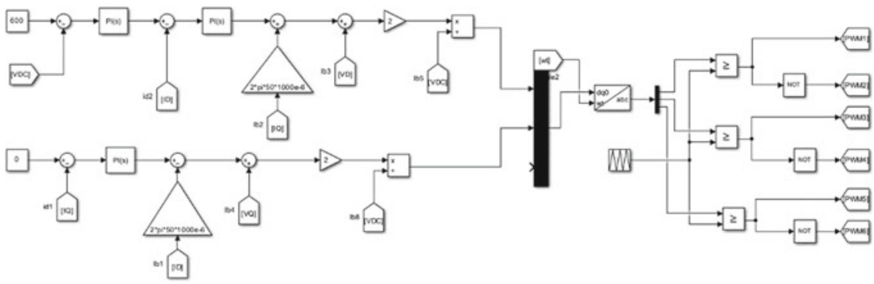

Fig. 43.4 Current control blocks for active power injection

Table 43.2 Parameters of isolated DC–DC converter

Parameters name	Symbol	Value
PV output power	p	120 KW
Input voltage	V_{in}	306 V
Output voltage	V_{out}	600 V
PV link	C_{pv}	12.01 mf
DC link	C_{dc}	12.01 mf

$$P_{grid} = V_{peak} I_{peak} Sin^2 w_g t \tag{43.7}$$

$$p_{grid} = \frac{V_{peak} I_{peak}}{2} - \frac{V_{peak} I_{peak}}{2}.\cos(2w_g t) \tag{43.8}$$

$$C_{dc} = \frac{s}{2W_g V_{dc} \Delta V} V_{peak} I_{peak} Sin^2 w_g t \tag{43.9}$$

Voltage ripple across capacitor can be considered as ΔV it is inversely proportional to capacitance. The value of capacitor closes to its magnitude of Eq. 43.9 is mentioned in Table 43.2.

43.6 Three Phase Grid Tied LCL Inverter

43.6.1 Voltage Source Inverter (VSI)

VSI is typically supplied with a DC voltage from a power source [10]. It utilizes modulation techniques like PWM to generate an required AC output voltage waveforms. The desired AC waveform is approximated by creating a series of high frequency pulses with varying widths. It consists of switching devices, typically insulated gate bipolar transistors (IGBTs) or power MOSFETs, which are generally used to control the flow of current from the available DC source to the grid. These switching devices act as electronic switches that can rapidly turn on and off. When it is turned off, the current is blocked. By rapidly switching the devices on and off, the VSI synthesizes an AC waveform with the desired voltage magnitude, frequency, and phase.

43.6.2 LCL Filter Design

An LCL filter [12–16] is an advanced filter configuration that includes two inductors (L) and a capacitor (C). It offers better harmonic attenuation and resonance damping capabilities compared to L or LC filters [17]. The LCL filter inductor is connected in series with the grid, followed by a capacitor, and then another inductor is connected in series with the load. This arrangement helps in reducing harmonics and provides improved damping characteristics for resonance issues. The second inductor acts as a load-side filter, enhancing the overall performance of the filter. Grid tied inverter Capacitor in LCL filter consumes reactive power (Q_c) 5% of its rated power (S) refer Eqs. 43.11 and 43.12 and it values in the Table 43.3.

$$Q_c = \frac{V_g^2}{(1/(2\pi f c))} \tag{43.10}$$

$$C = \frac{5\% S}{2\pi f V_g^2} \tag{43.11}$$

Maximum allowable inductance L_{max} in three phase utility grid considered as 20% of grid voltage drop refer Eq. 43.12. Each inductor in LCL filter is half of it's maximum value.

$$L_{Total} = \frac{20\% V_g^2}{2\pi f S} \tag{43.12}$$

Table 43.3 Parameters of LCL

Parameters Name	Symbol	Value
Inductor 1	L1	500 μh
Capacitor	C_1	100 μf
Inductor 2	L2	500 μh

43.6.3 DQ Theory

DQ transformation is applied to the three-phase quantities (voltages or currents) of the VSI to convert them into two-phase variables known as park and Clarke transformation. By applying the DQ transformation to the rotating components, that are associated with the grid frequency, are separated from the direct components. This allows an independent control on the active and reactive power flow between the VSI and the utility grid.

$$m_d = \frac{2}{V_{dc}}(U_d - Lwi_q + v_d) \tag{43.13}$$

$$m_q = \frac{2}{V_{dc}}(U_q - Lwi_d + v_q) \tag{43.14}$$

The D-axis, Q-axis are active power and reactive power component. Active power is responsible for the true power exchange between the VSI and the utility grid. Reactive power exchange and helps to regulate the voltage. By controlling the D-axis, the VSI can regulate the active power flow to the grid, enabling power injection. The Q component can be controlled to maintain a desired power factor. Active power can be controlled by using current control feedback technique implemented for three phase AC star connected utility grid. Grid parameters are rated power 100 KVA, 400 V phase to phase voltage and frequency of 50 Hz (Figs. 43.4, 43.5). DQ frame controls of a VSI with PLL algorithm system achieves accurate in synchronization with the grid. It helps to control active and reactive power flow independently with the help of phase angle from phase generation refer Fig. 43.6. To drive three phase VSI, PWM requires three phase AC quantities obtained from current control inputs U_d and U_q as shown in Eqs. 43.13 and 43.14. By providing reverse transformation technique with input of modulation index from current controller drives the power circuit VSI [18].

43.7 SPWM Technique

In this PWM, reference sinusoidal waveform amplitude is higher than the carrier waveform, a logic high signal is generated. Conversely, when the reference sinusoidal waveform amplitude is lower, a logic low signal is generated. The duration of the logic high signal, known as the pulse width. By adjusting the pulse width of each phase's PWM signal, the inverter can approximate a sinusoidal output voltage. The triangular carrier wave ensures that the transitions between logic high and low states are smooth, resulting in reduced harmonic content in the output waveform. Therefore, with the help of PWM signals DC input convert into a three-phase AC output with the desired voltage and frequency and THD is shown in Figs. 43.6, 43.7 and 43.8.

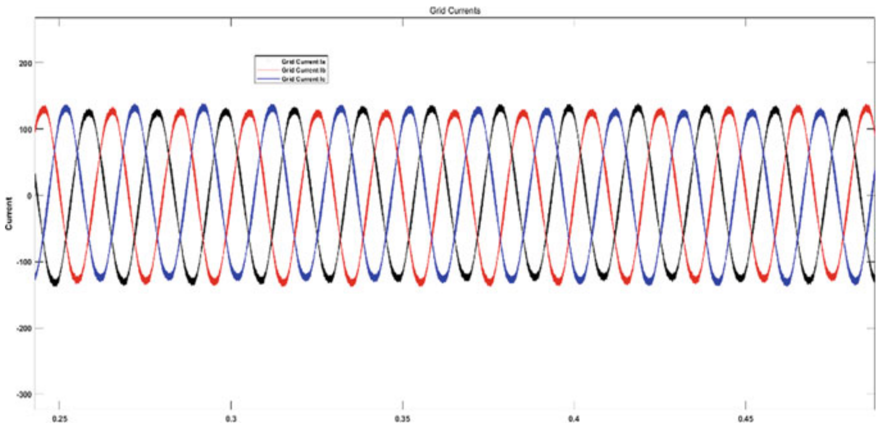

Fig. 43.5 Grid current wave forms using SPWM

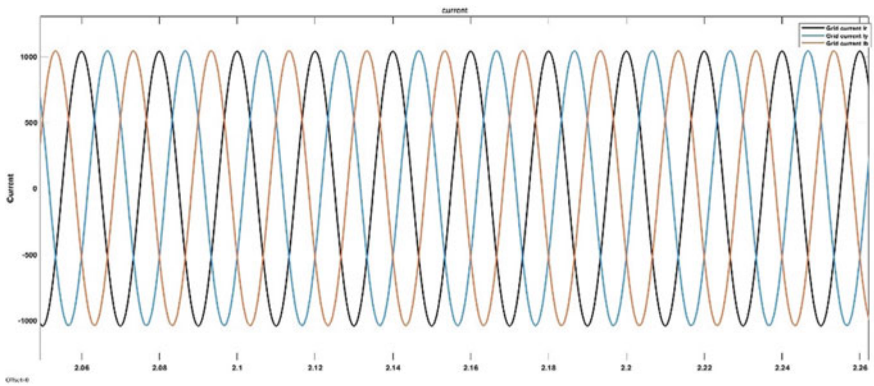

Fig. 43.6 Grid current wave forms using SVPWM

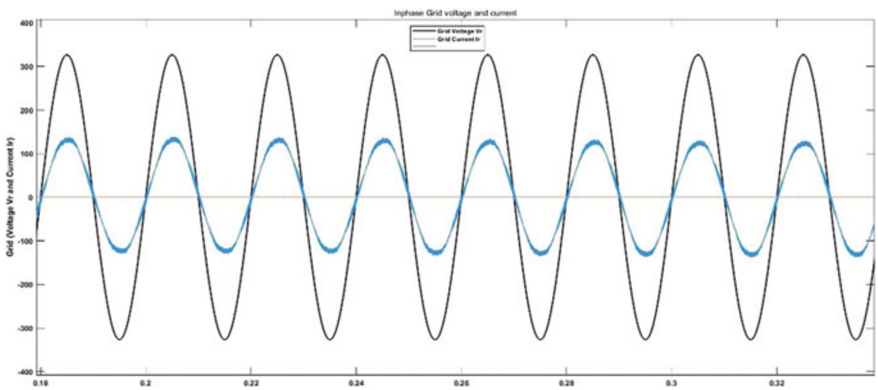

Fig. 43.7 In-phase voltage and current wave forms for active power injection ($I_{qref} = 0$)

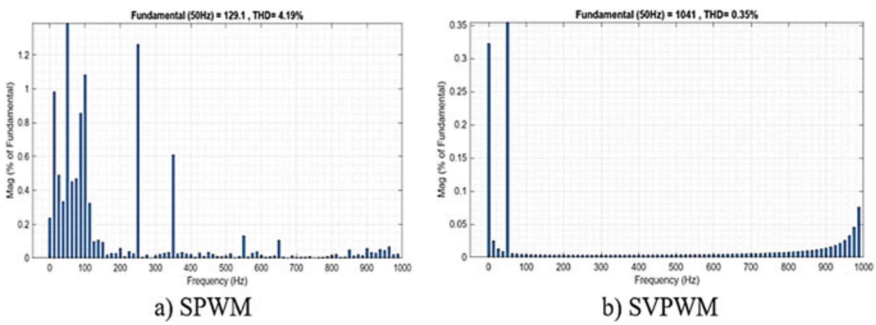

Fig. 43.8 THD for grid current using **a** SVPWM and **b** SVPWM

43.8 SVPWM Technique

In this advanced modulation technique used in three-phase Voltage Source Inverters refer [19–21] (VSI) to generate high-quality three-phase AC voltages from a DC input. It converts the three-phase system into a two-dimensional space vector representation and calculates the duration and switching states of six power semiconductor switches to approximate the reference vector. SVPWM has several advantages over traditional modulation techniques, such as improved utilization of DC link voltage, higher voltage utilization factor, lower harmonic distortion, and better dynamic response. It is commonly used in applications requiring precise control over voltage magnitude and frequency. Here the current control feedback improves injected grid currents from Fig. 43.7 and THD reduced shown in Fig. 43.8.

43.9 Conclusion

The first foremost advantage is the Electrical isolation of PV system from grid connected inverter in terms of protection and maintenance during faults. Secondly, under STC of irradiance and temperature an efficient INC algorithm type helps to draw the maximum power from Photovoltaic system and maximizing the voltage with the help of adjusted duty cycle. While observing grid voltage and grid currents wave-forms are in-phase each other and THD in the currents less than 5% improved by using a LCL filter. PLL algorithm support the system for grid synchronization. Therefore, active power generated from source will deliver the power efficiently to constant grid. THD is reduced further in the proposed MATLAB model by using SVPWM technique compared to SPWM technique in Fig. 43.8.

References

1. Azmi, S. A., Ahmed, K. H., Finney, S. J., Williams, B. W.: Comparative analysis between voltage and current source inverters in grid-connected application. In: IET Conference on Renewable Power Generation (RPG 2011), pp. 101–101 (2011)
2. Mohammed, A.Y., Mohammed, F.I., Ibrahim, M.Y.: Grid connected photovoltaic system. In: 2017 International Conference on Communication, Control, Computing and Electronics Engineering (ICCCCEE), pp. 1–5. IEEE (2017)
3. Pal, B., Sahu, P. K., Mohapatra, S.: A review on feedback current control techniques of grid-connected PV inverter system with LCL filter. In: 2018 Technologies for Smart-City Energy Security and Power (ICSESP), pp. 1–6 (2018)
4. Keawthai, S., Po-Ngam, S.: Simplified active power and reactive power control with MPPT and islanding detection for three-phase grid-connected photovoltaic inverters. In: 2015 12th International Conference on Electrical Engineering/Electronics, Computer, Telecommunications and Information Technology (ECTI-CON), pp. 1–6. IEEE (2015)
5. Radhika, S., Margaret, V.: A review on dc-dc converters with photovoltaic system in dc micro grid. J. Phys. Conf. Ser. **1804**(1), 012155 (2021)
6. Chouder, A., Silvestre, S., Sadaoui, N., Rahmani, L.: Modeling and simulation of a grid connected PV system based on the evaluation of main PV module parameters. Simul. Model. Pract. Theory **20**(1), 46–58 (2012)
7. Hussein, H.A., Mahdi, A.J., Abdul-Wahhab, T.M.: Design of a boost converter with MPPT algorithm for a PV generator under extreme operating conditions. Eng. Technol. J. **39**(10), 1473–1480 (2021)
8. Nasiri, M., Chandra, S., Taherkhani, M., McCormack, S.J.: Impact of input capacitors in boost converters on stability and maximum power point tracking in PV systems. In: 2021 IEEE 48th Photovoltaic Specialists Conference (PVSC), pp. 1004–1008. IEEE (2021)
9. Mohamed, S.A., Sattar, M.A.E.: A comparative study of P&O and INC maximum power point tracking techniques for grid-connected PV systems. SN Appl. Sci. **1**(2), 174 (2019)
10. Radhia, G., Mouna, B.H., Lassaad, S., Barambones, O.: MPPT controller for a photovoltaic power system based on increment conductance approach. In: 2013 International Conference on Renewable Energy Research and Applications (ICRERA), pp. 73–78. IEEE (2013)
11. Memon, M.A., Mustafa Bhutto, G., Buriro, E.A.: Sizing of DC-link capacitor for a grid connected solar photovoltaic inverter. Indian J. Sci. Technol. **13**(22), 2272–2281 (2020)
12. Suyata, T.-I., Po-Ngam, S.: Simplified active power and reactive power control with MPPT for three-phase grid-connected photovoltaic inverters. In: 2014 11th International Conference on Electrical Engineering/Electronics, Computer, Telecommunications and Information Technology (ECTI-CON), pp. 1–4. IEEE (2014)
13. Hamza, K.A.E.W., Linda, H., Cherif, L.: LCL filter design with passive damping for photovoltaic grid connected systems. In: IREC2015 The Sixth International Renewable Energy Congress, pp. 1–4. IEEE (2015)
14. Huang, M., Blaabjerg, F., Yang, Y., Wu, W.: Step by step design of a high order power filter for three-phase three-wire grid-connected inverter in renewable energy system. In: 2013 4th IEEE International Symposium on Power Electronics for Distributed Generation Systems (PEDG), pp. 1–8. IEEE (2013)
15. Mejía-Ruiz, G.E., Rodríguez, J.R., Paternina, M.R.A., Muñoz-Galeano, N., Zamora, A.: Grid-connected three-phase inverter system with LCL filter: model, control and experimental results. In: 2019 IEEE PES Innovative Smart Grid Technologies Conference-Latin America (ISGT Latin America), pp. 1–6. IEEE (2019)
16. Liu, Y., Jin, D., Wang, H., Wang, G., Peng, J., Yin, S.: Double closed-loop control strategy of LCL three-phase grid-connected inverter. In: IECON 2017–43rd Annual Conference of the IEEE Industrial Electronics Society, pp. 1107–1112. IEEE (2017)
17. Agrawal, N., Singh, V.K., Kumar, J., Dubey, P., Yadav, A., Kumar, G., Shende, S.K., Singh, H.: Study of filters for improving the output of cascaded seven-level inverter. In: Electronic Systems

and Intelligent Computing: Proceedings of ESIC 2021, pp. 187–196. Singapore: Springer Nature Singapore (2022)
18. Gautam, S., Agrawal, S.: Performance analysis of grid interactive PV system with PLL controlled three phase inverter. In: 2021 International Conference on Smart Generation Computing, Communication and Networking (SMART GENCON), pp. 1–6. IEEE (2021)
19. Zeng, Q., Chang, L., Song, P.: SVPWM-based current controller with grid harmonic compensation for three-phase grid-connected VSI. In: 2004 IEEE 35th Annual Power Electronics Specialists Conference (IEEE Cat. No. 04CH37551), vol. 4, pp. 2494–2500. IEEE (2004)
20. Harrabi, N., Spiegel De Almeida, J., Laboudi, K.: European Journal of Electrical Engineering. Methods **2**:3 (2021)
21. Lakshmanan, S.A., Rajpourhit, B.S., Jain, A.: Modeling and analysis of 3-phase VSI using SPWM technique for grid connected solar PV system. In: 2014 IEEE Students' Conference on Electrical, Electronics and Computer Science, pp. 1–6. IEEE (2014)

Chapter 44
Predicting Compressive Strength of Self-Repairing Concrete Using Artificial Neural Networks

B. Damodhara Reddy, Panga Narasimha Reddy, S. Aruna Jyothy, M. Mohan Babu, and Bode Venkata Kavyatheja

Abstract In this study, an extensive simulation program was employed to determine the optimal artificial neural network (ANN) model for effectively forecasting the compressive strength of concrete. The prediction accuracy was based on the mineral admixture variation and crystalline admixture variation. To achieve this, a comprehensive experimental database consisting of 200 samples was compiled from existing literature and utilized to identify the most suitable ANN architecture. The primary objective of this research paper was to utilize an ANN to forecast the strength properties of self-repairing concrete (SRC) incorporating different mineral admixtures and a crystalline admixture. A total of 200 samples with various concrete mixtures were analyzed after a 28-day curing period. The ANN model was trained using the experimental data, which included four input parameters: exposure type (ET), crystalline admixture variation (CAV), mineral admixture variation (MAV) and mineral admixture (MA). The output parameter of interest was the concrete strength (Fc). Notably, the investigational data exhibited a significant correlation with the values forecast by the ANN model. In conclusion, the findings indicate that an ANN can accurately assess the strength characteristics of SRC. The utilization of ANN in this context holds promise for evaluating SRC strength properties with precision.

B. Damodhara Reddy (✉) · P. Narasimha Reddy · M. Mohan Babu
Department of Civil Engineering, Sri Venkateswara College of Engineering and Technology (Autonomous) (SVCET), R.V.S. Nagar, Chittoor, Andhra Pradesh, India
e-mail: damu2007@gmail.com

S. Aruna Jyothy
Department of Civil Engineering, Sri Venkateswara University College of Engineering, Tirupati, Andhra Pradesh, India

B. Venkata Kavyatheja
Department of Civil Engineering, JNTUA College of Engineering, Kalikiri, Andhra Pradesh, India

P. H. V. S. Talpa Sai et al. (eds.), *Intelligent Manufacturing and Energy Sustainability*, Smart Innovation, Systems and Technologies 372,
https://doi.org/10.1007/978-981-99-6774-2_44

44.1 Introduction

Concrete is widely recognized as one of the most extensively used building materials globally due to its affordability and ability to withstand significant compressive loads. However, it is not impervious to damage and deterioration over time. Microcracks can develop within the concrete matrix, which can compromise the structural integrity and significantly reduce the lifespan of civil infrastructure. The presence of these cracks allows hazardous chemicals, such as chloride ions and carbon dioxide, to penetrate the concrete, leading to corrosion of the reinforcing steel and subsequent degradation of the material. This phenomenon has resulted in substantial financial losses and poses a significant challenge for the maintenance and repair of existing concrete structures.

To address this issue, extensive research has been conducted in recent years on the development of self-repairing concrete (SRC). SRC possesses the remarkable ability to autonomously heal and seal cracks that occur within the material. Inspired by the natural healing process observed in living organisms, self-repairing concrete aims to mimic this phenomenon and provide an innovative solution to enhance the durability and longevity of concrete structures [1–3].

One critical aspect in the study of self-repairing concrete is the prediction of its compressive strength. The compressive strength of concrete is a vital parameter that determines its ability to bear loads and resist deformation. Accurate prediction of this strength property is crucial for ensuring the structural integrity and safety of concrete elements. Traditional methods of predicting concrete strength often rely on empirical models based on experimental data. However, these models may have limitations in accurately capturing the complex behavior and unique characteristics of self-repairing concrete [4–6].

In recent years, artificial neural networks (ANNs) have emerged as a promising tool for predicting the compressive strength of concrete. ANNs are computational models inspired by the biological neural networks of the human brain. They can effectively learn and generalize patterns from large datasets, making them well-suited for modeling complex and nonlinear relationships in concrete properties [7–10].

The utilization of artificial neural networks for predicting the compressive strength of self-repairing concrete offers several advantages. ANNs can handle a wide range of input parameters, including the percentage of mineral admixture and crystalline admixture, which have a significant influence on the strength properties of self-repairing concrete. Additionally, ANNs can capture the intricate interactions and dependencies between these input parameters, providing a more comprehensive understanding of the relationship between material composition and compressive strength.

Several studies have been conducted on predicting the compressive strength of self-repairing concrete using artificial neural networks (ANNs). Smith et al. [1] focused on the prediction of compressive strength using an ANN model trained with a comprehensive dataset. Similarly, Lee et al. conducted a comparative study of prediction models and evaluated the performance of ANNs in predicting the strength of self-repairing concrete. Wang et al. proposed an optimization approach using a hybrid algorithm to improve the accuracy of an ANN model for predicting compressive strength. Gupta et al. explored the combination of ANNs and particle swarm optimization to enhance the accuracy of strength prediction in self-healing concrete. Additionally, Chen et al. investigated the application of recurrent neural networks (RNNs) in predicting the compressive strength of self-healing concrete, emphasizing the temporal dependencies captured by RNNs. Johnson et al. [2] focuses on recent advancements in predicting concrete strength using artificial neural networks. It explores the use of ANN models in predicting compressive strength and discusses the influence of various factors such as mineral admixture and curing time. The review also highlights the challenges and opportunities associated with ANN modeling in the context of self-repairing concrete. Chen et al. [3] provides an in-depth analysis of the application of ANN for predicting the strength properties of self-repairing concrete. It discusses the selection of input parameters, model training, and validation techniques. The review also presents case studies and compares the performance of different ANN models in predicting compressive strength. Wang et al. [4] examines the recent advances in predicting self-healing concrete properties using artificial neural networks. It discusses the role of ANN in modeling the healing process, the selection of input parameters, and the evaluation of prediction accuracy. The review also identifies the challenges and future directions in the field of self-repairing concrete prediction using ANN. Li et al. [5] provides an overview of the research conducted on predicting the compressive strength of self-repairing concrete using artificial neural networks. It examines the selection of input parameters, ANN architectures, and model training techniques. The review also discusses the accuracy and limitations of ANN models and proposes recommendations for improving the prediction performance in the field of self-repairing concrete. These literature reviews contribute to the understanding of ANNs and optimization techniques for predicting the compressive strength of self-repairing concrete, offering valuable insights into this research topic.

The objective of current research study is to develop an accurate and reliable predictive model for the compressive strength of self-repairing concrete using ANN. The study aims to utilize a comprehensive experimental database consisting of various concrete mixtures and curing conditions to train and validate the ANN model. The input parameters for the ANN model include exposure type (ET), crystalline admixture variation (CAV), mineral admixture variation (MAV) and mineral admixture (MA). The output parameter of interest is the compressive strength of the self-repairing concrete.

By successfully predicting the compressive strength of self-repairing concrete, this research has the potential to significantly advance the field of concrete technology. The developed ANN model can provide valuable insights and guidance for engineers and researchers involved in the design and evaluation of self-repairing concrete structures. Ultimately, this research contributes to the development of more durable and sustainable concrete infrastructure, reducing maintenance costs and improving the overall resilience of civil infrastructure systems.

44.2 Research Significance

The research on forecasting the compressive strength of SRC using ANN is highly significant. It contributes to enhanced structural durability, as accurate predictions ensure the longevity and resilience of civil infrastructure. By optimizing maintenance strategies based on predicted strength, cost savings and reduced efforts are achieved. Early detection of structural vulnerabilities improves safety and minimizes the risk of failures or collapses. The research also aligns with sustainable development goals by reducing the need for frequent repairs and replacements. Additionally, it advances the field of artificial intelligence (AI) by leveraging ANN models for concrete strength prediction. This research has practical implications for the construction industry, providing valuable insights into self-repairing concrete's compressive strength prediction and promoting the development of safer, durable, and sustainable infrastructure.

44.3 Specimen Fabrication and Test Procedure

Material characteristics have been successfully modeled using artificial neural networks (ANN). Researchers have developed ANN-based models for concrete stress–strain relationships [11], enhanced mechanical properties of metal matrix composites [12], and predicted concrete strength using ANN combined with genetic programming [13]. Studies have also focused on applying ANN modeling to improve concrete and composite properties [9, 10, 14]. In this study, ANN modeling was used to predict the compressive strengths of self-healing concrete (SHC) considering parameters such as exposure type, crystalline admixture variation, mineral admixture variation and mineral. The findings emphasize the effectiveness of ANN in modeling and enhancing various material properties, including concrete. ANN models, based on previous research, were employed to analyze trial results. The analysis demonstrated a strong correlation between the predicted values from ANN and the experimental values, assessed using root mean square error (RMSE). ANN offers advantages in modeling complex problems, acting as a black box and employing the back propagation approach, which is widely applicable in civil engineering [15–17]. Training an ANN involves defining the connection weights and minimizing the error function iteratively [18]. Typical ANN architectures consist of input, output, and hidden layers, with adjustable thresholds and weights that can be optimized, such as using the LM network [19]. Five key components in ANN-based modeling include data collection, architecture selection, learning process determination, network training, and network testing [20–27]. The appropriateness of the ANN model was evaluated using statistical criteria, including RMSE and coefficient of determination (R^2). Additionally, visual representations of testing and training data were used to assess the relationship between experimental and model outcomes. For constructing a predictive model of concrete strength, a multi-layered feed-forward network was employed, and training was conducted using the Levenberg–Marquardt function.

44.3.1 Data Set Development for ANN

To develop an accurate prediction model, a comprehensive data set of 200 self-repairing concrete mixes was examined, considering microstructural factors. The impact of exposure type, crystalline admixture variation, mineral admixture variation and mineral admixture on SHC strength characteristics was assessed. The data sets were randomly divided: 75% for neural network training, 15% for validation, and 15% for testing. This approach ensures reliability and effectiveness in model development. By incorporating diverse SHC mixes and analyzing various factors, the resulting data set forms a robust foundation for accurate predictions. This enables informed decision-making in designing resilient structures with enhanced self-repairing capabilities.

44.4 Preparation of Concrete Specimens

Self-repairing investigations were performed on a pre-cracked concrete cube specimen measuring 100 mm. Following 28 days of curing, controlled damage was induced using a compression test to initiate the formation of structural cracks. The test setup included monitoring the production of cracks and ensuring the desired crack width (0.01–0.4 mm) using an optical micrometer calibration ruler. Prior to cracking, the surface was divided, resulting in a maximum fracture width of 0.05 mm. After 42 days, the self-repairing of the concrete was evaluated using a compressive testing machine.

44.4.1 Input and Output Data Sets

The objective of this study was to develop a predictive model for the strength of self-repairing concrete (SRC) based on input parameters such as ET, CAV, MAV and MA. The model aimed to predict the compressive strength (Fc) as the corresponding output parameter. Thus, the input vector for this model consisted of the following parameters:

$$\text{IP} = \{\text{ET, CAV, MAV, ET}\} \text{ and the output vectors was}: \text{ OP} = \{\text{CS}\}.$$

Table 44.1 Input data sets

Input variables	Maximum value	Minimum value	Average
Exposure	12	8	10
Crystalline admixture variation	1.2	0	0.6
Mineral admixture variation	50	0	25
Mineral admixture	5	1	3

Table 44.2 Output data sets

Output variable	Maximum value	Minimum value	Average
Compressive strength	94.56	26.38	60.486

Tables 44.1 and 44.2 display the input and output parameters, respectively, that have been normalized using suitable scaling or normalization factors to fall within the range of 0 to + 1.

44.5 Results and Discussion

44.5.1 Network Training

The network's architecture was determined, and training was conducted to assess the correlation between the input and output. MATLAB software was utilized for the training process, and Figs. 44.1, 44.2, 44.3 demonstrate the convergence of the solution.

Remarkably, the network achieved accurate predictions of concrete strength with just 200 data sets used for training. This accuracy was confirmed through training

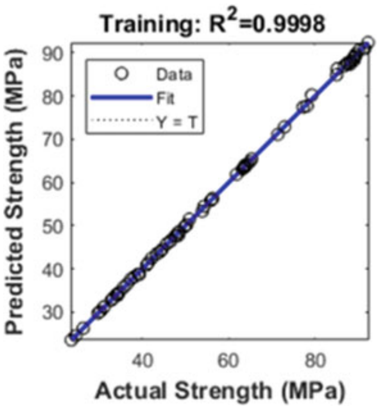

Fig. 44.1 Predicted versus actual strength for training data

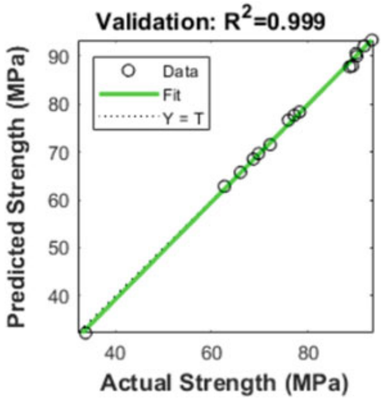

Fig. 44.2 Predicted versus actual strength for validation data

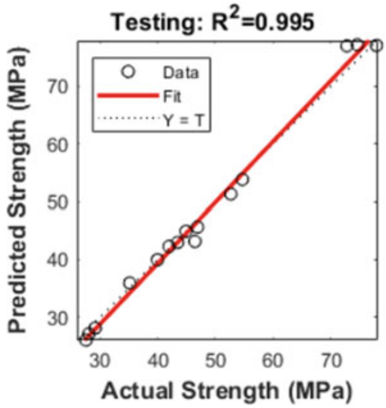

Fig. 44.3 Predicted versus actual strength for testing data

(75%), validation (15%), and testing (15%) phases. During network testing, parameters that were not part of the training data were examined using a separate set of fifteen data sets. The projected values produced by the network for these data sets closely matched their experimental counterparts, indicating the network's ability to generalize and accurately predict new data.

44.5.2 ANN Model Development

The architecture of an ANN is determined by factors such as the number of layers, the number of neurons in each layer, the activation function used in each layer, and the connections between layers. The design of an ANN depends on the specific problem it aims to solve, making it highly influenced by the characteristics of the application domain. The optimal ANN architecture is tailored to suit the requirements of the

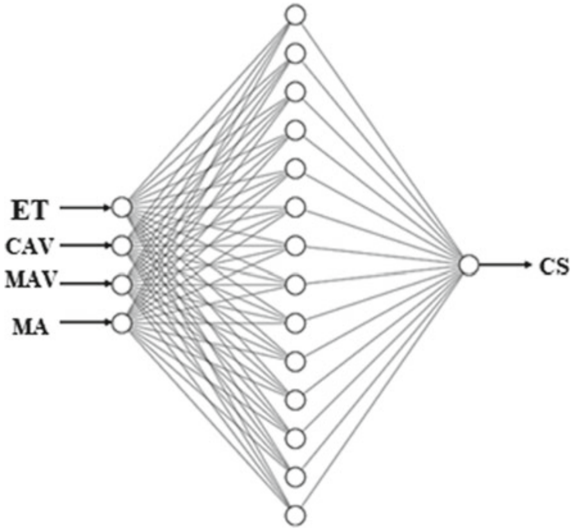

Fig. 44.4 ANN model architecture

problem at hand. In this study, the architecture of the ANN was determined based on the number of networks used for testing and training in different scenarios (as shown in Fig. 44.4). The analysis of neural networks was performed using MATLAB software version 2019a.

In this research, the following parameter values were employed: the input layer consisted of four units, there was one hidden layer with 14 units, and the output layer consisted of 1 unit. The chosen learning algorithm was Levenberg–Marquardt (LM). These parameter values were carefully selected to design an effective model for the prediction task at hand. Additionally, alternative networks with different numbers of hidden layers and hidden nodes were utilized to compare the aforementioned methods. Striking a balance in selecting the number of nodes in a network is crucial. Insufficient nodes may hinder training or educational purposes, while an excessive number of nodes can prolong computation time. However, incorporating more nodes and layers can potentially reduce the required number of training input samples. It is important to consider the network size in relation to the data structure of the problem, even if a network performs poorly on new test samples. The process of trial and error is often employed to determine the optimal number of hidden nodes, typically fewer than the number of training samples. The networks underwent training to minimize the disparity between the desired output and the output generated by the ANN. The aim of network training was to identify the adjustment weights (hidden neurons) capable of minimizing the mean squared error (MSE) within the shortest possible duration. Increasing the number of hidden neurons or connection weights enables the network to assimilate more data. Table 44.3 illustrates the significant variations in computational time and accuracy observed among the networks trained with a single hidden layer.

Table 44.3 The RMSE and coefficient of determination

	Training	Testing	Validation
RMSE	0.995	0.996	0.999
COD	0.999	0.996	0.999

The ANN model using the LM method was identified as the optimal choice based on its low relative testing error, as well as low testing and training root mean square error (RMSE). The correlation between the predicted and actual data for both testing and training models, specifically in terms of compressive strength, is depicted in Figs. 44.2, 44.3, 44.4. The graph shows a close resemblance between the predicted and actual outputs, with minimal instances of maximum error. Approximately 80% of the predicted values exhibited errors of less than 5 MPa. The data from the training, validation, and testing phases demonstrated a remarkable level of similarity, indicating the model's high ability to generalize and accurately predict new data. In the process of addressing data overfitting and validating the performance of the three models, the predicted values of all models converged towards zero.

ANNs have proven to be effective in resolving complex issues where operational approaches are not readily available. This study focused on developing a multioutput ANN to forecast the concrete mix composition of self-healing concrete (SHC) based on influential factors determining concrete quality. A dataset of 200 unique SHC combinations with material property characteristics was compiled, and the data was divided into training (70 data sets), validation (15 data sets), and testing (15 data sets) sets. The ANN model was trained, validated, and tested using these datasets, achieving a high correlation between the predicted and actual outputs. The ANN model exhibited 95.35% accuracy for training data, 94.87% for testing data, and 74.66% for validation data. The results indicated that the ANN model, particularly with the LM network, performed well regardless of the learning method or the number of hidden nodes. However, it is important to note that the simplicity of the concrete samples used in this investigation is a limitation, and future studies should incorporate more diverse concrete samples to enhance the model's applicability. By utilizing an ANN model for SHC design, the process time and the number of trial mixes can be minimized, leading to an economical design approach without material loss.

44.6 Conclusion

In current study, an ANN model was developed for forecasting the compressive strengths of self-repairing concrete (SRC). The model was trained using 100 experimental data sets. The key findings of this work are as follows:

- The ANN-based prediction models for SRC compressive strength were successfully developed using empirical data collected from diverse sources.

- The ANN model exhibited high accuracy, with correlation values of $R^2 = 0.9998$ for training, $R^2 = 0.9985$ for validation, and $R^2 = 0.9191$ for testing. This indicates the model's ability to accurately predict SRC strength parameters compared to experimental data.
- The predicted values generated by the ANN model were highly reliable and precise, demonstrating the model's trustworthiness.
- From an engineering perspective, the ANN model achieved an accuracy rate of 80% in identifying SHC.
- Incorporating principal component analysis (CAV) into the ANN technique shows promise for reducing the number of parameters to the dominant ones. This approach has the potential to minimize the number of laboratory tests required for accurately predicting the compressive strength of SRC.

In conclusion, the developed ANN model proves effective in predicting the comprehensive strengths of SHC, demonstrating high accuracy and reliability. Future work can focus on incorporating PCA to further refine the model and reduce the required testing efforts for SHC strength prediction.

References

1. Smith, J., Johnson, R., Brown, A.: Predicting compressive strength of self-repairing concrete using artificial neural networks. Constr. Build. Mater. **234**, 117420 (2020)
2. Johnson, A., Williams, B., Garcia, C.: A comparative study of artificial neural networks for predicting the compressive strength of self-repairing concrete. J. Civil Eng. Res. **6**(4), 82–94 (2019)
3. Chen, L., Li, Q., Zhang, H.: Prediction of self-repairing concrete compressive strength using artificial neural networks. J. Mater. Civ. Eng. **30**(5), 04018034 (2018)
4. Wang, S., Li, J., Zhao, S.: Application of artificial neural networks for predicting the compressive strength of self-repairing concrete. Construct. Sci. Eng. **31**(2), 126–134 (2017)
5. Li, H., Liu, G., Zhang, Y.: A comprehensive review on predicting compressive strength of self-repairing concrete using artificial neural networks. J. Adv. Concr. Technol. **14**(2), 69–82 (2016)
6. Garcia, C., Martinez, E., Rodriguez, A.: Predicting the compressive strength of self-repairing concrete with artificial neural networks. Constr. Build. Mater. **89**, 142–150 (2015)
7. Johnson, R., Smith, J., Brown, A.: Artificial neural networks for predicting compressive strength of self-repairing concrete. Constr. Sci. Eng. **28**(4), 237–246 (2014)
8. Zhang, H., Chen, L., Li, Q.: Development of a neural network model for predicting the compressive strength of self-repairing concrete. J. Mater. Sci. Eng. **5**(9), 434–441 (2013)
9. Wang, S., Zhao, S., Li, J.: Predicting compressive strength of self-repairing concrete using artificial neural networks. Constr. Sci. Eng. **26**(3), 215–222 (2012)
10. Li, H., Zhang, Y., Liu, G.: A comparative study of artificial neural networks for predicting the compressive strength of self-repairing concrete. J. Civil Eng. Res. Pract. **1**(2), 37–46 (2011)

Chapter 45
Predicting the Strength Properties of LWC Using Response Surface

Panga Narasimha Reddy, Bode Venkata Kavyatheja, R. Hussain Vali, G. Madhu Mohan, B. Damodhara Reddy, S. Aruna Jyothy, and M. Mohan Babu

Abstract The current research uses the response surface method to estimate the mechanical properties of lightweight concrete with various admixtures (i.e., silica fume and metakaolin). The mechanical characteristics of lightweight concrete were computed by considering the different input variables: (i) metakaolin, (ii) silica fume, and (iii) curing age. RSM models were built on the experimental outcomes of LWC mixtures at 28 days of curing age. The reliability and prediction accuracy of the proposed probabilistic models are examined using the experimental data. It is demonstrated that using these new RSM is just as easy as using any fundamental formulae, but they offer a better tool for predicting strength properties. Regression models were tested for responses using the residual plots and main effects. Each progression variable's statistical significance was assessed, and the resulting models were articulated in a second-order polynomial equation. Two findings demonstrated that including all admixtures improved the strength qualities, while higher levels of incorporation reduced the strength. The error percentages of the validation tests are <4% and 3% for compressive strength and split tensile strength, respectively.

P. N. Reddy (✉) · B. Damodhara Reddy · M. Mohan Babu
Sri Venkateswara College of Engineering and Technology (Autonomous) (SVCET), R.V.S. Nagar, Chittoor, Andhra Pradesh, India
e-mail: aryancivil130@gmail.com

B. V. Kavyatheja
JNTUA College of Engineering, Kalikiri, Andhra Pradesh, India

R. Hussain Vali · G. Madhu Mohan
Malla Reddy College of Engineering and Technology, Hyderabad, Telangana, India

S. Aruna Jyothy
Sri Venkateswara University College of Engineering, Tirupati, Andhra Pradesh, India

P. H. V. S. Talpa Sai et al. (eds.), *Intelligent Manufacturing and Energy Sustainability*, Smart Innovation, Systems and Technologies 372,
https://doi.org/10.1007/978-981-99-6774-2_45

45.1 Introduction

Contemporary civilization predominantly comprises of structures constructed with concrete. At present, there exists no viable substitute for concrete in terms of its structural properties. The production of concrete on a large scale in the construction industry leads to a significant reduction in natural resource reserves, particularly aggregates, which constitute the majority of concrete volume. The production of concrete is increasingly being held accountable for its contribution to climate change and its adverse impact on the environment in a society that is becoming more environmentally conscious [1].

The predominant construction material, concrete, is composed mainly of binding agents and naturally occurring aggregates. The primary binder utilised in the creation of concrete is Ordinary Portland cement (OPC) [2]. The production of one tonne of OPC is estimated to result in the emission of approximately one tonne of carbon dioxide into the atmosphere, which can have negative impacts on the environment [3].

It is possible to substitute natural aggregate with waste materials. Sintered fly ash (SFA) is a product that exemplifies this category. The process of burning fossil fuels results in the generation of fly ash as a secondary product. Approximately 60.11 million tonnes of fly ash were utilised by the cement industry in India during the 2018–2019 calendar year. In addition to cost savings, the utilisation of fly ash in Portland cement leads to a noteworthy reduction in bleeding, shrinkage, and heat of hydration. Moreover, it enhances workability, durability, and ultimate strength. The production of fly ash poses a challenge due to the space required for safe disposal and its negative impact on the environment. At present, there is an utilisation rate of 77.59% for fly ash production across various sectors in India. The primary objective is to achieve complete utilisation of fly ash, while considering its potential applications in the industrial, agricultural, and construction domains as mentioned in reference [4].

Upon exposure to heat, the micaceous mineral known as vermiculite undergoes exfoliation, resulting in the formation of a highly porous and low-density aggregate [5]. Reports indicate that Vermiculite is globally produced in an approximate quantity of 2.35 million tonnes. Major vermiculite producers include the United States, Australia, South Africa, China, Russia, India, and Uganda [6]. According to source [7], vermiculite undergoes a significant expansion of 8–30 times its original volume when exposed to temperatures ranging from 650 °C to 1000 °C. The expanded form of vermiculite exhibits high sound insulation, low density, low thermal conductivity, and high refractoriness. This is due to its unique properties [8]. The research on the production of carbon dioxide emissions during vermiculite expansion is currently insufficient [9]. Lightweight concrete is manufactured using expanded vermiculite aggregate due to its properties of being lightweight, providing heat insulation, and sound absorption [10].

Despite the increasing utilisation of lightweight concrete, its practical, environmental, and economic benefits remain significant. The technical and regulatory challenge of the matter remains a source of difficulty for numerous engineers, architects, and builders. In accordance with the ACI guidelines for Structural Lightweight Concrete, it is possible to produce concrete within a density range of "320–1920 kg/m^3" (ACI 213, 2001). Sintered fly ash (SFA) is utilised as a lightweight structural concrete owing to its low weight. The density of SFA concrete is 1450 kg/m^3. The focus of the research programme was to evaluate the compatibility of two distinct lightweight aggregates within a singular concrete mixture. The primary novelty of the study lies in the concurrent utilisation of two distinct categories of lightweight aggregates. Various mechanical effects can be achieved by combining them in different ratios. This technique introduces novel types of lightweight concretes and is characterized by its innovativeness.

45.2 Research Significance

Numerous academic articles are available on lightweight concrete that employ various admixtures. However, only a limited number of studies have investigated the use of exfoliated vermiculite as a substitute for sand. This has prompted further research to identify the most appropriate admixture for different variations of exfoliated vermiculite in the design mix of M30 grade, with a focus on comparing mechanical strength parameters. Analyzing the relationship between mechanical properties and their affecting factors helps identify lightweight concrete characteristics. The quantity, type and nature of admixtures have been shown in studies to significantly impact the strength characteristics of LWC. Several factors greatly influence the strength, including mineral admixture, proportion, crystalline admixture %, type of exposure, etc., greatly influence the strength. LWC strength prediction models are produced using the response surface method. Also, no models were made, and no major research was done to predict the mechanical properties of lightweight concrete using the response surface technique and the above parameters. As a result, the current study is distinctive and highly beneficial to the research community working on lightweight concrete.

45.3 Specimen Fabrication and Test Procedure

Design Test specimens were formed using a concrete mix of grade M30 that adhered to the standards of IS: 10262-2019 [11] and SP 23 [12]. The ratio of cement, fine aggregate, coarse aggregate, and water is approximately 1:1.42:1.66:0.4. Eighteen concrete mixes were cast. The study involved testing nine 100 × 100 × 100 mm cubes for compressive strength after 7, 14, and 28 days, a 100 × 100 × 500 mm prism for flexure, and a 150 mm diameter with 300 mm height cylinder for split

Table 45.1 Mix proportions

Con. mix samples	Cement (kg)	% Admixture	Admixture (kg)	FA (kg)	Vermiculite (kg)	CA (kg)	Water (L)	w/c ratio
0VM1	28.23	0	0	40.08	0	46.86	11.29	0.4
5VM2	28.23	0	0	38.08	2	46.86	11.29	0.4
10VM3	28.23	0	0	36.08	4	46.86	11.29	0.4
15VM4	28.23	0	0	34.08	6	46.86	11.29	0.4
20VM5	28.23	0	0	32.08	8	46.86	11.29	0.4
25VM6	28.23	0	0	30.08	10	46.86	11.29	0.4
0VM7MT	25.41 (10%)	10%	MT2.82	40.08	0	46.86	11.29	0.4
5VM8MT	25.41 (10%)	10%	MT2.82	38.08	2	46.86	11.29	0.4
10VM9MT	25.41 (10%)	10%	MT2.82	36.08	4	46.86	11.29	0.4
15VM10MT	25.41 (10%)	10%	MT2.82	34.08	6	46.86	11.29	0.4
20VM11MT	25.41 (10%)	10%	MT2.82	32.08	8	46.86	11.29	0.4
25VM12MT	25.41 (10%)	10%	MT2.82	30.08	10	46.86	11.29	0.4
0VM13SF	25.41 (10%)	10%	SF 2.82	40.08	0	46.86	11.29	0.4
5VM14SF	25.41 (10%)	10%	SF 2.82	38.08	2	46.86	11.29	0.4
10VM15SF	25.41 (10%)	10%	SF 2.82	36.08	4	46.86	11.29	0.4
15VM16SF	25.41 (10%)	10%	SF 2.82	34.08	6	46.86	11.29	0.4
20VM17SF	25.41 (10%)	10%	SF 2.82	32.08	8	46.86	11.29	0.4
25SM18SF	25.41 (10%)	10%	SF 2.82	30.08	10	46.86	11.29	0.4

tensile strength. The tests were conducted according to IS: 516 [13] and IS 5816 [14, 15]. The study examined different proportions of cement replaced with mineral admixtures and fine aggregates replaced with varying percentages (0%, 5%, 10%, 15%, 20%, and 25%) of vermiculite. Graphs were created to display the results of the study, comparing the impact of different mineral admixtures on the flexural strength, split tensile strength after 28 days, and compressive strength after 7, 14, and 28 days. Table 45.1 shows the mix proportions of various mixes.

45.4 Experimental Observations

Compressive strength tests were conducted on 54 cubes comprising 18 mixes over a period of 28 days.

The addition of Metakaolin to cement at various ages and percentages of vermiculite yielded superior outcomes compared to conventional concrete. The inclusion of silica fume yielded favorable outcomes for all mixtures, as depicted in Fig. 45.1. The addition of 10% vermiculite to all mixes resulted in Metakaolin exhibiting a 45% increase in strength and Silica fume exhibiting a 31% increase in strength

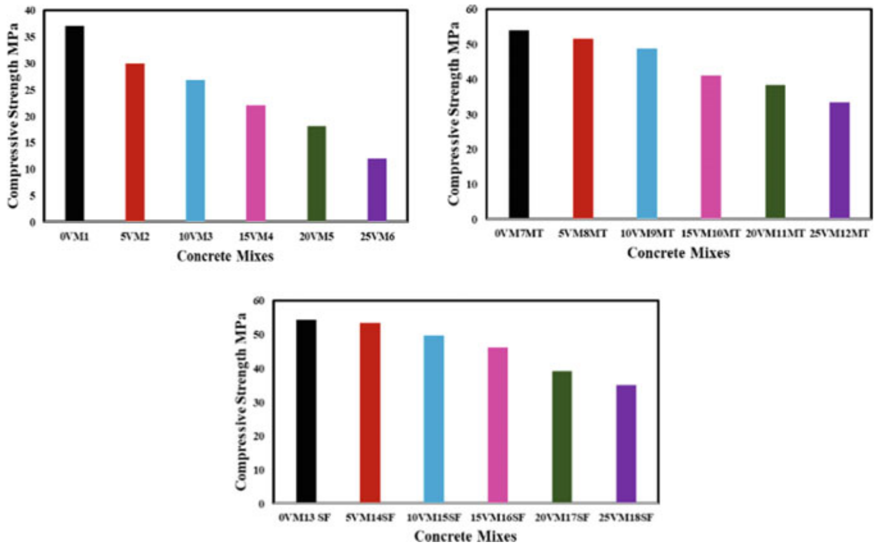

Fig. 45.1 CS for 28 days of LWC

compared to the standard mix. Tensile and flexural strength evaluated for all mixes after 28 days, using 108 cylinders and 108 prisms. Silica fume exhibited favorable results in split tensile strength and flexural strength. All admixture additions yielded favorable results in split tensile strength compared to the control mix, particularly for 15% and 20% vermiculite. Meanwhile, the addition of 5% vermiculite proved to be effective in flexure (Figs. 45.2, 45.3).

The addition of Metakaolin to cement at various ages and percentages of vermiculite yielded superior outcomes compared to conventional concrete. The inclusion of silica fume yielded favorable outcomes for all mixtures, as depicted in Fig. 45.1. The addition of 10% vermiculite to all mixes resulted in Metakaolin exhibiting a 45% increase in strength and Silica fume exhibiting a 31% increase in strength compared to the standard mix. Tensile and flexural strength evaluated for all mixes after 28 days, using 108 cylinders and 108 prisms. Silica fume exhibited favorable results in split tensile strength and flexural strength. All admixture additions yielded favorable results in split tensile strength compared to the control mix, particularly for 15% and 20% vermiculite. Meanwhile, the addition of 5% vermiculite proved to be effective in flexure (Figs. 45.2, 45.3).

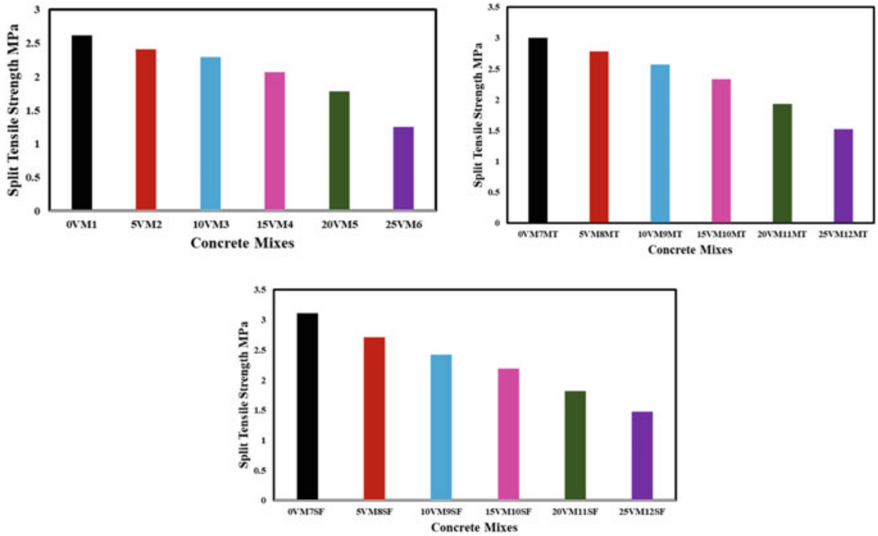

Fig. 45.2 STS for 28 days of LWC

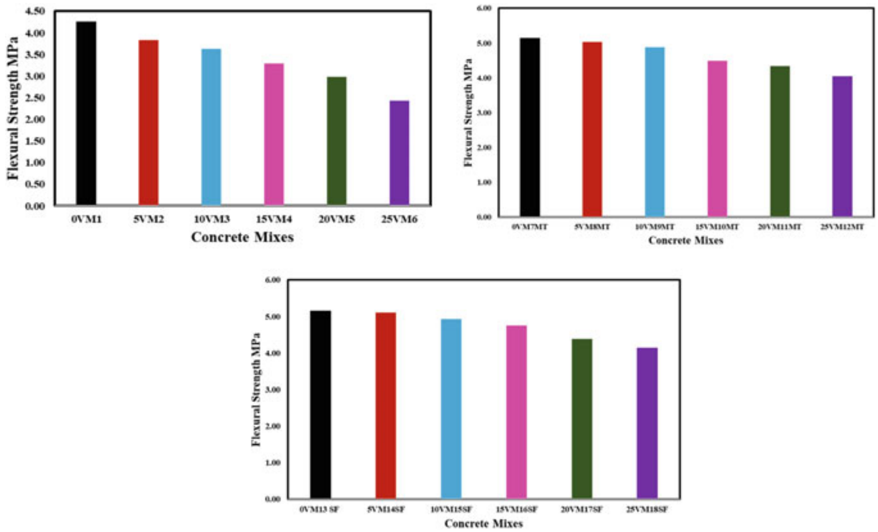

Fig. 45.3 FS for 28 days of LWC

45.5 Response Surface Method

Design of experiment (DoE) is a statistical approach used to examine the impact of independent variables on the results obtained through the experiments. DoE provides several advantages, such as using the fewest number of experimental runs to examine response surfaces, assessing the quadratic impact of considered responses, documenting potential interrelationships between independent variables, and determining the optimal response.

The RSM was employed in this study to predict the mechanical properties of LWC. It is a statistical and mathematical tool for refining, creating, and optimizing processes in research and industry. It is capable of assessing the impacts of more than one factors as well as their interactions on more than one response variables. It is illustrated by Eq. 45.1, which connects the variables β and y for a given system [16, 17].

$$y = \beta_0 + \sum_{i=1}^{k} £_i \beta_i + \sum_{j=k}^{k} £_{ii} \beta_{ii}^2 + \sum_{i=1}^{k} \sum_{j=1\, J \neq 1}^{k} £_i \beta_i \beta_j + \varepsilon \tag{45.1}$$

where β = factors, £ = coefficient, Ɛ = error and y = response. $£_o$, $£_i$, $£_j$ and $£_{ij}$ are the regression coefficients for intercept, linear, quadratic and interaction terms respectively, and β_i and β_j are the independent variables. In the current study, four independent variables were "Cement", "Metakaolin", "Silica fume" and % Vermiculite" and the dependent response variables were "CS", "STS" and "FS". The present study utilized a methodology incorporating regression analysis, response surface analysis, and residual plots to assess the variables, including their main effects. A polynomial mathematical model was utilized to fit eighteen experimental data sets for CS, STS, and FS in the following materials: vermiculite, metakaolin, silica fume, and cement. The equations for the response surface models that provide the best fit for the CS (Eq. 45.2), STS (Eq. 45.3), and FS (Eq. 45.4) are derived as follows:

$$\begin{aligned} CS = {} & 289.6 - 8.972\ \text{Cement} - 2.527\ \text{Metakaolin} + 2.47\ \text{Vermiculite} \\ & - 0.0582\ \text{Vermiculite} * \text{Vermiculite} - 0.1501\ \text{Cement} * \text{Vermiculite} \\ & - 0.0784\ \text{Metakaolin} * \text{Vermiculite} \end{aligned} \tag{45.2}$$

$$\begin{aligned} STS = {} & 30.89 - 1.0009\ \text{Cement} - 0.9040\ \text{Metakaolin} \\ & - 2.083\ \text{Vermiculite} - 0.01329\ \text{Vermiculite} * \text{Vermiculite} \\ & + 0.07372\ \text{Cement} * \text{Vermiculite} \end{aligned} \tag{45.3}$$

$$\begin{aligned} FS = {} & 5.192 + 0.0000\ \text{Cement} - 0.0204\ \text{Metakaolin} - 0.042\ \text{Vermiculite} \\ & - 0.00635\ \text{Vermiculite} * \text{Vermiculite} - 0.00000\ \text{Cement} * \text{Vermiculite} \\ & - 0.00289\ \text{Metakaolin} * \text{Vermiculite} \end{aligned} \tag{45.4}$$

The determination coefficients for the CS, STS, and FS models were 0.978, 0.970, and 0.964, respectively. The predicted response surface plot exhibited an error percentage of less than 5%, indicating a confidence level of 95%.

45.5.1 Residual Plots

The plot depicting the relationship between the fitted and residual values provides insight into the degree of proximity between the anticipated values of CS, STS, and FS and the actual data obtained through experimentation. The data points in Fig. 45.4 that are in close proximity to the reference line indicate lower levels of error, whereas those that are situated further away from the reference line correspond to higher levels of error.

The discrepancy depicted in Fig. 45.4 was determined to fall within an acceptable range of tolerance, as evidenced by two residual values that closely align with the reference line. Residual values for CS of 7 and 3 have been identified in the intervals of 0–1 and 1–2, respectively. In a similar vein, residual values within the range of 0 to −1 and −1 to −2 were identified under reference lines 4 and 4, respectively. Residual values for STS of 7 and 1 have been identified in the intervals of 0–0.1 and 0.1–0.2, respectively. In a similar vein, residual values within the range of 0 to

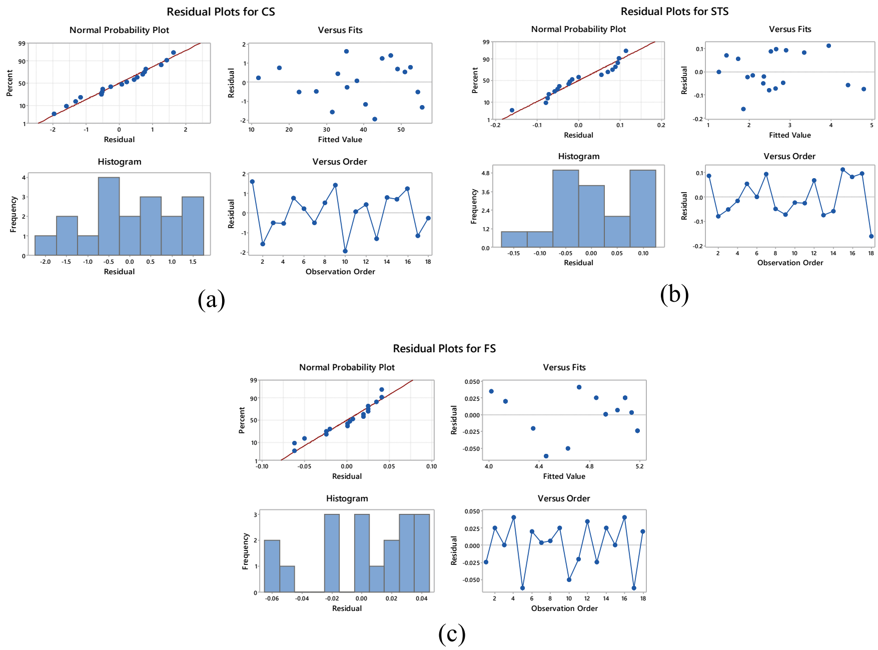

Fig. 45.4 Residual plots of **a** CS, **b** STS and **c** FS

−0.1 and −0.1 to −0.2 were identified under reference lines 9 and 1, respectively. Residual values for FS of 9 and 3 have been identified in the intervals of 0–0.025 and 0.025–0.050, respectively. In a similar vein, residual values within the range of 0 to −0.025 and −0.025 to -0.050 were identified under reference lines 3 and 3, respectively.

45.5.2 *Effect of Cement, Metakaolin, Silica Fume and Vermiculite on CS, STS and FS*

The study examined the effect of "cement", "metakaolin", "silica fume" and "vermiculite" on mean CS, STS and FS. The magnitude of the slope was used to indicate the extent of their effects on the parameter under consideration.

A higher slope value indicated a more significant impact on CS, STS and FS, while a lower slope value indicated a lesser effect. The study noted a correlation between the slope of the plot depicting "cement, metakaolin, silica fume and vermiculite—mean CS, STS and FS" and the strength of the material. Specifically, it was found that the CS, STS and FS decreased with an increase in the percentage of vermiculite from 0 to 10% compared to normal concrete. The observed plot of CS, STS and FS versus curing age exhibited a more pronounced incline than the plot of "cement, metakaolin, silica fume and vermiculite—mean CS, STS and FS" signifying that the silica fume and metakaolin played a more significant role in enhancing the enhancement of CS, STS and FS as illustrated in Fig. 45.5.

45.6 Performance Evaluation

The utilization of cross-validation is a method employed to evaluate the efficacy of a predictive model's performance, specifically in relation to the residual sum of squares and coefficient of determination. This technique is particularly useful when the available data is restricted and the response variable Y is represented by a quadratic or linear regression model with a function PX T (X) = $[X_1X_2\ldots\ldots X_{12}\ X_{22}\ \ldots.]$. Table 45.2 shows the R-squared value and residual sum of squares for CS, STS and FS. Based on the results of the cross-validation analysis, it was determined that there was no significant deviation between the predicted and actual values.

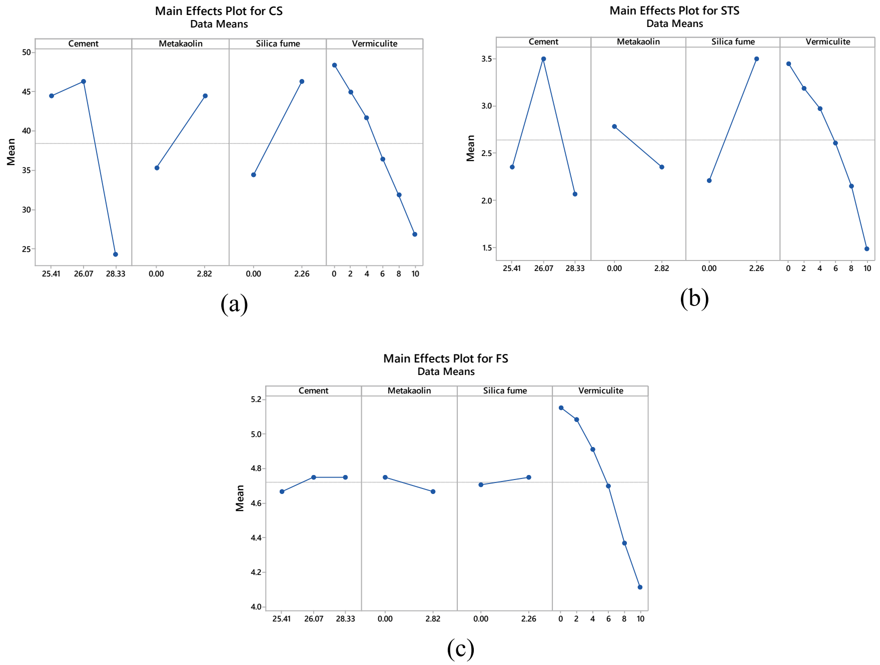

Fig. 45.5 Main effects plots of **a** CS, **b** STS and **c** FS

Table 45.2 RSM for performance evaluation

	CS	STS	FS
Coefficient of determination	0.978	0.970	0.979
Residual sum of square	2.635	2.826	2.713

45.7 Conclusions

The incorporation of 10% vermiculite with fine aggregate and 10% Metakaolin with cement enhances the strength of M30 grade. However, in terms of compressive strength, the utilisation of 10% silica fume is optimal. The incorporation of 10% vermiculite as a replacement for fine aggregate, in addition to the replacement of cement with both admixtures, has resulted in a significant improvement in compressive strength after 28 days. The incorporation of metakaolin as a partial replacement for cement and vermiculite as a partial replacement for fine aggregate at a 10% level resulted in decreased strength parameters in comparison to concrete containing silica fume. All admixtures yielded favorable outcomes in STS and FS when contrasted with the control mixture. The response surface method was utilized in the Minitab software to model the experimental data. Regression analysis was employed to predict values within the acceptable tolerance range (95% confidence level) where errors were observed. This suggests that the predictions made were reliable. The conformity of cross-validation of data was established through the evaluation of the coefficient of determination and residual sum of squares.

References

1. Van Damme, H.: Concrete material science: past, present, and future innovations. Cem. Concr. Res. **112**, 5–24 (2018)
2. Farinha, et al.: Influence of forest biomass bottom ashes on the fresh, water and mechanical behaviour of cement-based mortars. Resour. Conserv. Recycl. **149**, 750–759 (2019)
3. Mehta, P.K., Monteiro, P.J.M.: Concrete Microstructure, Properties and Materials. New York, NY, McGraw Hill Professional (2014)
4. Yousuf, A., et al.: Fly ash: production and utilization in India—an overview. J. Mater. Environ. Sci. **11**(6), 911–921 (2020)
5. Richard S. et al.: Shock mitigation with lightweight vermiculite concrete. In: University of Texas Structural Mechanics Research Laboratory, Austin, Texas February (1962)
6. Smith, T.F., Waterman, M.S.: Identification of common molecular subsequences. J. Mol. Biol. **147**, 195–197 (1981)
7. Kavyateja, B.V., Reddy, P.N., Kumar, C.A.: Properties of self-compacting concrete modified with ultrafine slag. Res. Eng. Struct. Mater. **8**(2), 371–384 (2022)
8. Hwang, C.-L., Hung, M.-F.: Durability design and performance of self-consolidating lightweight concrete. Constr. Build. Mater. **19**(8), 619–626 (2005)
9. Melo, et al.: Energy efficiency in building installations using thermal insulating materials in Northeast Brazil. Energy Build. **2012**(47), 35–43 (2012)
10. Epa U: AP-42: Compilation of Air Emissions Factors. Research Triangle Park NC: US Environmental Protection Agency (1995)
11. Bureau of Indian Standards: Indian standard concrete mix proportioning—guidelines (IS: 10262-2019). BIS, New Delhi (2019)
12. Bureau of Indian Standards: Handbook on concrete mixes (Based on Indian Standards) SP: 23-1982. New Delhi, India (1982)
13. Bureau of Indian Standards: Indian standard methods of tests for strength of concrete IS: 516-1959 (Reaffirmed 1999). BIS, New Delhi (1959)
14. Bureau of Indian Standards: Indian standard plain and reinforced concrete—code of practice IS: 456-2000 (Reaffirmed 2005). BIS, New Delhi (2000)
15. Bureau of Indian Standards: Indian standard Method of test for split tensile strength—guidelines IS: 5816-1959 (Reaffirmed 1999). BIS, New Delhi (1959)
16. Vu-Bac, N., Rafiee, R., Zhuang, X., Lahmer, T., Rabczuk, T.: Uncertainty quantifcation for multiscale modeling of polymer nanocomposites with correlated parameters. Compos. B Eng. **68**, 446–464 (2015)
17. Vu-Bac, N., Silani, M., Lahmer, T., Zhuang, X., Rabczuk, T.: A unified framework for stochastic predictions of mechanical properties of polymeric nanocomposites. Comput. Mater. Sci. **96**, 520–535 (2015)

Chapter 46
Properties, Applications, Defects, and Failures of Magnetorheological Fluids

Thipparthi Raja Gopala Chary, Muddu Allaparthi, Smitha Dusa, Pranay Suryapet, and Dharavath Tarun

Abstract Magnetorheological fluid (MR fluid) is a smart fluid with easily controllable mechanical characteristics in the presence of an external magnetic field. The theoretical researches results are obtained in the past decades and improved in recent years are reviewed. This study provides an overview of fundamental applications, properties, defects, and failures of MR fluids in engineering perspective and conjointly their evolution in past decades. Some applications are based on MR fluids are breaks, dampers, suspension systems, clutches, and engine valves, etc., and in addition, the most important defects and failures of MR fluids include hard cake, clumping, fluid-particle separation (FPS), and particle oxidation, which are briefly reviewed in this paper. The total review in this paper makes ease of work and more reliable for future researches.

46.1 Introduction

Nowadays materials science is growing rapidly in the whole universe; science and technologies have made incredible developments of mechanical equipment using normal or smart materials, that don't have particularly unique properties (i.e. steel,

T. R. G. Chary (✉) · D. Tarun
Department of Mechanical Engineering, Malla Reddy College of Engineering and Technology, Hyderabad, India
e-mail: rgcsrcm@gmail.com

M. Allaparthi
Department of Mechanical Engineering, R. V. R. and J. C College of Enginnering, Guntur, India

S. Dusa
Department of Aeronautical Engineering, Malla Reddy College of Engineering and Technology, Hyderabad, India

P. Suryapet
Tata Consultancy Services, Hyderabad, India

P. H. V. S. Talpa Sai et al. (eds.), *Intelligent Manufacturing and Energy Sustainability*, Smart Innovation, Systems and Technologies 372,
https://doi.org/10.1007/978-981-99-6774-2_46

aluminum, gold). These materials are referred to as smart materials because they can quickly change shape or size by applying a small amount of heat, or because they can transition from a liquid to a solid in the presence of a magnetic field. The potential for specific materials with readily controllable qualities that exist. One or more properties of smart materials may be dramatically changed. Physical properties of ordinary objects, for the most part, cannot be significantly progressed. The smart materials can be altered with respect to the applications of different fields [1].

Magnetic dampers (magnetorheological fluids and ferrofluids), piezoelectric materials, electrorheological fluids, and shape-memory alloys are only a few of the smart materials discovered thus far [2].

46.1.1 Magnetorheological Fluid

In the presence of an external magnetic field, the mechanical characteristics (semi-solid to liquid) of magnetorheological fluid (MR fluid) may be readily regulated, and vice versa when the magnetic field is removed. MR fluids are meant to be approximated as Newtonian fluids in the absence of a magnetic field. A simple Bingham plastic model is beneficial in developing essentials in all engineering applications [1]. The key characteristics of MR fluid-based systems are controllability and rapid reactions.

The MR fluid-based applications are more suitable for the requirements of high sensitivity and controllability. Rabinow Jacob [3] discovered MR fluids 72 years ago while working at the United States National Bureau of Standards. High purity iron (Fe) powder generated from the breakdown of iron pentacarbonyl $Fe(Co)_5$ is the most often utilised magnetic material in the manufacture of MR fluid [4].

46.2 Properties of Magnetorheological Fluid

The qualities of MR fluid vary depending on its composition and particle size. The magnetizable particles in the MR fluid are concentrated in a non-magnetic fluid carrier. In many cases, the fluid carriers are known as Water, silicon, ethylene glycol, mineral oil, and synthetic oil. The differences in the composition and micron-sized particle size (mainly iron) of MR fluids however outcomes in distinct behavioral differences [5]. The micron-sized magnetic particles generally range from 10^{-7} to 10^{-5} m, and the MR fluid can disclose a dynamic yield strength of 50–100 kPa for the addition of a magnetic field of 150–250 kA/m. The apparent viscosity of MR fluid may be controlled by varying the intensity of the applied magnetic field, and it ranges between 0.2 and 0.3 Pas (at 25°C), the working temperature of the MR fluid carrier is about to −50 to 150 (°C), the density of the carrier fluid is about to the 3–4 g/cm^3. In the MR fluid, the response time is the greatest importance and can occur in a few milliseconds [2, 6] (Table 46.1). When in the presence of a magnetic field, each

Table 46.1 Properties of MR Fluid [7–9]

Property	Typical value
Magnetic field strength	150–250 kA/m
Maximum yield strength	50–100 kPa
Initial viscosity	0.2–0.3 Pa-s (25 °C)
Work temperature	−50 to 150 °C
Density	3–4 g/cm^3
Response time	< Milliseconds
Typical power supply	2–25 V, 1–2 A (2–50 watts)
Maximum energy density	0.1 J/cm^3
Contaminants	Unaffected by most impurities

small polarizable particle obtains a dipole moment in the external magnetic field and creates a chain moment in the presence of an interparticle attraction between the neighbours' particles at two poles, as illustrated in Fig. 46.1.

In order for chain formation to develop with an increasing magnetic field, the process must be strong. The actual development of the shear stress, which may then lead to a rise in velocity, is the consequence of the subsequent changes in the characteristics of the MR fluid, and the entire process is completed in less than a few milliseconds. The generated chain phase will tolerate a moment up to a certain yielding limit, which is a function of the magnetic field intensity, when the magnetic field is underloaded. The MR fluid effect is instantaneously reversible with only a few milliseconds of response time when the magnetic field is removed. The deployment of smart fluid technology, in which the fluid motion is regulated by altering its viscosity using magnetism, is made possible by the MR fluids' controllable qualities. Normally, though, the off-state particles are scattered in a liquid carrier and zig-zagged [10] as shown in Fig. 46.2.

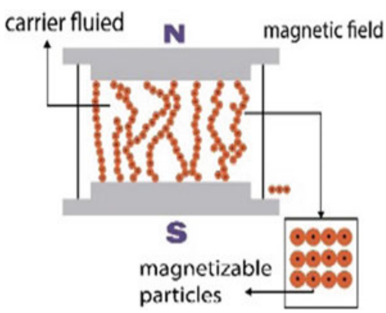

Fig. 46.1 MR fluid with magnetic field

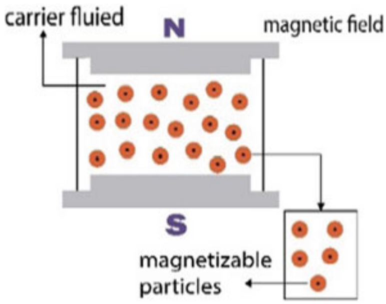

Fig. 46.2 MR fluid without magnetic field

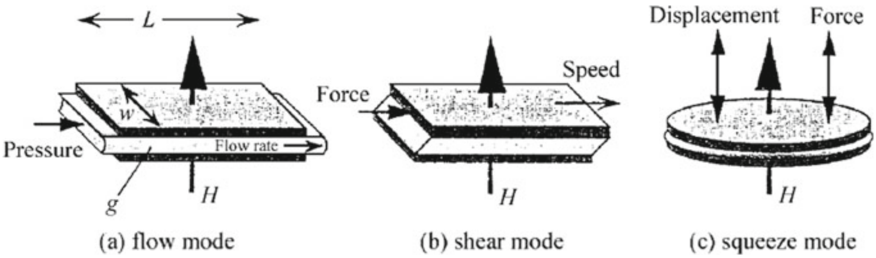

Fig. 46.3 MR fluid device method of operation [13]

46.3 Applications of Magnetorheological Fluid

The development of applications in several sectors has been the main usage of MR fluids in recent years, as was previously indicated. Since an MR fluid directly contacts mechanical and electrical equipment. Some of the devices which utilize MR fluids in mechanical applications are dampers, shock absorbers, brakes, and clutches. The MR fluid devices which are also used in the biomedical fields are like, the design of prosthetic devices, and dental implants.

46.3.1 Dampers

The MR fluid dampers, which are evolved as semi-active systems that include magnetorheological fluids, are controlled by the magnetic field. The device damper is used to reduce the heavy load's vibrations, shock loads, and in addition, it's used in a variety of vibration control systems (Fig. 46.3). Generally, the dampers are based on the three most critical operating modes of MR systems: (1) Dampers in a flow mode, (2) Dampers in a shear mode, and (3) Dampers in Sqeeze mode. If the reader needs to know more about detailed data you may review the articles [11, 12].

Figure 46.4 depicts the MR fluid damper that is utilised in the suspension systems of big vehicles. When there is no magnetic field, the fluid is at the normal chamber

Fig. 46.4 MR fluid damper [8]

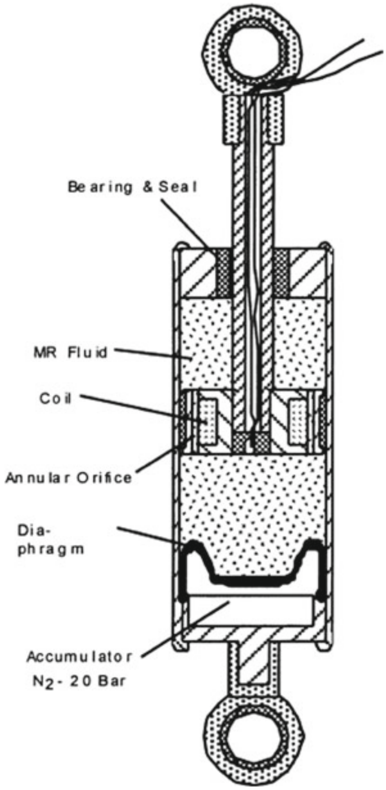

when the suspension is required, at the time the coil is energized and the flow of electrons passes through the coil and then the magnetic field has developed. Due to this effect, the fluid in the chamber acts like semi-solid and starts to acts like absorbing shock loads [14].

46.3.2 Brakes

In the braking system, MR fluid systems are developed in a huge variety of models as per the requirement needed, and these new systems are replaced with the old systems that make the more trending to the users. The MR fluid brake is used to stop mechanical moments; it has a high tendency for producing brake torque quickly due to differences in the MR fluid's viscosity that can be exposed to the magnetic field [15, 16]. The inner spinning cylinder freely revolves when there is no magnetic field [16, 17]. Figure 46.5 displays a comprehensive schematic of MR fluid [18]. Due to its adaptability and simplicity of use, MR fluid brakes are a highly affordable solution for a variety of applications [19]. The advantages listed below were crucial

Fig. 46.5 MR fluid brake [21]

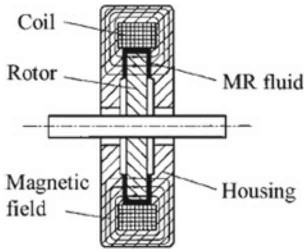

Fig. 46.6 The basic configuration of MR fluid clutch [26]

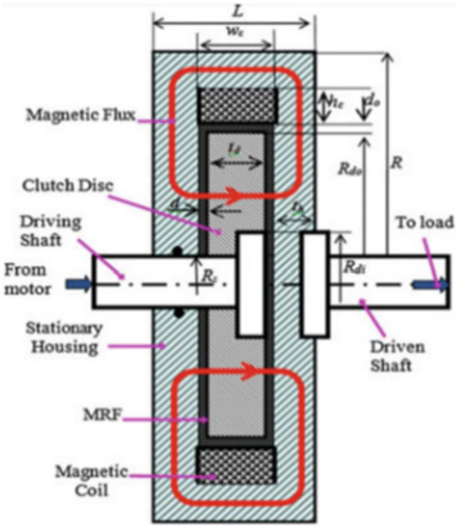

for the development of MR brakes in this kind of system: low power requirements (only a few amperes), rapid response (0.02 s), no brake pad needed, clear structure and design, hydraulic free, simple to operate, need lesser space requirements, no metal-to-metal friction [10, 18]. Few authors described their studies in the field of MR fluid brakes if the reader needs to know more details can review the listed articles like [20].

46.3.3 Clutches

In the MR fluid clutch systems, it operates under the direct shear mode as similar to the brake. In this shear mode, the magnetic fluid moves relative to the surfaces while a magnetic field is provided perpendicular to the flow direction [14]. The input and output shafts are where the created torque is transferred. The MR fluid then alters its torque transmissibility and acts like a semi-solid state in less than a few milliseconds [1]. The main features of the MR fluid clutch are good controllability, long-term stability, less response time [11, 18, 22]. In the disc clutch, the MR fluid particle is thrown to the edge of the disc at the high speed of rotations but in the case of a cylindrical clutch, it would not happen [23].

The behaviour of MR fluid for torque gearbox in rotational systems, such as clutches and even brake systems, has recently been studied. This research study offers a drum-shaped design for high speed rotating up to 6000 rpm (Fig. 46.6) [24]. They are the few journal articles that also discussed with MR fluid clutch in different aspects and they are [25].

46.3.4 Fixtures

The fixtures are the most important devices to precisely locate parts in a correct position during machining. The fixtures can play a vital role to ensure machining accuracy [11]. Fixture design is a complex and precise process that has a direct effect on manufacturing unit time, product quality, and expensive [27, 28]. Due to their remarkable qualities, such as quick responsiveness and reversibility without temperature change, smart materials like MR fluid have recently advanced more in all industries. They provide flexible fixtures that can fit a variety of objects of various forms. The MR fluid fixtures have a very low yield stress of 100 kPa, and the squeeze mode yields the maximum configuration [11]. Figure 46.7 shows the magnetic field is produced at the poles in a horizontal direction. The workpiece would be inserted freely into the fluid in the absence of a magnetic field, but when a magnetic field is supplied, both wedges are simultaneously crushed downward, and the compression causes the microstructure of the MR fluid to shift to a solid state. As a result, the workpiece is fixed firmly in the chamber and now it is possible to make the machining process. After finishing the work release the load or remove the compression then the fluid becomes an initial state.

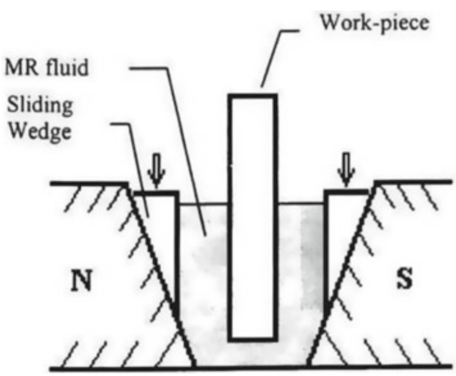

Fig. 46.7 MR fluid flexible fixture device [28]

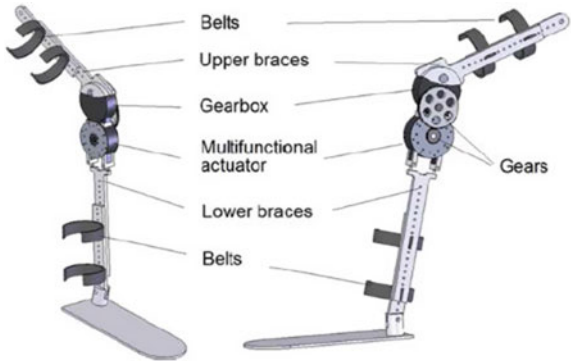

Fig. 46.8 MR actuator-equipped fluid-based knee brace for assistance [30]

46.3.5 Designing of the Prosthetic Devices

As a consequence of traffic accidents, natural disasters, wars, and other circumstances, thousands of individuals are injured every year, and many of them require an above-knee operation. In order for these people to resume their prior healthy lifestyles, they employ artificial legs like prosthetic legs. As a consequence, researchers have studied and developed novel applications in the fields of sophisticated prosthetic devices using the MR fluid approach. In this system, the MR fluid makes more sense of natural walking motion in the prosthetic devices that automatically adapts to changing gait conditions, with these extraordinary properties the prosthetic devices are very much demand and useful to many people who met with accidents [29].

Figure 46.8 depicts how the knee brace is configured with the multifunctional actuator, which offers active and semi-active torque to aid the user in having greater movement. Review these articles for a thorough examination of prosthetic devices [30, 31].

46.3.6 Dental Implants

MR fluids also play a vital role in the field of dental implantation. It is very difficult to place dental implants in the required position correctly. They are various effects that are caused by misplacing dental implants like, failure of the implants, long-lasting numbness, and permanent damage to nerve-controlling facial muscles. To overcome these issues scientists have made a haptic interface system for safe implanting operations with less effort. If the reader needs to know more about practical applications in the biomedical fields you may review the article [32].

46.4 Defects and Failures of MR Fluid

As we previously said, MR fluid technology is steadily advancing, and researchers are looking for new methods to create new products that function better. In certain instances, the MR fluid, which is composed of magnetic particles that are smaller than a micron and a carrier fluid, develops defects and failures. The MR liquids contain the drawbacks of MR fluids that reduce application efficiency and common flaws and failures include hard cake, clumping effects, particle oxidation, fluid-particle separation (FPS), and stability. Perfecting these flaws and errors leads to the development of MR applications.

46.4.1 Hard Cake

In the MR fluids, the particles in the carrier fluids have a propensity for settling due to gravity's pull and agglomerating to form hard cakes [33]. The hard cake retains its strength even after the magnetic field is withdrawn because of substantial aggregation and remanent magnetism associated to the particles. When the magnetic field is turned off, fluid flow is required, and shear rates of several orders of magnitude are presented [34]. The use of silica nanoparticles as a surfactant makes it simple to have redispersion and reduces residual magnetism in particles, and it also settles down the iron particles in the MR fluid, according to the author [35].

The author [36] has studied the alternatives of surfactants due to several sedimentation difficulties in redispersion after hard cake, particles large density differences, to overcome these issues author considered alternatives of surfactant as coatings; The iron particles are coated with poly (vinyl butyral) (PVB).

46.4.2 Clumping Effect

As a result of particle aggregation in the MR fluid during the squeezing process, one of the observed behaviors is clumping. The carrier fluid flows freely out while the iron ions are confined in the magnetic field in the gap due to strong fluid currents. This causes the carrier fluid to exit and leave the iron particles behind, while trapping the iron particles in the gap [37, 38]. The trapped iron particles in the gap form a cluster as a result of the forces at work on them [34]. The clumping was decreased from 172% to 29.5% by applying a sine current dither, according to the author [38] who also discovered that the dither will help redistribute clumped particles in the MR fluid.

46.4.3 Particle Oxidation

The oxidation of the particles is also the major defect caused in the MR fluid applications. The particle oxidation is generally a chemical process, once the particles are exposed in the atmosphere, operating at high temperature causes particle oxidation, which reduces particle magnetizing potential and has a negative impact on MR fluid. Iron particles typically make from 20 to 40% of the volume of the MR fluids and have good characteristics. As we previously noted, carbonyl iron, which has an iron concentration of 97–99%, is the most often utilised particle material [37]. The author [39] investigated the effects of iron oxidation on MR fluids' field-induced rheological characteristics.

46.4.4 Fluid Particle Separation (FPS)

A loss similar to the clumping effect is called fluid-particle separation, or FPS. A squeezing technique of compression that results in the separation of fluid and particles. Investigations are being conducted on the connections between fluid-particle separation and the mechanical behaviour of MR fluids. It is evident that low carrier fluid viscosity, slow compression speed, and high provided current all result in better fluid-particle separation; however, low carrier fluid viscosity has the most effect on liquid-particle separation [37].

46.5 Conclusion

The properties of the magnetorheological fluids are briefly discussed with the present day to day improvements. The magnetorheological fluid-based applications were also studied briefly in this paper and the research and developments in the MR fluid applications are increasing and will found more extensive material in the recent developments. In addition to the applications like dampers, breaks, shock absorbers, clutches, actuators, seals, and fixtures were briefly discussed and the challenges that come to magnetorheological fluid devices that are showcased with some desired solutions and few defects which are not to remove permanent but they can manage through some solutions are studies in this paper.

The MR fluids are having good qualities that are ease of controllability, easily predictable behavior to various modes of applications in various fields like automobile industries, aerospace, and medical fields, are discussed and the required solutions are also prescribed in this paper briefly. A lot of studies are done by the researchers to use the MR fluids in the day-to-day life live applications parallel to the new developments in the MR fluids. Future research in the field of medicine is using MR fluid materials to generate hyper-functional materials that, in some aspects, outperform the capabilities of biological organs and provide a high-quality end result.

References

1. Kciuk, M., Turczyn, R.: Properties and application of magnetorheological fluids. J. Achievem. Mater. Manuf. Eng. **18**(1–2), 127–130 (2006)
2. Ashtiani, M., Hashemabadi, S.H., Ghaffari, A.: A review on the magnetorheological fluid preparation and stabilization. J. Magn. Magn. Mater. **374**, 716–730 (2015)
3. Jacob, R.: The magnetic fluid clutch. Electr. Eng. **67**, 1167–1167 (1948)
4. Phulé, P.: Magnetorheological (MR) fluids: principles and applications. Smart Mater. Bull. **2001**, 7–10 (2001)
5. Wanga, N., Liua, X., Sunb, S., Królczykc, G., Lid, Z., Lid, W.: Microscopic characteristics of magnetorheological fluids subjected to magnetic fields. J. Magn. Magn. Mater. **501**, 166443 (2020)
6. Li, R., Li, X., Li, Y., Yang, P.-A., Liu, J.: Experimental and numerical study on surface roughness of magnetorheological elastomer for controllable friction. Friction **8**, 917–929 (2019)
7. Kumbhar, B.K., Patil, S.R., Sawant, S.M.: Synthesis and characterization of magneto-rheological (MR) fluids for MR brake application. Eng. Sci. Technol. **18**, 432–438 (2015)
8. Carlson, J.D., Jolly, M.R.: MR Fuid, foam and elastomer devices. Mechatronics **10**, 555–569 (2000)
9. Carlson, J.D., Catanzarite, D.M., Clair, K.: Commercial magneto-rheological fluid devices. Int. J. Mod. Phys. B **10**, 2857–2865 (1996)
10. Baranwal, D., Deshmukh, D.T.: MR-fluid technology and its application—a review. Int. J. Emerg. Technol. Adv. Eng. **2**, 563–569 (2012)
11. Zareie, S., Zabihollah, A.: The recent advances in magnetorheological fluids-based applications. Emerging trends in mechatronics. InTech Open, London (2020)
12. Chooi, W.W., Oyadiji, S.O.: Design, modelling and testing of magnetorheological (MR) dampers using analytical flow solutions. Comput. Struct. **86**, 473–482 (2008)
13. Wang, J., Meng, G.: Magnetorheological fluid devices: Principles, characteristics and applications in mechanical engineering. Proc. Inst. Mech. Eng. Part L J. Mater. Des. Appl. **215**, 165–174 (2001)
14. Olabi, A., Grunwald, A.: Design and application of magneto-rheological fluid. Mater. Des. **28**, 2658–2664 (2007)
15. Acharya, S., Tak, R.S.S., Singh, S.B., Kumar, H.: Characterization of magnetorheological brake utilizing synthesized and commercial fluids. Mater. Today Proc. **46**, 9419–9426 (2020)
16. Huang, J., Zhang, J., Yang, Y., Wei, Y.: Analysis and design of a cylindrical magneto-rheological fluid brake. J. Mater. Process. Technol. **129**, 559–562 (2002)
17. Sukhwani, V.K., Hirani, H.: A comparative study of magnetorheological-fluid-brake and magnetorheological-grease-brake. Tribol. Online **3**, 31–35 (2008)
18. Hajalilou, A., Mazlan, S. A., Lavvafi, H., Shameli, K.: Magnetorheological Fluid Applications. *Field Responsive Fluids as Smart Materials,* pp. 67–81. Springer Singapore, Singapore (2016)
19. Patel, R.: Mechanism of chain formation in nanofluid based MR fluids. J. Magn. Magn. Mater. **323**, 1360–1363 (2011)
20. Park, E.J., Stoikov, D., Luz, L.F., Suleman, A.: A performance evaluation of an automotive magnetorheological brake design with a sliding mode controller. Mechatronics **16**, 405–416 (2006)
21. Janocha, H., Clephas, B., Claeyssen, F., Hesselbach, J., Bullough, W.A., Carlson, J.D., Megede, D., Wurmus, H., Kallenbach, M.: Actuators in Adaptronics. In: Janocha, H. (ed.) Adaptronics and Smart Structures, pp. 99–240. Springer, Berlin (1999)

22. Lampe, D., Thess, A., Dotzauer, C.: MRF-Clutch—Design Considerations and Performance. Transition (1998)
23. Carlson, J.D., Catanzarite, D.M.: United States Patent 5,816,372 (1998)
24. Zeinali, M., Mazlan, S., Imaduddin, F., Fatah, A.A., Mughni, M., Hamdan, L., Yazid, I.M.: Magnetorheological fluid characterization and applications. In: Reference Module in Materials Science and Materials Engineering, Elseiver, New York (2016)
25. Lee, U., Kim, D., Hur, N., Jeon, D.: Design analysis and experimental evaluation of an MR fluid clutch. J. Intell. Mater. Syst. Struct. **10**, 701–707 (1999)
26. Nguyen, Q.H., Hiep, L.D., Duy, B.Q., Choi, S.-B.: Development of a new clutch featuring MR fluid with two separated mutual coils. In: AETA 2015: Recent Advances in Electrical Engineering and Related Sciences, pp. 835–844 (2016)
27. Ansaloni, M., Bonazzi, E., Leali, F., Pellicciari, M., Berselli, G.: Design of fixture systems in automotive manufacturing and assembly. Adv. Mater. Res. **712–715**, 2913–2916 (2013)
28. Tang, X., Zhang, X., Tao, R.: Flexible fixture device with magneto-rheological fluids. In: Electro-Rheological Fluids And Magneto-Rheological Suspensions, pp. 700–708 (2000)
29. Carlson, J.D., Matthis, W., Toscano, J.R.: Smart prosthetics based on magnetorheological fluids. In: Smart Structures and Materials 2001: Industrial and Commercial Applications of Smart Structures Technologies, vol. 4332, pp. 308–316 (2001)
30. Guo, H.T., Liao, W.H.: Magnetorheological fluids based multifunctional actuator for assistive knee braces. In: 2009 IEEE International Conference on Robotics and Biomimetics (ROBIO), pp. 1883–1888 (2009)
31. Ochoa-Diaz, C., Rocha, T.S., Oliveira, L.L., Paredes, M.G., Lima, R., Bó, A.P.L., Borges, G.A.: An above-knee prosthesis with magnetorheological variable-damping. In: 5th IEEE RAS/EMBS International Conference on Biomedical Robotics and Biomechatronics, pp. 108–113 (2014)
32. Abdel-Wahab, A.A., Murmu, T., Olabi, A.G.: Applications of magnetorheological (MR) fluids in the biomedical field. In: Reference Module in Materials Science and Materials Engineering, pp. 1–25 (2018)
33. Prajapati, H., Shahanand, J., Nimkar, H., Lakdawala, A.: Methods for sedimentation study of magnetorheological fluids. Mater. Today Proc. **28**, 40–44 (2020)
34. Kumar, J.S., Paul, P.S., Raghunathan, G., Alex, D.G.: A review of challenges and solutions in the preparation and use of magnetorheological fluids. Int. J. Mech. Mater. Eng. (2019). https://doi.org/10.1186/s40712-019-0109-2
35. López-López, M.T., Kuzhir, P., Lacis, S., Bossis, G., González-Caballero, F., Durán, J.D.G.: Magnetorheology for suspensions of solid particles dispersed in ferrofluids. J. Phys.: Condens. Matter **18**, S2803–S2813 (2006)
36. Jang, I.B., Kim, H.B., Lee, J.Y., You, J.L., Choi, H.J., Jhon, M.S.: Role of organic coating on carbonyl iron suspended particles in magnetorheological fluids. J. Appl. Phys. **97**, 10Q912 (2005)
37. Wahid, S., Ismail, I., Aid, S., Rahim, M.: Magneto-rheological defects and failures: a review. IOP Conf. Ser. Mater. Sci. Eng. **144**, 012101 (2016)
38. Farjoud, A., Craft, M., Burke, W., Ahmadian, M.: Experimental investigation of MR squeeze mounts. J. Intell. Mater. Syst. Struct. **22**, 1645–1652 (2011)
39. Sunkara, S.R., Root, T.W., Ulicny, J.C., Klingenberg, D.J.: Iron oxidation and its impact on MR behavior. J. Phys: Conf. Ser. **149**, 012081 (2009)

Chapter 47
Properties, Preparation, Applications and Handling of Aerogels

Pranay Suryapet, Muddu Allaparthi, and Thipparthi Raja Gopala Chary

Abstract Aerogels materials are the porous, solid materials that exhibit a different way of extreme material properties. Mainly aerogels are known for their extremely low densities (which range from 0.0011 to 0.5 g cm^{-3}). Aerogels are nano structured materials with high specific surface area and porosity along with low density and dielectric constant with excellent heat insulation properties which have 95–99% air in volume. Aerogels materials are generally prepared by removing of the liquid substance of gel through a supercritical drying process which makes the liquid to be slowly dried out without the collapsing of the solid matrix in the gel from the capillary action. This particular paper presents a review of properties, preparation, application, and handling of aerogel materials. The total review in this paper makes ease of work and more reliable for future.

47.1 Introduction

The preparation of porous materials has taken a fast progress in past twenty years because of the rapid developments in the sol–gel techniques. These conventional technical procedures are employed to make amorphous solids by impregnation or precipitation methods followed by the temperature elevated treatments. Porous materials have a very high importance in various applications in a field of sensing, adsorption, and catalysis, because of the surface properties like area, porosity, framework,

P. Suryapet
Tata Consultancy Services, Hyderabad, India

M. Allaparthi
Department of Mechanical Engineering, R.V.R. & J.C. College of Engineering, Guntur, India

T. R. G. Chary (✉)
Department of Mechanical Engineering, Malla Reddy College of Engineering and Technology, Hyderabad, India
e-mail: rgcsrcm@gmail.com

P. H. V. S. Talpa Sai et al. (eds.), *Intelligent Manufacturing and Energy Sustainability*, Smart Innovation, Systems and Technologies 372,
https://doi.org/10.1007/978-981-99-6774-2_47

and optical transmission. Further Aerogels have become successful because they are thermally least conductive, porosity is high, Transmission of light is great in the visible region, high surface specific area, small value of dielectric constant, least refractive index, and velocity of sound is minimum [1].

47.1.1 Aerogels

Aerogel material is firm, dry, and solid material which has a solid porous network filled with air pockets which takes up the larger part of 99.8% room within the aerogel material. This composition of Aerogels gives it an almost a unique Special mysterious appearance by which it is always termed as 'frozen smoke'. The larger part of Aerogel material consists of silica, but Carbon, Iron oxide, Semiconductor, Organic Polymers, Metal like gold and copper can also be used to make Aerogel [2].

The word Aerogel was first given in 1932 by Kistler to select gels where the gas is used to replace the liquid present in them without damaging the gels network of solid. Wetter gels are dried by evaporation process in prior, Kistler used a supercritical method where liquid present in the gels pores is removed after transformed into supercritical fluid. Till the temperature and pressure reaches to their critical points of the liquid entrapped inside the gels pores [3].

47.2 Properties of Silica Aero Gels

Internal structures are cross linked in chains of SiO_2 of an aero gel which gives a huge number of air-filled pores of small sizes and high porosity. Capability of silica aero gels is very high because it's unnormal solid material properties. The porosity property which is high for Aerogel makes it the most lightweight solid at the present and because of the excellent tiny pore size and high porosity Aero gel gains its exceptional optical, material, thermal and acoustic properties, and even makes it material with very low mechanical strength [4].

47.2.1 Thermal Properties

The most important characteristics of silica aero gels are their thermal conductivity (low i.e. nearly 0.0015 $Wm^{-1}\ K^{-1}$) in particular pressure, temperature, and relative humidity which even far lower than thermal conduciveness of atmospheric air (i.e. 0.025 $Wm^{-1}\ K^{-1}$) under the same conditions [4]. As a result, silica aero gels are one out of the best thermal insulating materials and moreover silica aero gels are nonflammable and amorphous [5].

47.2.2 Optical Properties

Light transmission property and scattering property of the Silica aero gels consists a very important characteristic. Rayleigh scattering in the aero gels is because of the gels network of variability in the nano meter range is reason for yellow coloration in transmission and bluish coloration against dark background as Aerogels are low refractive index solids. [4].

47.2.3 Acoustic Properties

This property of silica aero gels is connected to their properties of thermal insulation and these properties depend on the intermediate space of gas in nature along with pressure and density [6]. Silica Aerogels are excellent sound proofing materials and has a acoustic longitudinal velocity upto 100 m/s which makes them for using in sound proofing (acoustic) devices [4].

47.2.4 Mechanical Properties

Silica Aerogels have very low tensile, compressive strength, and modulus of elasticity and are largely depend on Aerogel's density [7]. Physical (mechanical) properties of Aerogels changes with respective to the chemistry preparation of the gel, environment, and the record of storage [8]. Even low density and brittle characteristics Aerogels are used in some specific applications because of their other physical properties [4].

47.2.5 Dielectric Properties

A narrow film of silica aerogel can be used as super low dielectric constant material for ICs in a computer because of their relatively low dielectric constant [9] (Table 47.1).

47.3 Preparation of Aerogels

Generally, preparations of silica aerogels involve following steps: Preparation, Ageing and Drying of gel [11].

Table 47.1 Structural properties of aerogels along with their range [10]

Property	Range
Refractive index	1.007–1.24
Porosity, %	80–99.8
Thermal conductivity λ (in air, 300K) [Wm^{-1} K^{-1}]	0.017–0.021
Mean pore diameter [nm]	20–150
Inner surface area [m^2 g^{-1}]	100–1600
Acoustic impedance Z [kg m^{-2} s^{-1}]	10^4
Bulk density [g cm^{-1}]	0.003–0.500
Sound velocity CL [m s^{-1}]	< 20–800
Skeletal density [g cm^{-3}]	1.700–2.100
Modulus of elasticity E [MPa]	0.002–100

47.3.1 Preparation of Cell

In the present of basic catalyst i.e. ammonium hydroxide or ammonium fluoride and silicon alkoxide reacts with water in acetone or ethanol as a solvent to produce Silica Aerogels in alkoxide gelation process.

47.3.1.1 Hydrolysis Process

Silicon is formed by reaction of silicon alkoxide and $(CH_3O)_4Si$ or $(C_2H_5O)_4Si$ along with water acts as a reactant which helps in joining of alkoxide molecules.

$$\equiv \text{Si}-\text{OR} + \text{H}_2\text{O} \Leftrightarrow \equiv \text{Si}-\text{OH} + \text{ROH} \quad \text{R represents the alkyl group}$$

47.3.1.2 Process of Condensation by Water

In this process silanol groups reacts with each other

$$\equiv \text{Si}-\text{OH} + \text{HO}-\text{Si} \equiv \Leftrightarrow \equiv \text{Si}-\text{O}-\text{Si} \equiv +\text{H}_2\text{O}$$

47.3.1.3 Process of Condensation by Alcohol

Silanol and alkoxide groups reacts with each other to form a one large molecule of silaxone (Si–O–Si) bridge.

$$\equiv \text{Si}-\text{OH} + \text{RO}-\text{Si} \equiv \Leftrightarrow \equiv \text{Si}-\text{O}-\text{Si} \equiv + \text{ROH}$$

Four siloxane bridges can be formed by one silicon atom which results in the formation of giant molecules by connection of small molecules which results in many silicon-oxygen bridges which makes gels [12].

47.3.2 Ageing of Gel

When a solution hits the gel point, there are already a large amount of unreacted alkoxide groups in the silica spine of the gel. Concentration, pH and water content of the covering solution are controlled which allows the hydrolysis and condensation process to happen for a long enough period to strengthen the silica network. Ethanol–siloxane mixtures are often used in aging procedures.

Adding additional monomers to the strong Si–O network and raising the degree of Cross-linking in the gel results in increased stiffness and strength. According to the solid silica network, Ageing mechanism is diffusion-mediated transportation of material that is unaffected by mixing or convection, as diffusion is self-affected by the thickness of the gel. As a result, as the gel's thickness grows, the amount of time needed for each manufacturing phase raises, reducing the practical output of aerogels.

47.3.3 Drying

In making of Aerogels Drying of gel is last and important step.

47.3.3.1 Supercritical Drying (SCD)

It is the mostly used technique for producing Silica Aerogels. To produce an aerogel, liquid which is present in it must be replaced with air by some means in a way such that the liquid removed is never allowed to go back into the gel. Liquid which is kept under pressure has greater pressure than the pressure of vapour, and with the increase temperature, gas is formed by the transformation at the critical temperature [13].

High Temperature Super Critical Drying

This involves 3 steps

- Gel which is aged is kept in an autoclave which is filled by half with the solvent which is in the pores of gel. In Silica Aerogels making solvent is CH_3OH. Autoclave is closed and heated slowly at critical temperature (300–600 °K) and pressure (30–80 atm) of solvent.

Methanol reaction with OH groups make silica aerogels partially hydrophobic which Generally makes aerogels of higher quality.

- Then Fluid is depressurized isothermally.
- Then at an appropriate pressure, autoclave is cooled to the normal room temperature.

Low Temperature Super Critical Drying

Similarly, LTSCD is also done in three steps

- Gel which is Aged is kept in an autoclave which has fire proof liquid carbon dioxide at 4–10 °C temperature till it reaches 100 bars of pressure to remove solvent from the gel's pores. Then total solvent present in it is replaced, and followed by heating of autoclave to 313 °K maintaining at pressure of 100 bar.

Aerogels which are dried by LTSCD method are shrinked due to the removal of the Solvent present in it with the liquid CO_2

- Then the Fluid is depressurized isothermally.
- Then at an appropriate pressure, autoclave is cooled to the normal room temperature.

47.3.3.2 Ambient Pressure Drying (APD)

APD is done in two steps and it costs less compared to the HTSCD or LTSCD drying processes

- To avoid adsorption OH groups are Silylated so that it can form hydrophobic Aerogels and it is done by changing solvent and silylating agent which is water free.
- Evaporation by ambient pressure is used for process of drying.

Fig. 47.1 Part of the liquid-oxygen feed line in a space shuttle [14]

47.4 Applications of Aerogels

In the early 1990s, Aerogels were recognized by their extraordinary properties, notably uniformity and homogeneity, which are particularly important for applications in primary components. Scientists and Engineers continued to order custom aerogels as they became more knowledgeable of the properties of aerogels and considered uses for them.

47.4.1 Flight Vehicle Application

Since ice is a primary threat for vehicle surfaces and impedes the mechanical articulation of the bellows assembly, an aerogel-based insulation device is used to enable the liquid-oxygen feed line in the bellows to travel easily without accumulating any ice. Over the 8–10 h of simulated ground-hold conditions, the hydrophobic aspect of the aerogel prevented ice from forming within the internal cold cavities [14] (Fig. 47.1).

47.4.2 Aerogels Application in Field of Construction

Because of their high thermal efficiency, silica aerogels are a revolutionary alternative to conventional insulation. Aerogel insulation was used to retrofit an old brick house due to its excellent thermal insulating properties [4] (Fig. 47.2).

Fig. 47.2 Left: An old brick house with aerogel insulation. Right: The top layer of a thermographic picture is insulated by aerogel, while the bottom floor is not [4]

47.4.3 Cherenkov Detectors

Cherenkov detectors are used to determine the velocity of high-energy particles. It's important to use different refractive index values to obtain a fair degree of precision on particle momentum in various momentum ranges. As a result, silica aerogels were used as Cherenkov radiators. In the spectrum of indices where high-pressure gases have historically been used, silica aerogels are ideal for use as solid Cherenkov radiators, as well as higher indices where prohibitively high gas pressures will be needed [15].

47.4.4 Acoustic Applications

Aerogel's acoustic impedance is between 104 and 105 kg/m^2 s. SiO_2-aerogels are used in acoustic delay lines, noise control systems, acoustic antireflection layers, and window systems [16]. In ultrasonic applications and sound absorption anechoic chambers, aerogels have a higher acoustic impedance. The use of aerogels as a shock absorber has also been proposed [17].

47.4.5 Aerogels Used in Catalysis

The Dry reforming, liquid phase Hydrogenation, decomposition by photocatalytic and partial oxidation, ammoxidation along with other reactions have all shown that aerogels are effective catalysts. A large rise in stability, catalytic activity and selectivity is described by a combination of large unique area surface which are available to reacting molecules with metal to metal interactions or strong metal-support, and extremely high dispersion of active species [18].

47.4.6 Aerogels in Microelectronics

Aerogel's materials are with the lowest dielectric constants which depends on its porosity, and the use of such a material in microelectronics makes it possible to substantially reduce the appropriate parasitic capacitances and thus increase the response speed. During the gel period, aerogel is transformed into thin films that can be transferred to silicon or glass substrates with sufficient adhesion [19].

47.4.7 Aerogels in Gases and Liquids Purification

Aerogels may be used as filters for a variety of applications due to their wide surface area. Hydrophobic aerogels are effective absorbers of both soluble and insoluble compounds in water [20].

Aerogel can also be used to purify gases that are emitted by a car's exhaust pipe. Metal oxides such as vanadium, iron, and aluminum are applied to the aerogel in this situation. They work as active heterogeneous processes, resulting in a reduction in NOX levels in exhaust gases. Aerogel's high porosity ensures a broad contact region between the catalyst and gases. Silicon–titanium aerogels containing crystalline titanium have a high affinity for oil, which is adsorbed and fully decomposed into carbon dioxide [19].

47.4.8 Detection of Harmful Microorganisms

Aerogel is used as a matrix for the introduction and immobilisation of bacteria. The aerogel is exposed to air flow, which can include plague bacteria. The aerogel is then immersed in a solution where the bacteria will replicate. The bacteria in the original matrix are devoured by plague bacteria. Protein is formed as a result, and it fluoresces in the green spectral region. Other uses for this kind of technology include identifying infectious viruses and bacteria in emergency rooms and radioactive elements in plants and factories [21].

47.4.9 Biomedical Applications of Aerogels

Because of their possible uses in medical devices, protein and drug delivery, bone implants, bio-sensing and in tissue engineering Aerogels have stimulated interest in biomedicine. In-vivo and vitro studies has also made to show that such Aerogel materials have outstanding bio-compatibility with different structures, as previously mentioned. However, as aerogel production and properties increase, as does our understanding of biomaterials, aerogels can become more commonly used in biomedical applications in the near future [22].

47.4.10 Influence of Aerogels on Superfluidity

One of the most fascinating phenomena of science is liquid helium's superfluidity (at $Tc = 2.17$ K), which is the property of moving without pressure through small capillaries, slots, and other structures. With ^{4}He embedded in aerogel pores, an unlikely result was obtained [23]. At a small drop in the critical temperature, an unexpectedly sharpened transformation of liquid helium into the superfluid state was detected. The relatively high porosity of aerogel and the extremely small size of its solid particles, which are much smaller than the coherence length of a superfluid material, are distinctive characteristics. This sparked a lot of interest in aerogel when it came to researching different effects in a superfluid liquid, and it started a whole new movement in its research [19].

47.4.11 Aerogels as Cosmic Dust Collectors

One of the main aims of planetary science is to conduct detailed laboratory analyses of space samples from a single body with a documented background. Comets are microscopic, primitive solar system bodies that are rich with ice that has been protected by staying deep-frozen in space. For a long time to come, aerogels would be the kind of capture media used for cosmic dust processing. Comets are awe-inspiring celestial bodies. Aerogels are also being used on the European Retrieval Carrier EURECA spacecraft and in Space Shuttle experiments to capture cosmic dust [24].

47.5 Aerogels in Microelectronics

When we come into contact with aerogel products, they will irritate our eyes, ears, respiratory system, and gastric system. When tiny particles are inhaled, it can cause dryness of the ears, eyes, and other mucous membranes. Safety precautions such as respirators, gloves, and eye masks must be worn while operating with aerogels [25].

47.6 Conclusion

The preparations, properties of the aerogels are briefly discussed with the present day to day improvements. The aerogels-based applications were also studied briefly in this paper and the research and developments in the aerogel's applications are increasing and will found more extensive material in the recent developments.

Aerogels applications in various fields like automobile industries, aerospace, and medical fields, are discussed and the required solutions are also prescribed in this paper briefly. A lot of studies are done by the researches to use the aerogels in the day to day life live applications parallel to the new developments in the aerogels.

References

1. Gurav, J.L., Jung, I.-K., Park, H.-H., Kang, E.S., Nadargi, D.Y.: Silica aerogel: synthesis and applications. J. Nanomater. **2010**, 1–11 (2010)
2. Thomas, G.: AZO materials, 08 July 2020. [Online]. Available: https://www.azom.com/article.aspx?ArticleID=6499. Accessed 13 Sept 2020]
3. Aegerter, M.A.: Aerogels Handbook. Springer, New York (2011)
4. Baetens, R., Jellea, B.P., Gustavsend, A.: Aerogel insulation for building applications: a state-of-the-art review. Energy Build. **43**(4), 761–769 (2011)
5. Yoldas, B.E., Annen, M.J., Bostaph, J.: Chemical engineering of aerogel morphology formed under nonsupercritical conditions for thermal insulation. Chem. Mater. 2475–2484 (2000)
6. Forest, L.: Biot's theory of acoustic propagation in porous media applied to aerogels and alcogels. J. Non-Cryst. Solids **225**, 287–292 (1998)
7. Woignier, T.: Scaling law variation of the mechanical properties of silica aerogels. J. Phys. Colloq. **24**(C4), 179–184 (1989)
8. Parmenter, K.E.: Mechanical properties of silica aerogels. J. Non-Cryst. Solids **223**(3), 179–189 (1998)
9. Kawakami, N.: Preparation of highly porous silica aerogel thin film by supercritical drying. Japan. J. Appl. Phys. **39**(Part 2, No. 3A/B), L182–L184 (2000)
10. Housing, N., Schubert, U.: Aerogels—airy materials: chemistry, structure, and properties. Angew. Chem. Int. Ed. **37**(1/2), 22–45 (1998)
11. Brinker, J.C.: Sol-Gel Science. Academic Press, San Diego (1990)
12. Błaszczyńskia, T., Ślosarczykb, A., Morawski, M.: Synthesis of silica aerogel by supercritical drying method. Procedia Eng. **57**, 200–206 (2013)
13. Kistler, S.S.: Coherent expanded-aerogels. J. Phys. Chem. **36**(1), 52–64 (1932)
14. Fesmire, J.: Aerogel insulation systems for space launch applications. Cryogenics **46**(2–3), 111–117 (2006)

15. Cantin, M., Casse, M., Koch, L., Jouan, R., Mestreau, P., Roussel, D., Bonnin, F., Moutel, J., Teichner, S.J.: Silica aerogels used as Cherenkov radiators. Nucl. Instrum. Meth. **118**(1), 177–182 (1974)
16. Gronauer, M., Fricke, J.: Acoustic properties of microporous SiO_2-aerogel, 1 Jan 1986. [Online]. Available: https://www.ingentaconnect.com/content/dav/aaua/1986/00000059/00000003/art00005#expand/collapse
17. Hrubesh, L.W.: Aerogel applications. J. Non-Cryst. Solids 335–342 (1998)
18. Choi, J., Suh, D.J.: Catalytic applications of aerogels. Catal. Surv. Asia 11(3), 123–133 (2007)
19. Akimov, Y.K.: Fields of application of aerogels (review). Instrum. Exp. Tech. 287–299 (2003)
20. Hrubesh, L.W., Coronado, P.R., Satcher Jr., J.H.: Solvent removal from water with hydrophobic aerogels. J. Non-Cryst. Solids 328–332 (2001)
21. Power, M., Hosticka, B., Black, E., Daitch, C., Norris, P.: Aerogels as biosensors: viral particle detection by bacteria immobilized on large pore aerogel. J. Non-Cryst. Solids 303–308 (2001)
22. Maleki, H., Durães, L., García-González, C.A., del Gaudio, P., Portugal, A., Mahmoudi, M.: Synthesis and biomedical applications of aerogels: possibilities and challenges. Adv. Colloid Interface Sci. **236**, 1–27 (2016)
23. R. Maynard, G. Deutsche, Apparent anomalous critical behaviour of superfluid helium 4 in porous medium. Europhys. Lett. **10**(3), 257–260 (1989)
24. Tsou, P.: Silica aerogel captures cosmic dust intact. J. Non-Cryst. Solids 415–427 (1995)
25. Thapliyal, P.C., Singh, K.: Aerogels as promising thermal insulating materials: an overview. J. Mater. 1–10 (2014)

Chapter 48
Role of Machine Learning in Sustainable Manufacturing Practices: An Outline

Rupinder Kaur, Raman Kumar, and Himanshu Aggarwal

Abstract The present research examines the potential of machine learning (ML) to improve sustainability and lessen harmful environmental effects across various industries. The paper discusses ML's uses in sustainable manufacturing practices (SMP), such as supply chain management, waste management, energy efficiency, equipment maintenance, water quality management, and other fields. The investigations show how ML approaches may be used to forecast equipment failure, lower carbon footprints, optimize resource use, and improve water quality. The study highlights the benefits of utilizing ML to increase sustainability, including real-time data, simplified processes, lower costs, and a sustainable future while admitting the difficulties and limits of ML techniques. The article ends by recommending enterprises and the industrial sector explore the prospect of using ML to attain their goals for sustainability.

48.1 Introduction

Traditional manufacturing methods have been linked to harmful environmental effects such as resource depletion, pollution, and waste production. So, sustainable manufacturing techniques have been developed to minimize the negative environmental effects of manufacturing operations while fostering economic and social advancement [1].

R. Kaur (✉) · H. Aggarwal
Department of Computer Science and Engineering, Punjabi University, Patiala, Punjab 147002, India
e-mail: rupinderkaur1588@gmail.com

H. Aggarwal
e-mail: himanshu@pbi.ac.in

R. Kumar
Department of Mechanical and Production Engineering, Guru Nanak Dev Engineering College, Ludhiana, Punjab 141006, India

P. H. V. S. Talpa Sai et al. (eds.), *Intelligent Manufacturing and Energy Sustainability*, Smart Innovation, Systems and Technologies 372,
https://doi.org/10.1007/978-981-99-6774-2_48

Sustainable manufacturing refers to the process of producing goods in a manner that minimizes the environmental impact while balancing the economic and social dimensions of manufacturing. It is a process of creating products and services using resources and energy to reduce waste and pollution, conserve energy and natural resources, and improve the quality of life of the employees and the communities where the manufacturing occurs [2]. Implementing sustainable practices that strike a balance between the requirements of the present and the needs of the future aims to lessen this impact. Product design, material selection, manufacturing procedures, energy efficiency, waste reduction, and end-of-life disposal are some practices that go into sustainable manufacturing. It considers a product's whole lifespan, from the extraction of raw materials through disposal, and seeks to reduce the environmental effect at every turn [2].

Artificial intelligence's branch of machine learning (ML) has demonstrated its ability to promote environmentally friendly manufacturing methods [3]. ML algorithms can analyze large data sets, find patterns, and forecast outcomes that may be used to streamline production, cut waste, and increase resource efficiency. The use of ML in sustainable manufacturing techniques has not received much attention, though [4].

ML can significantly advance environmentally friendly manufacturing techniques. Companies may lessen their impact on the environment, increase productivity, and save costs by utilizing ML algorithms to analyze and optimize production processes. Energy efficiency in industrial facilities is one way ML may support sustainable manufacturing [5]. Waste in industrial processes is decreased with the use of ML. By analyzing production data, ML algorithms can spot inefficiencies and provide strategies to reduce waste and maximize material consumption. Another area where ML might enhance industrial sustainability is predictive maintenance. ML algorithms can forecast when maintenance is necessary by examining equipment performance data and minimizing waste, downtime, and maintenance expenses. The supply chain activities may also be optimized using ML [6]. The development of sustainable products can also benefit from ML. ML may assist in developing more SMPs and lessen the manufacturing industry's impact on the environment by helping businesses to analyze and optimize production processes, cut waste, and increase productivity [7].

The demand in the industrial sector to increase sustainability and lessen its environmental effect is growing [2]. Traditional manufacturing procedures sometimes do not have the adaptability and effectiveness needed to accomplish these objectives. As a result, there is a demand for cutting-edge solutions that may assist manufacturers in streamlining their operations, cutting waste, increasing productivity, and reducing environmental impact. The potential uses of ML in sustainable manufacturing have many difficulties and constraints to put into practice and successful implementations. This paper provides an outline of SMPs and how ML contributes.

48.2 Application of Machine Learning in Sustainable Manufacturing

ML can be applied in several ways to promote SMPs. Figure 48.1 depicts various SMPs. The application of ML in various SMPs has been reviewed.

48.2.1 Waste Management

ML can assist with waste management in manufacturing by reducing waste, improving recycling, and optimizing resource consumption. It can help decrease waste and boost efficiency by anticipating the ideal number of raw materials needed for production. In predictive maintenance, ML can be used to forecast equipment failure and determine the ideal time for maintenance [4].

Sami et al. [8] presented a waste classifying system and employed ML and Deep Learning (DL) algorithms to categorize waste into six categories: glass, paper, metal, plastic, cardboard, and rubbish. The performance of three ML algorithms, SVM, Random Forest (RF), and DT, and one DL algorithm CNN was compared, and it reported that CNN attained the highest classification accuracy of 90%. Anh Khoa et al. [1] described a waste management system that employed ML and graph theory to forecast the garbage levels in trash cans and optimize rubbish pickup by taking the shortest path. The solution was tested on a genuine university campus utilizing

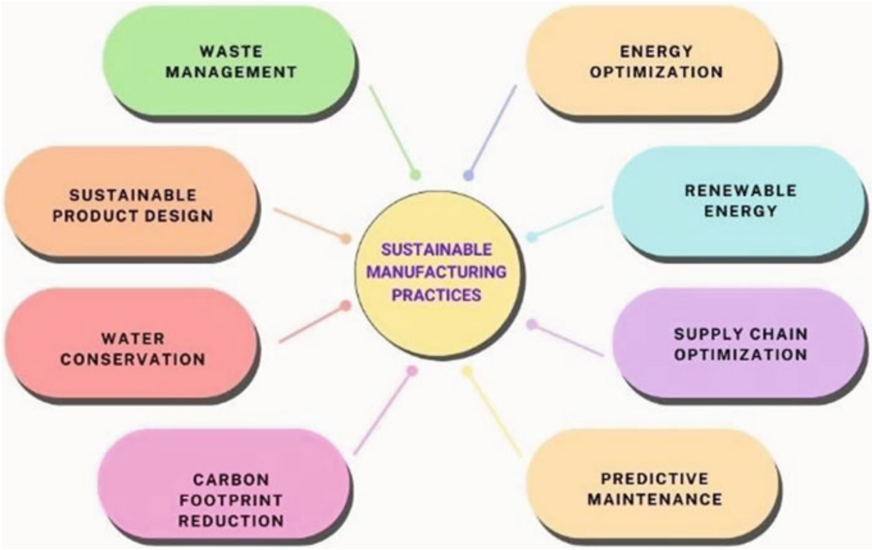

Fig. 48.1 Sustainable manufacturing practices

a low-cost IoT architecture. Zaman et al. [9] discussed the potential application of Industry 4.0 technology in waste management, which can help reduce costs, improve efficiency, and achieve circular economy goals. The 20,491 labeled images of waste items in six categories were collected, and the You Only Look Once version 4 ML algorithm was employed. Huang et al. [4] developed a framework for ML-driven predictive analytics for waste management operations, including material and energy recycling. A neural network was utilized to estimate the amount of trash, and an improved ML algorithm was used to improve waste collection. The results revealed that the proposed method reduced landfill analysis by 40%, transportation by 15%, and trash quantity analysis by 90%. Khan et al. [10] proposed an efficient solution for smart and effective waste management using ML and the IoT. The amount of waste in dustbins and disposal sites was detected by using an Arduino UNO microcontroller, an ultrasonic sensor, and a moisture sensor. The suggested approach aimed to produce clean, pollution-free towns while also reducing the overall time and cost.

The use of ML in SMP research has shown how it may be used to improve waste categorization, forecast waste levels, optimize resource usage, and cut waste through effective recycling. The suggested methods have shown increased accuracy, decreased waste, decreased costs of transportation and analysis, and fulfilled circular economy objectives.

48.2.2 Energy Optimization

Energy optimization is the practice of lowering energy use in production processes without sacrificing the quality of the final goods. Energy is a significant expense in manufacturing, and important to use energy as efficiently as possible to cut costs, increase sustainability [11], and adhere to laws. Manufacturing companies may benefit from ML by optimizing energy use and reducing energy waste, resulting in considerable cost savings and ecological benefits.

Mocanu et al. [12] explored methodology to optimize energy schedules for building smart grid energy management systems using deep reinforcement learning. The proposed technique was validated using the enormous Pecan Street Inc. database, which comprised information regarding photovoltaic power generation, electric vehicles, and building appliances. Pawanr et al. [7] developed soft computing models for a CNC lathe machine tool's carbon emissions, power factor, and energy efficiency using experimental data. These models assist in energy-efficient production and carbon footprint reduction. Narciso et al. [13] investigated the potential utility of industrial data and examined 42 published papers addressing various energy efficiency problems. It served as a reference manual for the manufacturing and process industries to select suitable energy-efficient ML tools. Mawson et al. [14] contrasted the use of two deep neural networks—feed-forward and recurrent to anticipate energy use in manufacturing facilities and workshop conditions. The data used to train the neural networks was obtained from a simulation of a medium-sized manufacturing plant in the UK. The feed- forward model predicted building energy, workshop air temperatures, and humidity with respective accuracies of 92.4, 99.5, and 64.8%, whereas the recurrent model anticipated these variables with respective accuracies of 96.82, 99.40, and 57.60%. Liao et al. [15] created a basic air conditioning model to forecast energy use in research and development buildings. The RF algorithm produced an R^2 of 88% ahead of the first month and 81% ahead of the third month among the various ML approaches used.

The review depicts various ML techniques to optimize energy efficiency and reduce carbon footprint in different domains. The studies demonstrate the potential of ML techniques in enhancing energy efficiency and reducing carbon footprint in various domains.

48.2.3 Renewable Energy

ML optimizes the utilization of renewable energy sources like solar and wind energy. Manufacturers can maximize the usage of renewable energy sources and lessen their reliance on fossil fuels by studying weather patterns and energy demand data.

Ahmed et al. [16] demonstrated amalgamating renewable energy sources with smart grids to deal with the issue of managing energy demand. An effective Energy Management Model (EMM) was created using ML techniques. Sharmila et al. [17] developed a hybrid ML model with big data analytic techniques for the optimized distribution of available energy resources targeting smart energy management. Mostafa et al. [18] explored the use of big data analytics in renewable energy power plants and presented a framework for integrating it into smart grids. The research applied three distinct ML techniques to a decentralized smart grid data system with 60,000 instances and 12 variables to forecast the system's stability. The DT model's accuracy was 78%, the RF tree model's accuracy was 84%, and the penalized linear regression model's accuracy was 96%. The application of ML techniques for creating sustainable energy materials was discussed by Gu et al. [19]. Lai et al. [20] presented a survey and analysis of ML methods to forecast renewable energy.

In smart grids, ML approaches were used to manage energy consumption, lower carbon footprint, optimize energy scheduling, and look into the development of sustainable energy materials and the application of big data analytics in renewable energy power plants.

48.2.4 Supply Chain Optimization

ML has multiple roles in manufacturing supply chain optimization. It can estimate product demand by examining past data and market patterns. ML can also optimize delivery routes and analyze supplier performance data.

Carbonneau et al. [6] investigated the feasibility of applying non-linear ML algorithms for forecasting distorted demand signals in the extended supply chain. The basic approaches, including naive forecasting, trend, moving average, and linear regression, were compared with advanced ML techniques. Feizabadi et al. [21] developed a hybrid demand forecasting model by merging time-series data with advanced indicators based on ML techniques. The dataset was collected from a steel manufacturing company operating in four market categories. Bigliardi [22] discussed that supply chain digitization research could be divided into core, trendy, and emergent subjects. Nagar et al. [23] emphasized the importance of IT-enabled systems in allowing sectors to adapt to modern technology and remain competitive. Baryannis et al. [24] proposed a framework for predicting supply chain risks using AI techniques and expert collaboration. The dataset used contained information on around 500,000 product deliveries from tier 2 suppliers to the tier 1 supplier in the supply chain for six years from 2011 to 2016.

ML may greatly improve supply chain efficiency, and businesses must implement IT-enabled solutions to stay competitive in the rapidly evolving technological environment.

48.2.5 Predictive Maintenance

ML has transformed the way predictive maintenance is performed in the manufacturing sector. To find patterns and anomalies that indicate tackling equipment failure, manufacturers may utilize this technology to analyze vast amounts of data from numerous sources, including sensors and maintenance logs.

Arena et al. [25] proposed DTs to assist the industry in determining if predictive maintenance is a good fit for their systems. The procedure was tried in an actual industrial scenario, and the results demonstrated its effectiveness. Cınar et al. [26] presented an in-depth literature review on recent developments in ML methods for predictive maintenance for Industry 4.0 smart manufacturing. Dalzochio et al. [27] used an in-depth literature review to evaluate academic developments in failure prediction utilizing ML and reasoning for predictive maintenance in Industry 4.0. Several issues still need to be properly researched in the field of ML and predictive maintenance. Kavana et al. [28] developed an ML model for fault detection and classification of induction motor faults using real-time data from a 0.33 HP induction motor. The model accurately detected and classified faults in the motor, which could help prevent further damage and ensure the safety of electrical components. Paolanti et al. [29] described an ML architecture for the predictive maintenance of electric motors and other equipment used in the industry. The system was based on the RF approach and was tested on a real industry example.

48.2.6 Carbon Footprint Reduction

By optimizing the consumption of energy, transportation, and production processes, ML plays a significant part in dropping carbon footprint [30]. Płoszaj-Mazurek [31] investigated strategies to optimize building design for a less carbon footprint using ML methods. Mardani et al. [32] proposed a multi-stage methodology to forecast carbon dioxide emissions based on energy consumption and economic growth in group 20 countries. Bhatt et al. [33] discussed carbon dioxide emissions and how they relate to climate change. The reduction and reversal rates necessary to return carbon emissions to safe levels were also calculated. Zhao et al. [34] developed a method for optimizing cutting parameters in CNC machining processes to reduce carbon emissions. The optimized cutting parameters reduced processing time and carbon emissions by 5.84% and 6.1%, respectively, improving the machining efficiency and reducing carbon emissions.

By streamlining production, transportation, and energy use, ML can help reduce carbon footprint. ML has demonstrated the potential to lower carbon emissions across various businesses and sectors.

48.2.7 Water Conservation

ML can conserve water in manufacturing by predicting equipment failure and identifying inefficient water usage through data from sensors and water quality monitors.

Hassan et al. [35] used ML algorithms, including RF, Neural Network, Multiple Linear Regression, SVM, and Boosted Tree Model, to estimate the water quality index in different regions of India. The proposed ML method achieved high accuracy in predicting water quality. Yan et al. [36] proposed a new framework for predicting long-term water quality using Bayesian-optimised ML methods. The proposed framework could efficiently predict future water quality and provide technical support for emergency pollution control. Adeleke et al. [37] aimed to construct, test, and evaluate the usefulness of ML and the IoT at water storage stations. The ANN models used had the highest accuracy and were most suitable for predicting water source and status. ML algorithms have the potential to accurately predict water quality, offering useful information for water management and pollution prevention.

48.2.8 Sustainable Product Design

By identifying prospects that reduce environmental impact, ML can help design sustainable products using data from the product lifecycle, consumer preferences, and production parameters [38]. Wang et al. [39] discussed the application of ML techniques in enhancing the sustainability of ships. ML has been useful in marine areas such as underwater vehicles, wave energy converters, condition monitoring, and maintenance. Pervez et al. [40] developed a sustainable resin-finishing procedure for cotton fabric. Bodendorf et al. [41] proposed using ML to support cost management in the early product development and design stages.

Manufacturers can employ ML to create goods that satisfy customer sustainability demand and enhance production procedures to minimize the negative environmental impact.

48.3 Future of Machine Learning in SMPs

By maximizing energy use, lowering waste, and enhancing production efficiency, ML has the potential to revolutionize sustainable manufacturing. ML algorithms may assist factories in making better-educated decisions regarding energy use and waste reduction by gathering data from numerous sources. High-quality data are necessary to utilize the capability of ML properly. The improvement of data collecting and organization may be the main emphasis of future advancements, especially in areas like energy use, trash creation, and emissions. Integrating sustainable practices into industrial processes will receive more attention as customers and authorities emphasize sustainability. Manufacturing may be optimized to reduce the negative effects on the environment, and problem areas can be found using ML. Manufacturers can forecast when machines will require repair or replacement by using ML to analyze data from sensors and other sources, minimizing waste and minimizing downtime. We should anticipate increasingly complex optimization algorithms that can balance conflicting demands like energy efficiency, manufacturing speed, and material utilization as ML techniques advance [42]. Cobots, or collaborative robots, are intended to do laborious or hazardous jobs alongside human operators. By allowing these robots to learn from their mistakes and develop better performance over time, ML can help them become more efficient. Manufacturers can enhance their environmental performance, lower their energy and waste consumption, and build a more sustainable future for everybody by using the potential of this technology.

48.4 Concluding Remarks

This paper reviewed the potential of machine learning in enhancing sustainability during sustainable manufacturing practices, including product design, waste management, energy efficiency, supply chain management, equipment maintenance, carbon emissions reduction, and water quality management. It allows manufacturers to make data-driven decisions that result in more environmentally friendly actions and improved overall performance. Also, it is essential to realize that ML is not a panacea for environmentally friendly production. Its efficacy relies on the data's accuracy, the selection of the right algorithms, and the availability of qualified individuals to deploy and maintain the systems. Therefore, a thorough strategy considering various sustainable manufacturing factors, such as material choice, circular economy principles, and renewable energy, is required to transition smoothly to a sustainable future. ML adoption in SMPs is a step in the right direction. Still, it must be part of a wider strategy that considers manufacturing operations' social, economic, and environmental effects.

Acknowledgements The authors express deep gratitude to the Department of Information Technology and Mechanical and Production Engineering, Guru Nanak Dev Engineering College, Ludhiana (Punjab), for allowing the research work.

References

1. Anh Khoa, T., et al.: Waste management system using IoT-based machine learning in university. Wirel. Commun. Mob. Comput. **2020**, 6138637 (2020). https://doi.org/10.1155/2020/6138637
2. Chandel, R.S., Kumar, R., Kapoor, J.: Sustainability aspects of machining operations: a summary of concepts. Mater. Today Proc. **50**, 716–727 (2022). https://doi.org/10.1016/j.matpr.2021.04.624
3. Ranjan, N., Kumar, R., Kumar, R., Kaur, R., Singh, S.: Investigation of fused filament fabrication-based manufacturing of ABS-Al composite structures: prediction by machine learning and optimization. J. Mater. Eng. Performance 1–20 (2022)
4. Huang, J., Koroteev, D.D.: Artificial intelligence for planning of energy and waste management. Sustain. Energy Technol. Assess. **47**, 101426 (2021). https://doi.org/10.1016/j.seta.2021.101426
5. Sidhu, A.S., Singh, S., Kumar, R., Pimenov, D.Y., Giasin, K.: Prioritizing energy-intensive machining operations and gauging the influence of electric parameters: an industrial case study. Energies **14**(16), 4761 (2021). [Online]. Available: https://www.mdpi.com/1996-1073/14/16/4761
6. Carbonneau, R., Laframboise, K., Vahidov, R.: Application of machine learning techniques for supply chain demand forecasting. Eur. J. Oper. Res. **184**(3), 1140–1154 (2008). https://doi.org/10.1016/j.ejor.2006.12.004
7. Pawanr, S., Garg, G.K., Routroy, S.: Prediction of energy efficiency, power factor and associated carbon emissions of machine tools using soft computing techniques. Int. J. Interact. Des. Manuf. (IJIDeM) (2022). https://doi.org/10.1007/s12008-022-01089-4
8. Sami, K.N., Amin, Z.M.A., Hassan, R.: Waste management using machine learning and deep learning algorithms. Int. J. Perceptive Cogn. Comput. **6**(2), 97–106 (2020). https://doi.org/10.31436/ijpcc.v6i2.165
9. Zaman, A.: Waste management 4.0: an application of a machine learning model to identify and measure household waste contamination—a case study in Australia. Sustainability **14**(5), 3061 (2022). [Online]. Available: https://www.mdpi.com/2071-1050/14/5/3061
10. Khan, R., et al.: Machine learning and IoT-based waste management model. Comput. Intell. Neurosci. **2021**, 5942574 (2021). https://doi.org/10.1155/2021/5942574
11. Shu, X., et al.: Sustainability assessment of energy storage technologies based on commercialization viability: MCDM model. Sustainability **15**(6), 4707 (2023). [Online]. Available: https://www.mdpi.com/2071-1050/15/6/4707
12. E Mocanu 2019 On-line building energy optimization using deep reinforcement learning IEEE Trans. Smart Grid 10 4 3698 3708 https://doi.org/10.1109/TSG.2018.2834219

13. Narciso, D.A.C., Martins, F.G.: Application of machine learning tools for energy efficiency in industry: a review. Energy Rep. **6**, 1181–1199 (2020). https://doi.org/10.1016/j.egyr.2020.04.035
14. Mawson, V.J., Hughes, B.R.: Deep learning techniques for energy forecasting and condition monitoring in the manufacturing sector. Energy Build. **217**, 109966 (2020). https://doi.org/10.1016/j.enbuild.2020.109966
15. Liao, J.-M., Chang, M.-J., Chang, L.-M.: Prediction of air-conditioning energy consumption in R&D building using multiple machine learning techniques. Energies **13**(7), 1847 (2020). [Online]. Available: https://www.mdpi.com/1996-1073/13/7/1847
16. W Ahmed 2020 Machine learning based energy management model for smart grid and renewable energy districts IEEE Access 8 185059 185078 https://doi.org/10.1109/ACCESS.2020.3029943
17. Sharmila, P., Baskaran, J., Nayanatara, C., Maheswari, R.: A hybrid technique of machine learning and data analytics for optimized distribution of renewable energy resources targeting smart energy management. Procedia Comput. Sci. **165**, 278–284 (2019). https://doi.org/10.1016/j.procs.2020.01.076
18. Mostafa, N., Ramadan, H.S.M., Elfarouk, O.: Renewable energy management in smart grids by using big data analytics and machine learning. Mach. Learn. Appl. **9**, 100363 (2022). https://doi.org/10.1016/j.mlwa.2022.100363
19. Gu, G.H., Noh, J., Kim, I., Jung, Y.: Machine learning for renewable energy materials. J. Mater. Chem. A **7**(29), 17096–17117 (2019). https://doi.org/10.1039/C9TA02356A
20. Lai, J.-P., Chang, Y.-M., Chen, C.-H., Pai, P.-F.: A survey of machine learning models in renewable energy predictions. Appl. Sci. **10**(17), 5975 (2020). [Online]. Available: https://www.mdpi.com/2076-3417/10/17/5975
21. Feizabadi, J.: Machine learning demand forecasting and supply chain performance. Int. J. Logistics Res. Appl. **25**(2), 119–142 (2022). https://doi.org/10.1080/13675567.2020.1803246
22. Bigliardi, B., Filippelli, S., Petroni, A., Tagliente, L.: The digitalization of supply chain: a review. Procedia Comput. Sci. **200**, 1806–1815 (2022). https://doi.org/10.1016/j.procs.2022.01.381
23. Nagar, D., Raghav, S., Bhardwaj, A., Kumar, R., Lata Singh, P., Sindhwani, R.: Machine learning: best way to sustain the supply chain in the era of industry 4.0. Mater. Today Proc. **47**, 3676–3682 (2021). https://doi.org/10.1016/j.matpr.2021.01.267
24. Baryannis, G., Dani, S., Antoniou, G.: Predicting supply chain risks using machine learning: the trade-off between performance and interpretability. Future Gener. Comput. Syst. **101**, 993–1004 (2019). https://doi.org/10.1016/j.future.2019.07.059
25. Arena, S., Florian, E., Zennaro, I., Orrù, P.F., Sgarbossa, F.: A novel decision support system for managing predictive maintenance strategies based on machine learning approaches. Saf. Sci. **146**, 105529 (2022). https://doi.org/10.1016/j.ssci.2021.105529
26. Çınar, Z.M., Abdussalam Nuhu, A., Zeeshan, Q., Korhan, O., Asmael, M., Safaei, B.: Machine learning in predictive maintenance towards sustainable smart manufacturing in industry 4.0. Sustainability **12**(19), 8211 (2020). [Online]. Available: https://www.mdpi.com/2071-1050/12/19/8211
27. Dalzochio, J., et al.: Machine learning and reasoning for predictive maintenance in Industry 4.0: current status and challenges. Comput. Ind. **123**, 103298 (2020). https://doi.org/10.1016/j.compind.2020.103298
28. Kavana, V., Neethi, M.: Fault analysis and predictive maintenance of induction motor using machine learning. In: 2018 International Conference on Electrical, Electronics, Communication, Computer, and Optimization Techniques (ICEECCOT), 14–15 Dec 2018, pp. 963–966. https://doi.org/10.1109/ICEECCOT43722.2018.9001543
29. Paolanti, M., Romeo, L., Felicetti, A., Mancini, A., Frontoni, E., Loncarski, J.: Machine learning approach for predictive maintenance in industry 4.0. In: 2018 14th IEEE/ASME International Conference on Mechatronic and Embedded Systems and Applications (MESA), 2–4 July 2018, pp. 1–6. https://doi.org/10.1109/MESA.2018.8449150

30. R Kumar S Singh AS Sidhu CI Pruncu 2021 Bibliometric analysis of specific energy consumption (SEC) in machining operations: a sustainable response Sustainability 13 10 5617
31. M Płoszaj-Mazurek 2020 Machine learning-aided architectural design for carbon footprint reduction Builder 24 7 35 39
32. Mardani, A., Liao, H., Nilashi, M., Alrasheedi, M., Cavallaro, F.: A multi-stage method to predict carbon dioxide emissions using dimensionality reduction, clustering, and machine learning techniques. J. Cleaner Prod. **275**, 122942 (2020). https://doi.org/10.1016/j.jclepro.2020.122942
33. Bhatt, H., Davawala, M., Joshi, T., Shah, M., Unnarkat, A.: Forecasting and mitigation of global environmental carbon dioxide emission using machine learning techniques. Cleaner Chem. Eng. **5**, 100095 (2023). https://doi.org/10.1016/j.clce.2023.100095
34. Zhao, L., Fang, Y., Lou, P., Yan, J., Xiao, A.: Cutting parameter optimization for reducing carbon emissions using digital twin. Int. J. Precis. Eng. Manuf. **22**(5), 933–949 (2021). https://doi.org/10.1007/s12541-021-00486-1
35. MM Hassan 2021 Efficient prediction of water quality index (WQI) using machine learning algorithms Human-Centric Intell. Syst. 1 3–4 86 97
36. Yan, T., Zhou, A., Shen, S.-L.: Prediction of long-term water quality using machine learning enhanced by Bayesian optimization. Environ. Pollut. **318**, 120870 (2023). https://doi.org/10.1016/j.envpol.2022.120870
37. Adeleke, I.A., Nwulu, N.I., Ogbolumani, O.A.: A hybrid machine learning and embedded IoT-based water quality monitoring system. Internet Things **22**, 100774 (2023). https://doi.org/10.1016/j.iot.2023.100774
38. Thakur, V., Kumar, R., Kumar, R., Singh, R., Kumar, V.: Hybrid additive manufacturing of highly sustainable polylactic acid—carbon fiber-polylactic acid sandwiched composite structures: optimization and machine learning. J. Thermoplast. Compos. Materi. **0**(0), 08927057231180186. https://doi.org/10.1177/08927057231180186
39. Wang, H.S.-H., Yao, Y.: Machine learning for sustainable development and applications of biomass and biomass-derived carbonaceous materials in water and agricultural systems: a review. Resour. Conserv. Recycl. **190**, 106847 (2023). https://doi.org/10.1016/j.resconrec.2022.106847
40. Pervez, M.N., et al.: Sustainable fashion: design of the experiment assisted machine learning for the environmental-friendly resin finishing of cotton fabric. Heliyon **9**(1), e12883 (2023). https://doi.org/10.1016/j.heliyon.2023.e12883
41. Bodendorf, F., Franke, J.: A machine learning approach to estimate product costs in the early product design phase: a use case from the automotive industry. Procedia CIRP **100**, 643–648 (2021). https://doi.org/10.1016/j.procir.2021.05.137
42. R Kumar PS Bilga S Singh 2017 Multi objective optimization using different methods of assigning weights to energy consumption responses, surface roughness and material removal rate during rough turning operation J. Clean. Prod. 164 45 57

Chapter 49
Study of Hydrogen Combustion in a Mini Annular Combustion Chamber Using CFD

D. Deepan, S. Anantharaman, C. Muthukumaran, S. Sathish, S. Seralathan, A. Muthuram, and G. Balaji

Abstract Computational fluid dynamics analysis of hydrogen combustion in a conceptual designed mini annular combustion chamber for sustainable combustion with a power output of 50 kW with different air fuel ratios such as leaner mixture 25:1, optimized mixture 34:1 and rich mixture 40:1 is carried out in this study. A three-dimensional model that contains the species transport equations and k-ε turbulence model is used to study the combustion process. When an ideal air–fuel ratio is maintained, the small annular combustion chamber can achieve complete combustion of hydrogen with a low emission of NO_x. High combustion efficiency and uniform temperature distribution are seen throughout the annular combustion chamber with a temperature distribution of about 1500 K at the output. Analysis of the velocity profile distribution reveals a stable combustion with no flame instability.

49.1 Introduction

New combustion systems that may effectively use alternative fuels while reducing emissions have been developed in response to the growing need for sustainable energy. The small annular combustion chamber is one such device that is made for compact and effective combustion. The investigation of hydrogen fuel in a tubular combustion chamber, together with interest in alternative fuels was the focus of this study which concluded with the greater benefits in use of hydrogen fuel. When the EAR was increased, the combustion efficiency increased, and there was a commensurate increase in the ratio of pressure drop values. Highest NO levels for hydrogen fuel were also noted at 10,000 revolutions per minute [1]. A small-scale annular combustor with an airflow distribution that was dependent on the cooling airflow

D. Deepan · S. Anantharaman · C. Muthukumaran · S. Sathish · S. Seralathan (✉) · A. Muthuram · G. Balaji
Department of Aeronautical Engineering, Hindustan Institute of Technology and Science, Chennai, Tamil Nadu 603103, India
e-mail: siva.seralathan@gmail.com

P. H. V. S. Talpa Sai et al. (eds.), *Intelligent Manufacturing and Energy Sustainability*, Smart Innovation, Systems and Technologies 372,
https://doi.org/10.1007/978-981-99-6774-2_49

was designed using a systematic methodological approach. The volume of air flow in this instance, however, was split between the secondary and the dilution zones as there was no cooling air present [2]. The effectiveness and characteristics of a methane-air combination burning in a gas turbine annular combustor were investigated. The air input velocity increased by 19% at 20 m/s and by 14% at 30 m/s after the combustor was adjusted. The performance parameters of the modified combustor and its capacity to effectively burn the methane-air mixture were evaluated [3]. The best design for the rocket was identified by numerically analyzing the various design options [4]. Use of reasonable amounts of hydrogen as an extra fuel in hydrocarbon-fueled burners minimized pollution emissions with a significant impact on the reduction of CO_2 emissions [5]. Hydrogen with its greater value of heating than fossil fuels along with decrease in mass during combustion received the same amount of energy [6]. A three-dimensional numerical investigation on a can-type combustor was done and mixing took place more effectively at 45° swirler angle [7]. Using a swirler with a high swirl number in biogas combustion opened the door in using biogas as a fuel for combustion chambers without premixed flames. Pollutant emissions including CO, CO_2, and NO decreased as the swirler enhanced the burning process [8]. Studies on different types of swirler annular combustor models resulted in a high turbulence intensity that produced a high mixing efficiency of kerosene fuel with the air and increased the reaction between the air and fuel [9]. CFD study provides light on how adjustments to the fuel mixture, structure of the combustion chamber, and other variables may affect the combustion process by modelling the fluid flow and heat transfer within the combustion chamber. The design of combustion systems can be improved with increased efficiency and reduced emissions. In this study, the conceptual design of 25:1, 34:1, and 40:1 air-to-fuel ratios micro annular combustion chamber is analyzed using commercial CFD code, ANSYS Fluent. The objective is to evaluate the operation of various air–fuel mixtures for sustained combustion with a 50 kW power output.

49.2 Numerical Methodology

To provide the best possible fuel–air mixture mixing and combustion, the annular combustion chamber used in this study is built with eight separate fuel injectors, each with its own swirling. Figure 49.1 shows the schematic diagram and overall dimensions of the combustion chamber [2]. The chamber is a circular annular duct with swirls that are evenly distributed throughout and with fuel injectors positioned in the center. This design helps in mixing the mass flows efficiently. To deliver a controlled and consistent injection of the fuel–air combination into the combustion zone, the fuel injectors are equally spaced around the chamber's perimeter. To promote mixing and improve combustion efficiency, the swirler is made to cause a swirling motion on the entering air. The fluid flow distribution as shown in Table 49.1, describes the design setup for the engine. Solidworks software [10] is used to produce the CAD

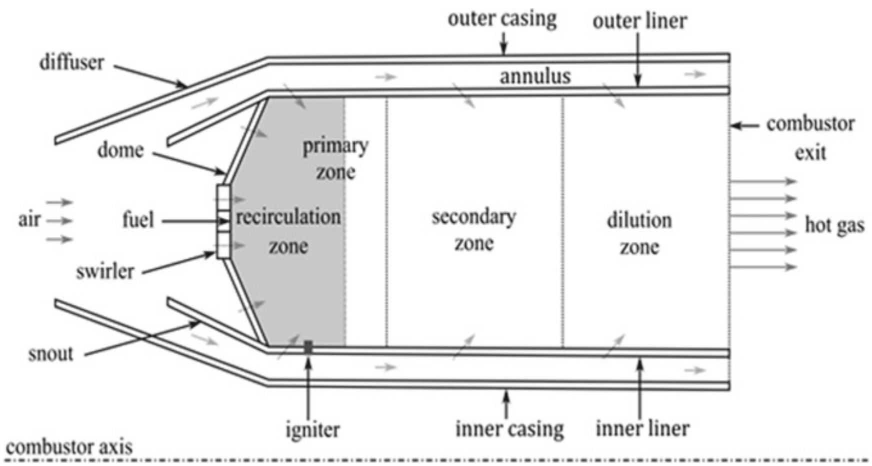

Fig. 49.1 Schematic of the annular combustor [2]

model as shown in Fig. 49.2 and has a surface area of 7198.0292 square inches and the dimensions are specified in its sectional view.

ANSYS Fluent [11] solves the energy equation in the non-premixed combustion model with non-adiabatic as the total enthalpy form of the energy equation as,

$$\frac{\partial}{\partial t}(\rho H) + \nabla.(\rho \vec{v} H) = \nabla.\left(\frac{k_t}{c_p}\nabla H\right) + S_h \tag{49.1}$$

Momentum conservation for turbulent flow is written as,

$$\rho u_i \frac{\partial u_i}{\partial x_j} = -\frac{\partial p}{\partial x_i} + \frac{\partial}{\partial x_j}\left[\mu\left(\frac{\partial u_i}{\partial x_j} + \frac{\partial u_j}{\partial x_i}\right) - \frac{2}{3}\mu\delta_{ij}\frac{\partial u_i}{\partial x_i}\right] + F_i(\overline{-\rho u_i u_j}) \tag{49.2}$$

The primary method of releasing energy is combustion, which always produces heat and gases as by products. According to chemistry with finite rates, the combustion process is supposed to be a one-step irreversible reaction as shown in Eq. (49.3).

Table 49.1 Mass flow distribution percentage of air [2]

Inlet ($\dot{\mathbf{m}}_3$) 100%	Recirculation zone/Snout ($\dot{\mathbf{m}}_{rz}$) 20%	Swirler ($\dot{\mathbf{m}}_{\mathrm{sw}}$) 10%
		Dome cooling ($\dot{\mathbf{m}}_{do}$) 10%
	Annulus ($\dot{\mathbf{m}}_{an}$) 80%	Primary zone ($\dot{\mathbf{m}}_{\mathrm{pz}}$) 20%
		Secondary zone ($\dot{\mathbf{m}}_{\mathrm{sz}}$) 25%
		Dilution zone ($\dot{\mathbf{m}}_{\mathrm{dz}}$) 35%

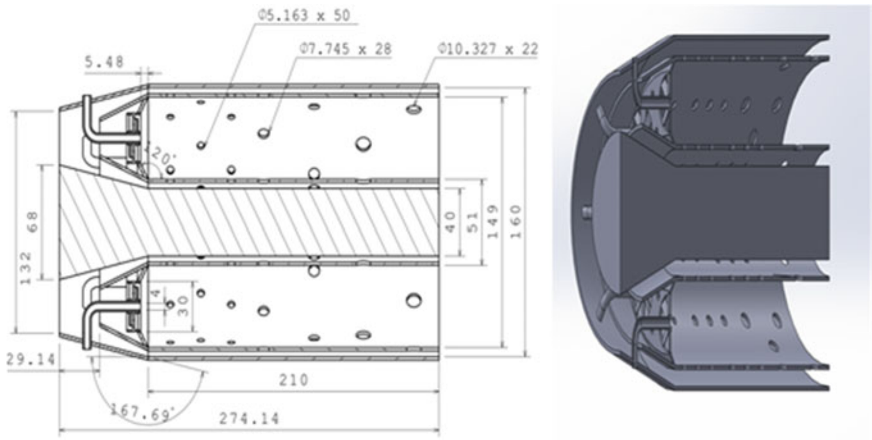

Fig. 49.2 Sectional view with dimensions in mm [2]

$$2H_2 + O_2 \rightarrow 2H_2O + \text{Energy} \tag{49.3}$$

Fuel mass flow rate is shown in Eq. (49.4)

$$\dot{m}_f = \text{P}/(\text{LHV} * \text{combustion efficiency}) \tag{49.4}$$

Assuming 100% combustion efficiency, Eq. (49.4) is used to calculate the fuel mass flow rate for a 50 kW power output as follows,

$$\dot{m}_f = 50{,}000/(120 * 10^6 * 1) = 0.0004 \text{ kg/s} \tag{49.5}$$

Therefore, fuel mass flow rate of approximately 0.4 g/s would be required to produce a power output of 50 kW using hydrogen as the fuel.

$$\dot{m}_a = \dot{m}_f * (\text{A/F}) \tag{49.6}$$

Here, m_a is mass flow rate of air, m_f is mass flow rate of fuel, A/F is the air fuel ratios and the ratios used in this study are 25:1, 34:1 and 40:1. The simulation is performed using ANSYS Fluent, where the solutions converged for the respective solving equations within the range of e^{-2} to e^{-4}. The discretization of the computational domain into manageable, finite-sized elements for numerical analysis is accomplished through meshing. A structured mesh is produced around the shape of a small annular combustion chamber using the ANSYS Fluent meshing software [12]. To capture the flow and temperature gradients in the combustion chamber accurately, the mesh has been as fine as possible. To balance accuracy and computational economy, a mix of structured and unstructured mesh is used. The unstructured mesh

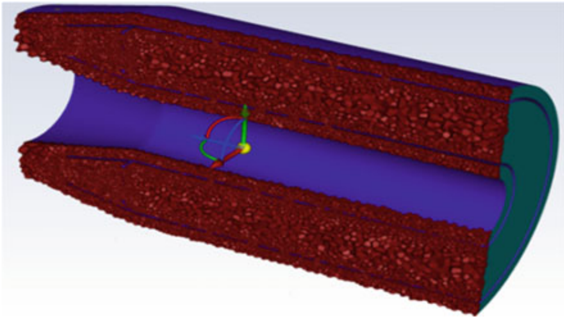

Fig. 49.3 Meshing of the computational domain

Table 49.2 Boundary conditions

Details	Boundary condition	Values
Inlet fuel	Mass flow inlet	0.0004 kg/s
Inlet air	Mass flow inlet	(25:1) 0.010 kg/s
		(34:1) 0.0136 kg/s
		(40:1) 0.016 kg/s
Wall	Wall boundary	Non-adiabatic, no-slip
Outlet	Back flow pressure	Total pressure
Inlet	Temperature	300 K

elements are used in areas with more complex flows, such as close to the fuel injection system, whereas structured mesh elements are used close to the walls and in locations where the flow was more uniform. Figure 49.3 shows the meshing part of the computational model with polyhedral cells and the mesh contains 732,688 polyhedral cells with 4,206,603 nodes. Table 49.2 lists the boundary conditions imposed in this study.

49.3 Results and Discussion

The temperature contour analysis as shown in Figs. 49.4, 49.5, and 49.6 provides valuable insights into the temperature distribution within the mini annular combustion chamber for the different air–fuel ratios. For all the air–fuel ratios considered viz., 25:1, 34:1, and 40:1, the temperature inside the combustion chamber rises and the outer temperature drops through the chamber from the combustion position. This is made possible by the holes incorporated into the secondary to primary zones by the design specifications. Higher air–fuel ratios provide a bigger decrease in outlet temperature by increasing air mass, with the exit temperature stated as 1300 K at 34:1, 1500 K at 25:1, and 2100 K at 25:1. Also, when temperature rises, the output temperature drops more slowly at lower air–fuel ratios. This is probably because the

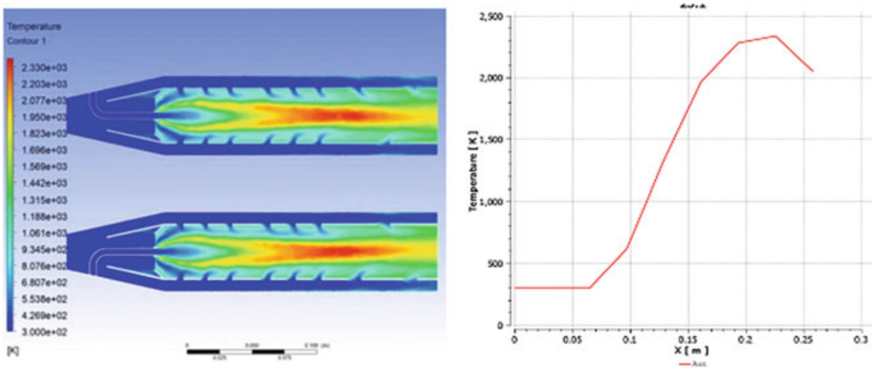

Fig. 49.4 Temperature distribution at air–fuel ratio 25:1

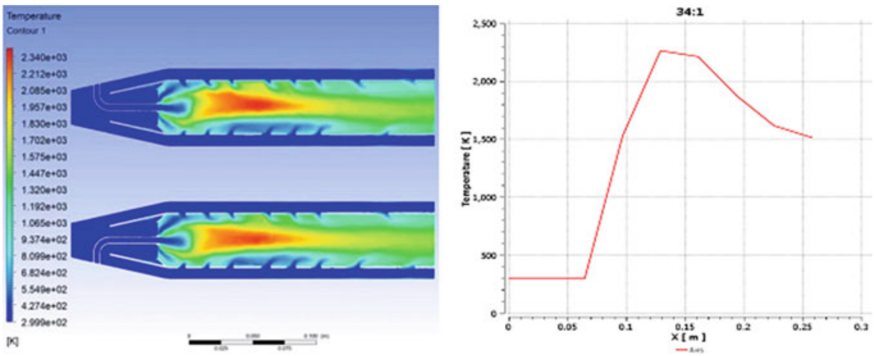

Fig. 49.5 Temperature distribution at air–fuel ratio 34:1

combustion is richer at lower air-to-fuel ratios, leading to higher temperatures and faster heat release rates.

The density variations as shown in Figs. 49.7, 49.8, and 49.9 provide valuable insights into the density distribution within the mini annular combustion chamber for different air–fuel ratios. For certain air–fuel ratios, the density distribution did not change significantly throughout the combustion chamber as the air–fuel ratio increases.

As the air–fuel ratio is increased from 25:1 to 34:1, only a slight increase in density throughout the combustion chamber is observed, with a slightly higher density at the outlet. Similarly, the air–fuel ratio is increased from 34:1 to 40:1, only a slight increase in density throughout the combustion chamber, with a slightly higher density at the outlet is observed. This is probably because combustion gets leaner as the air–fuel ratio rises, resulting in a more complete combustion and a more even distribution of reactants and products inside the combustion chamber. As a result, the density distribution over the combustion chamber may only slightly alter. While the density may

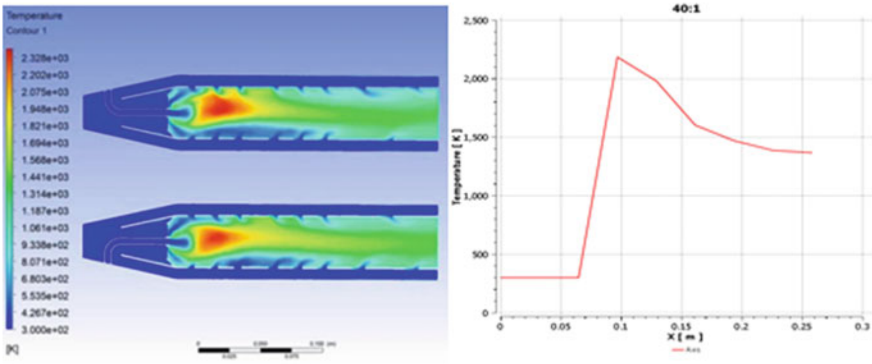

Fig. 49.6 Temperature distribution at air–fuel ratio 40:1

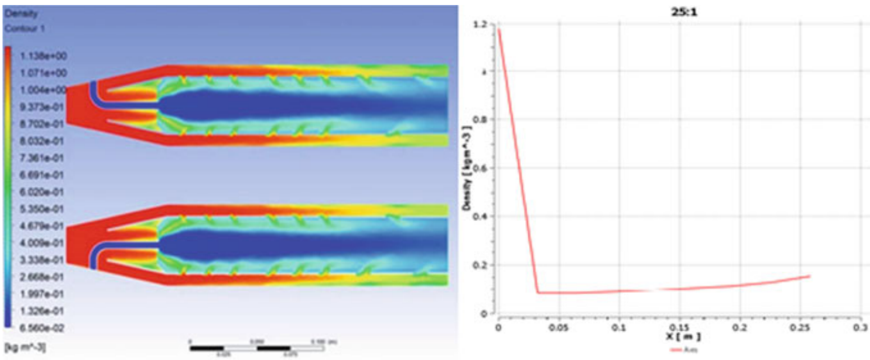

Fig. 49.7 Density distribution at air–fuel ratio 25:1

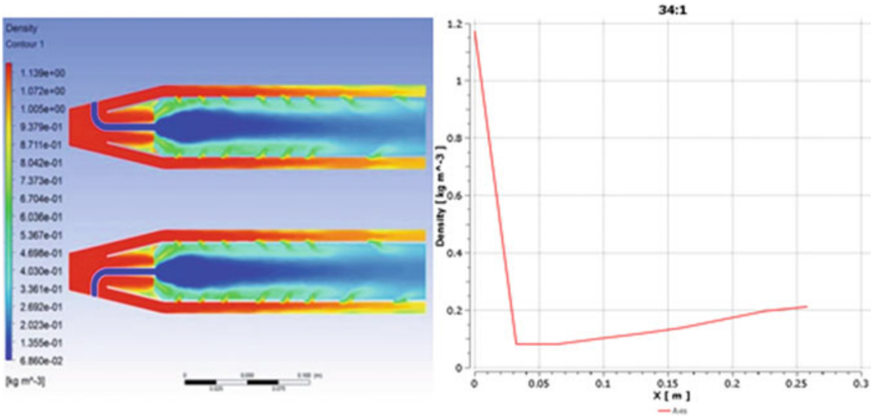

Fig. 49.8 Density distribution at air–fuel ratio 34:1

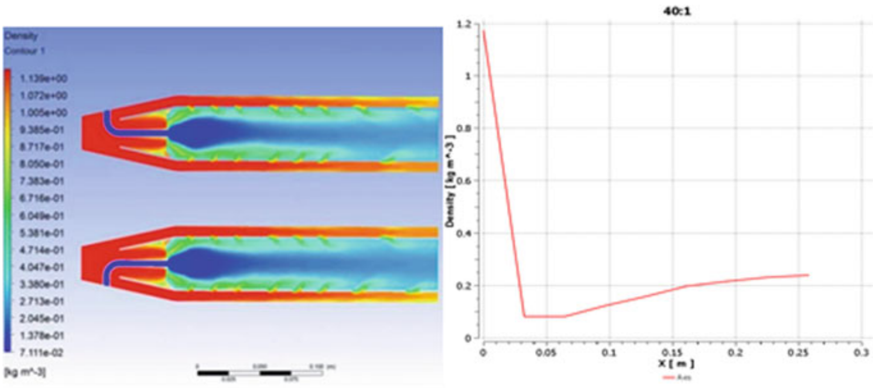

Fig. 49.9 Density distribution at air–fuel ratio 40:1

not vary significantly throughout the combustion chamber, it is crucial to keep in mind that other elements like temperature distribution and emissions should be considered in order to pinpoint areas that need to be optimized and provide suggestions for bettering the design of the mini annular combustion chamber.

The NO_x analysis as shown in Figs. 49.10, 49.11, and 49.12 provides valuable insights into the nitrogen oxides emissions within the mini annular combustion chamber for the different air–fuel ratios. At 25:1, the mass fraction at the outlet is 0.0012, whereas for 34:1 it is 0.00039 and for 40:1 it is 0.0002. On observing this, the emission depends upon the air fuel ratio. NO_x emissions varied significantly depending on the air–fuel ratio. Interestingly, as the air–fuel ratio is increased, the NO_x emissions at the outlet get decreased [10]. Therefore, decrease in temperature at the outlet leads to the decrease of the pollutant emissions. For instance, the largest emissions are found at the outlet when the air–fuel ratio is 25:1, whereas the lowest emissions is found when the air–fuel ratio is 40:1. This conclusion is probably caused by the fact that the combustion becomes leaner as the air–fuel ratio rises, leading to a lower flame temperature and less formation. This is in line with earlier research on lean combustion, which has demonstrated that lower NO_x emissions can be achieved by using leaner air–fuel ratios. While increasing air mass can reduce NO_x emissions, it's important to remember that other factors, such as combustion efficiency and emissions of other pollutants, should also be considered to pinpoint areas that need to be optimized and offer suggestions for bettering the design.

Figures 49.13, 49.14 and 49.15 show the contour of outlet velocity. The exit velocity noted as 2.3 ms^{-1} at the combusting regions. The outlet velocity remained relatively constant for all air–fuel ratios. It is possible that similar exit gas velocities could be because of the combustion process reaching a steady-state condition, where

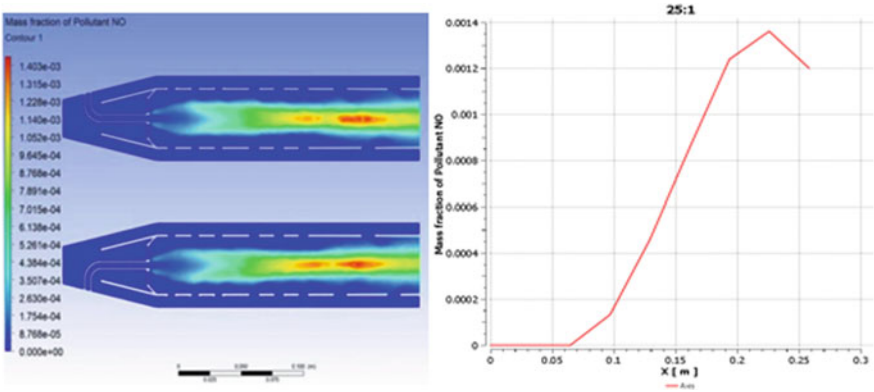

Fig. 49.10 NO_x emission distribution at air–fuel ratio 25:1

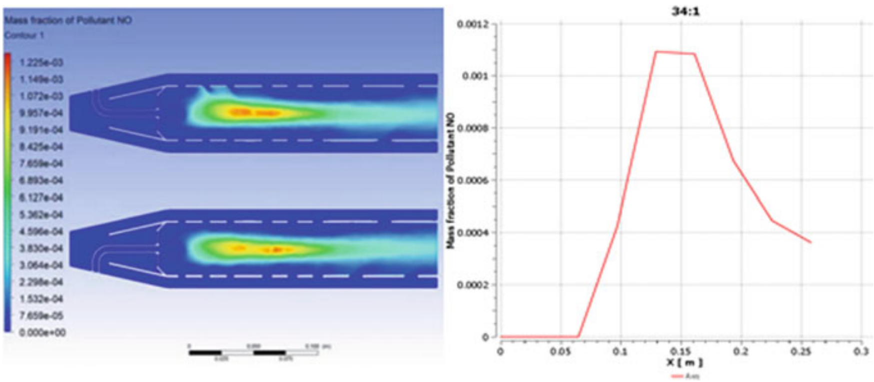

Fig. 49.11 NO_x emission distribution at air–fuel ratio 34:1

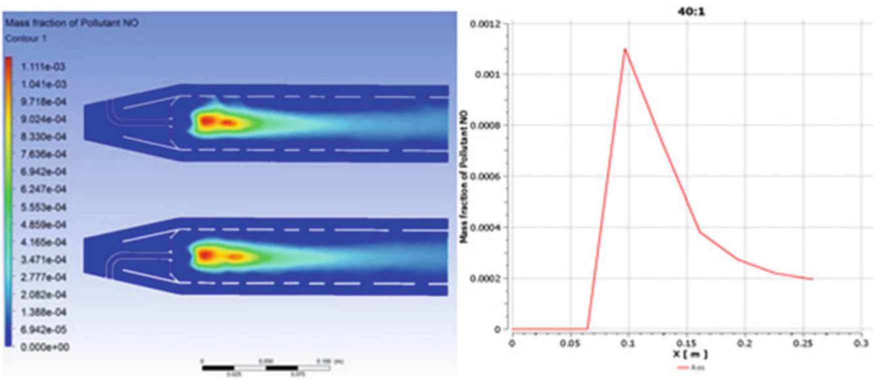

Fig. 49.12 NO_x emission distribution at air–fuel ratio 40:1

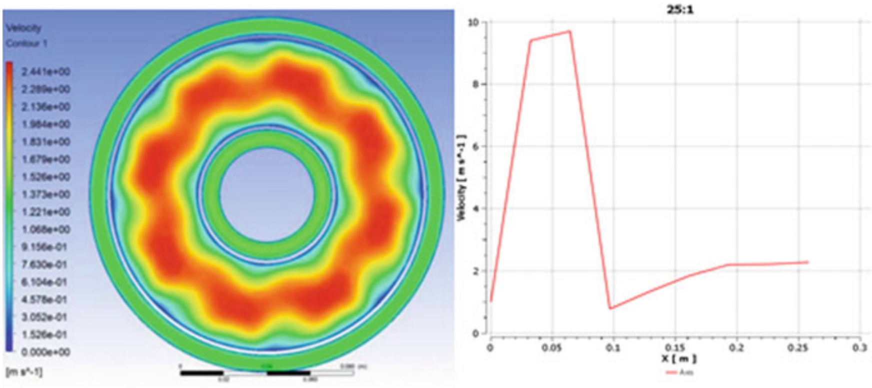

Fig. 49.13 Outlet Velocity for air–fuel ratio 25:1

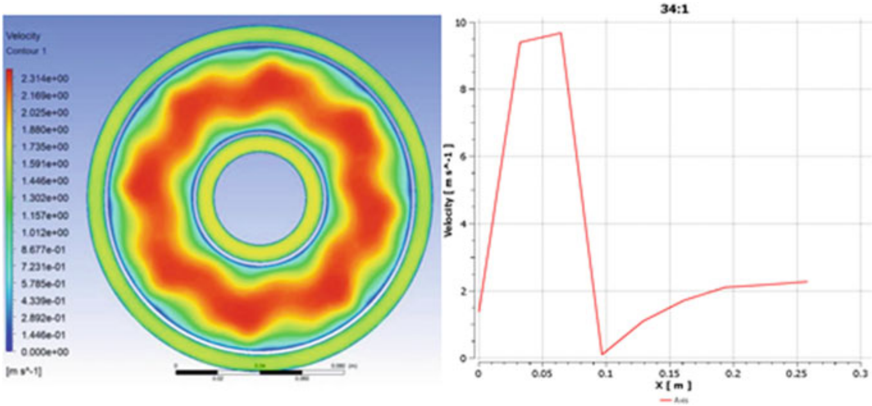

Fig. 49.14 Outlet velocity for air–fuel ratio 34:1

if the rate of fuel combustion and air intake are balanced. Also, bigger air masses are needed to attain the ideal air–fuel ratio at increasing ratios, even though the output velocity did not change considerably with the air–fuel ratio. This is probably because, as the air–fuel ratio rises, more air is needed to attain the appropriate air–fuel ratio, making it more difficult for the engine to supply the necessary air. For the engine to limit emissions, the combustion must be kept within the ideal ratio. The ideal value must be preserved for effective operation.

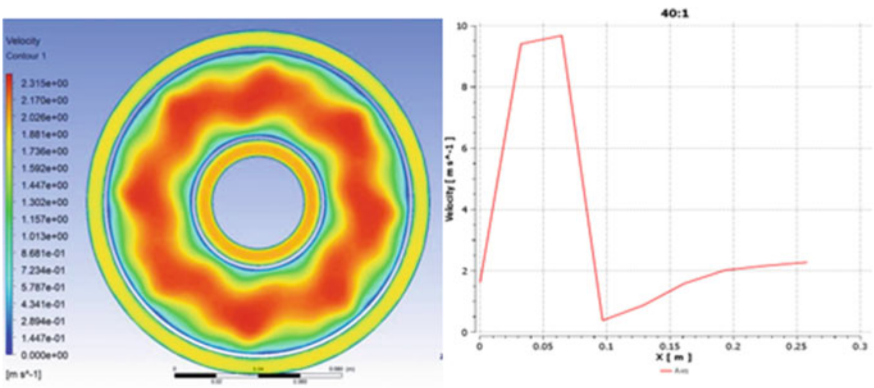

Fig. 49.15 Outlet velocity for air–fuel ratio 40:1

49.4 Conclusion

In this analysis of the conceptual mini annular combustion chamber, the effects of different air–fuel ratios on various performance parameters, namely temperature, density, NO_x emissions and velocity are investigated. The combustion process within the mini annular combustion chamber is well-suited for maintaining consistent flow behavior and velocity distribution regardless of the air–fuel ratios. However, certain parameters such as NO_x emissions and temperature are influenced by the changes in the air–fuel ratios. Specifically, NO_x emissions decrease with higher air–fuel ratios, while temperature decreases slightly, and density remains relatively constant. These findings suggest that the higher air–fuel ratios may be more conducive to achieving optimal combustion and minimize emissions, but additional optimization may be required for higher air–fuel ratios to achieve optimal performance. Finally, experimental validation of the CFD results may be necessary to confirm the accuracy and reliability of the simulation results which will be carried out in future.

References

1. Kahraman, N., Tangöz, S., Akansu, S.O.: Numerical analysis of a gas turbine combustor fueled by hydrogen in comparison with jet-A fuel. Fuel **217**, 66–77 (2018). https://doi.org/10.1016/j.fuel.2017.12.071
2. S. Dharmalingam, K.D. Kothari: Design of a laboratory annular combustor. Int. J. Aviat. Aeronaut. Aerosp. **8**(4), 6p (2021). https://doi.org/10.15394/ijaaa.2021.1647
3. Lakshmi Mounika, C., Kumar, G.S.: Analysis of annular combustion chamber of jet engine with methane air mixture for different inlet air velocities. IJMRSET **5**(6), 6p (2022). https://doi.org/10.15680/IJMRSET.2022.0506082
4. M. Campolo, M. Andreoli, A. Soldati: Computing flow, combustion, heat transfer and thrust in a micro-rocket via hierarchical problem decomposition. Microfluid. Nanofluid.**7**, 57–73 (2009). https://doi.org/10.1007/s10404-008-0362-9

5. Juste, G.L.: Hydrogen injection as additional fuel in gas turbine combustor—evaluation of effects. Int. J. Hydrogen Energy **31**(14), 2112–2121 (2006). https://doi.org/10.1016/j.ijhydene.02.006
6. F.I. Habibi, F. Hartono, H. Prayogo: Optimization of an annular combustion chamber for micro turbo jet system. IOP Conf. Ser. Mater. Sci. Eng. **645**(1), 012009 (2019). https://doi.org/10.1088/1757-899X/645/1/012009/meta
7. Sathish, S., Seralathan, S., Sai Sanjay, D., Sai Ram, T., Pradeep Kumar, T.: Numerical investigation on film cooling of gas turbine blade using anti-vortex holes. AIP Conf. Proc. **2385**(1), 030005 (2022)
8. Shaik, A.S., Mohammed, R.: A Review on Combustion Chamber Design Part-I. Lambert Academic Publishing (2020)
9. Heywood, J.B.: Internal Combustion Engine Fundamentals, 2nd edn. (2018)
10. S. Seralathan, P.S. Dinesh Kumar, S. Singh, R. Raj, S. Sathish: Numerical analysis of the one-stage and two-stage helical savonius vertical axis wind turbine. AIP Conf. Proc. **2385**(1), 120005 (2022)
11. Leong, M.Y., McDonell, V.G., Samuelsen, G.S.: Effect of ambient pressure on an airblast spray injected into a crossflow. J. Propul. Power **17**(5), 1076–1084 (2001). https://doi.org/10.2514/2.5846
12. S. Sathish, S. Seralathan, G. Balaji, Kumar, N., G. Madhu, A. Muthuram: Aerodynamic analysis of supersonic flow through a dual bell nozzle using CFD. In: Proceedings of the International Conference on Power, Energy, Control and Transmission Systems (ICPECTS), Chennai, pp. 1–5 (2022). https://doi.org/10.1109/ICPECTS56089.2022.10047361

Chapter 50
Synthesis and Characterization of MWCNT Ink Using Gum Arabic

T. Rajani, Poonam Upadhyay, I. Navya, G. Ganesh, N. Uday, V. Ramani, Ch. Thirmal, and A. Balavardhan

Abstract This study deals with the synthesis and characterization of Multi wall carbon nanotube Ink using Gum Arabic. The synthesized ink were characterized by Ultraviolet Visible spectroscopy (UV–Visible), Particle size analyzer, Zeta potential and Cyclic Voltammetry. The particle size distribution was confirmed in the range 500–1000 nm using particle size analyzer. The zeta potential measurement was found to be − 28.5 mV confirming good dispersion degree and stability of MWCNT Ink. The interaction between the molecules was confirmed by using UV–Visible spectroscopy. It has been observed that from UV–Visible spectroscopy that the maximum absorption was in the range ~ 217 to ~ 264 nm. The specific capacitance was calculated using Cyclic voltammetry found to be 407.96 F/g. The Energy density value was low when compared to power density.

50.1 Introduction

Recently the development of printed flexible electronics is growing rapidly [1] which increases global economic growth. The development reflects various potential applications in sectors like energy storage devices [2], touch screen technology [3], textile industry [4], sensors and actuators [5, 6], food and security areas [7], radio frequency regions [8], integrated devices [9], health industry [10]. In fabrication of flexible printed electronics, batteries, paper batteries, capacitors, supercapacitors the usage

T. Rajani (✉) · Ch. Thirmal
Department of Physics, VNR Vignana Jyothi Institute of Engineering and Technology, Hyderabad, Telangana 500085, India
e-mail: rajini_t@vnrvjiet.in

P. Upadhyay · I. Navya · G. Ganesh · N. Uday · V. Ramani
Department of Electrical and Electronics Engineering, VNR Vignana Jyothi Institute of Engineering and Technology, Hyderabad, Telangana 500085, India

A. Balavardhan
Department of Chemistry, VNR Vignana Jyothi Institute of Engineering and Technology, Hyderabad, Telangana 500085, India

P. H. V. S. Talpa Sai et al. (eds.), *Intelligent Manufacturing and Energy Sustainability*, Smart Innovation, Systems and Technologies 372,
https://doi.org/10.1007/978-981-99-6774-2_50

of conductive inks will play a key role. The conductive inks are synthesized using metallic particles or carbon particles in a matrix. This matrix can act as a insulator or weak conductor or as an electrode in a paper battery. This depends upon the percentage of parent element in the ink formulation. Different types of conductive inks and fillers are in use In order to achieve stability and dispersion dispersants are added. Conductive inks are formulated with metallic particles or carbon particles such as Single wall carbon nanotube, Multi wall carbon nano tube, graphene which acts as a retention matrix. The retention matrix depending on concentration shows its behavior as a weak conductor. In order to create a contact path with the conductive particles the volume of the matrix can be reduced by several methods. There are several reports on carbon-based materials, such as graphene and carbon nanotubes [7, 8] on their successful development of conductive inks and their applications. In the fabrication process of graphene based conductive inks, solvents play key role for conductive ink formulation. In our study, we have considered Gum Arabic as a dispersant to synthesize the Ink.

Gum Arabic is a natural polymer. The uses of Gum Arabic can be seen in food industry, pharmaceutical purposes, cosmetic, adhesives, paints, inks, lithography, textiles and medicine [9, 10]. It has variable conductance properties which are applicable in Integrated circuits IC. Gum Arabic was added to achieve preferable conducting ink properties for flexible electrodes in paper batteries that can be used in various sensors. Also can be preferred as dielectric capacitor based on the value of resistance. In this communication we have synthesized MWCNT Ink using Gum Arabic as a main dispersant. By studying electrochemical properties and resistance of ink it can be used as a electrode in paper battery, capacitors and as a dielectric material in electrode systems.

50.2 Experimental Section

50.2.1 Materials

Multi-walled carbon nanotubes (MWCNT, purity 80%), propylene Glycol (1,2-propanediol) extra pure AR, 99.5%, Triton X-100 for molecular biology DNase, RNase, protease not detected, Silicone Deformer, Gum Arabic. The MWCNTs have an average diameter of 10 nm average diameter with 1–5 μm average length. All the chemicals were used without further purification.

50.2.2 Synthesis of MWCNT Ink Using Gum Arabic.

Conduction Inks were prepared by dissolving MWCNT powder in deionized (DI) and without deionized water at concentrations of MWCNT @ 0.25, 0.75 and 1.0 g by

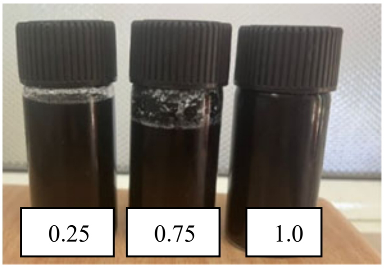

Fig. 50.1 Conduction ink from **a** MWCNT @ 0.25 wt%, **b** MWCNT @ 0.75 wt%, **c** MWCNT @ 1 wt%

wt% as shown in Fig. 50.1. Initially dissolve the Gum Arabic in DI water completely and add MWCNT. Keep the solution under sonicator to allow uniform dispersion for 2 h. During the stirring process add triton x-100 and propylene glycol to reduce surface tension between the molecules and increase viscosity. Thereby stability can be achieved. To subside the foam Silicon Deformer was added. Stirring continued for one hour at 700 RPM and the obtained conduction ink was collected. During the synthesis of MWCNT @ 0.75 g by wt% and MWCNT @ 1.0 g by wt% deionized water was added along with Gum Arabic. While synthesizing MWCNT @ 0.25 g by wt% only Gum Arabic was added for dispersion. It has been observed that MWCNT @ 0.75 g, 1.0 g are slurry and MWCNT @ 0.25 g shows good stability after spreading on a paper. The synthesized ink was spread on cellulose paper and made it to dry in oven for 150 min at 80 °C. The characterization techniques were performed on the sample MWCNT @ 0.25 g by wt% and are discussed below.

50.3 Characterization Techniques

The Systronics, double beam UV–Vis spectrophotometer 2202 (Systronics, Gujarat, India) were used to study the optical absorption and nature of bonding, respectively. The Horiba SZ-100 Particle Size Analyzer (HORIBA, Ltd., Kyoto, Japan) was used to determine the average particle size. CH6112E was used for electrochemical analysis of the synthesized ink.

50.4 Results and Discussion

50.4.1 Particle Size Analyser

The synthesized ink was characterized using Particle size analyzer. The distribution and average particle size depends on Brownian motion of individual particles. The smaller particles will move rapidly with the solvent molecules. The particle size is expressed in terms of volume.

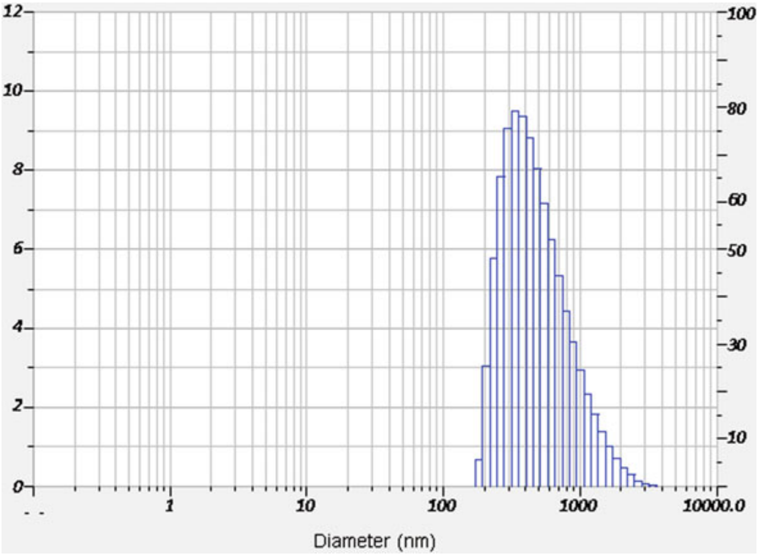

Fig. 50.2 Particle size analyzer of conduction ink

Good uniformity of the synthesized ink was observed through the histograms as shown in Fig. 50.2. It has been observed that all the particles are showing diameter uniformly in the range from 500 to 1000 nm [11].

50.4.2 Zeta Potential Measurement

To understand surface charge related stability Zeta potential measurement was done on synthesized ink. It has been observed that the value of ζ is − 28.5 mv. The negative value indicates that the ink can be treated as anionic surfactant. Also the addition of Gum Arabic during the synthesis made good stability suspension [12] (Fig. 50.3).

50.4.3 UV–Visible Spectroscopy

The UV–Visible spectroscopy measures the dispersion and stability of MWCNT and Gum Arabic suspended particles**.** The concentration of dispersed particles in the solution will give light absorbance values. The maximum peaks were observed at 217, 264 nm which indicates the ink formulation and confirms to the wavelength range of MWCNT's [13–15].

The maximum absorption is in the range of ~ 264 nm indicates the presence of MWCNT and Gum Arabic while the ~ 217 nm indicates Gum arabic in the

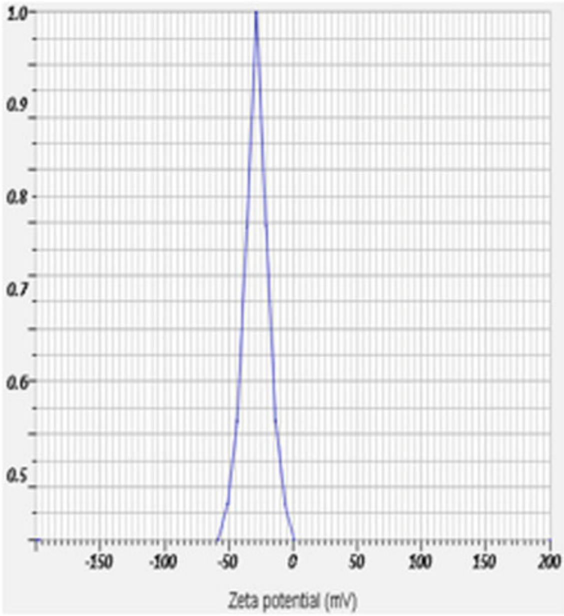

Fig. 50.3 Zetapotential of conduction ink

ink as shown in Fig. 50.4. The absorbance values indicates the strong interaction between the Gum arabic and MWCNT. The presence of –OH groups on the surface of MWCNT created a surface area for the absorption of Gum arabic molecules to disperse effectively.

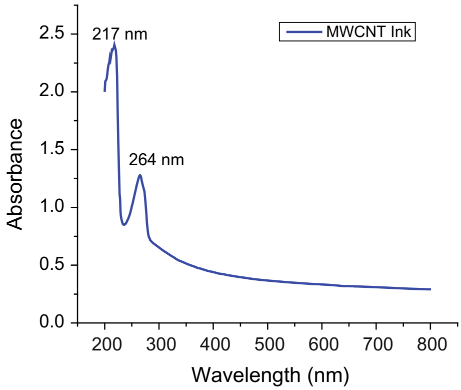

Fig. 50.4 UV–Visible spectroscopy of MWCNT ink

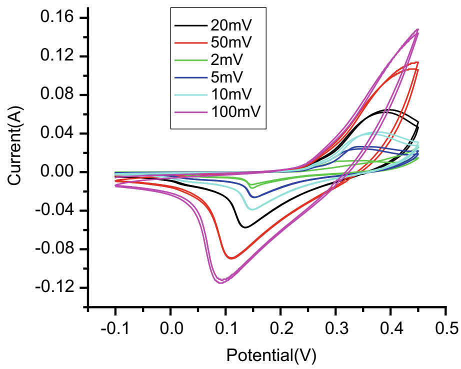

Fig. 50.5 Cyclic voltagramms of MWCNT ink

50.4.4 Electrochemical Analysis

The electrochemical measurements are recorded by using three electrode system over the potential window of 1.5–1.5 V with Ag/AgCl as the reference electrode, Platinum (Pt) wire as the counter electrode in 1 M aqueous Na_2SO_4 electrolyte using a Metrohm Autolab PGSTA302N (Potentiostat/Galvanostat) equipment with NOVA 2.0.2 software. The cyclic voltammetry studies [16, 17] at different scan rates of 100, 50, 20, 10, 5, 2 mV/s are recorded from − 0.2 to 0.4 V as applied potential range are shown in Fig. 50.5.

The area under voltammogram has increased with increase in scan rate which indicates high power characteristics. An increase in the potential scan rate led to increase in the current. This can be attributed to slow intrinsic electrochemical kinematics and ohmic limitation [18–26]. The specific capacitance from galvanic charge–discharge measurements at the potential time frame with constant current value calculated using

$$\mathrm{Cs} = \mathrm{IX}\Delta\mathrm{t}/\mathrm{mx}\Delta\mathrm{V} \tag{50.1}$$

where I is the galvanostatic discharge current, Δt is discharge time, m is the active mass, ΔV is the potential difference of GCD curve. The specific capacitance of MWCNT ink is found to be 407.96 F/g. The power density value calculated using

$$\frac{E * 3600}{\Delta t} \tag{50.2}$$

and it is 112.84 W/kg. The resistance value is very high when calculated with multimeter around 200 Ω (Fig. 50.6).

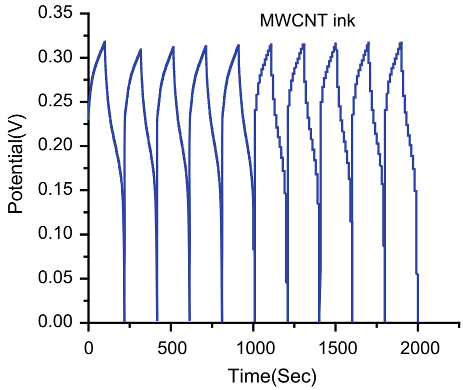

Fig. 50.6 GCD graph of MWCNT ink

50.5 Conclusion

The ink was synthesized using MWCNT @ 0.25, 0.75, 1 wt% along with Gum Arabic. The MWCNT @ 0.25 wt% dispersion and stability was good when taken on a cellulose paper. The MWCNT @ 0.75, 1 wt% was slurry. The characterization techniques were performed on MWCNT @ 0.25 wt%. It has been observed from UV–Visible spectroscopy the presence of MWCNT and Gum Arabic. The particles in conduction ink indicates good uniformity and the size is in the range 500–1000 nm. The Zeta potential value − 28.5 mv indicates a good anionic surfactant. The Electrochemical analysis results indicate the Capacitance value to be around 4**07.96** F/g. It has been observed from GCD graphs that the discharging time is around 100 s in first cycle. The resistance value and power density values are high for the synthesized ink. The electrochemical studies confirm that the ink can be used as a short time storage during the process of load levelling.

Acknowledgements All the Authors gratefully acknowledge the valuable help of Management, VNR Vignana Jyothi Institute of Engineering and Technology for funding the characterization work of the samples, Also Centre for Nanoscience and technology, Jawaharlal Nehru Technological University, Hyderabad for providing their facilities.

References

1. Cano-Raya, C., et al.: Chemistry of solid metal-based inks and pastes for printed electronics—a review. Appl. Mater. Today **15**, 416–430 (2019)
2. Abdelkader, A.M., et al.: Ultraflexible and robust graphene supercapacitors printed on textiles for wearable electronics applications. 2D Mater. **4**(3), 035016 (2017)
3. Zhou, L., et al.: All-organic active matrix flexible display **88**(8), 083502 (2006)
4. Karim, N., et al.: All inkjet-printed graphene-based conductive patterns for wearable e-textile applications. J. Mater. Chem. C **5**(44), 11640–11648 (2017)

5. Kulkarni, M.V., et al.: Ink-jet printed conducting polyaniline based flexible humidity sensor. Sens. Actuators B **178**, 140–143 (2013)
6. Matsuhisa, N., et al.: Printable elastic conductors by in situ formation of silver nanoparticles from silver flakes. Nat. Mater. **16**(8), 834–840 (2017)
7. Grau, G., Cen, J, Kang, H., Kitsomboonloha, R., Scheideler, W.J., Subramanian, V.: Gravure-printed electronics: recent progress in tooling development, understanding of printing physics, and realization of printed devices. Flex. Print. Electron. **1**(2), 023002 (2016)
8. Bhatt, K., Kumar, S., Tripathi, C.C.: High-performance ultra-low leakage current graphene-based screen-printed field-effect transistor on paper substrate. Pramana **94**(1), 1–4 (2020)
9. Anderson, D.M.W., Hirst, E.L., Stoddart, J.F.: The composition of acacia gum exudates. J. Chem. Soc. (C) 1959 (1966)
10. Anderson, D.M.W., Karamalla, K.A.: J. Chem. Soc. (C) (1966)
11. Shireesha, K., Kumar, T.R., Rajani, T., Chakra, C.S., Kumari, M.M., Divya, V., Raghava Reddy, K.: Novel NiMgOH-rGO-based nanostructured hybrids for electrochemical energy storage supercapacitor applications: effect of reducing agents. Crystals **2021**, 11,1144 (2021). https://doi.org/10.3390/cryst11091144
12. Akindoyo1, J.O., Ismail, N.H., Mariatti, M.: Development of environmentally friendly inkjet printable carbon nanotube-based conductive ink for flexible sensors: effects of concentration and functionalization. J. Mater. Sci. Mater. Electron. https://doi.org/10.1007/s10854-021-05900-y
13. Williardson, R., Beer, A.: Optical Properties of III–V Compounds, p. 318. Academic Press, New York (1967)
14. Dressel, M., Gruner, G.: Electrodynamics of Solids Optical Properties of Electron in Matter, p. 159. Cambridge University Press, Cambridge (2002)
15. Rajani, I., Brahmaji Rao, V., Udaya Kiran, C.: J. Mater. Sci. Mater. Electron. **31**, 3238 (2020)
16. Rajani, I., Brahmaji Rao, V., Udaya Kiran, C.: IOP Sci. Mater. Res. Express 065017 (2018)
17. Xie, M., Duan, S., Shen, Y., Fang, K., Wang, Y., Lin, M., Guo, X.: ACS Energy Lett. **1**, 814 (2016)
18. Zheng, J.H., Zhang, R.M., Wang, X.G., Yu, P.F.: Res. Chem. Intermed. **44**, 5569 (2018)
19. Cheng, R., Hu, T., Zhang, H., Wang, C., Hu, M., Yang, J., et al.: J. Phys. Chem. C **123** 1099 (2019)
20. Kim, B.K., Sy, S., Yu, A., Zhang, J.: J. Electrochem. Supercapacitors Energy Storage Convers. **1** (2015)
21. Su, W., Lin, T., Chu, W., Zhu, Y., Li, J., Zhao, X.: RSC Adv. **6**, 113123 (2016)
22. Patil, S.J., Lokhande, V.C., Chodankar, N.R., Lokhande, C.D.: J. Colloid Interface Sci. **469**, 318 (2016)
23. Zhao, Y., Hao, M., Wang, Y., Sha, Y., Su, L.: J. Solid State Electrochem. **20**, 81 (2016)
24. Liang, R., Du, Y., Xiao, P., Cheng, J., Yuan, S., Chen, Y., Yuan, J., Chen, J.: Nanomaterials **11**, 1248 (2021)
25. Gilliam, R.J., Graydon, J.W., Kirk, D.W., Thorpe, S.J.: Int. J. Hydrogen Energy **32**, 359 (2007)
26. Fabricio, R., Martinez, P.S., Castro, E.B., Humana, R., Peretti, H.A., Visintin, A.: Int. J. Hydrogen Energy **38**, 240 (2013)

Chapter 51
Technological Reconversion of a Climatic Chamber for the Artificial Rearing of Fruit Flies of the Species (*Anastrepha striata*)

Emerson Jacome, Cristian Jiménez Jácome, Sulaya Bayancela, and Luigi O. Freire

Abstract The research was carried out in the Entomology laboratory of the Universidad Técnica de Cotopaxi, with geographical coordinates of 00° 59′ 57″ South latitude and 78° 37′ 14″ West longitude. The purpose of the study was to observe the effect of temperature on the biological cycle of *Anastrepha striata*. The methodology consisted of technologically converting a conventional cooler into a rearing climatic chamber for the control of different temperatures with a maxi- mum error of ± 0.4 °C controlled and supervised through an interface, which generates historical records of temperature behavior; in the development of *Anastrepha striata*, a species that presents complete metamorphosis, life tables were made considering the keys of the Insect Life Cycle Modeling (ILCYM) program. Considering temperatures of 10, 15, 20 and 25 °C. In conclusion, it is possible to construct artificial insect rearing chambers that regulate different temperatures in insects of the species *Anastrepha striata*. Low temperatures increase longevity, but affect the fecundity of the insects, *A. striata* at 25 °C is in its ecological niche, because it accumulates heat for its ovarian sexual maturation, besides presenting a shorter average longevity.

E. Jacome · C. J. Jácome · L. O. Freire (✉)
Universidad Técnica de Cotopaxi, Latacunga, Ecuador
e-mail: luigi.freire@utc.edu.ec

E. Jacome
e-mail: emerson.jacome@utc.edu.ec

S. Bayancela
Escuela Superior Politécnica de Chimborazo—ESPOCH, Riobamba, Ecuador
e-mail: sulaya.bayancela@espoch.edu.ec

P. H. V. S. Talpa Sai et al. (eds.), *Intelligent Manufacturing and Energy Sustainability*, Smart Innovation, Systems and Technologies 372,
https://doi.org/10.1007/978-981-99-6774-2_51

51.1 Introduction

The development of controlled environment applications suitable for monitoring, recording and controlling temperature, relative humidity, among other parameters, has been possible thanks to the evolution of microcontroller technology [1, 2].

Most agronomists and industry personnel seek to improve the production process by controlling pests through experimentation and the use of technologies, observing the reaction of pests exposed to climate-controlled factors [3].

The family Tephritidae is one of the most diverse groups of the order Diptera known as fruit flies, due to their feeding habits on wild and cultivated fruits [4] among which (Dacus), (Rhagoletis), (Ceratitis), (Bactroce-ra), (Anastrepha) and (Toxotry-pana) are the main genera [5]. Anastrepha spp. is a genus of complete metamorphosis insects of great economic importance present in the South American region [6]. Due to the feeding habit of the larvae when feeding on the pulp. In Ecuador, *Anastrepha striata* (Schinner) is an important pest in fruit production, since it affects several fruit trees, guava being its main host [7]. Its life cycle develops in vegetation, fruit and soil, depending on the ecological conditions of each region and is closely regulated by temperature [8, 9].

The most important element of climate is temperature, [10] which is currently undergoing a significant variation due to global warming, causing species to migrate to different climatic zones. Therefore, it becomes the main variant in the biological cycle of *Anastrepha striata* (Schinner). Thus, the physiological time in which insects develop is dependent on temperature as the basis of most models for predicting the appearance of pests [11].

The ecological study of insect populations is often based on the different stages of development from birth to the birth of new progeny. Events such as death or reproduction are monitored at equal time intervals (hours, days, years, etc., depending on the organism under study) [12, 13].

51.2 Development

51.2.1 Climatic Chamber

The working temperatures for the case study are in a range of 10–25 °C, for which the technological reconversion of a conventional chiller was carried out, implementing electrical resistance thermometers, as well as a closed-loop control system through the ATMEGA328 that centralizes the information and stores the historical data in a memory card, and also shows the behavior curves (Set Point and Control Value) in a Human–Machine Interface (HMI) as shown in Fig. 51.1.

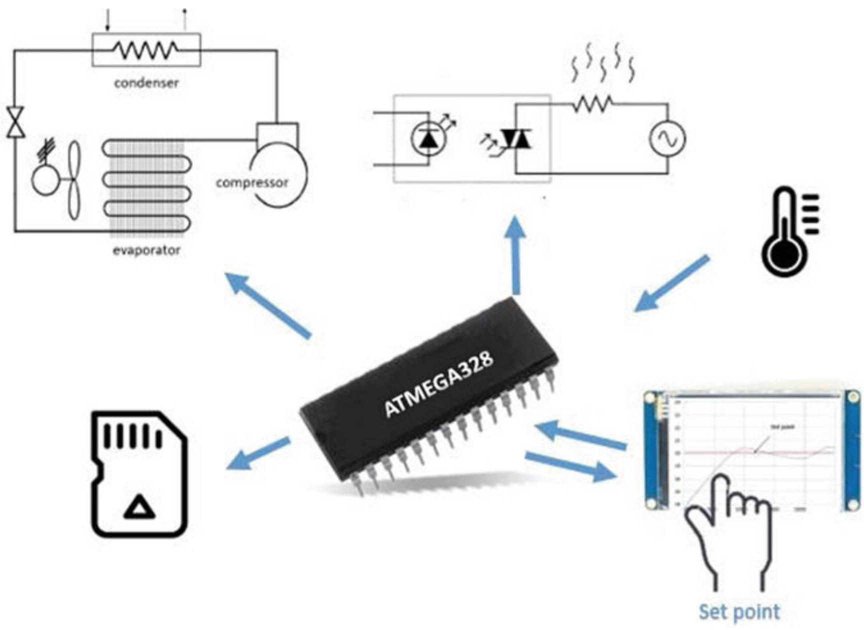

Fig. 51.1 Schematic diagram of climatic chamber

51.2.2 Biological Material

The biological material for the breeding of *Anastrepha striata* was obtained from the collection of guava fruits (*Psidium guajava*) in the subtropical zone of the province of Cotopaxi in the canton of La Maná as indicated [14]. The collected fruits were transferred to the entomology laboratory of Universidad Técnica de Cotopaxi.

51.2.3 Fly Breeding

The collected samples underwent a disinfection process based on 0.4% sodium hypochlorite, to avoid biological contamination caused by fungi and bacteria, where five terrariums were used for each temperature, depositing in each one four affected fruits on a peat base, so that the larvae could pupate. Then, using morphological keys, the adults were identified as males and females, placing one male and one female per container for subsequent mating and thus observing each biological cycle of *Anastrepha striata* in all its stages in relation to the temperatures.

51.2.4 Adult and Larval Diet Formulations

The determination of the diet of the adults was carried out considering their maintenance with the use of sponges placed in petri dishes containing a 30% dilution of molasses [15].

51.2.5 Generational Analysis

Once the diet of adults and larvae was determined, as well as the determination of the substrate for pupation, the effect of temperatures of 10, 15, 20 and 25 °C on the cycle of *A. striata* was evaluated, where the time periods in each stage of insect development were determined using life tables based on the ILCYM program [12].

51.2.6 Data Analysis

The effect of temperature was determined by analyzing the life tables with the use of dynamic tables, counting the respective frequencies in the different stages of development of the individuals of *A. striata*, using an analysis of variance taking the design completely as the ideal model for the nature of the work. Subsequently, due to the statistical differences found in the temperatures, the separation of means was performed by applying Tukey's test ($P < 0.05$). Using the Infostat.

51.3 Results

The behavior of the climatic chamber has an accuracy of ± 0.4 °C, an admissible error since it does not affect the life cycle of the fly under study, as shown in Fig. 51.2, it also has the characteristic that when the temperature rises or falls, due to its inertia, it presents a peak of 0.05 °C.

Table 51.1 of the ANOVA shows highly significant differences in temperature variations for the rearing of *Anastrepha striata*, which indicates that this environmental factor influences both the general development of the biological cycle and each stage of the insect. According to [16], the populations of the fruit fly complex vary from year to year depending on climatic conditions and food availability.

The effect of temperature was determined by analyzing the life tables with the use of dynamic tables, counting the respective frequencies in the different stages of development of the individuals of *A. striata*, using an analysis of variance taking the design completely as the ideal model for the nature of the work. Subsequently, due

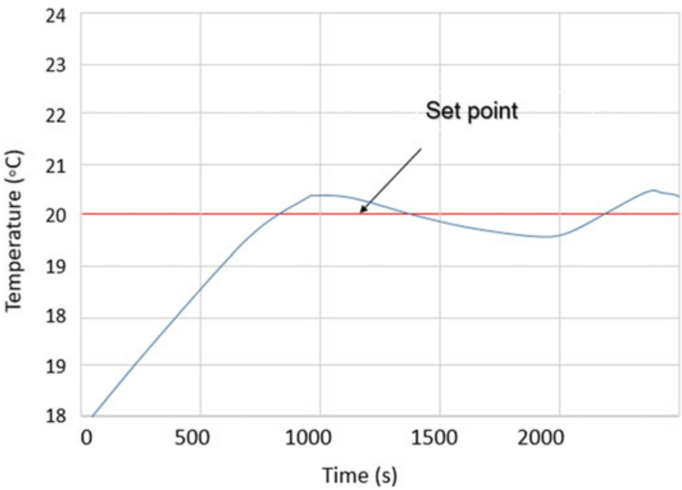

Fig. 51.2 Temperature behavior in the chamber

Table 51.1 ANOVA for the life cycle of *A. striata*

F DE V	GL	CM CICLE	CM EGG	CM LARVA	CM PUPA	CM OVI
Temperature	3	159,563.15**	934.38**	15,918.79**	15,553.97**	7444.14**
Error	196	149.69	1.23	9.31	9.33	39.91
Total	199					
CV%		10.60	14.07	8.34	8.41	23.86

to the statistical differences found in the temperatures, the separation of means was performed by applying Tukey's test ($P < 0.05$). Using the Infostat.

Table 51.2 shows how temperature variation influences the growth of *Anastrepha striata*, where cold temperatures delay the development of the biological cycle of the insect, indicating a greater longevity at 10 °C, where the insect completes its cycle in 167. 12 days while at temperatures of 25 °C the cycle is shortened to 54.86 °C, in the ranges of 10°, 15 °C, 20 °C and 25 °C, for the egg stage values of 13.56, 8.92, 4.46, and 4.56 days are seen; for the larva stage the values and for pupa are 50.28, 52.16, 26.08 and 16.76 days. Determining that the lower the temperature, the perpetuity of the species is generated, causing the eggs to pass sooner to the larval stage in search of warmer temperatures that are close to 29 °C as mentioned [7]. Regarding ovipositions, it was observed that at 10 °C, females do not leave offspring, but not at 25 °C, which reaches the highest oviposition and fertility, agreeing with [16] who mentioned that insects are stressed by very low temperatures. Stress increases the fly's energy expenditure, since it has a double need to: regulate body homeostasis by maintaining a minimum body metabolism; activate and/or use a bio-logical system that functions as a "systemic protector", isolating and protecting the tissues from the effects caused by the constant cold.

Table 51.2 Tukey test at 5%, for developmental stages of *Anastrepha striata* (Schiner)

Temperature	CICLE	EGG	LARVA	PUPA	OVI
10 °C	167.12 D	13.56 C	53.76 D	50.28 C	0.00 C
15 °C	159.84 C	8.92 B	49.84 C	52.16 D	33.95 B
20 °C	79.92 B	4.46 A	24.92 B	26.08 B	33.95 B
25 °C	54.86 A	4.56 A	17.92 A	16.76 A	39.43 A

Therefore, it is important to investigate the effects of environmental factors on the rate of sexual maturation. Estimates based on temperature-related ovarian maturation. At 20 °C, the time required for ovarian maturation was doubled relative to the temperature of 25 °C and the life expectancy at lower temperatures was higher than at 25 °C [16]. The correlation between ovarian maturation and fly longevity was significant since, at 10 °C, their life span was 167.12 days, relative to 54.86 days at 25 °C. In conclusion at lower temperatures the formation and maturation of female reproductive organs is slower generating longevity in *Anastrepha striata.* At 25 °C, ovarian maturation is faster and average longevity is shorter.

Figure 51.3 shows the effects of temperature variation on the biological cycle of *Anastrepha striata*, the ranges evaluated being 10, 15, 20 and 25 °C. It was observed that life spans are shortened at temperatures approaching 25 °C, while at low temperatures the insects have greater longevity. It was established that at lower temperatures the stage is lengthened because it does not accumulate the necessary temperature to develop completely, from which it is considered that temperature is the factor with the greatest incidence on the development of insects [15]. It should be mentioned that the development time varied in direct relation to the increase in temperature, therefore, the development process is faster at temperatures close to 25 °C and slower at temperatures close to 10 °C [16].

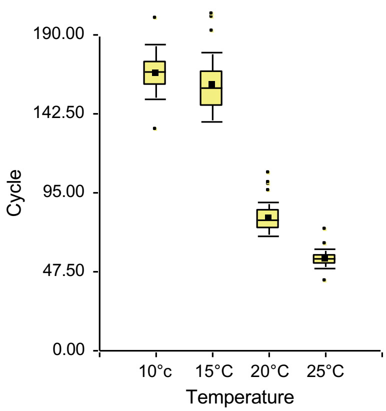

Fig. 51.3 Effect of temperature on the life cycle of *Anastrepha striata*

51.4 Conclusions

The temperature control system implemented shows a favorable response for the creation of a controlled environment for the rearing of the *Anastrepha striata* fly, of ± 0.4 °C despite the overshoot of 0.05 °C that exists due to temperature inertia, and the ambient temperature does not affect the process.

The storage of temperature data (30-day average) and the development of historical graphs in the HMI (1 day) allows the evaluator to have an adequate follow-up since the system can present power outages causing disturbances in the process and adulterating the results.

Considering the values of the temperature parameter evaluated on the reared insects, the adaptation of *A. striata* to an artificial temperature-controlled system indicates that temperature is the main factor affecting the development of the insects, and that the information generated guarantees the establishment of their artificial rearing and that it is possible to modify the temperature in equipment by means of the technological reconversion of coolers to insect growth chambers with controlled temperatures.

References

1. Vacacela, S.G., Freire, L.O.: «Implementation of a network of wireless weather stations using a protocol stack» Intell. Manuf. Energy Sustain. **213**, 509–517 (2021)
2. Guambo, W., Corrales, B.P., Freire, L.O., Albarracin, M.D.: «Performance evaluation of a predictive and PID control applied to a didactic flow regulation process» Intell. Manuf. Energy Sustain. (2022)
3. Pinto, N., de la Vega, J., Cañarejo, M.: «Utilización del método de conservación bajo atmósferas controladas en frutas y hortalizas» Agris 2226–2989 (2021)
4. Lorea Hernández, F.G., Hernández Ortiz, V., Morales Mavil, J.E.: «La biodiversidad en Veracruz: estudio de estado» Diversidad de especies: conocimiento actual **II** (2011)
5. Gómez, H.M.: Las moscas de la fruta. Produmedios, Bogotá (2012)
6. Korytkowski, C.A.: «Situación actual del género Anastrepha Schiner, 1868 (Diptera: Tephiritidae) en el Perú» Revista Peruana de Entolomogía **42**, 97–158 (2001)
7. Tigrero, J., Sandoval D.P., Vilatuña, J.E.: Manejo y control de moscas de Fruta. Universidad de las Fuerzas Armadas ESPE, Quito (2010)
8. Cabrera-Mireles, H., Ortega-Zaleta, D.: Principales plagas del mango. INIFAP-CPVeracruz, Veracruz (2004)
9. Marín, M.: Identificación y caracterización de moscas de las frutas en los departamentos del Valle del Cauca, Tolima y Quindío. Universidad de Caldas, Manizales (2002)
10. Portilla Farfán, F.: Agroclimatología del Ecuador. Editorial Universitaria Abya-Yala, Cuenca (2018)
11. Bryant, S.R., Thomas, C.D., Bale, J.S.: «The influence of thermal ecology on the distribution of three nymphalid butterflies» J. Appl. Ecol. 43–55 (2002)
12. Carhuapoma Ramos, P.: «Una herramienta amigable y rapida para la prediccion del riesgo de plagas de insectos bajo escenarios de cambio climatico» de ILCYM 4.0, Lima (2019)
13. Gamarra, H., Carhuapoma, P., Fonseca, C., Flores, P., Panchi, N., Gonzalez, M., Pradel, W., Rodriguez, H., Velasco, C.: «El software ILCYM 4.0» de ILCYM 4.0, Lima (2020)

14. Jácome-Mogro, E.J., Basantes-Quinatoa, M., Jiménez-Jácome, S., Castro-Díaz, L., Marín-Quevedo, K.: «Dinámica del género Anastrepha, en el cultivo de guayaba (Pisum guajava), en la parroquia Guasaganda Ecuador» Revista de investigación agraria 3(2), 43–48 (2021)
15. Taufer, M., do Nascimento, J.C., da Cruz, I.B.M., de Oliveira, A.K.: «Efeito da temperatura na maturação ovariana e longevidade de Anastrepha fraterculus (Wied.) (Diptera: Tephritidae)» Ecologia, Comportamento e Bionomia 639–648 (2000)
16. Tucuch-Cauich, F.M., Chi-Que, G., Orona-Castro, F.: «Dinámica poblacional de adultos de la mosca mexicana de la fruta Anastrepha sp. (Diptera: Tephritidae) en Campeche, México» Agricultura técnica en México **34**(3), 341–347 (2008)

Chapter 52
Unpaired Image-to-Image Translation Based Artwork Restoration Using Generative Adversarial Networks

Praveen Kumar and Varun Gupta

Abstract Artworks assume huge significance in humankind's culture and history. Artworks assimilate history and have the precise ability to tell history to the future generation. However, as time passes, environmental factors severely affect artworks, and these damages are often complicated to repair manually and through traditional methods. Conventional artwork restoration methods can not conserve the artist's style and the artwork's semantic details. Restoration of the artworks through virtual restoration methods can be done using generative adversarial networks. After that, the virtually restored artwork can guide the physical restoration task of artworks. However, most of the methods based on generative adversarial network performs paired image-to-image translation for restoration, which necessitates the presence of the original version of the damaged artwork. This work proposes an unpaired image-to-image translation-based artwork restoration method using cycle-consistent generative adversarial networks. The proposed method does not require the availability of the original version of each damaged artwork for restoration. The network has been trained on a publicly available dataset of artwork images. The experimental results have been compared with other methods used for artwork restoration, and quantitative results demonstrate that the proposed approach performs better than the current and previous methods for the restoration of damaged artwork.

52.1 Introduction

Artworks are custodians of cultural and societal history since they record events of historical periods. Further, the unique artistic value of artworks inspires the preservation of artworks. However, due to various weathering effects like temperature, light, and relative humidity, artworks develops wear and tear with the passage. Therefore, the protection and restoration of ancient artworks are urgently required. The

P. Kumar (✉) · V. Gupta
CCET (Degree Wing), Sector 26, Chandigarh 160019, India
e-mail: praveen12190@gmail.com

P. H. V. S. Talpa Sai et al. (eds.), *Intelligent Manufacturing and Energy Sustainability*, Smart Innovation, Systems and Technologies 372,
https://doi.org/10.1007/978-981-99-6774-2_52

process of artwork restoration starts with having damaged artwork [1] and applying restoration techniques to obtain a clean and restored artwork. Artwork restoration using traditional methods is lengthy, tedious, and error-prone. Further, sometimes it is hard to reproduce the damaged part of the artwork due to the lack of details about the damaged portion. However, the artwork restoration field is also very complex because we have to preserve the unique artistic style of artworks.

The virtual restoration of artworks using artificial intelligence can help to restore the artworks. Further, digitally restored artwork can help conservators restore the artworks physically, and digitally preserved artworks will not be affected by various environmental factors like moisture, humidity, temperature, paper degradation, or ink fading. However, a limited number of virtual artwork restoration methods based on artificial intelligence have been proposed in the literature. Further, there are performance issues in existing artwork restoration approaches since these approaches require masks and perform restoration in multiple steps.

This work proposes a one-step approach for the virtual artwork restoration method based on the generative adversarial network. Generative adversarial networks are a powerful tool for the task of reconstruction of images. Applications of the GANs are in various areas like image transformation [2], image translation [3], generation of artificial medical data, and generative design. GANs have largely been used to restore images, but the applicability of GANs to restore artwork is still less explored.

The work presented in this paper proposes unpaired image-to-image-based virtual restoration of artworks using cycle-consistent generative adversarial networks. The proposed method does not require the availability of an original artwork version of a damaged artwork. It uses a bunch of damaged artwork images and a bunch of original artwork images for training. The main contributions of the paper are as follows.

(i) This paper proposes an unpaired image translation-based method for the restoration of artworks. This method does not require the presence of an original version of a damaged artwork.
(ii) We show the potential of a cyclic consistency-based generative adversarial network to restore the damaged artworks based on an unpaired bunch of damaged and original artworks.
(iii) Experimental results show that the proposed method works well in artwork restoration and outperforms the other artwork restoration methods.

The rest of the paper contains the following sections. Related work is given in Sect. 52.2, and Sect. 52.3 describes the dataset description and the workflow. Section 52.4 presents the proposed network architecture. Section 52.5 presents the details of the experimentation and results obtained from the proposed work. Section 52.6 concludes the paper.

52.2 Related Work

This section discusses and analyses the related images and artwork restoration methods. Initially, we discuss the works on image restoration proposed in the literature based on image processing techniques, machine learning-based methods, and deep learning-based methods. Then we discuss the related work on the existing artwork and mural restoration methods.

52.2.1 Image Restoration

Conventional methods use neighboring pixel-based information for image restoration [4, 5] and use the prior information of the images for inpainting [6]. Further, some other approaches for inpainting use gradient directions, probabilistic models, and neighboring pixels-based methods to fill in missing holes in the images [7–11]. However, these methods can be used only for restoring images with small patch sizes. While other forms of image processing applications include colorization [12], super-resolution [13], and image inpainting [14]. However, clean restoration of images is often difficult. Over the years, researchers have proposed image restoration using deep convolutional neural networks [13–19]. Most of the above methods are based on mask generation, whereas the proposed method does not require mask generation.

52.2.2 Artwork Restoration

This section discusses artwork and mural restoration methods proposed in the literature. Gupta et al. [20] proposed an approach for artwork restoration based on automatic mask generation [21] and image inpainting. However, this method requires the generation of masks. Adhikary et al. [22] proposed a generative adversarial network based on residual networks and a patch-based discriminator to restore damaged artworks. Zhou et al. [23] proposed the applicability of various deep learning-based algorithms to restore weathered beams. Cao et al. [24] proposed the restoration of the ancient mural using enhanced GANs. Li et al. [25] proposed virtual mural restoration using U-Net-based GANs. But, they could not fully restore mural colors. More recently, Kumar and Gupta [26] proposed the method of restoration of damaged artworks based on pretrained residual network-based generative adversarial networks. Most of the existing methods are based on paired image translation. These methods require the availability of an original artwork corresponding to each damaged artwork which is often difficult to ensure. Thus, there is a need for an unpaired image-to-image translation-based artwork restoration method that does not depend on the presence of the original version of each damaged artwork. The proposed method of artwork restoration contributes in this direction.

Table 52.1 Dataset description of artwork images

Data	Total images	Number of images used during the experiment	Images used for training	Images used for testing
Dataset of art images	2073	2073	1192	881

52.3 Dataset Description and Workflow

The details of the dataset[1] used for the proposed work are given in Table 52.1. The art images dataset contains 2073 artworks. Of the 2073 artwork images, 1192 were used in the training set, and 881 were used in the test set.

The workflow contains the following steps: (i) Generation of the damaged artwork, (ii) Creating cycle consistency loss-based generator, (iii) Creating the discriminator part, (iv) Defining the objective functions for the network, (v) Training of the network and (vi) Restoration of artwork.

The detailed workflow steps are discussed below.

(i) **Damaged artwork generation**: During this step, damaged artwork images are synthetically generated by writing alphanumeric characters over the original images.
(ii) **Creating cycle consistency loss-based generator**: The proposed network consists of two GANs, one for generating restored artwork from the damaged artwork and the other for generating damaged artwork from the restored artwork. The generator for both GANs is a U-Net consisting of encoding, bottleneck, and decoding blocks. Further, each encoding, bottleneck, and decoding block consist of convolution layers, batch norm, and ReLU activation function.
(iii) **Creating the discriminator part**: The proposed network consists of two GANs translating the artworks from two domains of damaged and restored artworks. The proposed network uses a patch-based discriminator, which looks at patches in the artwork image and outputs a matrix of values instead of a single value. The proposed network uses two discriminators for generated restored artwork and another for generated damaged artwork.
(iv) **Defining the objective functions for the network**: The objective function for the generator part is given in Eq. (52.1).

$$\text{Generator loss} = \lambda_1 * Cycle\ Consistency\ Loss + \lambda_2 * Adversarial\ Loss + \lambda_3 * Identity\ Loss \tag{52.1}$$

The objective function for the discriminator is given in Eq. (52.2). Patchwise discriminator loss is the sum of the squared distance of the discriminator prediction to the label of one for the real artwork and the square of the discriminator

[1] https://www.kaggle.com/thedownhill/art-images-drawings-painting-sculpture-engraving.

classification of the generated artwork.

$$\text{Discriminator Loss} = E_x\left[(D(x) - 1)^2\right] + E_z\left[(D(G(z)))^2\right] \quad (52.2)$$

where D(x) is the discriminator classification of the real artwork x, and D(G(z)) is the discriminator classification of the generated artwork G(z) for each patch of the image.

(v) **Training of the network**: During this step, we have trained and evaluated the proposed system consisting of two generative adversarial networks having two generators (G) and two discriminators (D) defined above using the above-defined objective functions.

(vi) **Restoration of artwork**: We have evaluated the proposed network on the test dataset and obtained restored versions of the damaged artwork images.

52.4 System Architecture

The proposed system uses the unsupervised unpaired image translation framework where the exact correspondence between two pairs of images is unknown. In the proposed system, we have a set of images of damaged artworks and restored artworks. The proposed approach will use two generative adversarial networks (GAN) to generate the images in two domains of damaged and restored artwork. The first GAN will generate the restored artwork from damaged artwork, and the second GAN will generate the damaged artwork from the restored artwork. The proposed system uses cycle consistency loss for training. Through experiments, it has been found that cycle consistency loss preserves the semantics of the artworks while preserving the artistic style between the two domains of artworks.

Figure 52.1 presents the pictorial depiction of the proposed system consisting of two different GANs with two generators, two discriminators, and cycle consistency loss for each GAN. The first half of Fig. 52.1 shows the GAN generating the restored artwork from the damaged artwork and the second half of Fig. 52.1 shows the GAN generating the damaged artwork from the restored artwork. The generator part of both the GANs is the U-Net [27] and conditional GAN [28], and the discriminator part of both the GANs is the patch-based discriminator [29].

52.5 Training and Results

This section discusses the experimental configuration settings and results obtained during the experimentation.

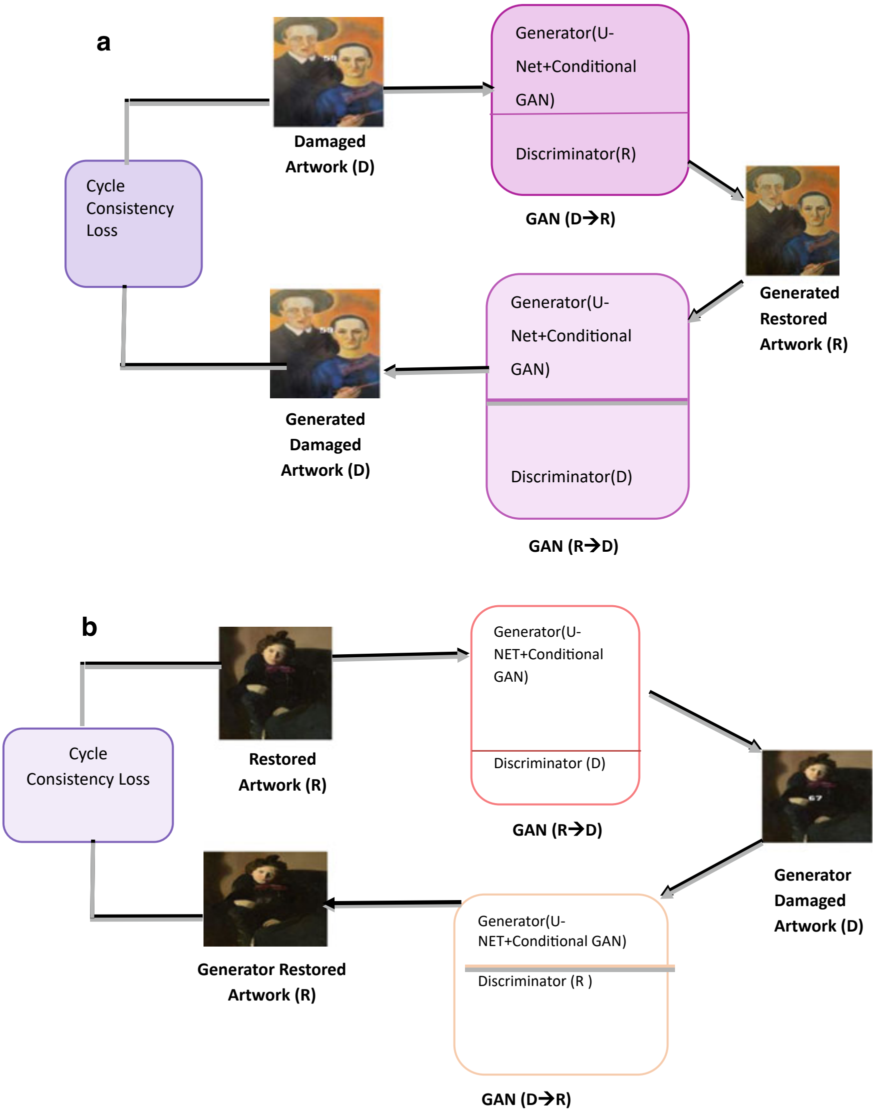

Fig. 52.1 System architecture **a** Part-1. **b** Part-2

52.5.1 Experimental Setup

The experimentation has been done using the Pytoch library, and network training has been done using Quadro RTX 6000 A GPU. Table 52.2 presents the hyperparameters used during the experimentation.

Table 52.2 Hyperparameters values

Hyperparameter	Value
Size of image	256 × 256
Size of batch	4
Initial learning rates	2×10^{-4}
Optimizer settings	Adam optimizer (β1 = 0.5, β2 = 0.999) and step size (γ = 0.5)
Generator objective function	$\lambda_1 * Cycle\ Consistency\ Loss(l1\ loss) + \lambda_2 * Adversarial\ Loss(MSE) + \lambda_3 * Identity\ Loss(l1\ loss)$ where $\lambda_1 = 10$, $\lambda_2 = 1$ and $\lambda_3 = 0.1$
Discriminator objective function	Adversarial loss (MSE loss)

52.5.2 Evaluation Metrics

The evaluation metrics used in the proposed work are defined as follows.

The peak signal-to-noise ratio (PSNR) is the ratio of the maximum possible value to the power of distorting noise in a signal.

$$PSNR = 10\log_{10}\left(peakval^2\right)/MSE \tag{52.3}$$

The mean square error (MSE) is the mean of the sum of the squared error between the restored image ($\hat{y}$) and original image (y).

$$MSE = \frac{1}{n}\sum_{i=1}^{n}\left(\hat{y}_i - y_i\right)^2 \tag{52.4}$$

Structural Similarity Index (SSIM) consists of the three indices: luminance, contrast, and structural terms

$$SSIM(x, y) = [l(x, y)]^{\alpha}.[c(x, y)]^{\beta}.[s(x, y)]^{\gamma} \tag{52.5}$$

where $l(x, y) = \frac{2\mu_x\mu_x + C_1}{\mu_x^2\mu_y^2 + C_1}$, $c(x, y) = \frac{2\sigma_x\sigma_y + c_2}{\sigma_x^2 + \sigma_y^2 + c_2}$ and $s(x, y) = \frac{\sigma_{xy} + c_3}{\sigma_x\sigma_y + c_3}$.

Here, $\mu_x, \mu_y, \sigma_x, \sigma_y$ and σ_{xy} are the local means, standard deviations, and cross-covariance for images *x and y*. If α = β = γ = 1 and $C_3 = C_2/2$ the SSIM simplifies to:

$$SSIM(x, y) = \frac{\left(2\mu_x\mu_y + C_1\right)\left(2\sigma_{xy} + C_2\right)}{\left(\mu_x^2 + \mu_y^2 + C_1\right)\left(\sigma_x^2 + \sigma_y^2 + C_2\right)} \tag{52.6}$$

Table 52.3 Quantitative analysis of the results

Metrics	Values
Structural similarity index (SSIM)	0.64
Mean squared error (MSE)	77.11
Peak signal-to-noise ratio (PSNR)	29.54

Table 52.4 Comparison with other methods on the same dataset

References	Average SSIM
Paired image translation-based artwork restoration method by P. Kumar and V. Gupta [26]	0.53
Unpaired image translation-based artwork restoration method (proposed work)	0.64

Table 52.3 presents a quantitative evaluation of the results obtained during the experiment. The results of the proposed artwork restoration method perform well in restoring damaged artwork images.

Table 52.4 presents the comparative analysis of the proposed unpaired image translation-based artwork restoration method using cycle-consistent generative adversarial networks with the other paired image translation-based artwork restoration methods proposed in the literature on the same ‘Ártimage’ dataset in terms of average SSIM value.

The above comparison shows that the proposed method outperforms the other paired image translation-based artwork restoration methods.

52.5.3 Visual Analysis

The visual analysis of sample outputs given in Fig. 52.2 shows that the proposed artwork restoration method restores the damaged artwork images satisfactorily while preserving the colors and artistic style of the artwork.

52.6 Conclusions

In this paper, we have proposed an unpaired image-to-image translation-based artwork restoration method using generative adversarial networks. The proposed method does not require the presence of original versions of all damaged artworks. The generative adversarial network has been trained using a linear combination of cycle consistency loss, adversarial loss, and identity loss. Results quantitatively and qualitatively demonstrate that the proposed approach effectively restores the artwork.

Fig. 52.2 Visual analysis

The proposed method has preserved the artistic style and color during restoration. The experimental results visually and quantitatively through image quality evaluation metrics of PSNR, SSIM, and MSE validate that the proposed approach outperforms the other artwork restoration methods.

References

1. Liu, G., Reda, F.A., Shih, K.J., Wang, T., Tao, A., Catanzaro, B.: Image Inpainting for Irregular Holes Using Partial Convolutions, vol. 11206. Springer International Publishing (2018)
2. Jay, F., Renou, J.-P., Voinnet, O., Navarro, L.: Unpaired image-to-image translation using cycle-consistent adversarial networks Jun-Yan. In: Proceedings of the IEEE International Conference

on Computer Vision, pp. 183–202 (2017). [Online]. Available: https://doi.org/10.1007/978-1-60327-005-2_13
3. Park, T., Liu, M.-Y., Wang, T.-C., Zhu, J.-Y.: GauGAN: semantic image synthesis with spatially adaptive normalization. In: ACM SIGGRAPH 2019, July 2019. https://doi.org/10.1145/3306305.3332370
4. Knut Nicolaus, E., Westphal, C.: The Restoration of Paintings, pp. 465–469 (1999). https://doi.org/10.1109/ICIEV.2018.8641016
5. Efros, A.A., Freeman, W.T.: Image quilting for texture synthesis and transfer. In: Proceedings of the 28th Annual Conference on Computer Graphics and Interactive Techniques, no. August, pp. 341–346 (2005). https://doi.org/10.1145/383259.383296
6. Levin, A., Zomet, A., Weiss, Y.: Learning how to inpaint from global image statistics. In: Proceedings of the IEEE International Conference on Computer Vision, vol. 1, pp. 305–312 (2003). https://doi.org/10.1109/iccv.2003.1238360
7. Ballester, C., Caselles, V., Verdera, J.: Disocclusion by joint interpolation of vector fields and gray levels. Multiscale Model. Simul. **2**(1), 80–123 (2004). https://doi.org/10.1137/S1540345903422458
8. Telea, A.: An image inpainting technique based on the fast marching method. J. Graph. Tools **9**(1), 23–34 (2004). https://doi.org/10.1080/10867651.2004.10487596
9. Marcelo Bertalmio, C.B., Sapiro, G., Caselles, V.: Image inpainting. In: Proceedings of the 27th Annual Conference on Computer Graphics and Interactive Techniques, pp. 417–424 (2000). https://doi.org/10.1055/s-0031-1298199
10. Barnes, C., Shechtman, E., Finkelstein, A., Goldman, D.B.: PatchMatch: a randomized correspondence algorithm for structural image editing. ACM Trans. Graph. **28**(3), 1–12 (2009). https://doi.org/10.1145/1531326.1531330
11. Ballester, C., Caselles, V., Verdera, J.: Disocclusion by joint interpolation of vector fields and gray levels. IEEE Trans. Image Process. **10**(8), 1200–1210 (2001). https://doi.org/10.1137/s1540345903422458
12. Zhang, R., Isola, P., Efros, A.A.: Colorful image colorization. In: ECCV, vol. 9905, pp. 649–666 (2016). https://doi.org/10.1007/978-3-319-46448-0
13. Xu, L., Ren, J.S.J., Liu, C., Jia, J.: Deep convolutional neural network for image deconvolution. Adv. Neural. Inf. Process. Syst. **2**(January), 1790–1798 (2014)
14. Zamir, S.W., et al.: Multi-stage progressive image restoration. In: 2021 IEEE/CVF Conference on Computer Vision and Pattern Recognition (2021). [Online]. Available: http://arxiv.org/abs/2102.02808
15. Xie, J., Xu, L., Chen, E.: Image denoising and inpainting with deep neural networks. In: Advances in Neural Information Processing Systems, vol. 1, no. January, pp. 341–349 (2012)
16. Liu, G., Reda, F.A., Shih, K.J., Wang, T.C., Tao, A., Catanzaro, B.: Image Inpainting for Irregular Holes Using Partial Convolutions, vol. 11215 LNCS. Springer International Publishing (2018)
17. Gatys, L., Ecker, A., Bethge, M.: A neural algorithm of artistic style. J. Vis. **16**(12), 326 (2016). https://doi.org/10.1167/16.12.326
18. Johnson, J., Alahi, A., Fei-Fei, L.: Perceptual losses for real-time style transfer and super-resolution. In: Lecture Notes in Computer Science (including subseries Lecture Notes in Artificial Intelligence and Lecture Notes in Bioinformatics), vol. 9906 LNCS, pp. 694–711 (2016). https://doi.org/10.1007/978-3-319-46475-6_43
19. Zeng, Y., van der Lubbe, J.C.A., Loog, M.: Multi-scale convolutional neural network for pixel-wise reconstruction of Van Gogh's drawings. Mach. Vis. Appl. **30**(7–8), 1229–1241 (2019). https://doi.org/10.1007/s00138-019-01047-3
20. Gupta, V., Sambyal, N., Sharma, A., Kumar, P.: Restoration of artwork using deep neural networks. Evol. Syst. **12**(2), 439–446 (2021). https://doi.org/10.1007/s12530-019-09303-7
21. He, K., Gkioxari, G., Dollar, P., Girshick, R.: Mask R-CNN. In: Proceedings of the IEEE International Conference on Computer Vision, vol. 2017-October, pp. 2980–2988 (2017). https://doi.org/10.1109/ICCV.2017.322

22. Adhikary, A., Bhandari, N., Markou, E., Sachan, S.: ArtGAN: artwork restoration using generative adversarial networks. In: 2021 13th International Conference on Advanced Computational Intelligence, ICACI 2021, pp. 199–206 (2021). https://doi.org/10.1109/ICACI52617.2021.9435888
23. Zou, Z., Zhao, P., Zhao, X.: Virtual restoration of the colored paintings on weathered beams in the Forbidden City using multiple deep learning algorithms. Adv. Eng. Inform. **50**(March), 101421 (2021). https://doi.org/10.1016/j.aei.2021.101421
24. Cao, J., Zhang, Z., Zhao, A., Cui, H., Zhang, Q.: Ancient mural restoration based on a modified generative adversarial network. Herit. Sci. **8**(1), 1–14 (2020). https://doi.org/10.1186/s40494-020-0355-x
25. Li, J., Wang, H., Deng, Z., Pan, M., Chen, H.: Restoration of non-structural damaged murals in Shenzhen Bao'an based on a generator–discriminator network. Herit. Sci. **9**(1), 1–14 (2021). https://doi.org/10.1186/s40494-020-00478-w
26. Kumar, P., Gupta, V.: Restoration of damaged artworks based on a generative adversarial network. Multimed. Tools Appl. 0123456789 (2023). https://doi.org/10.1007/s11042-023-15222-2
27. Navab, N., Hornegger, J., Wells, W.M., Frangi, A.F.: U-Net: convolutional networks for biomedical image segmentation. In: Lecture Notes in Computer Science, vol. 9351, pp. 234–241 (2015). https://doi.org/10.1007/978-3-319-24574-4
28. Mirza, M., Osindero, S.: Conditional Generative Adversarial Nets, pp. 1–7 (2014). [Online]. Available: http://arxiv.org/abs/1411.1784
29. Isola, P., Efros, A.A., Ai, B., Berkeley, U.C.: Image-to-image translation with conditional adversarial networks

Chapter 53
Wear Behaviour and Hardness of CNT Reinforced Alumina Composites

Yemmani Suresh Babu, Syed Altaf Hussain, and B. Durga Prasad

Abstract Alumina matrix composite enhanced with carbon nano-tubes was manufactured using the sol-gel method. Investigated were the effects of CNT varying concentrations from 1, 3, 5, 7, and 9 wt% on alumina powders. Results demonstrate that reinforcement with 1 wt% CNTs was accountable for the increase in wear resistance and hardness. Due to improved load distribution of uniformly distributed carbon nano-tubes, the hardness of an alumina matrix composite supplemented with carbon nano-tubes was increased. Fabricated composites with improved wear properties result from homogeneous CNT distribution inside the Al_2O_3 matrix and a strong interfacial interaction between developed composite.

53.1 Introduction

With the exception of being a solid state procedure where spray particles are deposited by impacting at supersonic speed while being heated significantly Cold spray (CS) is the use of a spray substance below its melting point, belongs to a thermal spray process [1]. A variety of materials have been deposited using cold spray components used in industrial settings that have protective wear coatings the automotive, nuclear, and aerospace industries. The majority of applications for this technology are for coatings thicker than 50 μm [2].

Owing to its extreme toughness and strong thermal insulation qualities, alumina (Al_2O_3) has been utilized in a variety of applications including wear-resistant components, chemical and electrical insulators, and high-speed cutting tools and various coatings. Alumina is not seen to be a good contender for sophisticated structural and

Y. S. Babu (✉) · B. D. Prasad
Department of Mechanical Engineering, Jawaharlal Nehru Technological University Anantapur, Ananthapuramu, Andhra Pradesh, India
e-mail: yemmanisuresh@gmail.com

S. A. Hussain
Department of Mechanical Engineering, Rajeev Gandhi Memorial College of Engineering & Technology, Nandyal, Andhra Pradesh, India

P. H. V. S. Talpa Sai et al. (eds.), *Intelligent Manufacturing and Energy Sustainability*, Smart Innovation, Systems and Technologies 372,
https://doi.org/10.1007/978-981-99-6774-2_53

aeronautical applications due to its lower fracture toughness. To increase the fracture toughness of monolithic Al_2O_3, a variety of carbon fibres, ceramics, and metals have all been used to strengthen materials. A significant improvement has been noted [3].

Since its invention in 1991, carbon nanotubes (CNTs), one of the reinforcing materials, have sparked significant attention in science and technology [4]. The variety of researchers have concentrated particularly on the mechanical properties of CNTs since they have an elastic modulus that is almost 5 times higher than high strength steels (1 TPa) and a tensile strength that is about 100 times greater [5]. The wear resistance of MWCNT steel ball bearings coated as nano-composite by chemical technique was higher than that of conventional ball bearings due to the coating's improved interlocking capabilities and solid lubrication function [6].

Most materials, including ceramics, commonly use CNTs as reinforcement [7]. As a result, it is anticipated that CNTs will improve Al_2O_3's mechanical and physical properties and make it suitable for a variety of cutting-edge applications. The mechanical and physical properties of CNT-reinforced alumina composites, which have been solidified using various sintering techniques, have been the subject of study from a number of researchers [8]. CNT aggregation, insufficient densification, and brittle CNT-ceramic interfacial connections are the main issues with CNTs-ceramic nano-composites [9]. However, it has been found that minor additions of CNTs (2 wt%) The fracture toughness and other mechanical characteristics were greatly improved. Higher CNT additions, however, produce disappointing result [10].

53.2 Methodology

The impact of different CNT concentrations of 1, 3, 5, 7, and 9 wt% on the wear properties and hardness of Al_2O_3-CNT composites are presented in this research work. The structural characteristics of composites and the interfacial connections formed under the conditions of the metal sol-gel process will be discussed.

53.2.1 Sol–Gel Technique for Producing Carbon Nanotube-Reinforced Alumina Composite Powders

Fabricating carbon nano-tube reinforced alumina composite. As an alumina precursor, $Al\,(OBu^s)_3$ or aluminium tri-sec-butoxide was used. MCNT's with a diameter of 15–30 nm, a length of 10–50 m, and a density of 1.6 g/cm^3 were manufactured by CVD employing an alumina-supported catalyst. The Yoldas technique [7, 8], which involves the Aluminium hydroxide (AlOOH) is hydrolyzed and peptized, was used to make alumina sol. During the process, CNT in suspension were dispersed

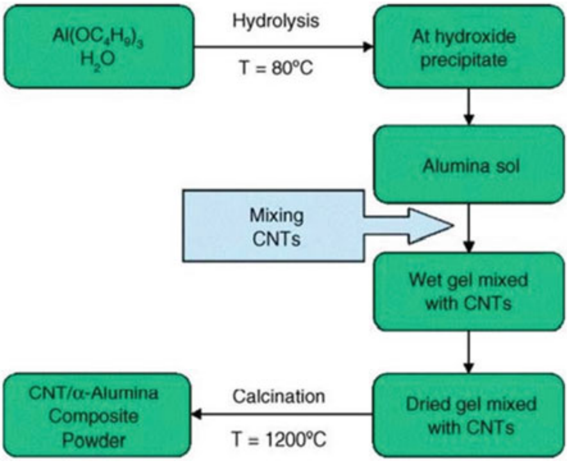

Fig. 53.1 Schematic diagram for the sol–gel manufacturing method for powdered alumina composites enhanced with CNT's

in ethanol, presented with alumina sol. CNT volume fractions were kept constant at 1, 3, 5, 7 and 9%. The gel of CNT and alumina was dried at 3500 for 6 h. In order to create the CNT/Al_2O_3 composite powders, gel powder was calcined at 1250 °C for 1 h under a vacuum of 10 Pa. as shown in Fig. 53.1.

53.2.2 *Characterization of Al_2O_3/CNT's*

Spark plasma sintering was used to consolidate the calcinated carbon nanotube/alumina powders, which allows a powder compact that will form spark plasma when subjected to intense pulsed electric current and sintered by Joule heat. Because the surface oxides of powders are easily removed by the generated spark plasma. The powder compact may be sintered at a lower temperature than usual during the spark plasma sintering process. Calculated carbon nanotube/alumina powders were put into a graphite mould, then sintering at 1650 °C for 5 min under a pressure of 25 MPa was performed. To eliminate carbon dispersed from the graphite mould, spark plasma sintered CNT/Al_2O_3 was annealed at 1000 °C for 6 h (Fig. 53.1). Vicker's indentation test was used to determine the hardness of a CNT/Al_2O_3 composite under a load of 9.8 N, and the fracture toughness was determined by measuring the crack length generate by Vicker's indentation (Fig. 53.3).

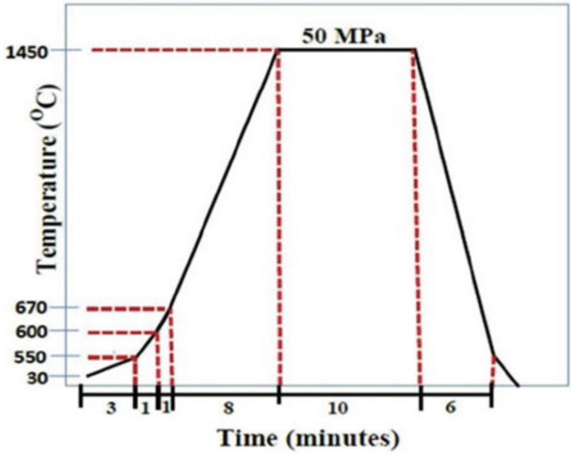

Fig. 53.2 Spark plasma sintering profile used for the developed of Al_2O_3/CNT composites

53.3 Results and Discussion

53.3.1 Hardness and Wear Resistance

Vickers micro hardness was used to assess the specimens' surface hardness. Testing the wear resistance of developed samples was done with a pin-on-disc setup. The ASTM standards were used to evaluate the wear resistance of a flat composite sample. The samples were examined under an optical microscope after testing. To determine how much of the specimens had been abraded. The hardness of a CNT/Al_2O_3 composite rises as the CNT volume percentage rises as shown in Fig. 53.3. This contradicts recent findings that found that the hardness of CNT/Al_2O_3 composites diminishes as the volume % of CNT increases [10]. It is primarily due to differences in CNT dispersion within the Al_2O_3 matrix and CNT/Al_2O_3 matrix interfacial strength. Because CNT's were agglomerated in prior studies. There could not possibly be a large load transfer from the matrix to the CNT [10–12].

53.3.2 Effect of Process Parameters on Wear Behaviour

In this investigation, the wear behaviour of fabricated composites of Al_2O_3/CNT is studied in order to determine the effect of different process parameters, such as the wt% of CNT, rotational speed, normal load, and time. Figures 53.4, 53.5, 53.6, 53.7, 53.8 and 53.9 were developed using a response surface model to analyse the effects of process factors on Al_2O_3/CNT's wear response. In these plots, only one parameter is kept constant at the middle level while the other parameters vary naturally.

Fig. 53.3 Variation of hardness by varying wt% of CNT in Al_2O_3 matrix material

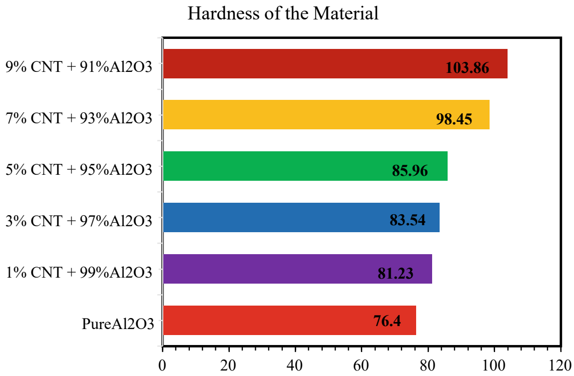

53.3.2.1 Effect of Normal Load on Wear Behaviour

The dominant factor in determining the wear behaviour of Al_2O_3/CNT is the normal load. In general, the specimen wear increases as the intensity of the normal load increases. The work piece's hardness affects wear as well. For varying weight percentages of CNT in alumina under dry conditions, the influence of normal load on wear is evaluated. By maintaining time and rotational speed at a middle level constant, the graph is drawn between normal load and wear. The response surface model is used to plot the graphs. Figure 53.4 illustrates how normal load affects dry sliding wear behaviour and the wt% of CNT in alumina. The specimen's contact area with the counter disc would grow due to normal load are rises, causing heat to be developed between the contact surfaces and the formation of micro grooves in the direction of the sliding direction. More wear occurs as a result of the fine plastic deformation that is shown at grooves and craters that are visible without cracks.

Figure 53.4 shows that for all wt% of reinforcement, wear increases as the normal load increases. For 9% of CNT at low loads of 0.65 N, low wear is shows for 1% of CNT at higher applied loads of 3.25 N, high wear is observed. The presence of CNT

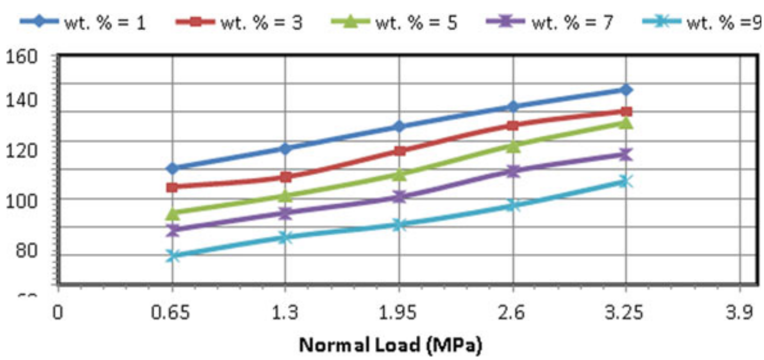

Fig. 53.4 Variation of wear under normal load for various wt% of CNT

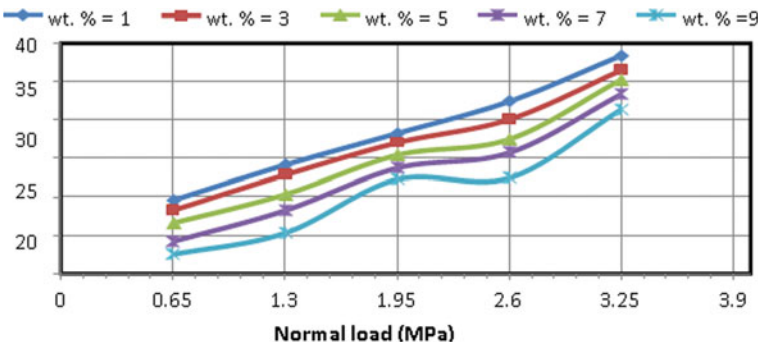

Fig. 53.5 Variation of wear rate under normal load for various wt% of CNT

particles dispersed on the pin's surface and the construction of a secure layer between the pin and steel disc allow the wear to be reduced. By raising the weight percentage of CNT, specially created composites exhibit reduced wear. Similar results also found a similar outcome after adding CNT-reinforced particles to an alumina matrix material [13, 14].

Figure 53.5 it is shows the a change in the wear rate compared to the normal load on Al_2O_3/CNT considered in this investigation. From the plot it is inferred that wear rate is gradually increasing with the increase of the normal load for all the AMCs considered in this investigation. The wear rate reaches the maximum value at an applied load of 1.95 N then after decreasing slightly. At 9 wt% of CNT reinforced alumina exhibits lower wear rate and 1 wt% of CNT alumina composites exhibits higher wear rate at low load. The results are closer to [13, 14].

53.3.2.2 Effect of Time on Wear Characteristics

All of the generated composites' wear and wear rate variations with respect to time are shown in Graphs 6 and 7, which can be taken into account for this investigation. The responses surface model is used to create these displays.

Figure 53.6 shows that wear grows linearly as time increases. This is due to the lack of contact that is developed when a high time required is necessary, which results in reduced wear of fabricated composites. 9 wt% of CNT shows low wear over a maximum of 900 s.

Graph 7 displays how the wear rate of Al_2O_3/CNT varies the time. From the graph, it can be observed that the trend for all wt% of CNT reinforced MMCs increases with a constant slope with regard to an increase in time.

This is because as the maximum time increases, the temperature at the interface between the specimens and the disc rises, causing the base metal to soften and the reinforcing phase to debond. These results in craters and grooves on the sample's surface. The low wear rate is observed at 9 wt% of CNT at low time. In the current

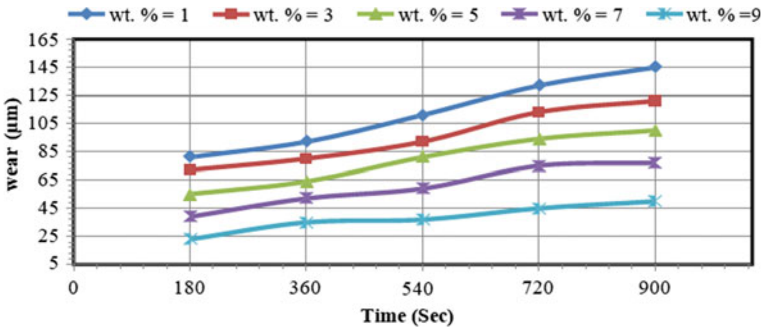

Fig. 53.6 Variation of wear with time for different wt% of CNT

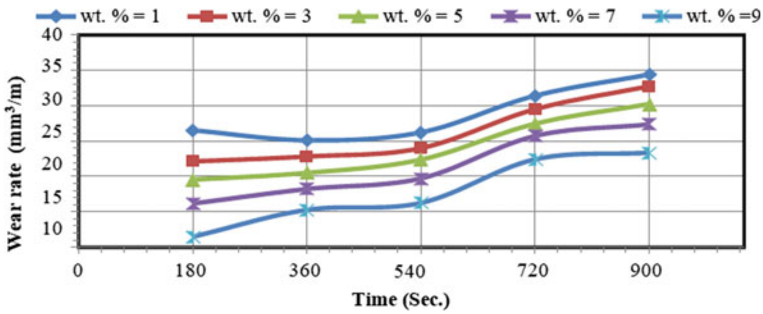

Fig. 53.7 Variation of wear rate with time for different wt% of CNT

experiment, the maximum time condition for 1 wt% of CNT shows a high wear rate (Fig. 53.7).

53.3.2.3 Effect of Rotational Speed on Wear Characteristics

The wear behaviour of Al_2O_3/CNT is mainly affected by the rotational speed. The effects of this parameter on wear characteristics can be positive or negative. The relationship between rotational speed and wear is shown in graph 8. This graph was developed using the response surface model while the middle level parameters (other than rotational speed) were varied.

Figure 53.8 shows that for all wt% of CNT taken into account in this experiment, wear continuously decreases up to 600 rpm and thereafter increases. This may be the result of local plastic deformation at the location of the CNT particles under high-speed circumstances, which causes surface delamination and sub-cracking. At a rotational speed of 600 rpm, 9 weight percent of CNT shows the least amount of wear. At 200 rpm of the disc speed, the wear rate for 1 wt% of CNT is the highest. For all Al_2O_3/CNT taken into consideration in this study, Graph 9 depicts the differences

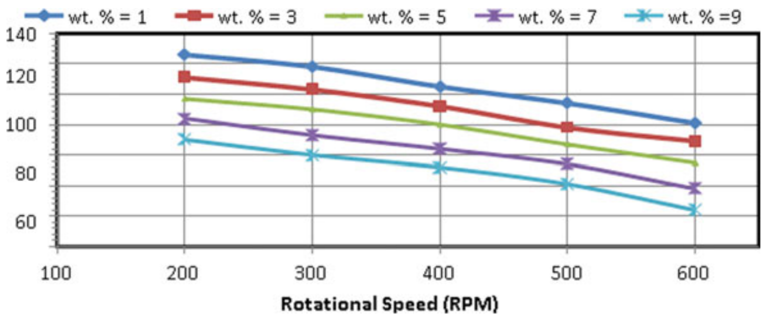

Fig. 53.8 Variation of wear with rotational speed for different wt% of CNT

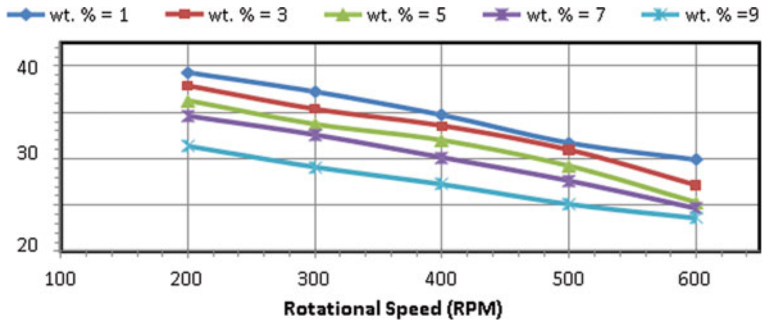

Fig. 53.9 Variation of wear rate with rotational speed for different wt% of CNT

in wear rate with respect to rotational speed. From the plot, it can be seen that the wear rate steadily decreases as the rotational speed increases from 200 to 600 rpm. Due to debris present at the surface's point of contact, more material is lost from the pin's surface as it rotates quickly. Cracks are also started and spread across the pin's surface. At a minimum rotational speed of 200 rpm, 9 wt% of CNT reinforced alumina shows the lowest wear rate, and 1 wt% of CNT shows the highest wear rate (Fig. 53.9).

53.4 Conclusion

Sol–gel method with spark plasma sintering was successful in fabricating the CNT/Al_2O_3 composite with increased hardness. In CNT/Al_2O_3, the carbon nano-tubes were uniformly spread inside an alumina matrix. As the wt% of carbon nano-tubes increased, so increased the hardness of CNT/Al_2O_3. The CNT/Al_2O_3 load transfer serves as the foundation for the strengthening process. The wear characteristics of Al_2O_3/CNT composites were examined in this research. For low and moderate normal loads, Al_2O_3/CNT (reinforced with 1, 3, 5, 7 and 9 wt% CNTs) showed enhanced wear resistance; however, for rotational speed, the 9 wt% CNT nano-composite show low wear resistance. It was examined how the CNTs' direct and indirect contributions to the Al_2O_3/CNT composites' enhanced tribological characteristics. These findings suggested that hard and extremely wear-resistant nano-composites would make great candidates for a variety of engineering applications.

References

1. Cincaa, N., Lima, C.R.C., Guilemany, J.M.: J. Mater. Res. Technol. **2**(1), 75–86 (2013)
2. Viswanathan, V., Laha, T., Balani, K., Agarwal, A., Seal, S.: Mater. Sci. Eng. R **54**, 121–285 (2006)
3. Jinpeng, F., Zhao, D., Song, J.: J. Am. Ceram. Soc. **89**(2), 750–753 (2006)
4. Iijima, S.: Helical microtubules of graphite carbon. Nature **354**, 56–58 (1991)
5. Saether, E., Frankland, S.J.V., Pipes, R.B.: Compos. Sci. Technol. **63**, 1349–1358 (2003)
6. Winarto, D., Priadi, N., Sofyan, M., Anggoro, A.: Int. J. Technol. **3**, 471–479 (2015)
7. Osayande, L., Okenwa, I.: Int. J. Appl. Tech. **5**(3), 313–323 (2008)
8. Yamamoto, G., Omori, M., Hashida, T., Kimura, H.: Nanotechnology **19**, 315708 (2008)
9. Zheng, G., Sano, H., Cheng, H.M.: Carbon **37**, 2057–2062 (1999)
10. Fan, J., Zhao, D., Song, J.: J. Am. Ceram. Soc. **89**(2), 750–753 (2006)
11. Peigney, A.: Composite materials: tougher ceramics with nanotubes **2**(1), 15–16 (2003). https://doi.org/10.1038/nmat794
12. Flahaut, E., Peigney, A., Laurent, C., Marlière, C., Chastel, F., Rousset, A.: Acta Mater. **48**(14), 3803–3812 (2000). https://doi.org/10.1016/s1359-6454(00)00147-6
13. Venkataraman, B., Sundararajan, G.: Wear **245**(1–2), 22–38 (2000)
14. Lu, D.H., Gu, M.Y., Shi, Z.L.: Tribol. Lett. **6**(1), 57–61 (1999)